Metallo-Supramolecular and Bioinspired Coordination Compounds for H_2O Oxidation

A thesis submitted to the University of Dublin for the degree of Doctor of Philosophy

Rory Elliott

School of Chemistry

University of Dublin

2020

An artistic impression of solar fuel synthesis.
Artwork by Michael Hagelberg, used by permission.

Declaration

I declare that this thesis has not been submitted as an exercise for a degree at this or any other university and it is entirely my own work.

I agree to deposit this thesis in the University's open access institutional repository or allow the library to do so on my behalf, subject to Irish Copyright Legislation and Trinity College Library conditions of use and acknowledgement.

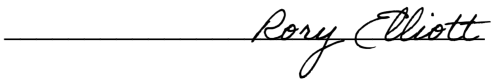

Rory Elliott

Acknowledgements

Firstly, I would like to express my sincere gratitude to my advisor Prof. Wolfgang Schmitt for the steady guidance generously given throughout my time here at Trinity College, and for offering me the opportunity to continue exploring this fascinating subject at the Ph.D level. Also, for granting me the intellectual freedom to explore my own ideas (and learn from my inevitable mistakes) I thank you.

I also have my whole family to thank, without whom I undoubtedly wouldn't be in this position. In particular, my Mum and Dad for their belief in me at every stage of my education, and for cultivating an environment in which learning was valued. Also, my big brother Dill for looking out for me, my older sister Leah for her inspiring determination, and my brothers Tim and Nathan for their encouragement and support. And my ally Mary Ellen – thank you for your exceptional kindness, patience and love.

Many of the results discussed in this report are the culmination of collaborative efforts, and thus would not have been possible without the contributions of several individuals in the Schmitt Lab and the School of Chemistry. Therefore, I acknowledge Dr. Amal Cherian Kathalikkattil for many late evenings spent building and tinkering with the light-driven water splitting system, Dr. Joaquín Soriano-López for electrochemical measurements and computational analyses, Dr. Colm Healy, Swetanshu Tandon, Dr. Ako Manase Ayuk and Dr. Lei Zhang for the preparation of Mn- and Co-based complexes discussed in Chapters 3 and 4, Dr. Brendan Twamley, Dr. Nianyong Zhu, Friedrich Steuber and Paul Wix for carrying out single crystal X-ray studies, Prof. Mathias Senge and Dr. Aoife Ryan for the provision of porphyrin ligands in the early stages of this project, Dr. John O'Brien and Dr. Manuel Ruether for NMR measurements and training in various instrumental techniques, Dr. Martin Feeney and Dr. Gary Hessman for mass spectroscopy measurements, Ann Connolly and Rónán Crowley at UCD for microanalysis and Éadaoin Whelan and Debobroto Sensharma for their help proofreading this thesis.

I also wish to thank all my talented and helpful colleagues in the Schmitt Group. Thanks to Colm, Kevin, Debo, Mariah, Joe, Éadaoin, Muhammed, Camelia, Ximo, Friedrich, Luana, Paul, Zubair, Jom, Amal, Ako, Guanghua, Aneela, Sebastien, Lauren, Greg, Xiao-Ping and Adam – it has been a pleasure to work alongside all of you.

I have been very fortunate to have supervised two excellent students who worked on this project. I would therefore like to acknowledge Aviral for his encouraging attitude and insight, and Jérémy for his hard work and diligence.

Finally, I would like to thank everybody else in the School of Chemistry for their help with technical, teaching and administrative aspects, including Teresa McDonnell, Margaret Brehon, Dr. Peter Brien, Frederick Cowzer, Maura Boland, Dr. Sinead Boyce, Anne Marie Farrell and Ben Power.

Summary

Ever-increasing energy demands and associated climate change issues impose imperative scientific challenges to society. Switching to an economy based on the carbon-free, high-density energy carrier H_2 represents a promising solution to the problems posed by fossil fuel consumption. However, current methods of H_2 production are expensive and unsustainable. Solar H_2O splitting presents an attractive approach for renewably generating H_2 in abundance. Despite this, current technological breakthroughs in this area are hampered by a lack of efficient, cost-effective catalysts for the endergonic, proton-coupled 4-electron O_2 evolution half-reaction (OER). Therefore, the development of H_2O oxidation catalysts (WOCs) based on earth-abundant materials to provide low-energy pathways for the OER is of utmost importance to satisfy global energy needs in an environmentally friendly manner.

Due to the thermodynamic and kinetic barriers to the OER, current catalysts for this reaction suffer from poor activity or instability. Moreover, many state-of-the-art WOCs rely on costly rare-earth elements. Metal-organic frameworks (MOFs) are metallo-supramolecular materials with well-defined cavities and unprecedented surface areas which can incorporate redox-active building units. Thus, MOFs represent a hopeful class of compounds to catalyse H_2O oxidation. This thesis aims to prepare and use metallo-supramolecular assemblies such as MOFs, metal-oxo clusters and complexes constructed using earth-abundant elements as catalysts for the challenging OER. The results presented in this thesis include the synthesis and structural characterisations of several metalloenzyme-inspired materials. Moreover, the exploration of these hybrid organic-inorganic systems as WOCs towards artificial photosynthetic applications is described. Ultimately, post-catalytic experiments are discussed which attribute the observed OER activities to various molecular species.

Chapter 1 contains a discussion of the historical context of this work and outlines the concepts drawn upon by this thesis. A literature review follows, giving an impression of the current state-of-the-art. The chapter concludes with a delineation of this project's aims and objectives.

In Chapter 2, the synthesis of a dicarboxylic acid-functionalised porphyrin 15-di(4-carboxyphenyl)-10,20-diphenylporphyrin H_4**L1** and several metalloporphyrin complexes H_2**L1**-Cu^{II}, H_2**L1**-Ni^{II} and H_2**L1**-Pt^{II} are described. The ligand H_2**L1**-Cu^{II} is then used to synthesise two novel Co^{II}-based MOFs, $[Co^{II}_4$(**L1**-$Cu^{II})_4(H_2O)_7]\cdot$2DEA·8MeOH (**1**) and

$[Co^{II}(\mathbf{L1}\text{-}Cu^{II})(DEA)]\cdot H_2O\cdot 3MeOH$ (**2**). Following this, the developed methodology to assess light-driven H_2O splitting catalysis is described. An investigation of the photocatalytic H_2O splitting properties of **1** is then discussed, as this compound was rationalised as more promising than **2** for this purpose. This study reveals that **1** performs as an effective catalyst for light-driven H_2O oxidation, yielding excellent turnover characteristics. Ultimately, post-catalytic characterisation experiments support the assignment of **1** as a genuine WOC.

Chapter 3 outlines the evaluation of a variety of Mn-oxo coordination compounds for photocatalytic H_2O oxidation activity. The study reveals nine compounds (**3** – **11**) that display apparent catalytic activity towards H_2O oxidation. The nonadecanuclear Mn-oxo cluster $[Mn^{III}_{12}Mn^{II}_7(\mu_4\text{-}O)_8(\mu_3\text{-}OCH_3)_2(\mu_3\text{-}Br)_6(H\mathbf{L2})_{12}(MeOH)_5(MeCN)]Br_2\cdot 9MeCN\cdot MeOH$ (**11**) reveals the highest catalytic activity of **3** – **11**. Therefore, further investigations into the catalytic properties of this compound were conducted, which illustrate that **11** is a genuine molecular H_2O oxidation catalyst with an activity that is superior to that of any heterogeneous Mn-oxo cluster previously reported in the literature.

In Chapter 4, the synthesis and characterisation of a trinuclear disc-shaped complex $[Co^{II}_3(\mathbf{L3})_2(H_2O)_6]^{6+}$ are discussed. This supramolecule assembles in the solid state through an extensive network of halogen and hydrogen bonding interactions to form the water insoluble halide-MOF $[Co^{II}_3(\mathbf{L3})_2(H_2O)_6]Cl_6\cdot DMF\cdot 6H_2O$ (**12**). The catalytic H_2O oxidation properties of **12** under photo- and electro-chemical conditions are then described, in addition to a series of post-catalytic characterisation experiments which indicate that **12** is indeed a true OER catalyst. Finally, a computational analysis is described which proposes a catalytic mechanism for O_2 formation that agrees well with empirical data.

Chapter 5 details the synthesis and characterisation of four novel supramolecular assemblies $[Mn^{II}(H\mathbf{L1}\text{-}Cu^{II})_2(DEA)_2]\cdot DEA$ (**13**), $[Mn^{II}(\mathbf{L1}\text{-}Cu^{II})(MeOH)_2]\cdot DEA\cdot MeOH$ (**14**), $[Mn^{II}(H\mathbf{L1}\text{-}Ni^{II})_2(DMF)_2]\cdot 3DMF$ (**15**) and $[Mn^{II}(\mathbf{L1}\text{-}Ni^{II})(DMF)_2]\cdot 4DMF$ (**16**) which comprise Mn^{II}-based building units connected by ditopic porphyrin ligands. The light-driven H_2O splitting properties of these compounds is assessed, although only modest catalytic activity was revealed. In the next section of this chapter, two novel supramolecular structures $[Zn^{II}_4O(\mathbf{L1}\text{-}Zn^{II})_3(H_2O)_3]$ (**17**) and $(TEAH)_2[In^{III}(H\mathbf{L1}\text{-}Cu^{II})_2(Ac)_2]Cl\cdot H_2O$ (**18**) are discussed.

In Chapter 6, details of the experimental materials and methods are described.

Chapter 7 concludes on the results described in this thesis and outlines some possible avenues for future work.

Table of Contents

Abbreviations

1D	One-Dimensional
2D	Two-Dimensional
3D	Three-Dimensional
acac	Acetylacetonate
ADP	Adenosine diphosphate
ApyH	2-Aminopyridinium
ATP	Adenosine triphosphate
bpy	4,4'-Bipyridine
BVS	Bond Valence Sum
ca.	Approximately
CB	Conduction Band
CoO_x	Cobalt Oxide Species
Co–Pi	Cobalt Phosphate
CP	Carbon Paste
CSD	Cambridge Structural Database
CV	Cyclic Voltammetry
DCM	Dichloromethane
DEA	*N*,*N*-Diethylacetamide
deeb	Diethyl 2,2'-Bipyridine-4,4'-dicarboxylate
DFT	Density Functional Theory
DLS	Dynamic Light Scattering
DMF	*N*,*N*-Dimethylformamide
DPFP	5,15-Dipyridyl-10,20-bis(pentafluorophenyl)porphyrin
DSPEC	Dye-Sensitized Photoelectrochemical Cell
DUT	Dresden University of Technology
Eqn.	Equation
ESI	Electrospray Ionisation
et al.	and others
Fig.	Figure
FT-IR	Fourier Transform Infrared Spectroscopy
GHG	Greenhouse Gas
H_2bdt	1,4-Benzenedi(1*H*-1,2,3-triazole)
HEC	Hydrogen Evolution Catalyst

HER	Hydrogen Evolution Reaction
HOMO	Highest Occupied Molecular Orbital
I2M	Interaction of Two M – O Units
IRMOF	Isoreticular Metal-Organic Framework
ITO	Indium Tin Oxide
LHCI	Light-Harvesting Complex I
LHCII	Light-Harvesting Complex II
LSV	Linear Sweep Voltammetry
LUMO	Lowest Unoccupied Molecular Orbital
MALDI-TOF	Matrix-Assisted Laser Desorption/Ionization Time-of-Flight
Max.	Maximum
MeCN	Acetonitrile
MIL	Matérial Institut Lavoisier
MMPF	Metal-Metalloporphyrin Framework
MnO_x	Manganese Oxide Species
MOF	Metal-Organic Framework
MOP	Metal-Organic Polyhedra
MS	Mass Spectrometry
NAPDH	Nicotinamide Adenine Dinucleotide Phosphate
NHE	Normal Hydrogen Electrode
NMR	Nuclear Magnetic Resonance
NU	Northwestern University
OEC	Oxygen Evolving Complex
OER	Oxygen Evolution Reaction
OMS	Open Metal Site
P_{680}	Reaction Centre of Photosystem II
PCET	Proton-Coupled Electron Transfer
pcu	Primitive Cubic Topology
pts	Platinum Sulphide Topology
PEC	Photoelectrochemical Cell
PEM	Proton Exchange Membrane
Ph_2PH	Diphenylphosphine
Piv	Pivalic Acid
PIZA	Porphyrinic Illinois Zeolite Analogue
PLAL	Pulsed Laser Ablation in Liquids
PQH_2	Plastoquinol

PS I	Photosystem I
PS II	Photosystem II
PS	Photosensitiser
PSM	Post Synthetic Modification
PXRD	Powder X-Ray Diffraction
Py	Pyridine
Q_A	Bound Plastoquinone Electron Carrier of PS II
Q_B	Mobile Plastoquinone Electron Carrier of PS II
rpm	Revolutions Per Minute
RPM	Robust Porphyrinic Material
SBU	Secondary Building Unit
SC 1	Anodic Semiconductor Electrode of PEC
SC 2	Cathodic Semiconductor Electrode of PEC
SEA	Sacrificial Electron Acceptor
SED	Sacrificial Electron Donor
SMM	Single-Molecule Magnet
TBA	Tetrabutylammonium
TCP	*Meso*-tetrakis(4-cyanophenyl)-21*H*,23*H*-porphyrin
TCPP	*Meso*-tetrakis(4-carboxyphenyl)porphyrin
TDP	4,4'-Trimethylenedipyridine
TEA	Triethylamine
TEAH	Triethylammonium
TEMPO	2,2,6,6-Tetramethylpiperidine-1-oxyl
TEOA	Triethanolamine
TFA	Trifluoroacetic Acid
TGA	Thermogravimetric Analysis
THF	Tetrahydrofuran
TLC	Thin Layer Chromatography
TMPP	*Meso*-tetrakis(4-methoxycarbonylphenyl)porphyrin
TOF	Turnover Frequency
TON	Turnover Number
VB	Valence Band
vs.	*Versus*
WNA	Water Nucleophilic attack
WOC	Water Oxidation catalyst
Y_z	A Redox-Active Tyrosine Residue on the D1 Subunit of PS II

Units & Symbols

$\Delta G°$	Standard free energy change
°C	Degrees Celsius
Å	Angstrom
a.m.u.	Atomic Mass Units
b	Empirical Bond Valence Parameter
B_0	Idealised Bond Distance
B_i	Individual Bond Distance
$E°$	Standard Cell Potential
eV	Electron Volt
j	Current Density
M	Molarity
pH	Negative Log of the Hydrogen Ion Concentration
s	Seconds
ε	Molar Absorptivity
η	Overpotential
λ	Wavelength

List of Formulae

$$\text{Bond Valence Sum (BVS)} = \sum \exp \frac{(B_0 - B_i)}{(b)}$$

$$\text{Turnover Number (TON)} = \frac{\Delta\,[O_2]}{[\text{catalyst}]}$$

$$\text{Turnover Frequency (TOF)} = \frac{\Delta\,[O_2]}{[\text{catalyst}]\ \times \text{time}}$$

$$O_2\text{Yield (\%)} = \frac{\Delta\,[O_2]\ \times 2}{[Na_2S_2O_8]} \times 100$$

List of Compounds

Organic Ligands

H_4**L1** – 5,15-Bis(4-carboxyphenyl)-10,20-diphenylporphyrin

H_3**L2** – 2,6-Bis(hydroxymethyl)-*p*-cresol

L3 – *N*,*N*',*N*''-Tris-(1-methyl)-1*H*-imidazol-4-ylmethylene)-1,3,5-triphenyl benzene

Inorganic Complexes and Frameworks

1 – $[(\mathbf{L1}\text{-}Cu^{II})_4Co^{II}_4(H_2O)_4]\cdot 2DEA\cdot 8MeOH$

2 – $[(\mathbf{L1}\text{-}Cu^{II})Co^{II}(DEA)]\cdot H_2O\cdot 3MeOH$

3 – $[Mn^{II}Mn^{III}_{12}(\mu_4\text{-}O)_8(\mu_4\text{-}Cl)_6(t\text{BuPO}_3)_8]$

4 – $[Mn^{II}_3Mn^{III}_{10}(\mu_4\text{-}O)_6(\mu_3\text{-}O)(\mu_3\text{-}OH)(\mu_4\text{-}Cl)_4(Cl)(t\text{BuPO}_3H)(t\text{BuPO}_3)_9]^{3-}$

5 – $[Mn^{II}_3Mn^{III}_{11}(\mu_4\text{-}O)_6(\mu_3\text{-}O)(\mu_3\text{-}OH)(\mu_2\text{-}OH)(\mu_4\text{-}Cl)_4(t\text{BuPO}_3H)(t\text{BuPO}_3)_{10}(Apy)]^{2-}$

6 – $[(Mn^{II}_{0.5}Mn^{III}_{0.5})Mn^{III}_{12}(\mu_4\text{-}O)_6(\mu\text{-}OH)_2(\mu\text{-}OMe)_4(MeOH)_2(t\text{BuPO}_3)_{10}(Pic)_4]^{0.5+}$

7 – $[(Mn^{II}_{0.5}Mn^{III}_{0.5})Mn^{III}_{12}Ca^{II}_2(\mu_4\text{-}O)_6(\mu_3\text{-}O)_2(\mu\text{-}OMe)_4(MeOH)_6(t\text{BuPO}_3)_{10}(Piv)_2(Ph_2PO_2)_2]$

8 – $[Mn^{III}_{11}Mo^{VI}_2O_2(\mu_4\text{-}O)_2(\mu_3\text{-}O)_4(\mu\text{-}O)_4(\mu\text{-}OH)_2(t\text{BuPO}_3)_{10}(Py)_4]^{-}$

9 – $[(Mn^{II}_{0.5}Mn^{III}_{0.5})Mn^{III}_{12}(\mu_4\text{-}O)_6(\mu\text{-}OH)_2(\mu\text{-}OMe)_4(MeOH)_2(t\text{BuPO}_3)_{10}(TDP)_4]^{0.5+}$

10 – $[Mn^{III}_{12}Mn^{II}_6Sr^{II}(\mu_4\text{-}O)_8(\mu_3\text{-}Cl)_8(H\mathbf{L2})_{12}(MeCN)_6]^{2+}$

11 – $[Mn^{III}_{12}Mn^{II}_7(\mu_4\text{-}O)_8(\mu_3\text{-}OCH_3)_2(\mu_3\text{-}Br)_6(H\mathbf{L2})_{12}(MeOH)_5(MeCN)]^{2+}$

12 – $[Co^{II}_3(\mathbf{L3})_2(H_2O)_6]Cl_6\cdot DMF\cdot 6H_2O$

13 – $[Mn^{II}(H\mathbf{L1}\text{-}Cu^{II})_2(DEA)_2]\cdot DEA$

14 – $[Mn^{II}(\mathbf{L1}\text{-}Cu^{II})(MeOH)_2]\cdot DEA\cdot MeOH$

15 – $[Mn^{II}(H\mathbf{L1}\text{-}Ni^{II})_2(DMF)_2]\cdot 6DMF$

16 – $[(Mn^{II}(\mathbf{L1}\text{-}Ni^{II})(DMF)_2]\cdot 4DMF$

17 – $[Zn_4O(H\mathbf{L1}\text{-}Zn^{II})_3(H_2O)_3]$

18 – $(TEAH)_2[In^{III}(H\mathbf{L1}\text{-}Cu^{II})_2(Ac)_2]Cl\cdot H_2O$

Chapter One

Introduction

1.1 Motivation and Global Context

The dawn of the industrial revolution in the mid-18th century profoundly and permanently changed humanity's relationship with Nature. Harnessing energy stored within fossil fuels for many millions of years impacted every aspect of civilisation; not least in terms of population, which surged from *ca*. 750 million to over 7.5 billion in just a handful of generations. This rapid growth was accompanied by an exponential rise in energy consumption, which is forecasted to exceed 27 TW by 2050.[1]

Today, more than 80% of the energy produced globally stems from the combustion of carbonaceous fuels with a low (coal), medium (oil) or high (natural gas) hydrogen content.[2] This exothermic process converts chemical energy of C – C and C – H bonds into heat while evolving the greenhouse gasses (GHGs) H_2O and CO_2. The rate of anthropogenic CO_2 emission greatly exceeds the rate of CO_2 partitioning into the biosphere and oceans. Because of this, current atmospheric concentrations of this GHG have reached their highest levels in between 650,000 to 20,000,000 years.[3–6]

It is widely acknowledged that the accumulation of CO_2 in our atmosphere can significantly disrupt the earth's climate system, eliciting far-reaching consequences such as sea level and temperature rises, ocean acidification, tropical cyclone intensification and increased drought frequency and severity with deleterious effects on biodiversity.[7–10] Coupled with energy security concerns and increasing air pollution mortality rates associated with burning fossil fuels, an enormous societal challenge is presented. It is therefore a scientific imperative to pursue concepts for harnessing energy sources that are both renewable and carbon-neutral.[11,12]

1.1.1 Modern Sustainable Energy Technologies

There is much contemporary research into the development of environmentally friendly and renewable energy options such as solar, wind, hydrothermal, tidal and geothermal power.[13] Solar energy represents a particularly promising energy source as it is clean and inexhaustible. The total power striking the earth exceeds 100,000 TW. This surpasses the current global demand of 15 TW by many orders of magnitude.[14] The sunlight that reaches earth every hour thus delivers almost as much energy as humanity uses in a year.[15]

At present, the most widely implemented devices for utilizing solar radiation are photovoltaic systems.[16] Photovoltaic cells capture solar radiation to generate an electric current by exploiting the photovoltaic effect.[17] While this technology has made impressive strides since its first conception, with steady improvements in efficiency through multiple generations (from <1% to >40% for state-of-the-art modern devices), they are not without their disadvantages.[18, 19] Because of the high price of their manufacture and the reliance of some devices on extracting rare-earth elements such as indium and tellurium (which have natural abundancies within the earth's crust of *ca*. 150 and 1 parts per billion, respectively),[20,21] solar energy remains more expensive than grid power in most countries.[22]

The manufacturing costs of photovoltaic devices are decreasing.[23] However, a greater challenge comes with the fact that photovoltaic cells can only produce electricity during daylight hours, whereas energy is consumed constantly. Moreover, the vast majority of the energy society's energy use comes in the form of liquid fuels (*ca*. 80%), which are used for transportation and other purposes, whereas only around 20% of energy is used as electricity. Therefore, an efficient method for storing, transporting and quickly releasing solar energy as needed is required.[24]

H_2 has been suggested as an attractive energy carrier of the future because it is carbon-free and has a very high gravimetric energy density (142 MJ kg^{-1} for H_2 compared to 46 MJ kg^{-1} for petrol). However, the current industrial methods relied upon to produce this gas are costly and non-renewable.[25,26] One promising solution for this is to rearrange the bonds of H_2O into H_2 and O_2 using solar energy. Using a small pool ($4 \times 3 \times 1$ m^2) of H_2O as feedstock, enough H_2 could be generated to satisfy the annual energy requirements of one person.[27] Harnessing and storing sunlight in solar fuels by splitting H_2O is the basis of photosynthesis, and offers an opportunity for sustainably satisfying civilisation's energy expenditure.

1.1.2 Solar Energy Storage

In 1912, the Italian photochemist Giacomo Luigi Ciamician delivered a public address in which he presciently predicted:

> "*On arid lands, there will spring up industrial colonies without smoke and without smokestacks; forests of glass tubes will extend over the plants and glass buildings will rise everywhere; inside of these will take place the photochemical processes that hitherto have been the guarded secret of the plants, but that will have been mastered by human industry which will know how to make them bear even more abundant fruit than Nature, for Nature is not in a hurry and mankind is. And if in a distant future the supply of coal becomes completely exhausted, civilization will not be checked by that, life and civilization will continue as long as the sun shines!*"[28]

Ciamician was perhaps one of the first scientists to recognise how capturing sunlight within chemical bonds could alter the trajectory of humanity. More than a century later, there has never been a greater urgency for renewably produced solar fuels. Whilst Ciamician sought to secure our energy supply beyond the exhaustion of earth's finite fossil fuel reserves, a more pressing problem has arisen from the combustion of these substances at such a scale that it has significantly perturbed the composition of earth's atmosphere.

Nature's approach of storing energy from the sun within energy-rich chemical fuels could be adapted to inspire the design of artificial photosynthetic devices.[11] Such systems offer an avenue to replace fossil fuels with less polluting, carbon-free energy carriers. Additionally, photosynthetic fuels could be produced from two essentially inexhaustible resources: sunlight and water.[29] However, current devices implementing this process are impeded by high production costs, poor stability or slow reaction rates, rendering them impractical solutions for solar fuel generation in their current state.[30]

To advance artificial photosynthetic technologies, it is necessary to understand the underlying mechanistic details of how Nature achieves H_2O splitting. In the century following Ciamician's address, this "*guarded secret of the plants*" has been painstakingly unravelled using modern spectroscopic and X-ray techniques, granting us insights he may only have speculated upon. In the following section, the highly sophisticated and specialised mechanisms and architectures which have evolved to accomplish photosynthesis are outlined.

1.2 Photosynthesis in Nature

The advent of oxygenic photosynthesis *ca*. 2.5 billion years ago marks one of the most significant transitions in evolutionary history.[31] The process was pioneered by cyanobacteria, which use sunlight to transform H_2O and CO_2 into energy-rich carbohydrates, releasing O_2 as a waste product according to Eqn. 1.1.[32,33] The success of these prokaryotic photoautotrophs (which were to evolve into chloroplasts of the photosynthetic eukaryotes higher plants, algae and euglena *via* endosymbiotic incorporation) resulted in an accumulation of atmospheric O_2 and the formation of a protective ozone layer.[34] This shift, known as the 'Great Oxidation Event' simultaneously triggered earth's largest known extinction event, whilst paving the way for the development of complex multicellular aerobic life.[35]

$$6CO_2 + 6H_2O \xrightarrow{h\nu} C_6H_{12}O_6 + 6O_2 \quad \text{(Eqn. 1.1)}$$

The carbohydrates formed during photosynthesis constitute the building blocks of all living organisms, and fossil fuels.[36] Cyanobacteria and eukaryotic photosynthetic organisms have mastered the exploitation of solar energy using an intricate electron-proton transport chain, mediated by an assembly of highly specialised thylakoid membrane-bound protein complexes and cofactors.[37] A schematic representation of the structures involved is depicted in Fig. 1.1.

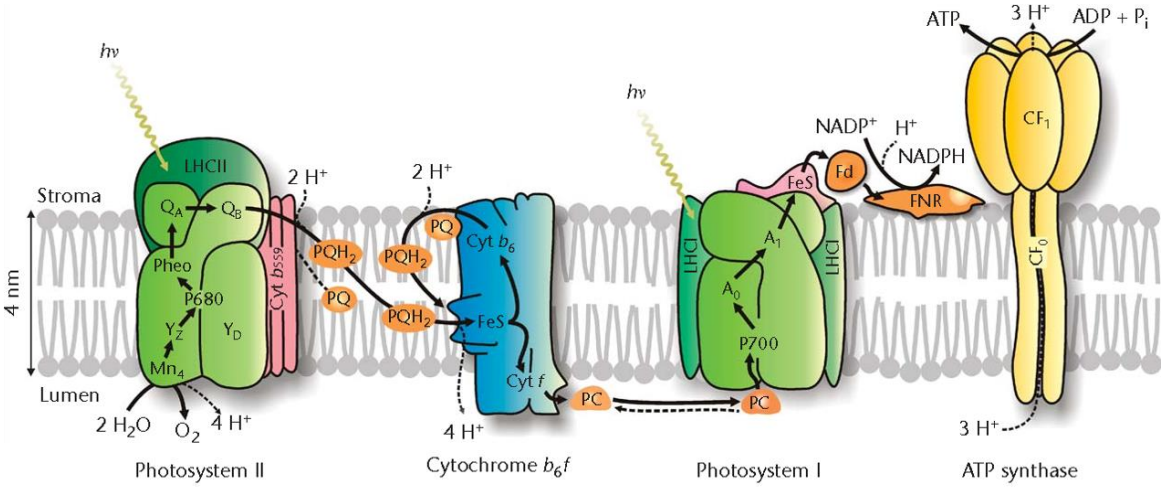

Figure 1.1: Schematic representation of the light-driven electron-proton transport processes occurring between membrane-bound proteins and cofactors in the thylakoid membrane of photosynthetic organisms. Adapted from Ref. 37.

In natural photosynthesis, the two reaction centres photosystem II (PS II) and photosystem I (PS I), which are linked by cytochrome b_6f and other mobile electron carriers, transfer electrons from H_2O to nicotinamide–adenine dinucleotide phosphate ($NADP^+$). This process is driven by solar photons that are absorbed by the porphyrin pigments chlorophyll *a* and chlorophyll *b* in light-harvesting complexes I and II (LHCI and LHCII), creating a photoinduced charge separation. Electron-hole pairs generated in LHCII are then funnelled through resonance energy transfer processes to a chlorophyll special pair (P_{680}), which acts as the primary electron donor of PS II.[38,39] Excitation of P_{680} precedes sequential electron transfers from P_{680}* to pheophytin (Pheo), followed by plastoquinone (Q_A and Q_B) electron acceptors, generating $P_{680}^{\bullet+}$, $Q_A^{\bullet-}$ and $Q_B^{\bullet-}$. The ground state P_{680} is then regenerated as electrons abstracted from H_2O by a $\{Mn_4\}$ cluster known as the oxygen evolving complex (OEC) are transferred to the excitonic dimer by a redox-active tyrosine residue on the D1 subunit of PS II (Y_z).[40]

Reduction of $Q_B^{\bullet-}$ affords the formation of plastoquinol (PQH_2), which travels across the thylakoid membrane where it is oxidised by cytochrome b_6f, which in turn reduces plastocyanin (PC). A 2nd light-driven reaction follows at P700, which is associated with LHCI of PS I. This reaction centre oxidises PC and reduces the electron carrier protein ferredoxin (Fd) *via* special a chlorophyll *a* (A_0) and vitamin K (A_1) cofactor, and an iron–sulfur protein (FeS). Ultimately, reduced Fd is used by ferredoxin–$NADP^+$ reductase (FNR) to reduce $NADP^+$ to NADPH. The energies of the electrons involved in this process are shown in Fig. 1.2. This series of redox reactions provides the basis of Nature's completely sustainable energy storage solution.[41]

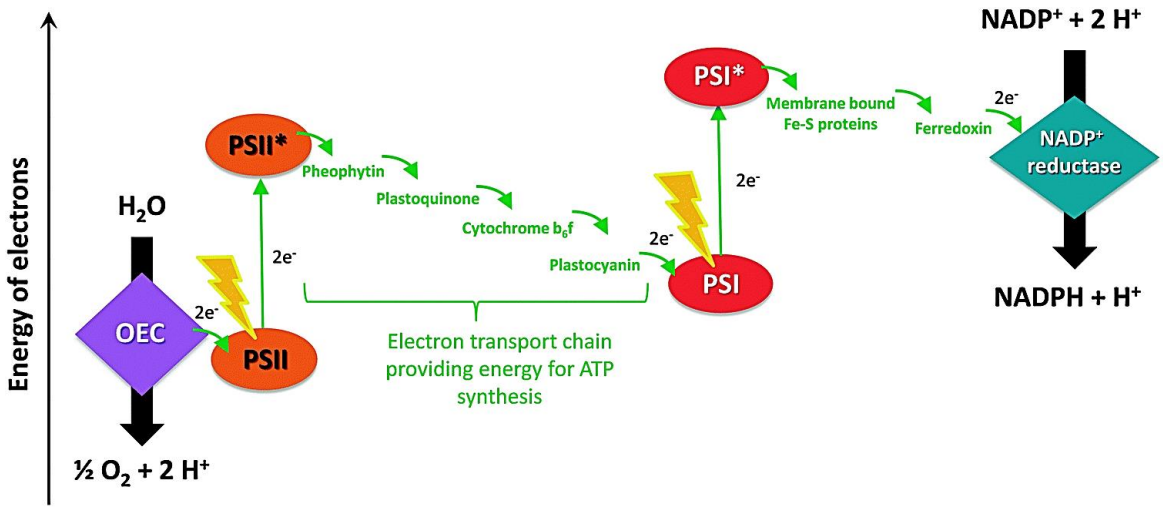

Figure 1.2: Schematic representation of the electron transport chain in natural photosynthesis showing the energy of electrons in a "Z-scheme". The light-absorbing reaction centres PS I and PS II drive the endergonic steps, ultimately transferring electrons from H_2O by the oxygen evolving complex (OEC) to $NADP^+$ reductase. Reproduced from Ref. 11.

The oxidation of H_2O by the OEC, the reduction of Q_A and Q_B, the oxidation of PQH_2 at cytochrome b_6f and the conversion of $NADP^+$ to NADPH all contribute towards the formation of a proton gradient across the thylakoid membrane. The energy stored within this gradient is used by ATP synthase to convert adenosine diphosphate (ADP) into adenosine triphosphate (ATP). The energy carriers ATP and NADH are ultimately consumed in the Calvin-Benson cycle, which fixes CO_2 from the atmosphere to create energy-rich carbohydrates.[42]

It is worth noting that the photoexcitation of P_{680} is a one-photon/one-electron process, however the reduction of PQ and the oxidation of H_2O are two- and four-electron processes, respectively. Hence, these chemical transformations require charge accumulation coupled to protonation reactions involving intermediates which are stabilized by their protein environment. Moreover, the initial light-driven splitting of H_2O is a highly endergonic process, with a Gibbs free energy change $\Delta G° = +237$ kJ per mole of H_2O decomposed.[43] Nature overcomes these challenges using PS II: a protein complex with an unequalled capacity for light-driven H_2O oxidation.[44]

1.2.1 Photosystem II

PS II is a highly specialised, dimeric thylakoid membrane-bound protein complex with a molecular weight of *ca*. 650 kDa.[45] The crystal structure of cyanobacterial PS II from *Thermosynechococcus elongatus* is presented in Fig. 1.3.[46] PS II is found in all photosynthetic organisms, and its overall function is to use solar energy to oxidise H_2O, liberating high-energy electrons for the reduction of plastoquinone.[47,48] Hence, PS II controls the first steps in the electron transport chain of photosynthesis.

Light-harvesting antennae complexes such as LHCII are vital to the operation of PS II. These structures are embedded with π conjugated metalloporphyrin and carotenoid chromophores that constitute an excitonically linked network which absorbs broadly in the visible region. Photosynthetic pigments are positioned to facilitate photon capture and funnelling of solar energy into the reaction centre P_{680} at the heart of PS II *via* resonance energy transfer.[49,50] This results in the formation of the cationic radical species $P_{680}^{\bullet+}$ with a high one-electron redox potential that provides the driving force for the highly endergonic H_2O splitting reaction.[51]

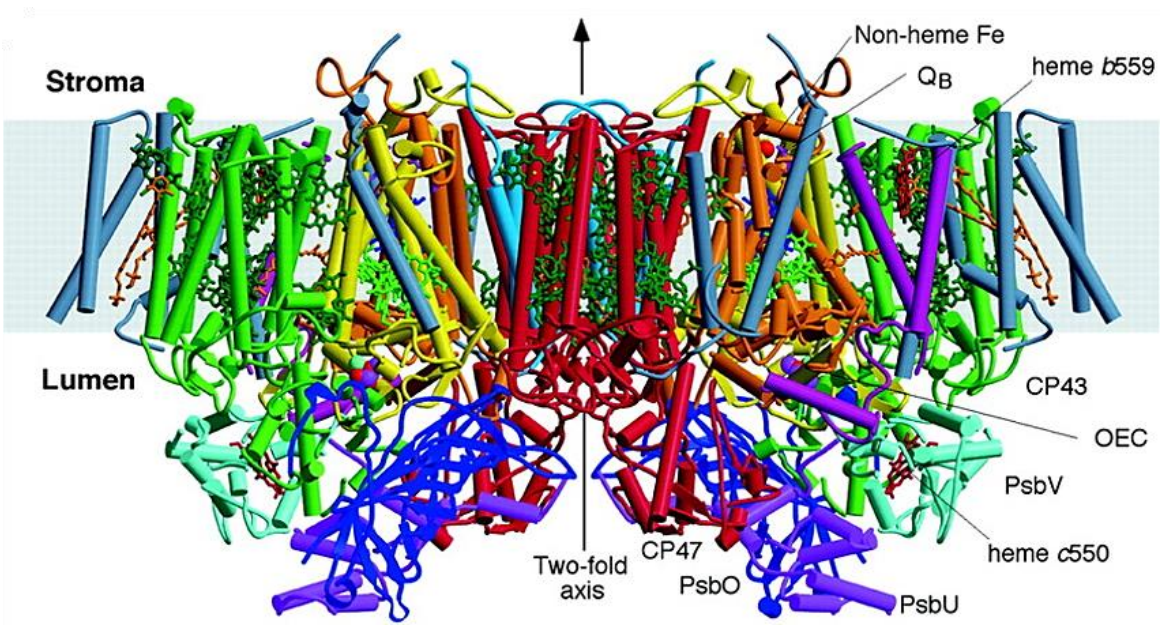

Figure 1.3: X-ray structure of the PS II dimer of the cyanobacterium *Thermosynechococcus elongatus* at 3.5 Å resolution. View is perpendicular to the membrane normal. Subunit colour scheme: D1 yellow, D2 orange, CP47 red, CP43 green, cyt b559 wine red, PsbL, PsbM, and PsbT medium blue, PsbH, PsbI, PsbJ, PsbK, PsbX, PsbZ, and PsbN grey, PsbO blue, PsbU magenta and PsbV cyan. α-Helices are represented as cylinders. Chlorophylls of the D1 and D2 reaction centre are light green, pheophytins are blue, chlorophylls of the antenna complexes are dark green, β-carotenes are orange, hemes are red, nonheme Fe is red, Q_A and Q_B are purple. The OEC is shown as the red (O atoms), magenta (Mn ions), and cyan (Ca ions) balls. Adapted from Ref. 46.

1.2.2 The Oxygen-Evolving Complex

Embedded within PS II is a Mn-oxo cluster known as the oxygen evolving complex (OEC).[52] This $\{Mn_4CaO_5\}$ cluster is used to oxidise H_2O at close-to-neutral pH with an efficiency that is unparalleled by any other synthetic system, with the OEC producing up to 500 molecules of O_2 every second.[46,53,] This remarkable, highly conserved catalyst is the only biological entity capable of creating an O – O bond from H_2O, and as such is the sole source of our atmosphere's 21% O_2.[54] Recent X-ray, spectroscopic and computational studies have yielded new structural and mechanistic insights into H_2O splitting catalysis by the naturally occurring OEC.[55–57]

The X-ray structure of the $\{Mn_4CaO_5\}$ OEC is presented in Fig. 1.4. The cuboidal complex features four oxo-bridged Mn atoms and one Ca atom which occupy four corners of the cube, whilst four bridging oxo atoms occupy the remaining corners. An additional, pentacoordinated 'dangler' Mn centre attaches to the cubane core through two oxo bridges.[58] This dangling Mn atom, which is also coordinated by two aqua ligands, is suspected of playing a pivotal role in O_2 evolution.[59,60] The overall structure of the OEC resembles a distorted chair.[61]

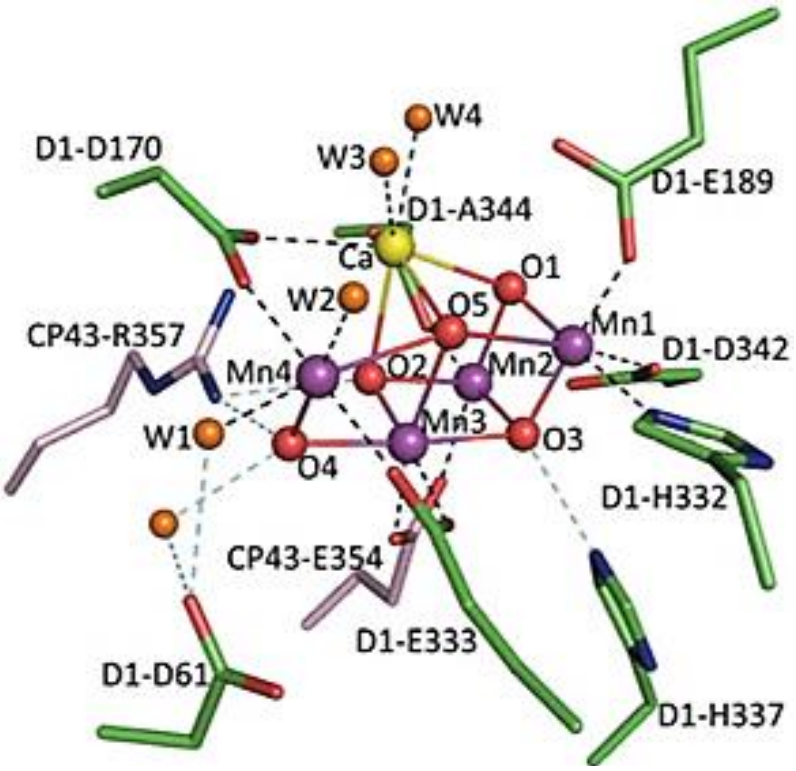

Figure 1.4: Crystallographically determined X-ray structure (1.9 Å resolution) of the cuboidal $\{Mn_4CaO_5\}$ OEC of PS II and its ligand environment. Colour scheme: Mn purple, Ca yellow, O red, N blue. D1 subunit C atoms are in green and the CP43 subunit C atoms are in pink. Adapted from Ref. 58.

Despite the challenges of H_2O oxidation, PS II mediates this process with exceptional efficiency. Therefore, the mechanism of catalysis by PS II has been intensely investigated.[62] In 1970, a catalytic cycle was proposed by Kok *et al*. based on flash-photolysis experiments performed the previous year by Joliot *et al*., which revealed that four sequential flashes of light induce O_2 evolution in a photosynthetic organism.[63,64] The Kok-Joliot cycle (Fig. 1.5) involves the sequential abstraction of four electrons from the $\{Mn_4CaO_5\}$ OEC by $P_{680}^{\bullet+}$ *via* Y_z. As oxidising equivalents are transferred to the OEC, it cycles through five storage states (S-states) from $S_0 - S_4$, where S_0 is the most reduced and S_4 is the most oxidised state of the Mn ions within the complex. In the final, light-independent transition from $S_4 - S_0$, O_2 is released and the ground state of the OEC is regenerated.[65] Due to the short-lived nature of the S_4 state, this transient intermediate is poorly characterised and still hotly debated.[66,67]

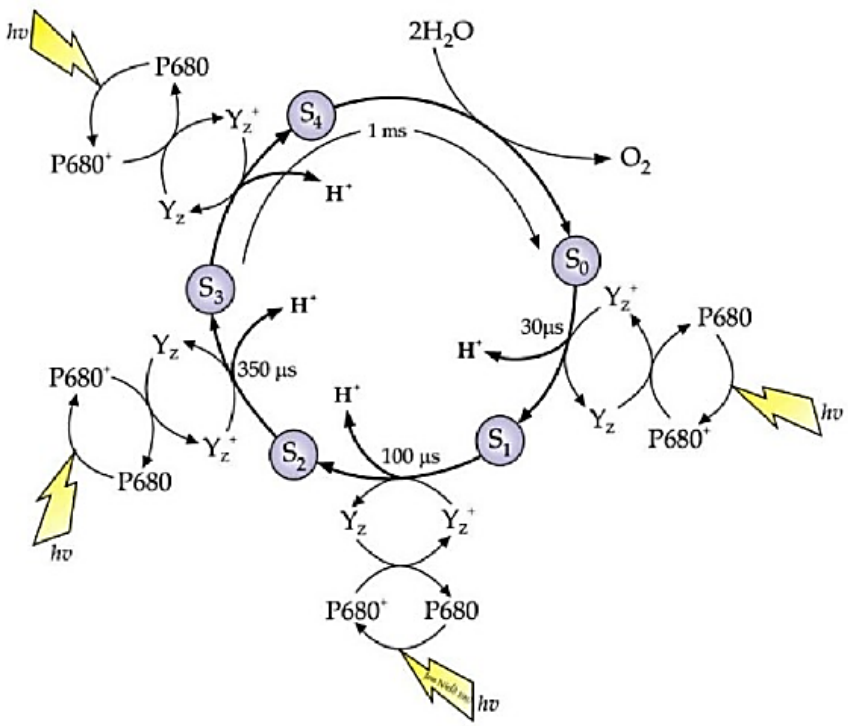

Figure 1.5: Kok cycle showing the five oxidation states ($S_0 - S_4$) of the OEC involved in H2O splitting. Solar energy is used to oxidise P680 to $P680^{\bullet+}$, which subsequently oxidises the $\{Mn_4CaO_5\}$ cluster of the OEC. Adapted from Ref. 68.

With each photo-driven S state change of the OEC, both a proton and an electron are removed from a bound H_2O molecule.[47] These proton-coupled electron transfers (PCETs) are pivotal to the proficiency of PS II, as for every electron that is transferred to $P_{680}^{\bullet+}$ by the OEC, a proton

is simultaneously transferred to the amino acid residues which surround the reaction centre.[69] Hence, PCETs allow for the accumulation of four oxidising equivalents whilst preventing large charges building up in the vicinity (and unduly destructive, high redox potentials). This synchronised shuffling of charge carriers is one way in which Nature accommodates a low-energy pathway for H_2O oxidation.[70]

The activity of the $\{Mn_4CaO_5\}$ vastly surpasses that of state-of-the-art modern synthetic catalysts for H_2O oxidation, which are also prone to decompose irreversibly.[71,72] The stability issues encountered with synthetic systems are unsurprising, considering that the OEC and its surroundings also constantly undergo degradation during O_2 evolution; however, self-repair mechanisms reconstitute the integrity of the OECs integrity, without which the cluster would become inactive within thirty minutes.[73] The stabilising protein subunits which surround the OEC are crucial to its activity.[74] The redox-active Y_z residue is intimately involved in the catalytic activity of the complex, as it links the OEC to P_{680} electronically, and is in close enough proximity that it may directly participate in catalysis.[75]

PS II and the OEC may serve as blueprints for the development of synthetic catalysts with analogous structural characteristics which mimic their function.[76] Indeed, many promising bioinspired H_2O oxidation catalysts (WOCs) have already been developed which comprise polynuclear Mn complexes, cubane motifs or non-innocent ligands.[60,71,77–79] In this thesis, the synthesis and characterisation of polynuclear Mn complexes containing redox-active ligands and frameworks based on porphyrins and transition metal species which could have potential as biomimetic water oxidation catalysts are investigated.

1.3 Artificial Photosynthesis

1.3.1 The H_2O Splitting Reaction

The ubiquitous presence of H_2O on earth in oceans, lakes and rivers means that the solvent of life harbours an essentially endless pool of redox equivalents. In Nature, PS II extracts high-energy protons and electrons from H_2O which, are ultimately employed in the synthesis of complex carbohydrates that serve several functions, including as energy carriers.[80] However, perhaps a more pragmatic approach would be to recombine reducing equivalents released from the decomposition of H_2O to produce H_2, which can be used as a carbon-free fuel and chemical feedstock.[81,82] This can be accomplished by coupling H_2O oxidation (Eqn. 1.2) with proton reduction (Eqn. 1.3), thus generating H_2 and O_2 (Eqn. 1.4).

$$2H_2O \rightarrow O_2 + 4H^+ + 4e^- \quad E° = 1.23\ \text{V vs. NHE (Eqn. 1.2)}$$

$$4H^+ + 4e^- \rightarrow 2H_2 \quad E° = 0.00\ \text{V vs. NHE (Eqn. 1.3)}$$

$$2H_2O \rightarrow O_2 + 2H_2 \quad E° = 1.23\ \text{V vs. NHE (Eqn. 1.4)}$$

1.3.2 Electrolytic H_2O Splitting

As early as 1789, the Dutch merchant Deiman and medical doctor van Troojstwijk established that passing an electric potential through H_2O results in its decomposition into its elemental constituent components H_2 and O_2.[83] In this experiment, a powerful electrostatic generator was discharged to a apply a voltage across two gold electrodes submerged in H_2O, resulting in the release of O_2 at the anode and H_2 at the cathode. This influential discovery had a far-reaching impact on the development of chemical theory. However, H_2O electrolysis is currently a prohibitively costly method of producing H_2.[84]

H_2O electrolysis is expensive due to the inherent stability of H_2O, meaning large amounts of power are needed to induce its decomposition. Under standard conditions, the free energy required to convert one mole of H_2O into H_2 and ½O_2 is $\Delta G° = 237.2$ kJ, which corresponds to a minimum electric potential of $E° = +1.23$ V per electron transferred according to the Nernst equation.[85] However, in practice, additional energy above this theoretical minimum potential, known as the overpotential (η), must also be applied to overcome the kinetic barriers associated with the destruction and creation of new chemical bonds.[86] This is particularly true for the

complex oxygen evolving reaction (OER), which involves the transfer of four electrons, the re-arrangement of multiple bonds and the formation of an O – O bond.[87,88]

The overpotentials of H_2O splitting can be reduced using a WOC or a H_2 evolution catalyst (HEC) in combination with an anode or cathode, respectively.[89] Electrocatalysts expedite H_2O splitting by allowing alternative, lower energy decomposition pathways, thus minimising the kinetic barriers of the OER or the hydrogen evolving reaction (HER). WOCs and HECs, therefore, reduce the energy required to carry out H_2O splitting.

The efficiency of an electrocatalyst can be determined by the necessary overpotential required to elicit a catalytic response. HECs and WOCs operating at potentials close to their Nernstian potentials of $E°$ = 1.23 and 0.00 V vs. NHE, respectively are highly desirable.[90] Further, the applied potential required to reach a current density flowing through an electrode of 10 mA cm^{-2} is often used as an indication of a catalyst's activity.[91] Finally electrocatalysts constructed from cheap, non-toxic materials that retain activity over prolonged periods of use are particularly promising.

However, even with the use of effective catalysts conventional electrolysers still require significant energy inputs. Without coupling H_2O electrolysis to a renewable energy source, this process alone does not represent a sustainable solution to the energy crisis.[92] Using solar energy to drive this process presents an opportunity to generate H_2 without relying on fossil fuels. Although the potential advantages afforded by such artificial photosynthetic systems are enormous, vast technological challenges are also presented.

1.3.3 The Photo-Electrochemical Cell

A major technological milestone towards light-driven H_2O splitting came in 1972 with the discovery of Honda-Fujishima effect and the subsequent development of the photo-electrochemical cell (PEC).[93] A PEC can convert solar radiation into energy stored in chemical bonds. Therefore, this breakthrough provided the first tangible indication that artificial photosynthesis could become a practicable reality. A typical PEC comprises two semiconductor electrodes which are immersed in an aqueous electrolyte solution and connected *via* an external circuit (Fig. 1.6).[94]

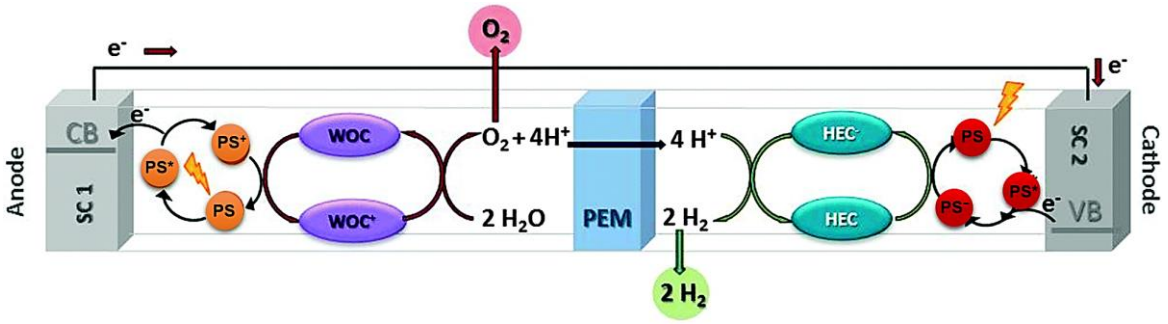

Figure 1.6: Schematic representation of a PEC for overall light-driven H_2O splitting. Adapted from Ref. 11.

In a PEC, a proton exchange membrane (PEM) divides the device into two sections: an anodic compartment in which the OER occurs and a cathodic compartment where the HER takes place. Physically separating the sites of H_2O oxidation and reduction is advantageous, as a highly efficient WOC may be inactive towards the HER, whilst an excellent HEC may be inappropriate for mediating the OER. In addition, having two different compartments for H_2 and O_2 evolution is beneficial, as it allows H_2 to be obtained in high purity and is safer, as it prevents the violent recombination of the two gasses. The driving force for H_2O splitting is provided by photons which are absorbed by either a semiconductor photoelectrode (SC 1 or SC 2) with an appropriate bandgap or an associated photosensitiser (PS). The efficiency of the system can be improved using either a WOC, a HEC or both by lowering the energy required to evolve O_2 and H_2.[95]

In Honda and Fujishima's pioneering study, the decomposition of H_2O into H_2 and O_2 was achieved without applying an external current using a PEC comprising an n-type TiO_2 photoanode connected to a Pt cathode. In this device, UV-illumination of the semiconductor

anode leads to the promotion of electrons from the conduction band (CB) to the valence band (VB), forming photoexcited electron and positive hole pairs. Four photogenerated holes then combine with the valence electrons of two H_2O molecules at the surface of the anode, releasing O_2 and four protons. Simultaneously, excited electrons migrate *via* the external circuit to the cathode where protons produced by the OER are reduced, releasing gaseous H_2.

Since their initial conception, PECs have been explored extensively for H_2O splitting.[96,97] Despite significant technological advances, achieving a solar-to-hydrogen efficiency of over 10% and long-term stability using these systems is challenging.[98,99,] Moreover, due to the large bandgaps of the semiconductor materials employed in PEC electrodes, substantial sections of the solar spectrum cannot be harnessed. For example, the n-type TiO_2 photoanodes of Honda and Fujishima's prototypal PEC display a bandgap of 3.0 – 3.2 eV, and therefore can only absorb UV-light (which accounts for just 5% of the energy content of sunlight).[100,101] For these reasons, PECs do not yet represent an economically viable means to produce H_2.[102]

To make H_2O splitting PECs cost-effective, much contemporary research is being carried out to improve the efficiency of these systems.[94,95,103] This could be achieved by developing efficient molecular WOCs and HECs to lower the overpotentials associated with H_2O splitting. Homogeneous catalysts could be incorporated into a working PEC by dissolving the WOC in the electrolyte, whilst heterogeneous catalysts can be anchored to electrodes to increase H_2 production.[11] In addition, integration of a light-absorbing PS may allow a greater portion of the solar spectrum to be utilised.[104] It is also desirable that WOCs, HECs and PSs used in PECs are constructed from inexpensive, earth-abundant and non-toxic materials for the technology to be widely adopted.[105,106] In the following section, some practical considerations for studying light-induced H_2O splitting catalysis are discussed.

1.3.4 Photocatalytic H_2O Splitting

Solar H_2O splitting is currently a highly active area of materials and catalysis research.[107] A commonly employed strategy is to investigate and optimise catalysts for each half-reaction separately. In practice, this is achieved using homogeneously dispersed PSs and sacrificial reagents. Using sacrificial reagents is advantageous as it allows OER or HER catalysts to be studied and optimised independently of one another. Under these conditions, electrons flow through the WOC or HEC in the same manner as in a PEC. However, fewer variables need to be controlled than in a complete H_2O splitting cell, and counterproductive charge-carrier recombination processes are prevented. Moreover, this allows the O_2 and H_2 evolving reactions to be studied in isolation as evolved gasses do not need to be separated. Once each catalyst has been optimised, a WOC and a HEC can be combined in a working PEC.[76]

Catalysts for the four-electron H_2O oxidation reaction are typically assessed as part of a three-component photocatalytic system comprising a WOC, PS and sacrificial electron acceptor (SEA) such as $Na_2S_2O_8$. A buffer solution is also commonly employed to counteract pH changes.[108] Fig. 1.7 illustrates the flow of electrons in such a three-component system: Absorption of a photon by a PS generates PS^*, which will reduce the SEA resulting in the formation of PS^+ and permanent decomposition of the SEA. Provided that its redox potential is sufficient, PS^+ can then sequentially abstract four electrons from the WOC. Acquisition of four photogenerated holes by the WOC allows it to mediate the multielectron OER.[11]

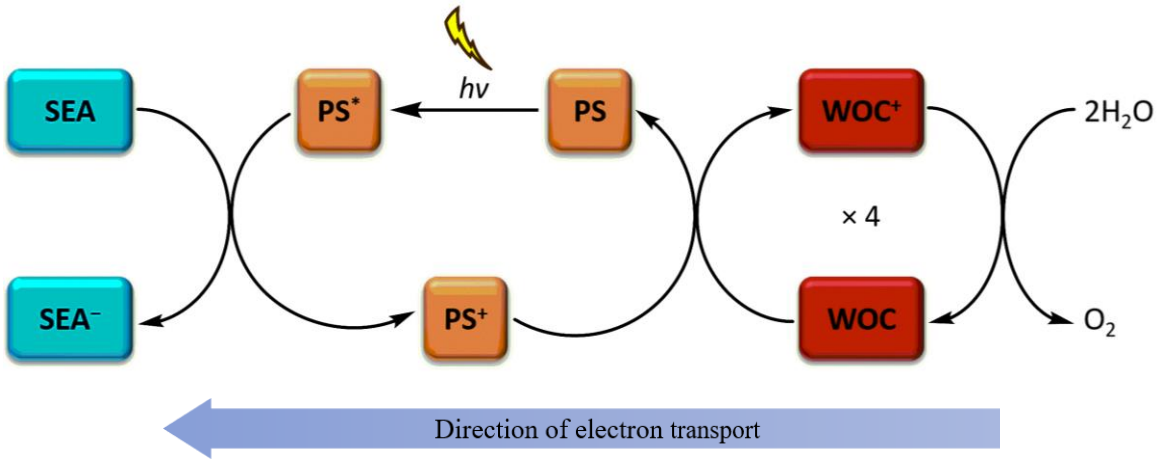

Figure 1.7: Series of expected interactions between a PS, SEA and WOC leading to light-driven H_2O oxidation. Absorption of a photon by PS absorbs causes it to enter an excited state PS*, which then transfers an electron to the SEA and becomes PS^+. The WOC is activated by four consecutive one-electron transfers to PS^+. By abstracting electrons from the PS, the SEA adopts an analogous role to H^+ as the final electron acceptor.

Similarly, when testing PS/HEC combinations a sacrificial electron donor (SED) such as methanol (MeOH), triethylamine (TEA) or triethanolamine (TEOH) can be employed, facilitating detailed HER studies. In this case, electrons flow from the SED to the HEC *via* the PS, generating HEC^-. The reduced catalyst may then be able to transfer electrons to H^+, simultaneously forming H_2 and regenerating the ground state of the catalyst.

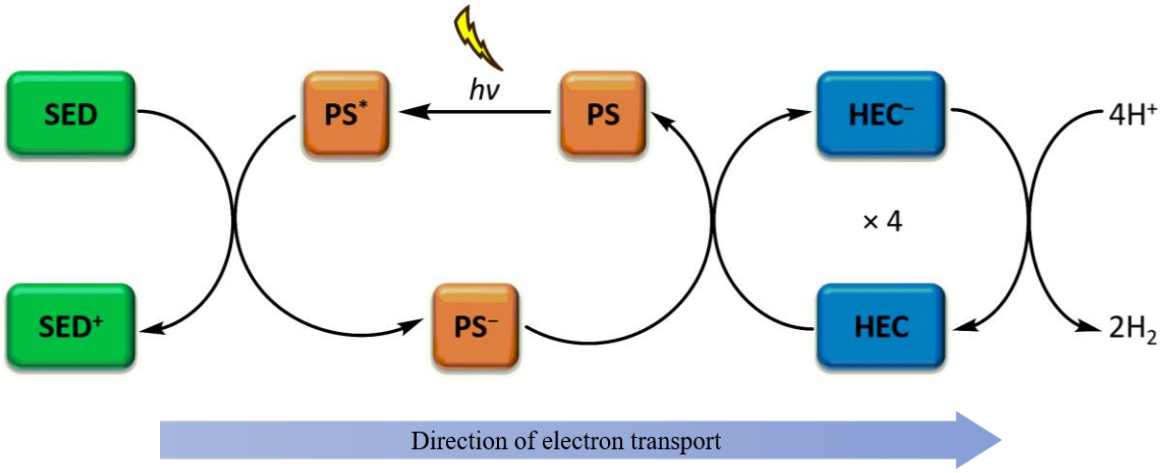

Figure 1.8: Series of reactions involved in the light-driven HER using a HEC, PS and SED. Absorption of a photon by the PS causes the species to enter an excited state, PS*. The SED then reduces PS*, resulting in the formation of the species PS^-. This reduced species may then transfer an electron to the HEC, which in turn reduces H^+ to H_2.

Kinetic monitoring of light-driven H_2O splitting reactions can be achieved using a Clark electrode inserted into the photocatalytic reaction mixture.[109–112] To quantitatively compare H_2O splitting catalysts in the literature, different metrics may be considered. These aspects relate to the intrinsic activity of a catalyst and its robustness. The overpotential η (see Section 1.3.2) and the turnover frequency (TOF) are associated with a catalyst's activity, whilst the turnover number (TON) relates to its robustness. The TON and TOF of a WOC are defined below:[113]

$$\text{Turnover Number (TON)} = \frac{\text{Moles of } O_2 \text{ Evolved}}{\text{Moles of WOC Employed}}$$

$$\text{Turnover Frequency (TOF)} = \frac{\text{Moles of } O_2 \text{ Evolved}}{\text{Moles of WOC Employed} \times \text{Time Elapsed}}$$

1.3.5 Photosensitisers for H_2O Splitting

A light-harvesting PS is a crucial component of any photocatalytic H_2O splitting system.[114] Absorption of a photon by a PS generates a photoinduced charge separation, which leads to the oxidation or reduction of a WOC or a HEC, respectively. Thus, these species provide the driving force for the photocatalytic OER and HER.[76]

Several stringent requirements must be satisfied for a PS to be suitable for solar-driven H_2O splitting: Effective chromophores should absorb a broad range of visible light, have a high molar extinction coefficient (ε) in this region, display a redox potential sufficiently high to facilitate electron transfer from a WOC or to a HEC, manifest long-lived excited-states that are adequate to affect intermolecular processes and exhibit photostability to allow prolonged use. Ideally, a PS should also be constructed from cheap and abundant, non-toxic materials.[115,116]

A large number of chromophores have been used as PSs for light-driven H_2O splitting in the literature, including Ru- and Ir-based polypyridyl complexes, porphyrins, phthalocyanines, quantum dots and others.[117–121] The structures of some of these PSs are shown in Fig. 1.8. Perhaps the most well-studied PS for molecular H_2O splitting catalytic studies is $[Ru(bpy)_3]Cl_2$ (bpy = 4,4'-bipyridine).[122,123] This homoleptic polypyridyl Ru complex is employed extensively in the literature, as it satisfies most of the conditions outlined above. However, $[Ru(bpy)_3]Cl_2$ is prone to decomposition under the working conditions of the OER and is expensive to use as it contains the rare-earth element Ru.[124]

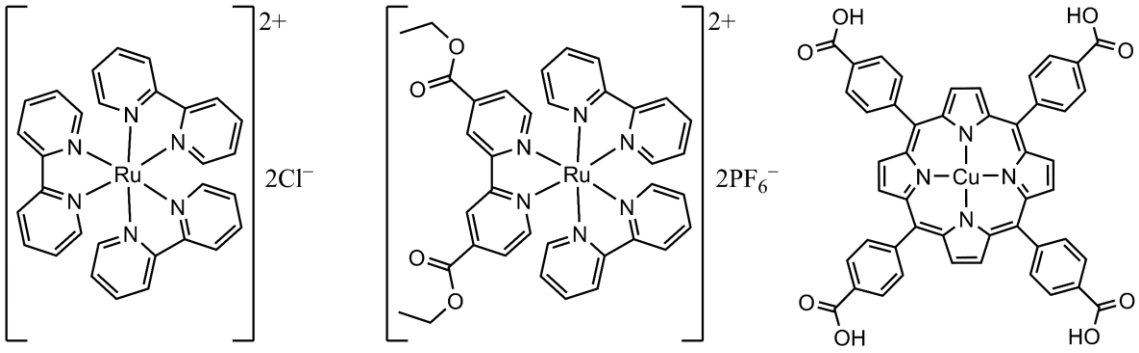

Figure 1.8: Structures of three PSs which have been employed in light-driven H_2O splitting studies (left) $[Ru(bpy)_3]Cl_2$, (middle) $[Ru(bpy)_2(deeb)](PF_6)_2$ and (right) [*meso*-tetra(4-carboxyphenyl)porphyrinato]-Cu^{II}.

Another attractive chromophore for sensitising H_2O splitting catalysts is the heteroleptic ester-functionalised PS, $[Ru^{II}(bpy)_2(deeb)](PF_6)_2$ (deeb = diethyl 2,2′-bipyridine-4,4′-dicarboxylate). This PS is structurally similar to $[Ru^{II}(bpy)_3]Cl_2$, however, it displays a greater redox potential in its one-electron oxidised state. Whilst the redox potential of the homoleptic PS is $E_{1/2}$ $[Ru^{III}(bpy)_3]^{3+}/[Ru^{II}(bpy)_3]^{2+}$ = 1.26 V vs. NHE, the heteroleptic PS has a redox potential of $E_{1/2}$ $[Ru^{III}(bpy)_2(deeb)]^{3+}/[Ru^{II}(bpy)_2(deeb)]^{2+}$ = 1.40 V vs. NHE. As the latter PS displays the greater redox potential, this species is expected to provide stronger driving force for thermodynamically uphill H_2O splitting reactions. Åkermark *et al*. demonstrated the superior photosensitising ability of $[Ru^{II}(bpy)_2(deeb)](PF_6)_2$ over $[Ru^{II}(bpy)_3]Cl_2$ in a series of photocatalytic OER experiments.[122]

The expected interactions of the one-electron PS $[Ru(bpy)_2(deeb)]^{2+}$ with the two-electron SEA $S_2O_8^{2-}$ and a WOC during the light-driven OER are displayed in Scheme 1.9. O_2 evolution is preceded by the consecutive abstraction of four electrons from the WOC by the PS. However, numerous alternative non-catalytic pathways exist. For example charge carrier recombination events or PS/WOC decomposition processes can all have diminutive effects on OER activity.[124]

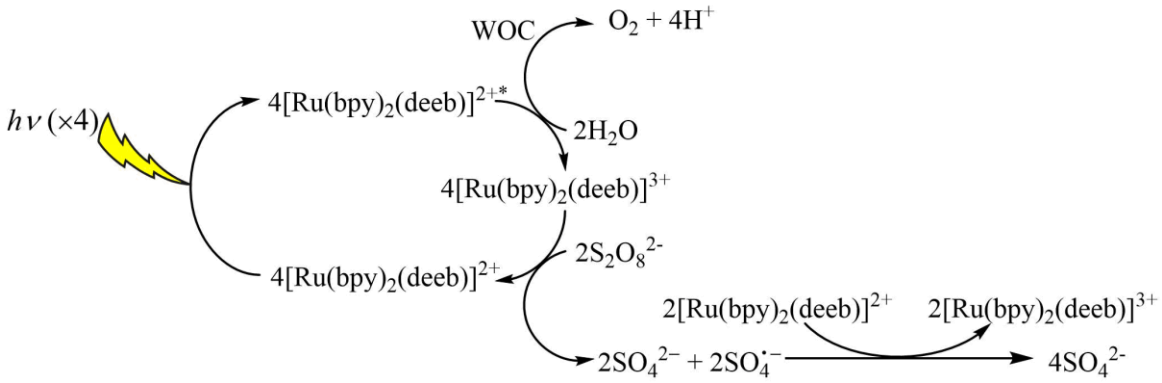

Scheme 1.9: General pathway to photocatalytic O_2 formation using (a) $[Ru(bpy)_2(deeb)]^{2+}$ or (b) $[Ru(bpy)_2(deeb)]^{2+}$ as a PS in presence of a WOC and $S_2O_8^{2-}$ as a SEA in the presence of a WOC.

In addition to these polypyridyl chromophores, there is growing interest in PS II-inspired porphyrins as PSs for light-driven H_2O splitting catalysis.[125] Metalloporphyrins offer advantages over Ru- and Ir-based dyes as they do not necessitate the use of rare-earth metals, and may demonstrate heightened photostability compared to other well-established PSs.[115,126] For example, in 2015 Brouwer *et al.* demonstrated that two related Pt^{II}-based metalloporphyrin

complexes TCPP-Pt^{II} (TCPP = [*meso*-tetrakis(4-carboxyphenyl)porphyrinato]) and TMPP-Pt^{II} (TMPP = [*meso*-tetrakis(4-methoxycarbonylphenyl)porphyrinato]) function as effective PSs for H_2O oxidation when used in combination with two homogeneous Ir- and Co-based WOCs.[119] Under the working conditions of the OER, TCPP-Pt^{II} and TMPP-Pt^{II} displayed excellent photostability which was superior to that of $[Ru^{II}(bpy)_3]Cl_2$. In addition, TMPP-Pt^{II} exhibited triple the photon capture ability and a redox potential which exceeded the redox potential of the commonly used PS $[Ru^{II}(bpy)_3]Cl_2$ by 240 mV.

The following year, an investigation led by the same group revealed that metalloporphyrin PSs comprising earth-abundant, first-row transition metals demonstrate promising photosensitising abilities when used with heterogeneous, Co-based WOCs.[118] In this study, analogues of TMPP-Cu^{II} and TMPP-Ni^{II} which were tetrachlorinated at the β-pyrrole positions outperformed their Pt^{II}-based predecessors in terms of photostability, molar absorptivity and redox potential. Moreover, in 2015 Natali *et al*. demonstrated the photosensitising potential of a Zn^{II}-based metalloporphyrin [*meso*-tetrakis(*N*-methyl-4-pyridyl)porphyrinato]-Zn^{II}.[115] Irradiation of this PS in the presence of a Ru-based polyoxometalate WOC and $Na_2S_2O_8$ SEA resulted in the evolution of modest quantities of O_2. These studies illustrate that metalloporphyrins may be exploited as earth-abundant PSs for H_2O splitting reactions.

1.4 Catalysts for H_2O Oxidation

The OER is the current bottleneck to light-driven H_2O splitting.[11,127] Whilst many competent catalysts exist for the HER, effectively catalysing the thermodynamically demanding OER is more challenging.[128–130] This is largely due to the endergonic and complex nature of this reaction, which is illustrated by the large overpotentials associated with the individual reaction steps.[87,88,131] Moreover, an effective WOC must be robust enough to endure highly oxidising conditions, accumulate four oxidising equivalents and withstand attack by high-energy intermediates without its activity diminishing.[76,132,133] The development of cheap, stable WOCs therefore has the potential to instigate a paradigm shift in sustainable energy production.[134–137] Therefore, this report predominantly addresses catalysts for the more challenging OER.

1.4.1 Metal Oxide WOCs

In 1978, Grätzel and Kiwi reported an early example of catalytic O_2 evolution from H_2O.[138] In this study, colloidal suspensions of the precious metal oxides IrO_2 and PtO_2 displayed photocatalytic OER activity using Ce^{IV} as an oxidant. The following year, RuO_2 was discovered to act as an efficient WOC under similar conditions.[139] The performance of these catalysts is intrinsically linked to their surface areas: catalysts displaying higher surface areas exhibit favourable activities.[132] These WOCs represent some of the most active OER catalysts in the literature, and as such these materials are considered benchmarks.[140] However, their prohibitive price and instability at high anodic potentials renders the industrial implementation of precious metal oxide WOCs economically infeasible.[95,141]

Several earth-abundant transition metal oxide species have also successfully been used to catalyse the OER. For example, in 1977 Morita *et al*. discovered that MnO_2 could be used as an electrocatalyst for H_2O oxidation, albeit with higher overpotentials than IrO_2 or RuO_2.[142] Many Mn oxide materials (MnO_x) have since demonstrated catalytic O_2 evolution capabilities.[143,144] Another attractive group of earth-abundant WOCs are Co oxides (CoO_x). These compounds display decent OER activity, and as such have been studied intensely over the last several decades.[91,145,146] In 2008, Nocera *et al*. deposited a Co oxide-phosphate catalyst (Co – Pi) on the surface of an indium tin oxide (ITO) electrode. This WOC efficiently evolved O_2, delivering 1 mA cm^{-2} at an applied overpotential of 410 mV at pH = 7.[147] Transition metal oxide WOCs are appealing due to their relatively low cost, however their moderate activities limit their practical applicability as OER catalysts.[148]

1.4.2 Molecular WOCs

To prepare WOCs which are active and stable enough to make wide-scale solar H_2 production cost-effective, extensive efforts have been devoted to the development of molecular WOCs which emulate the OEC.[72,133] These discrete systems typically constitute redox-active metal centres and stabilising organic ligands.[11] Unlike their bulk metal oxide counterparts, molecular WOCs benefit from having tunable electronic properties, and their ability to be anchored to the anodes of sophisticated H_2O splitting devices.[149,150] The first example of a molecular WOC reported in the literature is a dinuclear ruthenium complex with the formula $[(bpy)_2(H_2O)Ru^{III}ORu^{III}(H_2O)(bpy)_2]^{4+}$ (Fig. 1.10) which was prepared by Meyer *et al.* in 1982.[151,152] Dubbed the "blue dimer" due to its characteristic colour in solution, this WOC operates with a TOF = 4.2×10^{-3} s^{-1} and a TON = 13.2.[153]

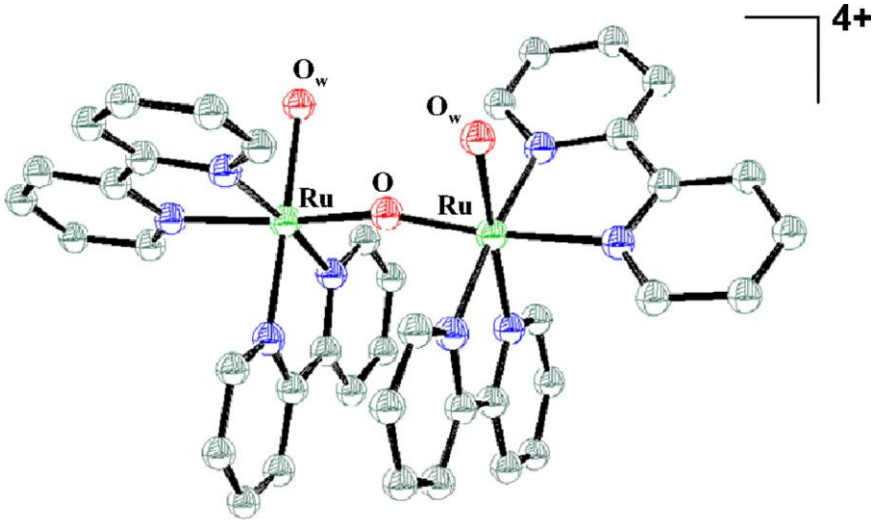

Figure 1.10: Crystal structure of the Ru-based "blue dimer" $[(bpy)_2(H_2O)Ru^{III}ORu^{III}(H_2O)(bpy)_2]^{4+}$, the first molecular WOC. Hydrogen atoms omitted for clarity. Colour scheme: C white, N blue, O red, Ru green. Reproduced from Ref. 154.

Over the decades following the discovery of the blue dimer, a plethora of poly- and mononuclear WOCs have been prepared, which display TONs and TOFs that have increased by over five orders of magnitude.[155] Particularly pertinent to the pursuit of striking a balance between high efficiency and low cost are catalysts constructed from earth-abundant and non-toxic elements.[95] To this end, many first-row transition metals have been used to fabricate OER catalysts, including Cr,[156] Mn,[157–162] Fe,[163,164] Ni,[165] Co,[166–169] and Cu.[170,171] This report primarily focuses on Mn- and Co-based WOCs.

1.4.3 Mn-Based Molecular WOCs

Mn is the 12th most abundant metal in the earth's crust and can be found in its elemental form in polymetallic nodules on the ocean floor.[172,173] Bioinspired molecular Mn-oxo clusters are therefore highly attractive as WOCs due to the high abundance and low cost of Mn.[174] Previously studied synthetic Mn catalysts include a diarylphosphinate-stabilised cubane-like {Mn_4O_4} cluster,[175] an acetate-stabilized tetramanganese polyoxometalate with an onset overpotential of 530 mV under electrochemical conditions and a TOF of 2.84 x 10^{-3} s^{-1} under photochemical conditions,[176] a tetranuclear cubane-like Mn-based WOC with a TON of 25,[177] and a Mn-based Weakley-type polyoxometalate OER catalyst that operates at neutral pH.[178]

Some of the most interesting and active Mn-based WOCs are derived from the dodecanuclear Mn-oxo cluster [$Mn_{12}O_{12}(OAc)_{16}(H_2O)_4$] (Fig 1.11).[179] Recently, Maayan *et al.* demonstrated that substituting the acetate ligands of this complex with di- or trihydroxybenzoate ligands increases the stability and solubility of the {Mn_{12}} system.[180,181] These di- and trihydroxybenzoate-substituted derivatives displayed TONs of 13.2 and 15.5, respectively, and onset overpotentials as low as 74 mV for the OER. Whilst these dodecanuclear derivatives still show signs of decomposition under working conditions, they possess high stability compared to previously reported Mn-oxo clusters. This approach provides an excellent example of rational ligand modification to tune the stability and OER performance of a molecular WOC.[182]

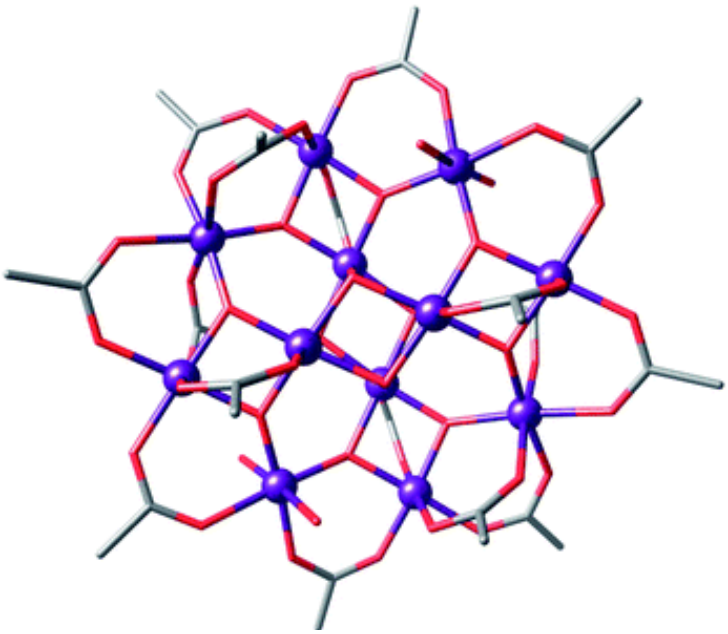

Figure 1.11: Crystal structure of the dodecanuclear Mn-oxo cluster [$Mn_{12}O_{12}(OAc)_{16}(H_2O)_4$]. Colour scheme: C grey, O red, Mn purple. Adapted from Ref. 183.

Mn-oxo cluster WOCs often suffer from stability issues under harsh working conditions due to the inherent lability of Mn complexes.[178] This may lead either to the *in-situ* formation of catalytically active heterogeneous Mn oxide species (MnO*x*) or catalyst decomposition into inactive species. Hence, correct catalyst assignment is crucial.[184,185] Various spectroscopic techniques such as Raman and UV-vis spectroscopy are frequently employed in the literature to distinguish true molecular WOCs from precatalytic species.[186–189] High-nuclearity Mn-oxo clusters with several substrate-accessible sites are especially desirable as molecular OER catalysts. These characteristics allow H_2O to coordinate to a cluster which acts as a reservoir of oxidising equivalents spread out over multiple metal centres.[180] In analogy to the OEC, many effective synthetic Mn-based WOCs in the literature constitute cubane motifs.[77,79,190]

1.4.4 Co-Based Molecular WOCs

Many Co-based molecular WOCs also demonstrate impressive O_2 evolution activity.[191–195] For example, in 2017, Galán-Mascarós *et al*. demonstrated the electrocatalytic OER activity of the polyoxometalate salt $Ba_8[Co_9(H_2O)_6(OH)_3(HPO_4)_2(PW_9O_{34})_3]\cdot 55H_2O$ (Fig 1.12).[196] When blended into carbon paste (CP) electrodes, this noble metal-free WOC displays excellent OER activity, which exceeds that of state-of-the-art catalysts such as IrO_2 by delivering a large current density of 1 mA cm^{-1} at an overpotential of just 189 mV under acidic conditions.

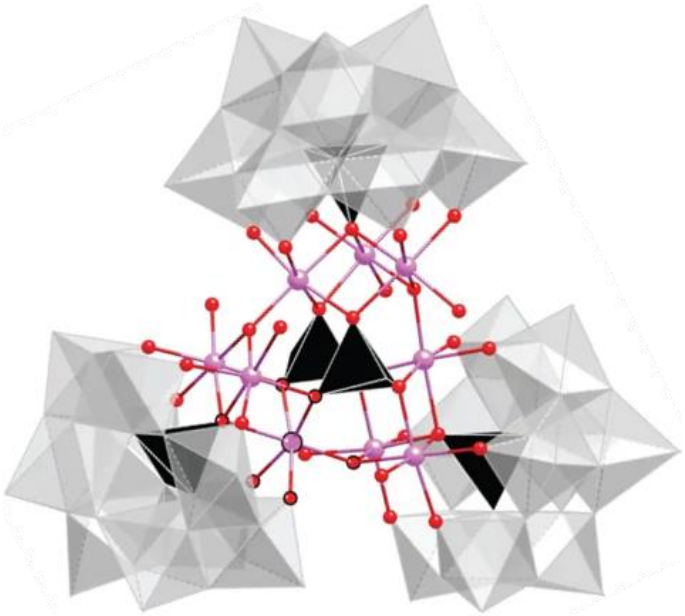

Figure 1.12: Crystal structure of the Co-based polyoxometalate WOC $[Co_9(H_2O)_6(OH)_3(HPO_4)_2(PW_9O_{34})_3]^{16-}$. Colour Scheme: Co pink, O red, WO_6 grey octahedra; PO_4, black tetrahedra. Reproduced from Ref. 196.

1.4.5 Porphyrin-Based Molecular WOCs

The heterocyclic macrocycles porphyrins are ubiquitous in biological systems, in which they are used for redox-catalysis, light-harvesting and transport.[197,198] The structural and electronic properties of these tetrapyrrolic molecules have been long exploited for diverse applications, including photodynamic therapy,[199] tumour imaging,[200] photovoltaics,[201] catalysis,[202] and artificial photosynthesis.[115,203] Their strong absorbance of visible light and redox-activity has led to their use in bio-inspired systems for photocatalytic H_2O splitting.[204,205]

For example, in 1994, Natura *et al*. developed a series of Mn^{III}-based porphyrin dimers which are active towards catalytic H_2O oxidation. Under electrochemical conditions, these metalloporphyrin WOCs evolved O_2 with a TOF of 1.8×10^{-3} s^{-1}. Moreover, in 2013 Sakai *et al.* demonstrated the photocatalytic OER activities of three Co^{II} metalloporphyrin complexes in the presence of $Na_2S_2O_8$ SEA and $[Ru(bpy)_3](NO_3)_2$ PS. This study indicated these Co-containing metalloporphyrins are effective WOCs, with TOFs ranging between 0.118 – 0.170 s^{-1}.[206] In a later study by the same group, the stabilities of these single-site Co^{II} WOCs were improved by introducing Cl atoms at the 2 and 6 positions of the porphyrin's aryl groups. These halogenated metalloporphyrins exhibited enhanced TOFs of up to 1.7 s^{-1}.[207]

Further, in 2019 Cao *et al*. demonstrated the electrocatalytic OER activity of the Cu^{II} complex of *meso*-tetra(4-*N*-methylpyridyl)porphyrin (Fig. 1.13).[208] This inexpensive, earth-abundant WOC exhibited efficient O_2 evolution behaviour, demonstrating catalytic activity at an applied overpotential of just 310 mV vs. NHE at pH = 7. These studies show that porphyrin complexes of first-row transition metals make promising molecular catalysts for H_2O oxidation.

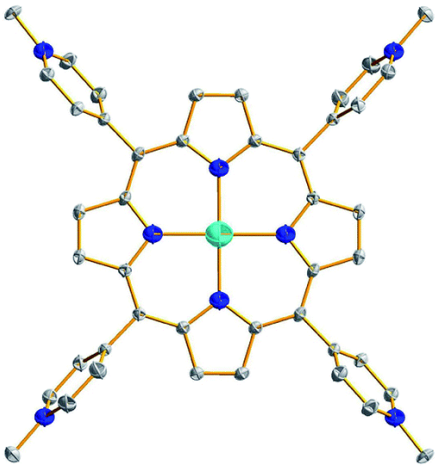

Figure 1.13: Thermal ellipsoid plot (50% probability) of the WOC [*meso*-tetra(4-*N*-methylpyridyl)porphyrinato]-Cu^{II}. Hydrogen atoms omitted for clarity. Colour scheme: C grey, N blue, Cu turquoise. Adapted from Ref. 208.

1.4.6 Mechanistic Considerations for H_2O Oxidation Catalysis

Several reaction mechanisms have been suggested for O – O bond formation in H_2O oxidation.[65,209] Two primary pathways have been identified using computational modelling studies (Fig. 1.14). These mechanisms involve either a nucleophilic attack by H_2O on a metal-oxo moiety (WNA pathway) or O – O bond formation *via* an interaction between two metal-oxo units (I2M pathway). Both of these mechanisms comprise four separate steps, each of which has an associated $\Delta G°$ value. For both the I2M and WNA mechanisms, the catalytic cycle begins with two PCETs, yielding a metal-oxo species (M = O). In the case of the WNA pathway, this M = O moiety undergoes nucleophilic attack by H_2O and a PCET to form a hydroperoxo species. This intermediate then regenerates the catalyst by releasing O_2 in a final PCET. For the I2M mechanism, two M = O moieties interact to form a peroxo unit, which subsequently evolves O_2 and reforms the catalyst.

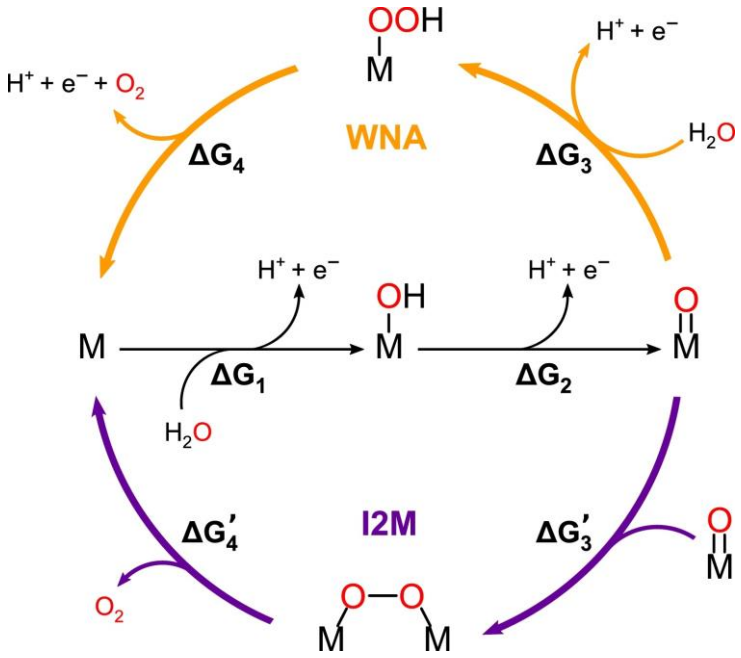

Figure 1.14: Catalytic cycle of the two main pathways to O_2 evolution by a WOC. Reproduced from Ref. 210.

Most homogeneous or single-site heterogeneous WOCs mediate the OER according to the WNA pathway. However, WOCs which exhibit second-order kinetics may evolve O_2 through the I2M mechanism.[211] In a recent study by Siegbahn *et al.*, the activation barriers of O_2 formation by the $\{Mn_4CaO_5\}$ cluster of the OEC according to either the WNA or I2M pathway

were compared.[56] Density functional theory (DFT) calculations revealed that the energy requirement was significantly higher for nucleophilic attack by a solvent H_2O molecule than it was for the coupling of an oxyl radical and a bridging oxo moiety (29.8 kcal mol^{-1} for WNA compared to 6.2 kcal mol^{-1} for I2M, using the same model). This investigation suggests that O_2 formation in PS II proceeds according to the I2M mechanism.[212]

1.4.7 Chromophore – Catalyst Dyad Complexes

Several processes within light-driven H_2O oxidation can constitute the bottleneck of O_2 evolution. Limburg *et al*. recently demonstrated that for highly active WOCs, the rate-limiting step is the oxidation of the WOC by PS^+.[124] Further, this investigation revealed that a slow rate of electron transfer from a WOC to PS^+ results in an accumulation of PS^+, which undergoes rapid decomposition, thus reducing the photocatalytic system's overall stability. Therefore, improving the electronic communication between these moieties may significantly enhance the efficiency of the OER.

One promising strategy to alleviate this bottleneck is to directly tether a PS to a WOC through coordinative or covalent bonds.[11] The effectiveness of this approach has been demonstrated by several studies which show that supramolecular assemblies comprising antennae PSs that are chemically linked to WOCs exhibit greater activity than their intermolecular equivalents.[213–216] For example, Thummel *et al*. reported a diruthenium PS – WOC dyad photocatalyst which exhibited a TON = 134 over six hours.[217] This activity is twenty times greater than the activity of an analogous multicomponent system under identical conditions. Once optimised, such PS – WOC dyads can be integrated into dye-sensitized photoelectrochemical cells (DSPECs) to convert solar energy and H_2O into H_2 and O_2.[218,219]

Metal-organic frameworks (MOFs) are highly customisable, hybrid organic-inorganic materials which offer a platform for the incorporation of a PS and a WOC within a highly ordered supramolecular assembly.[220] In the next section, this important and versatile class of compounds is introduced, and the relevance of these materials for designing highly active heterogeneous H_2O splitting catalysts is outlined.

1.5 Metal-Organic Frameworks

1.5.1 Definitions and Overview

In recent years, MOFs have attracted significant scientific attention.[221–223] Members of this exciting class of modular, metallo-supramolecular polymeric materials can be conceptualised as repeating combinations of inorganic secondary building units (SBUs or 'nodes') bridged by multitopic organic ligands (or 'linkers').[224] This generates infinitely extended multidimensional network structures which demonstrate long-range order and high crystallinity (Fig. 1.15).[225] The unprecedented tunability and surface areas of MOFs make them versatile tools for advancing divergent emergent technologies to tackle several substantial scientific challenges.[226–228]

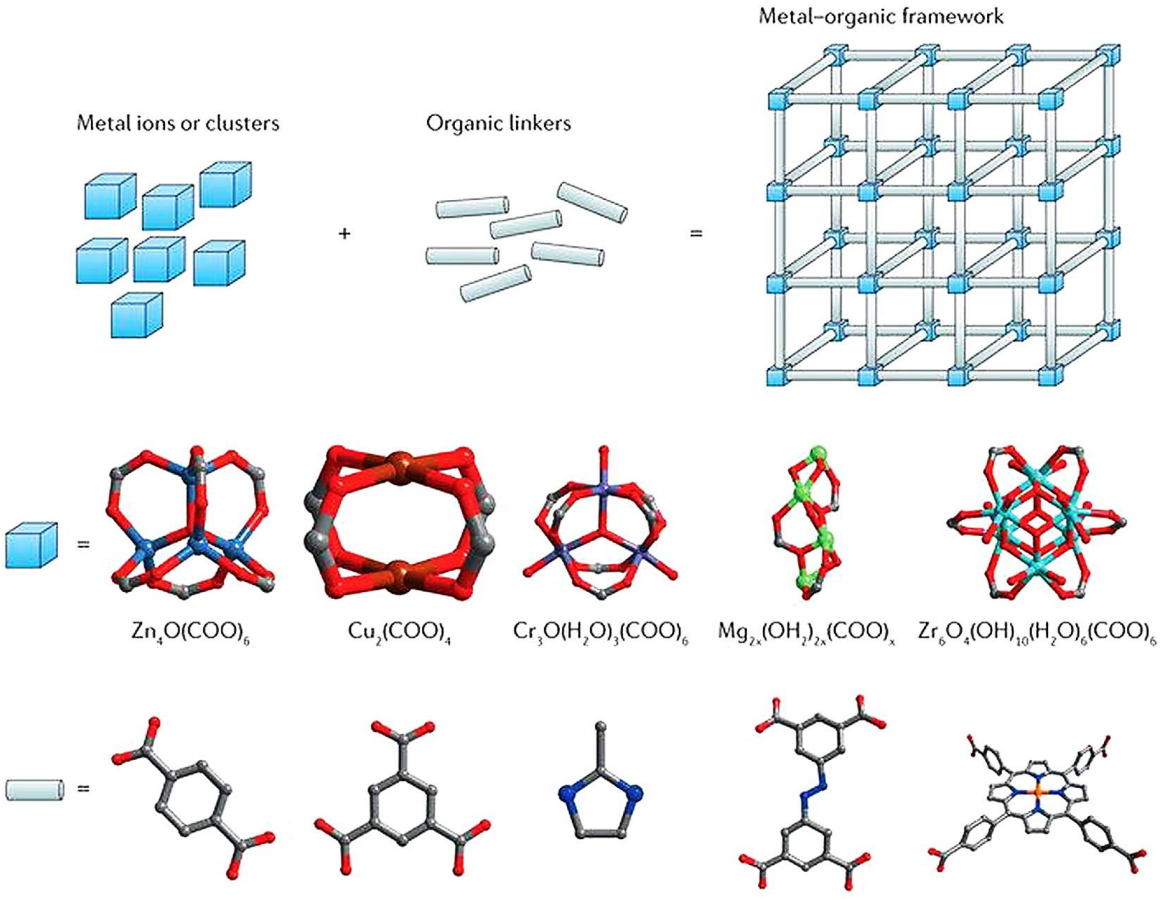

Figure 1.15: Model depicting the assembly of inorganic and organic components to give an infinitely extended MOF (top). Some representative SBU clusters featuring Zn^{II}, Cu^{II}, Mg^{II} Cr^{III} and Zr^{IV} metal ions are shown (middle), in addition to a selection of ligands typically employed in MOF synthesis (bottom), which commonly contain carboxylate, imidazolate, azolate, phosphonate or porphyrin functional groups. Colour scheme: C grey, O red, N blue, Zn^{II} light blue, Cu^{II} orange, Cr^{III} purple Mg^{II} green Zr^{IV} teal. Reproduced from Ref. 229.

1.5.2 Historical Perspective

Coordination polymers such as Prussian Blue dyes and other porous materials such as naturally occurring zeolite minerals have been studied since the early 18th century.[230] However, their structures were not successfully elucidated until the 1970s with the debut of suitable X-ray and spectroscopic techniques.[231,232] At this time, the developing field of crystal engineering sought to discover: 'Can the structures of crystalline solids be predicted from a knowledge of their chemical compositions?'.[233] Despite the apparent simplicity of this question, definitively answering it has proved elusive.[234–236]

In 1989, Robson and Hoskins reported the first deliberately designed framework structure.[237] Robson intended to generate an infinitely extended 3D network constructed from components displaying analogous connectivity to the carbon atoms of diamond. To achieve this, the tetranitrile ligand $C(C_6H_4CN)_4$ was selected to complex with the metal ion Cu^I, which typically adopts tetrahedral coordination environments. Adding the ligand $C(C_6H_4CN)_4$ to $Cu(MeCN)_4BF_4$ (MeCN = acetonitrile) in MeCN, before allowing the solvent to slowly evaporate afforded crystals which were subsequently characterised by Hoskins using single crystal X-ray diffraction. This analysis revealed that, as intended, an infinitely extended framework structure $[Cu^I(C(C_6H_4CN)_4)]BF_4$ had formed which displayed the desired diamondoid topology depicted in Fig. 1.16a.[238]

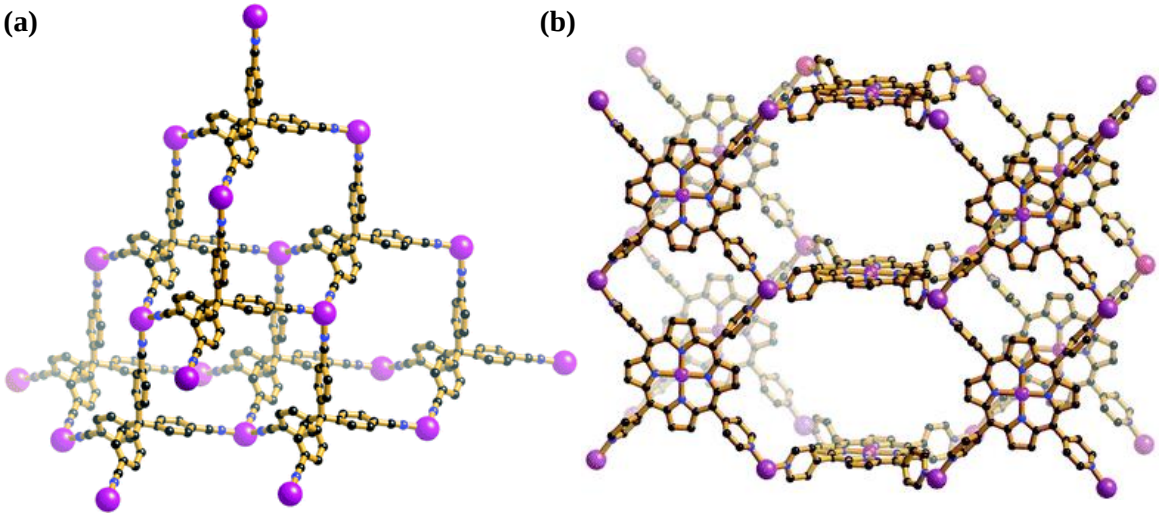

Figure 1.16: Two infinitely extended network structures prepared by Robson *et al.* (a) diamondoid $[Cu^I(C(C_6H_4CN)_4)]BF_4$ structure and (b) porphyrin-based $[Cu^I(TCP\text{-}Cu^{II})]BF_6$ framework featuring **pts** topology (TCP-Cu^{II} = *meso*-tetrakis(4-cyanophenyl)-21*H*,23*H*-porphyrinato]-Cu^{II}). H atoms, counterions and solvents omitted for clarity. Colour scheme: C black, N blue, Cu purple. Adapted from Ref. 238.

The following year, Robson *et al*. prepared a range of rationally constructed 3D network structures comprising metallic building units connected *via* organic linkers.[239–242] Included among the growing number of reported coordination polymers was a porous 3D framework featuring [5,10,15,20-tetrakis(4-cyanophenyl)-21*H*,23*H*-porphyrinato]-Cu^{II} linkers and mononuclear Cu^{I} nodes (Fig. 1.16b). This MOF was envisioned as having possible applications for heterogeneous catalysis due to the potential redox functionality of its porphyrin linkers.[243] Ahead of these pivotal discoveries, Robson predicted that a wide range of frameworks could be created simply by varying the nature of organic ligands and metallic nodes employed.[244,245]

In 1995, the term "metal-organic framework" was coined by Yaghi *et al*. in a paper describing a porous 3D interpenetrated network comprising Cu^{I} nodes and bpy ligands formulated as $Cu(bpy)_{1.5}{\cdot}NO_3(H_2O)_{1.25}$.[246] In 2003, O'Keeffe and co-workers articulated the principle that MOF architectures could be controlled through judicious selection of linkers and nodes in an approach known as "reticular synthesis".[247] This principle is elegantly exemplified by the isoreticular series of MOF-5 analogues (Fig. 1.17).[248] MOF-5 ($[Zn^{II}_4O(BDC)_3]$, BDC = 1,4-benzenedicarboxylate) is a 3D porous MOF with primitive cubic (**pcu**) topology, which features octahedral $\{Zn^{II}_4O\}$ SBUs bridged by ditopic BDC linkers.[249]

Following the discovery of MOF-5 in 1999 many isostructural analogues of this framework have been prepared using different ditopic linkers, demonstrating that the number of possible MOF structures is essentially infinite.[250,251] The ability to design MOFs with predetermined structures and cavities, combined with the demonstration of their permanent porosity by Kitagawa *et al*. triggered a rapid expansion of the field.[252] Since the pioneering work of Robson,[239] O'Keeffe,[222] Fujita,[253] Zaworotko,[254] Kitagawa[255] and Yaghi,[256] over 60,000 different MOFs have been reported in the Cambridge Structural Database (CSD).[257]

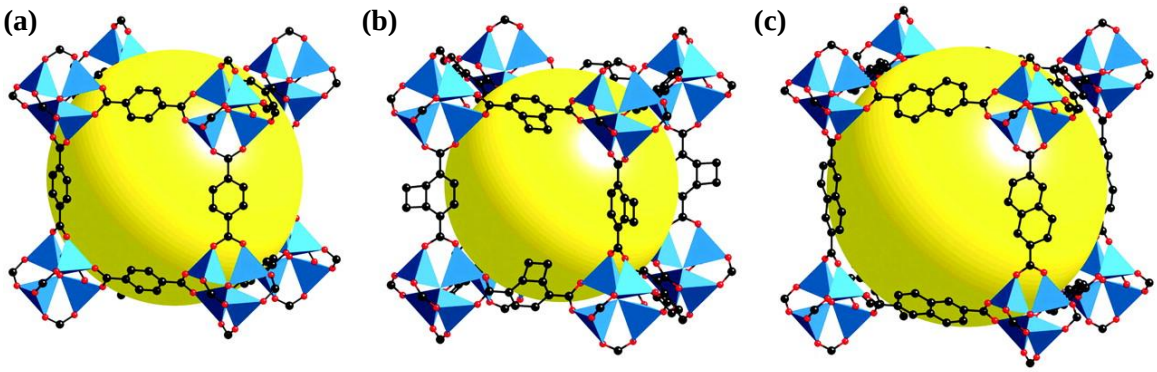

Figure 1.17: Crystal structures of the isoreticular series (a) MOF-5, (b) IRMOF-6 and (c) IRMOF-8 (IRMOF = isoreticular metal-organic framework). Hydrogen atoms have been omitted for clarity. Colour scheme: C black, O red, Zn^{II} centres are displayed as blue polyhedra. The void space is represented by yellow spheres. Reproduced from Ref. 248.

1.5.3 Synthesis of Metal-Organic Frameworks

MOFs are typically synthesised in the liquid-phase by combining a metal salt with an organic ligand in a suitable solvent system. This mixture is then kept at a certain temperature either below the boiling point of the solvent (classical method),[258] or above the boiling point of the solvent in a sealed vessel (solvothermal method).[259] Under suitable conditions, this will lead to the formation of crystalline MOF compound *via* a self-assembly process.[260,261] As the substitution of terminal ancillary ligands by polytopic ligands results in the formation of higher dimensional frameworks, heating favours MOF self-assembly for entropic reasons.[262] Other structure-directing factors which affect MOF synthesis are pH values, the nature of the solvent and the presence of counter ions or other templating auxiliary molecules in the reaction mixture.[258,263,264] Although conventional, elevated-temperature liquid phase MOF synthesis is currently the most widely employed method,[265] several other techniques exist such as electrochemical,[266] microwave assisted,[267] mechanochemical[268] and sonochemical synthesis.[269]

A MOF's SBUs provide directional information and can comprise one or more metal ions to form clusters with a range of geometric configurations, such as square paddle-wheels, octahedra, infinite rods and others.[270–272] Several cationic species can constitute a MOF's nodes, for example alkaline earth metals, transition metals and lanthanides.[258,273] Organic linkers extend the framework by connecting inorganic nodes through coordinative bonds, thus generating infinitely repeating arrays.[274] Ligands typically employed in MOF synthesis are polytopic, multifunctional moieties bearing binding groups such as carboxylates, phosphonates, pyridyls or imidazolates.[275] Rigid aromatic ligands are often favourable to flexible linkers, as the former can confer crystallinity, porosity and stability to the MOF.[221,276]

One synthetic strategy which is commonly applied to access permanently porous 3D MOFs is to pillar 2D layered frameworks using ditopic linkers such as bipyridine derivatives.[277–279] Choe *et al*. demonstrated this approach with the synthesis of three porphyrin paddle-wheel (PPF) MOFs; PPF-3, PPF-4 and PPF-5.[280] A reaction between either tetrakis(4-carboxyphenyl)porphyrin or [tetrakis(4-carboxyphenyl)porphyrinato]-Pd^{II} and Zn^{II} or Co^{II} nitrate under solvothermal conditions generates a 2D network with a 'checkerboard' pattern comprising $\{M_2(COO)_4\}$ paddlewheel SBUs (where M = Co^{II} or Zn^{II}) that are bridged by tetratopic porphyrin linkers. This layered structure can then be pillared using 4,4′-bipyridine (bpy) linkers, affording the formation of three 3D MOFs. Interestingly, the presence of Co^{III}, Zn^{II} or Pd^{II} in the macrocyclic cavity determines the network's topology (Fig. 1.18).

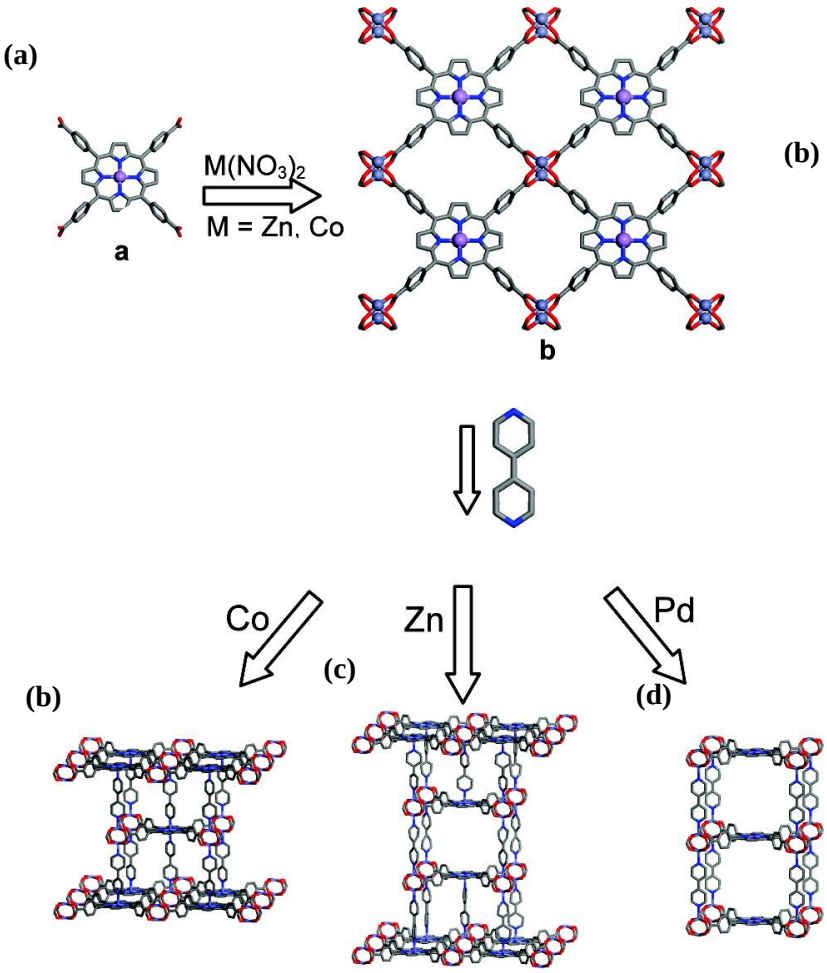

Figure 1.18: Scheme showing the reaction between (a) porphyrin ligands and metal nitrates giving (b) infinite 2D sheets. These 'checkerboard' layers are then pillared using bpy to generate (c) PPF-3, (d) PPF-4 and (e) PPF-5. The stacking arrangements of these 3D MOFs is dictated by the preferred coordination geometry of the metalloporphyrin's cation. Colour scheme: C grey, O red, N blue M (Co, Zn or Pd) purple. Adapted from Ref. 280.

In addition to their facile synthesis and (in many cases) favourable thermal and chemical stabilities,[281] one of the key desirable features of MOF structures is their ability to be rationally designed.[222] Through careful preselection of appropriate building blocks, predetermined network architectures with tunable compositions and desirable properties can be prepared.[277] The extent to which the final structure of a MOF can be predicted is still the subject of debate.[258] However, the degree of synthetic control offered by MOFs is unparalleled in other important porous materials such as zeolites.[282] Through application of the principle of reticular synthesis, an enormous range of MOFs with diverse topologies and chemical constituents can be prepared that display diverse properties and potential applications.[247]

1.5.4 Properties

MOFs are highly tunable, crystalline, and porous materials which therefore often display unprecedented properties.[283] These materials can exhibit extremely low densities and exceptional surface areas, which are unmatched by any other material. For example, the MOFs NU-110 (NU = Northwestern University) and DUT-60 (DUT = Dresden University of Technology) exhibit surface areas of just under 8000 $m^2\ g^{-1}$.[284–286] The surface areas of these materials vastly exceed that of any other porous materials such as zeolites or activated charcoal, which typically exhibit surface areas of under 1000 $m^2\ g^{-1}$.[287–289]

The stability of a MOF is dictated by its topology and the nature of the ligands and SBUs from which it is constructed.[249] Several early MOFs comprising Cu^{II}- or Zn^{II}-based SBUs (including MOF-5) displayed promising characteristics, although were restricted from many applications due to their poor hydrolytic stabilities.[290] However, selecting linkers which form strong coordinative bonds to highly connected nodes can afford frameworks which are highly durable under a range of conditions.[291] For example, in 2005 Férey *et al*. reported a highly porous and hydrolytically stable MOF, MIL-101 (MIL = Matérial Institut Lavoisier) with the formula $[Cr_3F(H_2O)_2O(BDC)_3]$.[292] Submerging this material in H_2O at ambient temperatures for many months does not cause the framework to decompose.[293,294] In addition, the framework UiO-66 (UiO = University of Oslo) which is formulated as $[Zr_6O_6(OH)_4(BDC)]$ can tolerate being boiled in H_2O for several hours without the BDC ligands being displaced by the solvent.[220,295]

1.5.5 Applications

The unique properties of MOFs give them a wide range of potential applications in areas such as CO_2 storage, H_2 storage, molecular separation, drug delivery and spintronics.[296–299] MOFs are also particularly promising for catalytic applications, as they represent a rational synthetic avenue to afford highly ordered structures with well-defined catalytically active sites.[300] Following the discovery of the first catalytically active MOF of the formula $[Cd(bpy)_2](NO_3)_2$ by Fujita *et al*. in 1994,[301] this area has expanded significantly and many more catalytically active frameworks have since been reported in the literature.[302,303,304]

The exceptional surface areas and porosities of MOFs allow them to mediate heterogeneous catalytic processes at very high reaction rates, as MOF structures can be prepared that are densely populated with substrate-accessible active sites.[303,305,306] Moreover, many MOFs

contain SBUs with coordination sites that are bound by labile solvent moieties, known as open metal sites (OMSs).[307] These sites facilitate catalytic reactions because ligand exchange at an OMS allows a substrate to interact with an SBU without compromising the MOF's structural integrity. Therefore, an OMS acts as a Lewis acid catalyst. Hence, OMSs can facilitate catalytic transformations of a substrate within a MOF.

Alternatively, catalytic OMSs can be incorporated within a MOF's linkers, as is the case for frameworks constructed from metalloporphyrin ligands.[221,308] A MOF displaying OMSs can have an activity comparable to a homogeneous catalyst, whilst retaining the practical advantages of a heterogeneous catalyst. These advantages include facile separation of catalyst from the reaction mixture and improved activity and stability owing to spatial separation of the MOF's active sites.[302,309,310] As the morphology of a MOF's pores can be predetermined, MOF catalysts offer an additional advantage as they can be designed to selectively catalyse only substrates of the right size and shape to enter their pores.[311]

1.5.6 Metal-Metalloporphyrin Frameworks

Metal-metalloporphyrin frameworks (MMPFs) are a special class of MOF in which porphyrin moieties are incorporated into a framework as functional constituents.[221,277,312] MMPFs can be prepared by introducing coordinating functional groups at a porphyrin's *meso*-positions, giving polytopic porphyrin ligands capable of bridging metallic nodes.[313,314] The synthetic principals developed for MOFs such as reticular synthesis translate to MMPF synthesis: Rigid building blocks are combined giving rationally designed, supramolecular architectures with desirable properties.[247] The metal ion of a metalloporphyrin may also act as a mononuclear SBU.[315]

The first MMPF was reported in 1991 by Robson *et al*. Reacting [*meso*-tetra(4-pyridyl)porphinato]-Pd^{II} (MTPP-Pd^{II}) and $Cd(NO_3)_2{\cdot}4H_2O$ in a mixture of boiling MeOH and H_2O generated a 3D framework with the formula $[Cd^{II}_2(MTPP\text{-}Pd^{II})(NO_3)_4(H_2O)_4]{\cdot}5H_2O$. This MMPF comprises mononuclear Cd^{II} nodes bridged by palladium tetrapyridyl porphyrin linkers.[244] Since the synthesis of this prototypal framework, many fascinating MMPFs have been created for diverse applications such as molecular separation,[314] light-harvesting,[316] and heterogeneous catalysis.[317–320]

MMPFs offer many advantages when exploited as catalytic systems.[318,321] This is a result of the favourable characteristics of MOFs for catalysis, combined with the easily manipulatable

light-harvesting and redox properties of metalloporphyrins.[222] Catalytic transformations mediated by MMPF's can occur either at an OMS within a node or at a metalloporphyrin moiety.[322] Moreover, as the macrocyclic cavity of a porphyrin ligand can be pre-synthetically metallated with an array of metal ions, additional functionality can be conferred to the MMPF. Therefore, MMPFs are highly tunable materials which can display high OMS densities.

The literature contains many examples of MMPFs which have been successfully employed as heterogeneous, biomimetic catalysts for a broad range of oxidation reactions.[221] Pioneering studies by O'Keeffe *et al*.,[323] Eddaoudi *et al*.,[324] Hupp *et al*.,[325] Zhou *et al*.[326] and Wu *et al*.[327] demonstrate the promising potential of this class of compounds as oxidation catalysts. A selection of notable MMPFs which display redox-catalytic activity are discussed below.

In 2012, Chen *et al*. demonstrated the heterogeneous biomimetic oxidation catalytic activity of the 3D MMPF MMPF-6 (Fig. 1.19a).[328] MMPF-6 is constructed from tetracarboxylate TCPP-$Fe^{III}Cl$ (TCPP = [*meso*-tetrakis(4-carboxyphenyl)porphyrinato]) linkers which bridge hexanuclear $\{Zr_6O_8(CO_2)_8(H_2O)_8\}$ SBUs and is formulated as $[(Zr_6O_8(H_2O)_8(TCPP\text{-}Fe^{III}Cl)_2)]\cdot 6H_2O$. This framework features large 1D hexagonal and triangular channels with diameters of *ca*. 36 and 12 Å, respectively. MMPF-6 exhibits excellent catalytic activity towards the peroxidation of 1,2,3-trihydroxybenzene, and can be recycled multiple times.

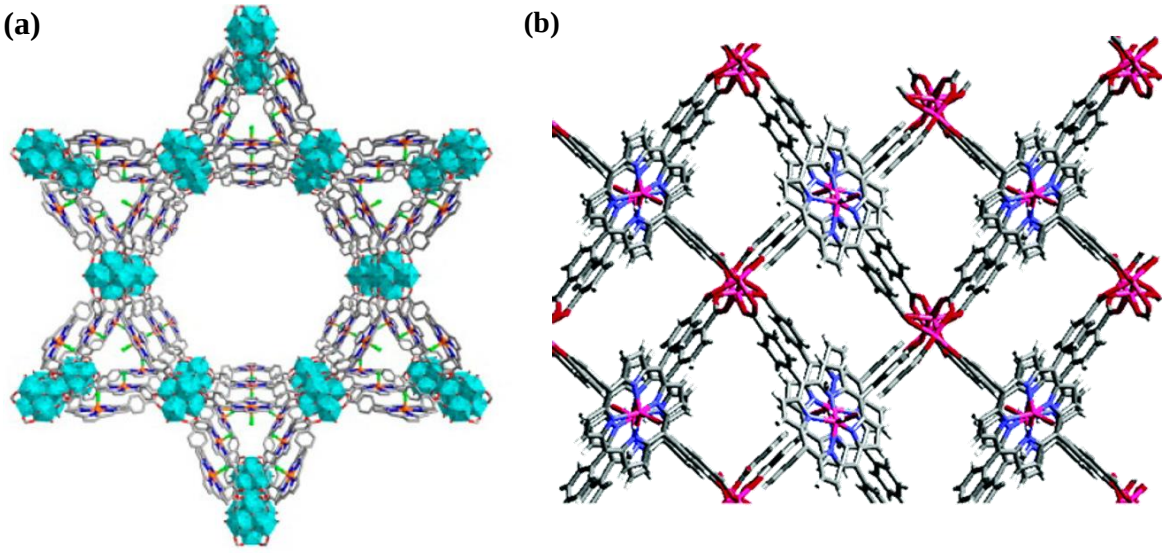

Figure 1.19: Crystal structures of two MMPFs which demonstrate oxidation catalytic activity (a) MMPF-6, formulated as $[(Zr_6O_8(H_2O)_8(TCPP\text{-}Fe^{III}Cl)_2)]\cdot 6H_2O$ and (b) PIZA-3, which is of the formula $[Mn_{1.5}(TCPP\text{-}Mn^{III})(DMF)]\cdot 5DMF$. Constitutional and coordinated solvent molecules have been omitted for clarity. Colour scheme: C, grey, O, red, N blue, Cl, green; Zr, turquoise polyhedra, Mn pink. Reproduced from Refs. 329 and 328.

Suslick *et al*. prepared a catalytically active MMPF PIZA-3 (PIZA = porphyrinic Illinois zeolite analogue) of the formula $[Mn_{1.5}(TCPP\text{-}Mn^{III})(DMF)]\cdot 5DMF$ (DMF = *N*,*N*-dimethylformamide).[329] This compound comprises trinuclear Mn^{II}-based SBUs bridged by tetratopic TCPP-Mn^{III} ligands, which gives rise to an open framework structure with small (< 10 Å) channels (Fig. 1.19b). PIZA-3 is a robust heterogeneous catalyst for the oxidation of a range of linear and cyclic alkanes, and the epoxidation of cyclic alkenes. The activity of this MMPF is moderate, with catalytic yields comparable to that of homogeneous Mn^{III} porphyrins. This was rationalised to be due to the framework's relatively small pore diameter, which restricts substrates from entering the channels of this MMPF. Therefore, the substrate is instead oxidised at the surface of PIZA-3. This study illustrates the importance of large channels and substrate-accessibility of the active sites for a catalytically active framework.[329]

In 2011, Hupp *et al*. demonstrated the catalytic potential of the MMPF ZnMn-RPM (RPM = Robust Porphyrinic Material).[330] This framework comprises Zn paddlewheels bridged by tetracarboxylate TCPP linkers giving rise to 2D sheets. These sheets are pillared by ditopic DPFP-Mn^{III} (DPFP-Mn^{III} = [5,15-dipyridyl-10,20-bis(pentafluorophenyl)porphyrinato]-Mn^{III}) ligands generating a 3D porous structure of the formula $[Zn^{II}_2(TCPP)(DPFP\text{-}Mn^{III})]$. Catalytic studies revealed that ZnMn-RPM is an effective catalyst for the epoxidation of styrene and the oxidation of cyclohexane in the presence of the oxidant 2-(*tert*-butylsulfonyl)iodosylbenzene (Fig. 1.20). This MMPF achieved TONs which were more than double that of the homogeneous porphyrin [5,10,15,20-tetrakis(pentafluorophenyl)porphyrinato]-Mn^{III}Cl. However, an induction period of *ca*. 250 minutes was observed before the activity reached its *max*. rate, which was attributed to the time taken for the reactants penetrate the channels of ZnMn-RPM.

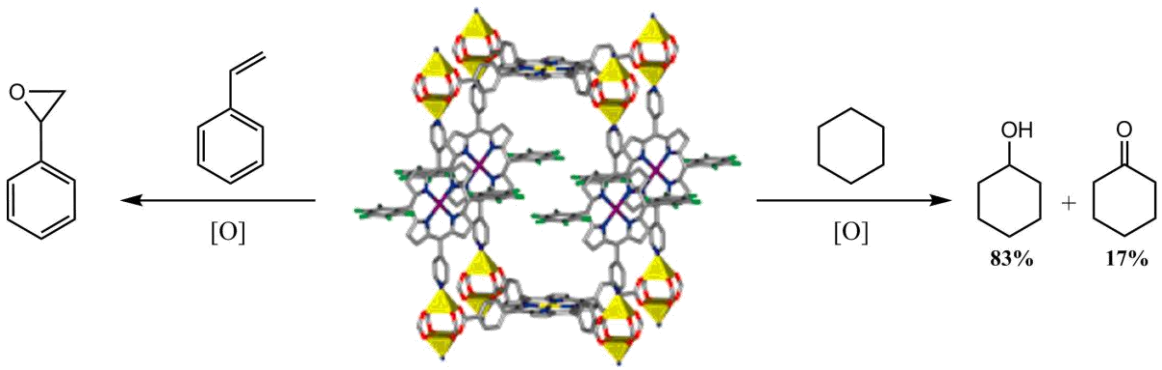

Figure 1.20: Catalytic transformations mediated by ZnMn-RPM in the presence of 2-(*tert*-butylsulfonyl)iodosylbenzene oxidant ([O]). ZnMn-RPM is catalytically active towards the epoxidation of styrene (left) and the oxidation of cyclohexane to form cyclohexanol and cyclohexanone with a selectivity of 83% and 17%, respectively (right). Colour scheme: Zn yellow polyhedra, Mn purple, F green, C grey, N blue O red, H white. Adapted from Ref. 330.

1.5.7 MOFs for H_2O Splitting Catalysis

In recent years, the structural versatility, porosity and hydrolytic stability of many MOFs has led to their use as catalysts for H_2O splitting.[220] Their high surface areas facilitate fast catalytic kinetics, whilst their tunable light absorption and redox properties make MOFs a promising platform for designing OER or HER photocatalysts.[331–333] Moreover, the modularity of MOFs provides an avenue to integrate the components required for light-induced H_2O splitting into a combined heterogeneous supramolecular system.

A framework comprising redox-active SBUs acting as WOCs or HECs stabilised by photoactive linkers acting as PSs may display intrinsic catalytic activity.[334] Combining a PS with a WOC or a HEC in a MOF ensures the close spatial proximity of these species, thus promoting charge transfer and therefore catalytic activity.[335] The tunability of MOFs is also advantageous, as Aziz *et al*. recently demonstrated using computational simulations that the bandgap of an MMPF can be aligned to facilitate the photocatalytic OER or HER by changing the identity of the metal ion present in the metalloporphyrin linkers.[336]

A number of recent investigations demonstrate the potential of MOFs as H_2O splitting catalysts.[337,338,339] For example, Chi *et al*. reported the photocatalytic H_2O oxidation activity of MIL-101(Fe).[340] Upon irradiation of this WOC the presence of $[Ru(bpy)_3](ClO_4)_2$ PS and $Na_2S_2O_8$ SEA This MOF achieved a *max*. TON = 27.3 and a TOF = 0.1 s^{-1}. Under electrochemical conditions, the *max*. current density achieved using MIL-101(Fe) was 4.2 mA cm^{-2}.

Several Co-containing MOFs have successfully been used as earth-abundant catalysts for the OER which display excellent activity.[341,342,343] For example, in 2017 Jiang *et al*. demonstrated the excellent OER activity of a cobalt-citrate MOF constructed from a $\{Co_4O_4\}$ cubane SBUs under electrochemical conditions.[344] At an applied overpotential of 408 mV, this MOF delivered a current density of 10 mA cm^{-2}. The OER activity of this MOF is greater than that observed using the benchmark transition metal-based WOC, Co_3O_4.

In September 2019, Huang *et al*. demonstrated the exceptionally high activity of a Co^{II}-based MOF towards catalytic H_2O oxidation.[345] A reaction between $Co(OAc)_2$ and 1,4-benzenedi(1*H*-1,2,3-triazole) (H_2bdt) under solvothermal conditions generated a framework comprising $\{Co^{II}_8OH_6\}$ SBUs connected by triazolate ligands with the formula $[Co_8(OH)_6(bdt)_4(Hbdt)_2]$ (Fig. 1.21). The high durability and surface area, and the presence of open metal sites prompted an investigation into the OER properties of this framework.[346]

Irradiating $[Co_8(OH)_6(bdt)_4(Hbdt)_2]$ in the presence of $[Ru(bpy)_3]SO_4$ PS and $Na_2S_2O_8$ SEA at pH = 9 rapidly resulted in O_2 production. In this photochemical test, the MOF exhibited an apparent TOF = 3.05 s^{-1} and a TON = 1.2 × 10^6. The TON of this MOF exceeds that of any previously reported WOC by two orders of magnitude. Moreover, in electrochemical experiments the framework induced a current density of 2.0 mA cm^{-1} at a very low overpotential of 353 mV. These studies highlight the powerful potential of MOF structures to mediate H_2O oxidation catalysis.

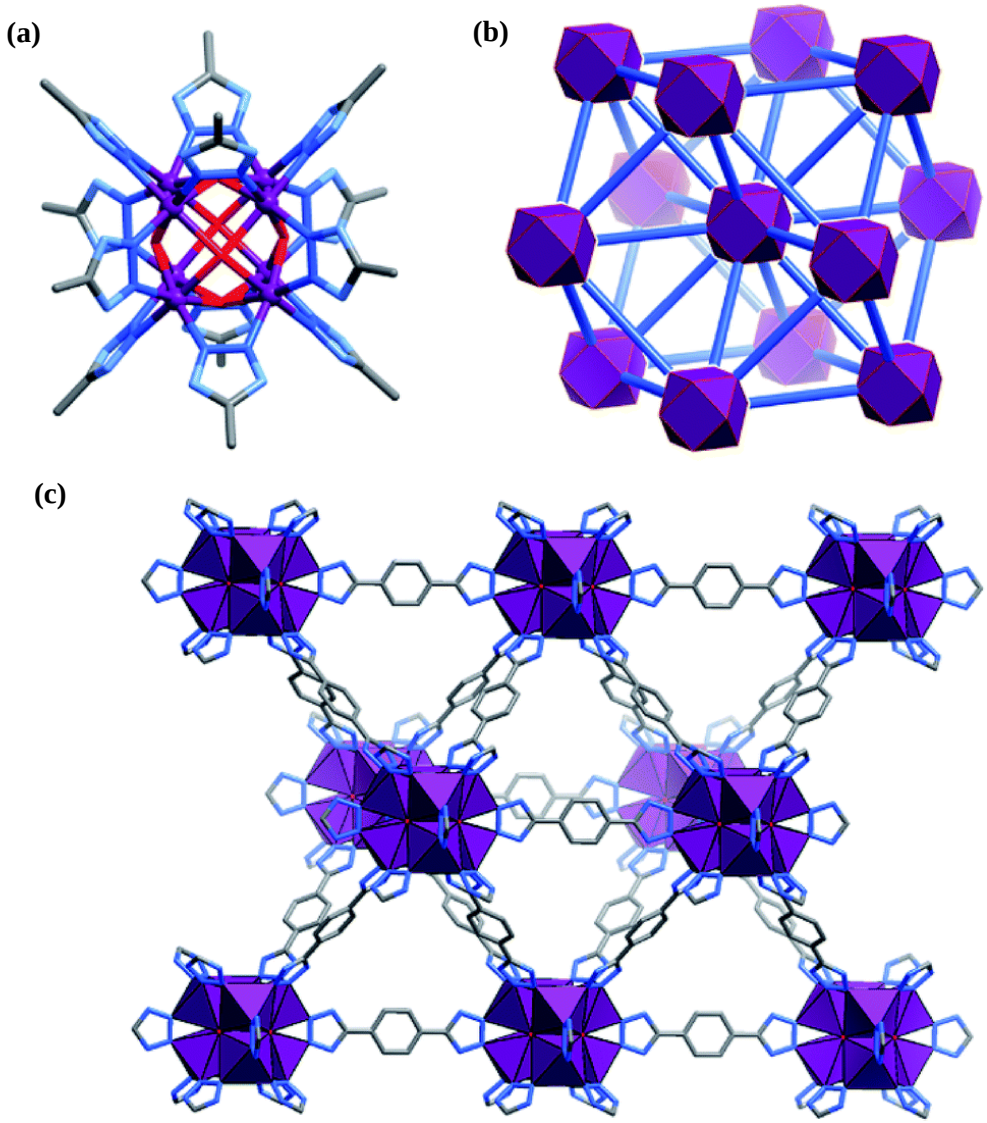

Figure 1.21: Crystal structure of the OER active MOF $[Co_8(OH)_6(bdt)_4(Hbdt)_2]$ showing (a) the 12-connected octacobalt cluster, (b) a topological reduction of the framework in which $\{Co^{II}_8OH_6\}$ SBUs are presented as violet polyhedra and triazolate linkers are simplified as blue sticks and (c) the 3D structure of the coordination framework in which Co^{II} centres displayed as violet polyhedra. Hydrogen atoms have been omitted for clarity. Adapted from Ref. 345.

1.6 Aims and Objectives

The overarching aim of this research project was to synthesise ditopic porphyrin ligands to use in the preparation of novel MMPFs, coordination polymers and complexes with potential catalytic applications. A further aim was to identify Co- and Mn-based metallo-supramolecular structures which may display catalytic H_2O oxidation activity. The ultimate aim of this investigation was to discover novel H_2O splitting catalysts based on bioinspired coordination compounds constructed from earth-abundant elements.

A delineation of the specific aims (❖) and associated objectives (➢) of this work follows:

❖ To prepare novel MMPFs, coordination polymers, complexes and clusters.

- ➢ The synthesis of the freebase and Cu^{II}-, Ni^{II}- and Pt^{II}-metallated complexes of the dicarboxylate porphyrin 5,15-bis(4-carboxyphenyl)-10,20-diphenylporphyrin (H_4**L1**).
- ➢ The use of these porphyrin ligands to synthesise MMPFs, coordination polymers and complexes that contain Co^{II} or Mn^{II} centres, and OMSs.
- ➢ Employing the ligands 2,6-bis(hydroxymethyl)-*p*-cresol (H_3**L2**) and *N*,*N*',*N*''-tris-(1-methyl)-1*H*-imidazol-4-ylmethylene)-1,3,5-triphenyl benzene (**L3**) in the synthesis of metallo-supramolecular clusters and complexes.
- ➢ To characterise novel compounds using single crystal X-ray diffraction and other physicochemical characterisation methods.

❖ To identify compounds with potential catalytic H_2O splitting properties.

- ➢ Examining the structures of novel MMPFs and porphyrin-based coordination polymers for motifs likely to confer catalytic H_2O splitting activity. Structures featuring potentially redox-active Co^{II}- or Mn^{II}-based SBUs, large channels, substrate-accessible OMSs were selected to test for catalytic OER or HER activity.
- ➢ Selection of polynuclear coordination complexes from the literature whose structural characteristics relate to those of PS II to use as biomimetic OEC model systems for H_2O oxidation, paying particular attention to high-nuclearity Mn-oxo clusters stabilised by non-innocent ligands which feature cubane-motifs and labile solvent sites.

- Following on from this, the final aim of this project was to determine the catalytic H_2O splitting properties of compounds identified as promising for this purpose, with a particular focus on OER catalysis. The following objectives were set out to achieve this:

  - To develop an experimental methodology to quantitively characterise photocatalytic H_2O splitting activity in terms of TONs and TOFs.
  - To test the light-driven H_2O splitting catalytic activities of Co- and Mn-based materials.
  - To further assess the catalytic properties of any compounds displaying light-driven OER activity under electrochemical conditions.
  - To conduct post-catalytic tests using spectroscopic techniques to rationally assign the true O_2 evolving catalyst in OER experiments.

The porphyrin, *p*-cresol and imine ligands used in the preparation of materials tested for catalytic H_2O splitting activity are presented in Fig. 1.22.

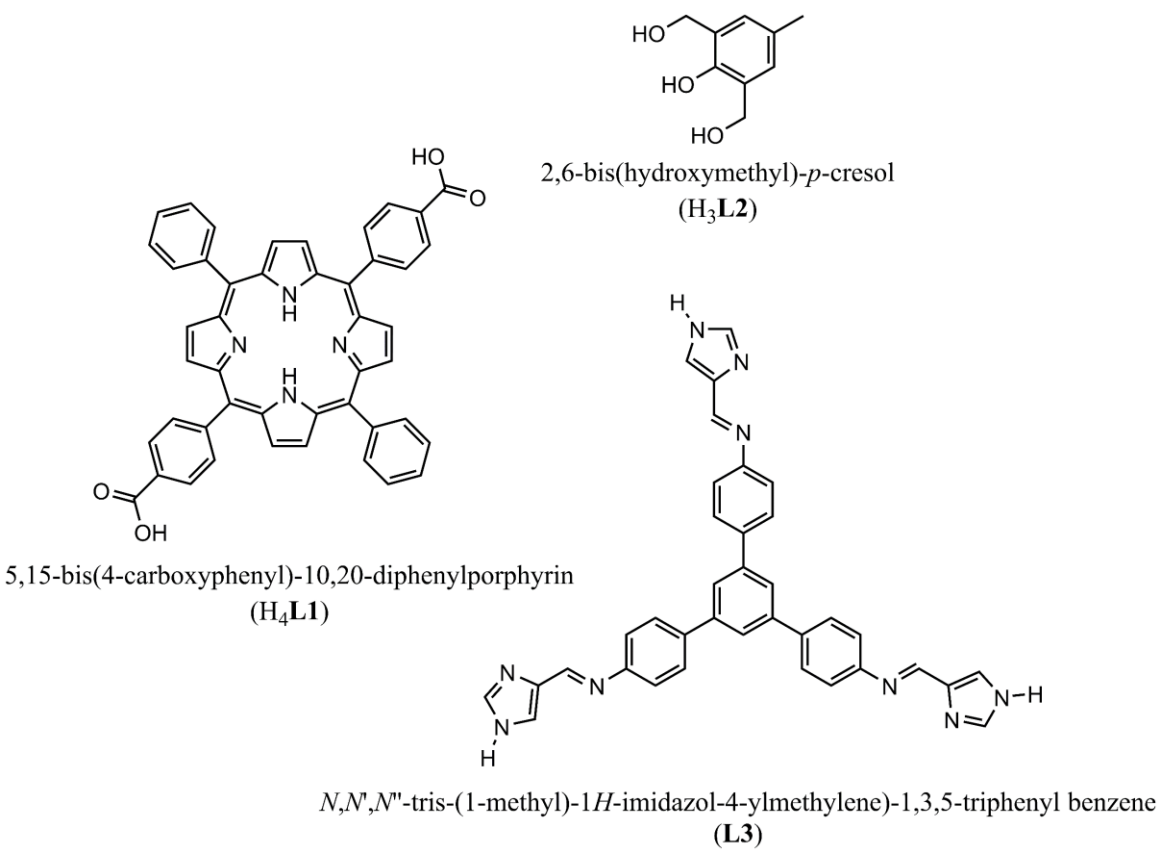

Figure 1.22: Structures of the ligands H_4**L1**, H_3**L2** and **L3** employed in the synthesis of coordination complexes, polymers and frameworks. Several transition metal complexes of the porphyrin H_4**L1** were also prepared, affording the metalloporphyrin ligands H_2**L1**-Cu^{II}, H_2**L1**-Ni^{II} and H_2**L1**-Pt^{II}, which were used in the synthesis of novel compounds.

Chapter 2 describes the synthesis of the porphyrin linkers H_4**L1**, H_2**L1**-Cu^{II}, H_2**L1**-Ni^{II} and H_2**L1**-Pt^{II}. The ligand H_2**L1**-Cu^{II} was then employed to synthesise two novel Co^{II}-based MMPFs (**1** and **2**) which are characterised using single crystal X-ray diffraction and other physicochemical characterisation techniques. Following this, the experimental setup and protocol developed to measure light-driven H_2O oxidation catalysis is briefly outlined. Using this setup, the light-induced O_2 evolution properties of **1** are established, and subsequent characterisation experiments rule out the possibility of catalytically active CoO_x species being the source of the observed O_2 evolution.

Chapter 3 details a series of catalytic OER screening experiments which identified nine Mn-based, catalytically active compounds (**3** – **11**). The most active of these materials (**11**) was resynthesized and characterised to facilitate further catalytic testing, which resulted in the discovery of a novel polymorph of this bioinspired Mn-oxo cluster. The chapter concludes with an investigation of the catalytic properties of **11**, which revealed that this compound yields exceptionally high catalytic OER activity.

Chapter 4 discusses the synthesis of a trinuclear, imine-stabilised Co^{II}-based complex (**12**) which exhibits high catalytic OER activity. The H_2O oxidation behaviour of this material was probed in photochemical and electrochemical experiments. Ultimately, computational modelling was applied to elucidate the mechanism of O_2 evolution by **12**.

Chapter 5 deals with several Mn^{II}- (**13** – **16**), Zn^{II}- (**17**) and In^{III}-based (**18**) MMPFs, coordination polymers and complexes which were prepared using the porphyrin ligands H_4**L1**, H_2**L1**-Cu^{II} and H_2**L1**-Ni^{II}. Examination of the crystal structures of **13** – **16** revealed that these compounds contained Mn^{II} centres and OMSs. Hence, the light-driven catalytic OER or HER activities of these materials were assessed.

1.7 References

1 N. S. Lewis and D. G. Nocera, *Proc. Natl. Acad. Sci.*, 2006, **103**, 15729–15735.

2 R. J. Detz, J. N. H. Reek and B. C. C. van der Zwaan, *Energy Environ. Sci.*, 2018, **11**, 1653–1669.

3 H. Hellevang and P. Aagaard, *Sci. Rep.*, 2015, **5**, 17352.

4 U. Siegenthaler, T. F. Stocker, E. Monnin, D. Lüthi, J. Schwander, B. Stauffer, D. Raynaud, J.-M. Barnola, H. Fischer, V. Masson-Delmotte and J. Jouzel, *Science*, 2005, **310**, 1313–1317.

5 R. Heede, *Clim. Change*, 2014, **122**, 229–241.

6 D. Schimel, B. B. Stephens and J. B. Fisher, *Proc. Natl. Acad. Sci.*, 2015, **112**, 436–441.

7 G. A. Meehl, W. M. Washington, W. D. Collins, J. M. Arblaster, A. Hu, L. E. Buja, W. G. Strand and H. Teng, *Science*, 2005, **307**, 1769–1772.

8 S. Solomon, G.-K. Plattner, R. Knutti and P. Friedlingstein, *Proc. Natl. Acad. Sci.*, 2009, **106**, 1704–1709.

9 V. Ramanathan and Y. Feng, *Proc. Natl. Acad. Sci.*, 2008, **105**, 14245–14250.

10 J. Hansen, M. Sato, R. Ruedy, P. Kharecha, A. Lacis, R. Miller, L. Nazarenko, K. Lo, G. A. Schmidt, G. Russell, I. Aleinov, S. Bauer, E. Baum, B. Cairns, V. Canuto, M. Chandler, Y. Cheng, A. Cohen, A. Del Genio, G. Faluvegi, E. Fleming, A. Friend, T. Hall, C. Jackman, J. Jonas, M. Kelley, N. Y. Kiang, D. Koch, G. Labow, J. Lerner, S. Menon, T. Novakov, V. Oinas, J. Perlwitz, J. Perlwitz, D. Rind, A. Romanou, R. Schmunk, D. Shindell, P. Stone, S. Sun, D. Streets, N. Tausnev, D. Thresher, N. Unger, M. Yao and S. Zhang, *Atmos. Chem. Phys.*, 2007, **7**, 2287–2312.

11 S. Berardi, S. Drouet, L. Francas, C. Gimbert-Surinach, M. Guttentag, C. Richmond, T. Stoll and A. Llobet, *Chem. Soc. Rev.*, 2014, **43**, 7501–7519.

12 S. C. Anenberg, P. Achakulwisut, M. Brauer, D. Moran, J. S. Apte and D. K. Henze, *Sci. Rep.*, 2019, **9**, 11552.

13 R. Eisenberg, H. B. Gray and G. W. Crabtree, *Proc. Natl. Acad. Sci.*, 2019, 201821674.

14 A. Cho, *Science*, 2010, **329**, 786–787.

15 T. Grewe, M. Meggouh and H. Tüysüz, *Chem. Asian J.*, 2016, **11**, 22–42.

16 M. Kumar, A. Dubey, N. Adhikari, S. Venkatesan and Q. Qiao, *Energy Environ. Sci.*, 2015, **8**, 3134–3159.

17 B. Parida, S. Iniyan and R. Goic, *Renew. Sustain. Energy Rev.*, 2011, **15**, 1625–1636.

18 B. O'Regan and M. Gratzel, *Nature*, 1991, **353**, 737–740.

19 R. R. King, D. C. Law, K. M. Edmondson, C. M. Fetzer, G. S. Kinsey, H. Yoon, R. A. Sherif and N. H. Karam, *Appl. Phys. Lett.*, 2007, **90**, 183516.

20 A. M. Alfantazi and R. R. Moskalyk, *Miner. Eng.*, 2003, **16**, 687–694.

21 Z. He, Y. Yang, J.-W. Liu and S.-H. Yu, *Chem. Soc. Rev.*, 2017, **46**, 2732–2753.

22 K. Branker, M. J. M. Pathak and J. M. Pearce, *Renew. Sustain. Energy Rev.*, 2011, **15**, 4470–4482.

23 H. Apostoleris, S. Sgouridis, M. Stefancich and M. Chiesa, *Nat. Energy*, 2019, **4**, 833–834.

24 N. Cox, D. A. Pantazis, F. Neese and W. Lubitz, *Interface Focus*, 2015, **5**, 20150009.

25 I. Staffell, D. Scamman, A. Velazquez Abad, P. Balcombe, P. E. Dodds, P. Ekins, N. Shah and K. R. Ward, *Energy Environ. Sci.*, 2019, **12**, 463–491.

26 M. A. Rosen and S. Koohi-Fayegh, *Energy Ecol. Environ.*, 2016, **1**, 10–29.

27 M. W. Kanan and D. G. Nocera, *Science*, 2008, **321**, 1072–1075.

28 G. Ciamician, *Science*, 1912, **36**, 385–394.

29 D. Narzi, D. Bovi and L. Guidoni, *Proc. Natl. Acad. Sci.*, 2014, **111**, 8723–8728.

30 H. Anthony, *Philos. Trans. R. Soc. A Math. Phys. Eng. Sci.*, 2013, **371**, 1996.

31 P. M. Shih, J. Hemp, L. M. Ward, N. J. Matzke and W. W. Fischer, *Geobiology*, 2017, **15**, 19–29.

32 R. M. Soo, J. Hemp, D. H. Parks, W. W. Fischer and P. Hugenholtz, *Science*, 2017, **355**, 1436–1440.

33 R. Buick, *Philos. Trans. R. Soc. B Biol. Sci.*, 2008, **363**, 2731–2743.

34 J. F. Allen, W. B. M. de Paula, S. Puthiyaveetil and J. Nield, *Trends Plant Sci.*, 2011, **16**, 645–655.

35 M. S. W. Hodgskiss, P. W. Crockford, Y. Peng, B. A. Wing and T. J. Horner, *Proc. Natl. Acad. Sci.*, 2019, **116**, 17207–17212.

36 J. Barber and P. D. Tran, *J. R. Soc. Interface*, 2013, **10**, 20120984.

37 Govindjee, J. F. Kern, J. Messinger and J. Whitmarsh, *eLS*, 2010.

38 J. Barber and M. D. Archer, *J. Photochem. Photobiol. A Chem.*, 2001, **142**, 97–106.

39 T. Renger, V. May and O. Kühn, *Phys. Rep.*, 2001, **343**, 137–254.

40 M. Grabolle and H. Dau, *Biochim. Biophys. Acta*, 2005, **1708**, 209–218.

41 H. Inoue, T. Shimada, Y. Kou, Y. Nabetani, D. Masui, S. Takagi and H. Tachibana, *ChemSusChem*, 2011, **4**, 173–179.

42 M. P. Johnson, *Essays Biochem.*, 2016, **60**, 255–273.

43 U. Ulmer, T. Dingle, P. N. Duchesne, R. H. Morris, A. Tavasoli, T. Wood and G. A. Ozin, *Nat. Commun.*, 2019, **10**, 3169.

44 G. Renger and T. Renger, *Photosynth. Res.*, 2008, **98**, 53–80.

45 L.-X. Shi and W. P. Schröder, *Biochim. Biophys. Acta*, 2004, **1608**, 75–96.

46 K. N. Ferreira, T. M. Iverson, K. Maghlaoui and J. Barber, *Science* 2004, **303**, 1831–1839.

47 M. M. Najafpour and Govindjee, *Dalt. Trans.*, 2011, **40**, 9076–9084.

48 K. Saito, A. W. Rutherford and H. Ishikita, *Proc. Natl. Acad. Sci.*, 2013, **110**, 7690–7695.

49 H. van Amerongen and R. Croce, *Photosynth. Res.*, 2013, **116**, 251–263.

50 G. A. Jones and D. S. Bradshaw, *Front. Phys.*, 2019, **7**, 100.

51 H. Ishikita, W. Saenger, J. Biesiadka, B. Loll and E.-W. Knapp, *Proc. Natl. Acad. Sci.*, 2006, **103**, 9855–9860.

52 K. M. Davis and Y. N. Pushkar, *J. Phys. Chem. B*, 2015, **119**, 3492–3498.

53 D. J. Vinyard, G. M. Ananyev and G. Charles Dismukes, *Annu. Rev. Biochem.*, 2013, **82**, 577–606.

54 F. A. Armstrong, *Philos. Trans. R. Soc. B Biol. Sci.*, 2008, **363**, 1263–1270.

55 M. Barra, M. Grabolle, M. Haumann, P. Liebisch, C. Mu and H. Dau, *Science*, 2005, **310**, 1019–1021.

56 P. E. M. Siegbahn, *Proc. Natl. Acad. Sci.*, 2017, **114**, 4966–4968.

57 R. D. Britt, K. A. Campbell, J. M. Peloquin, M. L. Gilchrist, C. P. Aznar, M. M. Dicus, J. Robblee and J. Messinger, *Biochim. Biophys. Acta*, 2004, **1655**, 158–171.

58 Y. Umena, K. Kawakami, J.-R. Shen and N. Kamiya, *Nature*, 2011, **473**, 55–60.

59 E. M. Sproviero, J. A. Gascón, J. P. McEvoy, G. W. Brudvig and V. S. Batista, *J. Am. Chem. Soc.*, 2008, **130**, 3428–3442.

60 S. Paul, F. Neese and D. A. Pantazis, *Green Chem.*, 2017, **19**, 2309–2325.

61 H. Bao and R. L. Burnap, *Proc. Natl. Acad. Sci.*, 2015, **112**, 6139–6147.

62 J. Kern, R. Chatterjee, I. D. Young, F. D. Fuller, L. Lassalle, M. Ibrahim, S. Gul, T. Fransson, A. S. Brewster, R. Alonso-Mori, R. Hussein, M. Zhang, L. Douthit, C. de Lichtenberg, M. H. Cheah, D. Shevela, J. Wersig, I. Seuffert, D. Sokaras, E. Pastor, C. Weninger, T. Kroll, R. G. Sierra, P. Aller, A. Butryn, A. M. Orville, M. Liang, A. Batyuk, J. E. Koglin, S. Carbajo, S. Boutet, N. W. Moriarty, J. M. Holton, H. Dobbek, P. D. Adams, U. Bergmann, N. K. Sauter, A. Zouni, J. Messinger, J. Yano and V. K. Yachandra, *Nature*, 2018, **563**, 421–425.

63 P. Joliot, G. Barbieri and R. Chabaud, *Photochem. Photobiol.*, 1969, **10**, 309–329.

64 B. Kok, B. Forbush and M. McGloin, *Photochem. Photobiol.*, 1970, **11**, 457–475.

65 J. P. McEvoy and G. W. Brudvig, *Chem. Rev.*, 2006, **106**, 4455–4483.

66 H. Dau and M. Haumann, *Coord. Chem. Rev.*, 2008, **252**, 273–295.

67 K. M. Davis, B. T. Sullivan, M. C. Palenik, L. Yan, V. Purohit, G. Robison, I. Kosheleva, R. W. Henning, G. T. Seidler and Y. Pushkar, *Phys. Rev. X*, 2018, **8**, 41014.

68 J. Barber, *Biochim. Biophys. Acta*, 2004, **1655**, 123–132.

69 T. J. Meyer, M. H. V. Huynh and H. H. Thorp, *Angew. Chem. Int. Ed.*, 2007, **46**, 5284–5304.

70 M. Amin, L. Vogt, W. Szejgis, S. Vassiliev, G. W. Brudvig, D. Bruce and M. R. Gunner, *J. Phys. Chem. B*, 2015, **119**, 7366–7377.

71 M. M. Najafpour, A. N. Moghaddam, S. I. Allakhverdiev and Govindjee, *Biochim. Biophys. Acta*, 2012, **1817**, 1110–1121.

72 M. Schulze, V. Kunz, P. D. Frischmann and F. Würthner, *Nat. Chem.*, 2016, **8**, 576–583.

73 S. V. Baranov, G. M. Ananyev, V. V. Klimov and G. C. Dismukes, *Biochemistry*, 2000, **39**, 6060–6065.

74 K. Ifuku and T. Noguchi, *Front. Plant Sci.*, 2016, 7, 84.

75 H. Kühne and G. W. Brudvig, *J. Phys. Chem. B*, 2002, **106**, 8189–8196.

76 M. D. Kärkäs, O. Verho, E. V Johnston and B. Åkermark, *Chem. Rev.*, 2014, **114**, 11863–12001.

77 G. C. Dismukes, R. Brimblecombe, G. A. N. Felton, R. S. Pryadun, J. E. Sheats, L. Spiccia and G. F. Swiegers, *Acc. Chem. Res.*, 2009, **42**, 1935–1943.

78 J. S. Kanady, E. Y. Tsui, M. W. Day and T. Agapie, *Science*, 2011, **333**, 733–736.

79 C. Zhang, C. Chen, H. Dong, J.-R. Shen, H. Dau and J. Zhao, *Science*, 2015, **348**, 690–693.

80 S. Trouvelot, M.-C. Héloir, B. Poinssot, A. Gauthier, F. Paris, C. Guillier, M. Combier, L. Trdá, X. Daire and M. Adrian, *Front. Plant Sci.*, 2014, **5**, 592.

81 D. Zhao, D. Yuan and H.-C. Zhou, *Energy Environ. Sci.*, 2008, **1**, 222–235.

82 F. Ausfelder and A. Bazzanella, *Hydrogen in the Chemical Industry*, Wiley, New Jersey, 2016.

83 R. de Levie, *J. Electroanal. Chem.*, 1999, **476**, 92–93.

84 H. A. M. Snelders, *Ambix*, 1979, **26**, 116–133.

85 P. Tang and J. Arbiol, *Nanoscale Horiz.*, 2019, **4**, 1256–1276.

86 C. Xiang, K. M. Papadantonakis and N. S. Lewis, *Mater. Horizons*, 2016, **3**, 169–173.

87 H. Tributsch, in *Advances in Photoelectrochemical Water Splitting: Theory, Experiment and Systems Analysis*, The Royal Society of Chemistry, 2018, pp. 1–28.

88 J. H. Kim, D. Hansora, P. Sharma, J.-W. Jang and J. S. Lee, *Chem. Soc. Rev.*, 2019, **48**, 1908–1971.

89 N.-T. Suen, S.-F. Hung, Q. Quan, N. Zhang, Y.-J. Xu and H. M. Chen, *Chem. Soc. Rev.*, 2017, **46**, 337–365.

90 B. You and Y. Sun, *Acc. Chem. Res.*, 2018, **51**, 1571–1580.

91 X. Deng and H. Tüysüz, *ACS Catal.*, 2014, **4**, 3701–3714.

92 S. Chu, Y. Cui and N. Liu, *Nat. Mater.*, 2017, **16**, 16–22.

93 A. Fujishima and K. Honda, *Nature*, 1972, **238**, 37–38.

94 B. Zhang and L. Sun, *Chem. Soc. Rev.*, 2019, **48**, 2216–2264.

95 I. Roger, M. A. Shipman and M. D. Symes, *Nat. Rev. Chem.*, 2017, **1**, 3.

96 K. Park, Y. J. Kim, T. Yoon, S. David and Y. M. Song, *RSC Adv.*, 2019, **9**, 30112–30124.

97 C. S. Tan, K. W. Kemp, M. R. Braun, A. C. Meng, W. Tan, C. E. D. Chidsey, W. Ma, F. Moghadam and P. C. McIntyre, *Sustain. Energy Fuels*, 2019, **3**, 1490–1500.

98 X. Shi, H. Jeong, S. J. Oh, M. Ma, K. Zhang, J. Kwon, I. T. Choi, I. Y. Choi, H. K. Kim, J. K. Kim and J. H. Park, *Nat. Commun.*, 2016, **7**, 11943.

99 R. Fan, S. Cheng, G. Huang, Y. Wang, Y. Zhang, S. Vanka, G. A. Botton, Z. Mi and M. Shen, *J. Mater. Chem. A*, 2019, **7**, 2200–2209.

100 X. Chen and S. S. Mao, *Chem. Rev.*, 2007, **107**, 2891–2959.

101 S. Hoang, S. Guo, N. T. Hahn, A. J. Bard and C. B. Mullins, *Nano Lett.*, 2012, **12**, 26–32.

102 B. A. Pinaud, J. D. Benck, L. C. Seitz, A. J. Forman, Z. Chen, T. G. Deutsch, B. D. James, K. N. Baum, G. N. Baum, S. Ardo, H. Wang, E. Miller and T. F. Jaramillo, *Energy Environ. Sci.*, 2013, **6**, 1983–2002.

103 A. Hossain, K. Sakthipandi, A. K. M. Atique Ullah and S. Roy, *Nano-Micro Lett.*, 2019, **11**, 103.

104 J. Luo, S. K. Karuturi, L. Liu, L. T. Su, A. I. Y. Tok and H. J. Fan, *Sci. Rep.*, 2012, **2**, 451.

105 Z. Li, W. Luo, M. Zhang, J. Feng and Z. Zou, *Energy Environ. Sci.*, 2013, **6**, 347–370.

106 C. Jiang, S. J. A. Moniz, A. Wang, T. Zhang and J. Tang, *Chem. Soc. Rev.*, 2017, **46**, 4645–4660.

107 Y. Wang, A. Vogel, M. Sachs, R. S. Sprick, L. Wilbraham, S. J. A. Moniz, R. Godin, M. A. Zwijnenburg, J. R. Durrant, A. I. Cooper and J. Tang, *Nat. Energy*, 2019, **4**, 746–760.

108 M. Yagi, E. Tomita, S. Sakita, T. Kuwabara and K. Nagai, *J. Phys. Chem. B*, 2005, **109**, 21489–21491.

109 L. C. Clark, R. Wolf, D. Granger and Z. Taylor, *J. Appl. Physiol.*, 1953, **6**, 189–193.

110 D. Ressnig, M. Shalom, J. Patscheider, R. Moré, F. Evangelisti, M. Antonietti and G. R. Patzke, *J. Mater. Chem. A*, 2015, **3**, 5072–5082.

111 J. Li, R. Güttinger, R. Moré, F. Song, W. Wan and G. R. Patzke, *Chem. Soc. Rev.*, 2017, **46**, 6124–6147.

112 S. I. Shylin, M. V Pavliuk, L. D'Amario, F. Mamedov, J. Sá, G. Berggren and I. O. Fritsky, *Chem. Commun.*, 2019, **55**, 3335–3338.

113 C. Costentin, G. Passard and J.-M. Savéant, *J. Am. Chem. Soc.*, 2015, **137**, 5461–5467.

114 S. T. Kochuveedu, *J. Nanomater.*, 2016, **12**, 4073142.

115 M. Natali, E. Deponti, D. Vilona, A. Sartorel, M. Bonchio and F. Scandola, *Eur. J. Inorg.*

Chem., 2015, **2015**, 3467–3477.

116 J. Corredor, M. J. Rivero, C. M. Rangel, F. Gloaguen and I. Ortiz, *J. Chem. Technol. Biotechnol.*, 2019, **94**, 3049–3063.

117 H. Junge, N. Rockstroh, S. Fischer, A. Brückner, R. Ludwig, S. Lochbrunner, O. Kühn and M. Beller, *Inorganics*, 2017, **5**, 14.

118 H.-C. Chen, J. N. H. Reek, R. M. Williams and A. M. Brouwer, *Phys. Chem. Chem. Phys.*, 2016, **18**, 15191–15198.

119 H.-C. Chen, D. G. H. Hetterscheid, R. M. Williams, J. I. van der Vlugt, J. N. H. Reek and A. M. Brouwer, *Energy Environ. Sci.*, 2015, **8**, 975–982.

120 G. Landrou, A. A. Panagiotopoulos, K. Ladomenou and A. G. Coutsolelos, *J. Porphyr. Phthalocyanines*, 2016, **20**, 534–541.

121 B. C. M. Martindale, G. A. M. Hutton, C. A. Caputo and E. Reisner, *J. Am. Chem. Soc.*, 2015, **137**, 6018–6025.

122 M. D. Kärkäs, T. M. Laine, E. V Johnston and B. Åkermark, *Visible Light-Driven Water Oxidation Catalyzed by Ruthenium Complexes*, InTech, Rijeka, 2016.

123 E. Deponti and M. Natali, *Dalt. Trans.*, 2016, **45**, 9136–9147.

124 B. Limburg, E. Bouwman and S. Bonnet, *ACS Catal.*, 2016, **6**, 5273–5284.

125 S. Hamad, N. C. Hernandez, A. Aziz, A. R. Ruiz-Salvador, S. Calero and R. Grau-Crespo, *J. Mater. Chem. A*, 2015, **3**, 23458–23465.

126 K. J. Young, L. A. Martini, R. L. Milot, R. C. S. Iii, V. S. Batista, C. A. Schmuttenmaer, R. H. Crabtree and G. W. Brudvig, *Coord. Chem. Rev.*, 2012, **256**, 2503–2520.

127 A. Izgorodin, O. Winther-Jensen and D. R. MacFarlane, *Aust. J. Chem.*, 2012, **65**, 638–642.

128 M. Nippe, R. S. Khnayzer, J. A. Panetier, D. Z. Zee, B. S. Olaiya, M. Head-Gordon, C. J. Chang, F. N. Castellano and J. R. Long, *Chem. Sci.*, 2013, **4**, 3934–3945.

129 W. Liu, E. Hu, H. Jiang, Y. Xiang, Z. Weng, M. Li, Q. Fan, X. Yu, E. I. Altman and H. Wang, *Nat. Commun.*, 2016, **7**, 10771.

130 J. Deng, P. Ren, D. Deng, L. Yu, F. Yang and X. Bao, *Energy Environ. Sci.*, 2014, **7**, 1919–1923.

131 H. Dau and I. Zaharieva, *Acc. Chem. Res.*, 2009, **42**, 1861–1870.

132 K. C. Mavrokefalos and R. G. Patzke, *Inorganics*, 2019, 7.

133 J. D. Blakemore, R. H. Crabtree and G. W. Brudvig, *Chem. Rev.*, 2015, **115**, 12974–13005.

134 T. R. Cook, D. K. Dogutan, S. Y. Reece, Y. Surendranath, T. S. Teets and D. G. Nocera, *Chem. Rev.*, 2010, **110**, 6474–6502.

135 M. G. Walter, E. L. Warren, J. R. McKone, S. W. Boettcher, Q. Mi, E. A. Santori and N. S. Lewis, *Chem. Rev.*, 2010, **110**, 6446–6473.

136 J. H. Montoya, L. C. Seitz, P. Chakthranont, A. Vojvodic, T. F. Jaramillo and J. K.

Nørskov, *Nat. Mater.*, 2017, **16**, 70–81.

137 Z. W. Seh, J. Kibsgaard, C. F. Dickens, I. Chorkendorff, J. K. Nørskov and T. F. Jaramillo, *Science*, 2017, **355**, eaad4998.

138 J. Kiwi and M. Grätzel, *Angew. Chem. Int. Ed.*, 1978, **17**, 860–861.

139 J. Kiwi and M. Grätzel, *Angew. Chem. Int. Ed.*, 1979, **18**, 624–626.

140 A. Harriman, I. J. Pickering, J. M. Thomas and P. A. Christensen, *J. Chem. Soc. Faraday Trans. 1*, 1988, **84**, 2795–2806.

141 F. Lu, M. Zhou, Y. Zhou and X. Zeng, *Small*, 2017, **13**, 1701931.

142 M. Morita, C. Iwakura and H. Tamura, *Electrochim. Acta*, 1977, **22**, 325–328.

143 M. Wiechen, M. M. Najafpour, S. I. Allakhverdiev and L. Spiccia, *Energy Environ. Sci.*, 2014, **7**, 2203–2212.

144 M. Wiechen, I. Zaharieva, H. Dau and P. Kurz, *Chem. Sci.*, 2012, **3**, 2330–2339.

145 B. M. Hunter, H. B. Gray and A. M. Müller, *Chem. Rev.*, 2016, **116**, 14120–14136.

146 P. W. Menezes, A. Indra, D. González-Flores, N. R. Sahraie, I. Zaharieva, M. Schwarze, P. Strasser, H. Dau and M. Driess, *ACS Catal.*, 2015, **5**, 2017–2027.

147 J. J. H. Pijpers, M. T. Winkler, Y. Surendranath, T. Buonassisi and D. G. Nocera, *Proc. Natl. Acad. Sci.*, 2011, **108**, 10056–10061.

148 A. Moysiadou and X. Hu, *J. Mater. Chem. A*, 2019, **7**, 25865–25877.

149 B. Wurster, D. Grumelli, D. Hötger, R. Gutzler and K. Kern, *J. Am. Chem. Soc.*, 2016, **138**, 3623–3626.

150 S. W. Sheehan, J. M. Thomsen, U. Hintermair, R. H. Crabtree, G. W. Brudvig and C. A. Schmuttenmaer, *Nat. Commun.*, 2015, **6**, 6469.

151 S. W. Gersten, G. J. Samuels and T. J. Meyer, *J. Am. Chem. Soc.*, 1982, **104**, 4029–4030.

152 J. A. Gilbert, D. S. Eggleston, W. R. Murphy, D. A. Geselowitz, S. W. Gersten, D. J. Hodgson and T. J. Meyer, *J. Am. Chem. Soc.*, 1985, **107**, 3855–3864.

153 J. P. Collin and J. P. Sauvage, *Inorg. Chem.*, 1986, **25**, 135–141.

154 J. J. Concepcion, J. W. Jurss, J. L. Templeton and T. J. Meyer, *Proc. Natl. Acad. Sci.*, 2008, **105**, 17632–17635.

155 B. Limburg, E. Bouwman and S. Bonnet, *Coord. Chem. Rev.*, 2012, **256**, 1451–1467.

156 M. Shamsipur, A. A. Taherpour, H. Sharghi, V. Lippolis and A. Pashabadi, *Electrochim. Acta*, 2018, **265**, 316–325.

157 R. Brimblecombe, A. Koo, G. C. Dismukes, G. F. Swiegers and L. Spiccia, *J. Am. Chem. Soc.*, 2010, **132**, 2892–2894.

158 E. A. Karlsson, B.-L. Lee, T. Åkermark, E. V Johnston, M. D. Kärkäs, J. Sun, Ö. Hansson, J.-E. Bäckvall and B. Åkermark, *Angew. Chem. Int. Ed.*, 2011, **50**, 11715–11718.

159 K. J. Young, M. K. Takase and G. W. Brudvig, *Inorg. Chem.*, 2013, **52**, 7615–7622.

160 P. D. Frischmann, K. Mahata and F. Wurthner, *Chem. Soc. Rev.*, 2013, **42**, 1847–1870.

161 B. Schwarz, J. Forster, M. K. Goetz, D. Yücel, C. Berger, T. Jacob and C. Streb, *Angew. Chem. Int. Ed.*, 2016, **55**, 6329–6333.

162 J. Limburg, J. S. Vrettos, L. M. Liable-Sands, A. L. Rheingold, R. H. Crabtree and G. W. Brudvig, *Science*, 1999, **283**, 1524–1527.

163 J. L. Fillol, Z. Codolà, I. Garcia-Bosch, L. Gómez, J. J. Pla and M. Costas, *Nat. Chem.*, 2011, **3**, 807–813.

164 M. Okamura, M. Kondo, R. Kuga, Y. Kurashige, T. Yanai, S. Hayami, V. K. K. Praneeth, M. Yoshida, K. Yoneda, S. Kawata and S. Masaoka, *Nature*, 2016, **530**, 465–468.

165 X.-B. Han, Y.-G. Li, Z.-M. Zhang, H.-Q. Tan, Y. Lu and E.-B. Wang, *J. Am. Chem. Soc.*, 2015, **137**, 5486–5493.

166 Q. Yin, J. M. Tan, C. Besson, Y. V Geletii, D. G. Musaev, A. E. Kuznetsov, Z. Luo, K. I. Hardcastle and C. L. Hill, *Science*, 2010, **328**, 342–345.

167 D. K. Dogutan, R. McGuire and D. G. Nocera, *J. Am. Chem. Soc.*, 2011, **133**, 9178–9180.

168 D. Wang and J. T. Groves, *Proc. Natl. Acad. Sci.*, 2013, **110**, 15579–15584.

169 A. J. Esswein, Y. Surendranath, S. Y. Reece and D. G. Nocera, *Energy Environ. Sci.*, 2011, **4**, 499–504.

170 S. M. Barnett, K. I. Goldberg and J. M. Mayer, *Nat. Chem.*, 2012, **4**, 498–502.

171 P. Garrido-Barros, I. Funes-Ardoiz, S. Drouet, J. Benet-Buchholz, F. Maseras and A. Llobet, *J. Am. Chem. Soc.*, 2015, **137**, 6758–6761.

172 G. B. Haxel, J. B. Hedrick, G. J. Orris, P. H. Stauffer and J. W. Hendley II, *Rare earth elements: critical resources for high technology*, Fact Sheet., 2002.

173 P. Rybár, L. Domaracká, H. Hamrák and I. Šimko, eds. C. Drebenstedt and R. Singhal, Springer International Publishing, Cham, 2014, pp. 217–225.

174 M. M. Najafpour, G. Renger, M. Hołyńska, A. N. Moghaddam, E.-M. Aro, R. Carpentier, H. Nishihara, J. J. Eaton-Rye, J.-R. Shen and S. I. Allakhverdiev, *Chem. Rev.*, 2016, **116**, 2886–2936.

175 R. Brimblecombe, G. F. Swiegers, G. C. Dismukes and L. Spiccia, *Angew. Chem. Int. Ed.*, 2008, **47**, 7335–7338.

176 R. Al-Oweini, A. Sartorel, B. S. Bassil, M. Natali, S. Berardi, F. Scandola, U. Kortz and M. Bonchio, *Angew. Chem. Int. Ed.*, 2014, **53**, 11182–11185.

177 R.-Z. Liao, M. D. Kärkäs, B.-L. Lee, B. Åkermark and P. E. M. Siegbahn, *Inorg. Chem.*, 2015, **54**, 342–351.

178 S. Goberna-Ferrón, J. Soriano-López and J. Galán-Mascarós, *Inorganics*, 2015, **3**, 332–340.

179 R. Bagai and G. Christou, *Chem. Soc. Rev.*, 2009, **38**, 1011–1026.

180 G. Maayan, N. Gluz and G. Christou, *Nat. Catal.*, 2018, **1**, 48–54.

181 T. Ghosh and G. Maayan, *Angew. Chem. Int. Ed.*, 2019, **58**, 6476.

182 Y. Yan, J. S. Lee and D. A. Ruddy, *Inorg. Chem.*, 2015, **54**, 4550–4555.

183 F. Neese and D. A. Pantazis, *Faraday Discuss.*, 2011, **148**, 229–238.

184 R. K. Hocking, R. Brimblecombe, L. Y. Chang, A. Singh, M. H. Cheah, C. Glover, W. H. Casey and L. Spiccia, *Nat. Chem.*, 2011, **3**, 461–466.

185 K. J. Young, Y. Gao and G. W. Brudvig, *Aust. J. Chem.*, 2011, **64**, 1221.

186 S. Fukuzumi and D. Hong, *Eur. J. Inorg. Chem.*, 2014, **2014**, 645–659.

187 Y. Li, W. Qiu, F. Qin, H. Fang, V. G. Hadjiev, D. Litvinov and J. Bao, *J. Phys. Chem. C*, 2016, **120**, 4511–4516.

188 J. Soriano-López, F. Song, G. R. Patzke and J. R. Galan-Mascaros, *Front. Chem.*, 2018, **6**, 302.

189 S. Bernardini, F. Bellatreccia, A. Casanova Municchia, G. Della Ventura and A. Sodo, *J. Raman Spectrosc.*, 2019, **50**, 873–888.

190 A. Sartorel, M. Bonchio, S. Campagna and F. Scandola, *Chem. Soc. Rev.*, 2013, **42**, 2262–2280.

191 F. Evangelisti, R. Güttinger, R. Moré, S. Luber and G. R. Patzke, *J. Am. Chem. Soc.*, 2013, **135**, 18734–18737.

192 N. S. McCool, D. M. Robinson, J. E. Sheats and G. C. Dismukes, *J. Am. Chem. Soc.*, 2011, **133**, 11446–11449.

193 C.-F. Leung, S.-M. Ng, C.-C. Ko, W.-L. Man, J. Wu, L. Chen and T.-C. Lau, *Energy Environ. Sci.*, 2012, **5**, 7903–7907.

194 A. I. Nguyen, M. S. Ziegler, P. Oña-Burgos, M. Sturzbecher-Hohne, W. Kim, D. E. Bellone and T. D. Tilley, *J. Am. Chem. Soc.*, 2015, **137**, 12865–12872.

195 T. Ishizuka, A. Watanabe, H. Kotani, D. Hong, K. Satonaka, T. Wada, Y. Shiota, K. Yoshizawa, K. Ohara, K. Yamaguchi, S. Kato, S. Fukuzumi and T. Kojima, *Inorg. Chem.*, 2016, **55**, 1154–1164.

196 M. Blasco-Ahicart, J. Soriano-Lopez, J. J. Carbo, J. M. Poblet and J. R. Galan-Mascaros, *Nat. Chem.*, 2018, **10**, 24–30.

197 L. Smykalla, C. Mende, M. Fronk, P. F. Siles, M. Hietschold, G. Salvan, D. R. T. Zahn, O. G. Schmidt, T. Rüffer and H. Lang, *Beilstein J. Nanotechnol.*, 2017, **8**, 1786–1800.

198 W. Auwärter, D. Écija, F. Klappenberger and J. V Barth, *Nat. Chem.*, 2015, **7**, 105–120.

199 M. Ethirajan, Y. Chen, P. Joshi and R. K. Pandey, *Chem. Soc. Rev.*, 2011, **40**, 340–362.

200 K. Berg, P. K. Selbo, A. Weyergang, A. Dietze, L. Prasmickaite, A. Bonsted, B. O. Engesaeter, E. Angell-Petersen, T. Warloe, N. Frandsen and A. Hogset, *J. Microsc.*, 2005, **218**, 133–147.

201 S. Mathew, A. Yella, P. Gao, R. Humphry-Baker, B. F. E. Curchod, N. Ashari-Astani, I. Tavernelli, U. Rothlisberger, M. K. Nazeeruddin and M. Grätzel, *Nat. Chem.*, 2014, **6**, 242–247.

202 B. S. Lane and K. Burgess, *Chem. Rev.*, 2003, **103**, 2457–2474.

203 M. Iyoda, J. Yamakawa and M. J. Rahman, *Angew. Chem. Int. Ed.*, 2011, **50**, 10522–10553.

204 J. H. Kim, S. H. Lee, J. S. Lee, M. Lee and C. B. Park, *Chem. Commun.*, 2011, **47**, 10227–10229.

205 H. Inoue, S. Funyu, Y. Shimada and S. Takagi, *Pure Appl. Chem.*, 2005, **77**, 1019–1033.

206 T. Nakazono, A. R. Parent and K. Sakai, *Chem. Commun.*, 2013, **49**, 6325–6327.

207 T. Nakazono and K. Sakai, *Dalt. Trans.*, 2016, **45**, 12649–12652.

208 Y. Liu, Y. Han, Z. Zhang, W. Zhang, W. Lai, Y. Wang and R. Cao, *Chem. Sci.*, 2019, **10**, 2613–2622.

209 M. Schilling and S. Luber, *Front. Chem.*, 2018, 6, 100.

210 J. Soriano-López, W. Schmitt and M. García-Melchor, *Curr. Opin. Electrochem.*, 2018, **7**, 22–30.

211 D. W. Shaffer, Y. Xie and J. J. Concepcion, *Chem. Soc. Rev.*, 2017, **46**, 6170–6193.

212 J. P. McEvoy, J. A. Gascon, V. S. Batista and G. W. Brudvig, *Photochem. Photobiol. Sci.*, 2005, **4**, 940–949.

213 F. Li, Y. Jiang, B. Zhang, F. Huang, Y. Gao and L. Sun, *Angew. Chem. Int. Ed.*, 2012, **51**, 2417–2420.

214 Q. Chen, Q. Zhou, T.-T. Li, R. Liu, H. Li, F. Guo and Y.-Q. Zheng, *Transit. Met. Chem.*, 2019, **44**, 349–354.

215 D. L. Ashford, D. J. Stewart, C. R. Glasson, R. A. Binstead, D. P. Harrison, M. R. Norris, J. J. Concepcion, Z. Fang, J. L. Templeton and T. J. Meyer, *Inorg. Chem.*, 2012, **51**, 6428–6430.

216 M. R. Norris, J. J. Concepcion, D. P. Harrison, R. A. Binstead, D. L. Ashford, Z. Fang, J. L. Templeton and T. J. Meyer, *J. Am. Chem. Soc.*, 2013, **135**, 2080–2083.

217 N. Kaveevivitchai, R. Chitta, R. Zong, M. El Ojaimi and R. P. Thummel, *J. Am. Chem. Soc.*, 2012, **134**, 10721–10724.

218 B. D. Sherman, D. L. Ashford, A. M. Lapides, M. V Sheridan, K.-R. Wee and T. J. Meyer, *J. Phys. Chem. Lett.*, 2015, **6**, 3213–3217.

219 B. D. Sherman, M. V Sheridan, K.-R. Wee, S. L. Marquard, D. Wang, L. Alibabaei, D. L. Ashford and T. J. Meyer, *J. Am. Chem. Soc.*, 2016, **138**, 16745–16753.

220 K. Meyer, M. Ranocchiari and J. A. van Bokhoven, *Energy Environ. Sci.*, 2015, **8**, 1923–1937.

221 L. R. MacGillivray and C. M. Lukehart, *Metal-Organic Framework Materials*, Wiley, New Jersey, 2014.

222 H. Furukawa, K. E. Cordova, M. O'Keeffe and O. M. Yaghi, *Science*, 2013, **341**, 1230444–1230444.

223 V. F. Cheong and P. Y. Moh, *Mater. Sci. Technol.*, 2018, **34**, 1025–1045.

224 M. Eddaoudi, *Science*, 2002, **295**, 469–472.

225 M. Eddaoudi, D. B. Moler, H. Li, B. Chen, T. M. Reineke, M. O'Keeffe and O. M. Yaghi, *Acc. Chem. Res.*, 2001, **34**, 319–330.

226 A. E. Baumann, D. A. Burns, B. Liu and V. S. Thoi, *Commun. Chem.*, 2019, **2**, 86.

227 P. Silva, S. M. F. Vilela, J. P. C. Tomé and F. A. Almeida Paz, *Chem. Soc. Rev.*, 2015, **44**, 6774–6803.

228 M. Bilal, M. Adeel, T. Rasheed and H. M. N. Iqbal, *J. Mater. Res. Technol.*, 2019, **8**, 2359–2371.

229 A. J. Howarth, Y. Liu, P. Li, Z. Li, T. C. Wang, J. T. Hupp and O. K. Farha, *Nat. Rev. Mater.*, 2016, **1**, 15018.

230 J. F. Keggin and F. D. Miles, *Nature*, 1936, **137**, 577–578.

231 B. M. Weckhuysen and J. Yu, *Chem. Soc. Rev.*, 2015, **44**, 7022–7024.

232 H. J. Buser, D. Schwarzenbach, W. Petter and A. Ludi, *Inorg. Chem.*, 1977, **16**, 2704–2710.

233 G. R. Desiraju, *J. Am. Chem. Soc.*, 2013, **135**, 9952–9967.

234 J. Maddox, *Nature*, 1988, **335**, 201.

235 G. R. Desiraju, *J. Chem. Sci.*, 2010, **122**, 667–675.

236 R. Haldar, A. Mazel, M. Krstić, Q. Zhang, M. Jakoby, I. A. Howard, B. S. Richards, N. Jung, D. Jacquemin, S. Diring, W. Wenzel, F. Odobel and C. Wöll, *Nat. Commun.*, 2019, **10**, 2048.

237 B. F. Hoskins and R. Robson, *J. Am. Chem. Soc.*, 1989, **111**, 5962–5964.

238 R. Robson, *Dalt. Trans.*, 2008, 5113–5131.

239 B. F. Hoskins and R. Robson, *J. Am. Chem. Soc.*, 1990, **112**, 1546–1554.

240 B. F. Hoskins, R. Robson and P. Smith, *J. Chem. Soc. Chem. Commun.*, 1990, 488–489.

241 R. W. Gable, B. F. Hoskins and R. Robson, *J. Chem. Soc. Chem. Commun.*, 1990, 1677–1678.

242 B. F. Abrahams, B. F. Hoskins and R. Robson, *J. Chem. Soc. Chem. Commun.*, 1990, **1**, 60.

243 B. F. Abrahams, B. F. Hoskins, D. M. Michail and R. Robson, *Nature*, 1994, **369**, 727–729.

244 B. F. Abrahams, B. F. Hoskins and R. Robson, *J. Am. Chem. Soc.*, 1991, **113**, 3606–3607.

245 R. Robson, B. F. Abrahams, S. R. Batten, R. W. Gable, B. F. Hoskins and J. Liu, *Supramol. Archit.*, 1992, **499**, 256–273.

246 O. M. Yaghi and H. Li, *J. Am. Chem. Soc.*, 1995, **117**, 10401–10402.

247 O. M. Yaghi, M. O'Keeffe, N. W. Ockwig, H. K. Chae, M. Eddaoudi and J. Kim, *Nature*, 2003, **423**, 705–714.

248 N. L. Rosi, *Science*, 2003, **300**, 1127–1129.

249 H. Li, M. Eddaoudi, M. O'Keeffe and O. M. Yaghi, *Nature*, 1999, **402**, 276–279.

250 R. L. Martin, L.-C. Lin, K. Jariwala, B. Smit and M. Haranczyk, *J. Phys. Chem. C*, 2013, **117**, 12159–12167.

251 H. Furukawa, Y. B. Go, N. Ko, Y. K. Park, F. J. Uribe-Romo, J. Kim, M. O'Keeffe and O. M. Yaghi, *Inorg. Chem.*, 2011, **50**, 9147–9152.

252 M. Kondo, T. Yoshitomi, H. Matsuzaka, S. Kitagawa and K. Seki, *Angew. Chem. Int. Ed.*, 1997, **36**, 1725–1727.

253 M. Fujita, D. Oguro, M. Miyazawa, H. Oka, K. Yamaguchi and K. Ogura, *Nature*, 1995, **378**, 469–471.

254 S. Subramanian and M. J. Zaworotko, *Angew. Chem. Int. Ed.*, 1995, **34**, 2127–2129.

255 H.-C. Zhou and S. Kitagawa, *Chem. Soc. Rev.*, 2014, **43**, 5415–5418.

256 M. Li, D. Li, M. O'Keeffe and O. M. Yaghi, *Chem. Rev.*, 2014, **114**, 1343–1370.

257 P. Z. Moghadam, A. Li, S. B. Wiggin, A. Tao, A. G. P. Maloney, P. A. Wood, S. C. Ward and D. Fairen-Jimenez, *Chem. Mater.*, 2017, **29**, 2618–2625.

258 G. Ferey, *Chem. Soc. Rev.*, 2008, **37**, 191–214.

259 A. Rabenau, *Angew. Chem. Int. Ed.*, 1985, **24**, 1026–1040.

260 T. R. Cook, Y.-R. Zheng and P. J. Stang, *Chem. Rev.*, 2013, **113**, 734–777.

261 H. Vardhan, M. Yusubov and F. Verpoort, *Coord. Chem. Rev.*, 2016, **306**, 171–194.

262 S. S.-Y. Chui, S. M.-F. Lo, J. P. H. Charmant, A. G. Orpen and I. D. Williams, *Science*, 1999, **283**, 1148–1150.

263 R. Seetharaj, P. V Vandana, P. Arya and S. Mathew, *Arab. J. Chem.*, 2016, **21**, 616–623.

264 J. Cepeda, G. Beobide, O. Castillo, A. Luque, S. Pérez-Yáñez and P. Román, *Cryst. Growth Des.*, 2012, **12**, 1501–1512.

265 N. Stock and S. Biswas, *Chem. Rev.*, 2012, **112**, 933–969.

266 M. Li and M. Dincă, *J. Am. Chem. Soc.*, 2011, **133**, 12926–12929.

267 J. Klinowski, F. A. Almeida Paz, P. Silva and J. Rocha, *Dalt. Trans.*, 2011, **40**, 321–330.

268 M. Klimakow, P. Klobes, A. F. Thünemann, K. Rademann and F. Emmerling, *Chem. Mater.*, 2010, **22**, 5216–5221.

269 W.-J. Son, J. Kim, J. Kim and W.-S. Ahn, *Chem. Commun.*, 2008, 6336–6338.

270 Y.-R. Lee, J. Kim and W.-S. Ahn, *Korean J. Chem. Eng.*, 2013, **30**, 1667–1680.

271 D. J. Tranchemontagne, J. L. Mendoza-Cortés, M. O'Keeffe and O. M. Yaghi, *Chem. Soc. Rev.*, 2009, **38**, 1257–1283.

272 N. L. Rosi, J. Kim, M. Eddaoudi, B. Chen, M. O'Keeffe and O. M. Yaghi, *J. Am. Chem. Soc.*, 2005, **127**, 1504–1518.

273 U. Mueller, M. Schubert, F. Teich, H. Puetter, K. Schierle-Arndt and J. Pastré, *J. Mater. Chem.*, 2006, **16**, 626–636.

274 H.-C. Zhou, J. R. Long and O. M. Yaghi, *Chem. Rev.*, 2012, **112**, 673–674.

275 H. Zhu and D. Liu, *J. Mater. Chem. A*, 2019, **7**, 21004–21035.

276 A. Kirchon, L. Feng, H. F. Drake, E. A. Joseph and H.-C. Zhou, *Chem. Soc. Rev.*, 2018, **47**, 8611–8638.

277 W.-Y. Gao, M. Chrzanowski and S. Ma, *Chem. Soc. Rev.*, 2014, **43**, 5841–5866.

278 D. Sun, F. S. Tham, C. A. Reed and P. D. W. Boyd, *Proc. Natl. Acad. Sci.*, 2002, **99**, 5088–5092.

279 A. M. Shultz, O. K. Farha, J. T. Hupp and S. T. Nguyen, *J. Am. Chem. Soc.*, 2009, **131**, 4204–4205.

280 E.-Y. Choi, P. M. Barron, R. W. Novotny, H.-T. Son, C. Hu and W. Choe, *Inorg. Chem.*, 2009, **48**, 426–428.

281 M. Bosch, M. Zhang and H.-C. Zhou, *Adv. Chem.*, 2014, **2014**, 8.

282 M. Eddaoudi, D. F. Sava, J. F. Eubank, K. Adil and V. Guillerm, *Chem. Soc. Rev.*, 2015, **44**, 228–249.

283 V. V Butova, M. A. Soldatov, A. A. Guda, K. A. Lomachenko and C. Lamberti, *Russ. Chem. Rev.*, 2016, **85**, 280–307.

284 O. K. Farha, A. Özgür Yazaydın, I. Eryazici, C. D. Malliakas, B. G. Hauser, M. G. Kanatzidis, S. T. Nguyen, R. Q. Snurr and J. T. Hupp, *Nat. Chem.*, 2010, **2**, 944–948.

285 O. K. Farha, I. Eryazici, N. C. Jeong, B. G. Hauser, C. E. Wilmer, A. A. Sarjeant, R. Q. Snurr, S. T. Nguyen, A. Ö. Yazaydın and J. T. Hupp, *J. Am. Chem. Soc.*, 2012, **134**, 15016–15021.

286 I. M. Hönicke, I. Senkovska, V. Bon, I. A. Baburin, N. Bönisch, S. Raschke, J. D. Evans and S. Kaskel, *Angew. Chem. Int. Ed.*, 2018, **57**, 13780–13783.

287 B. L. Dunicz, *J. Chem. Educ.*, 1961, **38**, 357.

288 D. Peralta, G. Chaplais, A. Simon-Masseron, K. Barthelet, C. Chizallet, A.-A. Quoineaud and G. D. Pirngruber, *J. Am. Chem. Soc.*, 2012, **134**, 8115–8126.

289 D. J. C. Yates, *Can. J. Chem.*, 1968, **46**, 1695–1701.

290 M. Ding, X. Cai and H.-L. Jiang, *Chem. Sci.*, 2019, **10**, 10209–10230.

291 C. Wang, X. Liu, N. Keser Demir, J. P. Chen and K. Li, *Chem. Soc. Rev.*, 2016, **45**, 5107–5134.

292 G. Férey, C. Mellot-Draznieks, C. Serre, F. Millange, J. Dutour, S. Surblé and I. Margiolaki, *Science*, 2005, **309**, 2040–2042.

293 Q. Liu, L. Ning, S. Zheng, M. Tao, Y. Shi and Y. He, *Sci. Rep.*, 2013, **3**, 2916.

294 S. Bhattacharjee, C. Chen and W.-S. Ahn, *RSC Adv.*, 2014, **4**, 52500–52525.

295 S. Chavan, J. G. Vitillo, D. Gianolio, O. Zavorotynska, B. Civalleri, S. Jakobsen, M. H. Nilsen, L. Valenzano, C. Lamberti, K. P. Lillerud and S. Bordiga, *Phys. Chem. Chem. Phys.*, 2012, **14**, 1614–1626.

296 R. J. Kuppler, D. J. Timmons, Q.-R. Fang, J.-R. Li, T. A. Makal, M. D. Young, D. Yuan, D. Zhao, W. Zhuang and H.-C. Zhou, *Coord. Chem. Rev.*, 2009, **253**, 3042–3066.

297 D. Aulakh, J. B. Pyser, X. Zhang, A. A. Yakovenko, K. R. Dunbar and M. Wriedt, *J. Am. Chem. Soc.*, 2015, **137**, 9254–9257.

298 J. L. C. Rowsell and O. M. Yaghi, *Angew. Chem. Int. Ed.*, 2005, **44**, 4670–4679.

299 J.-R. Li, R. J. Kuppler and H.-C. Zhou, *Chem. Soc. Rev.*, 2009, **38**, 1477–1504.

300 S. Kitagawa, R. Kitaura and S. Noro, *Angew. Chem. Int. Ed.*, 2004, **43**, 2334–2375.

301 M. Fujita, Y. J. Kwon, S. Washizu and K. Ogura, *J. Am. Chem. Soc.*, 1994, **116**, 1151–1152.

302 J. Liu, L. Chen, H. Cui, J. Zhang, L. Zhang and C.-Y. Su, *Chem. Soc. Rev.*, 2014, **43**, 6011–6061.

303 A. Corma, H. García and F. X. Llabrés i Xamena, *Chem. Rev.*, 2010, **110**, 4606–4655.

304 D. Farrusseng, S. Aguado and C. Pinel, *Angew. Chem. Int. Ed.*, 2009, **48**, 7502–7513.

305 A. Dhakshinamoorthy, M. Opanasenko, J. Čejka and H. Garcia, *Catal. Sci. Technol.*, 2013, **3**, 2509–2540.

306 A. Dhakshinamoorthy, Z. Li and H. Garcia, *Chem. Soc. Rev.*, 2018, **47**, 8134–8172.

307 M. H. Mohamed, Y. Yang, L. Li, S. Zhang, J. P. Ruffley, A. G. Jarvi, S. Saxena, G. Veser, J. K. Johnson and N. L. Rosi, *J. Am. Chem. Soc.*, 2019, **141**, 13003–13007.

308 L. R. MacGillivray, *Metal-Organic Frameworks: Design and Application*, Wiley, 2010.

309 P. Garcia-Garcia, M. Muller and A. Corma, *Chem. Sci.*, 2014, **5**, 2979–3007.

310 S. A. Burgess, A. Kassie, S. A. Baranowski, K. J. Fritzsching, K. Schmidt-Rohr, C. M. Brown and C. R. Wade, *J. Am. Chem. Soc.*, 2016, **138**, 1780–1783.

311 W. Zhang, G. Lu, C. Cui, Y. Liu, S. Li, W. Yan, C. Xing, Y. R. Chi, Y. Yang and F. Huo, *Adv. Mater.*, 2014, **26**, 4056–4060.

312 Z. Guo and B. Chen, *Dalt. Trans.*, 2015, **44**, 14574–14583.

313 B. J. Burnett and W. Choe, *CrystEngComm*, 2012, **14**, 6129–6131.

314 M. E. Kosal, J.-H. Chou, S. R. Wilson and K. S. Suslick, *Nat. Mater.*, 2002, **1**, 118–121.

315 G. I. Dzhardimalieva and I. E. Uflyand, *RSC Adv.*, 2017, **7**, 42242–42288.

316 H.-J. Son, S. Jin, S. Patwardhan, S. J. Wezenberg, N. C. Jeong, M. So, C. E. Wilmer, A. A. Sarjeant, G. C. Schatz, R. Q. Snurr, O. K. Farha, G. P. Wiederrecht and J. T. Hupp, *J. Am. Chem. Soc.*, 2013, **135**, 862–869.

317 Y. Xiao, W. Guo, H. Chen, H. Li, X. Xu, P. Wu, Y. Shen, B. Zheng, F. Huo and W. D. Wei, *Mater. Chem. Front.*, 2019, **3**, 1580–1585.

318 S. Nakagaki, G. Ferreira, G. Ucoski and K. Dias de Freitas Castro, *Mol.*, 2013, **18**, 7279.

319 D. W. Smithenry, S. R. Wilson and K. S. Suslick, *Inorg. Chem.*, 2003, **42**, 7719–7721.

320 K. A. D. Castro, F. Figueira, R. F. Mendes, J. A. S. Cavaleiro, M. da G. P. M. Neves, M. M. Q. Simões, F. A. Almeida Paz, J. P. C. Tomé and S. Nakagaki, *ChemCatChem*, 2017, **9**, 2939–2945.

321 M. Zhao, S. Ou and C.-D. Wu, *Acc. Chem. Res.*, 2014, **47**, 1199–1207.

322 C. Pereira, M. Simões, J. Tomé and F. Almeida Paz, *Mol.*, 2016, **21**, 1348.

323 X.-L. Yang, M.-H. Xie, C. Zou, Y. He, B. Chen, M. O'Keeffe and C.-D. Wu, *J. Am. Chem. Soc.*, 2012, **134**, 10638–10645.

324 M. H. Alkordi, Y. Liu, R. W. Larsen, J. F. Eubank and M. Eddaoudi, *J. Am. Chem. Soc.*, 2008, **130**, 12639–12641.

325 C. F. Pereira, F. Figueira, R. F. Mendes, J. Rocha, J. T. Hupp, O. K. Farha, M. M. Q. Simões, J. P. C. Tomé and F. A. A. Paz, *Inorg. Chem.*, 2018, **57**, 3855–3864.

326 D. Feng, Z.-Y. Gu, J.-R. Li, H.-L. Jiang, Z. Wei and H.-C. Zhou, *Angew. Chem. Int. Ed.*, 2012, **51**, 10307–10310.

327 M.-H. Xie, X.-L. Yang, C. Zou and C.-D. Wu, *Inorg. Chem.*, 2011, **50**, 5318–5320.

328 Y. Chen, T. Hoang and S. Ma, *Inorg. Chem.*, 2012, **51**, 12600–12602.

329 K. S. Suslick, P. Bhyrappa, J. H. Chou, M. E. Kosal, S. Nakagaki, D. W. Smithenry and S. R. Wilson, *Acc. Chem. Res.*, 2005, **38**, 283–291.

330 O. K. Farha, A. M. Shultz, A. A. Sarjeant, S. T. Nguyen and J. T. Hupp, *J. Am. Chem. Soc.*, 2011, **133**, 5652–5655.

331 M. Fuentes-Cabrera, D. M. Nicholson, B. G. Sumpter and M. Widom, *J. Chem. Phys.*, 2005, **123**, 124713.

332 A. Fateeva, P. A. Chater, C. P. Ireland, A. A. Tahir, Y. Z. Khimyak, P. V Wiper, J. R. Darwent and M. J. Rosseinsky, *Angew. Chem. Int. Ed.*, 2012, **51**, 7440–7444.

333 Z. Jin and H. Yang, *Nanoscale Res. Lett.*, 2017, **12**, 539.

334 M. A. Nasalevich, M. van der Veen, F. Kapteijn and J. Gascon, *CrystEngComm*, 2014, **16**, 4919–4926.

335 D. Kim, D. R. Whang and S. Y. Park, *J. Am. Chem. Soc.*, 2016, **138**, 8698–8701.

336 A. Aziz, A. R. Ruiz-Salvador, N. C. Hernández, S. Calero, S. Hamad and R. Grau-Crespo, *J. Mater. Chem. A*, 2017, **5**, 11894–11904.

337 J.-Q. Shen, P.-Q. Liao, D.-D. Zhou, C.-T. He, J.-X. Wu, W.-X. Zhang, J.-P. Zhang and X.-M. Chen, *J. Am. Chem. Soc.*, 2017, **139**, 1778–1781.

338 X.-L. Wang, L.-Z. Dong, M. Qiao, Y.-J. Tang, J. Liu, Y. Li, S.-L. Li, J.-X. Su and Y.-Q. Lan, *Angew. Chem. Int. Ed.*, 2018, **57**, 9660–9664.

339 Y. An, Y. Liu, P. An, J. Dong, B. Xu, Y. Dai, X. Qin, X. Zhang, M.-H. Whangbo and B. Huang, *Angew. Chem. Int. Ed.*, 2017, **56**, 3036–3040.

340 L. Chi, Q. Xu, X. Liang, J. Wang and X. Su, *Small*, 2016, **12**, 1351–1358.

341 R. K. Tripathy, A. K. Samantara and J. N. Behera, *Dalt. Trans.*, 2019, **48**, 10557–10564.

342 W. Chen, Y. Zhang, G. Chen, R. Huang, Y. Zhou, Y. Wu, Y. Hu and K. Ostrikov, *J. Mater. Chem. A*, 2019, **7**, 3090–3100.

343 Z. Wei, W. Zhu, Y. Li, Y. Ma, J. Wang, N. Hu, Y. Suo and J. Wang, *Inorg. Chem.*, 2018, **57**, 8422–8428.

344 J. Jiang, L. Huang, X. Liu and L. Ai, *ACS Appl. Mater. Interfaces*, 2017, **9**, 7193–7201.

345 N.-Y. Huang, J.-Q. Shen, Z.-M. Ye, W.-X. Zhang, P.-Q. Liao and X.-M. Chen, *Chem. Sci.*, 2019, **10**, 9859–9864.

346 X.-F. Lu, P.-Q. Liao, J.-W. Wang, J.-X. Wu, X.-W. Chen, C.-T. He, J.-P. Zhang, G.-R. Li and X.-M. Chen, *J. Am. Chem. Soc.*, 2016, **138**, 8336–8339.

Chapter Two

Co^{II} Metal-Metalloporphyrin Frameworks: Synthesis, Characterisation and H_2O Oxidation Properties

2.1 Introduction

The unique properties and structural versatility offered by MOFs has led to their use as photo- and electrocatalysts for both the OER and the HER.[1,2] Several attributes of MOFs engender these materials as excellent candidates for H_2O splitting catalysis. For example, their high surface area and crystallinity allows substrate-accessible catalytic sites to be atomically dispersed throughout a material.[3] This permits the simultaneous exposure of a large number of active sites to a substrate, thus facilitating favourable catalytic kinetics. Further, the physical separation of a MOF's catalytic sites prevents the occurrence of counterproductive charge recombination processes.[4]

In addition, the modularity of MOFs allows individual functional components to be combined forming efficient hybrid organic-inorganic catalysts.[5] For example, numerous Co-oxo clusters have demonstrated impressive OER activity.[6,7,8] The incorporation of such WOCs, or other redox-active Co-oxo clusters as SBUs within MOFs may generate heterogeneous catalysts with comparatively superior activity to the isolated cluster from which they are constructed.

In recent years, this strategy has been exploited with the synthesis of several Co-based MOFs that display OER activity.[9] For example, Ma *et al*. reported a 3D MOF $[Co_{1.5}(tib)(dcpna)]\cdot 6H_2O$ (tib = 1,3,5-tris(1-imidazolyl)-benzene, dcpna = 5-(3',5'-dicarboxylphenyl)nicotinic acid) featuring Co^{II} centres and 1D solvent-accessible channels.[10] Under electrochemical conditions, $[Co_{1.5}(tib)(dcpna)]\cdot 6H_2O$ exhibits catalytic activity towards the OER operating with a current density of 10 mA cm^{-2} at a low overpotential of 360 mV. In addition, Wang *et al*. showed that the Co-based MOF Co-ZIF-67 ($[Co(2\text{-}MeIm)_2]$, 2-MeIm = 2-methylimidazolate) functions as an effective catalyst for the light-driven OER in the presence of $[Ru(bpy)_3](ClO_4)_2$ PS and $Na_2S_2O_8$ SEA with a TOF = 0.035 s^{-1}.[11] However, in an investigation by D'Alessandro *et al*., mixed-valent Co_3O_4 was implicated as the true WOC in O_2 evolution experiments using Co-ZIF-67.[12] This underscores the importance of thorough post-catalytic characterisation to rule out the formation and participation of other OER active species.

Metal-metalloporphyrin frameworks (MMPFs) represent a resurging family of MOFs comprising porphyrin-based bridging ligands.[13] The diverse functionality and stability offered by porphyrins and metalloporphyrins make them attractive building blocks for the construction of catalytically active frameworks.[14] Recently, Cao *et al*. demonstrated the electrocatalytic O_2 evolution activity of a Cu^{II} complex of tetrakis(4-*N*-methylpyridyl)porphyrin.[15] This noble

metal-free metalloporphyrin functions as an effective homogeneous OER catalyst, operating with an onset overpotential of just 310 mV and a high faradaic efficiency (>93%) in neutral, phosphate-buffered aqueous media. Another example of an OER active MMPF is PCN-224 ($[Zr_6(TCPP\text{-}Ni^{II})_{1.5}]$, TCPP-$Ni^{II}$ = [*meso*-tetrakis(4-carboxyphenyl)porphyrinato]-Ni^{II}).[16] This framework was used for the electrochemical oxidation of H_2O. An investigation by Morris *et al*. found that PCN-224 is a competent OER catalyst which operates at a moderate overpotential of 450 mV under aqueous conditions.

In this chapter, the syntheses of a series of metalloporphyrin analogues of the ditopic linear linker 5,15-di(4-carboxyphenyl)-10,20-diphenylporphyrin (H_4**L1**, Fig. 2.1) are described. Additionally, the syntheses, crystal structures and physicochemical characterisation of two novel MMPFs (**1** and **2**) which incorporate Co^{II}-based nodes and the Cu^{II} metalloporphyrin linker (**L1**-Cu^{II})$^{2-}$ are discussed. Out of these two MMPFs, **1** was rationalised as a more promising candidate to conduct an H_2O oxidation catalysis study on. Following on from this, the experimental setup and methodology developed to carry out H_2O splitting catalytic investigations is described. In the final section of this chapter, the light-driven OER catalytic properties and post-catalytic physicochemical characterisation experiments using **1** are detailed.

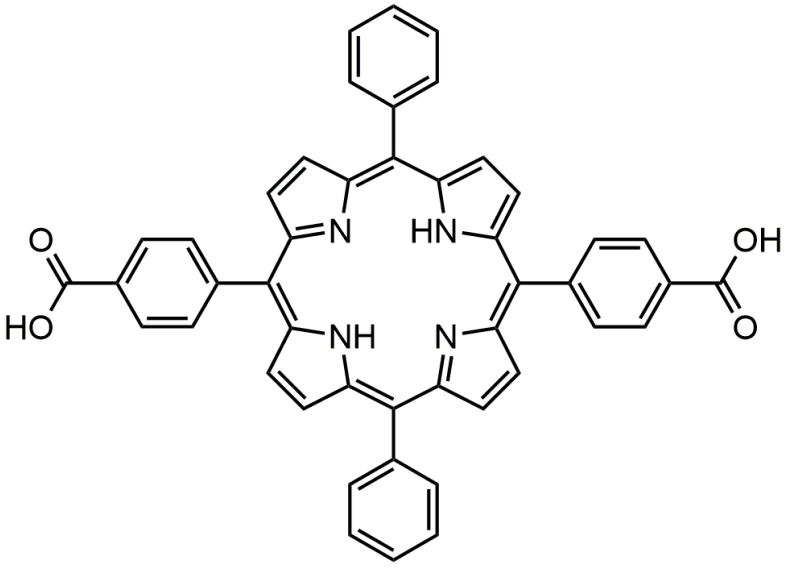

Fig 2.1: Structure of the freebase porphyrin (H_4**L1)** employed in the synthesis of compounds **1** and **2**.

2.2 Synthesis of the Linker 5,15-Bis(4-carboxyphenyl)-10,20-diphenylporphyrin (H_4**L1**) and Related Metalloporphyrin Ligands

In this work, the porphyrin 5,15-bis(4-carboxyphenyl)-10,20-diphenylporphyrin (H_4**L1**, Fig 2.1) and its metalloporphyrin analogues have been used as ligands in the synthesis of a range of MMPFs, coordination polymers and complexes based on Co^{II} (**1** and **2**), Mn^{II} (**5 – 9**), Zn^{II} (**10**) and In^{III} (**11**) ions. H_4**L1** comprises a tetrapyrrolic core which is substituted at each of its four *meso* positions; the 5 and 15 positions are substituted by non-functionalised phenyl groups, and the 10 and 20 positions are substituted by *para*-carboxylic acid-functionalised phenyl rings. This substitution pattern makes H_4**L1** a ditopic linear linker with two carboxylic acid groups situated at an angle of 180° with respect to each other.

Selection of the ligand H_4**L1** for the synthesis of MMPFs was rationalised as a means to access the rich chemical diversity previously attained using more rudimentary linear carboxylate linkers,[17,18] whilst exploiting the unique electronic and photophysical properties of porphyrins. Furthermore, as an array of metal ions can be hosted by the central cavity of H_4**L1**, additional tuning of the MMPFs is possible.[19] Despite these favourable characteristics, the MMPF chemistry of H_4**L1** remains relatively underexplored at the time of writing, with only two MMPF structures reported in the Cambridge Structural Database containing this linker, and no structures reported containing either Co- or Mn-based SBUs connected by H_4**L1** ligands.[20,21] This is in stark contrast to the large library of MMPFs reported featuring the tetrasubstituted carboxylic acid porphyrin linker, tetrakis(4-carboxyphenyl)porphyrin. This is most likely due to the relative ease of synthesis and purification of more highly symmetric porphyrins.

H_4**L1** and the related metalloporphyrin complexes H_2**L1**-Cu^{II}, H_2**L1**-Ni^{II} and H_2**L1**-Pt^{II} were accessed *via* either a three-step (H_4**L1**) or a four-step (H_2**L1**-Cu^{II}, H_2**L1**-Ni^{II} and H_2**L1**-Pt^{II}) synthesis beginning with the synthesis of the carbomethoxyphenyl-functionalised reactant 5-(4-carbomethoxyphenyl)dipyrromethane, which is outlined below.

2.2.1 Synthesis of 5-(4-Carbomethoxyphenyl)dipyrromethane

5-(4-Carbomethoxyphenyl)dipyrromethane was synthesized according to a modified procedure outlined by Lindsey *et al*.[22] (Scheme 2.1). Indium chloride was added to a solution of methyl 4-formylbenzoate in freshly distilled pyrrole under an inert atmosphere. This mixture was then shielded from light and stirred for three hours before adding an aqueous solution of NaOH to quench the reaction. After an additional hour of stirring, the reaction mixture was concentrated under reduced pressure and the excess pyrrole was recovered and put aside for later use. Purification of the crude product using silica gel column chromatography afforded 5-(4-carbomethoxyphenyl)dipyrromethane as an off-white powder in reasonable yield (50%). The product was characterised using NMR and FT-IR spectroscopy and mass spectrometry.

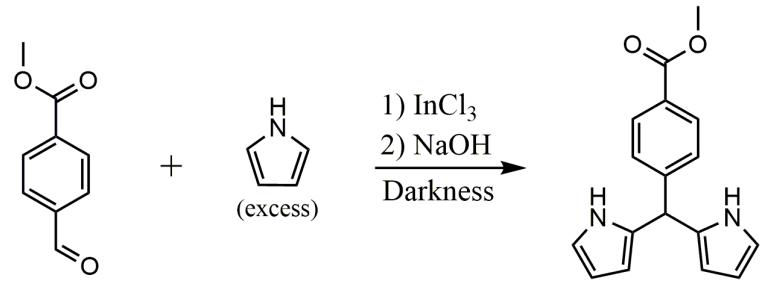

Scheme 2.1: Synthesis of 5-(4-carbomethoxyphenyl)dipyrromethene from methyl 4-formylbenzoate and pyrrole.

2.2.2 Synthesis of 5,15-Bis(4-carbomethoxyphenyl)-10,20-diphenylporphyrin (Me_2H_2L1)

5,15-Bis(4-carbomethoxyphenyl-10,20-diphenylporphyrin (Me_2H_2**L1**) was prepared in a MacDonald-type macrocyclization reaction according to an adapted literature procedure.[23] A dilute solution of 5-(4-carbomethoxyphenyl)dipyrromethene and benzaldehyde in DCM was acidified by adding TFA under an inert atmosphere while shielding from light (Scheme 2.2). This condensation reaction was stirred for three hours before the resulting porphyrinogen species was oxidised with the addition of *p*-chloranil. After stirring overnight, the reaction was quenched with TEA, before evaporating the solvent under reduced pressure.

Employing a low concentration of 5-(4-carbomethoxyphenyl)dipyrromethene in this synthesis favours the macrocyclization reaction over oligomerisation.[24] 5,15-bis(4-carbomethoxyphenyl-10,20-diphenylporphyrin forms as the major non-polymeric product of this reaction, however, several isomeric porphyrins were also detected in the reaction mixture,

including porphyrins with alternative substitution patterns such as 5,10-bis(4-carboxyphenyl)-15,20-diphenylporphyrin, α,β-linked "N-confused" porphyrins, as well as unsubstituted, mono-, tri- and tetra-carboxyphenyl substituted porphyrins, and other combinations of these variations.[25]

Purification of the crude product using a series of silica gel chromatographic separation steps afforded the product 5,15-bis(4-carbomethoxyphenyl)phenyl-10,20-diphenylporphyrin (Me_2H_2**L1**) in high purity and acceptable yield (17%). The product was subsequently characterised using NMR, FT-IR and UV-Vis spectroscopy, and mass spectrometry.

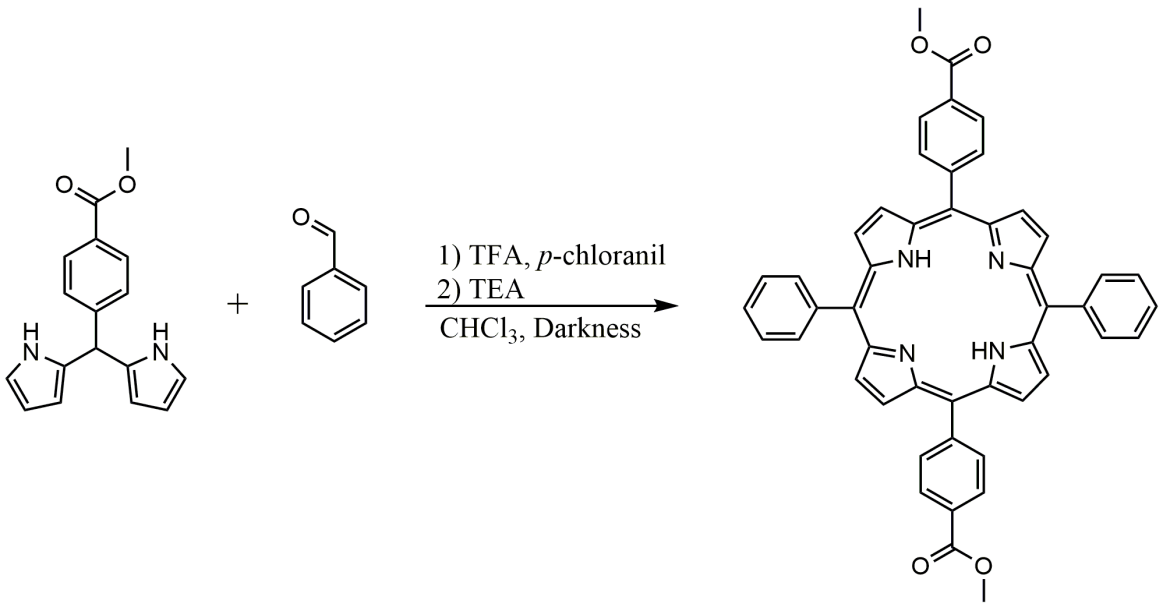

Scheme 2.2: Reaction between 5-(4-carbomethoxyphenyl)dipyrromethane and benzaldehyde yielding 5,15-bis(4-carbomethoxyphenyl)phenyl-10,20-diphenylporphyrin (Me_2H_2**L1**) as the major porphyrin product.

2.2.3 Synthesis of Metalloporphyrin Esters Me_2L1-Cu^{II}, Me_2L1-Ni^{II} and Me_2L1-Pt^{II}

The ester 5,15-bis(4-carbomethoxyphenyl)-10,20-diphenylporphyrin (Me_2H_2**L1**) can be hydrolysed without further modification to obtain the corresponding freebase porphyrin H_4**L1** (see section 2.2.4). Alternatively, the freebase ester Me_2H_2**L1** can be metallated with an array of metal ions which will each impart unique electronic, photophysical and redox properties to the molecule.[26] For example, Brouwer *et al*. demonstrated that metalloporphyrin complexes of Cu^{II} and Ni^{II} ions function as stable photosensitisers for the light-driven OER under neutral, phosphate-buffered conditions in the presence of a Co-based WOC.[27] Furthermore, Pt^{II}-based metalloporphyrin complexes have been highlighted as excellent photosensitisers for H_2O splitting.[28,29] It was rationalised that the high quantum yields and large redox potentials associated with Pt^{II}-based porphyrins justified their use, despite the increased investment costs associated with this noble metal.[30,31] For these reasons Cu^{II}, Ni^{II} and Pt^{II} ions were selected for complexation with Me_2H_2**L1**.

Reaction conditions vary slightly depending on the metal ion to be incorporated in the porphyrin and are summarized in Scheme 2.3. Applied synthetic procedures were adapted from Cheng *et al*. and, in general, involve the reflux of the ester Me_2H_2**L1** with an excess of the desired metal salt in an appropriate organic solvent until complete metalation is confirmed using TLC.[32]

Me_2L1-Cu^{II}

Me_2**L1**-Cu^{II} was prepared by refluxing Me_2H_2**L1** and $Cu(OAc)_2$ in a mixture of $CHCl_3$ and MeOH in absence of light for 24 hours, followed by removal of the solvent under reduced pressure. Subsequent recrystallisation of the solid residue in a mixture of DCM and MeOH afforded the formation of Me_2**L1**-Cu^{II} as an orange powder in high yield (86%).

Me_2L1-Ni^{II}

Me_2**L1**-Ni^{II} was synthesised by refluxing Me_2H_2**L1** with $Ni(acac)_2$ in toluene in the dark for 48 hours. Following this, the solvent was evaporated under reduced pressure and the solid residue was recrystallized in a mixture of $CHCl_3$ and MeOH to afford the formation of Me_2**L1**-Ni^{II} as an orange powder in high yield (84%).

Me_2L1-Pt^{II}

Me_2**L1**-Pt^{II} was prepared by refluxing a solution of Me_2H_2**L1** and $PtCl_2$ in benzonitrile under an inert atmosphere for six hours while protecting from light. Removal of the solvent under reduced pressure and recrystallisation of the solid residue in a mixture of $CHCl_3$ and MeOH afforded the formation of Me_2**L1**-Pt^{II} as a red powder in good yield (77%).

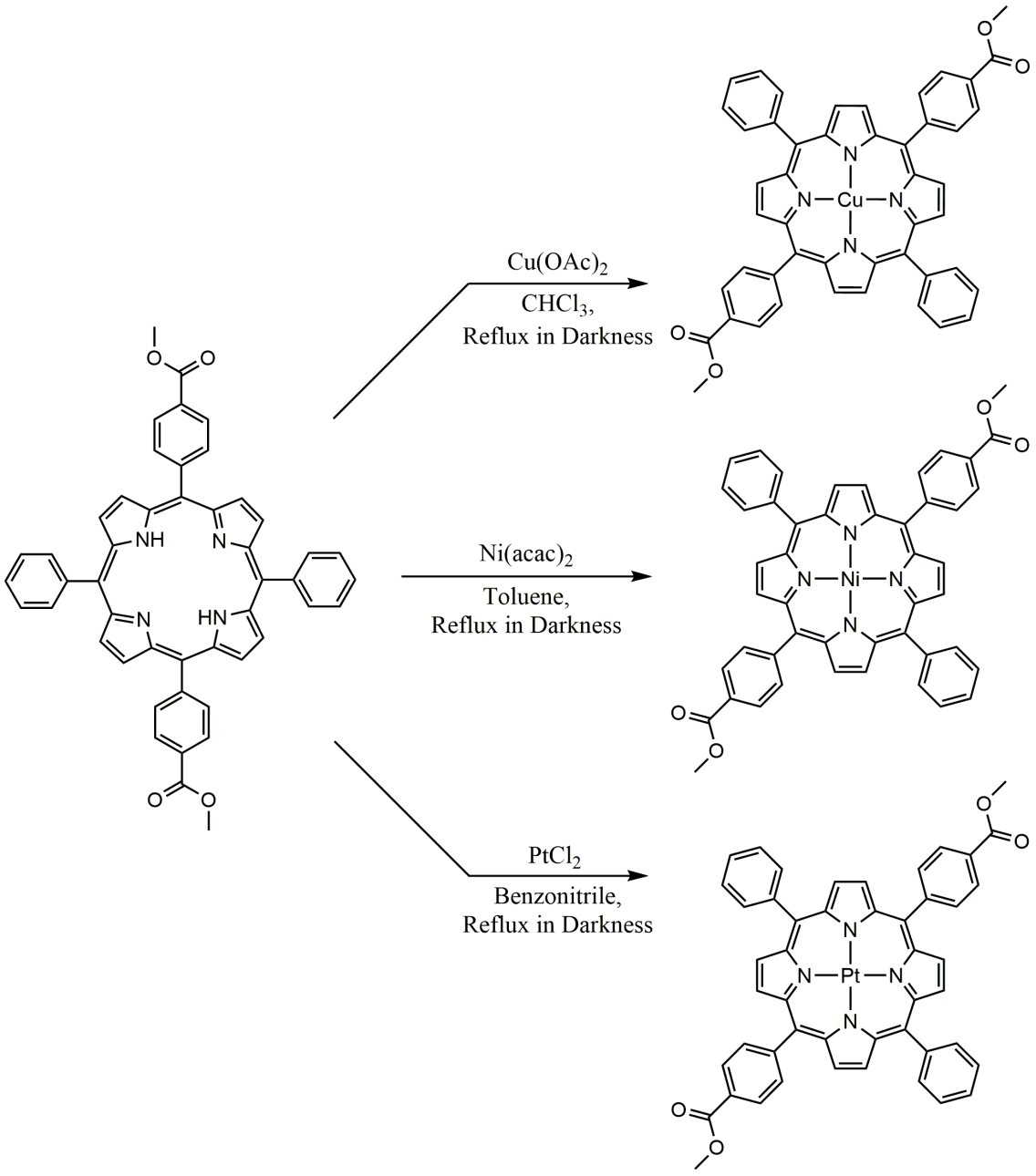

Scheme 2.3: Synthetic route to form the metalloporphyrin esters Me_2**L1**-Cu^{II}, Me_2**L1**-Ni^{II} and Me_2**L1**-Pt^{II} from Me_2H_2**L1.**

2.2.4 Synthesis of Carboxylic Acid Porphyrins H_4L1, Me_2H_2L1-Cu^{II}, Me_2H_2L1-Ni^{II} and Me_2H_2L1-Pt^{II}

Porphyrin esters were hydrolysed according to adapted literature procedures (Scheme 2.4).[33] The ester-functionalised porphyrins Me_2H_2**L1**, Me_2**L1**-Cu^{II}, Me_2**L1**-Ni^{II} and Me_2**L1**-Pt^{II} were each refluxed in mixtures of H_2O, KOH, THF and MeOH for up to 48 hours under darkness. The resulting dipotassium salts were then dissolved in water before being acidified with HCl, causing precipitation of the carboxylic acid products. These products were subsequently collected by filtration and washed with warm distilled water and hexane and (if necessary) recrystallised in EtOH and acetone, which afforded the formation of the deprotected metalloporphyrin ligands; H_4**L1** as a purple powder in 95% yield, H_2**L1**-Cu^{II} as an orange powder in 84% yield, H_2**L1**-Ni^{II} as an orange powder in 80% yield or H_2**L1**-Pt^{II} as a red powder in 74% yield. All compounds were characterised using NMR, FT-IR and UV-Vis spectroscopy, and mass spectrometry.

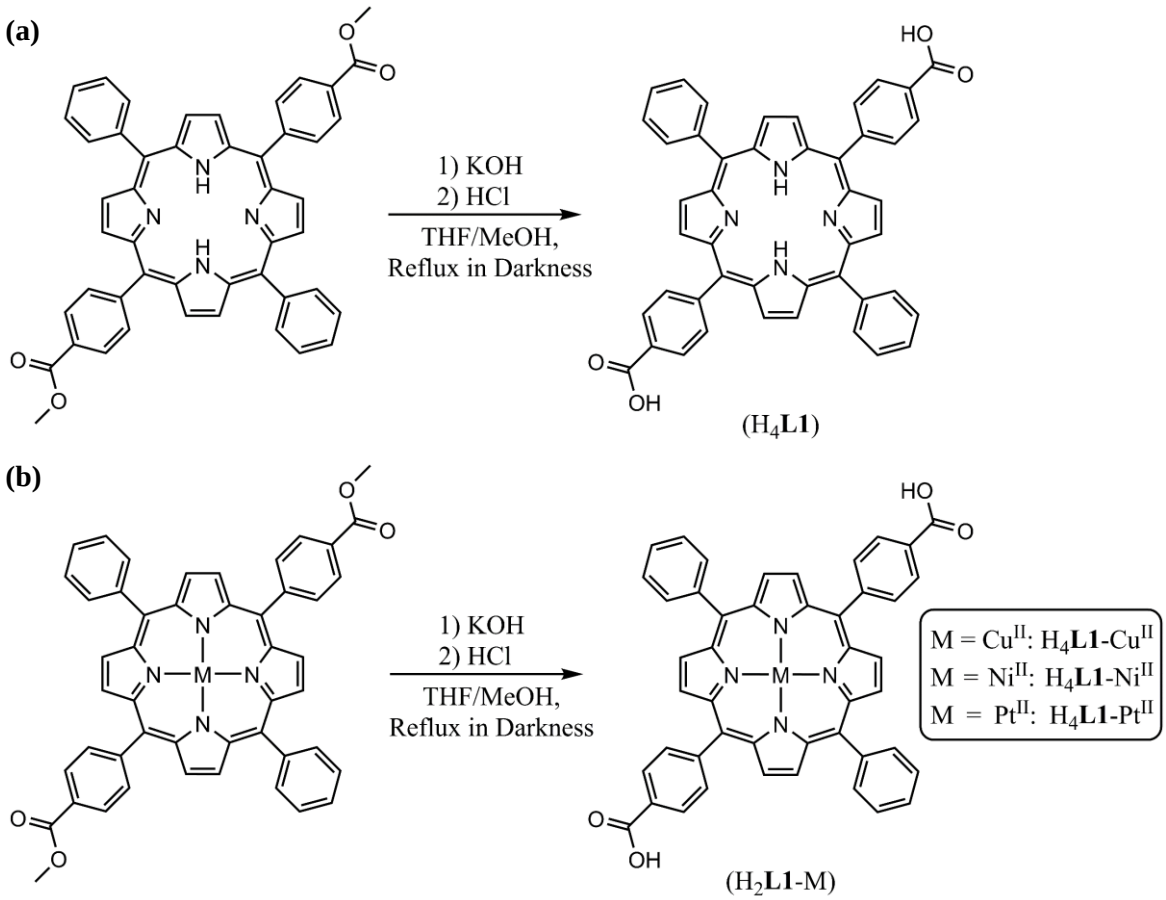

Scheme 2.4: Synthetic method employed to obtain (a) the dicarboxylate porphyrin H_4**L1** and (b) the dicarboxylate metalloporphyrins H_2**L1**-Cu^{II}, H_2**L1**-Ni^{II} and H_2**L1**-Pt^{II}.

2.3 $[Co^{II}_4(L1\text{-}Cu^{II})_4(H_2O)_7]\cdot 2DEA\cdot 8MeOH$ (1)

Following the successful synthesis and characterisation of the porphyrin ligands H_4**L1**, H_2**L1**-Cu^{II}, H_2**L1**-Ni^{II} and H_2**L1**-Pt^{II} in high purity, several attempts were made to incorporate these linkers into novel MMPFs containing redox-active Co^{II}-based SBUs. This aim was achieved for the first time with the synthesis of $[Co^{II}_4$(**L1**-$Cu^{II})_4(H_2O)_7]\cdot 2DEA\cdot 8MeOH$ (**1**).

2.3.1 Synthesis of $[Co^{II}_4(L1\text{-}Cu^{II})_4(H_2O)_7]\cdot 2DEA\cdot 8MeOH$ (1)

The 3D MMPF $[Co^{II}_4$(**L1**-$Cu^{II})_4(H_2O)_7]\cdot 2DEA\cdot 8MeOH$ (**1**) was synthesized in a reproducible reaction between H_2**L1**-Cu^{II} and $CoCl_2$ in a mixture of diethyl acetamide (DEA) and methanol. Heating this mixture to 80 °C in an autoclave for four days before slowly cooling to ambient temperature resulted in the formation of phase-pure, rod-shaped crimson crystals of **1** in good yield. The crystals were of suitable quality for analysis using single crystal X-ray diffraction.

2.3.2 Crystal Structure of $[Co^{II}_4(L1\text{-}Cu^{II})_4(H_2O)_7]\cdot 2DEA\cdot 8MeOH$ (1)

The crystal structure of $[Co^{II}_4$(**L1**-$Cu^{II})_4(H_2O)_7]\cdot 2DEA\cdot 8MeOH$ (**1**) was solved in the orthorhombic space group *Pbcn*. **1** is a 3D MMPF featuring tetranuclear $\{Co^{II}_4\}$ SBUs bridged by linear ditopic (**L1**-$Cu^{II})^{2-}$ porphyrin linkers and large, solvent-accessible hexagonal channels which extend in the direction of the crystallographic *a*-axis (Fig. 2.2).

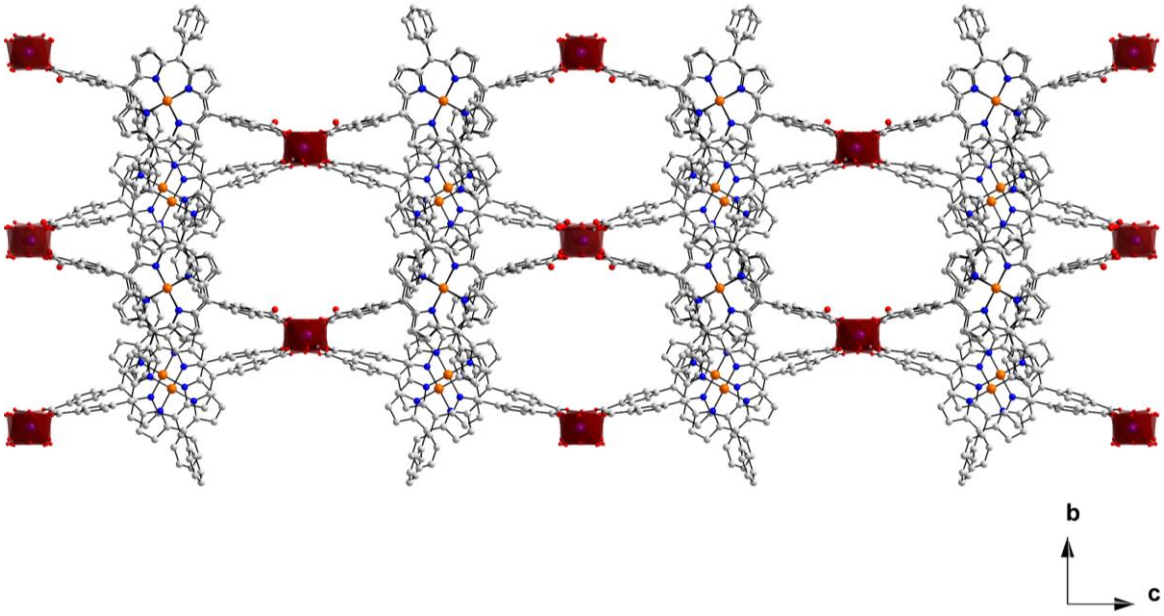

Figure 2.2: Ball-and-stick representation of the 3D structure of the MMPF $[Co^{II}_4$(**L1**-$Cu^{II})_4(H_2O)_7]\cdot 2DEA\cdot 8MeOH$ (**1**) viewed in the directions of the crystallographic *a*-axis highlighting the 1D channels of **1**. Solvent molecules and hydrogen atoms have been omitted for clarity. Colour scheme: C white, H grey, N blue, O red, Co violet, Cu orange. Co^{II} centres are represented as red polyhedra.

Each of the $\{Co^{II}_4\}$ SBUs of **1** are connected to eight other $\{Co^{II}_4\}$ nodes by eight bridging ditopic $(\mathbf{L1}\text{-}Cu^{II})^{2-}$ linkers. This generates the unique 3D architecture of **1** which can be seen in Fig. 2.3.

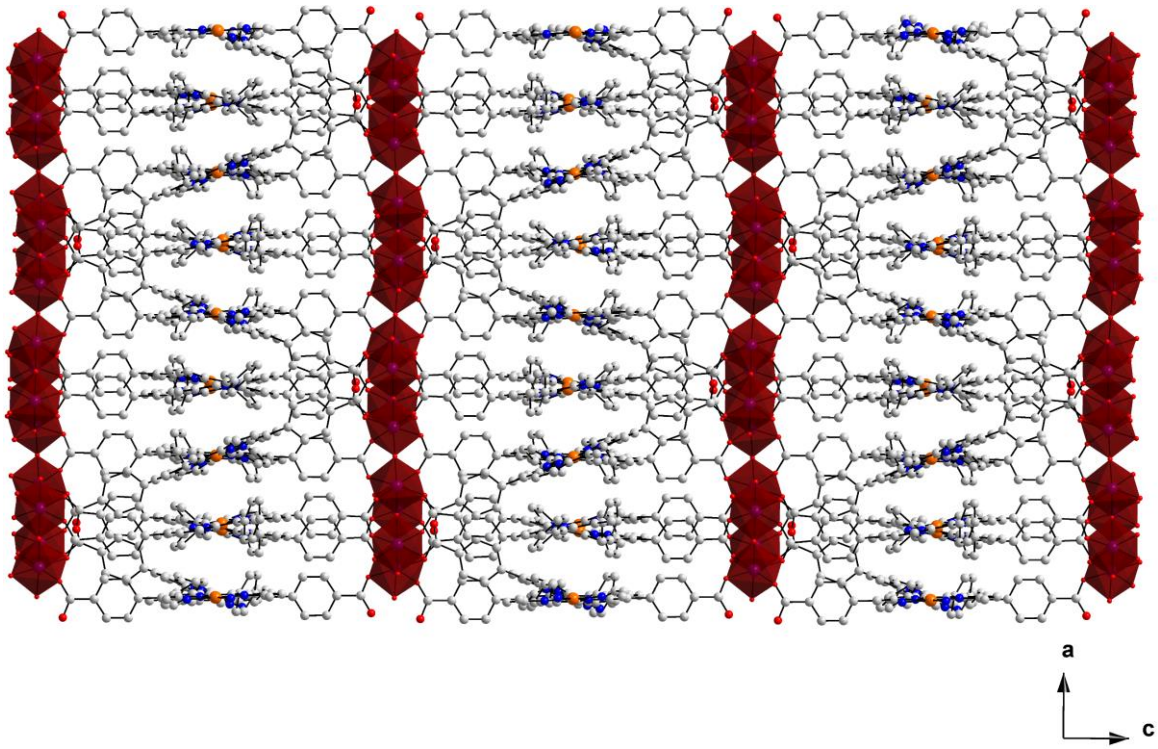

Figure 2.3: Ball-and-stick representation of the 3D structure of the MMPF **1** viewed in the directions of the crystallographic *b*-axis. Each of the tetranuclear $\{Co^{II}_4\}$ nodes in the framework are connected to 8 different $\{Co^{II}_4\}$ SBUs by 8 ditopic $(\mathbf{L1}\text{-}Cu^{II})^{2-}$ linkers. Solvent molecules and hydrogen atoms have been omitted for clarity. Colour scheme: C white, H grey, N blue, O red, Co violet, Cu orange. Co^{II} centres are represented as red polyhedra.

The asymmetric unit of **1** contains two crystallographically distinct Co^{II} centres which display distorted octahedral coordination environments, two doubly deprotonated $(\mathbf{L1}\text{-}Cu^{II})^{2-}$ ligands, one crystallographically fully-occupied μ_2-bridging H_2O molecule, one μ_2-bridging H_2O molecule with a crystallographic occupancy of ½ and two terminally coordinated H_2O molecules. The μ_2-bridging H_2O molecule with a crystallographic occupancy of ½ is located on a two-fold rotational axis. This C_2 symmetry element positioned on the central μ_2-bridging O-donor generates the linear tetranuclear $\{Co^{II}_4\}$ SBU of **1**. This SBU is stabilised by eight different μ_2-bridging $(\mathbf{L1}\text{-}Cu^{II})^{2-}$ ligands and seven H_2O molecules, three of which adopt a μ_2-bridging mode and four of which are terminally coordinated.

Eight linear ditopic (**L1**-Cu^{II})$^{2-}$ linkers connect each SBU with eight different tetranuclear SBUs (Fig. 2.4). Each of the two crystallographically independent linkers in **1** are doubly deprotonated and adopt two different coordination modes at their four different binding sites; three adopt a bidentate bridging mode and one adopts a monodentate binding mode. The hexagonal channels in **1** are occupied by disordered solvent molecules which could not be modelled, so were therefore accounted for using the OLEX2 implementation of BYPASS.[34]

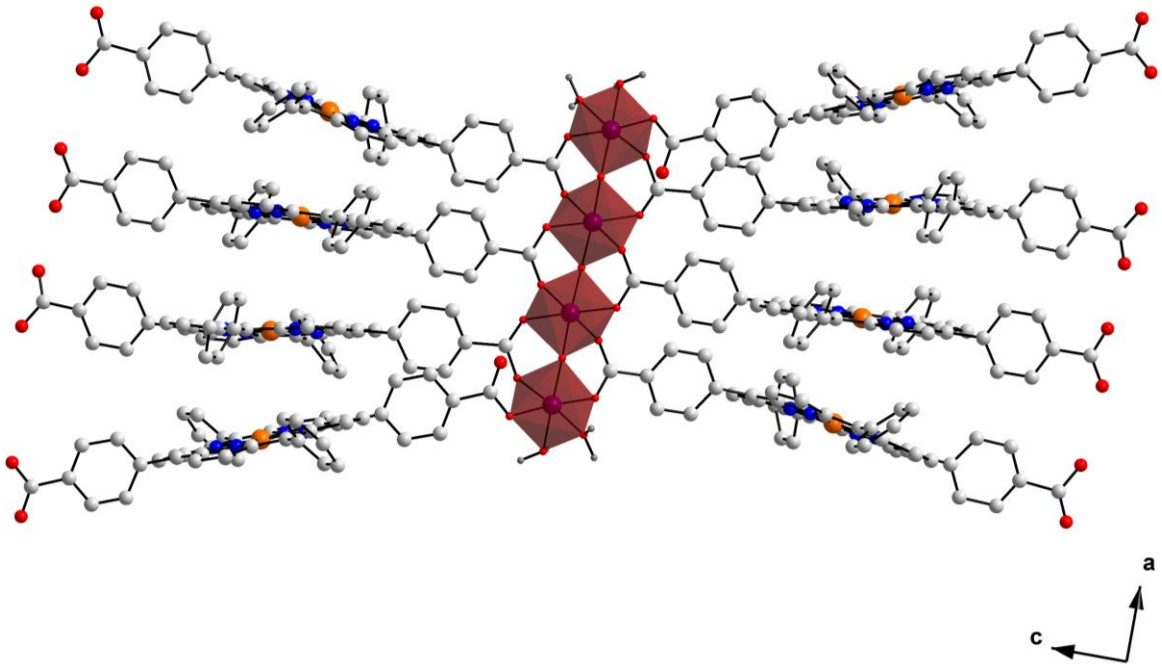

Figure 2.4: Ball-and-stick representation of {Co^{II}_4} SBU of [Co^{II}_4(**L1**-Cu^{II})$_4$(H_2O)$_7$]·2DEA·8MeOH (**1**) showing the arrangement the (**L1**-Cu^{II})$^{2-}$ linkers which surround the 8-connected tetranuclear {Co^{II}_4} node, viewed in the direction of the crystallographic *b*-axis. Solvent molecules and hydrogen atoms have been omitted for clarity. Colour scheme: C white, H grey, N blue, O red, Co violet, Cu orange. Co^{II} centres shown as red polyhedra.

A detailed representation of the {Co^{II}_4} SBU of **1** is presented in Fig. 2.5. The coordination geometry adopted by each of the four Co^{II} centres in the SBU of **1** is distorted octahedral. The four metal centres are bridged by six μ_2-bridging carboxylate moieties and three O-donors from three μ_2-bridging H_2O molecules. The central μ_2-bridging O-donor O(12) that bridges Co(2) and Co(2') is located on a 2-fold rotational axis. The SBU is also coordinated by four O-donors O(1), O(2), O(1') and O(2') that derive from four η^1 terminal capping H_2O molecules which are orientated towards the hexagonal channels of **1**.

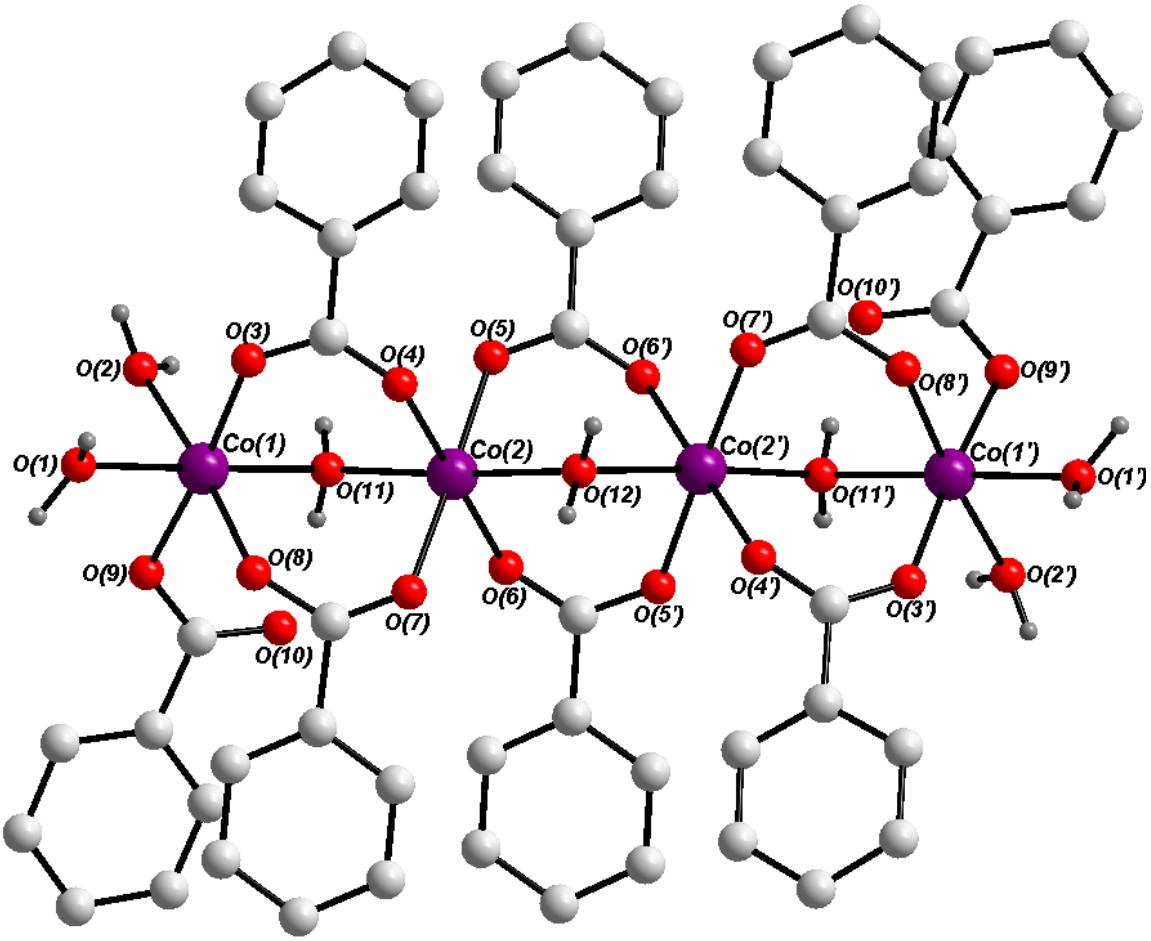

Figure 2.5: Ball-and-stick representation of the tetranuclear $\{Co^{II}_4\}$ SBU in **1**. Most of the hydrogen atoms have been omitted for clarity. Colour scheme: C white, H grey, O red, Co violet.

The coordination environment of Co(1) comprises two O-donors O(1) and O(2) of two *cis* terminally coordinated aqua ligands, two O-donors O(3) and O(8) that derive from two distinct bidentate *syn-syn* bridging carboxylate moieties which each adopt a μ_2-η^1:η^1 binding mode, one O-donor O(9) which derives from a monodentate carboxylate moiety and adopts a μ_1-η^1 binding mode, and one O-donor O(11) from a μ_2-bridging aqua ligand.

The bond distances between Co(1) and each of the O-donors of the two terminal H_2O molecules O(1) and O(2) are 2.112(7) Å and 2.126(5) Å for Co(1) – O(1) and Co(1) – O(2), respectively. In contrast, the bond distances between Co(1) and the O-donors of the two bidentate carboxylate moieties are 2.004(4) Å and 2.038(5) Å for Co(1) – O(3) and Co(1) – O(8), respectively. The distance between Co(1) and the monodentate carboxylate moiety O-donor

O(9) is 2.076(4) Å. The distance between Co(1) and the O-donors of the μ_2-bridging H_2O ligand O(11) is the longest bond distance in the coordination sphere of Co(1), which is 2.143(4) Å.

The bond angles surrounding Co(1) that deviate from the ideal octahedral angle of 90° are within the range of 86.36(2)° – 98.74(3)°. The bond angle surrounding Co(1) that deviates most significantly from the ideal octahedral angle of 180° is 174.3(2)° for O(2)-Co(1)-O(8).

The coordination environment of Co(2) is composed of four equatorial O-donors O(4), O(5), O(6) and O(7) that derive from four different bidentate *syn-syn* bridging carboxylate moieties which adopt μ_2-η^1:η^1 binding modes. Two axial O-donors O(11) and O(12) of two μ_2-bridging H_2O moieties complete the coordination sphere of Co(2).

The bond distances between Co(2) and the four O-donors of the bidentate bridging carboxylate moieties O(4), O(5), O(6) and O(7) are 2.058(4) Å, 2.025(4) Å, 2.046(4) Å and 2.060(4) Å, respectively. The bond distances between Co(2) and the O-donors of two μ_2-bridging H_2O moieties are 2.150(4) Å and 2.178(3) Å for Co(2) – O(1) and Co(2) – O(12), respectively.

The bond angles surrounding Co(2) which deviate from the ideal octahedral angle of 90° are within the range of 86.43(2)° – 94.43(2)°, and the bond angle surrounding Co(2) that deviates most significantly from the ideal octahedral angle of 180° is 176.88(2)° for O(2)-Co(2)-O(8). This binding geometry gives Co(2) an axially elongated, distorted octahedral coordination environment. The bond distances and angles surrounding Co(1) and Co(2) are within expected ranges and are consistent with comparable Co^{II} carboxylate complexes reported in the literature.[35]

The interatomic distance Co(1)···Co(2) is 3.587(1) Å, and the interatomic distance Co(2)···Co(2') is 3.575(5) Å. The bond angles Co(1)-O(11)-Co(2) and Co(2)-O(12)-Co(2') are 113.31(1)° and 110.36(1)°, respectively. These interatomic distances and angles within the SBU of **1** are similar to those reported for other analogous carboxylate-bridged Co^{II} complexes in the literature.[36]

Topologically, the tetranuclear SBU can be considered as an 8-connected node linked by ditopic (**L1**-Cu^{II})$^{2-}$ linkers, generating a uninodal framework with the overall point symbol of $\{4^{20}\cdot6^{8}\}$. A topological reduction of **1** is presented in Fig. 2.6. To the best of our knowledge, the topology of **1** is exceptionally rare. At the time of writing, 8-connected MOFs are scarcely described in the literature.[37,36,38] Further, this is also the first reported example of a MOF featuring the unique linear $\{Co^{II}_4\}$ SBU.

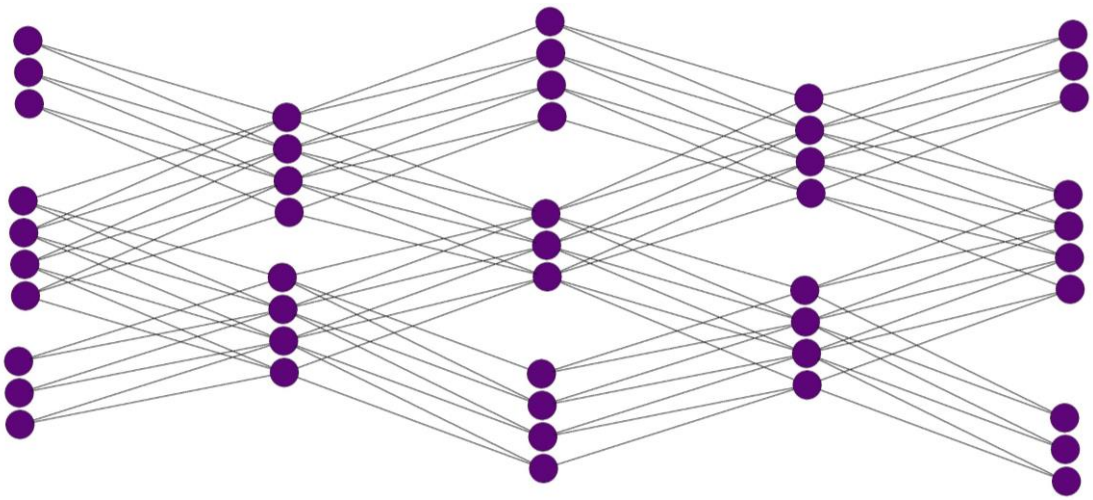

Figure 2.6: Topological reduction illustrating the connectivity of **1**. $\{Co^{II}_4\}$ nodes are represented as violet spheres connected by **(L1**-Cu^{II}**)**$^{2-}$ linkers.

Selected supramolecular interactions which stabilise **1** are shown in Fig. 2.7. Hydrogen bonding interactions within **1** are highlighted in Fig. 2.7a. The O-atom O(10) of the monodentate carboxylate moiety acts as a H-bond acceptor by forming a hydrogen bond with the μ_2-bridging water moiety comprising O(11), which acts as a H-bond donor. The hydrogen bond distance O(10)···H – O(11) is 2.564(2) Å, and the bond angle O(10)···H-O(11) is 160.3(5)°. These values are consistent with literature reported hydrogen bonding interactions of moderate strength.[39]

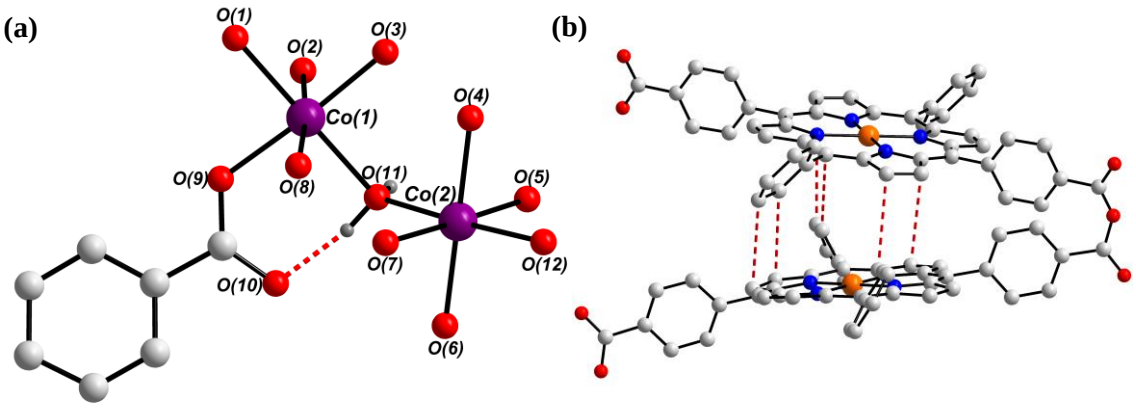

Figure 2.7: Ball-and-stick representation of the supramolecular forces within **1** highlighting (a) the hydrogen bonding interaction between the hydrogen bond acceptor O(10) and the hydrogen bond donor O(11), and (b) selected π – π stacking interactions between (**L1**-Cu^{II}**)**$^{2-}$ linker moieties which stabilise **1**. Hydrogen atoms not participating in hydrogen bonding and coordinated solvent molecules have been omitted for clarity. Hydrogen bonds and π – π interactions are represented as dashed red lines. Colour scheme: C white, H grey, N blue, O red, Co violet, Cu orange.

Further stabilisation of **1** occurs through π – π stacking interactions which extend approximately in the direction of the crystallographic *a*-axis. Some of these stacking interactions are highlighted in Fig. 2.7b. The non-functionalised *meso* phenyl rings of the (**L1**-Cu^{II})$^{2-}$ linkers display T-shaped π – π stacking interactions with neighbouring (**L1**-Cu^{II})$^{2-}$ porphyrin rings. The distance between these π – π stacking moieties is within the range of 3.47 – 3.67 Å. Neighbouring porphyrin moieties also display parallel displaced π – π stacking interactions which stabilise **1**. These interactions, which occur between the tetrapyrrolic systems of adjacent (**L1**-Cu^{II})$^{2-}$ moieties, are also highlighted in Fig. 2.7b. The average distance between these stacking porphyrins varies between 3.58 Å and 3.62 Å, and is consistent with π – π stacking interactions reported in the literature.[40,41]

The two distinct (**L1**-Cu^{II})$^{2-}$ linker moieties within the crystal structure of **1** are illustrated in Fig. 2.8. Each of the Cu^{II} ions Cu(1) and Cu(2) adopt square planar coordination geometries, and the metalloporphyrin moieties adopt planar configurations. The bond angles between the central Cu^{II} ions and the pyrrolic N-donors located at opposite corners of the macrocyclic cavity range between 179.22(18)° to 180.00(15)° for N(1)-Cu(1)-N(3) and N(5)-Cu(2)-N(7), respectively.

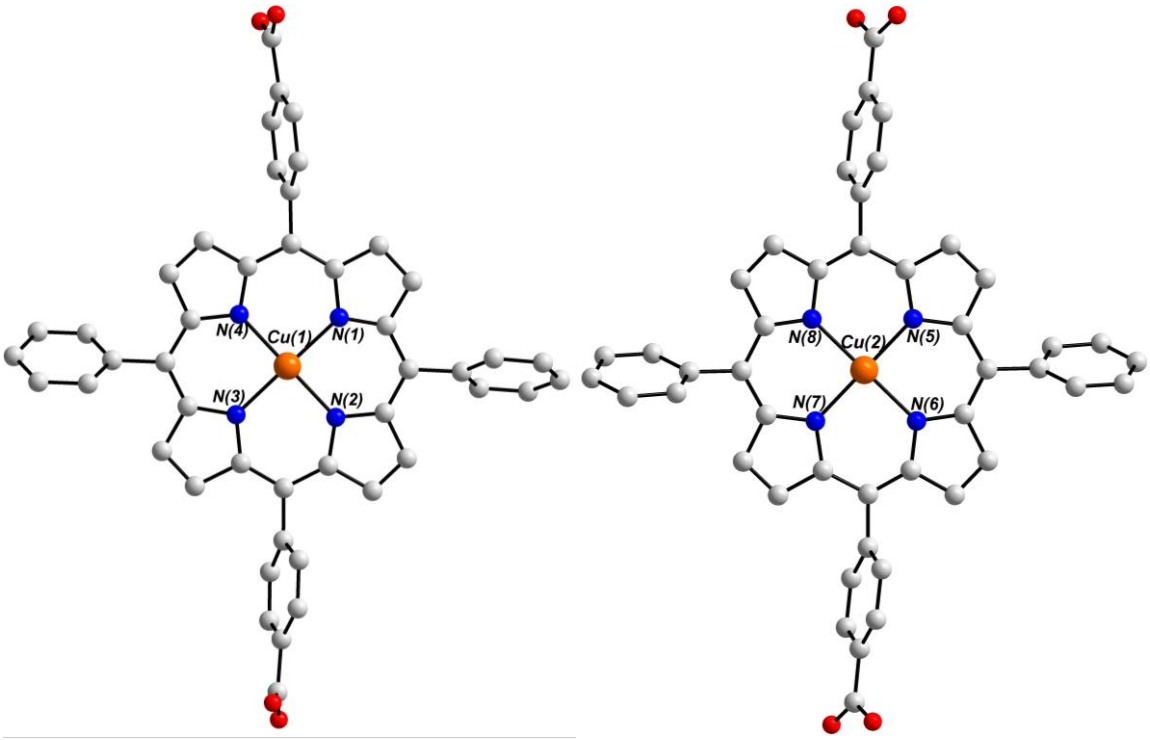

Figure 2.8: Ball-and-stick representations of the two distinct ditopic (**L1**-Cu^{II})$^{2-}$ metalloporphyrin linker moieties of **1**. Hydrogen atoms have been omitted for clarity. Colour scheme: C white, N blue, O red, Cu orange.

The dihedral angles between carboxylate-functionalised phenyl rings on opposite *meso* positions of the (**L1**-Cu^{II})$^{2-}$ ligands vary up to 9.94°, whereas the dihedral angles between the non-functionalised phenyl rings of the (**L1**-Cu^{II})$^{2-}$ linkers are within the range of 0.32° – 56.51°. This configuration facilitates increased stabilisation of the ligands through π – π stacking and hydrogen bonding interactions.

The two ditopic porphyrin linkers present in the asymmetric unit of **1** are both fully deprotonated. For each of the two (**L1**-Cu^{II})$^{2-}$ linkers, two carboxylic acid moieties and two pyrrole moieties of the porphyrin ring system are deprotonated. This gives a charge of −8, which is balanced by two Cu^{II} ions which occupy the central cavities of the metalloporphyrin rings, and two Co^{II} ions of the MMPF's SBU. **1** is therefore a neutral framework, and the assignment of the oxidation states for each of the Cu^{II} and Co^{II} ions were verified using BVS analysis calculations.

The packing of **1** is presented in Fig. 2.9. Viewing along the crystallographic *a*- *b*- and *c*-axes illustrates the 1D hexagonal channels of **1**. These channels extend in parallel with the crystallographic *a*-axis and constitute the void volume of **1**. The solvent-accessible void volume of **1** was calculated as *ca*. 4874 $Å^3$, which corresponds to 21.8% of the unit cell (using CCDC-mercury program and a probe radius of 1.2 Å).[42]

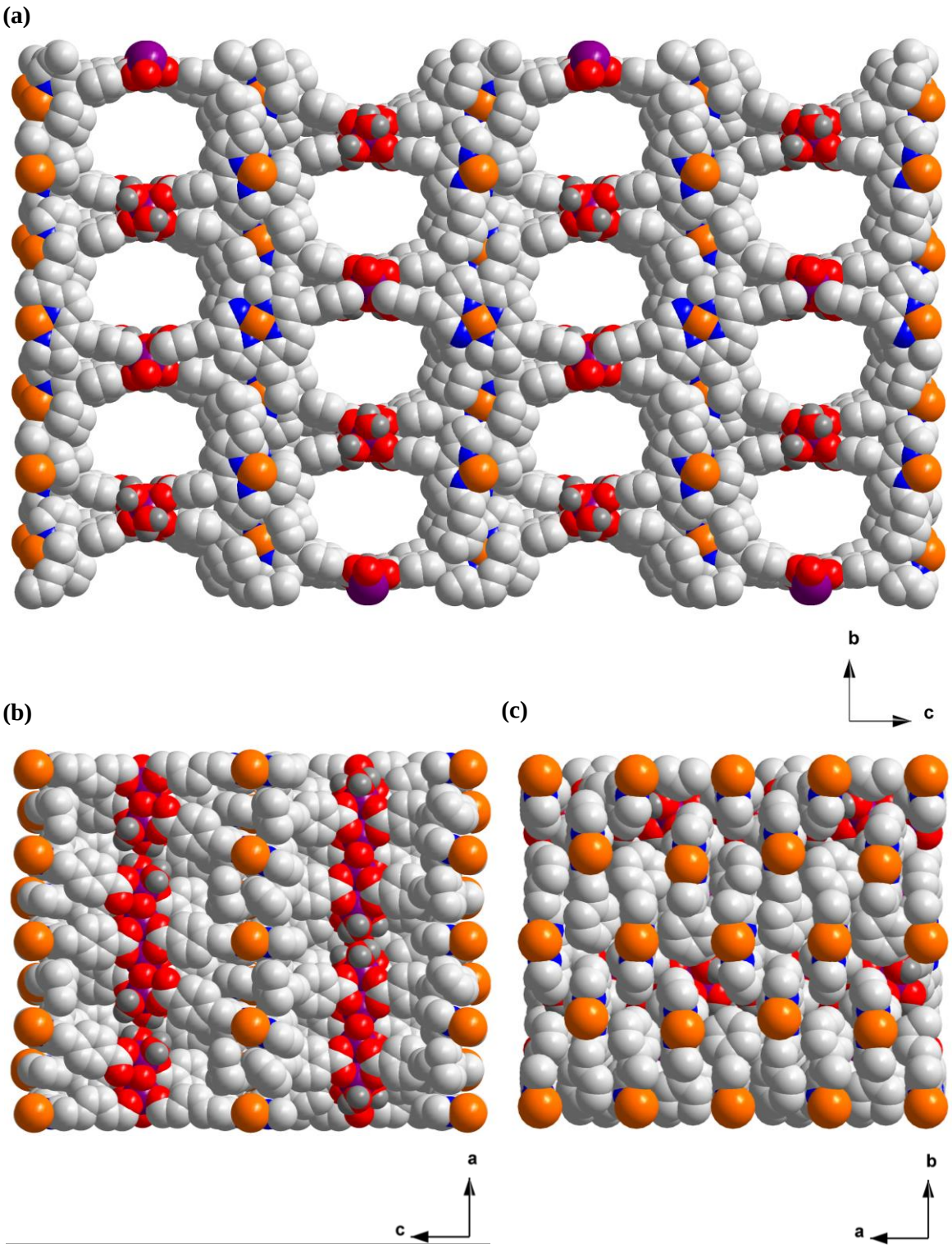

Figure 2.9: Space-filling representation of the packing of **1**, viewed along the crystallographic (a) *a*-axis, (b) *b*-axis and (c) *c*-axis. Colour scheme: C white, H grey, N blue, O red, Co violet, Cu orange.

2.3.3 Physicochemical Characterisation of 1

Infrared Spectroscopy

The MMPF **1** was characterised using IR spectroscopy. The FT-IR spectrum of **1** (Fig. 2.10) exhibits several characteristic signals: A weak, broad signal at around 3629 cm^{-1} was assigned to O – H stretching vibrations of the terminal and bridging H_2O molecules within the SBU of **1**, and constitutional solvent molecules. A signal at 3058 cm^{-1} can be assigned to aromatic C – H stretching vibrations of the (**L1**-Cu^{II})$^{2-}$ linker moieties. Two signals at 2972 and 1604 cm^{-1} can be attributed to a C – H vibration and a C = O vibration, respectively of the constitutional DEA solvent molecules which occupy the channels of **1**.[43] A band at 1575 cm^{-1} may be assigned to an asymmetric stretching vibrational mode of the η^1 binding carboxylate moiety of **1**.[44,45] Strong signals at 1533 and 1382 cm^{-1} were attributed to the asymmetric and symmetric stretching vibrations, respectively of the μ^2-η^1:η^1 bridging carboxylate moiety in **1**.[46] Two absorptions at 1342 and 996 cm^{-1} can be assigned to a C – N vibration, and to an in-plane deformation (ring breathing) of the (**L1**-Cu^{II})$^{2-}$ ligand, respectively.[47]

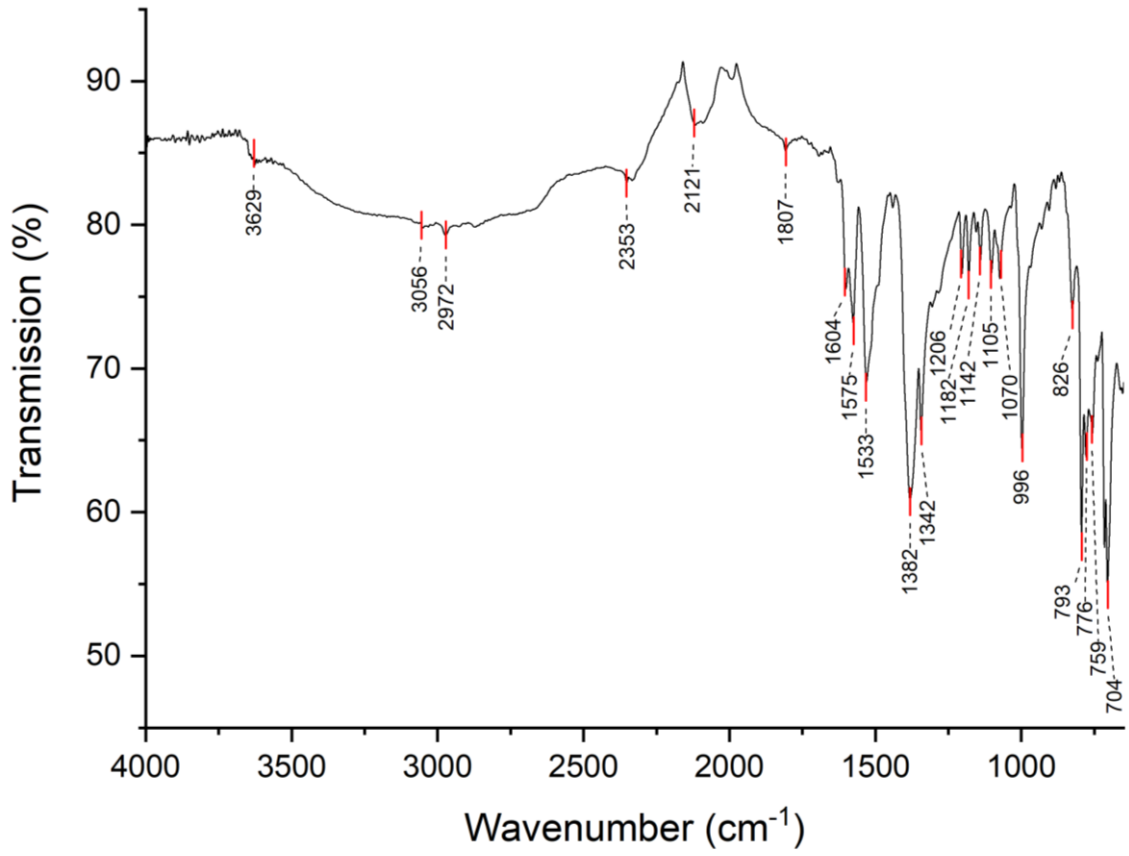

Figure 2.10: FT-IR spectrum of **1**.

Thermogravimetric Analysis

The thermal stability of **1** was assessed using thermogravimetric analysis (TGA). The analysis was conducted using a freshly prepared crystalline sample under a constant stream of N_2 in the temperature range 30 – 800 °C. The TGA trace (Fig. 2.11) reveals that as **1** is heated from 30 – 100 °C, a weight loss of 9.9% is observed. This weight loss can be accounted for by the loss of 8 methanol molecules from channels of **1** (calculated: 9.9%). Heating **1** further from 100 - 190 °C resulted in an additional weight loss of 9.2%, which can be attributed to the loss of two DEA solvent molecules from the channels in **1**, and the loss of the three μ_2-bridging and two terminal H_2O molecules from the SBU of **1** (calculated: 9.1%). Heating **1** above 350 °C results in decomposition of the organic ligands and is associated with a weight loss of 55%. A final decomposition step is noted from 480 - 800 °C, which is attributed to the formation of metal oxide species. The formula $[Co^{II}_4(\mathbf{L1}\text{-}Cu^{II})_4(H_2O)_7]\cdot 2DEA\cdot 8MeOH$ assigned to **1** was determined through the interpretation of these data.

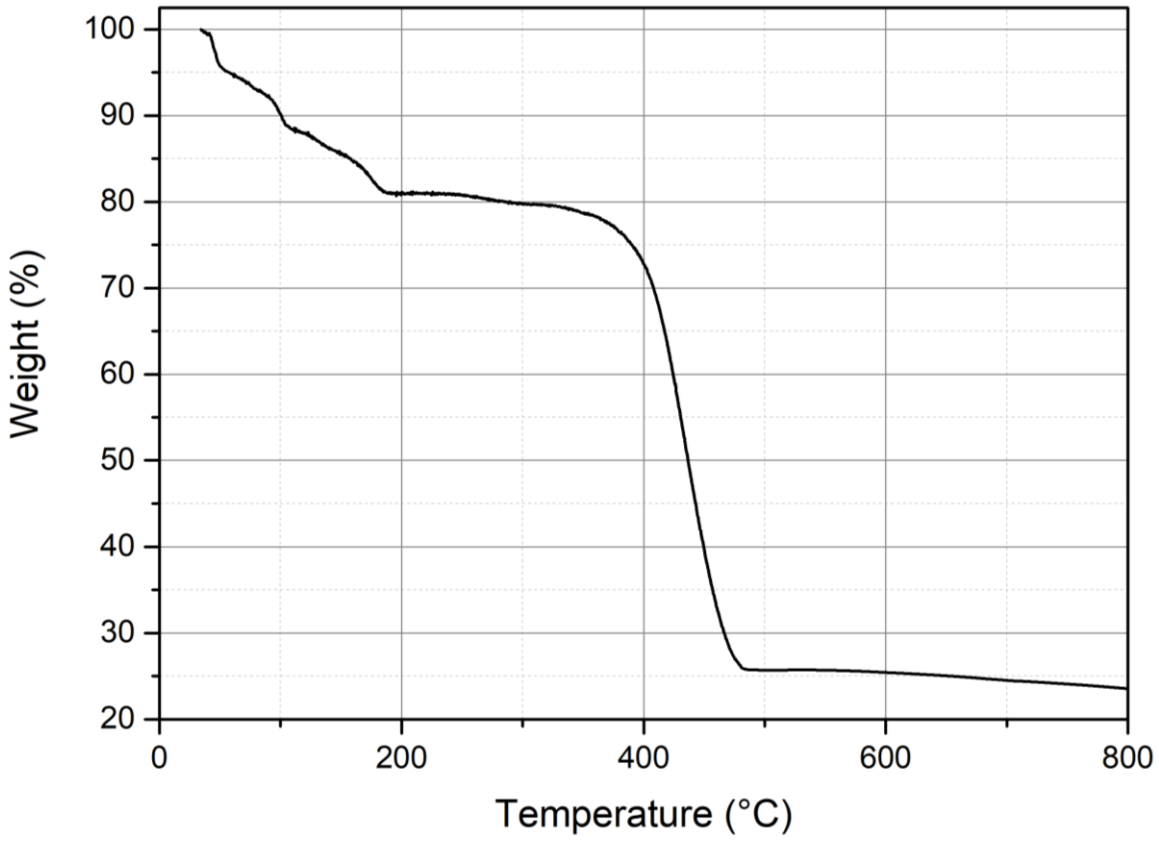

Figure 2.11: TGA trace for **1.**

Powder X-Ray Diffraction Analysis

Powder X-ray diffraction (PXRD) analysis was employed to determine the phase purity of **1** (Fig. 2.12). As **1** rapidly desolvates in air, the material was measured using a capillary. Comparison of the measured powder pattern with the simulated powder pattern (calculated from the crystal structure of **1**) shows that the two highest intensity signals in the calculated powder pattern at 2Θ = 6.13° and 8.45° are in good agreement with the measured powder pattern. The fine structure is not fully resolved in the powder pattern of **1**, however most of the high intensity signals are present in both the measured powder pattern and the simulated PXRD spectrum. This disparity may be due to preferred orientation effects in the measured sample. Alternatively, differences between the measured and simulated PXRD patterns could arise from unrefined disordered solvent molecules in the crystal structure of **1**. The results of this analysis indicate that **1** forms phase-pure using the synthetic approach outlined in Section 2.2.

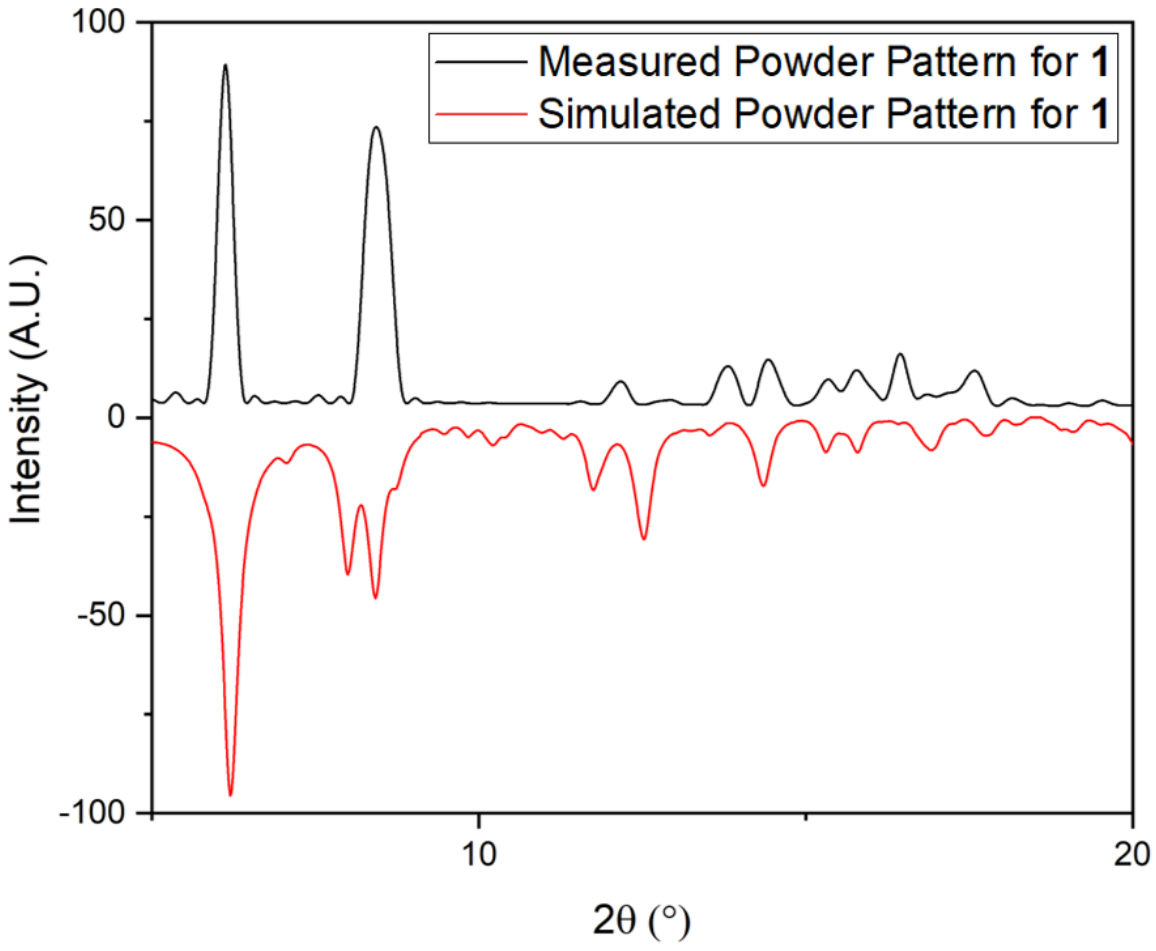

Figure 2.12: Powder X-ray diffraction analysis comparing the experimental powder pattern of **1** (black) with the simulated powder pattern calculated using the single crystal X-ray diffraction data of **1** (red).

2.4 $[Co^{II}(L1\text{-}Cu^{II})(DEA)]\cdot H_2O\cdot 3MeOH$ (2)

Initial attempts to synthesise novel 3D Co^{II}-based MMPFs using the relatively underexplored metalloporphyrin pro-ligand H_2**L1**-Cu^{II} were successful. After achieving this objective with the synthesis of **1**, further experiments were carried out to establish if other Co^{II}-based MMPFs could be generated using (**L1**-Cu^{II})$^{2-}$ as a ligand. These investigations led to the discovery of $[Co^{II}$(**L1**-Cu^{II})(DEA)]·H_2O·3MeOH (**2**).

Modification of the reaction conditions applied in the synthesis of **1** resulted in the generation of the 2D Co^{II}-based MMPF **2**. **2** forms from the same reactants as **1**, however at a higher temperature and in the presence of a modulator (acetic acid). In this section. the synthesis, structure and physicochemical characterisation of **2** are discussed.

2.4.1 Synthesis of $[Co^{II}(L1\text{-}Cu^{II})(DEA)]\cdot H_2O\cdot 3MeOH$ (2)

The 2D MMPF $[Co^{II}(\mathbf{L1}\text{-}Cu^{II})(DEA)]\cdot H_2O\cdot 3MeOH$ (**2**) was synthesised in a reproducible reaction between $H_2\mathbf{L1}\text{-}Cu^{II}$ and $CoCl_2\cdot 6H_2O$ in a mixture of DEA and methanol in the presence of acetic acid as a modulator. Heating this mixture to 120 °C under solvothermal conditions for three days led to the formation of red, plate-shaped crystals of **2** in moderate yields which were suitable for analysis using single crystal X-ray diffraction.

2.4.2 Crystal Structure of $[Co^{II}(L1\text{-}Cu^{II})(DEA)]\cdot H_2O\cdot 3MeOH$ (2)

The crystal structure of **2** was solved in the monoclinic space group *P*2/*c*. X-ray analysis revealed that **2** is a 2D MMPF featuring rod-shaped SBUs which are comprised of alternating tetrahedrally and octahedrally coordinated Co^{II} centres. The SBUs of **2** are bridged by$(\mathbf{L1}\text{-}Cu^{II})^{2-}$ linkers generating 2D sheets with a corrugated form (Fig. 2.13).

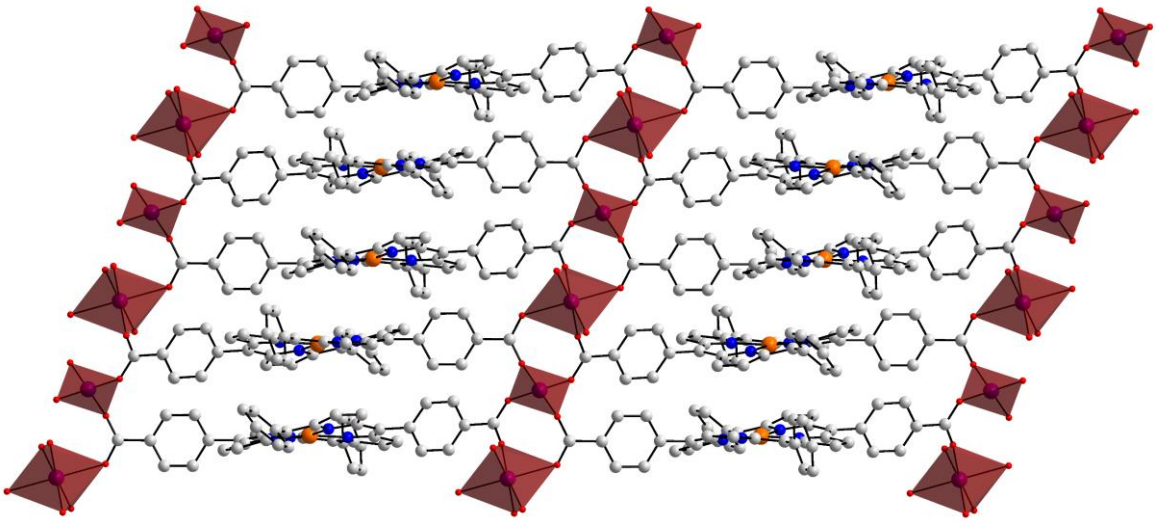

Figure 2.13: Ball-and-stick representation of the 2D MMPF $[Co^{II}(\mathbf{L1}\text{-}Cu^{II})(DEA)]\cdot H_2O\cdot 3MeOH$ showing a corrugated 2D sheet featuring rod-shaped SBUs connected by ditopic linear $(\mathbf{L1}\text{-}Cu^{II})^{2-}$ linkers. Coordinated solvent molecules and hydrogen atoms have been omitted for clarity. Colour Scheme: C white, O red, Co violet, Cu Orange. Co^{II} centres are represented as red polyhedra.

The asymmetric unit of **2** contains two crystallographically independent Co^{II} centres, each of which are located on two-fold rotational axes and have a crystallographic occupancy of ½. Also present in the asymmetric unit of **2** are one doubly deprotonated $(\mathbf{L1}\text{-}Cu^{II})^{2-}$ ligand and one terminally coordinated DEA solvent molecule. The constitutional solvent molecules were not

located in the crystal structure of **2** and were therefore masked using the Platon-Squeeze routine.[48]

Each of the Co^{II} centres within the MMPF **2** are coordinated by four different *syn-syn* bridging carboxylate moieties which adopt μ_2-η^1:η^1 binding modes. These carboxylate moieties connect the Co^{II} centres generating infinite 1D chains that extend in the direction of the crystallographic *a*-axis (Fig. 2.14). These rod-shaped SBUs stack in parallel with one another and are each connected within the 2D sheet along the [101] crystallographic directions to two neighbouring SBUs by ditopic (**L1**-Cu^{II})$^{2-}$ linkers.

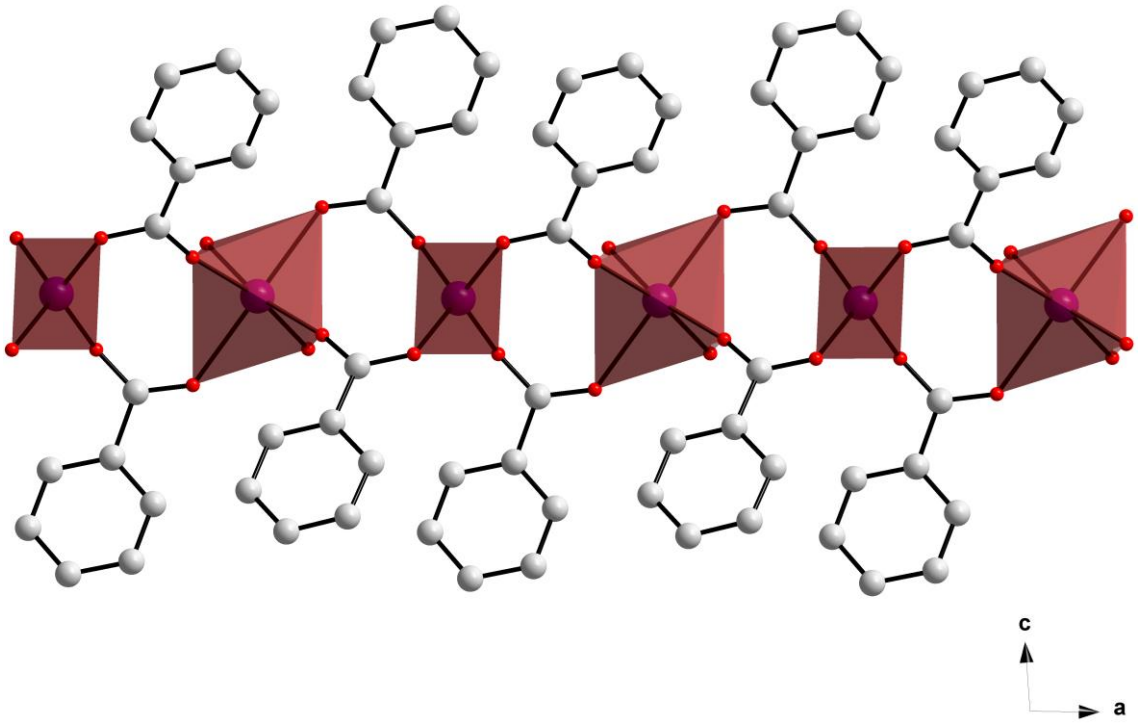

Figure 2.14: Ball-and-stick representation of the SBU of the 2D MMPF [Co^{II}(**L1**-Cu^{II})(DEA)]·H_2O·3MeOH (**2**) which features alternating tetrahedral and octahedral Co^{II} centres bridged by the carboxylate moieties of the (**L1**-Cu^{II})$^{2-}$ ligand. Coordinated solvent molecules and hydrogen atoms have been omitted for clarity. Colour Scheme: C white, O red, Co violet. Co^{II} centres are represented as red polyhedra.

The coordination environments of the two crystallographically ½ occupied Co^{II} centres, Co(1) and Co(2) of **2** are displayed in Fig. 2.15. The coordination geometry of Co(1) is distorted octahedral, and this ion's coordination environment comprises four O-donors O(1), O(1'), O(4) and O(4') which derive from four *syn-syn* bridging, μ_2-η^1:η^1 binding carboxylate moieties of

four different (**L1**-Cu^{II})$^{2-}$ ligands, and two O-donors O(5) and O(5') of two *cis*-coordinated DEA solvent molecules. The coordination geometry adopted by the other Co^{II} centre of **2**, Co(2), is distorted tetrahedral and is composed of four O-donors O(2), O(3), O(2') and O(3') of four different *syn-syn* bridging, μ_2-η^1:η^1 binding carboxylate moieties which derive from four different (**L1**-Cu^{II})$^{2-}$ linker moieties.

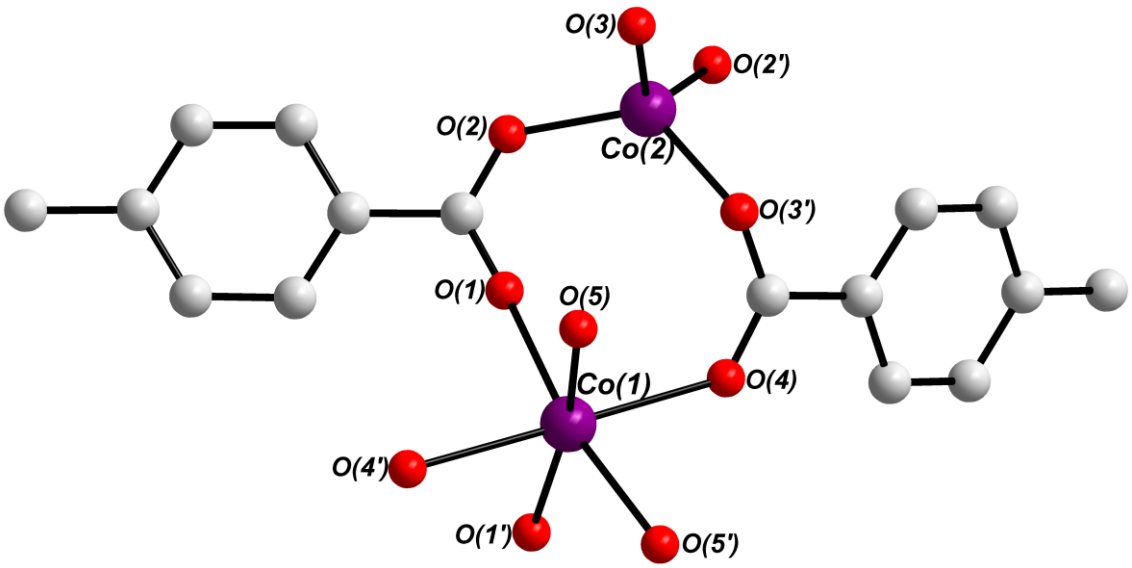

Figure 2.15: Ball-and-stick representation of the octahedral and tetrahedral coordination environments of the two Co^{II} centres Co(1) and Co(2) of **2**. Coordinated solvent molecules and hydrogen atoms have been omitted for clarity. Colour scheme: C white, O red, Co violet.

The octahedrally coordinated Co^{II} ion Co(1) is characterised by a bond distance between the metal centre and the carboxylate O-donors O(1) and O(1') of 2.2850(5) Å, whilst the bond distance between Co(1) and the carboxylate O-donors O(4) and (O4') is 2.3686(7) Å. The distance between Co(1) and the O-donors O(5) and O(5') which derive from the *cis* coordinated DEA solvent moieties is 2.2626(5) Å. The bond angles surrounding Co(1) which deviate most significantly from the ideal octahedral angle of 90° are 83.88(19)° and 97.86(19)° for O(4)-Co(1)-O(5') and O(4)-Co(1)-O(5), respectively. The bond angle surrounding Co(1) that deviates most significantly from the ideal octahedral angle of 180° is 169.22(19)° for O(5)-Co(1)-O(1').

The bond distances between the tetrahedrally coordinated Co^{II} centre Co(2) and the carboxylate derived O-donors O(2) and O(3) are 1.9604(5) Å and 1.9484(4) Å, respectively. The bond

angles surrounding Co(2) which differ the greatest amount from the ideal tetrahedral angle of 109.5° are 98.41(2)° for O(3)-Co(2)-(3') and 124.52(3)° for O(2')-Co(2)-O(3). The bond distances and angles surrounding the two Co^{II} centres within the SBU of **2** fall within expected ranges, and are typical in comparison with the bond distances and angles of other literature reported tetrahedral and octahedral Co^{II} carboxylate complexes.[49,50,51]

The interatomic distance between neighbouring Co^{II} centres within the same 1D chain Co(1)···Co(2) is 4.5020(14) Å. This interatomic distance is significantly longer than the average Co···Co interatomic distance within the tetranuclear Co^{II} SBU of **1** which is *ca.* 3.6 Å. The shortest distance between two connected rod-shaped SBUs (Co^{II} centre to Co^{II}) centre is *ca.* 22 Å.

The saddle-shaped metalloporphyrin linker (**L1**-Cu^{II})$^{2-}$ of **2** is depicted in Fig. 2.16. The porphyrin exhibits a ruffled configuration. The bond angles surrounding the central square planar Cu^{II} ion Cu(1) which deviate from the ideal angle of 180° are 173.33(3)° and 173.61(3)° for N(1)-Cu(1)-N(3) and N(2)-Cu(1)-N(4), respectively. The extent to which these bond angles differ from 180° is greater than the equivalent bond angles of **1**. Therefore, the porphyrin ligand of **2** adopts a less planar configuration in comparison with the linkers of **1**.

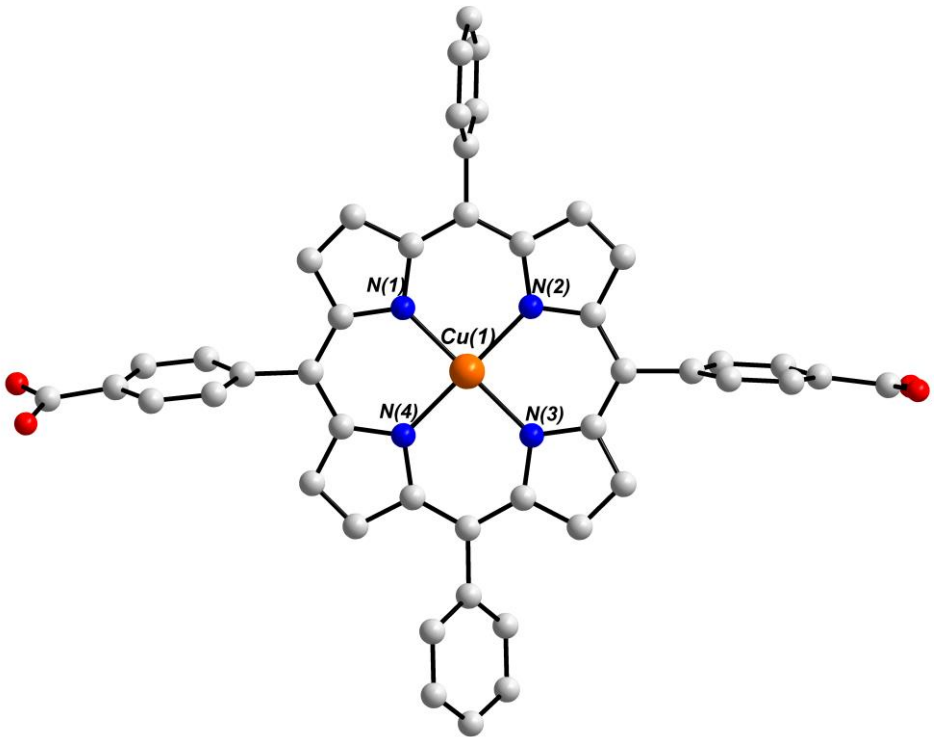

Figure 2.16: Ball-and-stick representation of the saddle-shaped, ditopic metalloporphyrin (**L1**-Cu^{II})$^{2-}$ linker of **2**. Hydrogen atoms have been omitted for clarity. Colour scheme: C white, N blue, O red, Cu orange.

The dihedral angle between carboxylate-functionalised *meso* phenyl rings within (**L1**-Cu^{II})$^{2-}$ is 13.9°, whilst the dihedral angle between the non-functionalised *meso* phenyl rings of (**L1**-Cu^{II})$^{2-}$ is 33.0°. This configuration facilitates the π – π stacking interactions which stabilise **2**.

Selected π – π stacking interactions within **2** are illustrated in Fig. 2.17. The tetrapyrrolic rings of adjacent porphyrin moieties within the 2D sheet stabilise each other through parallel displaced π – π stacking interactions which propagate along the crystallographic [101] direction. The distance between these π – π stacking moieties are within the range of 3.50 – 3.90 Å. Additionally, the carboxylate-functionalised *meso* phenyl rings form weak parallel displaced π – π stacking interactions with neighbouring carboxylate-functionalised *meso* phenyl rings in the same 2D sheet, further stabilising **2**. These π – π stacking interactions are characterised by interatomic distances which range between 3.70 and 3.92 Å.

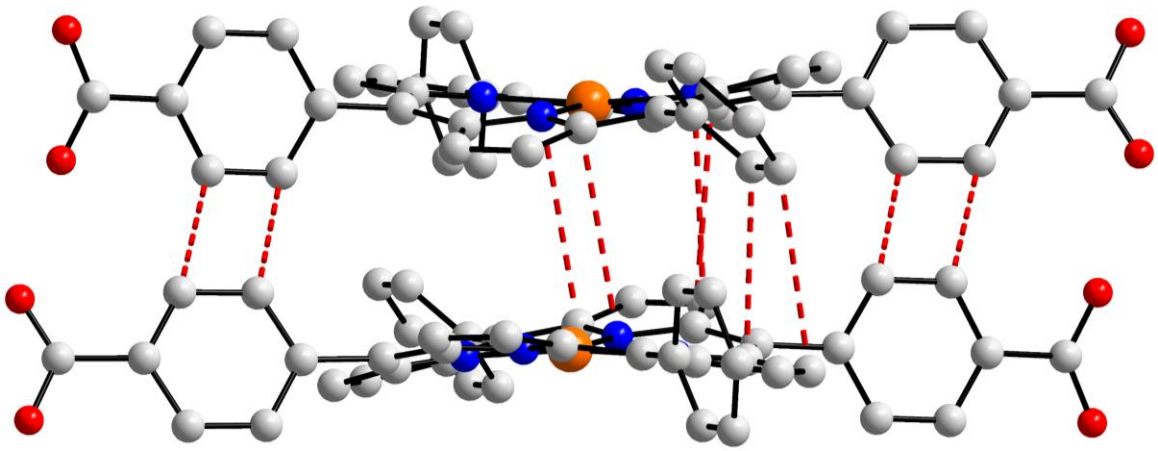

Figure 2.17: Ball-and-stick representation of selected supramolecular interactions in **2**, highlighting π – π stacking interactions between neighbouring (**L1**-Cu)$^{2-}$ porphyrin moieties within the 2D. Colour scheme: C white, N blue, O red, Cu orange. π – π interactions are represented as dashed red lines.

The non-functionalised *meso* phenyl rings of (**L1**-Cu^{II})$^{2-}$ are also stabilised through T-shaped π – π stacking interactions. These interactions occur between non-functionalised *meso* phenyl rings and the tetrapyrrolic ring systems of neighbouring porphyrin moieties within the 2D sheet. The distance between these π – π stacking interactions are within the range of 3.56 – 3.57 Å. T-shaped π – π stacking interactions also occur between non-functionalised phenyl rings and the tetrapyrrolic cores of porphyrin moieties of neighbouring 2D sheets. The distance between these π – π stacking interactions are within the range 3.67 – 3.96 Å. The

distances between all of the π – π stacking moieties discussed are within the expected range for π – π stacking interactions, and are consistent with literature reported values.[40]

The (**L1**-Cu^{II})$^{2-}$ linker in **2** is fully deprotonated, giving a charge of −4. This charge is balanced by the Cu^{II} ion Cu(1), and two crystallographically half-occupied Co^{II} ions Co(1) and Co(2) that form the rod-shaped SBU of **2**. As a result of this, the overall charge of **2** is neutral. Assignment of the oxidation states of each of the metal centres within **2** were confirmed using BVS analysis calculations.

The packing arrangement in the crystal structure of **2** is displayed in Fig. 2.18. 2D corrugated sheets pack densely, and the *meso* phenyl rings of porphyrin linkers interdigitate between neighbouring 2D layers. Small 1D channels locate between the 2D layers and extend in the direction of the crystallographic *a*-axis. These small channels are filled with constitutional solvent molecules.

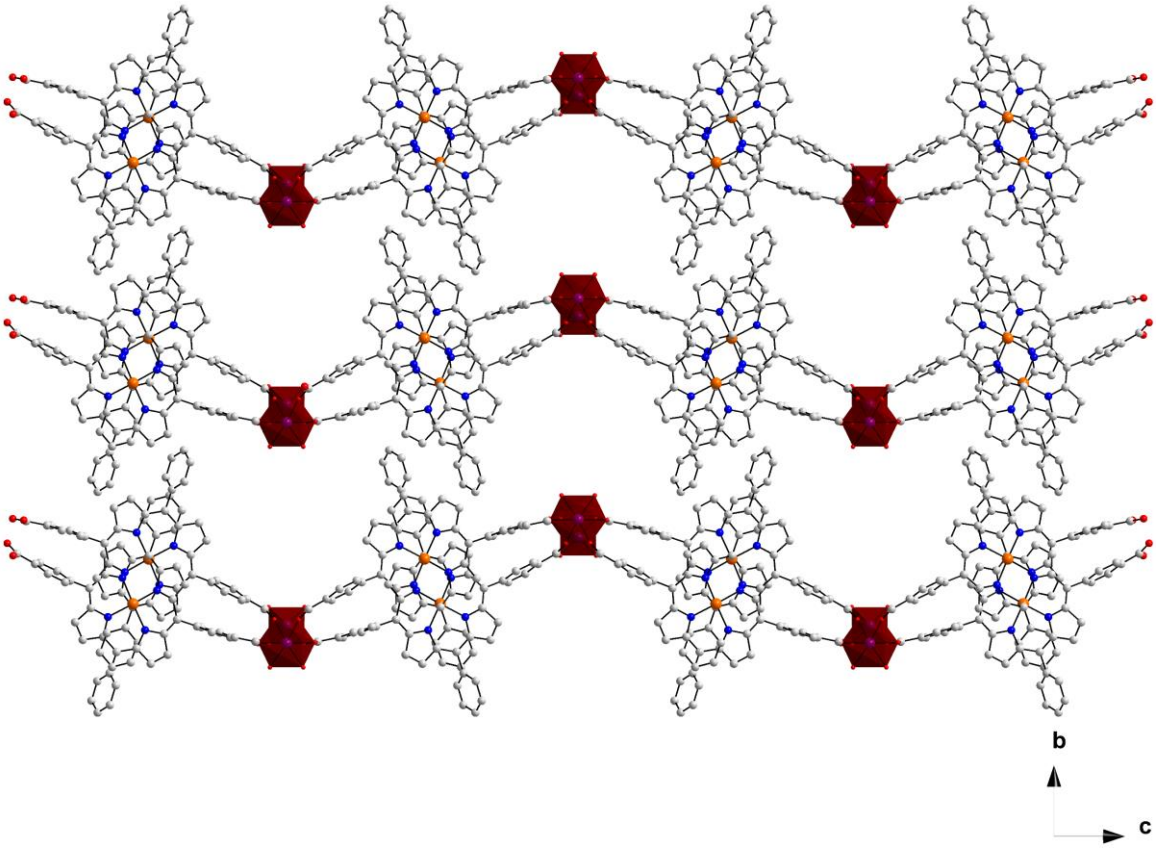

Figure 2.18: Ball-and-stick representation of the packing arrangement in **2** highlighting stacking interdigitated corrugated sheets and small 1D channels which extend in parallel with the crystallographic *a*-axis. View is in the direction of the crystallographic *a*-axis. Coordination solvent and hydrogen atoms have been omitted for clarity. Colour scheme: C white, N blue, O red, Co violet, Cu orange. Co^{II} centres are represented as red polyhedra.

2.4.3 Physicochemical Characterisation of 2

Infrared Spectroscopy

The 2D framework **2** was characterised using infrared spectroscopy. The FT-IR spectrum of **2** is presented in Fig. 2.19 and exhibits several characteristic signals. Broad signals around 3000 cm^{-1} can be attributed to aromatic C – H stretching vibrations of the (**L1**-Cu^{II})$^{2-}$ linker of **2**. A band at 1594 cm^{-1} can be assigned to a C = O stretching vibration of the DEA moieties within **2**.[43] Two signals at 1548 and 1373 cm^{-1} can be assigned to the asymmetric and symmetric vibrations, respectively, of the μ^2-η^1:η^1 carboxylate groups which bridge the Co^{II} centres of **2**.[44,46,52] A weak band at 1274 cm^{-1} can be attributed to a C – N stretching mode of the porphyrin linker of **2**, and a sharp signal at 994 cm^{-1} can be assigned to an in-plane vibration (ring breathing) of the (**L1**-Cu^{II})$^{2-}$ ligand.[47] Finally, a signal at 832 cm^{-1} can be assigned to a methine C – H bending vibration of the metalloporphyrin linkers of **2**.[53]

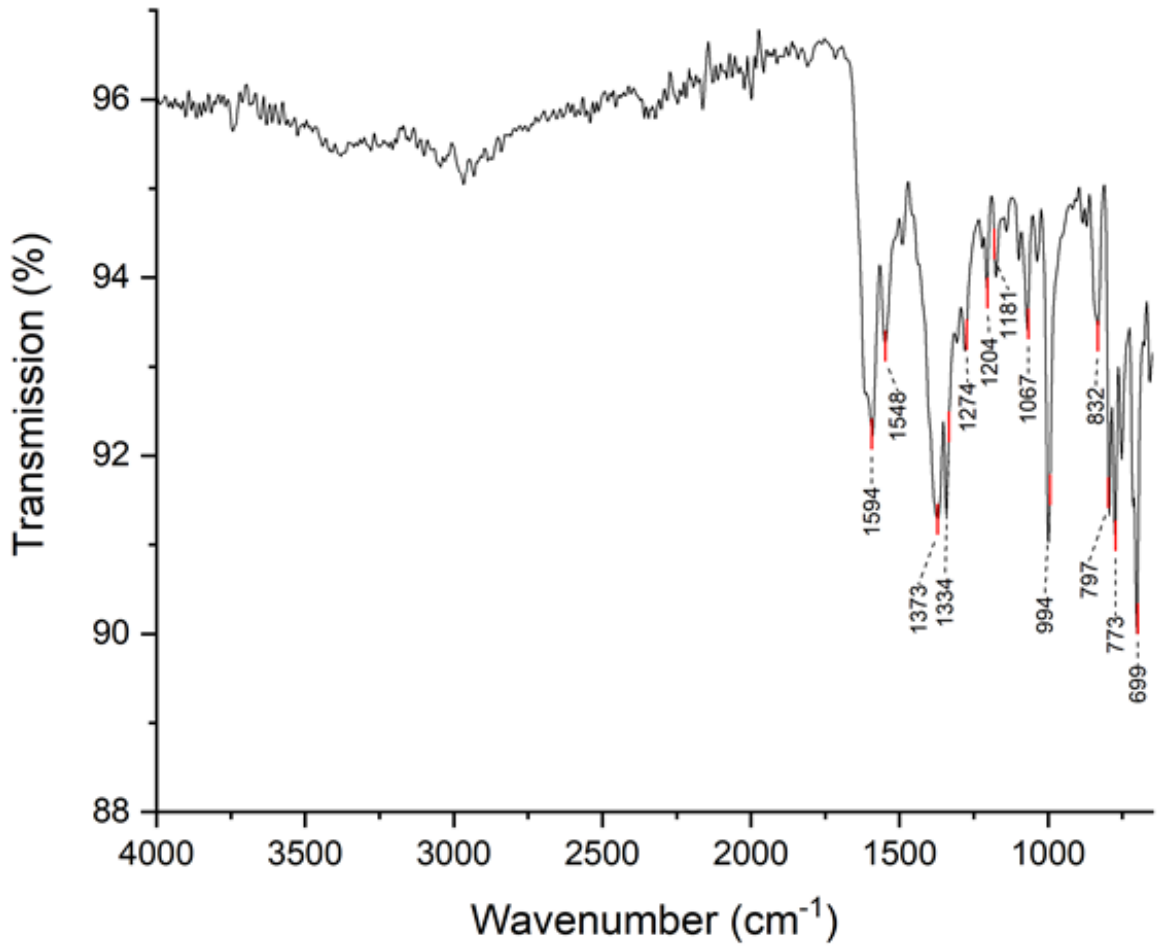

Figure 2.19: FT-IR spectrum of **2**.

Thermogravimetric Analysis

The thermal stability of **2** was assessed using TGA by heating a freshly prepared crystalline sample of **2** from 30 – 800 °C under a constant stream of N_2. The TGA trace is shown in Fig. 2.20 and reveals that the decomposition of **2** occurs in three distinct stages. Between 20 – 300 °C constitutional and coordinated solvent molecules are removed. The second decomposition stage occurs between *ca*. 350 – 470 °C and is associated with the decomposition of the organic ligands. A final thermogravimetric step occurs above 470 °C, which is attributed to the formation of metal oxide species.

As the sample is heated from 30 – 100 °C a mass loss of 11.6% is observed. This decrease in mass can be attributed to the loss of one water and three methanol constitutional solvent molecules (calculated 11.5%). When **2** is heated further from 100 – 210 °C a weight loss of 10.8% is observed. This weight loss can be associated with the loss of the coordinated DEA molecule of **2** (calculated 10.9%). Interpretation of these data led to the assignment of the molecular formula $[Co^{II}(\mathbf{L1}\text{-}Cu^{II})(DEA)]\cdot H_2O\cdot 3MeOH$ of **2**.

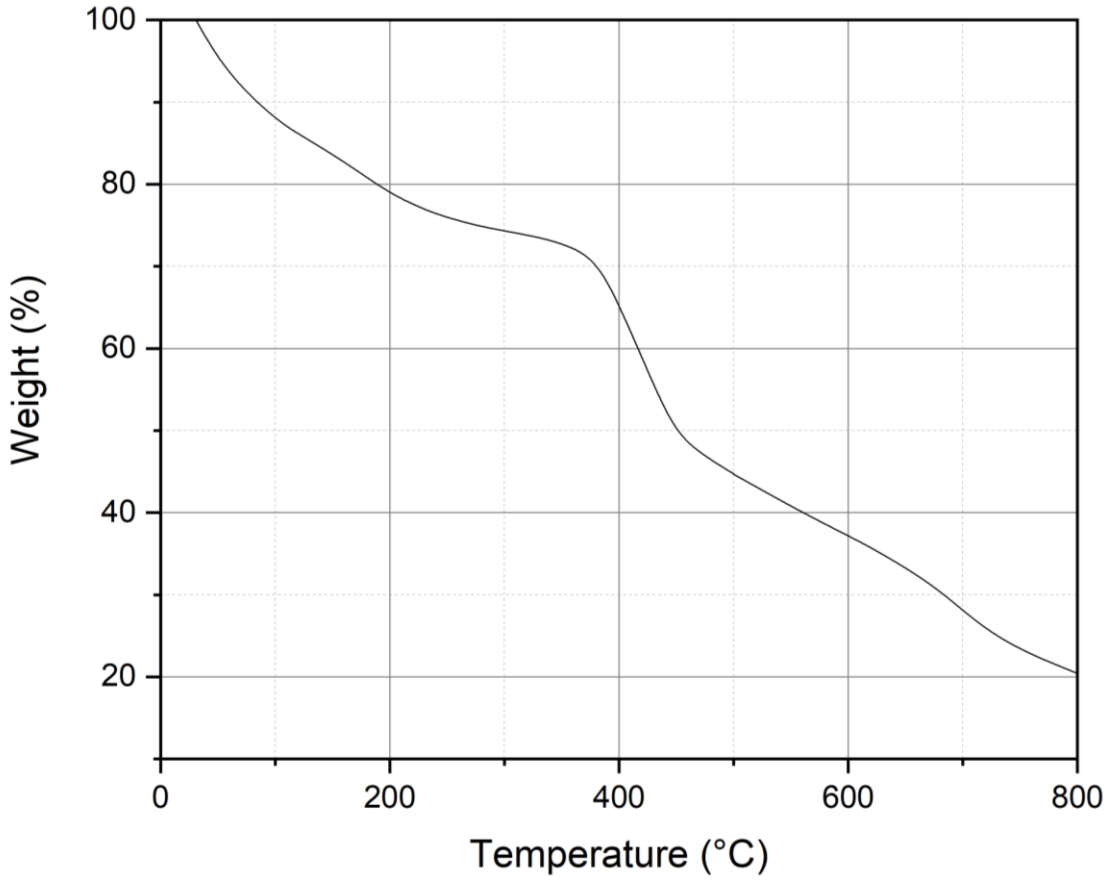

Figure 2.20: TGA trace for **2**.

Powder X-Ray Diffraction Analysis

The phase purity of **2** was evaluated using PXRD analysis. Removal of the mother liquor from **2** results in desolvation of the sample, therefore the PXRD spectrum of **2** was measured using a capillary. The experimental diffraction pattern of **2** and a simulated PXRD pattern calculated from the single crystal X-ray diffraction data of **2** are displayed in Fig. 2.21. Comparison of the experimental and simulated PXRD spectra reveals that all of the signals of high intensity present in the calculated powder pattern are also present in the measured powder pattern of **2**. Although the experimental and simulated spectra agree, a signal at 2Θ = 10.6° observed in the measured powder pattern was not observed in the calculated PXRD spectrum. This difference may be due to preferred orientation effects in the measured sample, or because the constitutional solvent molecules were not refined in the single crystal XRD structure of **2**.

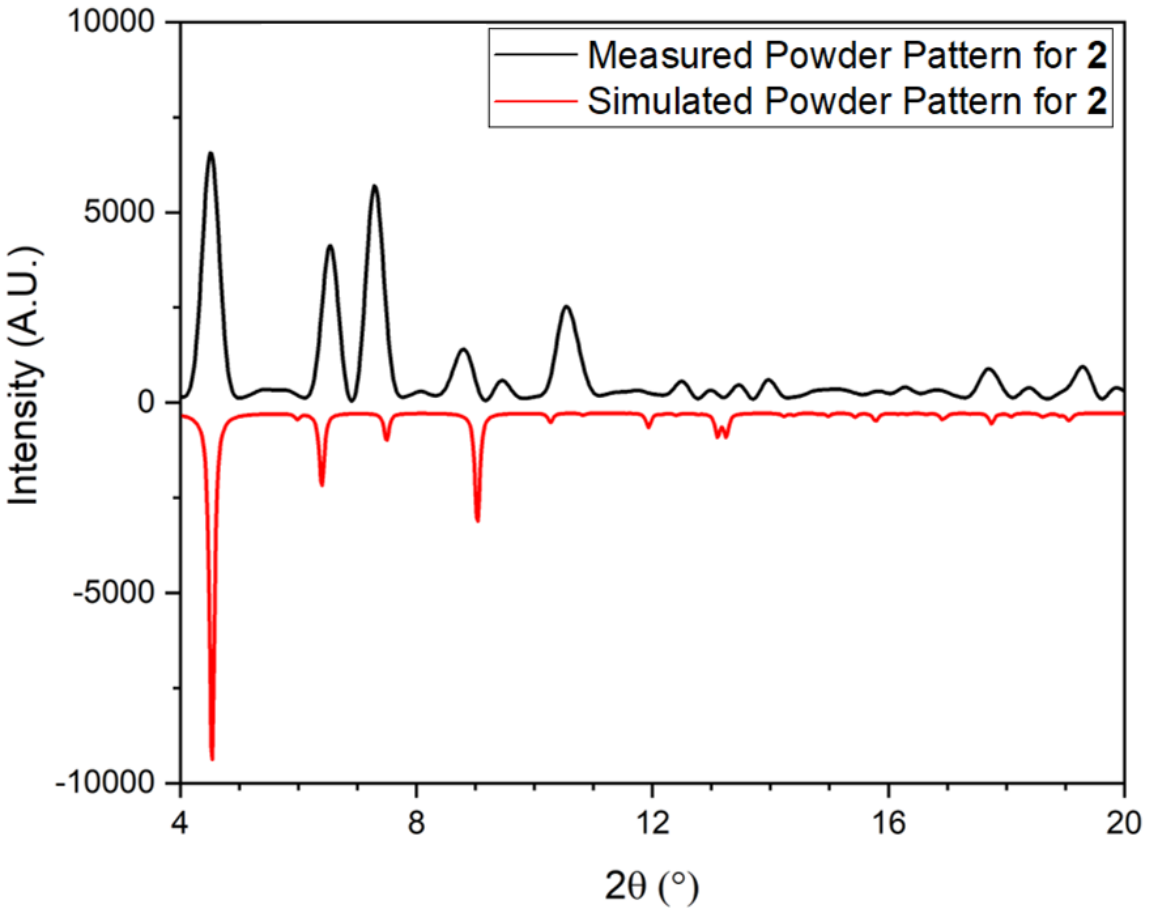

Figure 2.21: Powder X-ray diffraction analysis comparing the experimentally obtained diffraction pattern with a simulated spectrum obtained from the single crystal X-ray diffraction data of **2**.

2.5 H_2O Splitting Catalysis

Two central ambitions of this research project encompass the synthesis of materials with the potential to catalyse H_2O splitting reactions, and the quantification of newly discovered catalytic properties in terms of TON, TOF and % yield. To achieve these objectives, an experimental setup to establish the kinetics of light-driven OER or HER catalysis was designed. Using this system, prospective catalysts were tested as constituents of three-component photocatalytic mixtures according to adapted literature protocols.[54,55,56,57] The design and operation of the developed methodology are briefly outlined below. For further details of the experimental approach used to measure light-driven H_2O splitting, see Section 6.1.12.

2.5.1 Design of the H_2O Splitting Experimental Setup

A schematic representation of the setup used to assess H_2O splitting photocatalysis is presented in Fig. 2.22. The system comprises a reactor housing the reaction mixture under investigation (Fig. 2.22a) which is immersed in a water bath (Fig. 2.22b) kept at a constant temperature by a hotplate/stirrer (Fig. 2.22c). An LED coupled with a fibre optic tip (Fig. 2.18d) illuminates the reaction vessel as the dissolved O_2 or H_2 quantities are monitored in real-time using a Clark electrode (Fig. 2.22e). A monometer (Fig. 2.22f) and laptop (Fig. 2.22g) amplify and record the electrode's output. A grounding cable (Fig. 2.22h) grounds the reaction mixture.

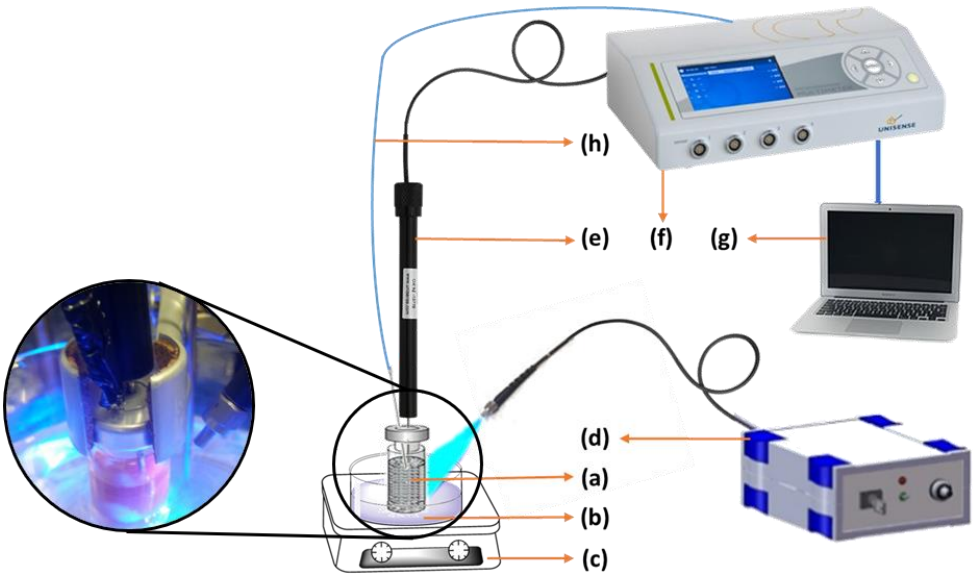

Figure 2.22: Schematic representation of the light-driven H_2O splitting setup. Labels: (a) Reaction vial housing photocatalytic mixture; (b) water bath; (c) hotplate/stirrer maintaining temperature and stirring rate of 25 °C and 500 rpm, respectively; (d) LED with optical fibre; (e) O_2 or H_2 sensing Clark electrode; (h) grounding cable protecting Clark electrode; (f) monometer; (g) laptop to record data. Inset: Photograph of the photocatalytic H_2O splitting setup in operation.

2.5.2 Methodology for Assessing H_2O Splitting Catalysis

Photocatalytic H_2O splitting experiments were carried out using three-component systems comprising a PS ($[Ru(bpy)_3]Cl_2$ or $[Ru(bpy)_2(deeb)](PF_6)_2$), a SEA or SED ($Na_2S_2O_8$ or ascorbic acid) and an OER or HER catalyst under phosphate-buffered, aqueous conditions. Mixtures under investigation were deaerated in the dark before hermetically sealing inside borosilicate reaction vessels equipped with stir bars. A Clark electrode fitted with a piercing needle tip was then inserted into the solution phase of the catalytic mixture *via* the septum of the reactor. Following this, the photocatalytic mixtures were irradiated using an LED whilst the dissolved O_2 or H_2 concentrations were recorded using the Clark electrode, thus providing quantitative information about the kinetics of H_2O splitting catalysis in real-time.

PS's used in catalytic light-driven H_2O splitting experiments included the commercially available, homoleptic PS $[Ru(bpy)_3]Cl_2$ and the heteroleptic PS $[Ru(bpy)_2(deeb)](PF_6)_2$. Both of these one-electron, Ru-polypyridyl complexes are well established in the literature as PS's for H_2O splitting catalysis.[57,58] The redox potentials of the ester-functionalised PS $[Ru(bpy)_2(deeb)](PF_6)_2$ and $Ru(bpy)_3]Cl_2$ are $E_{1/2}$ Ru^{III}/Ru^{II} = 1.40 V and 1.26 V vs. NHE, respectively. Due to the endergonic nature of the more challenging half-reaction of H_2O splitting, the OER ($E°$ = 1.23 V vs. NHE), it was rationalised that using a PS with a higher redox potential in H_2O oxidation experiments may improve the activity of a WOC. Therefore, the PS $[Ru(bpy)_2(deeb)](PF_6)_2$ was prepared in a three-step synthesis according to adapted literature procedures outlined by Ma *et al*.[59] and Meyer *et al*.[60] (for synthesis see Section 6.2).

Once assembled, control experiments were conducted using the setup to verify its suitability for measuring OER catalysis. The results of these experiments (presented in Section 6.13) confirm that various mixtures of PS's and SEA's do not evolve O_2 in the absence of a WOC. Further, in a functional test in which a literature-established OER catalyst (Co_3O_4 nanoparticles) was irradiated in the presence of a three-component catalytic system, significant O_2 evolution was detected.[61,62] These tests demonstrate that the developed methodology is suitable for assessing H_2O oxidation catalytic activity. Following this, a series of optimisation experiments in which a range of reaction parameters were individually modified were performed (see Section 6.1.14 for details). As a result of these tests, the photocatalytic OER experiments described herein were carried out under aqueous, phosphate-buffered conditions (0.01 M, initial pH = 7.0) using $Na_2S_2O_8$ (10 mM) as SEA and $[Ru(bpy)_2(deeb)](PF_6)_2$ (2 mg, 2.33 μmol) as PS, and irradiated using an LED (λ = 470) with a power of 10 mW cm^{-2}.

2.6 H_2O Oxidation Properties of 1

The H_2O oxidation half-reaction is considered a crucial bottleneck in the development of efficient artificial photosynthetic technologies.[63] Therefore, the discovery of highly active and robust WOCs is of paramount importance for generating H_2 in a sustainable, environmentally-friendly manner using H_2O as a feedstock, and to advance our understanding of this complex process.[64] Therefore, initial investigations intended to identify catalysts for the more challenging O_2 evolution reaction.

The two Co^{II}-based MMPFs discussed in this chapter **1** and **2** feature multiple characteristics rendering them promising candidates to catalyse the OER. Considering the structures of these compounds, each framework is constructed from potentially redox-active polynuclear Co^{II}-based SBUs, which are a common attribute among literature established molecular WOCs.[65] In addition, **1** and **2** are noble metal-free and heterogeneous under the aqueous conditions typically employed in H_2O oxidation. These properties are advantageous as they facilitate post-reaction catalyst recovery *via* filtration and also may lower potential investment costs.[66]

However, several features of **1** make this MMPF a more attractive compound to use as a heterogeneous catalyst for the OER compared to **2**. For example, the large solvent-accessible channels of the MMPF **1** permit the simultaneous exposure of a higher proportion of the Co^{II}-based SBUs to H_2O substrates than in **2**, which has a relatively denser structure. Furthermore, four aqua ligands coordinate to two Co^{II} centres in each of the $\{Co^{II}_4\}$ SBUs of **1**. The presence of these H_2O molecules bound directly to potentially active clusters is likely to promote O_2 evolution catalysis.[67]

The locations of the coordinated aqua ligands of **1** is also significant: Two terminally coordinated H_2O molecules comprising O(1) and O(2) cap each end of the $\{Co^{II}_4\}$ SBU and dangle into solvent-accessible channels. Two coordinated H_2O molecules comprising O(2) and O(11) are connected to two different Co^{II} centres and are held in close proximity to each other (interatomic distance O(2)···O(11) is 3.057(3) Å). This positioning allows the OER possibly to proceed *via* either the WNA or the I2M pathway.[68] Moreover, **1** forms phase-pure and in high yield whereby large individual crystals can be manually selected for use in catalytic studies, thus the homogeneity of the sample can be guaranteed. All of these factors underline that **1** is the most suitable candidate to be used in an OER catalysis investigation. Therefore, **1** was employed in a series of O_2 evolution experiments which are described in the following section.

2.6.1 Photocatalytic H_2O Oxidation Experiments

Light-Driven OER Control Experiments Using 1

The light-driven OER catalytic activity of **1** was assessed according to established literature procedures using the experimental setup described above.[56,69] O_2 evolution experiments were performed using large individual crystals of **1** which were manually selected from a freshly prepared sample, washed with DMF and ground into a fine powder using an agate mortar and pestle. The powdered crystals were then irradiated (λ = 405 or 470 nm, 10 mW cm^{-1}) in a hermetically sealed reaction vessel in the presence of $[Ru(bpy)_2(deeb)](PF_6)_2$ PS and $Na_2S_2O_8$ SEA in an anoxic, phosphate-buffered aqueous solution whilst the kinetics of O_2 evolution were monitored in real-time using an O_2-sensing Clark electrode.

Initially, several control experiments were performed using **1**. Photocatalytic tests were carried out in which individual components of the three-component system were excluded from reaction vial prior to irradiation of the reactants at λ = 470 nm. The results of these control experiments are summarised in Table 2.1 and reveal that significant quantities of O_2 were not evolved if any one photocatalytic component was not present in the reaction mixture. This confirms that the WOC, SEA and PS are all required for overall OER activity.

Table 2.1: Table highlighting how light-driven OER catalysis using 1 depends on the presence of an external PS, and on the wavelength of the LED light source.

WOC (**1**)	$Na_2S_2O_8$	$[Ru(bpy)_2(deeb)](PF_6)_2$	Irradiation (λ = 405 nm)	Irradiation (λ = 470 nm)	O_2 Evolution Observed
–	Yes	Yes	–	Yes	No
Yes	Yes	–	–	Yes	No
Yes	–	Yes	–	Yes	No
Yes	Yes	–	Yes	–	No
Yes	Yes	Yes	–	Yes	Yes

The presence of porphyrin linkers in **1**, which could potentially act as intrinsic photosensitising moieties prompted a photocatalytic experiment in which an external PS was excluded from the reaction mixture. In these tests, **1** was irradiated at $\lambda = 405$ nm in the presence of $Na_2S_2O_8$ as a SEA in phosphate-buffered aqueous solutions. Unfortunately, significant OER activity was not observed in this experiment. This could be due to intramolecular quenching of photoexcited porphyrins in **1**, or be because of the (**L1**-Cu^{II})$^{2-}$ ligand derivative of **1** not having a sufficient redox potential to provide an adequate thermodynamic driving force for H_2O oxidation to proceed.[70] As a result of this, the OER experiment was repeated using $[Ru(bpy)_2(deeb)](PF_6)_2$ as a PS and the reaction mixture was irradiated at $\lambda = 470$ nm, which resulted in the production of a significant quantity of O_2.

This experiment demonstrates that the presence of an external PS is necessary for O_2 evolution activity using **1**. Attempts were made to synthesise an analogous MMPF to **1** using H_2**L1**-Pt^{II} as a pro-ligand due to the higher redox potential associated with Pt^{II}-metallated porphyrins.[28] However, a sample of acceptable purity, as determined by PXRD analysis, could not be obtained.

Catalytic Loading Experiments

Significant quantities of O_2 were evolved when **1** was irradiated in the presence of $Na_2S_2O_8$ as a SEA and $[Ru(bpy)_2(deeb)](PF_6)_2$ as a PS at $\lambda = 470$ nm. Illumination of this three-component catalytic mixture resulted in the dissolved O_2 concentration inside the reactor to rise continuously for *ca*. 250 seconds at a rate dependent on the catalyst loading. After this time, the measured O_2 concentration reached a plateau, before finally decreasing slightly as the evolved O_2 diffused into the reaction vessel's headspace. Fig. 2.23 shows the kinetics of O_2 evolution upon irradiation of photocatalytic mixtures containing loadings of **1** of 0.04 mg, 0.08 mg and 0.12 mg.

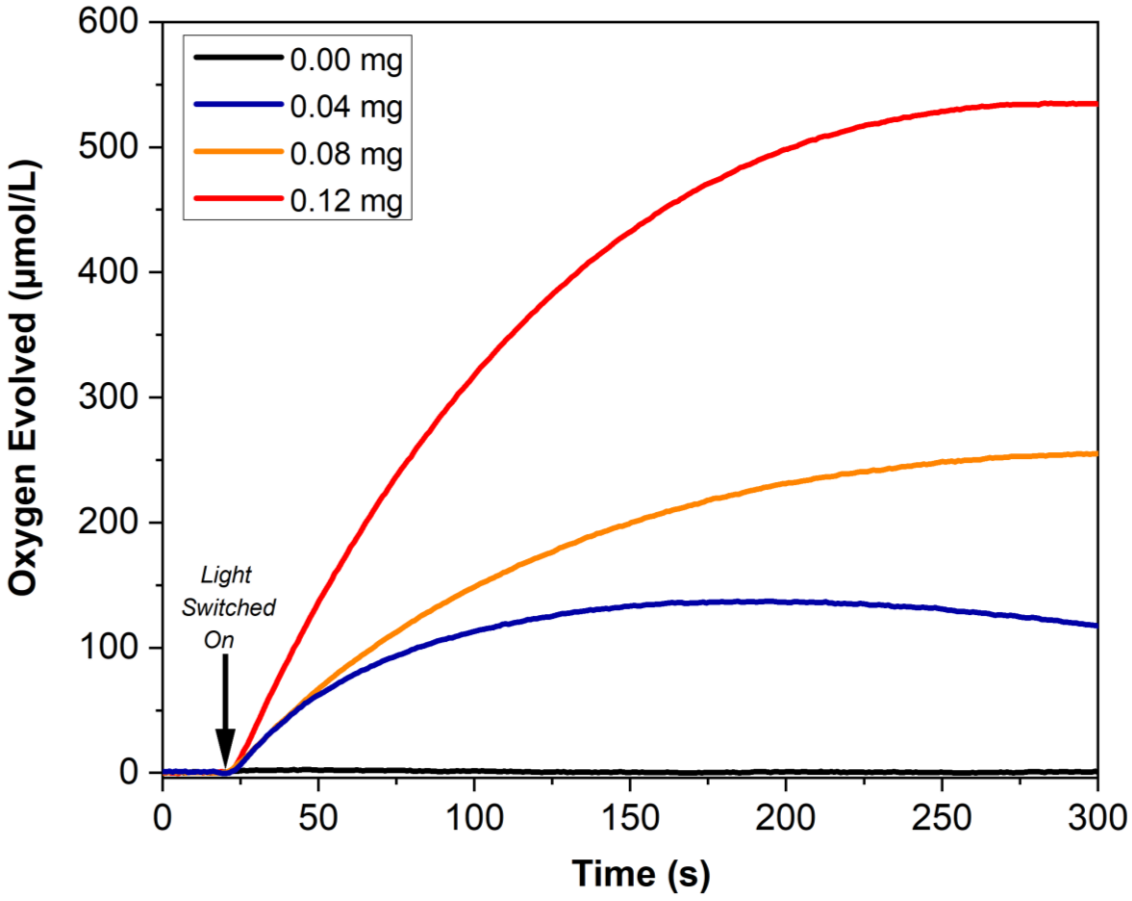

Figure 2.23: Kinetic monitoring (Clark electrode) of the light-driven OER using different loadings of **1** (0 mg, black; 0.04 mg, blue; 0.08 mg, orange; 0.08 mg, red). Conditions: LED lamp ($\lambda = 470$, 10 mW cm^{-2}), $[Ru(bpy)_2(deeb)](PF_6)_2$ PS (2 mg) and $Na_2S_2O_8$ SEA (11.9 mg) in 0.01 M phosphate buffer (starting pH = 7, 5 mL). Constant stirring at 500 rpm; a temperature of 25 °C was maintained by immersing the reaction vessel in a water bath.

These experiments reveal that **1** is as an effective photocatalyst for H_2O oxidation in the presence of a SEA and a PS. The TON, TOF and O_2 yields observed when employing various loadings of **1** are displayed in Table 2.2. Under the applied conditions, **1** produces a maximum quantity of 2.68 µmol O_2 at a catalyst loading of 0.12 mg. The highest TON and maximum O_2 yield were also observed at this catalyst loading, where **1** evolved 86.5 mol O_2 per mole of catalyst, corresponding to an O_2 yield of 10.7% based on the loading of $Na_2S_2O_8$.

The calculated TOF was found to be inversely correlated with the loading of the catalyst: The lowest TOF = 0.81 s^{-1} was observed at the highest loading of **1** (0.12 mg), whereas the largest TOF = 1.08 s^{-1} was observed at the lowest catalytic loading (0.04 mg). This trend has been observed in a number of different OER catalytic studies reported in the literature.[71,72] The maximum TON and TOF of **1** are remarkably high relative to other literature reported heterogeneous transition metal-based WOCs.[67,73]

Table 2.2: Comparison of the TON, TOF and % oxygen conversion at various loadings of 1.

Catalyst Loading (mg)	Turnover Number (TON)	Turnover Frequency (TOF, s^{-1})	Oxygen Conversion (%)
0.04	66.3	1.08	2.74
0.08	61.9	0.57	5.12
0.12	86.5	0.81	10.7

Recycling Experiments

In order to ascertain if the WOC **1** could be recycled, an established literature protocol was followed.[74] Fresh quantities of $Na_2S_2O_8$ SEA and $[Ru(bpy)_2(deeb)](PF_6)_2$ PS were added to the reaction vial after O_2 evolution had ceased, and the OER experiment was repeated. The observed O_2 quantity evolved fell to *ca*. 5% of the amount produced in the initial run, revealing that **1** does not appear to be a recyclable catalyst under these conditions. This could be attributed to many factors, such as catalyst decomposition under the highly oxidising experimental conditions, or reduced efficiency of the catalyst under the decreased pH working conditions of the post-OER catalytic supernatant.[75]

2.6.2 Catalytic Characterisation Experiments

The pre- and post-irradiated reaction mixtures from light-driven O_2 evolution experiments using **1** were characterised physicochemically in order to identify the true WOC. UV-Vis spectroscopy was used to detect *in-situ* leaching of Co^{II} ions from **1** into the supernatant, whereas Raman spectroscopy was employed to rule out the formation of trace quantities of OER active materials such as cobalt oxides (CoO_x) or cobalt phosphates (Co–Pi) during catalysis. Raman and UV-Vis spectroscopy are highly sensitive, well-established techniques within the H_2O oxidation catalysis literature which are routinely used in the identification of trace species or intermediates formed under turnover conditions.[76,77,78]

UV-Vis Spectroscopy

UV-Vis spectroscopy experiments were conducted to detect the presence of solvated Co^{II} ions in the catalytic mixture, which can act as a precatalyst by forming CoO_x particles *in-situ*.[79] Three-component photocatalytic mixtures containing the proposed WOC **1**, $[Ru(bpy)_2(deeb)](PF_6)_2$ PS and $Na_2S_2O_8$ SEA in an aqueous phosphate-buffered solution were analysed using UV-Vis spectroscopy both before and after O_2 evolution. The spectra of these mixtures, as well as the UV-Vis spectrum of an aqueous solution of $CoCl_2 \cdot 6H_2O$ are compared in Fig. 2.24. An absorption band at *ca*. 520 nm is observed in the UV-Vis spectrum of the aqueous solution of $CoCl_2 \cdot 6H_2O$. This signal is not present in the UV-Vis spectra of either the pre- or post-irradiated catalytic mixtures. This observation strongly indicates that significant quantities of Co^{II} ions do not leach into the supernatant from **1** prior to, or during the light-driven OER.

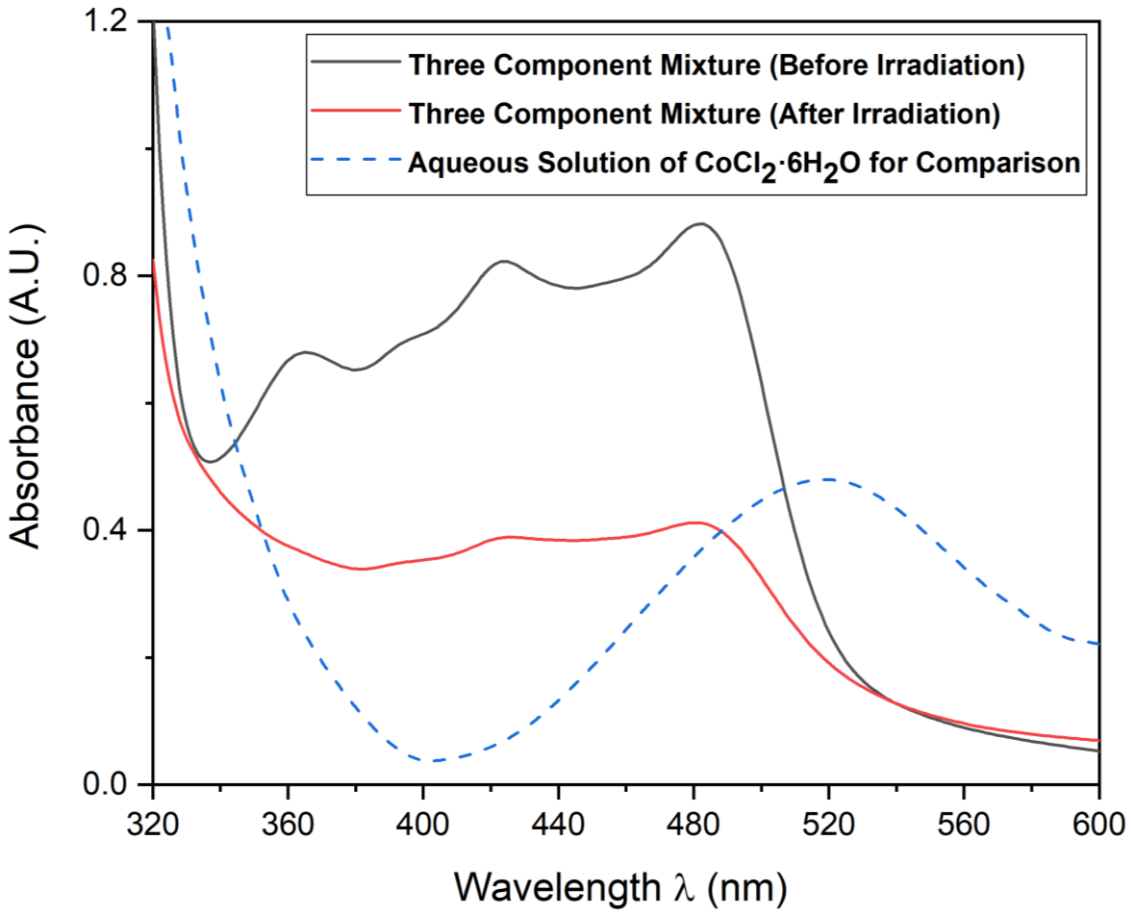

Fig. 2.24: UV-Vis spectra of the three-component photocatalytic mixtures in aqueous phosphate-buffered solutions before (black) and after (red) irradiation. The UV-vis spectrum of an aqueous solution of $CoCl_2 \cdot 6H_2O$ is also plotted for comparison (blue, dashed).

The UV-Vis spectra of the irradiated and non-irradiated samples differ in three absorption bands at *ca*. 360, 420 and 480 nm which are assigned to the PS $[Ru(bpy)_2(deeb)](PF_6)_2$. These signals appear reduced in intensity in the UV-Vis spectrum of the post-irradiated catalytic mixture relative to the intensity of the corresponding bands in the spectrum of the pre-irradiated catalytic mixture. The disparity between these two spectra indicates that the PS degrades during OER catalysis. This observation is consistent with other photocatalytic H_2O splitting systems in the literature which use Ru-based polypyridyl PS's.[57]

Raman Spectroscopic Analysis

To detect OER active species generated *in-situ* during catalytic experiments using **1**, Raman spectra were recorded of the dried residues of both pre- and post-irradiated catalytic mixtures. These spectra, in addition to the Raman spectra of **1**, $[Ru(bpy)_2(deeb)](PF_6)_2$, $Na_2S_2O_8$ and Na_2SO_4 are compared in Fig. 2.25.

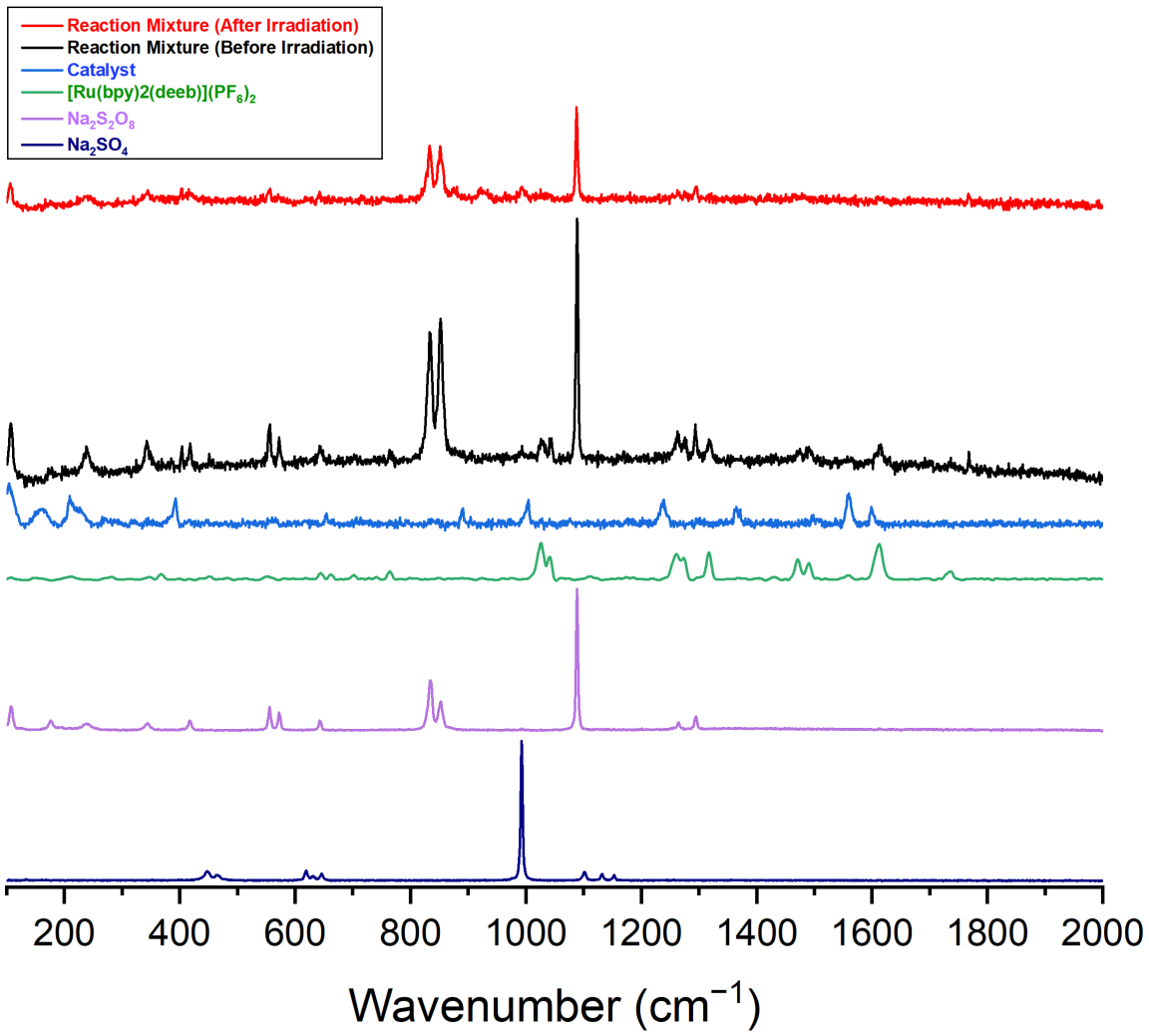

Fig. 2.25: Raman spectra of the dried residues of the three-component photocatalytic mixture both before (black) and after (red) irradiation. Solid samples of **1** (blue), $[Ru(bpy)_2(deeb)](PF_6)_2$ PS (green), $Na_2S_2O_8$ SEA (lilac) and Na_2SO_4 (navy) are also plotted for comparison.

Interpretation of the Raman spectra of pre- and post-irradiated catalytic mixtures reveals a number of key differences. Crucially, however, no additional signals in the Raman spectrum

of the post-irradiated sample (that are not present in the spectrum of the pre-irradiated sample) were observed within the range 400 – 600 cm^{-1}. As CoO_x compounds are highly vibrationally active in Raman spectroscopy in this region, this observation rules out the *in-situ* formation of CoO_x species which could be responsible for the OER activity observed.[77,80] Furthermore, bands deriving from Co–Pi could not be detected in the Raman spectra of either the pre- or post-irradiated catalytic mixtures.[81,82]

A number of signals in the Raman spectrum of the pre-irradiated reaction mixture can be assigned to the WOC **1**. Bands of low intensity at 1555, 992, 402 cm^{-1} and two shoulders at 888 and 202 cm^{-1} can be attributed to **1** in the pre-irradiated photocatalytic mixture. Most of these signals, with the exception of a shoulder at 888 cm^{-1} cannot be seen in the Raman spectrum of the post-irradiated reaction mixture, indicating that the WOC decomposes into OER inactive materials under the working conditions of O_2 evolution.

A series of vibrational bands attributed to $[Ru(bpy)_2(deeb)](PF_6)_2$ at 1767, 1614, 1493, 1475, 1317, 1277, 1263, 1045, 1030 and 767 cm^{-1} have significantly lower intensity in the Raman spectrum of the post-irradiated reaction mixture in comparison to the equivalent bands in the Raman spectrum of the pre-irradiated catalytic mixture. This indicates that the PS decomposes during O_2 evolution, which is known to occur when employing ruthenium polypyridyl-based compounds as PS's for H_2O oxidation catalysis.[57] This observation is also consistent with the UV-Vis spectroscopy analyses of pre- and post-irradiated catalytic samples.

Several signals in the Raman spectra of both the pre- and post-irradiated catalytic samples at 1296, 1264 1089, 854, 833, 571, 555 and 108 cm^{-1} can be assigned to $Na_2S_2O_8$. These bands reveal significantly lower intensity in the Raman spectrum of the post-irradiated three-component mixture when compared with the corresponding bands in the Raman spectrum of the pre-irradiated catalytic mixture. This disparity matches expectations, due to the irreversible degradation of $Na_2S_2O_8$ into Na_2SO_4 during O_2 evolution. The diminished intensities of the signals assigned to $Na_2S_2O_8$ in the Raman spectrum of the irradiated catalytic mixture indicates that the SEA is only partially consumed during the OER using **1**.

A signal at 993 cm^{-1} in the Raman spectrum of the post-irradiated three-component mixture is assigned to SO_4^{2-}. This is the only signal observed in the Raman spectrum of the irradiated catalytic mixture that is not present in the Raman spectrum of the pre-irradiated mixture. This is a result of decomposition of the SEA into Na_2SO_4 during light-driven O_2 evolution.

The *in-situ* formation of CoO_x or Co–Pi compounds during the light-driven OER using **1** could not be detected in Raman spectroscopy experiments. Furthermore, the leaching of Co^{II} ions into the supernatant during catalysis could not be detected using UV-Vis spectroscopy. The results of these experiments, combined with the exceptional TOF observed for **1** (which is significantly higher than TOFs reported in the literature for CoO_x nanoparticles[62] or Co–Pi species[83]) provides compelling evidence that **1** is a genuine WOC. It can therefore be concluded that **1** is not a precatalyst which decomposes into another OER active species under working conditions.

2.7 Conclusion and Future Work

In this chapter, the synthesis of a linear dicarboxylate-functionalised porphyrin 5,15-bis(4-carboxyphenyl)-10,20-diphenylporphyrin (H_4**L1**) is described. Further, the syntheses of a series of metalloporphyrin analogues H_2**L1**-Cu^{II}, H_2**L1**-Ni^{II} and H_2**L1**-Pt^{II} are outlined, and the Cu^{II} metalloporphyrin (H_2**L1**-Cu^{II}) was successfully used in the synthesis of two novel Co^{II}-based MMPFs, $[Co^{II}_4$(**L1**-$Cu^{II})_4(H_2O)_7]\cdot 2DEA\cdot 8MeOH$ (**1**) and $[Co^{II}$(**L1**-$Cu^{II})(DEA)]\cdot H_2O\cdot 3MeOH$ (**2**).

Single crystal X-ray diffraction resulted in the elucidation of the structures of **1** and **2**. **1** is a 3D MMPF featuring large, solvent-accessible 1D channels and unique 8-connected partially hydrated $\{Co^{II}_4\}$ SBUs. **2** is a 2D MMPF which is composed of infinite rod-shaped SBUs containing alternating tetrahedral and octahedral Co^{II} centres bridged by (**L1**-$Cu^{II})^{2-}$ linkers. The assembly of these SBUs results in corrugated sheets that stack and interdigitate in the crystal structure of **2**.

In addition, an experimental setup and methodology which was designed to assess the H_2O splitting catalytic properties of prospective WOCs or HECs was described. Following on from this, a photocatalytic OER study was carried out using **1**, as this compound was judged to be more likely to be active towards H_2O splitting catalysis than **2**. This investigation revealed that **1** functions as an effective WOC when irradiated (λ = 470 nm) in the presence of $[Ru(bpy)_2(deeb)](PF_6)_2$ PS and $Na_2S_2O_8$ SEA under neutral, aqueous phosphate-buffered conditions. A max. TON = 86.5 and TOF = 1.08 s^{-1} were achieved using **1** as a WOC; this activity is remarkable among literature reported transition metal-based WOCs.[84,67,73]

Finally, the pre- and post-irradiated catalytic mixtures from O_2 evolution experiments were characterised using Raman and UV-Vis spectroscopy. The results of these experiments ruled out the *in-situ* formation of catalytically active materials such as CoO_x or Co–Pi, implicating **1** as a genuine OER catalyst.

Future investigations may seek to characterise the OER activity of **1** under electrocatalytic conditions. Cyclic voltammetry and bulk electrolysis experiments might be used to establish the overpotential and stability of this WOC, in addition to facilitating further characterisation of the post-catalytic material. Energy-dispersive X-ray spectroscopy experiments on catalytic samples recovered following bulk electrolysis could allow precise elucidation of decomposition pathways undertaken by **1** during O_2 evolution. This information can then be used to design a more robust catalyst that is resistant to the identified decomposition pathway.

Additionally, the light-driven H_2O splitting activity of **2** could be determined and compared with the activity of **1**. Moreover, Zn^{II}- and Pt^{II}-based metalloporphyrin complexes may be used to synthesise novel MMPFs which are isostructural to **1** and **2**, and the light-driven OER properties of these novel compounds can be established. Gaining an understanding of how the catalytic activities of these isostructures relates to the H_2O splitting activities of **1** and **2** would provide insight into how the nature of the metal ion within the MMPF's linker influences the structures' overall catalytic activity.

2.8 References

1 K. Meyer, M. Ranocchiari and J. A. van Bokhoven, *Energy Environ. Sci.*, 2015, **8**, 1923–1937.

2 W. Wang, X. Xu, W. Zhou and Z. Shao, *Adv. Sci.*, 2017, **4**, 1600371.

3 Z. Liang, C. Qu, D. Xia, R. Zou and Q. Xu, *Angew. Chem. Int. Ed.*, 2018, **57**, 9604–9633.

4 T. Hisatomi, K. Takanabe and K. Domen, *Catal. Letters*, 2015, **145**, 95–108.

5 M. Ranocchiari and J. A. van Bokhoven, *Phys. Chem. Chem. Phys.*, 2011, **13**, 6388–6396.

6 M. Blasco-Ahicart, J. Soriano-Lopez, J. J. Carbo, J. M. Poblet and J. R. Galan-Mascaros, *Nat. Chem.*, 2018, **10**, 24–30.

7 G. La Ganga, F. Puntoriero, S. Campagna, I. Bazzan, S. Berardi, M. Bonchio, A. Sartorel, M. Natali and F. Scandola, *Faraday Discuss.*, 2012, **155**, 177–190.

8 V. Artero, M. Chavarot-Kerlidou and M. Fontecave, *Angew. Chem. Int. Ed.*, 2011, **50**, 7238–7266.

9 R. K. Tripathy, A. K. Samantara and J. N. Behera, *Dalt. Trans.*, 2019, **48**, 10557–10564.

10 Q. Meng, J. Yang, S. Ma, M. Zhai, J. Lu, Q. Meng, J. Yang, S. Ma, M. Zhai and J. Lu, *Polymers*, 2017, **9**, 676.

11 Q. Xu, H. Li, F. Yue, L. Chi and J. Wang, *New J. Chem.*, 2016, **40**, 3032–3035.

12 P. M. Usov, C. McDonnell-Worth, F. Zhou, D. R. MacFarlane and D. M. D'Alessandro, *Electrochim. Acta*, 2015, **153**, 433–438.

13 W.-Y. Gao, M. Chrzanowski and S. Ma, *Chem. Soc. Rev.*, 2014, **43**, 5841–5866.

14 C. Pereira, M. Simões, J. Tomé and F. Almeida Paz, *Mol.*, 2016, **21**, 1348.

15 Y. Liu, Y. Han, Z. Zhang, W. Zhang, W. Lai, Y. Wang and R. Cao, *Chem. Sci.*, 2019, **10**, 2613–2622.

16 P. M. Usov, S. R. Ahrenholtz, W. A. Maza, B. Stratakes, C. C. Epley, M. C. Kessinger, J. Zhu and A. J. Morris, *J. Mater. Chem. A*, 2016, **4**, 16818–16823.

17 W. Lu, Z. Wei, Z.-Y. Gu, T.-F. Liu, J. Park, J. Park, J. Tian, M. Zhang, Q. Zhang, T. Gentle III, M. Bosch and H.-C. Zhou, *Chem. Soc. Rev.*, 2014, **43**, 5561–5593.

18 A. Schoedel, M. Li, D. Li, M. O'Keeffe and O. M. Yaghi, *Chem. Rev.*, 2016, **116**, 12466–12535.

19 Q. H. Al-Galiby, H. Sadeghi, L. A. Algharagholy, I. Grace and C. Lambert, *Nanoscale*, 2016, **8**, 2428–2433.

20 K. Lu, C. He and W. Lin, *J. Am. Chem. Soc.*, 2014, **136**, 16712–16715.

21 J. M. Verduzco, H. Chung, C. Hu and W. Choe, *Inorg. Chem.*, 2009, **48**, 9060–9062.

22 J. K. Laha, S. Dhanalekshmi, M. Taniguchi, A. Ambroise and J. S. Lindsey, *Org. Process Res. Dev.*, 2003, **7**, 799–812.

23 S. Banfi, E. Caruso, L. Buccafurni, R. Murano, E. Monti, M. Gariboldi, E. Papa and P. Gramatica, *J. Med. Chem.*, 2006, **49**, 3293–3304.

24 V. Martí-Centelles, M. D. Pandey, M. I. Burguete and S. V Luis, *Chem. Rev.*, 2015, **115**, 8736–8834.

25 H. Furuta, T. Asano and T. Ogawa, *J. Am. Chem. Soc.*, 1994, **116**, 767–768.

26 P. Kar, S. Sardar, E. Alarousu, J. Sun, Z. S. Seddigi, S. A. Ahmed, E. Y. Danish, O. F. Mohammed and S. K. Pal, *Chem. – A Eur. J.*, 2014, **20**, 10475–10483.

27 H.-C. Chen, J. N. H. Reek, R. M. Williams and A. M. Brouwer, *Phys. Chem. Chem. Phys.*, 2016, **18**, 15191–15198.

28 H.-C. Chen, D. G. H. Hetterscheid, R. M. Williams, J. I. van der Vlugt, J. N. H. Reek and A. M. Brouwer, *Energy Environ. Sci.*, 2015, **8**, 975–982.

29 M. Zhu, Y. Lu, Y. Du, J. Li, X. Wang and P. Yang, *Int. J. Hydrogen Energy*, 2011, **36**, 4298–4304.

30 R. R. de Haas, R. P. M. van Gijlswijk, E. B. van der Tol, H. J. M. A. A. Zijlmans, T. Bakker–Schut, J. Bonnet, N. P. Verwoerd and H. J. Tanke, *J. Histochem. Cytochem.*, 1997, **45**, 1279–1292.

31 P. Chen, O. S. Finikova, Z. Ou, S. A. Vinogradov and K. M. Kadish, *Inorg. Chem.*, 2012, **51**, 6200–6210.

32 C. He, Q. He, C. Deng, L. Shi, D. Zhu, Y. Fu, H. Cao and J. Cheng, *Chem. Commun.*, 2010, **46**, 7536–7538.

33 J. Miao and L. Zhu, *Chem. Asian J.*, 2010, **5**, 1634–1641.

34 P. van der Sluis and A. L. Spek, *Acta Crystallogr. Sect. A*, 1990, **46**, 194–201.

35 Y.-C. He, N. Xu, F.-H. Zhao, W.-Q. Kan, H.-R. Liu and J. You, *Inorg. Chem. Commun.*, 2017, **86**, 78–81.

36 G. Nandi, R. Thakuria, H. M. Titi, R. Patra and I. Goldberg, *CrystEngComm*, 2014, **16**, 5244–5256.

37 Y. Zhang, Y. Wu, X. He, J. Ma, X. Shen and D. Zhu, *Acta Crystallogr. Sect. C*, 2018, **74**, 256–262.

38 L. Ma, D. J. Mihalcik and W. Lin, *J. Am. Chem. Soc.*, 2009, **131**, 4610–4612.

39 T. Steiner, *Angew. Chem. Int. Ed.*, 2002, **41**, 48–76.

40 C. A. Hunter and J. K. M. Sanders, *J. Am. Chem. Soc.*, 1990, **112**, 5525–5534.

41 M. S. Deenadayalan, N. Sharma, P. K. Verma and C. M. Nagaraja, *Inorg. Chem.*, 2016, **55**, 5320–5327.

42 C. F. Macrae, P. R. Edgington, P. McCabe, E. Pidcock, G. P. Shields, R. Taylor, M. Towler and J. van de Streek, *J. Appl. Crystallogr.*, 2006, **39**, 453–457.

43 M. B. Shundalau, A. I. Komyak, A. P. Zazhogin and D. S. Umreiko, *J. Appl. Spectrosc.*,

2012, **79**, 22–30.

44 H. Benalia and D. Barkat, *J. Dispers. Sci. Technol.*, 2017, **38**, 1247–1251.

45 V. Zeleňák, Z. Vargová and K. Györyová, *Spectrochim. Acta Part A Mol. Biomol. Spectrosc.*, 2007, **66**, 262–272.

46 B. Morzyk-Ociepa, M. Kokot, E. Różycka-Sokołowska, K. Giełzak-Koćwin, B. Filip-Psurska, J. Wietrzyk and D. Michalska, *Polyhedron*, 2014, **67**, 464–470.

47 L. J. Boucher and J. J. Katz, *J. Am. Chem. Soc.*, 1967, **89**, 1340–1345.

48 A. L. Spek, *Acta Crystallogr. Sect. C, Struct. Chem.*, 2015, **71**, 9–18.

49 S. O. H. Gutschke, D. J. Price, A. K. Powell and P. T. Wood, *Angew. Chem. Int. Ed.*, 2001, **40**, 1920–1923.

50 X.-W. Wang, Y. Chen, J.-Z. Chen, J.-H. Liu and L. Han, *Z. Naturforsch. B*, 2008, **63**, 129–133.

51 W.-H. Jiang, H.-Z. Zhang, G.-F. Hou, D.-S. Ma, B. Liu and Y.-H. Yu, *RSC Adv.*, 2017, **7**, 45641–45651.

52 M. Matzapetakis, M. Dakanali, C. P. Raptopoulou, V. Tangoulis, A. Terzis, N. Moon, J. Giapintzakis and A. Salifoglou, *J. Biol. Inorg. Chem.*, 2000, **5**, 469–474.

53 M. Aydin, ed. D. L. A. E.-M. T. Stauffer, IntechOpen, Rijeka, 2016, p. Ch. 7.

54 A. F. Abdel-Magied, A. Shatskiy, R.-Z. Liao, T. M. Laine, W. A. A. Arafa, P. E. M. Siegbahn, M. D. Kärkäs, B. Åkermark and E. V. Johnston, *ChemSusChem*, 2016, **9**, 3448–3456.

55 M. Orlandi, R. Argazzi, A. Sartorel, M. Carraro, G. Scorrano, M. Bonchio and F. Scandola, *Chem. Commun.*, 2010, **46**, 3152–3154.

56 M. D. Kärkäs, T. M. Laine, E. V Johnston and B. Åkermark, *Visible Light-Driven Water Oxidation Catalyzed by Ruthenium Complexes*, InTech, Rijeka, 2016.

57 B. Limburg, E. Bouwman and S. Bonnet, *ACS Catal.*, 2016, **6**, 5273–5284.

58 T. M. Laine, M. D. Kärkäs, R.-Z. Liao, T. Åkermark, B.-L. Lee, E. A. Karlsson, P. E. M. Siegbahn and B. Åkermark, *Chem. Commun.*, 2015, **51**, 1862–1865.

59 H. Xia, Y. Zhu, D. Lu, M. Li, C. Zhang, B. Yang and Y. Ma, *J. Phys. Chem. B*, 2006, **110**, 18718–18723.

60 B. P. Sullivan, D. J. Salmon and T. J. Meyer, *Inorg. Chem.*, 1978, **17**, 3334–3341.

61 X. Deng and H. Tüysüz, *ACS Catal.*, 2014, **4**, 3701–3714.

62 J. D. Blakemore, H. B. Gray, J. R. Winkler and A. M. Müller, *ACS Catal.*, 2013, **3**, 2497–2500.

63 J. H. Kim, D. Hansora, P. Sharma, J.-W. Jang and J. S. Lee, *Chem. Soc. Rev.*, 2019, **48**, 1908–1971.

64 H. Inoue, T. Shimada, Y. Kou, Y. Nabetani, D. Masui, S. Takagi and H. Tachibana, *ChemSusChem*, 2011, **4**, 173–179.

65 D. Nesterov and O. Nesterova, *Catalysts*, 2018, **8**, 602.

66 G. Maayan, N. Gluz and G. Christou, *Nat. Catal.*, 2018, **1**, 48–54.

67 M. D. Kärkäs and B. Åkermark, *Dalt. Trans.*, 2016, **45**, 14421–14461.

68 V. Kunz, D. Schmidt, M. I. S. Röhr, R. Mitrić and F. Würthner, *Adv. Energy Mater.*, 2017, **7**, 1602939.

69 M. Schulze, V. Kunz, P. D. Frischmann and F. Würthner, *Nat. Chem.*, 2016, **8**, 576–583.

70 S. M. Shaikh, A. Chakraborty, J. Alatis, M. Cai, E. Danilov and A. J. Morris, *Faraday Discuss.*, 2019, **216**, 174–190.

71 A. Sartorel, M. Bonchio, S. Campagna and F. Scandola, *Chem. Soc. Rev.*, 2013, **42**, 2262–2280.

72 F. Evangelisti, P.-E. Car, O. Blacque and G. R. Patzke, *Catal. Sci. Technol.*, 2013, **3**, 3117–3129.

73 J. Soriano-López, F. Song, G. R. Patzke and J. R. Galan-Mascaros, *Front. Chem.*, 2018, **6**, 302.

74 L. Yu, Y. Ding, M. Zheng, H. Chen and J. Zhao, *Chem. Commun.*, 2016, **52**, 14494–14497.

75 C. Spöri, J. T. H. Kwan, A. Bonakdarpour, D. P. Wilkinson and P. Strasser, *Angew. Chem. Int. Ed.*, 2017, **56**, 5994–6021.

76 J. Li, R. Güttinger, R. Moré, F. Song, W. Wan and G. R. Patzke, *Chem. Soc. Rev.*, 2017, **46**, 6124–6147.

77 K. S. Joya and X. Sala, *Phys. Chem. Chem. Phys.*, 2015, **17**, 21094–21103.

78 S. Fukuzumi, Y.-M. Lee and W. Nam, *Dalt. Trans.*, 2019, **48**, 779–798.

79 H. Liu, M. Schilling, M. Yulikov, S. Luber and G. R. Patzke, *ACS Catal.*, 2015, **5**, 4994–4999.

80 Y. Li, W. Qiu, F. Qin, H. Fang, V. G. Hadjiev, D. Litvinov and J. Bao, *J. Phys. Chem. C*, 2016, **120**, 4511–4516.

81 C.-Z. Yuan, Y.-F. Jiang, Z. Wang, X. Xie, Z.-K. Yang, A. B. Yousaf and A.-W. Xu, *J. Mater. Chem. A*, 2016, **4**, 8155–8160.

82 S. Zhao, C. Li, H. Huang, Y. Liu and Z. Kang, *J. Mater.*, 2015, **1**, 236–244.

83 Y. Surendranath, M. W. Kanan and D. G. Nocera, *J. Am. Chem. Soc.*, 2010, **132**, 16501–16509.

84 F. Lu, M. Zhou, Y. Zhou and X. Zeng, *Small*, 2017, **13**, 1701931.

Chapter Three

Bioinspired Mn-Oxo Clusters for H_2O Oxidation

3.1 Introduction

In recent years, Mn-based H_2O oxidation catalysts using the naturally occurring $\{Mn_4CaO_5\}$ cluster of the OEC as a blueprint for OER catalysis have attracted significant scientific attention.[1] Investigations of these bioinspired compounds are propitious, not only for enhancing our understanding of H_2O splitting in Nature but also because of the intrinsic properties of Mn. Owing to the high natural abundance and low toxicity of Mn, Mn-based WOCs offer many advantages over other WOCs constructed from prohibitively expensive rare-earth elements such as Ru and Ir.[2,3,4]

Mn-oxo clusters are particularly attractive for H_2O oxidation catalysis studies as they can be prepared in high yields from inexpensive, environmentally benign salts and solvents according to well-established procedures.[5] Moreover, Mn is endowed with a rich redox chemistry with several accessible oxidation states.[6] Consequently, polynuclear Mn-oxo complexes may function as redox reservoirs, carrying several oxidising equivalents across many Mn centres of a molecule. This allows multinuclear structures to mediate multiple-electron redox reactions such as the four-electron OER whilst avoiding high energy intermediates.[7] For example, in the OEC four photogenerated holes which are sequentially accumulated from $P_{680}^{\bullet+}$ are stored as Mn^{IV} ions within the $\{Mn_4CaO_5\}$ cluster prior to O_2 evolution in the catalytic cycle (Fig.1.5).[8]

Importantly for H_2O oxidation catalysis, all oxidation states above Mn^{II} are highly oxidising under certain conditions, and are stabilised to varying degrees by OH^- and O^{2-} ligands which are important prevailing moieties during the OER (see Fig. 1.14).[9] In the OEC, it is suspected that a highly oxidising Mn^{V} (or Mn^{IV}-oxyl) species provides the energy for the critical O – O bond formation step.[10] Additionally, the kinetics of ligand exchange at Mn^{II} sites is fast, particularly in the case of terminally coordinated ligands which is advantageous for H_2O oxidation.[11] Furthermore, aromatic redox-active ligands which coordinate directly to Mn-oxo core structures may be able to modulate catalytic activity by storing and transferring oxidising equivalents during the OER. This is analogous to the tyrosine (Y_z) residue which is closely associated with the catalytic action of the $\{Mn_4CaO_5\}$ cluster in PS II.[12,13] Moreover, Mn-oxo cubanes are exceptionally powerful oxidising agents (with more oxidising power than analogous non-cubane compounds of identical empirical composition).[14]

Under this purview, multinuclear Mn-oxo clusters comprising cubane-type core structures, terminally coordinated labile ligands to allow H_2O substrate exchange and non-innocent aromatic ligands are particularly appealing for OER catalysis studies.[15] In addition, H_2O

oxidation catalysts capable of operating heterogeneously under neutral aqueous conditions are advantageous for practical applications, as this facilitates their recovery from mild and environmentally-friendly reaction mixtures.[13,16]

Within the literature, a wealth of Mn-oxo aggregates which exhibit these attributes have been documented.[17] Their structures are regularly reported due to their high magnetic anisotropies which can give rise to single-molecule magnet (SMM) behaviour and potential data storage applications.[18,19,20,21] However, these materials have not yet satisfactorily been explored for catalytic purposes. Thus, the examination of previously published Mn-oxo clusters for H_2O oxidation catalytic properties presents a promising avenue for advancing artificial photosynthetic energy conversion concepts.[22]

One pertinent example of this is a dodecanuclear SMM $[Mn_{12}O_{12}(OAc)_{16}(H_2O)_4]$ which was originally synthesised in Lis in 1980.[23] Recently, Maayan *et al*. modified this cluster by incorporating hydrophilic di- or trihydroxybenzoate ligands. This resulted in soluble $\{Mn_{12}\}$ derivatives which demonstrate significant OER activity. Under electrochemical conditions, these compounds achieved TONs of 13.2 and 15.5 for the trihydroxybenzoate- and dihydroxybenzoate-substituted clusters, respectively.[24,25] These materials represent some of the most robust and active Mn-based H_2O oxidation catalysts in the literature which operate at neutral pH, however, they still show signs of decomposition under working conditions.

In this chapter, the screening for H_2O oxidation catalytic properties of a range of Mn-oxo compounds (**3** – **11**) is discussed. Following this preliminary investigation, the material which displayed the highest apparent activity and stability (**11**) was selected for use in a more in-depth OER study. As a result of this, **11** was resynthesized and characterised which resulted in the discovery of a novel polymorph containing the literature-known $\{Mn_{19}\}$ cluster core. The O_2 evolution properties of **11** under photochemical and electrochemical conditions are then outlined, in addition to a series of experiments which assign **11** as a genuine molecular WOC (see Sections 3.3 – 3.6).

3.2 Preliminary Screening of Mn-Oxo Materials for OER Catalytic Activity

A central aim of this research project was to determine the catalytic OER properties of Mn compounds with some structural similarities to the {Mn_4CaO_5} cluster of the OEC. The various advantages afforded by 'OEC mimicking' Mn-oxo clusters make their use in O_2 evolution catalysis studies attractive. Fortuitously, a diverse range of Mn-oxo clusters previously prepared within the Schmitt group were available for use in H_2O oxidation experiments. Using the experimental setup described in Chapter 2, an array of promising, potentially OER active Mn-oxo materials were screened for photocatalytic activity according to an established procedure.[26,27] Several of these structures are literature-known, however their OER catalytic properties had not been explored prior to this work.[28,29,30,31] To emulate the biological working conditions of the OEC, photocatalytic H_2O screening experiments were conducted under aqueous working conditions at pH = 7.

Mn-based coordination complexes and polymers bearing structural characteristics deemed likely to confer OER activity were screened as prospective WOCs. For example, clusters displaying solvent-accessible coordination sites,[32] cubane motifs,[14,33,34] polynuclearity,[35] Mn centres with high oxidation states[22,36] or non-innocent ligands[37] were preferentially selected. Several of the structures screened emerged as OER-inactive in these preliminary tests. However, nine Mn-oxo compounds (**3 – 11**) revealed catalytic O_2 evolution activity and are discussed in this section.

3.2.1 Cl^--Stabilised Mn-Oxo Coordination Clusters with Cuboctahedral Core Topologies

Three $t\text{BuPO}_3^{2-}$-stabilised ($t\text{BuPO}_3^{2-}$ = *tert*-butylphosphonate), mixed-valent Mn-oxo clusters with $\{Mn^{II}Mn^{III}_{12}\}$ (**3**), $\{Mn^{II}_3Mn^{III}_{10}\}$ (**4**) and $\{Mn^{II}_3Mn^{III}_{11}\}$ (**5**) core structures were selected.[28] These structures are displayed in Fig 3.1 and are formulated as:

$[Mn^{II}Mn^{III}_{12}(\mu_4\text{-O})_8(\mu_4\text{-Cl})_6(t\text{BuPO}_3)_8]$ (**3**),

$[Mn^{II}_3Mn^{III}_{10}(\mu_4\text{-O})_6(\mu_3\text{-O})(\mu_3\text{-OH})(\mu_4\text{-Cl})_4(\text{Cl})(t\text{BuPO}_3\text{H})(t\text{BuPO}_3)_9]^{3-}$ (**4**) and

$[Mn^{II}_3Mn^{III}_{11}(\mu_4\text{-O})_6(\mu_3\text{-O})(\mu_3\text{-OH})(\mu_2\text{-OH})(\mu_4\text{-Cl})_4(t\text{BuPO}_3\text{H})(t\text{BuPO}_3)_{10}(\text{Apy})]^{2-}$ (**5**, Apy = 2-aminopyridine).

For the full molecular formulae of Mn-oxo compounds used to calculate catalyst loadings in light-driven OER experiments, see Section 6.1.15 in the experimental section. Each unique cluster **3** – **5** exhibits an array of attributes engendering them likely catalysts for the OER, and their polynuclear Mn-based constitutions render them apt synthetic models of the Mn_4CaO_5 OEC of PS II.[38,5] However, heretofore the homogeneous OER catalytic properties of these clusters had not been investigated.

The three Mn-oxo clusters **3** – **5** were prepared *via* comproportionation reactions between $MnCl_2{\cdot}4H_2O$ and $KMnO_4$ in the presence of $t\text{BuPO}_3\text{H}_2$ and triethylamine (TEA) in acetonitrile (MeCN). The cluster which forms from this reaction mixture is determined by the ratio between the concentrations of Cl^- anions and $t\text{BuPO}_3\text{H}_2$ used in the synthesis. Therefore, a high degree of synthetic control is afforded, as the employed Cl^- anion concentration correlates with the Cl^- content and symmetry of the cluster generated. Employing Cl^-:phosphonate ratios of 6:1, 4:1 and 2:1 reproducibly results in the formation of **3**, **4** and **5**, respectively.

3 (Fig. 3.1a) is a highly symmetric, tridecanuclear $\{Mn^{II}Mn^{III}_{12}\}$ coordination cluster comprising a central Mn^{II} ion which is linked to an array of twelve cuboctahedrally arranged Mn^{III} ions through eight $\mu_4\text{-}O^{2-}$ oxo ligands. This cuboctahedron's six square faces are stabilised by six octahedrally arranged $\mu_4\text{-}Cl^-$ ligands, and its eight triangular faces are stabilised by eight $\mu_3\text{-}t\text{BuPO}_3^{2-}$ ligands which adopt a cubic configuration. Notably, **3** is an example of a Keplerate cluster, as it comprises endohedrally encapsulating arrangements of platonic ($\{Cl_6^-\}$ octahedron and $\{(t\text{BuPO}_3^{2-})_8\}$ cube) and Archimedean bodies ($\{Mn^{III}\}_{12}$ cuboctahedron).[39]

The Cl^- stabilised clusters **4** (Fig. 3.1b) and **5** (Fig. 3.1c) are structurally related to **3**. As in **3**,

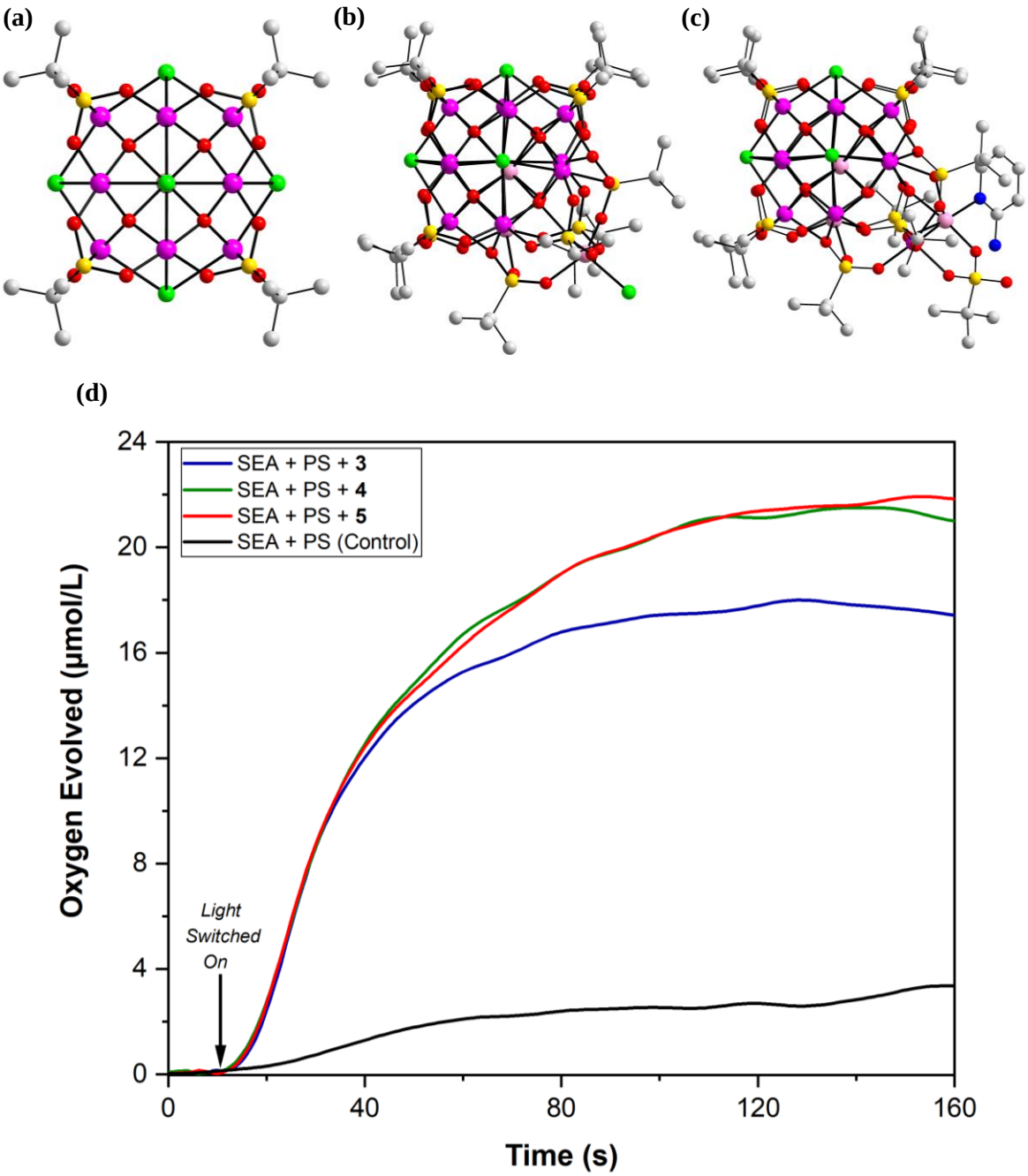

Figure 3.1: (a – c) Ball-and-stick representations of three structurally related, mixed-valent Mn-oxo clusters which were screened for light-induced OER activity: (a) **3**, (b) **4**, and (c) **5**. Hydrogen atoms and solvent molecules have been omitted for the purpose of clarity. Colour scheme: C white, O red, Cl green, P yellow, C orange, Mn^{II} pale pink, Mn^{III} magenta. (d) Kinetic monitoring (Clark electrode) of the O_2 evolution response of three Mn-oxo clusters **3** (blue), **4** (green) and **5** (red) in the presence of a SEA and a PS. The O_2 evolution response of a control experiment in which only the SEA and PS were irradiated is also plotted for comparison (black). Conditions: 1.2 µM WOC loading in a phosphate-buffered, aqueous solution (5 mL 0.01 M, initial pH = 7) with $Na_2S_2O_8$ SEA (10 mM) and $[Ru(bpy)_2(deeb)](PF_6)_2$ PS (2 mg, 2.33 µmol). LED lamp (λ = 470, 10 mW cm^{-2}). The photocatalytic mixture was stirred at a constant rate of 500 rpm and maintained at 25 °C by immersing the reaction vessel in a water bath.

both **4** and **5** are stabilised by eight cubically configured *t*$BuPO_3^{2-}$ ligands. However, two vertices of the {Cl_6^-} octahedron of **5** are absent in **4** and **3**. Therefore, these reduced symmetry structures have one fewer Mn^{III} vertex than the original {Mn^{III}}$_{12}$ cuboctahedron of **3**. The central Mn^{II} ions of **4** and **5** are linked to eleven Mn^{III} centres through one μ_3-OH^{2-} hydroxo, one μ_3-O^{2-} oxo and six μ_4-O^{2-} oxo ligands. **4** also features a pendant Mn^{II} ion which is attached to the cluster core by two additional phosphonate ligands. Similarly, **5** features a hanging dinuclear {Mn^{II}-OH-Mn^{III}} subunit which connects to the core through three phosphonates. The dangling Mn centres of **4** and **5** are reminiscent of the dangling Mn^{III} ion of the OEC.[38,40]

The OER catalytic properties of **3** – **5** were investigated for several reasons. For example, these clusters contain several high oxidation state Mn centres (twelve Mn^{III} (**3**), ten Mn^{III} (**4**) or eleven Mn^{III} (**5**)), which has been associated with favourable H_2O oxidation catalytic activity.[41,42] Moreover, the high nuclearities of **3** – **5** may allow the four redox equivalents required for H_2O oxidation to accumulate over multiple metal sites, thus preventing unfavourable large oxidation state changes to any individual Mn centre.[43] In addition, the stabilities of **3** – **5** in solution have been confirmed using electrospray-ionisation mass spectrometry (ESI-MS).[28] Finally, the dangling {Mn^{II}} and {Mn^{II}-OH-Mn^{III}} subunits of **4** and **5**, respectively, structurally resemble a feature of the OEC.[44]

The Mn-oxo clusters **3**, **4** and **5** were independently screened for homogeneous photocatalytic OER activity under neutral, aqueous phosphate-buffered conditions according to established literature procedures.[1,26,45,46,] Upon light-irradiation (LED lamp, λ = 470 nm, 10 mW cm^{-2}), deaerated 1.2 µM solutions of **3**, **4** or **5** containing $Na_2S_2O_8$ SEA and [$Ru(bpy)_2(deeb)$]$(PF_6)_2$ PS, the dissolved O_2 quantity inside the reactor rose continuously for *ca*. 120 seconds. The kinetics of O_2 evolution (monitored using a Clark electrode) by **3** (blue), **4** (green), **5** (red) and no catalyst (black) while all other conditions were kept constant are plotted in Fig. 3.1d.

In these screening experiments, the Mn-oxo clusters **3**, **4** and **5** produced significantly more O_2 than was liberated in a control experiment in which no catalyst was used, indicating that all three compounds demonstrate OER catalytic activity. **4** and **5** evolved the highest quantities of O_2, liberating *max*. 105 and 108 nmol of O_2, respectively. These closely matching activities correspond to a TON = 17.5 for **4** and a TON = 18 for **5**. The symmetric species **3** gave rise to the lowest quantity of O_2 of the three clusters, demonstrating a TON = 14.8 and a TOF = 0.35 s^{-1}. A comparison of the TONs, TOFs and % O_2 yield of the OER using **3**, **4** and **5** is presented in Table 3.1 on page 122.

The higher H_2O oxidation activities of **4** and **5** in comparison with the activity of **3** could arise due to a contribution from the 'dangling' Mn centres of these compounds. Also, as **4** and **5** feature two fewer outer stabilising Cl^- ligands relative to **3**, the cores of the former clusters may be more readily accessible by H_2O substrate molecules thus improving their OER performance. Finally, the nature of the bridging ligands which stabilise **3** – **5** could be of potential significance: Whilst **3** is stabilised exclusively by μ_3-*t*$BuPO_3^{2-}$ phosphonate ligand derivatives, **4** and **5** are stabilised by both μ_3-*t*$BuPO_3^{2-}$ and μ_2-*t*$BuPO_3H^-$ phosphonates. The labile latter ligand derivative may be substituted by H_2O substrates more easily, giving rise to the relatively higher catalytic activities observed using **4** and **5**.

3.2.2 Mn-Oxo Coordination Clusters featuring Brucite-Type Structural Motifs

Four investigated, structurally related, Mn-oxo clusters which were synthesised within the Schmitt group are of the formulae:

$[(Mn^{II}_{0.5}Mn^{III}_{0.5})Mn^{III}_{12}(\mu_4\text{-}O)_6(\mu\text{-}OH)_2(\mu\text{-}OMe)_4(MeOH)_2(t\text{BuPO}_3)_{10}(Pic)_4]^{0.5+}$ (**6**, Pic = 4-picoline),[29]

$[(Mn^{II}_{0.5}Mn^{III}_{0.5})Mn^{III}_{12}Ca^{II}_2(\mu_4\text{-}O)_6(\mu_3\text{-}O)_2(\mu\text{-}OMe)_4(MeOH)_6(t\text{BuPO}_3)_{10}(Piv)_2(Ph_2PO_2)_2]$ (**7**, Piv = pivalate, Ph_2PO_2 = diphenylphosphinate),

$[Mn^{III}_{11}Mo^{VI}_2O_2(\mu_4\text{-}O)_2(\mu_3\text{-}O)_4(\mu\text{-}O)_4(\mu\text{-}OH)_2(t\text{BuPO}_3)_{10}(Py)_4]^-$ (**8**, Py = pyridine) and

$[(Mn^{II}_{0.5}Mn^{III}_{0.5})Mn^{III}_{12}(\mu_4\text{-}O)_6(\mu\text{-}OH)_2(\mu\text{-}OMe)_4(MeOH)_2(t\text{BuPO}_3)_{10}(TDP)_4]^{0.5+}$ (**9**, TDP = 4,4'-trimethylenedipyridine).[29]

6 – **9** (Fig. 3.2a – d) were selected to use in OER screening experiments as they share several structural attributes with literature-known synthetic WOCs, and with the OEC of PS II.[2,47] Samples of **6** – **9** were prepared in high-yielding, reproducible reactions, and their catalytic properties were thus far undiscovered. The heterometallic clusters **7** and **8** are analogues of the homometallic Mn-oxo cluster **6**, whereas **9** is a cluster-based coordination polymer which is derived from **6**.

The core structure of **6** comprises a three-layered distorted cuboctahedral topology featuring a central, octahedrally coordinated Mn^{II} or Mn^{III} ion (1:1 ratio in the crystal structure) which is linked to six adjacent Mn^{III} ions *via* six μ_4-oxo ligands. The middle layer of **6** is a hexagonal "brucite"-type heptanuclear subunit that is connected to two triangular, outer layers through eight μ_4-phosphonate, six μ_4-oxo and four μ-methoxy ligands. The outermost layers of **6** are each composed of a dinuclear {Mn^{III}-O-Mn^{III}} subunit which is coordinated by two terminal picoline (Pic) ligands located at two Mn^{III} Jahn-Teller elongated binding sites, and a single tetragonally distorted Jahn-Teller Mn^{III} centre bound by a terminal labile MeOH ligand.

The heterometallic clusters **7** and **8** bear analogous core structures to **6**. However, the outer trinuclear layers of **7** are each capped by an octacoordinated Ca^{II} centre which connects through two μ_3-η^2:η^1-phosphonate ligands, one μ_2-η^1:η^1-diphenylphosphine ligand and a μ_3-oxo ligand. In **8**, the two outer isolated Mn^{III} ions are substituted by molybdate moieties. As a result of this, **7** and **8** each feature two fewer Mn^{III} Jahn-Teller distorted sites which are occupied by terminal labile ligands relative to **6**.

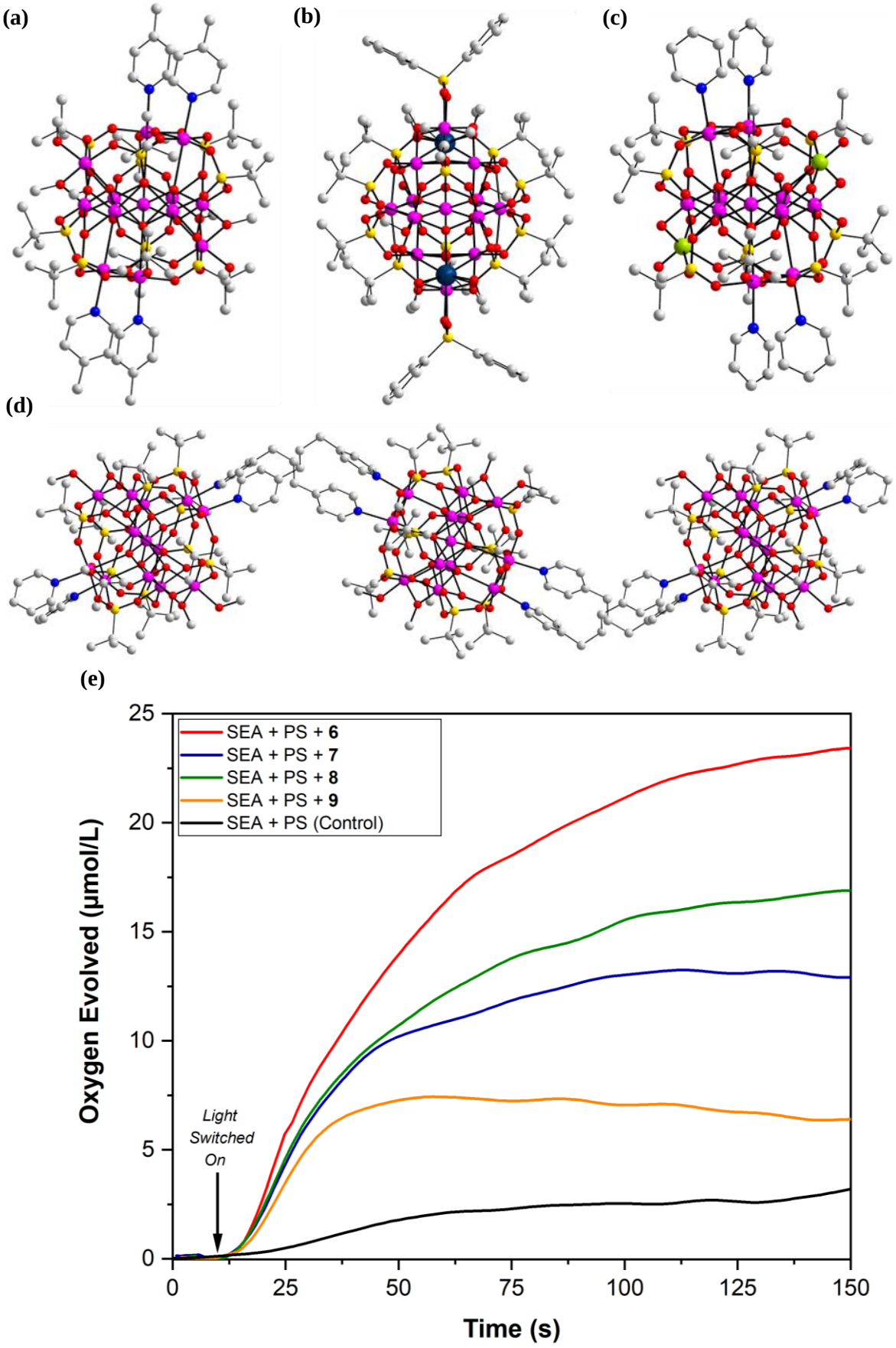

Figure 3.2: (a – d) Crystal structures (ball-and-stick representations) of four structurally related Mn-oxo compounds with brucite-type {Mn_7} core topologies: (a) **6**, (b) **7**, (c) **8** and (d) **9**. Hydrogen atoms and constitutional solvent molecules have been omitted for clarity. Colour scheme: C white, O red, N blue, Mo lime, P yellow, Mn^{II} pale pink, Mn^{III} magenta (Contd.)

Ca^{II} navy. (e) Kinetic monitoring (Clark electrode) of the photocatalytic OER response of **6** (red), **7** (blue), **8** (green) and **9** (orange) from H_2O oxidation screening tests in the presence of a SEA and PS. The O_2 evolution response of a control experiment in which the SEA and PS were irradiated without a WOC is also plotted for comparison (black). Conditions for O_2 evolution experiments: Homogeneous WOC loading (**6** – **9**), 1.2 μM; heterogeneous WOC loading (**9**), 30 nm in phosphate-buffered aqueous solutions (5 mL 0.01 M, initial pH = 7) containing $Na_2S_2O_8$ SEA (10 mM) and $[Ru(bpy)_2(deeb)](PF_6)_2$ PS (2 mg, 2.33 μmol). LED lamp ($\lambda = 470$, 10 mW cm^{-2}). A constant stirring rate and temperature of 500 rpm and 25 °C, respectively, were maintained throughout each experiment.

The coordination polymer **9** is generated by substituting the four terminal Pic ligands of **6** with ditopic 4,4'-trimethylenedipyridine (TDP) ligands. **9** comprises $\{Mn_{13}\}$ SBUs with virtually identical geometric parameters to **6** that are doubly bridged by μ-TDP linkers. The packing of **9** in the solid state gives rise to large solvent-filled channels with pore openings of *ca*. 10 × 12 Å. The inner surfaces of these cavities are decorated with two labile MeOH ligands at Mn^{III} Jahn-Teller sites per $\{Mn_{13}\}$ unit, and the solvent-accessible volume of **9** after removal of guest solvent molecules is *ca*. 38%.[48]

Several structural attributes of **6** – **9** make them attractive materials to test for H_2O oxidation activity. For example, all four compounds are high-nuclearity molecules with many Mn^{III} centres, and 'brucite'-type cores resembling the structures of previously published phosphate-stabilised OER catalysts.[49,50] Further, the presence of kinetically labile, monodentate ligands bound to tetragonally elongated Mn^{III} Jahn-Teller sites at the peripheries of **6** – **9** is a promising property, as participation in ligand-exchange reactions by these moieties with H_2O substrate molecules could precede OER catalytic transformations. Additionally, the presence of Ca^{II} ions in **7** make this structure an intriguing synthetic model for the $\{Mn_4CaO_5\}$ cluster of PS II. Finally, although **6**, **7** and **8** are homogeneous under aqueous conditions, the heterogeneous nature of **9** under these conditions could confer advantages as a H_2O splitting catalyst.[16]

The OER activities of **6** – **9** were screened in the same manner as **3** – **5**, according to adapted literature procedures.[45,46,26] Irradiation (LED lamp, $\lambda = 470$ nm) of anoxic, aqueous phosphate-buffered solutions containing **6**, **7**, **8** or **9** and $Na_2S_2O_8$ and $[Ru(bpy)_2(deeb)](PF_6)_2$ induced O_2 evolution, whereby the measured dioxygen concentration in solution continuously increased for either *ca*. 120 (**6**, **7** and **8**) or 60 seconds (**9**). The O_2 evolution profiles of **6** (red), **7** (blue), **8** (green), **9** (orange) and no catalyst (black) are plotted in Fig. 3.2e.

In these experiments, irradiation of each of the compounds **6** – **9** resulted in the production of several times more O_2 than was produced in a control experiment without a catalyst. This

suggests that all four compounds either exhibit catalytic OER activity or are precatalysts for other OER active materials. The largest quantity of O_2 (117 nmol) was liberated using **6**, which also displayed the highest TON = 19.5 and TOF = 0.48 s^{-1} of the compounds tested. The heterometallic clusters **7** and **8** evolved comparatively less O_2 than their homometallic analogue **6**: **7** and **8** evolved 65.0 and 84.5 nmol of O_2, respectively. The heterogeneous coordination polymer **9** generated the smallest quantity of O_2 (37.5 nmol). The TONs, TOFs and O_2 yields calculated from these screening experiments are shown in Table 3.1.

The magnitude of the OER activity manifested by **6** – **9** appears to be associated with the number of H_2O substrate-accessible Mn^{III} Jahn-Teller distorted sites on each cluster. The highest activity was demonstrated using **6** which contains six such sites, whereas equimolar amounts of **7** and **8** which each feature four of these sites evolved comparatively less O_2. **7** displayed greater OER activity than **8**, which may be due to steric shielding of the active sites of **8** by proximal capping Ca^{II} ions and hydrophobic Piv ligands. **9** exhibited the lowest turnover characteristics of **6** – **9** and also contains the fewest kinetically labile ligands located at Jahn-Teller sites. The slow kinetics of OER catalysis by this polymer may otherwise be attributed to its heterogeneity, as only the active sites located at the surface of **9** are accessible by H_2O substrate molecules.

3.2.3 Supertetrahedral Nonadecanuclear Mn-Oxo Coordination Clusters

Two final Mn-oxo clusters featuring {Mn_{19}} and {$Mn_{18}Sr$} core structures constructed from redox-active, tridentate 2,6-bis(hydroxymethyl)-*p*-cresol (H_3**L2**) ligands which are formulated as:

$[Mn^{III}_{12}Mn^{II}_{6}Sr^{II}(\mu_4\text{-}O)_8(\mu_3\text{-}Cl)_8(H\mathbf{L2})_{12}(MeCN)_6]^{2+}$ (**10**) and

$[Mn^{III}_{12}Mn^{II}_{7}(\mu_4\text{-}O)_8(\mu_3\text{-}OCH_3)_2(\mu_3\text{-}Br)_6(H\mathbf{L2})_{12}(MeOH)_5(MeCN)]^{2+}$ (**11**)

were assessed as light-induced OER catalysts (Fig. 3.3a & b). The mixed-valent complexes **10** and **11** are structural variants of a nonadecanuclear Mn-oxo aggregate which was initially investigated by Powell *et al*., due to its unprecedented ground spin state of S = 83/2.[30] The transition metal ions of **10** and **11** are organised to form high-nuclearity supertetrahedral structures with several substrate-accessible sites, and significant similarities to the {Mn_4CaO_5} cluster of the OEC (see Fig. 3.4). Additionally, the insolubility of these clusters in aqueous solutions and their facile preparation from inexpensive and environmentally benign starting materials make them attractive candidates for H_2O oxidation catalysis. The presence of Sr^{II} in **10** is also intriguing, as this is the only metal known which can replace Ca^{II} in the OEC without rendering the cluster catalytically inactive.[51]

Despite these promising properties, **10** and **11** have not been studied as WOCs. However, in a recent study by Mameri *et al*., two Mn-oxo complexes bearing analogous {$Mn_{18}Sr$} and {Mn_{19}} core structures to **10** and **11** were successfully employed in the electrocatalytic oxidation of benzyl alcohol into benzaldehyde using O_2 as an oxidant and TEMPO (2,2,6,6-tetramethylpiperidine-1-oxyl) as a co-catalyst.[31] This result suggests that aggregates with {$Mn_{18}Sr$} and {Mn_{19}} cluster cores are competent catalysts for oxidative transformations, further indicating that **10** and **11** are rational choices to screen for OER activity.

The heterogeneous photocatalytic H_2O oxidation activities of **10** and **11** were probed in an analogous manner to **3** – **9**, using aqueous phosphate-buffered working conditions at pH = 7, $Na_2S_2O_8$ as SEA and $[Ru(bpy)_2(deeb)](PF_6)_2$ as PS. The kinetics of O_2 evolution (monitored using a Clark electrode) by **10** and **11** are displayed in Fig. 3.3c. Under photocatalytic conditions, both **10** and **11** evolved significantly more O_2 than a control experiment without catalyst, indicating that both of these compounds are highly active catalysts towards the OER. Employing 5 nmol loadings of **10** and **11** liberated 103 and 129 nmol O_2, respectively, with corresponding TONs of 20.5 for **10** and 25.8 for **11**. Very high TOFs of 0.56 and 0.57 s^{-1} were

achieved using **10** and **11**, respectively. The turnover characteristics revealed by **10** and **11** in these catalytic experiments are listed in Table 3.1.

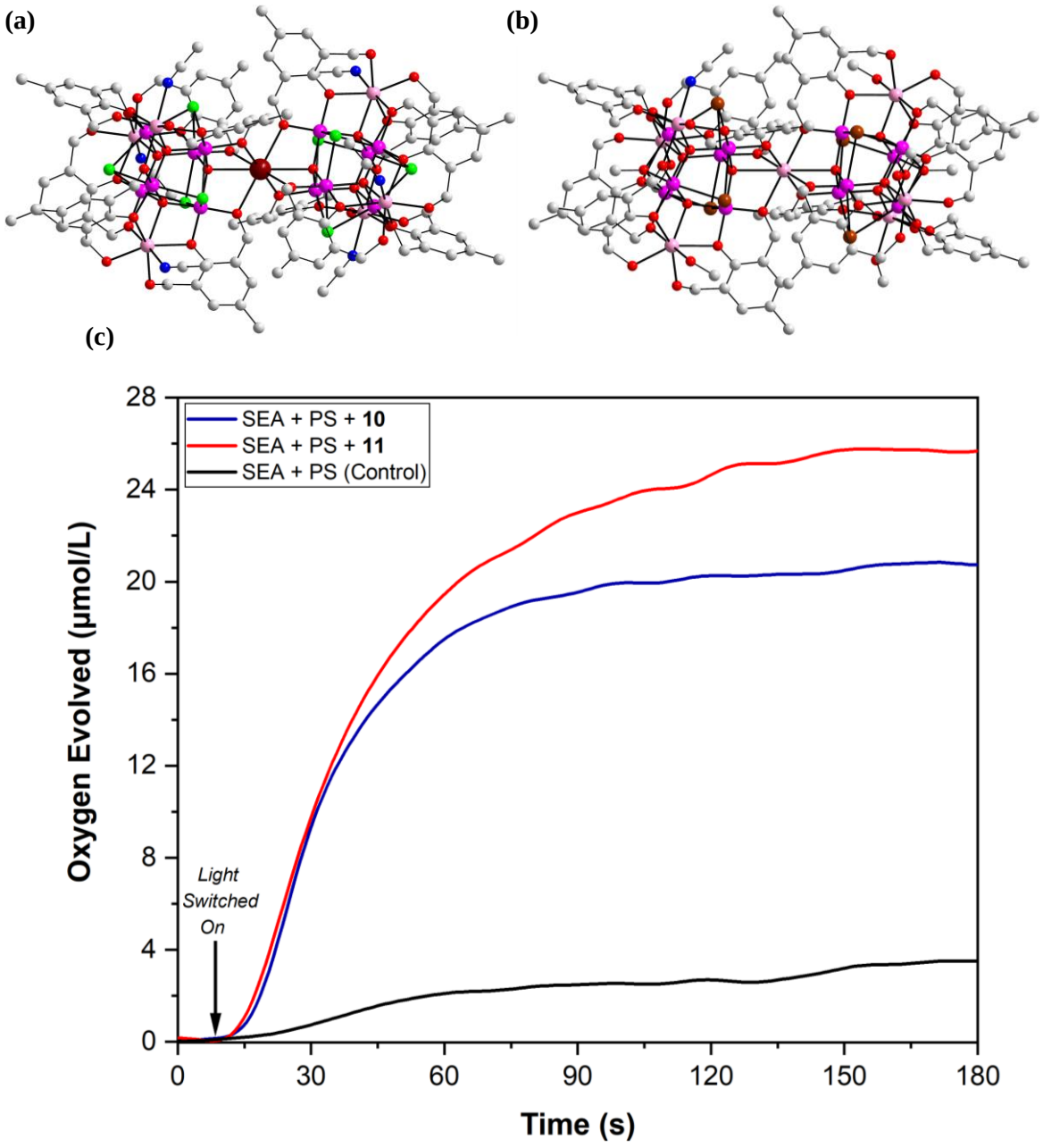

Figure 3.3: (a & b) Crystal structures (ball-and-stick representations) of two nonadecanuclear Mn-oxo clusters screened for light-driven OER catalytic activity: (a) **10** and (b) **11**. Hydrogen atoms and solvent of crystallisation have been omitted for clarity. Colour scheme: C white, O red, N blue, Cl green, Br brown, Mn^{II} pale pink, Mn^{III} pink, Sr crimson. (c) Kinetic monitoring (Clark electrode) of the light-driven O_2 evolution response of **10** (blue) and **11** (red). For comparison, the O_2 evolution response of a control experiment without a catalyst is also shown (black). Conditions: 5 nm WOC loading in a phosphate-buffered aqueous solution (5 mL 0.01 M, initial pH = 7) containing $Na_2S_2O_8$ SEA (10 mM) and $[Ru(bpy)_2(deeb)](PF_6)_2$ PS (2 mg, 2.33 µmol). Irradiated using an LED lamp ($\lambda = 470$, 10 mW cm^{-2}). The photocatalytic mixture was stirred at a constant rate of 500 rpm and maintained at 25 °C by immersing the reaction vessel in a water bath.

The exceptional OER activities observed using **10** and **11** could stem from several shared structural features. For example, both compounds comprise high-nuclearity cluster cores, allowing the four electrons which must be abstracted from H_2O to promote O_2 evolution to be distributed between either eighteen or nineteen redox-active Mn centres in **10** or **11**, respectively. This difference could underlie the marginally superior O_2 evolution activity displayed by **11** in comparison to **10**. In addition, each cluster contains twelve Mn^{III} centres, which are integral to catalytic H_2O oxidation in many WOCs including the OEC of PS II.[52,53] Furthermore, the geometric configurations of the Mn-oxo clusters **10** and **11** resemble the OEC: Two pseudocubane motifs appended by 'dangling' Mn^{II} centres which are coordinated by terminal, labile solvent molecules constitute a total of six substrate-accessible active sites per cluster of **10** and **11**. Finally, the presence of redox-active O-donor ligands which stabilise the cores structures of **10** and **11** represents an additional parallel between these clusters and the OEC.[38,54] The relevance of these features for H_2O oxidation catalysis are examined in greater detail in Section 3.3.

3.2.4 Relative Photocatalytic OER Activities of 3 – 11

The turnover characteristics of the Mn-oxo compounds which revealed photocatalytic H_2O oxidation activity (**3** – **11**) are detailed in Table 3.1.

Table 3.1 – Results of light-driven H_2O oxidation catalysis screening experiments using the Mn-oxo compounds 3 – 11 in the presence of $[Ru(bpy)_2(deeb)](PF_6)_2$ and $Na_2S_2O_8$.

Catalyst	O_2 Evolved (nmol)	TON	TOF (s^{-1})	O_2 Yield (%)
3 (6 nmol)	88.5	14.8	0.36	0.35
4 (6 nmol)	105	17.5	0.46	0.42
5 (6 nmol)	108	18.0	0.48	0.43
6 (6 nmol)	117	19.5	0.48	0.47
7 (6 nmol)	65.0	10.8	0.36	0.26
8 (6 nmol)	84.5	14.1	0.37	0.34
9 (30 nmol)	37.5	1.25	0.06	0.15
10 (5 nmol)	103	20.5	0.56	0.41
11 (5 nmol)	129*	25.8*	0.57*	0.52*

*Denotes the highest activity in terms of TON, TOF or O_2 yield of the Mn-oxo clusters **3** – **11**.

The Cl^--Stabilised Mn-oxo clusters **3** – **5** are good candidates to use in further OER catalytic studies on account of their facile synthesis and apparent favourable turnover characteristics (in particular **4** and **5**). However, as **3** – **5** are homogeneous under aqueous conditions they may display poor stability, and they are less easily recovered and recycled.[2] A number of other materials were also screened for catalytic H_2O oxidation activity to identify a structure displaying superior OER characteristics or heterogeneity for use in a more detailed H_2O oxidation catalysis study. Because of this, no further O_2 evolution experiments were carried out using **3** – **5**.

The screened Mn-oxo structures **6** – **9** also evidenced OER activity. A comparison of their relative activities highlights the tridecanuclear cluster **6** as a particularly promising homogeneous H_2O oxidation catalyst due to its high activity and apparent robustness relative to **7** – **9** and other literature-known WOCs.[43,55] After examining the Mn-oxo compounds **3** – **9** for OER activity, a correlation between favourable catalytic performance and high-nuclearity structures with several substrate-accessible sites became apparent. Therefore, two final nonadecanuclear Mn-oxo clusters with multiple substrate-accessible sites (**10** and **11**) were investigated for heterogeneous OER activity.

Comparison of the relative catalytic activities of **1** – **11** reveals that the turnover characteristics of **10** and **11** represent the highest OER catalytic activities of all of the Mn-oxo materials tested for catalytic H_2O oxidation. Moreover, Table 3.1 reveals that the O_2 evolution activity of **11** surpasses that of **3** – **10** in terms of TON, TOF and O_2 yield. In addition, due to the insolubility of this complex under aqueous conditions, the determined turnover characteristics do not represent the full catalytic potential of the material.

Considering the highly encouraging OER properties displayed by **11**, its insolubility in aqueous solutions at room temperature and its facile preparation from environmentally benign and cheap starting materials, **11** is an excellent candidate to employ in H_2O oxidation studies. Accordingly, the synthesis of **11** was reproduced and the product was characterised to afford an adequate quantity of phase-pure catalytic material for use in O_2 evolution experiments. This resulted in the discovery of a novel polymorph bearing a well-established cluster core. In the next section, the synthesis, characterisation and structural properties of **11** are detailed. Following on from this, a more detailed catalytic H_2O oxidation investigation using **11** as a WOC is outlined.

3.3 OER Catalytic Properties of $[Mn^{III}_{12}Mn^{II}_{7}(\mu_4\text{-}O)_8(\mu_3\text{-}OCH_3)_2(\mu_3\text{-}Br)_6(HL2)_{12}(MeOH)_5(MeCN)]Br_2\cdot 9MeCN\cdot MeOH$ (11)

In the previous section, an evaluation of the Mn-oxo compounds **3** – **11** highlighted several promising candidates for H_2O oxidation catalysis. This initial investigation indicated that **11** exhibits exceptional OER activity, exceeding that of **3** – **10**, and potentially outperforming many state-of-the-art literature-known transition metal-based WOCs.[25,56,57,58]

In this section, the synthesis and characterisation of **11** are outlined, prior to an in-depth examination of the cluster's OER properties. Catalytic experiments were carried out with three principal objectives: to optimise the H_2O oxidation activity of **11**, to quantitatively characterise the O_2 evolution behaviour of **11** and to identify the true WOC in this investigation.

3.3.1 Synthesis of $[Mn^{III}_{12}Mn^{II}_{7}(\mu_4\text{-}O)_8(\mu_3\text{-}OCH_3)_2(\mu_3\text{-}Br)_6(HL2)_{12}(MeOH)_5(MeCN)]Br_2\cdot 9MeCN\cdot MeOH$ (11)

$[Mn^{III}_{12}Mn^{II}_{7}(\mu_4\text{-}O)_8(\mu_3\text{-}OCH_3)_2(\mu_3\text{-}Br)_6(H\mathbf{L2})_{12}(MeOH)_5(MeCN)]Br_2\cdot 9MeCN\cdot MeOH$ (**11**) was prepared in a reproducible reaction, according to an adaptation of the general literature method for synthesising complexes with supertetrahedral $\{Mn_{19}\}$ core structures.[59,60,61] For this purpose, 2,6-bis(hydroxymethyl)-*p*-cresol ($H_3\mathbf{L2}$) was refluxed with $MnBr_2\cdot 4H_2O$ and trimethylamine in a mixture of acetonitrile and methanol for two hours. This reaction mixture was then slowly cooled to ambient temperature before filtering twice and leaving to crystallise by slow evaporation. After several days, uniform needle-shaped, deep red crystals of **11** had formed in the filtrate which were suitable for analysis using single crystal X-ray diffraction in moderate yield (23 %). Prior to catalytic experiments, the mother liquor was decanted, and individual crystals were manually selected and carefully washed with water. These crystals were subsequently dried in air and ground into a fine powder using a mortar and pestle.

3.3.2 Crystal Structure of $[Mn^{III}_{12}Mn^{II}_{7}(\mu_4\text{-}O)_8(\mu_3\text{-}OCH_3)_2(\mu_3\text{-}Br)_6(HL2)_{12}(MeOH)_5(MeCN)]Br_2\cdot 9MeCN\cdot MeOH$ (11)

The crystal structure of $[Mn^{III}_{12}Mn^{II}_{7}(\mu_4\text{-}O)_8(\mu_3\text{-}OCH_3)_2(\mu_3\text{-}Br)_6(H\mathbf{L2})_{12}(MeOH)_5(MeCN)]Br_2\cdot 9MeCN\cdot MeOH$ (**11**) was solved in the monoclinic space group $P2_1/n$. X-ray diffraction analysis revealed that **11** is a novel polymorph of a previously reported nonadecanuclear molecular $\{Mn_{19}\}$ species which can be regarded as a dimer of two supertetrahedral $\{Mn^{III}_6Mn^{II}_4\}$ units that share a central Mn^{II} vertex. A wire-frame representation of **11** and polyhedral representations of its cluster core are presented in Fig. 3.4.

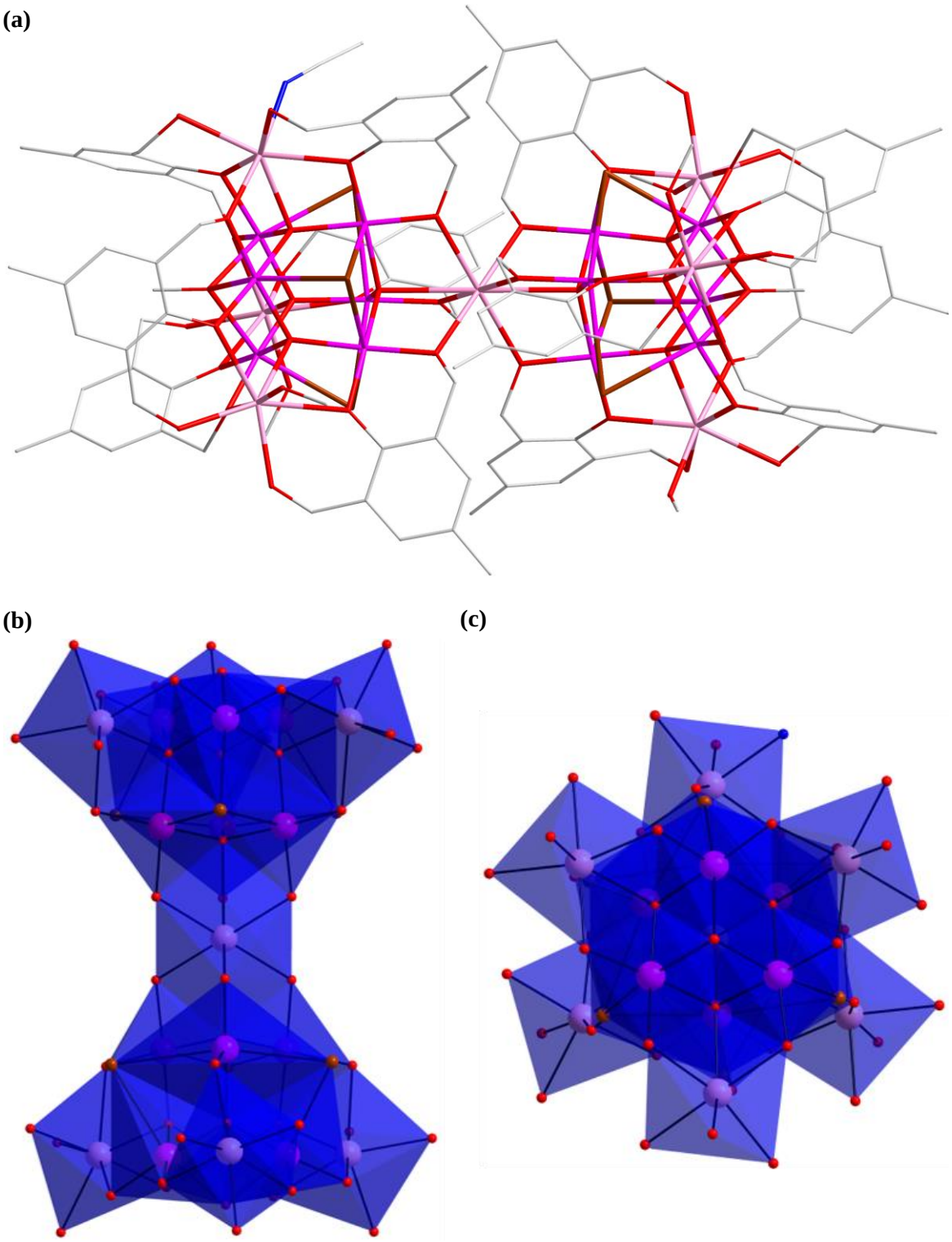

Figure 3.4: Single crystal X-ray structure of **11**. (a) Wire-frame representation of the nonadecanuclear cluster **11** comprising two $\{Mn^{III}_6Mn^{II}_4\}$ supertetrahedra which share a common Mn^{II} vertex and are surrounded by twelve stabilising triply-bridging $(H\mathbf{L2})^{2-}$ ligand derivatives. (b & c) Polyhedral representations of the core of **11**, viewed in the direction of the crystallographic: (b) *c*-axis and (c) *b*-axis. Hydrogen atoms and non-coordinated solvent molecules have been omitted for clarity. Colour scheme: C white, O red, N blue, Br brown, Mn^{II} pale pink, Mn^{III} pink. Mn centres are depicted as blue polyhedra in ball-and-stick representations (b & c).

The Mn-oxo cluster **11** comprises two $\{Mn^{III}_6Mn^{II}_4\}$ units which share a common vertex. The $\{Mn^{III}_6Mn^{II}_4\}$ unit is composed of a central $\{Mn^{III}_6\}$ assembly with octahedral atom arrangement. Four of the eight triangular faces of this octahedron are stabilised by μ_3-Br^- or μ_3-OCH_3^- ligands, whilst the remaining faces are capped by μ_4-O^{2-} oxo ligands that connect the inner $\{Mn^{III}_6\}$ unit to four outer Mn^{II} ions which adopt a tetrahedral $\{Mn^{II}_4\}$ topology. In contrast to the central 6-coordinate Mn^{II} ion that connects the two $\{Mn^{III}_6Mn^{II}_4\}$ supertetrahedra, each of the peripheral 7-coordinate Mn^{II} ions is coordinated by a MeOH or MeCN solvent molecule. The $\{Mn_{19}\}$ cation is stabilised by 12 partially deprotonated organic $(H\mathbf{L2})^{2-}$ ligand derivatives, whereby one methyl alcohol moiety remains protonated whilst the other methyl alcohol and the phenolic hydroxyl functional groups are deprotonated. The constitutional formula and the assignment of the oxidation states of **11** is unambiguous and in agreement with BVS analyses, observed geometrical parameters and charge balance considerations.

Structurally, **11** is similar to several previously reported supertetrahedral clusters comprising $\{Mn_{19}\}$ cores.[30,59,62,63,64] However, **11** differs from these clusters in terms of its μ_3-face-capping and terminal ligands. A complex which closely resembles **11** is the species $[Mn^{III}_{12}Mn^{II}_7(\mu_4\text{-}O)_8(\mu_3\text{-}OCH_3)_2(\mu_3\text{-}Br)_6(H\mathbf{L2})_{12}(MeOH)_6]Br_2$ which was very recently used by Mameri *et al*. to catalytically oxidise benzyl alcohol.[31] Both of these compounds comprise essentially identical core structures, however, **11** features five MeOH and one MeCN terminal ligands whilst the terminal ligands of the literature-known $\{Mn_{19}\}$ aggregate are exclusively methanolic.

Closer inspection of the supertetrahedral $\{Mn^{III}_6Mn^{II}_4\}$ unit (Fig. 3.5), which constitutes half of the cluster core of **11** reveals several key features which are likely to contribute towards its high H_2O oxidation activity. For example, the presence of three outer Mn^{II} centres which are coordinated by terminal labile MeOH or MeCN molecules (circled in orange in Fig. 3.5) allow direct coordination of several H_2O substrate moieties to a redox-active polynuclear cluster core. Furthermore, the exchange of these labile solvent molecules for H_2O can form up to six $\{Mn\text{-}O\text{-}Mn\text{-}OH_2\}$ motifs in **11**. This is significant as has been proposed that the $\{Mn\text{-}O\text{-}Mn\text{-}OH_2\}$ unit plays a critical role in OER catalysis by the $\{Mn_4CaO_5\}$ OEC and several synthetic Mn-based bioinspired WOCs.[25,56,65] These motifs could function as active centres for OER catalysis in **11** by facilitating O_2 formation *via* a coupling reaction between a $Mn^{IV} - O^{\cdot}$ and a μ-oxo species according to an I2M pathway.[66] One of the locations on the supertetrahedral $\{Mn^{III}_6Mn^{II}_4\}$

unit where a {Mn-O-Mn-OH_2} motif may arise following solvent exchange is highlighted in blue in Fig. 3.5, and represents one probable active site for H_2O oxidation catalysis by **11**.

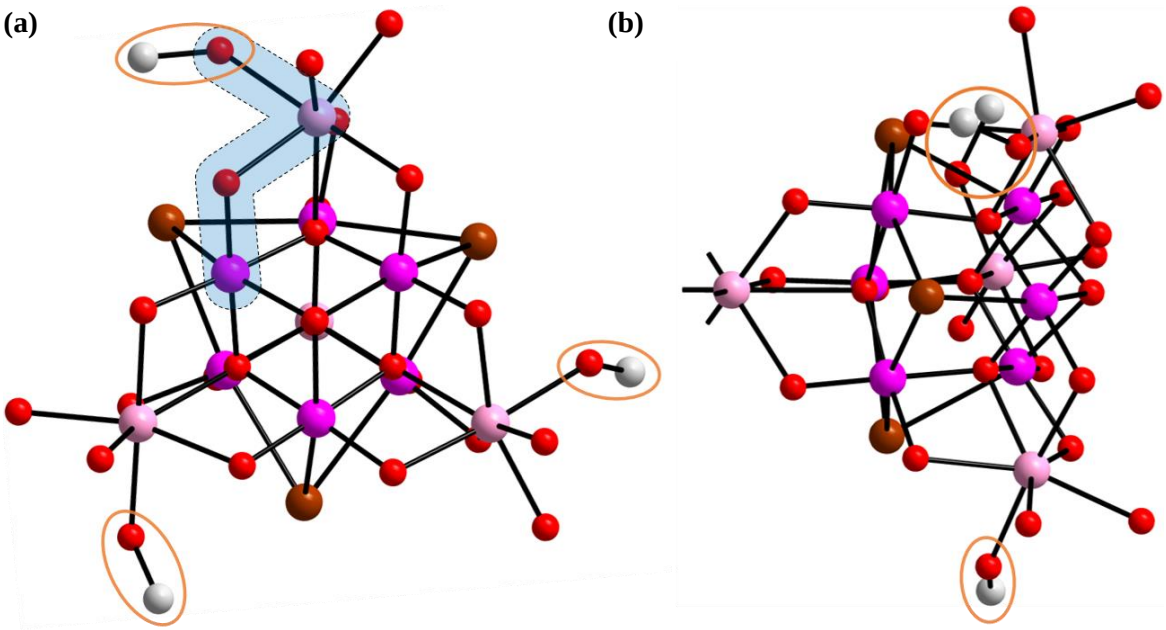

Figure 3.5: Ball-and-stick representation of the {$Mn^{III}_6Mn^{II}_4$} supertetrahedral unit of **11** viewed in the direction of the crystallographic (a) *b*-axis and (b) *a*-axis. Organic ligand derivatives and constitutional solvent molecules have been omitted for clarity. Labile terminal solvent molecules which bind to Mn^{II} centres are circled in orange, and a representative {Mn-O-Mn-O} moiety is highlighted in blue. Colour scheme: C white, O red, Br brown, Mn^{II} pale pink, Mn^{III} pink.

It has been demonstrated that non-innocent ligands coordinated to redox-active metal centres can constructively modulate the catalytic activity of a complex by storing redox equivalents during H_2O oxidation.[67] In particular, aromatic ligands bearing electron donating substituents have been shown to augment the OER activity of a WOC.[37] As the redox-active ligand derivative (H**L2**)$^{2-}$ which stabilises the core of **11** features these attributes, it is likely that these moieties contribute to the cluster's catalytic activity. Moreover, a number of metal-free organic catalysts have recently been explored as H_2O oxidation catalysts.[68,69] Among these, aromatic molecules bearing oxygen-containing functional groups such as C = O and C – OH have demonstrated good activity, although the mechanism of OER catalysis by these structures are not well understood.[70] It is therefore likely that the ligand derivative (H**L2**)$^{2-}$ synergistically enhances the O_2 evolution activity of **11**, either by storing redox equivalents thus preventing the formation of high energy states or by acting as direct catalysts for H_2O oxidation.

Several similarities can be drawn between **11** and the OEC of PS II (highlighted in Fig. 3.6). In the natural H_2O oxidation catalyst, a redox-active tyrosine (Y_z) residue is closely associated (<5 Å) with the $\{Mn_4CaO_5\}$ cluster has a critical function in O_2 formation.[71] This amino acid transfers electrons garnered from H_2O oxidation by the $\{Mn_4CaO_5\}$ cluster to the chlorophyll special pair ($P_{680}^{\bullet+}$), thus regenerating the ground state of the primary electron donor of PS II through rapid electron injection.[72] It is interesting to note that the 4-methylene phenol residue of Y_z closely resembles the $(H\mathbf{L2})^{2-}$ ligand derivatives which stabilise the Mn-oxo core of **11** (Fig. 3.6a). Therefore, the oxidizable *p*-cresol ligand $(H\mathbf{L2})^{2-}$ of **11** may functionally mimic Y_z in the OEC by tuning the conductivity of the $\{Mn_{19}\}$ cluster.[73]

In addition, the core topology of **11** bears resemblance to the $\{Mn_4CaO_5\}$ cluster which oxidises H_2O in Nature. Each supertetrahedral $\{Mn^{III}_6Mn^{II}_4\}$ unit of **11** comprises a pseudocubane motif (highlighted in Fig. 3.6b). These cubane-type arrangements are fused by a central Mn^{II} centre and, analogously to the OEC, feature partially-solvated 'dangling' Mn^{II} ions which could serve as catalytically active sites for H_2O oxidation by **11**. For comparison, the crystal structure of the $\{Mn_4CaO_5\}$ cluster of the OEC is shown in Fig. 3.6c.

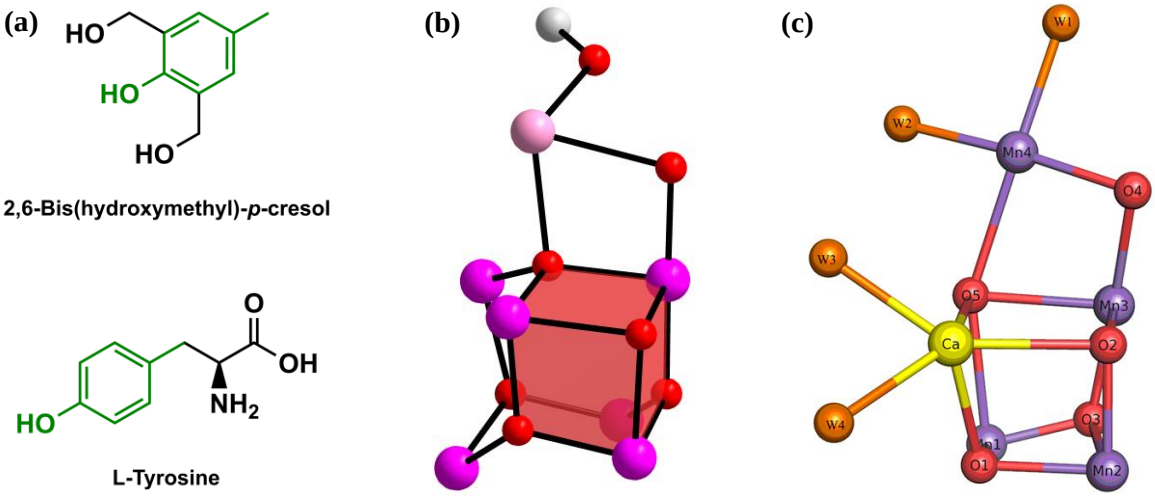

Figure 3.6: (a) Comparison of the structures of the redox-active *p*-cresol ligand $H_3\mathbf{L2}$ which stabilises the cluster core of **11**, and the Y_z amino acid which oxidises the $\{Mn_4CaO_5\}$ cluster of the OEC in PS II. Structural similarities are highlighted green. (b) Ball-and-stick representation highlighting the cubane-type arrangement within the supertetrahedral $\{Mn^{III}_6Mn^{II}_4\}$ unit of **11**, viewed in the direction of the crystallographic *b*-axis. This is compared with (c) the crystal structure of the OEC, reproduced from Ref. [74]. Colour scheme: C white, O red, Mn^{II} pale pink, Mn^{III} pink, Ca yellow.

The packing of **11** in the crystal structure is displayed in Fig. 3.7. In the solid state, small intercluster channels form which extend in the direction of the crystallographic *a*-axis. These channels are occupied by constitutional MeOH and MeCN solvent molecules.

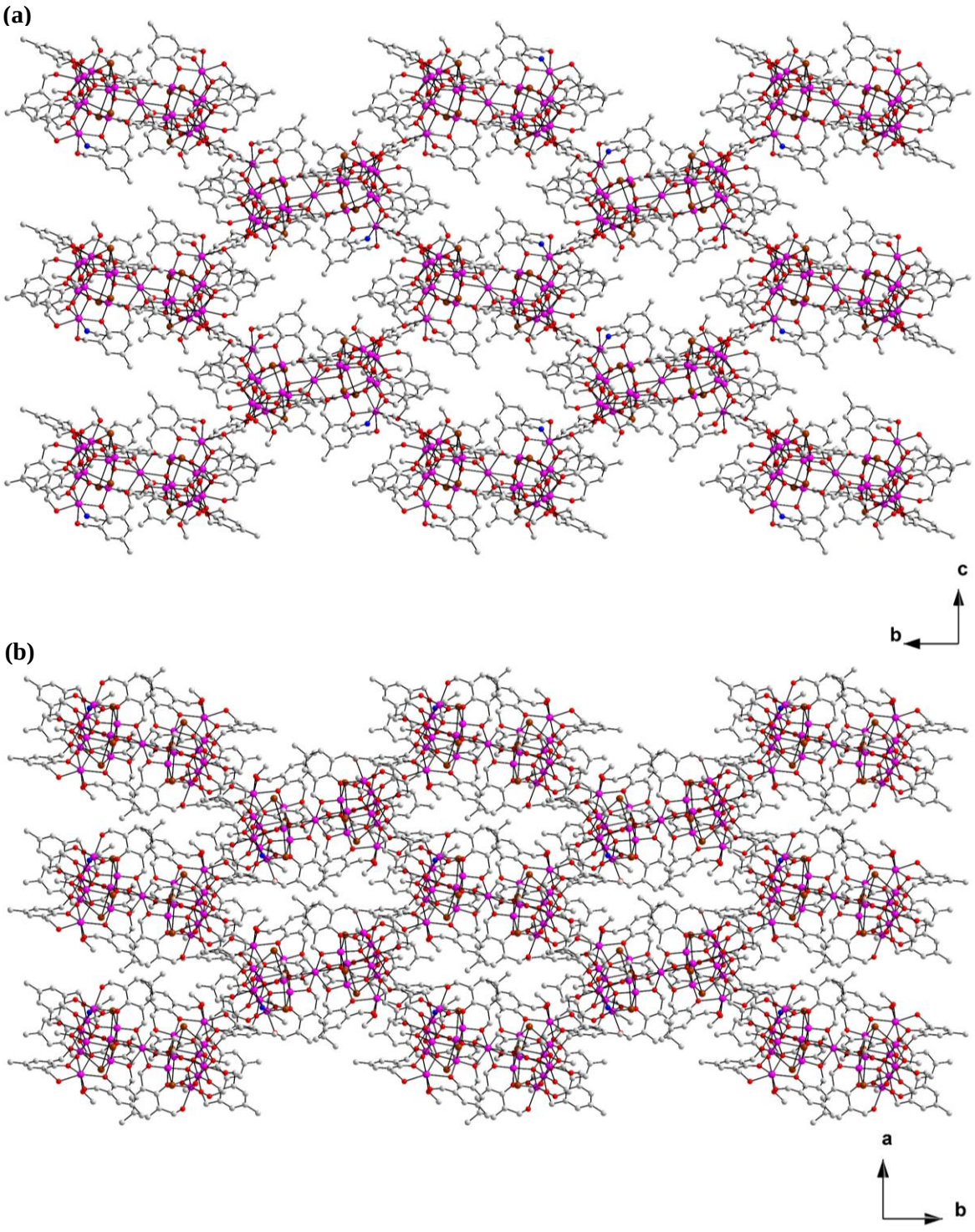

Figure 3.7: Ball-and-stick representation of the packing arrangement of **11** in the crystal structure, viewed in the direction of the crystallographic (a) *a*-axis and (b) *c*-axis. Crystallisation solvent molecules, Br^- counterions and hydrogen atoms have been omitted for clarity. Colour scheme: C white, O red, N blue, Cl green, Br brown, Mn^{II} pale pink, Mn^{III} pink.

3.3.3 Physicochemical Characterisation of 11

Infrared Spectroscopy

The Mn-oxo cluster **11** was characterised using infrared (IR) spectroscopy. The resulting spectrum is presented in Fig. 3.8 and reveals a number of characteristic signals. Firstly, a very broad band above 3000 cm^{-1} can be attributed to O – H stretching vibrations of the cresol ligand derivative $(H\mathbf{L2})^{2-}$ and constitutional solvent molecules which participate in hydrogen bonds. Several signals centred around 3000 cm^{-1} can be assigned to aromatic C – H stretching vibrations of the ligand derivative $(H\mathbf{L2})^{2-}$. Two bands at 1609 and 1468 cm^{-1} can be attributed to C – C stretching vibrations within the aromatic component of $(H\mathbf{L2})^{2-}$. A strong signal centred around 1250 cm^{-1} may be attributed to C – O stretching vibrations of the alcohol or phenol functionalities of $(H\mathbf{L2})^{2-}$. Several bands in the region 750 – 900 cm^{-1} could arise due to out-of-plane C – H bending vibrations from the aromatic ligands. Finally, signals between 470 – 640 cm^{-1} may arise due to Mn – O stretching and bending vibrations.[75]

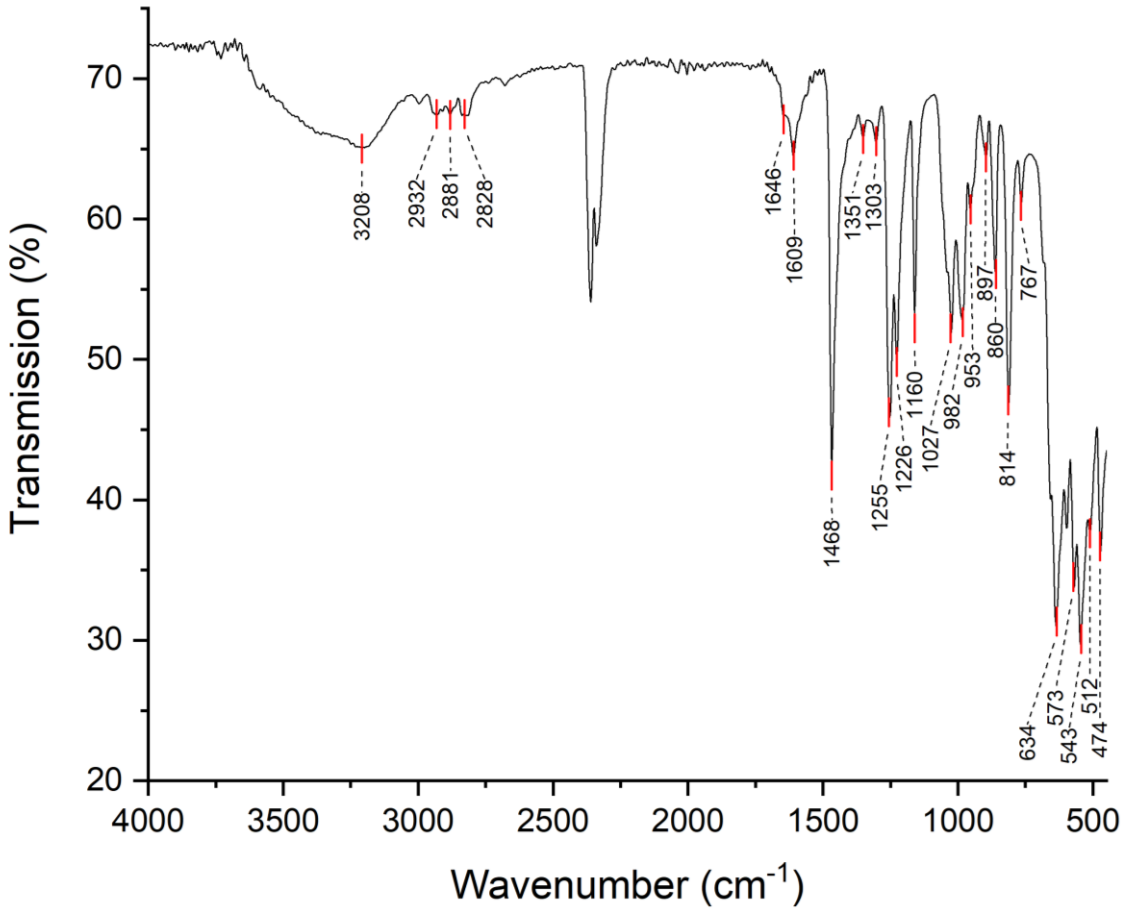

Figure 3.8: FT-IR spectrum of **11**.

Thermogravimetric Analysis

The thermal stability of **11** was assessed using thermogravimetric analysis (TGA) by heating a crystalline sample of **11** between 30 – 800 °C under a constant stream of N_2. The resulting TGA trace (Fig. 3.9) reveals that the decomposition of **11** occurs in several stages. The first stage, which occurs as the sample is heated from 30 to 100 °C can be associated with the loss of the constitutional solvent molecules of **11**. The second decomposition stage occurs as the sample is heated from 100 to 280 °C and can be associated with loss of the coordinated solvent molecules of **11**. Two final decomposition steps are observed between 280 to 470 °C and from 470 °C onwards, which can be attributed to decomposition of the *p*-cresol ligands of **11** and the formation of metal oxides, respectively.

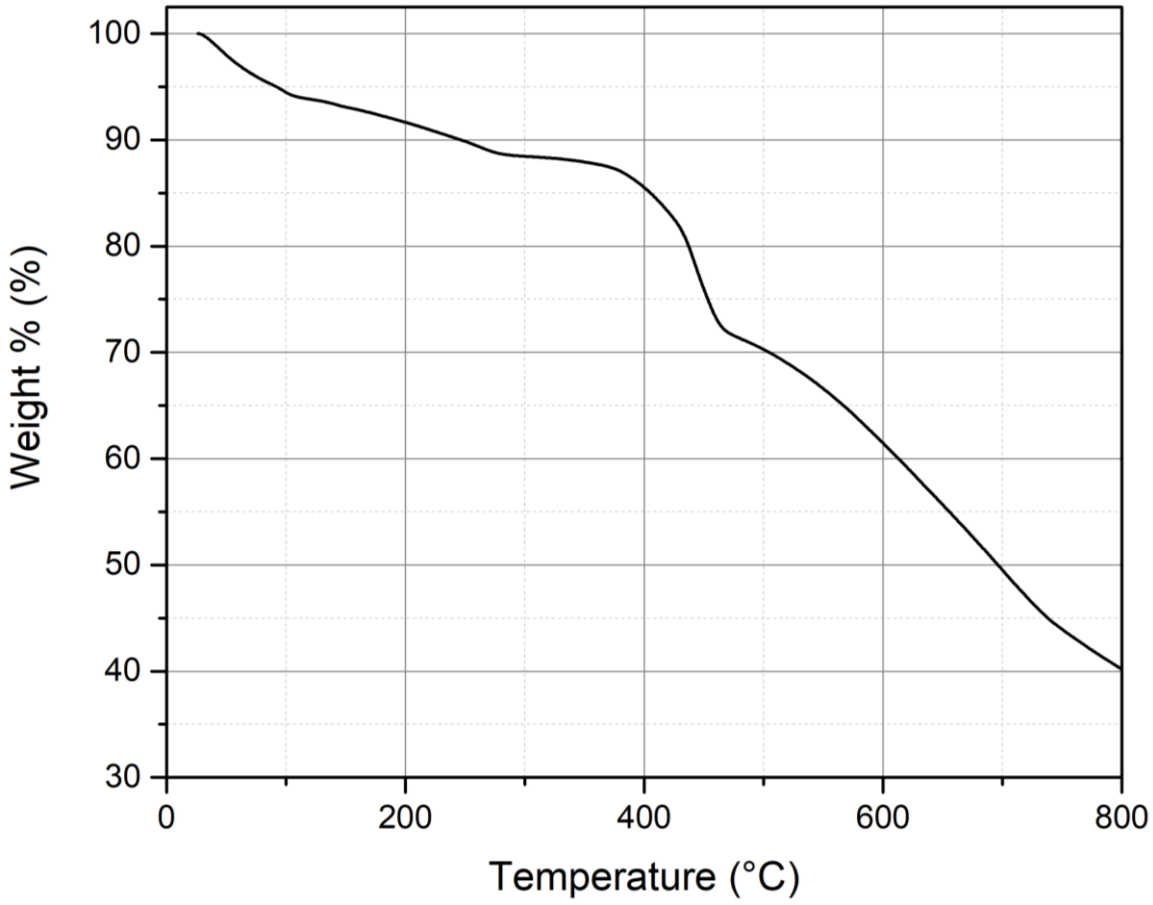

Figure 3.9: TGA trace for **11**.

Powder X-Ray Diffraction Analysis

Powder X-ray diffraction (PXRD) analysis was employed to determine the phase-purity of **11**. A finely ground sample of **11** was sealed in a glass capillary tube under solvent, before mounting the capillary on a goniometer head and recording the PXRD pattern. The measured PXRD pattern (black) is compared with a simulated powder pattern which was calculated from the single crystal X-ray diffraction data of **11** (red) in Fig. 3.10. The experimental and simulated spectra agree reasonably well, indicating bulk purity of the sample. However, the fine structure is not completely resolved in the experimental spectrum which is attributed to preferred orientation effects in the powdered sample and to the use of single crystals for data collection. To guarantee phase-purity of the material used in catalytic experiments, large single crystals of **11** were manually selected, washed with distilled H_2O before grinding into a powder prior to their use.

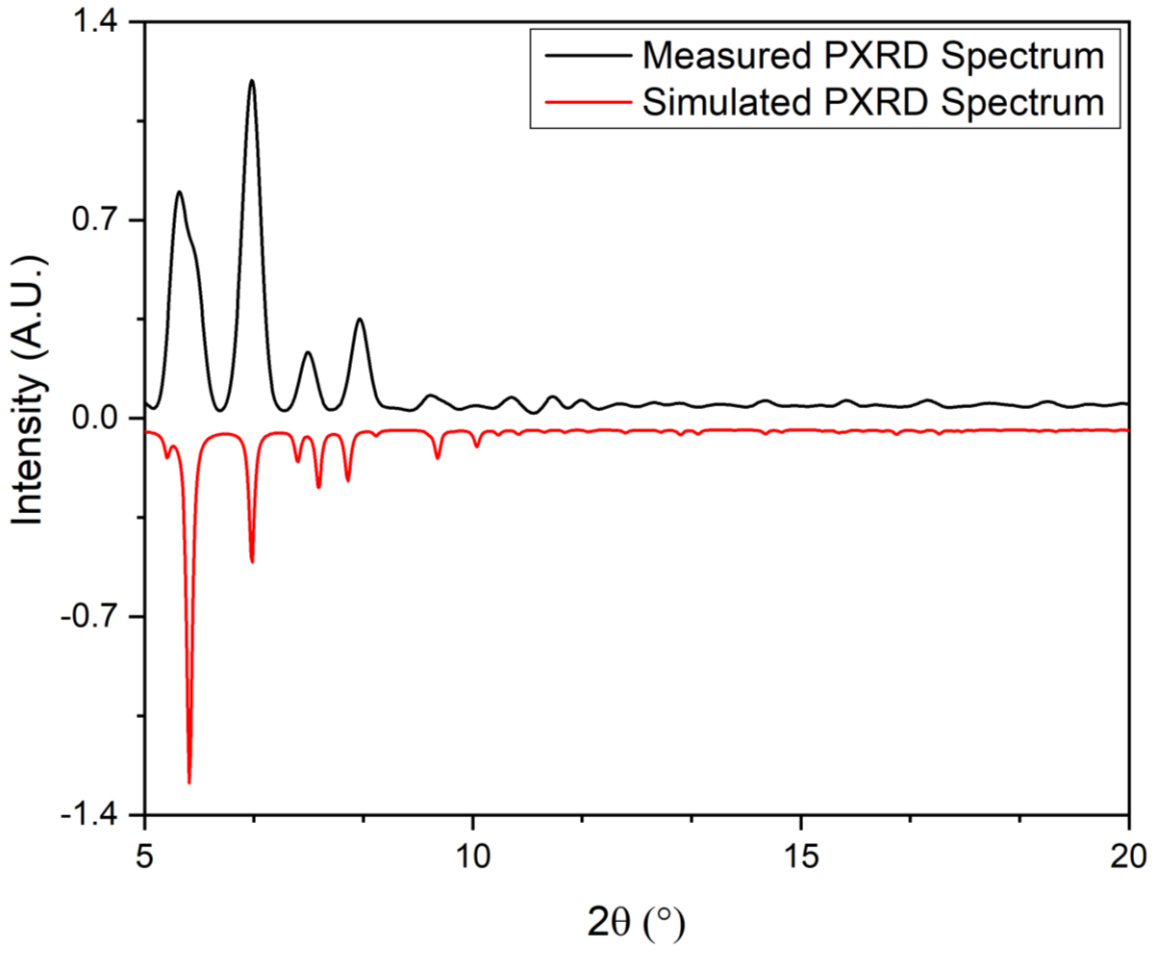

Figure 3.10: Powder X-ray diffraction analysis comparing the measured spectrum of **11** (black) with the simulated pattern (red) calculated from the single crystal X-ray diffraction data of **11**.

Dynamic Light Scattering

The hydrophobic $(H\mathbf{L2})^{2-}$ ligand derivatives of **11** provide a dielectric environment, preventing dissolution of the Mn-oxo cluster in aqueous solutions at ambient temperatures. This is advantageous for H_2O oxidation catalysis as it facilitates a more facile recovery of the catalytic material by filtration. To confirm this, the particle size distribution of **11** in Millipore water was measured using dynamic light scattering (DLS) at room temperature. The resulting DLS data is presented in Fig. 3.11 and reveals that the average particle size within the measured suspension is *ca*. 310 nm. This analysis substantiates that **11** is insoluble under the aqueous conditions applied in H_2O oxidation experiments.

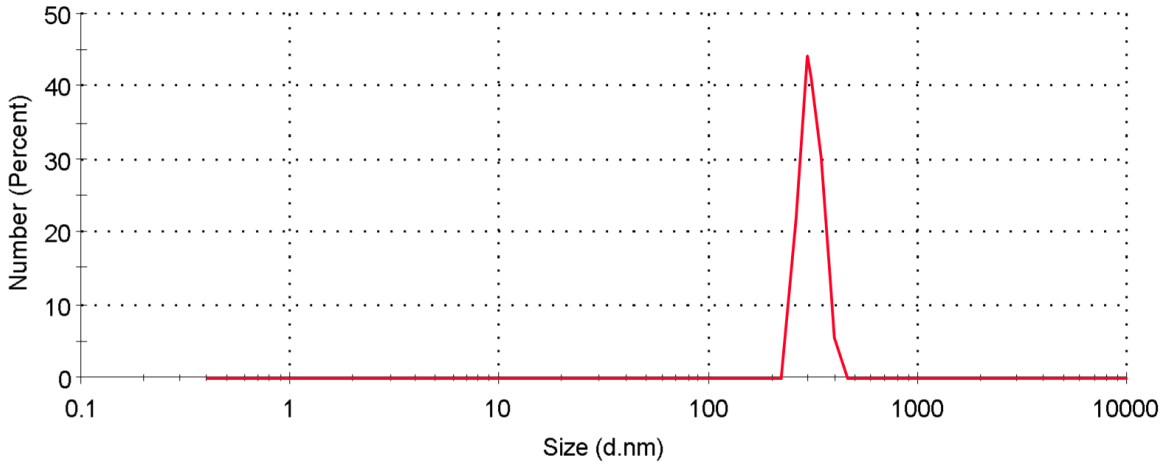

Figure 3.11: Number-weighted dynamic light scattering (DLS) measurement of a suspension of **11** (1 mg) in Millipore water (2 mL) which indicated that the mean particle diameter is 310 nm.

Mass Spectrometry

Positive-mode MALDI-TOF mass spectrometry was used to determine the hydrolytic stability of **11** under the aqueous conditions commonly employed in OER catalysis. To this end, **11** was suspended in an aqueous phosphate-buffered solution before the cluster was dissolved by adding *N*,*N*-dimethylformamide (DMF) to the suspension. The mass spectrum of the resulting mixture is presented in Fig 3.12. The detection of signals at *m/z* = 1874.075, 1897.498 and 1921.049 a.m.u. indicates that the supertetrahedral core of **11** retains its structural integrity in solution, whereby various numbers of coordinating solvents interact with the molecular species. The proposed assignments for each of these signals are given in Table 3.2.

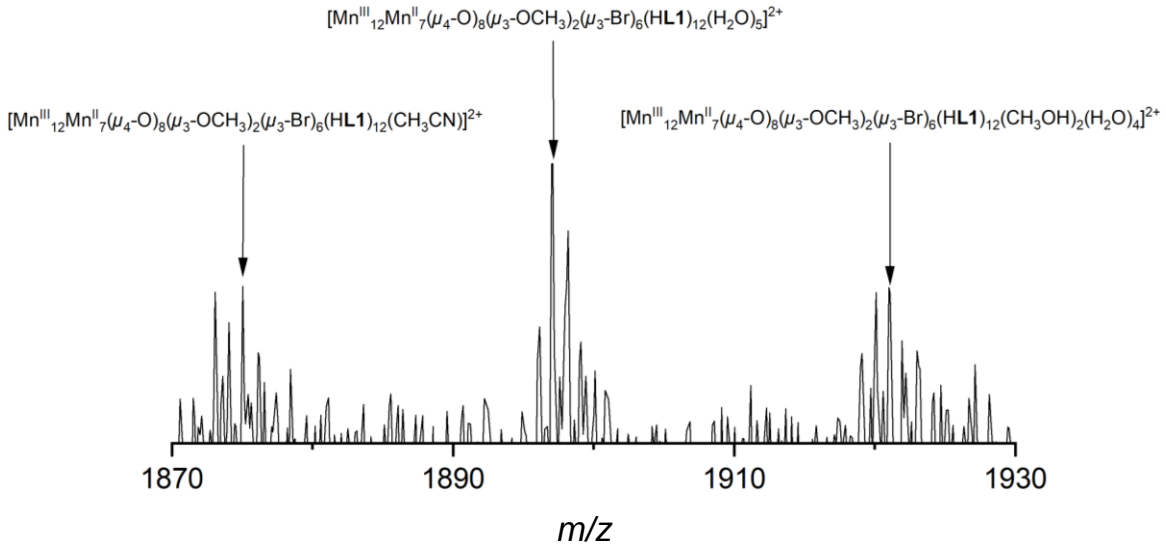

Figure 3.12: Positive-mode MALDI-TOF mass spectrum of **11** in a mixture of aqueous phosphate buffer and DMF.

Table 3.2: Proposed assignments of observed signals in MALDI-TOF MS analysis.

Species	*m/z* (Calcd.)	m/z (Found)
$[Mn^{III}_{12}Mn^{II}_{7}(\mu_4\text{-}O)_8(\mu_3\text{-}OCH_3)_2(\mu_3\text{-}Br)_6(H\mathbf{L2})_{12}(CH_3CN)]^{2+}$	1874.054	1874.075
$[Mn^{III}_{12}Mn^{II}_{7}(\mu_4\text{-}O)_8(\mu_3\text{-}OCH_3)_2(\mu_3\text{-}Br)_6(H\mathbf{L2})_{12}(H_2O)_5]^{2+}$	1897.568	1897.509
$[Mn^{III}_{12}Mn^{II}_{7}(\mu_4\text{-}O)_8(\mu_3\text{-}OCH_3)_2(\mu_3\text{-}Br)_6(H\mathbf{L2})_{12}(CH_3OH)_2(H_2O)_4]^{2+}$	1921.086	1921.049

3.4 Photocatalytic H_2O Oxidation Properties of 11

The highly encouraging O_2 evolution behaviour of **11** signified in a preliminary photocatalytic test described in Section 3.2, and the Mn-oxo cluster's various structural attributes (discussed in Section 3.3) which are indicative of its suitability as a WOC prompted further investigation into this compound's catalytic properties. To this end, the heterogenous H_2O oxidation activity of **11** was assessed under photocatalytic conditions using a range of catalyst loadings. Following this, recycling tests were conducted to establish whether the catalyst **11** maintains O_2 evolution activity for extended periods of time. In an attempt to replicate the mild aqueous operating conditions of PS II, OER experiments were conducted in aqueous phosphate buffer at pH 7.0.

Catalyst Loading Experiments

The light-induced OER activity of **11** at a range of catalyst loadings (1.25 nmol – 10.00 nmol) was established in a series of heterogeneous photochemical tests. The WOC was evaluated in the presence of a three-component photocatalytic system using the same method applied to determine catalytic H_2O oxidation activity described in Section 3.2.[76] The kinetics of O_2 evolution using various loadings of **11** are displayed in Fig. 3.13. Upon irradiation using an LED lamp (λ = 470 nm, 10 mW cm^{-2}), nanomolar loadings of **11** gave rise to a high activity whereby the dissolved O_2 concentration continuously rose for *ca*. 120 seconds before reaching a plateau. Net O_2 production increased with catalyst loading following pseudo first-order kinetics: Maximum O_2 liberation of 157 nmol was attained using 10.00 nmol **11**, with a corresponding TON = 15.7. This represents an activity which surpasses many cutting edge catalysts based on non-noble metals.[24,25]

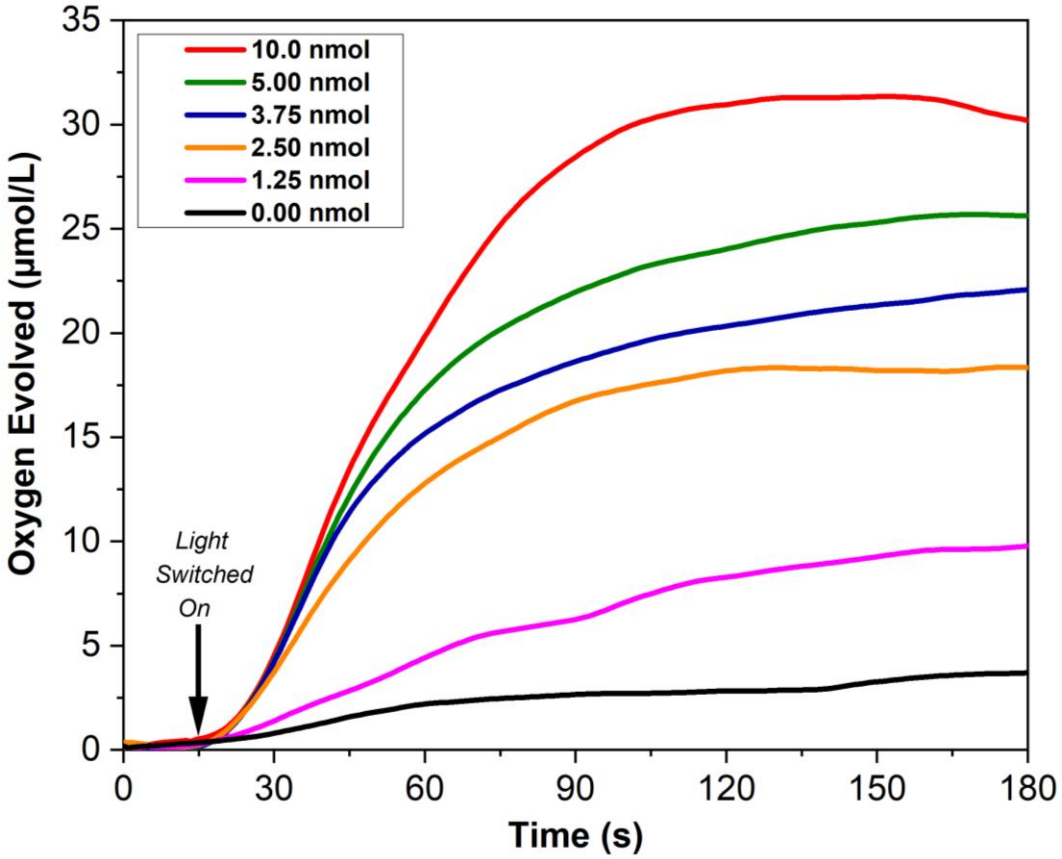

Figure 3.13: O_2 evolution profiles (recorded using a Clark O_2 sensor) of various loadings of **11** upon irradiation (LED, λ = 470, 10 mW cm^{-2}) in the presence of a SEA and a PS. Sample dispersed in aqueous phosphate buffer (5 mL, 0.01 M, initial pH = 7.0) containing $Na_2S_2O_8$ (10 mM) and $[Ru(bpy)_2(deeb)](PF_6)_2$ (2 mg, 2.33 µmol). The reaction mixture was stirred at a constant rate of 500 rpm and maintained at 25 °C by immersing the reaction vessel in a water bath.

Reducing the loading of **11** below 10.00 nmol coincided with improved turnover characteristics. For example, a very high TON = 40 was achieved using a catalyst loading of 1.25 nmol. This inverse relationship between catalyst loading and activity is frequently observed in H_2O oxidation catalysis studies.[77] The highest TOF = 0.71 s^{-1} was observed at a catalyst loading of 2.50 nmol. This TOF is several times higher than the TOFs of any previously reported MnO_x species, and higher than any other heterogeneously operating molecular Mn coordination cluster at neutral pH conditions;[2,78,79] hence these data corroborate the results of the preliminary screening studies and implicate **11** as a genuine OER catalyst. The TONs, TOFs and O_2 yields of **11** at various catalyst loadings are detailed in Table 3.3.

Table 3.3: Comparison of the TON, TOF and % oxygen conversion for light-induced OER catalysis experiments. Data were obtained at various loadings of 11.

Catalyst Loading (nmol)	O_2 Evolved (nmol)	TON	TOF (s^{-1})	O_2 Yield (%)
1.25	50.0	40.0	0.48	0.20
2.50	91.3	36.5	0.72	0.37
3.75	113	30.0	0.64	0.45
5.00	129	25.8	0.53	0.51
10.0	157	15.7	0.33	0.63

Despite the very high activity displayed by **11**, it is worth noting that the determined TONs and TOFs do not fully represent this cluster's activity. Considering that the complex is insoluble in aqueous systems, only a small proportion of its Mn sites are readily available to promote H_2O oxidation catalysis. Therefore, the TONs and TOFs presented in Table 3.3 are underestimated, and higher values would be expected using soluble derivatives of **11** in molecular solutions in which all of the catalytically active metallic centres are readily accessible by H_2O molecules.

The photocatalytic experiments described above reveal that **11** exhibits the highest OER activity under neutral pH conditions of any known molecular bio-inspired Mn system.[2,57,65] The exceptional turnover characteristics of **11** most likely derive from its structural attributes, in which six partially-solvated, 'dangling' Mn^{II} ions attached to cubane-type assemblies allow H_2O substrate binding, and in which closely-located μ-oxo-bridged Mn centres provide direct electronic pathways to distribute oxidation equivalents. Further, the electronic features of the *p*-cresol $(H\mathbf{L2})^{2-}$ ligand derivatives are expected to aid the abstraction of electrons from H_2O similarly to Y_z in the OEC, thus leading to enhanced catalytic activity.[80] Importantly, the OER characteristics of **11** are displayed under neutral pH conditions, which is advantageous for the development of photoanodes which operate using mild, environmentally-friendly electrolytes within artificial photosynthetic cells.[81]

Recycling Experiments

To ascertain if **11** maintains catalytic activity following light-driven H_2O oxidation, a series of recycling experiments were carried out according to a known literature procedure.[82] Following the cessation of O_2 evolution by **11** under photocatalytic conditions, fresh quantities of PS and SEA were added to the reaction vessel and the photocatalytic experiment was repeated until no significant O_2 evolution was observed. The kinetics of O_2 evolution from four catalytic tests using the same sample of **11** as WOC are plotted in Fig. 3.14. This experiment reveals that **11** is recyclable, evolving O_2 over three sequential catalytic tests. However, with each consecutive run, the quantity of O_2 evolved decreased by *ca*. 20% of the amount of O_2 evolved in the first test. Following the fourth run, the quantity of O_2 evolved using **11** was comparable that evolved by a SEA and PS alone, indicating that after this point the catalyst had fully decomposed into OER inactive species. The calculated TON achieved by **11** over three consecutive runs was 86, which is several times higher than the TON of any previously reported Mn-oxo cluster.[24,25,43]

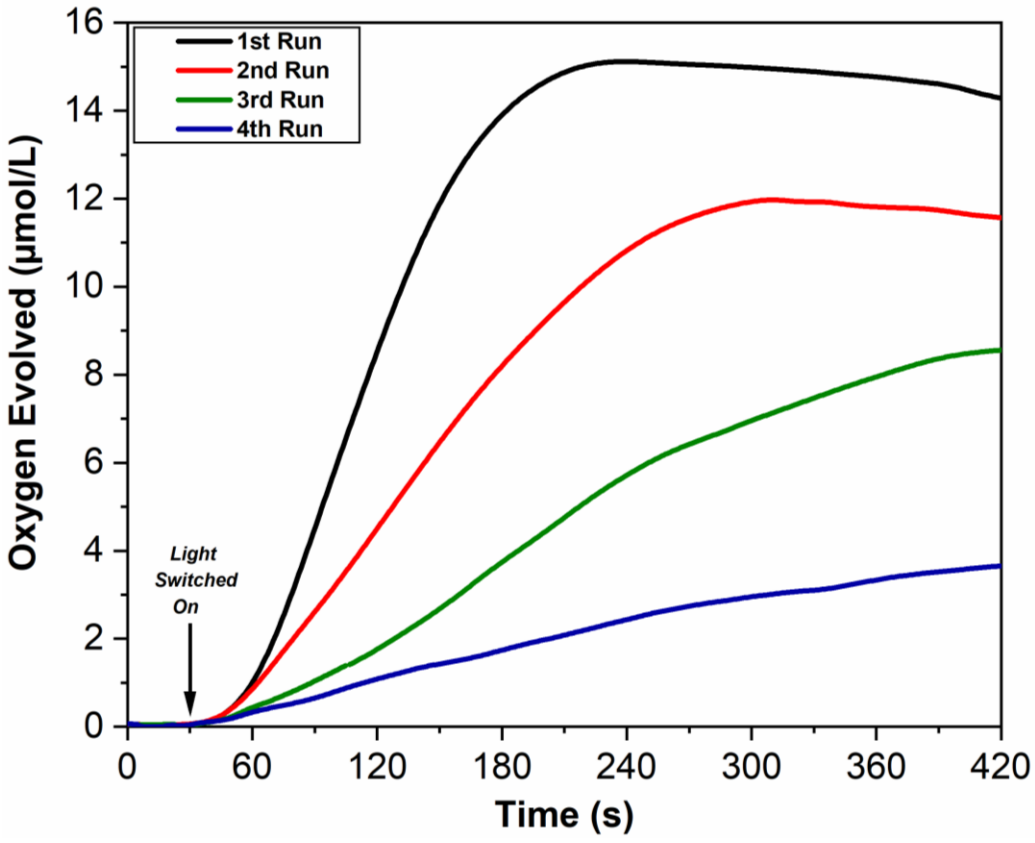

Figure 3.14: Kinetics of light-driven dioxygen formation during four recycling tests using **11**. Prior to each catalytic run, 2 mg $[Ru(bpy)_2(deeb)](PF_6)_2$, and 11.9 mg $Na_2S_2O_8$ were added to the reaction vial. Conditions: 2.5 nmol WOC loading in 5 mL 0.01 M phosphate buffer (starting pH = 7), LED lamp (λ = 470, 10 mW cm^{-2}), constant temperature of 25 °C and stirring rate of 500 rpm maintained throughout each catalytic run.

Additional Light-Driven H_2O Oxidation Experiments

To confirm that the O_2 evolved using **11** in photocatalytic experiments stems from catalytic H_2O oxidation activity of the cluster, equivalent quantities of **11** and its constituent components $MnBr_2{\cdot}4H_2O$ and H_3**L2** were measured under identical conditions. The O_2 evolution profiles from these tests are plotted in Fig. 3.15 and reveal that the O_2 yield using **11** was *ca*. threefold that of nineteen molar equivalents $MnBr_2{\cdot}4H_2O$, and over seven times the O_2 yield of twelve molar equivalents of H_3**L2**. This experiment demonstrates that the activity attributed to **11** does not stem from either *in-situ* generated MnO_x under the working conditions or from the ligand H_3**L2**. Furthermore, the result supports the assertion the excellent catalytic performance observed using **11** arises due to a synergistic effect between its polynuclear Mn-oxo core which contains pseudocubane motifs and the redox-active *p*-cresol $(H\mathbf{L2})^{2-}$ ligand derivatives which stabilise the cluster.

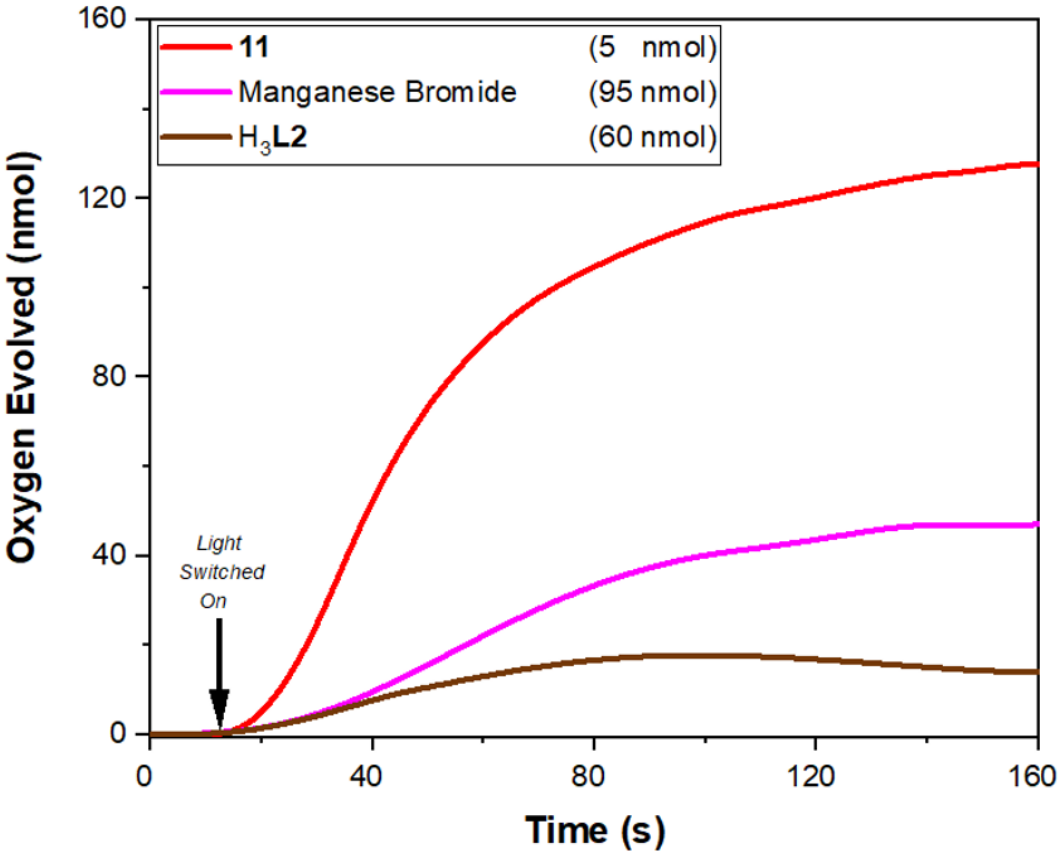

Figure 3.15: Comparison of the O_2 evolution response of equivalent quantities of **11** (red) and its constituent components: $MnBr_2{\cdot}4H_2O$ (pink) and H_3**L2** (brown). This experiment indicates that the observed H_2O oxidation catalytic activity must arise from **11**, as high excesses of $MnBr_2{\cdot}4H_2O$ or H_3**L2** are required to evolve comparable amounts of dioxygen.

Photosensitiser Comparison

Two literature-established Ru-based PS's ($[Ru(bpy)_3]Cl_2$ and $[Ru(bpy)_2(deeb)](PF_6)_2$) were employed in light-driven O_2 experiments using **11**.[45,83] In Fig. 3.16, the kinetics of O_2 evolution of **11** under neutral, aqueous phosphate-buffered conditions and in the presence of $Na_2S_2O_8$ SEA and either $[Ru(bpy)_3]Cl_2$ (red) or $[Ru(bpy)_2(deeb)](PF_6)_2$ (black) are displayed. All parameters excluding the nature of the PS were kept constant.

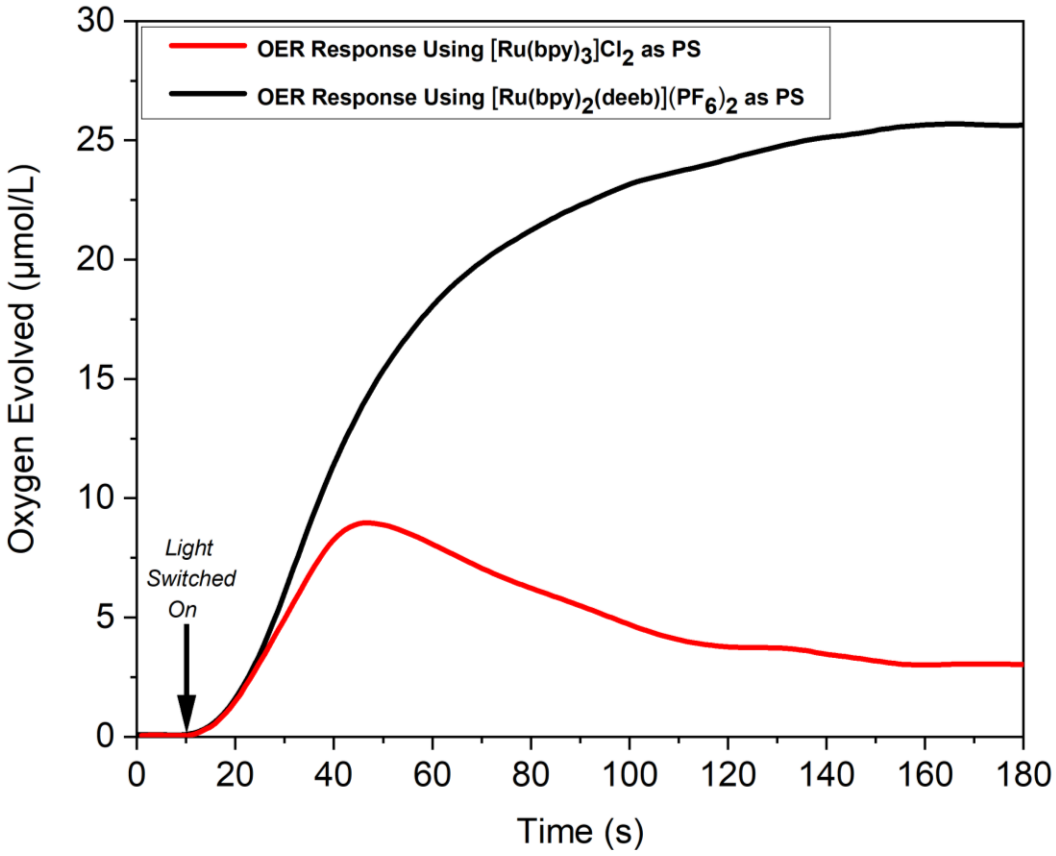

Figure 3.16: Kinetic monitoring (Clark electrode) of the light-driven OER by **11** (5 nmol) in the presence of either $Ru(bpy)_3]Cl_2$ (red) or $[Ru(bpy)_2(deeb)](PF_6)_2$ (black) as PS. Conditions: LED lamp ($\lambda = 470$, 10 mW cm^{-2}), 2.33 µmol PS and $Na_2S_2O_8$ (10 mM) in 5 mL of a 0.01 M phosphate-buffered aqueous solution (initial pH = 7). Constant stirring and temperature of 25 °C maintained by immersion of the reaction vessel in a water bath.

In this experiment under analogous conditions employing the homoleptic PS $[Ru(bpy)_3]Cl_2$ liberated 45 nmol O_2, whereas when using the heteroleptic PS $[Ru(bpy)_2(deeb)](PF_6)_2$ 129 nmol O_2 was evolved. This activity corresponds to TONs of 9 and 26 with $[Ru(bpy)_3]Cl_2$ and $[Ru(bpy)_2(deeb)](PF_6)_2$ as PS's, respectively. This outcome is in-line with expectations and can

be attributed to the contrasting redox potentials of the employed PS's: As the oxidation potential associated with $[Ru(bpy)_2(deeb)]^{2+}$ ($E_{1/2}$ Ru^{III}/Ru^{II} = 1.40 V vs. NHE) is higher than that of $[Ru(bpy)_3]^{2+}$ ($E_{1/2}$ Ru^{III}/Ru^{II} = 1.26 V vs. NHE) the former, stronger PS provides a greater driving force for the endergonic OER.[83] Therefore, it can be concluded that $[Ru(bpy)_2(deeb)](PF_6)_2$ is a more effective PS than $[Ru(bpy)_3]Cl_2$ for H_2O oxidation catalysis using **11**.

3.5 Post-Catalytic Characterisation

Light-induced H_2O oxidation experiments using **11** demonstrate that this compound displays excellent O_2 evolution behaviour under photocatalytic conditions, exhibiting apparent OER turnover characteristics which surpass those of any previously reported Mn-oxo cluster or MnO_x species under neutral pH conditions. However, possible cluster transformations were not ruled out during these activity assessments. To characterize the chemical transformations undergone by **11** under working conditions and to rule out the formation of catalytic metal oxide species, a post-catalytic analysis was performed using Raman spectroscopy.

Raman Spectroscopic Analysis

Raman spectroscopy is well-suited for detecting trace quantities of *in-situ* generated, catalytically active MnO_x compounds, as these species exhibit easily recognisable, characteristic signals in Raman spectra.[84] Therefore, to rule out the formation of OER active MnO_x species under the operating conditions of photocatalytic experiments using the Mn-oxo cluster **11**, Raman spectra were obtained from the dried residues of three-component photocatalytic mixtures both before and after irradiation. These spectra, in addition to the Raman spectra of the WOC **11**, $[Ru(bpy)_2(deeb)](PF_6)_2$, $Na_2S_2O_8$ and $NaSO_4$ are compared in Fig. 3.17.

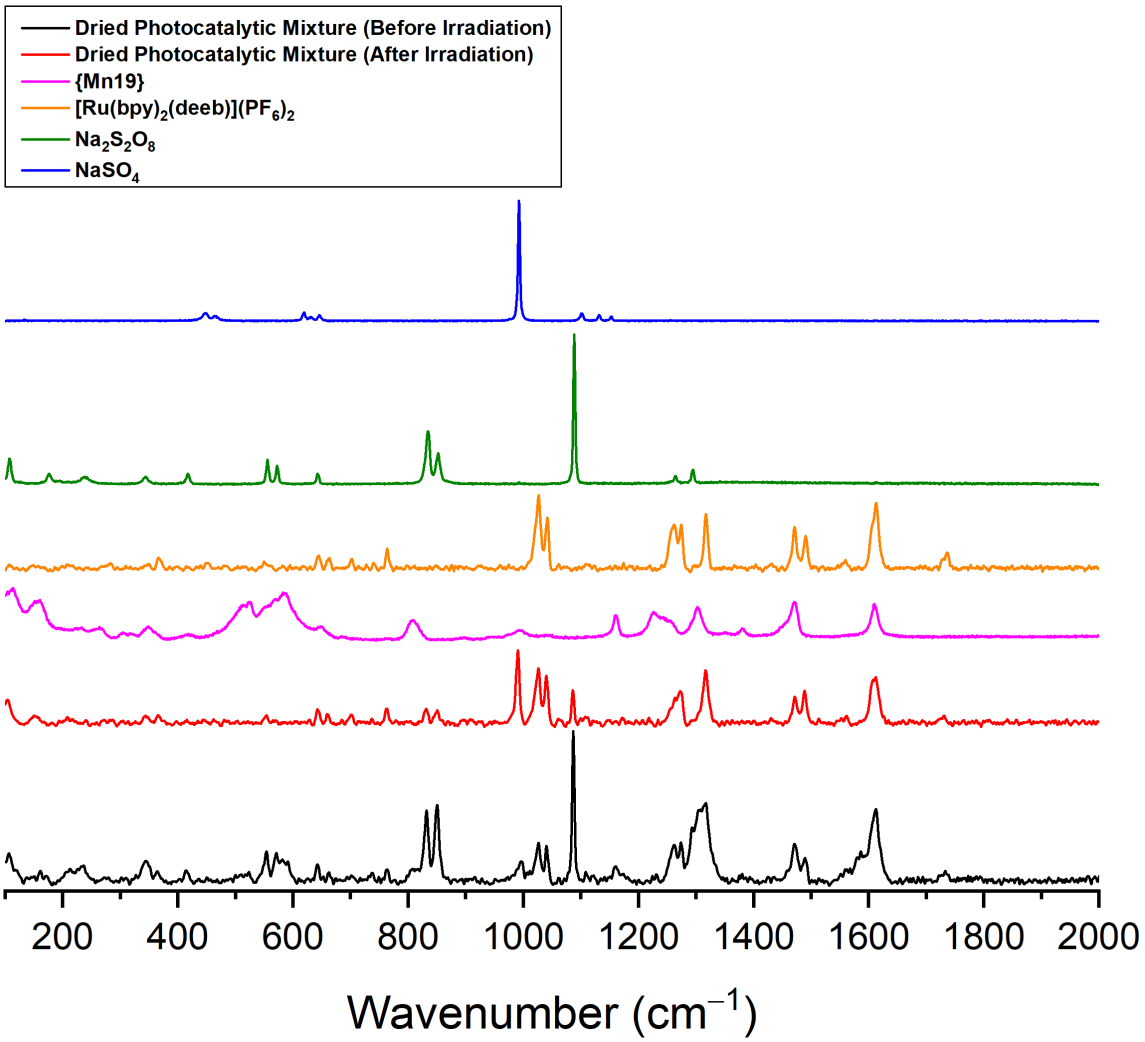

Figure 3.17: Raman spectra of the dried residues of the three-component photocatalytic mixture before (black) and after (red) irradiation. Also plotted for comparison are the Raman spectra of **11** (pink), $[Ru(bpy)_2(deeb)](PF_6)_2$ (orange), $Na_2S_2O_8$ (green) and $NaSO_4$ (blue).

Interpretation of the Raman spectra of pre- and post-catalytic three-component mixtures reveals a few key differences. Importantly, however, no signals in the region 200 – 750 cm^{-1} are present in the Raman spectrum of the post-irradiated catalytic mixture which cannot be located in the Raman spectrum of the pre-irradiated catalytic mixture. As MnO_x species are typically highly Raman active in this region, this observation rules out the *in-situ* formation of these compounds contributing towards the observed OER activity in light-driven O_2 evolution experiments using the cluster **11**.[84,85]

Several signals in the Raman spectrum of the pre-catalytic three-component mixture can be assigned to **11**: Weak bands at 160, 515, 575, 810, 1160, 1230 and 1380 cm^{-1}, and a shoulder at 810 cm^{-1} are attributed to the Mn-oxo cluster. However, in the Raman spectrum of the post-catalytic three-component mixture signals at 515, 575, 810 and 1380 cm^{-1} are either reduced in intensity relative to the intensity of the corresponding bands in the spectrum of the pre-catalytic mixture or not present. This supports the results of recycling and electrochemical (see Section 3.6) experiments carried out using **11**, further supporting the proposition that the cluster decomposes into catalytically inactive species during photocatalytic O_2 evolution.

A number of bands in the Raman spectrum of the pre- and post-irradiated catalytic mixture at 345, 365, 550, 645, 665, 700, 770, 1030, 1045, 1265, 1320, 1470, 1490, 1610, and 1740 cm^{-1} can be assigned to the PS $[Ru(bpy)_2(deeb)](PF_6)_2$. Three signals at 830, 850 and 1090 cm^{-1} in the Raman spectra of the pre- and post-irradiated catalytic mixtures are assigned to $Na_2S_2O_8$. These signals reveal significantly lower intensity in the Raman spectrum of the post-irradiated mixture relative to the intensity of the corresponding bands in the Raman spectrum of the pre-irradiated reaction mixture. This disparity is likely to be due to the irreversible decomposition of the SEA during the OER. The only signal which is significantly higher in intensity in the Raman spectrum of the post-irradiated catalytic mixture relative to the corresponding signal in the Raman spectrum of the pre-irradiated reaction mixture is a band at 995 cm^{-1}, which is assigned to SO_4^{2-}, which was generated as a result of SEA decomposition.

3.6 Electrocatalytic H_2O Oxidation Properties of 11

To corroborate the H_2O catalytic oxidation activity of **11** observed under photocatalytic conditions, the O_2 evolution activity of this Mn-oxo cluster was evaluated in electrochemical tests in collaboration with Dr. Joaquin Soriano-López. For this analysis, **11** was blended with commercial carbon paste (CP) at different weight ratios (wt.-%) to produce **11**-modified carbon paste (**11**/CP) electrodes. Linear sweep voltammetry (LSV) experiments were carried out using **11**/CP electrodes with 10, 20, or 30 wt.-% catalyst loading as working electrodes (Fig. 3.18).[86] Analogously to photochemical experiments, the mild aqueous operating conditions of PS II were emulated in electrocatalytic experiments by using aqueous phosphate buffer solutions at pH = 7.2 using KNO_3 (1 M) as electrolyte.

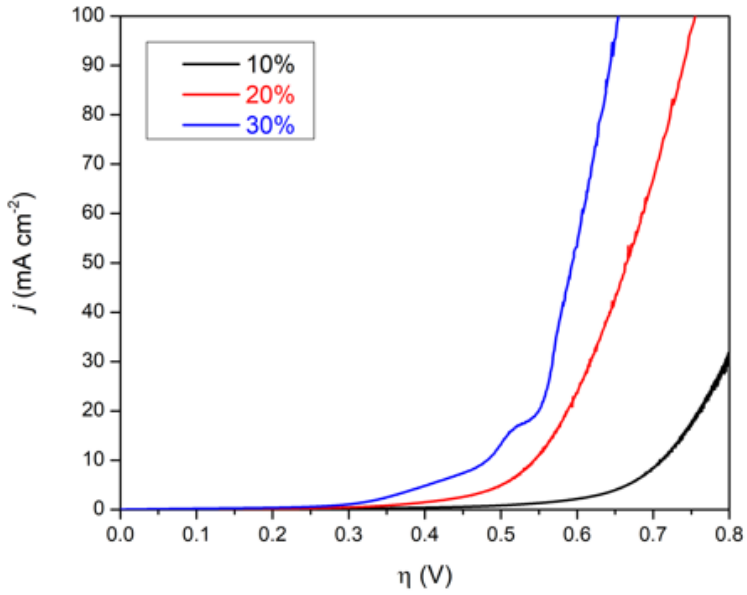

Figure 3.18: Linear sweep voltammetry using **11**/CP electrodes at 10, 20, or 30 wt.-% catalyst loadings.

As in photocatalytic experiments, employing higher loadings of **11** resulted in increased OER catalytic activity: 30 wt.-% **11**/CP electrodes displayed the best performance, promoting very high current densities at low overpotentials, yielding 1 mA cm^{-2} at η = 292 mV and even 100 mA cm^{-2} at η = 654 mV. Further, a remarkably low onset overpotential of just 255 mV was achieved using these electrodes. This is in contrast with a control LSV experiment in which an external potential was applied to a pure CP working electrode and no catalytic response was elicited. The overpotentials required for the onset of catalytic activity (η_{onset}), and to reach

current densities (j) of 1 and 100 mA cm^{-2} using **11**/CP working electrodes are displayed in Table 3.4.

In repeated LSV experiments performed using **11**/CP working electrodes, the cluster's catalytic OER activity was observed to diminish after multiple repetitions. This indicates that **11** decomposes into catalytically inactive species after prolonged use, which is in line with catalyst recycling experiments (see Section 3.4). Moreover, analysis using Raman spectroscopy performed on post-catalytic **11**/CP electrodes was unable to detect *in-situ* generated MnO_x species. This conforms with post-catalytic characterisation experiments performed on photocatalytic mixtures (see Section 3.5) and further supports the supposition that **11** is a genuine OER catalyst

Table 3.4: Comparison of the LSV data obtained using 11/CP working electrodes containing different catalyst loadings.

wt.-% **11**/CP	η_{onset} (mV)	η (mV) @ j = 1 mA cm^{-2}	η (mV) @ j = 100 mA cm^{-2}
10	438	521	–
20	297	367	755
30	255	296	654

The outlined electrochemical experiments exemplify that **11** facilitates electrocatalytic H_2O oxidation at low onset overpotentials and promote high current densities which exceed most of those reported for other OER catalysts at neutral pH values.[87] Furthermore, the diminishing activity of **11** in consecutive LSV experiments using **11**/CP electrodes, the absence of MnO_x species in post-catalytic samples and the high activity characteristics of **11** revealed in this electrocatalytic study substantiate the cluster's unprecedented turnover characteristics observed in photocatalytic experiments.

3.7 Conclusion

In this chapter, a series of catalytic H_2O oxidation screening experiments are described. These tests were carried out on Mn-based compounds with some structural similarities to the OEC. This initial investigation aimed to identify a bioinspired Mn-based material exhibiting light-driven OER activity at pH = 7 to employ in further catalytic studies.

As a result of this precursory assay, nine Mn-oxo materials (**3** – **11**) with previously unknown H_2O oxidation properties revealed OER activity when irradiated (λ = 470 nm) in the presence of a three-component photocatalytic system. The activities manifested by **3** – **11** varied considerably, displaying TONs within the range of 1.25 – 25.8 and TOFs ranging between 0.06 – 0.57 s^{-1}. A correlation was noted between high-nuclearity structures with several substrate-accessible sites and favourable OER activity, as compounds featuring these attributes generally liberated greater quantities of O_2 in these experiments.

Out of all of the materials tested, the Mn-oxo cluster **11** revealed the most exciting turnover characteristics, with an activity surpassing that of **3** – **10** and many Mn-based literature WOCs.[43] **11** is also attractive for practical H_2O oxidation applications as its preparation is facile and involves inexpensive environmentally-friendly starting materials, and because of its insolubility and stability under neutral aqueous conditions. Further, structural characteristics of **11** such as the presence of substrate-accessible sites, non-innocent ligands and cubane motifs were highly encouraging. Due to these propitious properties, **11** was chosen for further catalytic studies. The OER characteristics of **3** – **10** may be investigated in greater detail in future work, however **11** was the only compound considered following preliminary screening experiments.

To facilitate further examination of the catalytic properties of **11**, this Mn-oxo cluster was synthesised and characterised using single crystal X-ray diffraction, FT-IR spectroscopy, PXRD, TGA, MALDI-TOF mass spectrometry and DLS. This analysis revealed that **11** is a new polymorph containing a recently reported cluster core and confirmed the phase-purity and stability of the sample.[31] Following on from this, the catalytic H_2O oxidation properties of **11** were scrutinised in a series of heterogeneous photocatalytic experiments. In this investigation, a high TON = 40 and TOF = 0.72 s^{-1} were achieved using catalyst loadings of 1.25 and 2.50 nmol, respectively. In the presence of $[Ru(bpy)_3]Cl_2$ instead of $[Ru(bpy)_2(deeb)](PF_6)_2$ as PS, **11** was evolved significantly less O_2 under otherwise analogous conditions (45 vs. 129 nmol O_2 evolved). This disparity can be explained by the higher redox potential of the PS $[Ru(bpy)_2(deeb)](PF_6)_2$.

To establish if **11** could be reused, a series of catalytic recycling tests were carried out. Following O_2 evolution by **11**, fresh quantities of PS and SEA were added to the reaction vial and the OER experiment was repeated. This experiment revealed that **11** maintains catalytic activity over a prolonged period of time, however the activity fell significantly each time the reaction mixture was irradiated. After the third test, the quantity of O_2 liberated was comparable to the amount of O_2 evolved in a control experiment without a WOC, indicating that **11** had decomposed into catalytically inactive species. Over three photocatalytic tests, a combined total TON = 86 was achieved using a 2.5 nmol loading of **11**.

To verify that **11** is a genuine WOC, three-component photocatalytic mixtures were dried and characterised before and after irradiation using Raman spectroscopy. Critically, characteristic vibrational bands typical of MnO_x species were undetectable in the Raman spectrum of the catalytic mixture following irradiation. This signifies that **11** is the source of the evolved O_2, and not a precatalyst which forms MnO_x species under the working conditions.[88] Bands which were assigned to **11** in the Raman spectrum of the pre-irradiated photocatalytic mixture were of lower intensity in the Raman spectrum of the irradiated sample, suggesting that **11** decomposes into inactive materials. This observation is consistent with recycling experiments.

Further, the O_2 evolution activities of equivalent molar quantities of **11**, $MnBr_2{\cdot}4H_2O$ and H_3**L2** were examined under analogous conditions. In this experiment, the OER activity of **11** vastly surpassed the activity of either the redox-active ligand or metal salt. This experiment provides strong evidence that **11** or a compound closely related to it is the species responsible for O_2 evolution. As the activity of **11** is far greater than the combined activities of its metallic and organic constituents, this suggests that the activity of **11** stems from a synergistic effect between its Mn-oxo core and redox-active stabilising *p*-cresol ligands.

Under electrochemical conditions as part of modified carbon paste electrodes, **11** gives rise to a very low onset potential for catalytic H_2O oxidation. Using 30 wt.-% **11**/CP electrodes, a remarkably low onset overpotential of just 255 mV was achieved. Moreover, high current densities were delivered at low overpotentials, yielding 100 mA cm^{-2} at η = 654 mV. Further, the overpotential of the **11**/CP electrodes can be reduced by increasing the catalyst loading within the carbon blend, as demonstrated by LSV experiments. Therefore, the observed OER activity directly correlates with the quantity of **11** within the modified electrodes, which supports photochemical experiments using this Mn-oxo cluster.

The remarkable turnover characteristics displayed by **11** under photochemical conditions and H_2O oxidation activity at low overpotentials in electrochemical experiments at pH = 7 most likely arises due to a synergistic effect between the bioinspired Mn-oxo cluster and the stabilising redox-active organic ligands. Furthermore, this activity can be attributed the polynuclear core of **11** which contains 'dangling' Mn^{II} centres that interact with H_2O substrates and can accumulate charge equivalents over multiple metallic centres, hence facilitating multi-electron redox processes. The latter characteristic is one of the most important features of natural enzymes to facilitate rapid multiple electron transformations and is well-established for molecular oxo clusters such as polyoxometalates.[7,89,90,91,92]

Also pertinent to the reactivity of **11** are the oxidizable *p*-cresol $(H\mathbf{L2})^{2-}$ ligand derivatives which likely promote electron abstraction from the $\{Mn_{19}\}$ cluster core in an analogous manner to the natural Y_z functionality of PS II. Hence, **11** replicates key features of the OEC's environment within PS II. It is important to note that this study was carried out at neutral pH values at 1 atm and ambient temperature, where **11** has shown unprecedented OER performance under electro- and photochemical conditions. This is highly desirable for the development of artificial photosynthetic cells for direct solar-to-fuel applications.

Maayan *et al*. demonstrated some of the most active Mn-based OER catalysts in the literature. Dodecanuclear $[Mn_{12}O_{12}(OAc)L_x(H_2O)_4]$ complexes (where L = di- or trihydroxybenzoate) exhibit TONs of up to 15.5 under electrochemical conditions, which is several times lower than the highest TON exhibited by **11**.[22,25] One of the most attractive noble metal-free OER catalysts operating under neutral pH conditions is a cobalt oxide-phosphate catalyst (Co-P_i) which was established by Nocera *et al*.[93] Co-P_i catalyses H_2O oxidation under electrochemical conditions, delivering 1 mA cm^{-2} at an applied overpotential of 410 mV at pH = 7. The equivalent current density was delivered by **11**/CP electrodes at an overpotential of just 255 mV. The high OER activity of **11** is an important discovery for the development of effective, renewable technologies for H_2 production from H_2O using inexpensive and environmentally friendly methods. However, it must be acknowledged that the performance of a WOC is linked to the experimental conditions applied.[94]

In this investigation, a synthetic avenue to a highly active WOC using abundant, non-toxic metal ions and inexpensive organic ligands has been highlighted. This approach can be applied to a wide range of clusters and diverse potentially non-innocent ligands. In future investigations, the ligand $H_3\mathbf{L2}$ could be synthetically modified to tune the performance of **11**

under catalytic conditions. This may be achieved by adding electron donating substituents to stabilise the Mn-oxo core during catalysis or using more robust binding groups such as carboxylates to improve the activity of the cluster.[37] Further, the influence of incorporating heterometallic ions such as Ca^{II} or Ba^{II} into the $\{Mn_{19}\}$ system on its catalytic activity could be explored.[95] Finally, computational modelling could be applied to elucidate mechanistic analogies or differences between **11** and the OEC.

3.8 References

1 A. Singh and L. Spiccia, *Coord. Chem. Rev.*, 2013, **257**, 2607–2622.

2 M. M. Najafpour, G. Renger, M. Hołyńska, A. N. Moghaddam, E.-M. Aro, R. Carpentier, H. Nishihara, J. J. Eaton-Rye, J.-R. Shen and S. I. Allakhverdiev, *Chem. Rev.*, 2016, **116**, 2886–2936.

3 I. Roger, M. A. Shipman and M. D. Symes, *Nat. Rev. Chem.*, 2017, **1**, 3.

4 L. C. Seitz, C. F. Dickens, K. Nishio, Y. Hikita, J. Montoya, A. Doyle, C. Kirk, A. Vojvodic, H. Y. Hwang, J. K. Norskov and T. F. Jaramillo, *Science*, 2016, **353**, 1011–1014.

5 E. Y. Tsui, J. S. Kanady and T. Agapie, *Inorg. Chem.*, 2013, **52**, 13833–13848.

6 F. A. Armstrong, *Philos. Trans. R. Soc. B Biol. Sci.*, 2008, **363**, 1263–1270.

7 J. P. McEvoy and G. W. Brudvig, *Chem. Rev.*, 2006, **106**, 4455–4483.

8 J. Kern, R. Chatterjee, I. D. Young, F. D. Fuller, L. Lassalle, M. Ibrahim, S. Gul, T. Fransson, A. S. Brewster, R. Alonso-Mori, R. Hussein, M. Zhang, L. Douthit, C. de Lichtenberg, M. H. Cheah, D. Shevela, J. Wersig, I. Seuffert, D. Sokaras, E. Pastor, C. Weninger, T. Kroll, R. G. Sierra, P. Aller, A. Butryn, A. M. Orville, M. Liang, A. Batyuk, J. E. Koglin, S. Carbajo, S. Boutet, N. W. Moriarty, J. M. Holton, H. Dobbek, P. D. Adams, U. Bergmann, N. K. Sauter, A. Zouni, J. Messinger, J. Yano and V. K. Yachandra, *Nature*, 2018, **563**, 421–425.

9 J. P. McEvoy, J. A. Gascon, V. S. Batista and G. W. Brudvig, *Photochem. Photobiol. Sci.*, 2005, **4**, 940–949.

10 R. Gupta, T. Taguchi, B. Lassalle-Kaiser, E. L. Bominaar, J. Yano, M. P. Hendrich and A. S. Borovik, *Proc. Natl. Acad. Sci.*, 2015, **112**, 5319–5324.

11 M. M. Najafpour, M. A. Isaloo, J. J. Eaton-Rye, T. Tomo, H. Nishihara, K. Satoh, R. Carpentier, J.-R. Shen and S. I. Allakhverdiev, *Biochim. Biophys. Acta*, 2014, **1837**, 1395–1410.

12 D. Wang and C. O. Bruner, *Inorg. Chem.*, 2017, **56**, 13638–13641.

13 Y. Liu, Y. Han, Z. Zhang, W. Zhang, W. Lai, Y. Wang and R. Cao, *Chem. Sci.*, 2019, **10**, 2613–2622.

14 G. C. Dismukes, R. Brimblecombe, G. A. N. Felton, R. S. Pryadun, J. E. Sheats, L. Spiccia and G. F. Swiegers, *Acc. Chem. Res.*, 2009, **42**, 1935–1943.

15 M. Wiechen, H.-M. Berends and P. Kurz, *Dalton Trans.*, 2011, **41**, 21–31.

16 S. Fukuzumi and D. Hong, *Eur. J. Inorg. Chem.*, 2014, **2014**, 645–659.

17 S. Mukhopadhyay, S. K. Mandal, S. Bhaduri and W. H. Armstrong, *Chem. Rev.*, 2004, **104**, 3981–4026.

18 C.-I. Yang, W. Wernsdorfer, G.-H. Lee and H.-L. Tsai, *J. Am. Chem. Soc.*, 2007, **129**, 456–457.

19 C. J. Milios, A. Vinslava, W. Wernsdorfer, S. Moggach, S. Parsons, S. P. Perlepes, G. Christou and E. K. Brechin, *J. Am. Chem. Soc.*, 2007, **129**, 2754–2755.

20 L. A. Kushch, V. D. Sasnovskaya, A. I. Dmitriev, E. B. Yagubskii, O. V Koplak, L. V Zorina and D. W. Boukhvalov, *Dalt. Trans.*, 2012, **41**, 13747–13754.

21 D. Maniaki, E. Pilichos and S. P. Perlepes, *Front. Chem.*, 2018, **6**, 461.

22 G. Maayan and G. Christou, *Inorg. Chem.*, 2011, **50**, 7015–7021.

23 T. Lis, *Acta Crystallogr. Sect. B*, 1980, **36**, 2042–2046.

24 T. Ghosh and G. Maayan, *Angew. Chem. Int. Ed.*, 2019, **58**, 6476.

25 G. Maayan, N. Gluz and G. Christou, *Nat. Catal.*, 2018, **1**, 48–54.

26 M. D. Kärkäs, T. M. Laine, E. V Johnston and B. Åkermark, *Visible Light-Driven Water Oxidation Catalyzed by Ruthenium Complexes*, InTech, Rijeka, 2016.

27 M. Schulze, V. Kunz, P. D. Frischmann and F. Würthner, *Nat. Chem.*, 2016, **8**, 576–583.

28 L. Zhang, R. Clérac, P. Heijboer and W. Schmitt, *Angew. Chem. Int. Ed.*, 2012, **51**, 3007–3011.

29 L. Zhang, R. Clérac, C. I. Onet, M. Venkatesan, P. Heijboer and W. Schmitt, *Chem. - A Eur. J.*, 2012, **18**, 13984–13988.

30 A. M. Ako, I. J. Hewitt, V. Mereacre, R. Clérac, W. Wernsdorfer, C. E. Anson and A. K. Powell, *Angew. Chem. Int. Ed.*, 2006, **45**, 4926–4929.

31 E. Chevallot-Beroux, A. M. Ako, W. Schmitt, B. Twamley, J. Moran, B. Corinne, L. Ruhlmann and S. Mameri, *Dalt. Trans.*, 2019, **48**, 4830–4836.

32 D. Lukács, Ł. Szyrwiel and S. J. Pap, *Catalysts*, 2019, 9.

33 R. Brimblecombe, A. M. Bond, G. C. Dismukes, G. F. Swiegers and L. Spiccia, *Phys. Chem. Chem. Phys.*, 2009, **11**, 6441–6449.

34 F. Song, R. Moré, M. Schilling, G. Smolentsev, N. Azzaroli, T. Fox, S. Luber and G. R. Patzke, *J. Am. Chem. Soc.*, 2017, **139**, 14198–14208.

35 J. Li, R. Güttinger, R. Moré, F. Song, W. Wan and G. R. Patzke, *Chem. Soc. Rev.*, 2017, **46**, 6124–6147.

36 P. Garrido-Barros, C. Gimbert-Suriñach, R. Matheu, X. Sala and A. Llobet, *Chem. Soc. Rev.*, 2017, **46**, 6088–6098.

37 P. Garrido-Barros, I. Funes-Ardoiz, S. Drouet, J. Benet-Buchholz, F. Maseras and A. Llobet, *J. Am. Chem. Soc.*, 2015, **137**, 6758–6761.

38 S. Paul, F. Neese and D. A. Pantazis, *Green Chem.*, 2017, **19**, 2309–2325.

39 A. Müller, S. Sarkar, S. Q. N. Shah, H. Bögge, M. Schmidtmann, S. Sarkar, P. Kögerler, B. Hauptfleisch, A. X. Trautwein and V. Schünemann, *Angew. Chem. Int. Ed.*, 1999, **38**, 3238–3241.

40 Y. Umena, K. Kawakami, J.-R. Shen and N. Kamiya, *Nature*, 2011, **473**, 55–60.

41 Y. Yan, J. S. Lee and D. A. Ruddy, *Inorg. Chem.*, 2015, **54**, 4550–4555.

42 D. R. J. Kolling, N. Cox, G. M. Ananyev, R. J. Pace and G. C. Dismukes, *Biophys. J.*, 2012, **103**, 313–322.

43 M. M. Najafpour, G. Renger, M. Hołyńska, A. N. Moghaddam, E.-M. Aro, R. Carpentier, H. Nishihara, J. J. Eaton-Rye, J.-R. Shen and S. I. Allakhverdiev, *Chem. Rev.*, 2016, **116**, 2886–2936.

44 B. Zhang and L. Sun, *Dalt. Trans.*, 2018, **47**, 14381–14387.

45 B. Limburg, E. Bouwman and S. Bonnet, *ACS Catal.*, 2016, **6**, 5273–5284.

46 M. Orlandi, R. Argazzi, A. Sartorel, M. Carraro, G. Scorrano, M. Bonchio and F. Scandola, *Chem. Commun.*, 2010, **46**, 3152–3154.

47 J. D. Blakemore, R. H. Crabtree and G. W. Brudvig, *Chem. Rev.*, 2015, **115**, 12974–13005.

48 A. L. Spek, *J. Appl. Crystallogr.*, 2003, **36**, 7–13.

49 M. W. Kanan, J. Yano, Y. Surendranath, M. Dincă, V. K. Yachandra and D. G. Nocera, *J. Am. Chem. Soc.*, 2010, **132**, 13692–13701.

50 F. Song, M. M. Busch, B. Lassalle-Kaiser, C.-S. Hsu, E. Petkucheva, M. Bensimon, H. M. Chen, C. Corminboeuf and X. Hu, *ACS Cent. Sci.*, 2019, **5**, 558–568.

51 A. Boussac, F. Rappaport, P. Carrier, J.-M. Verbavatz, R. Gobin, D. Kirilovsky, A. W. Rutherford and M. Sugiura, *J. Biol. Chem.*, 2004, **279**, 22809–22819.

52 I. Zaharieva, M. M. Najafpour, M. Wiechen, M. Haumann, P. Kurz and H. Dau, *Energy Environ. Sci.*, 2011, **4**, 2400–2408.

53 I. Zaharieva, D. González-Flores, B. Asfari, C. Pasquini, M. R. Mohammadi, K. Klingan, I. Zizak, S. Loos, P. Chernev and H. Dau, *Energy Environ. Sci.*, 2016, **9**, 2433–2443.

54 K. N. Ferreira, T. M. Iverson, K. Maghlaoui and J. Barber, 2004, **303**, 1831–1839.

55 Y. Gao, R. H. Crabtree and G. W. Brudvig, *Inorg. Chem.*, 2012, **51**, 4043–4050.

56 A. K. Poulsen, A. Rompel and C. J. McKenzie, *Angew. Chem. Int. Ed.*, 2005, **44**, 6916–6920.

57 R. Brimblecombe, A. Koo, G. C. Dismukes, G. F. Swiegers and L. Spiccia, *J. Am. Chem. Soc.*, 2010, **132**, 2892–2894.

58 J. Limburg, J. S. Vrettos, L. M. Liable-Sands, A. L. Rheingold, R. H. Crabtree and G. W. Brudvig, *Science*, 1999, **283**, 1524–1527.

59 S. Mameri, A. M. Ako, F. Yesil, M. Hibert, Y. Lan, C. E. Anson and A. K. Powell, *Eur. J. Inorg. Chem.*, 2014, **2014**, 4326–4334.

60 A. M. Ako, B. Burger, Y. Lan, V. Mereacre, R. Clérac, G. Buth, S. Gómez-Coca, E. Ruiz, C. E. Anson and A. K. Powell, *Inorg. Chem.*, 2013, **52**, 5764–5774.

61 A. M. Ako, V. Mereacre, R. Clérac, W. Wernsdorfer, I. J. Hewitt, C. E. Anson and A. K. Powell, *Chem. Commun.*, 2009, **0**, 544–546.

62 A. M. Ako, Y. Lan, O. Hampe, E. Cremades, E. Ruiz, C. E. Anson and A. K. Powell, *Chem. Commun.*, 2014, **50**, 5847–5850.

63 C.-H. Ge, Z.-H. Ni, C.-M. Liu, A.-L. Cui, D.-Q. Zhang and H.-Z. Kou, *Inorg. Chem. Commun.*, 2008, **11**, 675–677.

64 J. Dreiser, A. M. Ako, C. Wäckerlin, J. Heidler, C. E. Anson, A. K. Powell, C. Piamonteze, F. Nolting, S. Rusponi and H. Brune, *J. Phys. Chem. C*, 2015, **119**, 3550–3555.

65 M. D. Kärkäs and B. Åkermark, *Dalt. Trans.*, 2016, **45**, 14421–14461.

66 R. Tagore, R. H. Crabtree and G. W. Brudvig, *Inorg. Chem.*, 2007, **46**, 2193–2203.

67 M. D. Kärkäs, R.-Z. Liao, T. M. Laine, T. Åkermark, S. Ghanem, P. E. M. Siegbahn and B. Åkermark, *Catal. Sci. Technol.*, 2016, **6**, 1306–1319.

68 Y. Lin, K.-H. Wu, Q. Lu, Q. Gu, L. Zhang, B. Zhang, D. Su, M. Plodinec, R. Schlögl and S. Heumann, *J. Am. Chem. Soc.*, 2018, **140**, 14717–14724.

69 J. Zhang, Z. Zhao, Z. Xia and L. Dai, *Nat. Nanotechnol.*, 2015, **10**, 444.

70 L. Li, H. Yang, J. Miao, L. Zhang, H.-Y. Wang, Z. Zeng, W. Huang, X. Dong and B. Liu, *ACS Energy Lett.*, 2017, **2**, 294–300.

71 D. Narzi, D. Bovi and L. Guidoni, *Proc. Natl. Acad. Sci.*, 2014, **111**, 8723–8728.

72 S. Styring, J. Sjöholm and F. Mamedov, *Biochim. Biophys. Acta*, 2012, **1817**, 76–87.

73 R.-Z. Liao, M. D. Kärkäs, B.-L. Lee, B. Åkermark and P. E. M. Siegbahn, *Inorg. Chem.*, 2015, **54**, 342–351.

74 M. M. Najafpour and Govindjee, *Dalt. Trans.*, 2011, **40**, 9076–9084.

75 H. Visser, C. E. Dubé, W. H. Armstrong, K. Sauer and V. K. Yachandra, *J. Am. Chem. Soc.*, 2002, **124**, 11008–11017.

76 A. F. Abdel-Magied, A. Shatskiy, R.-Z. Liao, T. M. Laine, W. A. A. Arafa, P. E. M. Siegbahn, M. D. Kärkäs, B. Åkermark and E. V. Johnston, *ChemSusChem*, 2016, **9**, 3448–3456.

77 B. Schwarz, J. Forster, M. K. Goetz, D. Yücel, C. Berger, T. Jacob and C. Streb, *Angew. Chem. Int. Ed.*, 2016, **55**, 6329–6333.

78 L. Y. S. Lee and K.-Y. Wong, in *Organometallics and Related Molecules for Energy Conversion*, ed. W.-Y. Wang, Springer Berlin Heidelberg, 2015, pp. 365–394.

79 M. M. Najafpour, S. Nayeri and B. Pashaei, *Dalt. Trans.*, 2011, **40**, 9374.

80 P. E. M. Siegbahn and M. R. A. Blomberg, *Biochim. Biophys. Acta*, 2004, **1655**, 45–50.

81 J. J. H. Pijpers, M. T. Winkler, Y. Surendranath, T. Buonassisi and D. G. Nocera, *Proc. Natl. Acad. Sci.*, 2011, **108**, 10056–10061.

82 L. Yu, Y. Ding, M. Zheng, H. Chen and J. Zhao, *Chem. Commun.*, 2016, **52**, 14494–14497.

83 T. M. Laine, M. D. Kärkäs, R.-Z. Liao, T. Åkermark, B.-L. Lee, E. A. Karlsson, P. E. M. Siegbahn and B. Åkermark, *Chem. Commun.*, 2015, **51**, 1862–1865.

84 S. Bernardini, F. Bellatreccia, A. Casanova Municchia, G. Della Ventura and A. Sodo, *J. Raman Spectrosc.*, 2019, **50**, 873–888.

85 F. Buciuman, F. Patcas, R. Craciun and D. R. T. Zahn, *Phys. Chem. Chem. Phys.*, 1999, **1**, 185–190.

86 J. Soriano-López, S. Goberna-Ferrón, L. Vigara, J. J. Carbó, J. M. Poblet and J. R. Galán-Mascarós, *Inorg. Chem.*, 2013, **52**, 4753–4755.

87 Z. Codolá, J. Lloret-Fillol and M. Costas, *Non-Noble Met. Catal.*, 2019, 425–451.

88 A. Ramírez, P. Hillebrand, D. Stellmach, M. M. May, P. Bogdanoff and S. Fiechter, *J. Phys. Chem. C*, 2014, **118**, 14073–14081.

89 X. López, J. J. Carbó, C. Bo and J. M. Poblet, *Chem. Soc. Rev.*, 2012, **41**, 7537.

90 M. Martin-Sabi, J. Soriano-López, R. S. Winter, J.-J. Chen, L. Vilà-Nadal, D.-L. Long, J. R. Galán-Mascarós and L. Cronin, *Nat. Catal.*, 2018, **1**, 208–213.

91 H. Lv, J. Song, Y. V. Geletii, J. W. Vickers, J. M. Sumliner, D. G. Musaev, P. Kögerler, P. F. Zhuk, J. Bacsa, G. Zhu and C. L. Hill, *J. Am. Chem. Soc.*, 2014, **136**, 9268–9271.

92 S. Goberna-Ferrón, L. Vigara, J. Soriano-López and J. R. Galán-Mascarós, *Inorg. Chem.*, 2012, **51**, 11707–11715.

93 M. W. Kanan and D. G. Nocera, *Science*, 2008, **321**, 1072–1075.

94 R. Pokhrel, M. K. Goetz, S. E. Shaner, X. Wu and S. S. Stahl, *J. Am. Chem. Soc.*, 2015, **137**, 8384–8387.

95 M. Blasco-Ahicart, J. Soriano-Lopez, J. J. Carbo, J. M. Poblet and J. R. Galan-Mascaros, *Nat. Chem.*, 2018, **10**, 24–30.

Chapter Four

Metallo-Supramolecular Co^{II} Polygons for H_2O Oxidation

4.1 Introduction

Metal-organic polygons and polyhedra (MOPs) are a class of discrete metallo-supramolecular compounds comprising metal ions or polynuclear complexes linked by organic ligand moieties which form *via* self-assembly mechanisms.[1] Judicious selection of organic linkers and SBUs allows the self-assembly process to be directed, thus affording control over the structural, topological and electronic properties of the final material.[2] In recent years, application of this directed synthetic approach has led to the development of MOPs with a wide variety of potential applications including catalysis,[3,4,5] drug delivery,[6] sensing[7] and many others.[8,9]

The organic linkers employed in the synthesis of MOPs are often adapted from those typically used in the reticular synthesis of MOFs,[10] and include carboxylate-,[11] pyridine-[12] and imine-[13] functionalised organic ligands. Literature investigations of imine-based MOPs have demonstrated that the nature of the metal ion within the SBUs of these structures has a significant impact on the physicochemical characteristics of the material. Recently, tritopic imine-containing MOPs featuring Zn^{II} or Fe^{II} have been explored.[14,15]

To develop novel and efficient WOCs, the construction of MOPs comprising Co^{II}-based SBUs presents an attractive opportunity. Despite the extensively demonstrated favourable redox properties of Co^{II} for H_2O oxidation catalysis,[16,17,18] this metal remains relatively underexplored within imine-based MOP chemistry. The low toxicity and high abundance of Co compared with other noble-metals commonly employed in OER catalysis such as Ru and Ir presents additional advantages.[19] These attributes make Co^{II}-based MOPs promising candidates for OER catalysis. Therefore, this investigation focusses on the development of Co^{II}-based MOPs comprising imine ligands for catalysing H_2O oxidation.

In this chapter, a novel class of heterogeneous WOC is described. The synthetic methodology involves a Co^{II}-directed self-assembly using the Schiff base ligand *N*,*N*',*N*''-tris-(1-methyl)-1*H*-imidazol-4-ylmethylene)-1,3,5-triphenyl benzene (**L3**). This process generates the disc-shaped supramolecule $[Co^{II}_3(\mathbf{L3})_2(H_2O)_6]^{6+}$ which features partially hydrated Co^{II} centres. In the solid state, this molecule assembles through an extensive network of hydrogen and halogen bonding interactions to form the stable, water-insoluble halide-metal-organic framework $[Co^{II}_3(\mathbf{L3})_2(H_2O)_6]Cl_6 \cdot DMF \cdot 6H_2O$ (**12**). The capability of **12** to catalyse OER is then assessed under photo- and electrochemical conditions and a computational analysis is applied to elucidate the mechanism of O_2 evolution using this compound. Finally, DFT calculations attribute the observed OER activity to a Co^{III}-oxyl species.

4.2 Synthesis and Structural Characterisation of $[Co^{II}_3(L3)_2(H_2O)_6]Cl_6 \cdot DMF \cdot 6H_2O$ (12)

The supramolecular assembly **12** comprises {Co^{II}/imine} polygons connected through supramolecular interactions to form a 3D framework. The structure was known to the Schmitt group, however in this study the compound's catalytic properties are probed for the first time.[20] The synthesis, structure and physicochemical characterisation of **12** are outlined in this section.

4.2.1 Synthesis of $[Co^{II}_3(L3)_2(H_2O)_6]Cl_6 \cdot DMF \cdot 6H_2O$ (12)

The supramolecular complex $[Co^{II}_3$(**L3**)$_2(H_2O)_6]Cl_6 \cdot DMF \cdot 6H_2O$ (**12**) was prepared in collaboration with Dr. Ako M. Ayuk. Initially, the ligand *N*,*N*',*N*''-tris-(1-methyl)-1*H*-imidazol-4-ylmethylene)-1,3,5-triphenyl benzene (**L3**) was prepared by refluxing 1,3,5-tris(4-aminophenyl)benzene and 4-imidazolecarboxaldehyde overnight in a solution of MeOH and acetic acid. Nucleophilic addition of the primary amine to the aldehyde afforded the formation of the Schiff base ligand. **L3** was then heated with $CoCl_2 \cdot 6H_2O$ in DMF, before filtering the solution and slowly diffusing THF into the filtrate over several days. This afforded orange crystals of **12** in good yield that were suitable for analysis using single crystal X-ray diffraction.

4.2.2 Crystal Structure of $[Co^{II}_3(L3)_2(H_2O)_6]Cl_6 \cdot DMF \cdot 6H_2O$ (12)

The crystal structure of **12** was solved in the hexagonal space group $P6_522$. The asymmetric unit of **12** contains two distinct Co^{II} centres: one of which is crystallographically fully occupied, whilst the other has a crystallographic occupancy of ½ and is located on a 2-fold rotational axis. Also found within the asymmetric unit of **12** are one **L3** ligand, three coordinated H_2O molecules, DMF and H_2O constitutional solvent molecules and Cl^- counterions.

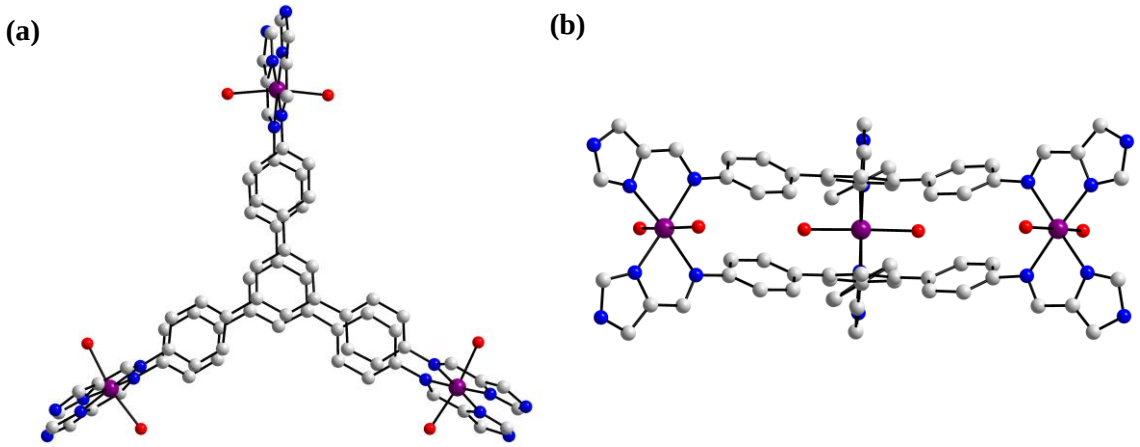

Figure 4.1: Ball-and-stick representation of the trinuclear disc-like structure $[Co^{II}_3$(**L3**)$_2(H_2O)_6]^{6+}$ viewing from (a) top and (b) side. Hydrogen atoms have been omitted for clarity. Colour scheme: C white, N blue, O red, Co violet.

A C_2 symmetry element extending between the two **L3** ligands generates the trinuclear complex $[Co^{II}_3(\mathbf{L3})_2(H_2O)_6]^{6+}$ which exhibits the disk-like structure depicted in Fig. 4.1a. In the solid state, this trinuclear complex assembles through halogen and hydrogen bonding interactions to form the stable, water insoluble halide-metal-organic framework compound, $[Co^{II}_3(\mathbf{L3})_2(H_2O)_6]Cl_6 \cdot DMF \cdot 6H_2O$ (**12**). Each of the Co^{II} centres of **12** are coordinated by two different imidazolate **L3** ligands, and the aromatic ring systems of each of these ligands are aligned in parallel with one another (Fig. 4.1b). The distances between the centroids of the aromatic rings of the ligand moieties are within the range 3.628(8) – 3.678(2) Å. These distances are consistent with π – π stacking interactions previously reported in the literature.[21]

The coordination environments of the two crystallographically independent Co^{II} centres of the trinuclear complex $[Co^{II}_3(\mathbf{L3})_2(H_2O)_6]^{6+}$ are shown in Fig. 4.2. Both Co(1) and Co(2) adopt distorted octahedral coordination geometries which are composed of two imine N-donors, two imidazole N-donors and two O-donors of two coordinated H_2O molecules. The four N-donor atoms are located at the equatorial plane of the Co^{II} centres, with the imine-imidazolate functionality acting as a *cis*-coordinating bidentate functionality.

The apical binding sites of each of the Co^{II} centres are occupied by two O-donors from two H_2O moieties which coordinate *trans* with respect to each other. The bond distances surrounding Co(1) and Co(2) range between 2.10 – 2.22 Å. The bond angles which surrounding Co(1) and Co(2) that deviate most significantly from the ideal octahedral angles of 90° and 180° are within the ranges 76.6° – 105.6° and 169.2° – 190.8°, respectively. These bond distances and angles are consistent with other Co^{II} imidazolate and imine complexes previously reported in the literature.[22,23,24]

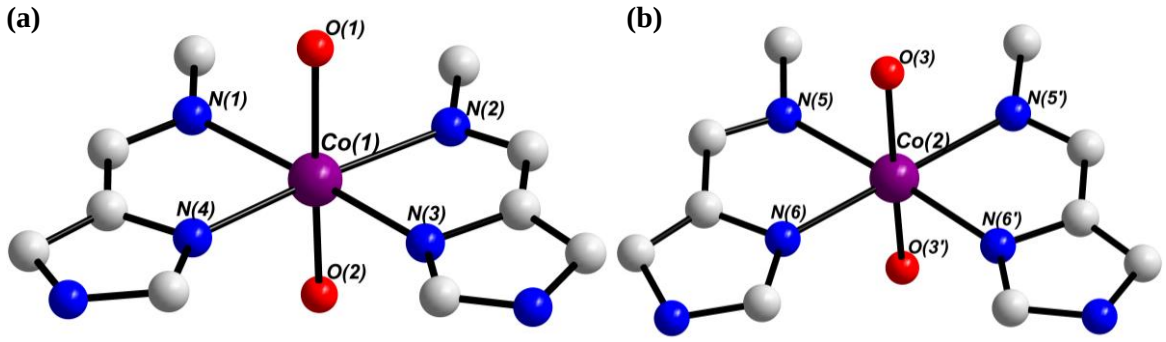

Figure 4.2: Ball-and-stick representation of the coordination environments of the Co^{II} centres in compound **12** ((a) Co(1) and (b) Co(2)). Hydrogen atoms have been omitted for clarity. Colour scheme: C white, N blue, O red, Co violet.

The trinuclear complex $[Co^{II}_3(\mathbf{L3})_2(H_2O)_6]^{6+}$ is stabilised by an extensive network of halogen bonding interactions between Cl^- counterions and imidazole H atoms of the **L3** moieties of **12**. These interactions connect trinuclear complexes along the crystallographic *ab* plane to form layers, which are then further connected by halogen bonding interactions that extend in the direction of the crystallographic *c*-axis to form the 3D halide-metal-organic framework structure $[Co^{II}_3(\mathbf{L3})_2(H_2O)_6]Cl_6$ (**12**). The Cl^- – CH halogen bond distances of **12** are within the range of 2.58 – 2.62 Å, which is typical for halogen bonding interactions previously reported in the literature.[25]

The stacking of the 2D layers within the framework **12** gives rise to large helical channels which are displayed in Fig. 4.3. These helical channels extend in parallel with the crystallographic *c*-axis and have a 6_3 screw symmetry. The presence of these channels in **12** gives the structure a large solvent-accessible void volume which comprises *ca*. 58% of the unit cell volume (calculated using CCDC-mercury program and a probe radius of 1.2 Å).[26]

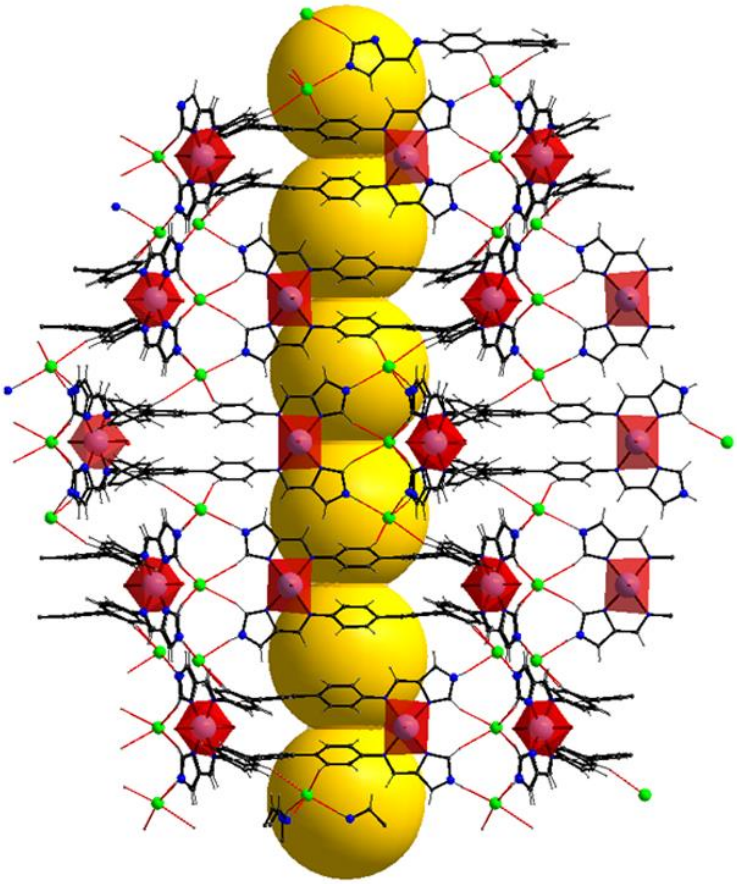

Figure 4.3: Ball-and-stick representation of **12** highlighting the large helical channels which extend in the direction of the crystallographic *c*-axis. Constitutional and coordinated solvent molecules have been omitted for clarity. Colour Scheme: C grey, H white, N blue, Cl green, Co^{II} centres are shown as red polyhedra and yellow spheres highlight void space.

The halide-metal-organic framework **12** is further stabilised by a network of hydrogen bonding interactions between the six coordinated H_2O ligands and constitutional solvent molecules which locate within the channels of **12**. The hydrogen bond distances $O_{(water)} – H\cdots O_{(solvent)}$ are within the range 2.56 – 2.73 Å, which is consistent with hydrogen bonding interactions previously reported in the literature.[27]

Each of the two imidazolate ligands **L3** in **12** are protonated in the crystal structure and are therefore not charged. Each of the three cobalt centres was determined to have an oxidation state of +II using BVS analysis calculations, giving an overall positive charge of +6. This charge is balanced by the presence of 6 Cl^- anions in the crystal structure which stabilise the halide-metal-organic framework **12** through halogen bonding interactions. Therefore, the overall charge of **12** is neutral.

The packing of the halide-metal-organic framework **12** is displayed in Fig. 4.3. The trinuclear complex $[Co^{II}_3(\mathbf{L3})_2(H_2O)_6]^{6+}$ is connected *via* hydrogen and halogen bonding interactions which arrange the complexes into hexagonal layers, whereby three $[Co^{II}_3(\mathbf{L3})_2(H_2O)_6]^{6+}$ complexes align to form individual hexagons (Fig. 4.4a). These honeycomb-shaped layers assemble through Cl^- – CH interactions in the direction of the crystallographic *c*-axis, which stack on top of one another giving rise to the helical channels of **12** (Fig. 4.4b). The distance between neighbouring honeycomb layers (centre to centre) is *ca*. 9.8 Å.

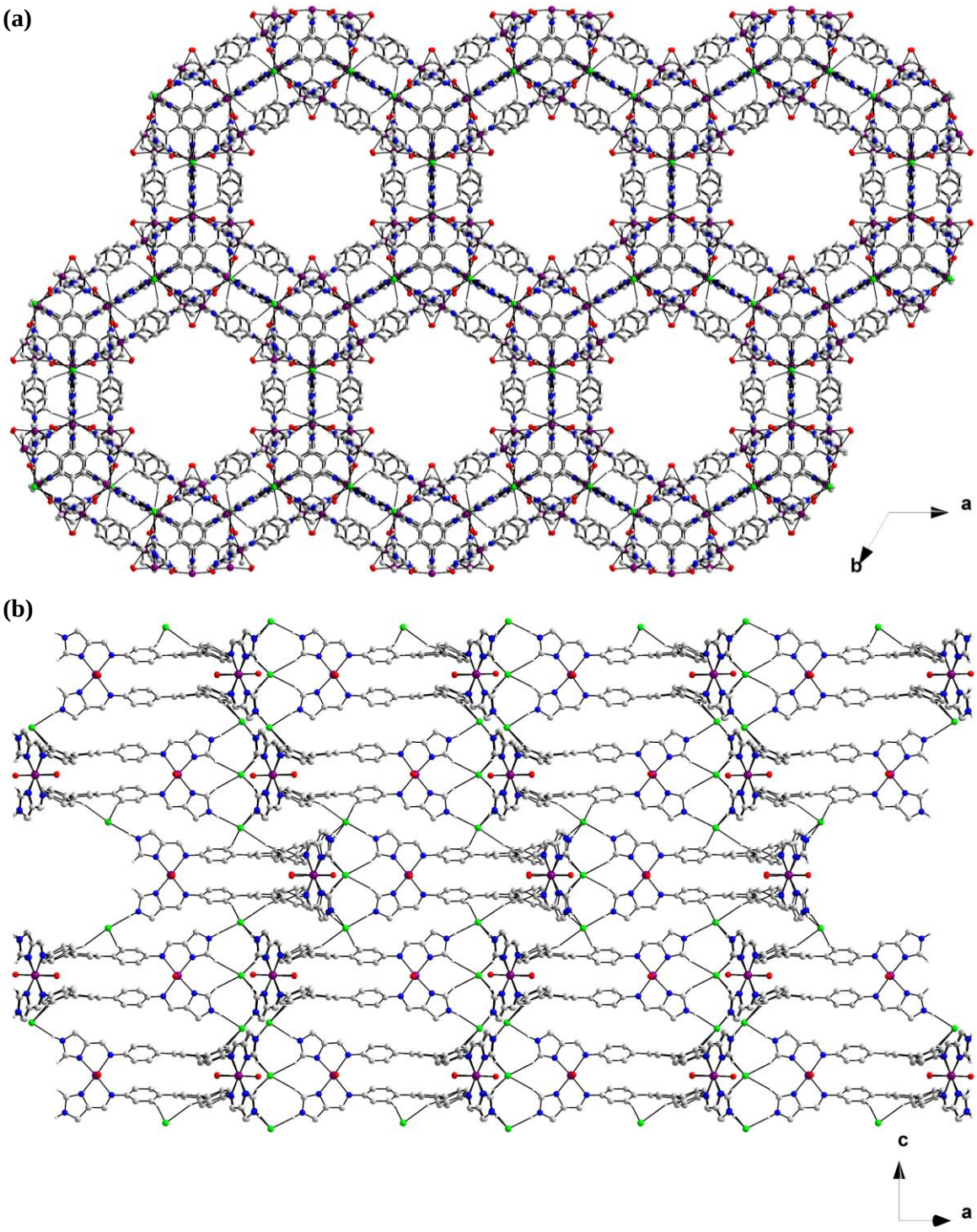

Figure 4.4: Ball-and-stick representation of the packing arrangement of **12**, viewed in the direction of the crystallographic (a) *c*-axis and (b) *b*-axis. Constitutional solvent molecules, coordinated solvent molecules and non-hydrogen bonding hydrogen atoms have been omitted for clarity. Colour scheme: C grey, H white, N blue, O red, Co violet, Cl green.

4.2.3 Physicochemical Characterisation of 12

Infrared Spectroscopy

The halide-metal-organic framework **12** was characterised using FT-IR spectroscopy, and the resulting spectrum is presented in Fig. 4.5. In this spectrum, broad signals above 3200 cm^{-1} can be assigned to vibrations of the hydrogen bonding apically coordinated and constitutional H_2O moieties. In addition, several characteristic signals can be attributed to the ligand **L3** in the FT-IR spectrum of **12**: A signal at 3127 cm^{-1} can be assigned to an aromatic C – H stretching vibration from the ligand, an absorption at 2979 cm^{-1} can be attributed to N – H stretching from the imidazole functionality of **L3**, a signal at 1622 cm^{-1} is assigned to the imine functionality of **L3**, and a signal at 1319 cm^{-1} can be associated with a C – N stretching vibration of the imidazole functionality of **L3**.[28] Two signals at 1157 and 895 cm^{-1} were assigned to the in-plane and out-of-plane N – H bending modes from the imidazole moiety of **L3**, respectively.[29]

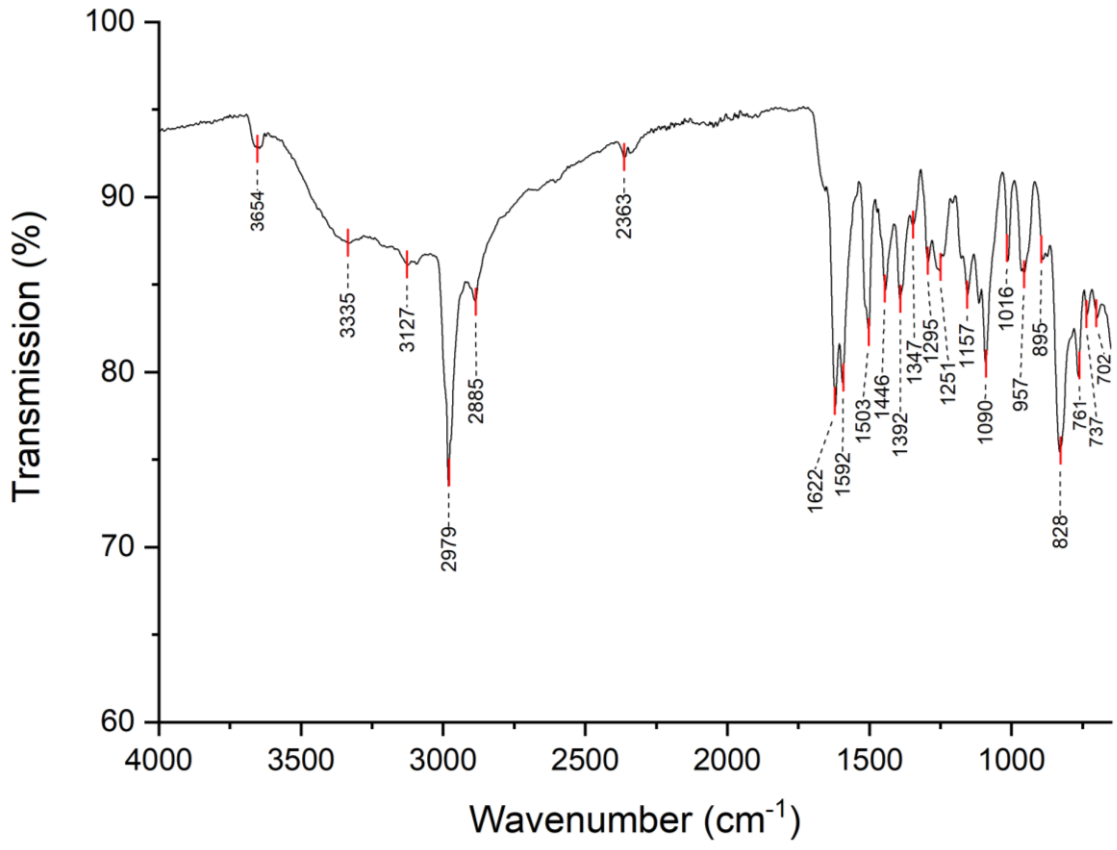

Figure 4.5: FT-IR spectrum of **12**.

Thermogravimetric Analysis

The thermal stability of **12** was assessed using thermogravimetric analysis (TGA) of a freshly prepared, crystalline sample. The analysis was conducted under a constant stream of N_2 in the temperature range 30 – 800 °C. The TGA trace (Fig. 4.6) reveals that as compound **12** is heated from 30 – 100 °C, a weight loss of 12.0% is observed. This weight loss is attributed to the loss of six constitutional H_2O solvent molecules, and the six apically coordinated H_2O molecules from **12** (calculated 11.7%). As compound **12** is heated further from 100 – 160 °C, an additional weight loss of 3.9% is observed, which is associated with the loss of one DMF constitutional solvent molecule (calculated 3.9%). The thermal decomposition of **12** then proceeds in two further stages: Decomposition of the imidazole ligands occurs between 160 – 570 °C, and final decomposition step occurs between 570 – 800 °C which is associated with the formation of metal oxide species. Interpretation of the TGA trace obtained led to the determination of the molecular formula of **12**, $[Co^{II}_3(\mathbf{L3})_2(H_2O)_6]Cl_6 \cdot DMF \cdot 6H_2O$.

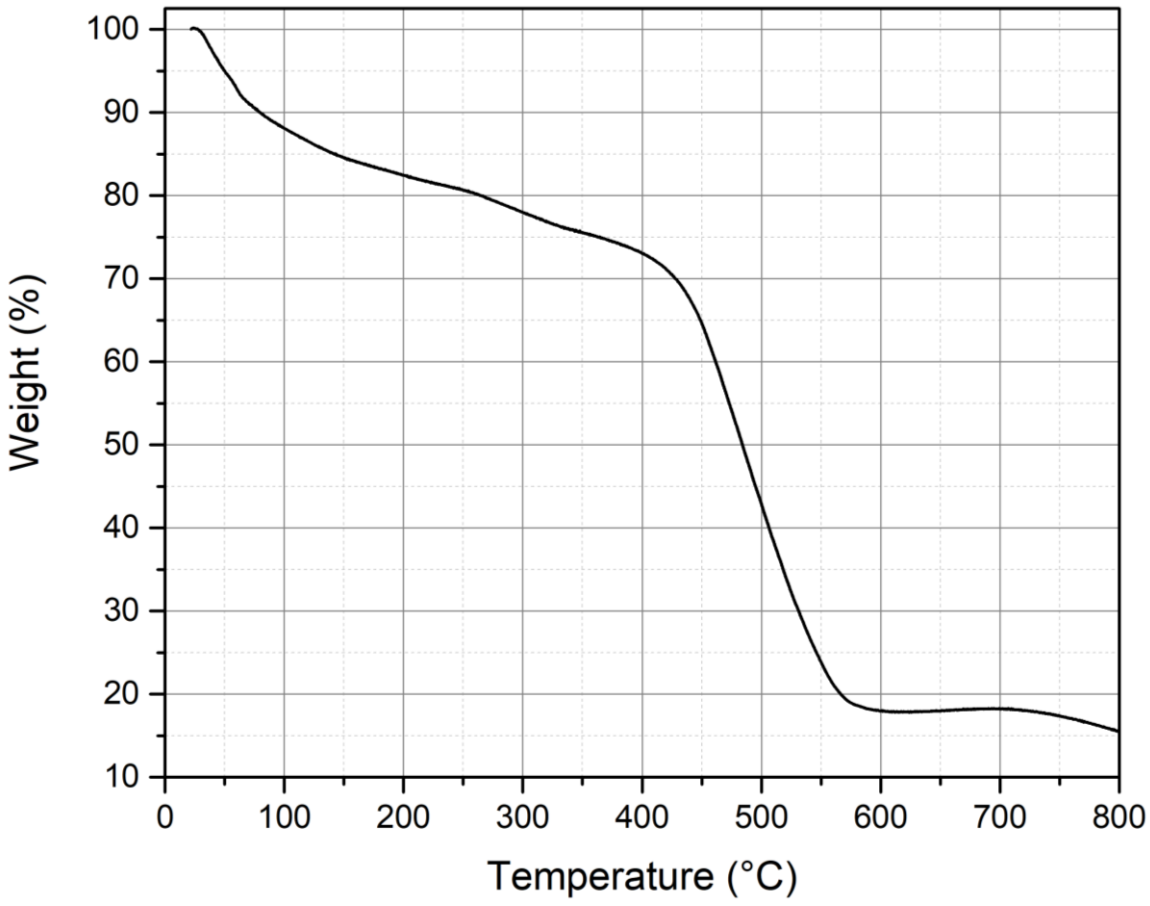

Figure 4.6: TGA trace of **12**.

Mass Spectrometry

The halide-metal-organic framework **12** was found to be insoluble in both aqueous solutions and alcohols. However, upon heating **12** in DMF, small quantities of the material went into solution which were detected using positive ion MALDI mass spectrometry (Fig. 4.7). A weak signal observed at *m/z* = 1633.48 was assigned to the species $\{[Co_3\mathbf{L3}_2(H_2O)_6]Cl_5\}^+$ (calculated *m/z* = 1633.47), confirming that **12** maintains its structural integrity in aqueous solutions.

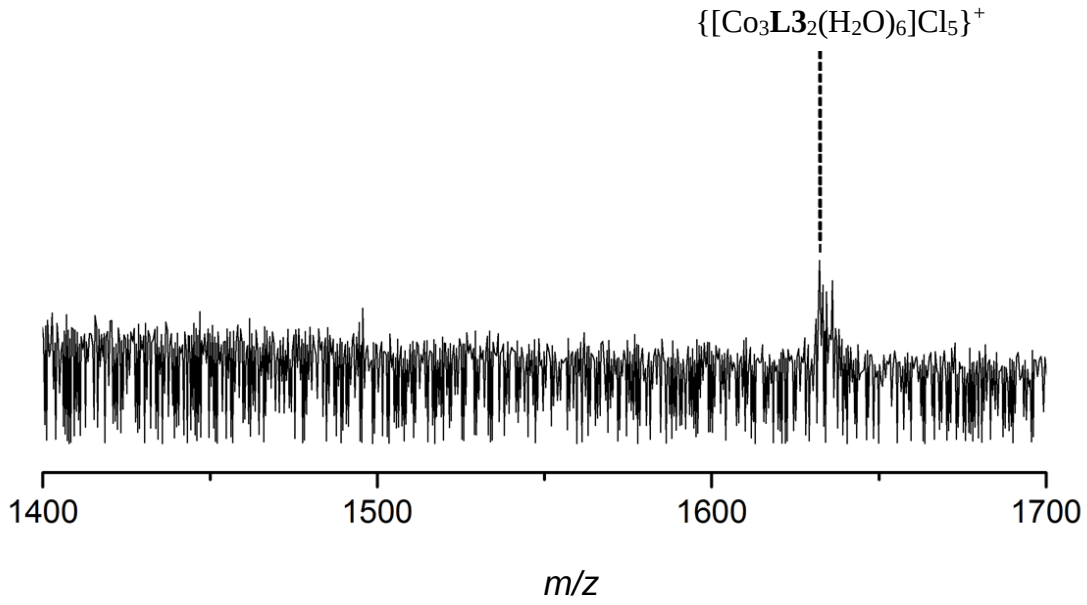

Figure 4.7: Positive ion MALDI of **12** dissolved in DMF highlighting the species $\{[Co_3\mathbf{L3}_2(H_2O)_6]Cl_5\}^+$, $\{Co_3C_{72}H_{66}N_{18}O_6Cl_5\}^+$ (calculated *m/z* = 1633.47, found *m/z* = 1633.48).

4.3 H_2O Oxidation Catalytic Experiments

The halide-metal-organic framework **12** features several structural attributes indicative of its capacity to catalyse the OER. For example, the large, solvent-accessible channels within the 3D open-framework structure of **12**, coupled with the presence of partially hydrated Co^{II} centres in the structure were significative of the material's catalytic potential. Furthermore, the facile synthesis, noble-metal-free nature and heterogeneity of **12** under aqueous conditions all suggested that the material could prove to be a valuable WOC. These observations prompted an investigation into the H_2O oxidation properties of **12** under both photo- and electrochemical conditions. The experiments described in this section demonstrate that **12** functions as an efficient heterogeneous catalyst for the OER.

4.3.1 Visible Light-Induced H_2O Oxidation Catalytic Properties of 12

The light-driven H_2O oxidation activity of **12** was assessed according to a procedure which was analogous to the protocol applied to determine the photocatalytic OER activity of **1**. A three-component system comprising the WOC (**12**), a PS ($[Ru(bpy)_2(deeb)](PF_6)_2$) and a two-electron SEA ($Na_2S_2O_8$) was employed under phosphate-buffered aqueous conditions at pH = 7.0.[30] O_2 evolution activity was monitored in real-time using a Clark electrode whilst the reactor was irradiated with an LED lamp (λ = 470 nm).

Control experiments were conducted in which one of each of the three components of the photocatalytic system were removed. This resulted in negligible O_2 evolution, demonstrating that each component is vital for overall OER activity (Table 4.1). Preliminary OER experiments using **12** with $[Ru(bpy)_3]Cl_2$ as a PS or in borate-buffered solutions resulted in less O_2 evolution compared to analogous experiments conducted using $[Ru(bpy)_2(deeb)](PF_6)_2$ as a PS or phosphate-buffered solutions. For this reason, subsequent experiments were conducted using $[Ru(bpy)_2(deeb)](PF_6)_2$ in phosphate-buffered aqueous solutions.

Table 4.1: Table highlighting the relationship between O_2 evolution the presence of each component of the three-component photocatalytic system and light irradiation.

12	$Na_2S_2O_8$	$[Ru(bpy)_2(deeb)](PF_6)_2$	Light Irradiation (λ = 470 nm)	OER Activity Observed
Yes	Yes	Yes	–	No
Yes	Yes	–	Yes	No
Yes	–	Yes	Yes	No
–	Yes	Yes	Yes	No
Yes	Yes	Yes	Yes	Yes

Kinetics of the Light-Driven OER

Photocatalytic experiments using **12** revealed that the material exhibits optimal OER performance using a catalyst loading of between 0.04 – 0.08 mg in the presence of $[Ru(bpy)_2(deeb)](PF_6)_2$ (2 mg) PS and $Na_2S_2O_8$ SEA (10 mM) in an aqueous phosphate-buffered solution (5 mL, 0.01 M, initial pH = 7). Fig. 4.8 displays the kinetics of the light-driven OER using **12** when employing catalytic loadings of 0.00, 0.04, 0.06, and 0.08 mg. When the light is switched on, the measured O_2 concentration in the solution containing the three-component catalytic mixture continuously rises for *ca*. 200 seconds, before levelling off and eventually decreasing as a result of equilibration with the headspace of the reactor. The relationship between the loading of **12** and net O_2 production follows pseudo first-order kinetics, indicating that the mechanism of the OER by **12** proceeds *via* a WNA pathway as opposed to an I2M pathway, which would be expected to exhibit 2nd order reaction kinetics.[31]

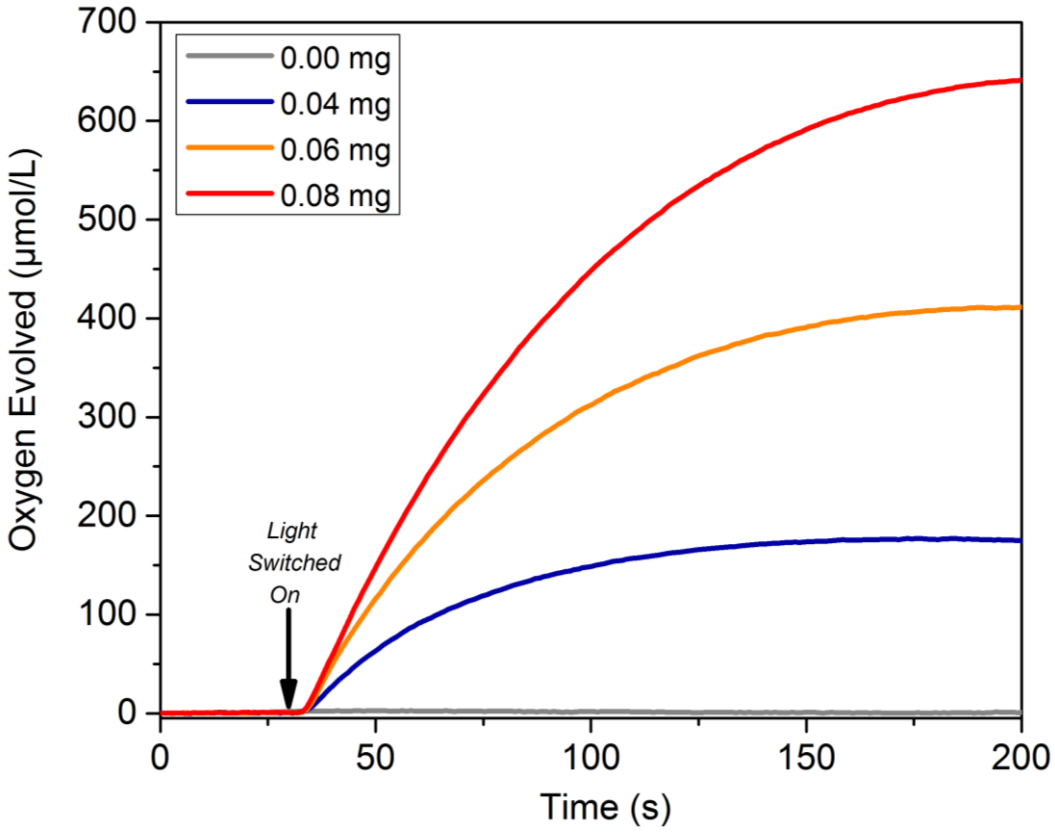

Figure 4.8: Kinetic monitoring (Clark electrode) of light-driven dioxygen formation using different WOC loadings of **12** (0 mg, grey; 0.04 mg, blue; 0.06 mg, orange; 0.08 mg red). Conditions LED lamp (λ = 470, 10 mW cm^{-2}), $[Ru(bpy)_2(deeb)](PF_6)_2$ (2 mg), $Na_2S_2O_8$ (10 mM) in phosphate-buffered aqueous solution (5 mL, 0.01 M, pH = 7.0). Constant stirring rate of 500 rpm and temperature of 25 °C maintained by immersion of the reaction vessel in a water bath.

Kinetics of the Light-Driven OER: High Catalyst Loadings

Increasing the loading of **12** above 0.08 mg resulted in diminishing catalytic turnover characteristics. The kinetics of O_2 evolution by **12** at loadings higher than 0.08 mg are plotted in Fig. 4.9. Increasing the amount of **12** above the optimal loading for the OER resulted in a decrease in the TON (TON = 24.7 using 0.15 mg loading of **12** compared to TON = 44.1 with a loading of **12** of 0.09 mg), the TOF (TOF = 0.30 s^{-1} for 0.15 mg WOC loading compared to TOF = 0.57 s^{-1} for 0.09 mg WOC loading) and overall dioxygen evolution by the catalyst (O_2 conversion = 8.58% for 0.09 mg loading compared to O_2 conversion of 8.02% for 0.15 mg loading). Similar behaviour has previously been reported in other investigations of catalysts for the light-driven OER, and the behaviour has been attributed to aggregate formation between the catalyst and the PS species, which decreases the overall efficiency of the photocatalytic system.[32,33,34]

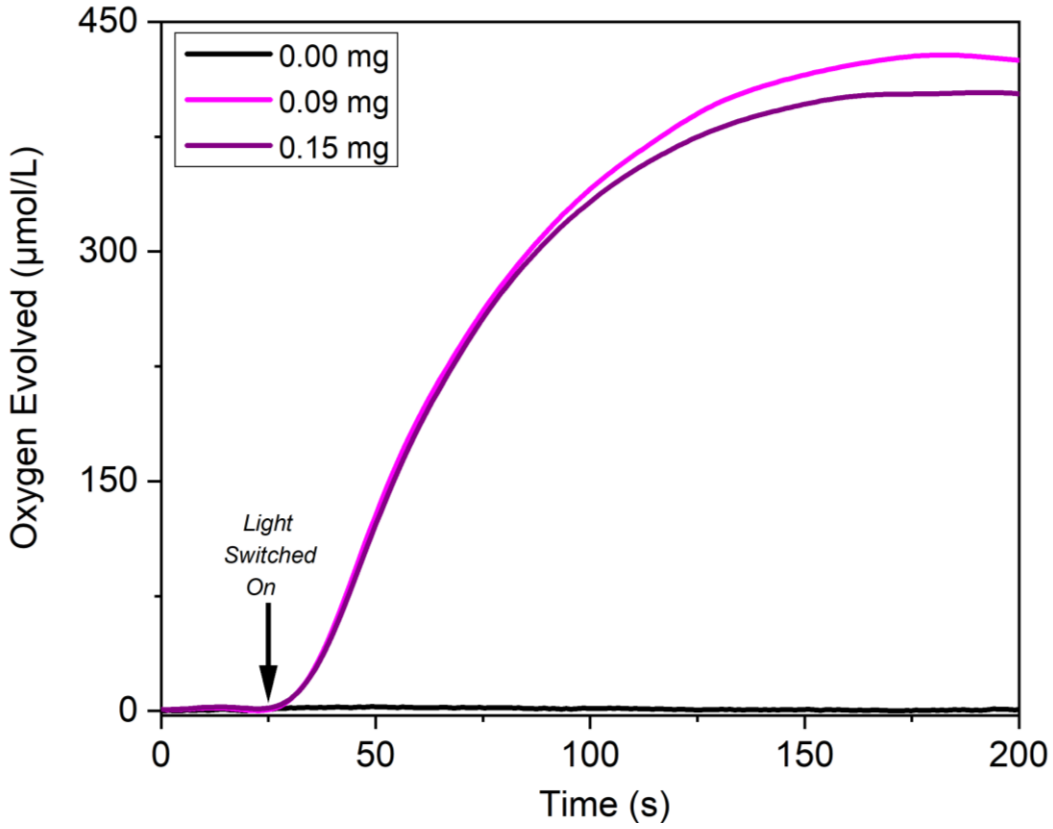

Figure 4.9: Kinetic monitoring (Clark electrode) of light-driven dioxygen formation using high loadings of **12** (0 mg, black; 0.09 mg, magenta; 0.15 mg purple) showing the negative correlation between OER activity and catalyst loading above the optimal catalytic loading. Conditions LED lamp (λ = 470, 10 mW cm^{-2}), $[Ru(bpy)_2(deeb)](PF_6)_2$ (2 mg), $Na_2S_2O_8$ (10 mM) in phosphate-buffered aqueous solution (5 mL, 0.01 M, pH = 7.0). Constant stirring rate of 500 rpm and a temperature of 25 °C maintained by immersion of the reaction vessel in a water bath.

The light-driven OER experiments described demonstrate that **12** functions as an efficient H_2O oxidation catalyst, operating with a maximum TOF = 1.21 s^{-1} when employing catalyst loading of 0.06 mg, and a maximum TON = 74.3 and O_2 yield of 12.8% when employing a loading of 0.08 mg (Table 4.2).

The halide-metal-organic framework **12** exhibits superior catalytic performance in terms of TON and TOF towards the light-driven OER relative to many other transition metal-based WOCs previously reported in the literature.[35] The maximum TOF of **12** towards the OER is exceptional among earth-abundant heterogeneous WOCs.[36,37] For example, Blakemore *et al*. prepared quantum-confined Co_3O_4 nanoparticles (< 5 nm diameter) for electrocatalytic H_2O oxidation using pulsed-laser ablation in liquids (PLAL).[38] The TOF of this WOC is 0.21 s^{-1} per mole of surface-accessible Co atoms, which is among the highest reported TOF for Co_3O_4 nanoparticles.

Even if the assumption is made that all of the Co^{II} ions of **12** are surface-accessible, the TOF per Co^{II} centre in **12** is still significantly higher than the reported TOF of the PLAL generated Co_3O_4 nanoparticles under most of the applied experimental conditions. A lower TOF was only observed when using the highest loadings of **12** (0.09 mg and 0.15 mg). The moderate TON and very high TOF displayed by **12** suggests that structural modifications to increase the robustness of this WOC would be beneficial for generating a highly efficient OER catalyst.

Table 4.2 – TON, TOF and % oxygen conversion at different loadings of 12.

Catalyst Loading (mg)	Turnover Number (TON)	Turnover Frequency (TOF, s^{-1})	Oxygen Conversion (%)
0.04	41.6	0.98	3.60
0.06	64.0	1.21	8.30
0.07	59.8	1.01	9.00
0.08	74.3	1.09	12.8
0.09	44.1	0.57	8.58
0.15	24.7	0.30	8.02

Recycling Experiments

In order to ascertain if **12** could be recycled, fresh quantities of $[Ru(bpy)_2(deeb)](PF_6)_2$ and $Na_2S_2O_8$ were added to the reaction vial following the conclusion of a light-driven H_2O oxidation experiment. The OER response of this reaction mixture was then recorded, before repeating this process until no more O_2 evolution could be detected. The kinetics of the OER for these experiments is shown in Fig. 4.10 and reveals that **12** maintains activity after the first cycle, however oxygen evolution fell significantly (net oxygen yield fell to 23% and 10% of the 1st cycle for the 2nd and 3rd cycle, respectively). The combined total turnover number exhibited by **12** over three catalytic tests was calculated as 23.0. This number is lower than may be expected as it was necessary to employ a buffer solution with a higher than optimal ionic strength in order to avoid a significant decrease in pH of the catalytic mixture over several successive catalytic runs.

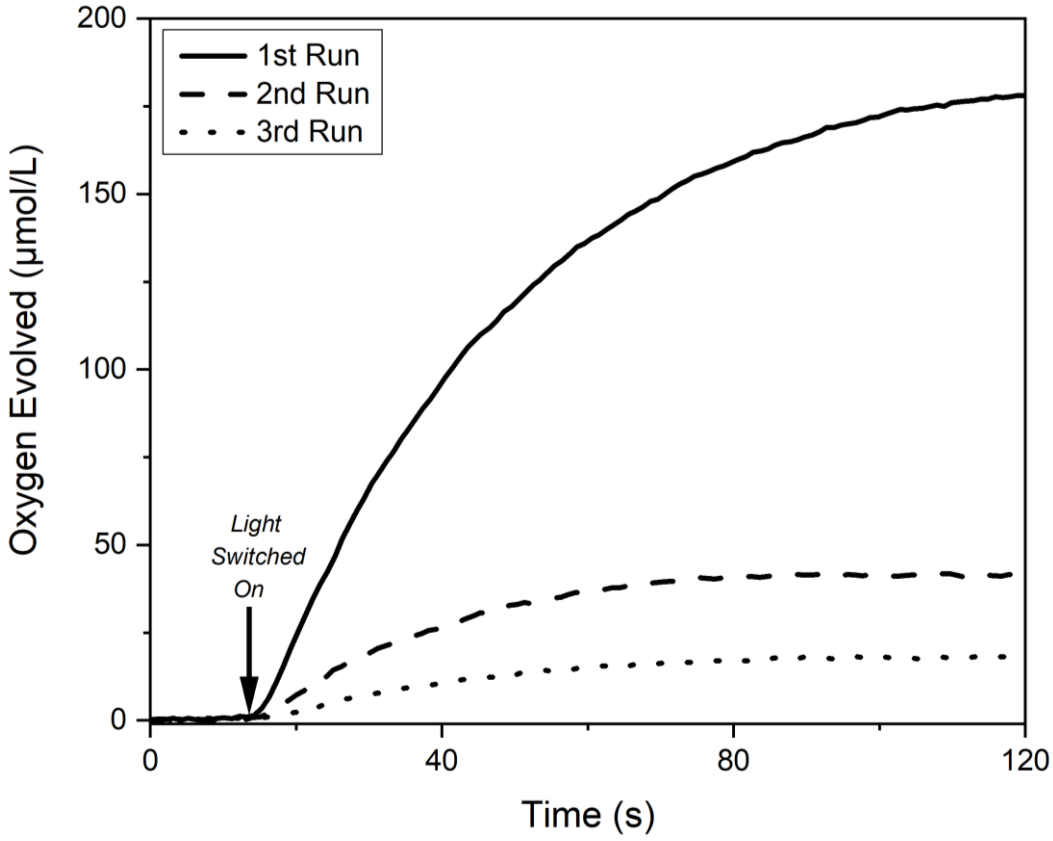

Fig. 4.10: Kinetics of light-driven dioxygen formation during four recycling tests using **12**. Prior to each catalytic run, 2 mg $[Ru(bpy)_2(deeb)](PF_6)_2$, and 11.9 mg $Na_2S_2O_8$ were added to the reaction vial. Conditions: 0.086 mg WOC loading in 5 mL 0.05 M phosphate buffer (starting pH = 7), LED lamp (λ = 470, 10 mW cm^{-2}), a constant temperature of 25 °C and a stirring rate of 500 rpm was maintained throughout each catalytic run.

Subsequent attempts to reuse the catalytic material after the 3rd run by adding additional SEA and PS and irradiating resulted in negligible O_2 evolution. The suspected reason for this is that **12** decomposes into catalytically inactive or less active species when repeatedly subjected to the harshly oxidising working conditions of the OER. To verify this hypothesis, the recycled inactive catalytic material was taken into DMF and analysed using positive ion ESI mass spectroscopy (Fig. 4.11). As expected, no signals could be assigned to the intact catalytic species in the resulting mass spectrum, and two new signals emerged at *m/z* = 96.03 and 352.18, which were assigned the protonated organic decomposition products of **12**: 4-imidazolecarboxaldehyde (calculated *m/z* = 96.03) and 1,3,5-tris(4-aminophenyl)benzene (calculated *m/z* = 352.18), respectively.

This observation provides a useful insight into the decomposition pathway of **12** during the OER. It also reveals a potential weakness in the WOC of the imine moiety, which could be substituted for a more robust functional group to confer additional stability to **12** under the working conditions of light-driven OER. Such modifications could lead to the synthesis of more robust WOCs which are analogous to **12** in future studies.

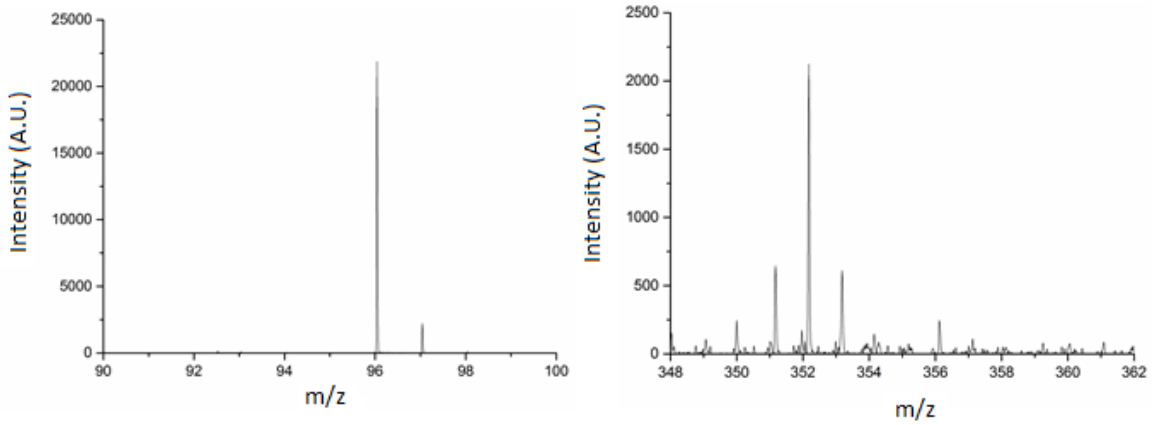

Figure 4.11: Positive ion ESI-MS of the solid particles taken into DMF after the third run of the light-driven OER recycle test highlighting (a) the peak at *m/z* = 96.03 corresponding to protonated 4-imidazolecarboxaldehyde fragment of the Schiff Base ligand $\{C_4H_4N_2O\}^+$ 96.03 (calculated), 96.03 (found), and (b) the peak at *m/z* = 352.17 corresponding to protonated triamine fragment of the Schiff Base $\{C_{24}H_{22}N_3\}^+$ 352.18 (calculated), 352.17 (found).

4.3.2 Post-Catalytic Characterisation

After establishing the O_2 evolving properties of **12** under photochemical conditions, it was vital to verify that **12** is indeed the true OER active species responsible for the observed catalytic activity. To rule out the *in-situ* formation of trace quantities of heterogeneous OER competent catalysts such as CoO_x or Co–Pi, Raman spectroscopic analysis was performed on catalytic samples before and after light-driven O_2 evolution. Moreover, UV-Vis spectroscopy was conducted on aqueous solutions containing three-component catalytic mixtures at several stages of the light-driven OER to measure Co^{II} leaching from **12**. The detection of catalytic leaching is integral to ascertain the true origin of any observed O_2 evolution, as Co^{II} ions have been demonstrated as precatalysts for the formation of CoO_x species.[39,40,41] At the end of this section, the kinetics of light-driven O_2 evolution by **12** and Co_3O_4 nanoparticles under analogous conditions are compared. This comparison is used to determine if the OER activity of **12** could arise due to the participation of Co_3O_4 nanoparticles which form in low levels below the detection limit of Raman spectroscopic analysis.

Raman Spectroscopic Analysis

Raman spectroscopic analysis was carried out on a freshly prepared crystalline sample of **12**, and a sample of **12** that had been employed in the light-driven OER (Fig. 4.12). Post-catalytic material was recovered by collecting the solid material remaining in the irradiated three-component mixture by filtration and subsequently washing with distilled H_2O. Raman spectroscopic analysis is well suited to detect trace amounts of either CoO_x species or Co–Pi that may form *in-situ* due to the high surface sensitivity of this technique.[42]

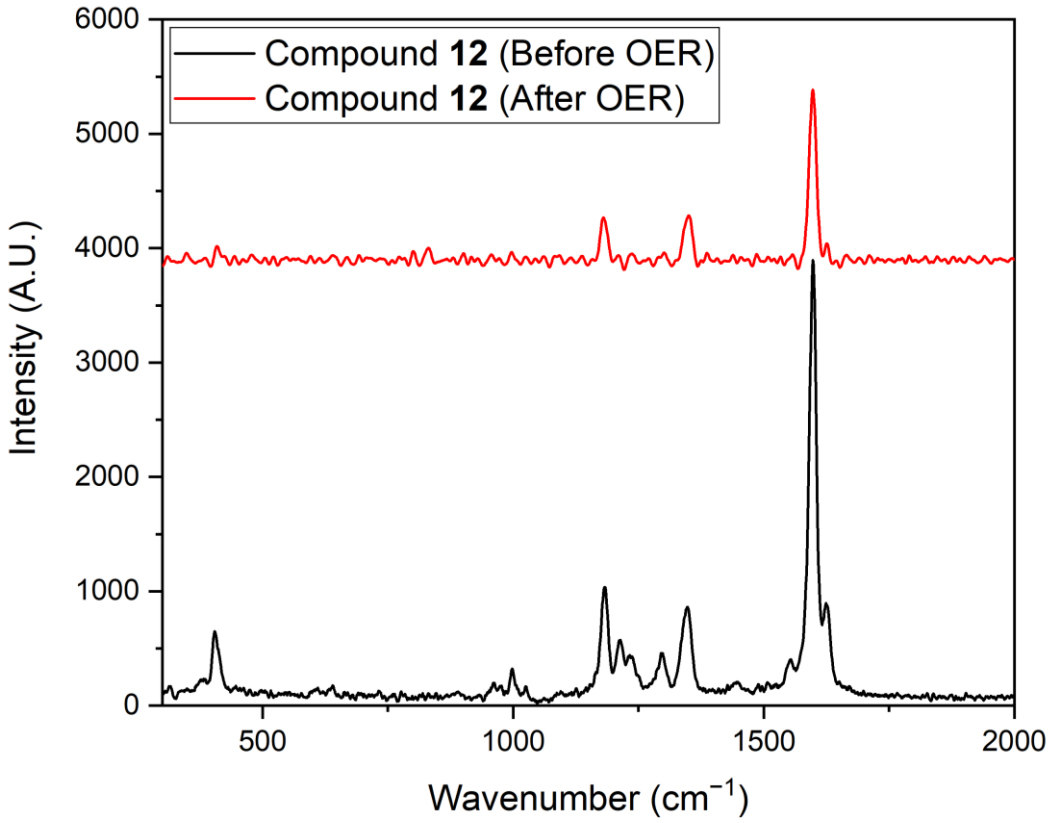

Figure 4.12: Raman spectroscopic analysis of **12** (black) and solid particles of the catalyst recovered after use in the light-driven OER (red).

Comparison of the two spectra reveals that the highest intensity signals arising from **12** at 410 cm^{-1}, 1180 cm^{-1}, 1350 cm^{-1}, and 1600 cm^{-1} are present in both the freshly prepared and the post-OER catalytic samples. This indicates that **12** retains its structural integrity at least in part following the OER. However, due to the diminished intensity of these signals in the post-irradiated catalytic sample, and because many of the lower intensity signals present in the

Raman spectrum of the fresh catalytic material are not present in the Raman spectrum of the irradiated sample it seems probable that partial decomposition of the catalyst occurs during the light-driven OER. This is observation is consistent with the catalyst recycling experiments in which the activity of **12** was observed to decrease over multiple catalytic runs.

Crucially, no signals were observed in the Raman spectrum of the post-irradiated catalytic sample in the region 400 – 600 cm^{-1}, which is the region in which CoO_x species are typically highly vibrationally active in Raman spectroscopy.[43] Furthermore, no signals could be assigned to Co–Pi in the Raman spectrum of the post-irradiated catalytic sample, which typically features two distinct signals at 971 cm^{-1} and 1056 cm^{-1} that arise from the $[PO_4]^{3-}$ groups of Co–Pi.[44,45] The absence of signals that could be assigned to either CoO_x species or Co–Pi in the Raman spectrum of the recovered post-catalytic material strongly suggests that the observed OER activity arises directly from **12**, which is a true molecular WOC.

UV-Vis Spectroscopy

The supernatant of various suspensions of **12** were analysed using UV-Vis spectroscopy to detect leaching of Co^{II} ions from the WOC into the aqueous phase. Initially, a suspension of **12** (10 mg) in aqueous phosphate buffer (5 mL, 0.01 M, pH = 7) was stirred for 15 minutes before measuring the UV-Vis spectrum of the supernatant of this suspension (Fig. 4.13, black). For comparison, the UV-Vis spectrum of a $CoCl_2 \cdot 6H_2O$ (10 μM) in an aqueous phosphate-buffered solution (0.01 M, initial pH = 7) was also measured (Fig. 4.13, blue). Importantly, a characteristic absorption detected in the UV-Vis spectrum of the $CoCl_2 \cdot 6H_2O$ solution at λ = 520 nm cannot be seen in the UV-Vis spectrum of the supernatant of the WOC suspension. This result indicates that significant quantities of Co^{II} do not leach from **12** under the aqueous phosphate-buffered conditions employed in photocatalytic OER experiments.

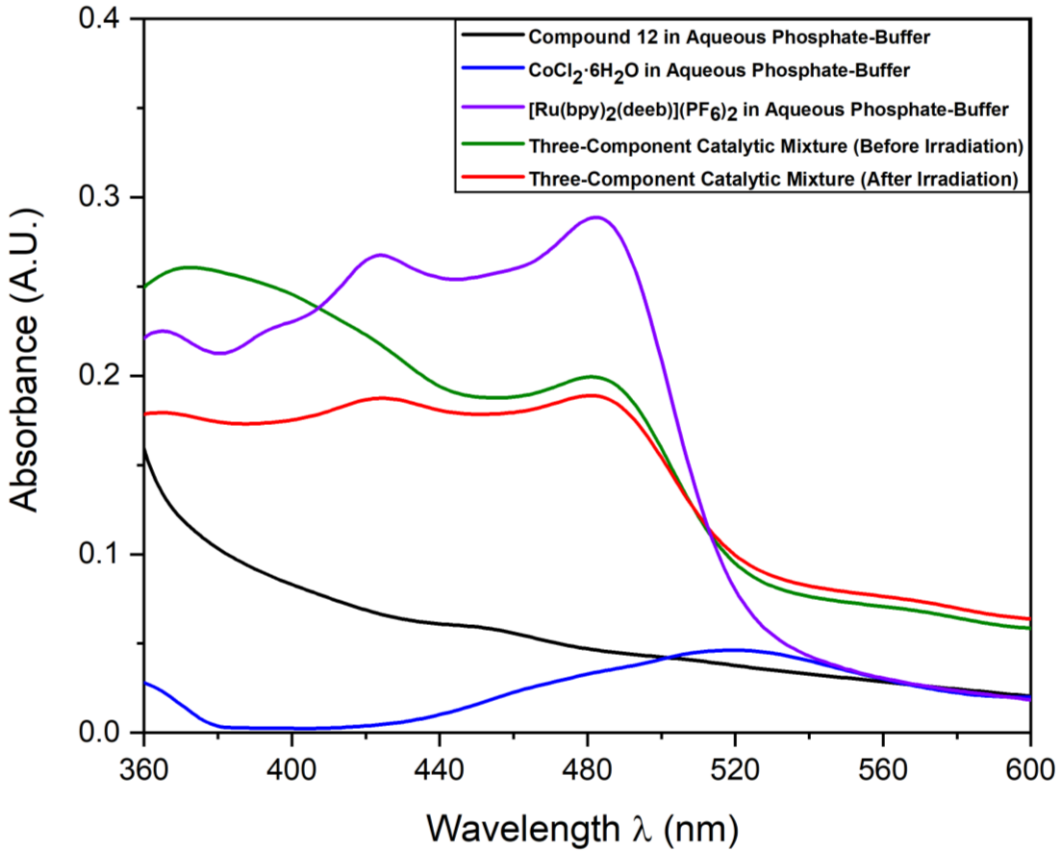

Figure 4.13: Comparison of the UV-Vis spectra of various catalytic mixtures and components, including the supernatant of a suspension of **12** in an aqueous phosphate-buffered solution (black), a three-component photocatalytic mixture in an aqueous phosphate-buffered solution both before (green) and after (red) irradiation. The UV-Vis spectra of aqueous phosphate-buffered solutions containing the PS $[Ru(bpy)_2(deeb)](PF_6)_2$ (purple) and $CoCl_2 \cdot 6H_2O$ (blue) are also plotted for comparison.

Following this, UV-Vis spectroscopy was used to detect Co^{II} leaching from **12** under the highly oxidising working conditions of light-driven OER experiments. To this end, the UV-Vis spectra of three-component photocatalytic mixtures in aqueous phosphate buffer were obtained before (Fig. 4.13, green) and after (Fig. 4.13, red) O_2 evolution. The UV-Vis spectrum of the PS $[Ru(bpy)_2(deeb)](PF_6)_2$ in aqueous phosphate buffer is plotted for comparison (Fig. 4.13, violet). The characteristic maxima of aqueous Co^{II} ions at λ = 520 nm is not observed in the UV-Vis spectra of the pre-, or the post- irradiated three-component catalytic mixtures. This indicates that Co^{II} leaching from **12** does not occur under the working conditions of the OER.

Comparison of the Catalytic OER Activity of 12 and Co_3O_4 Nanoparticles

In order to gather further, indirect evidence that the participation of *in-situ* formed Co_3O_4 nanoparticles do not contribute significantly to the H_2O oxidation activity observed for **12**, the catalytic activity of equimolar Co quantities of **12** and commercially sourced Co_3O_4 nanoparticles (50 – 80 nm particle size) were assessed under analogous conditions. The kinetics of the light-driven OER catalysed by 84 nmol of either Co_3O_4 or **12** in the presence of $[Ru(bpy)_2(deeb)](PF_6)_2$ (2 mg) in 5 mL and $Na_2S_2O_8$ (10 mM) in a phosphate-buffered aqueous solution (5 mL, 0.01 M) with an initial pH = 7 are displayed in Fig. 4.14.

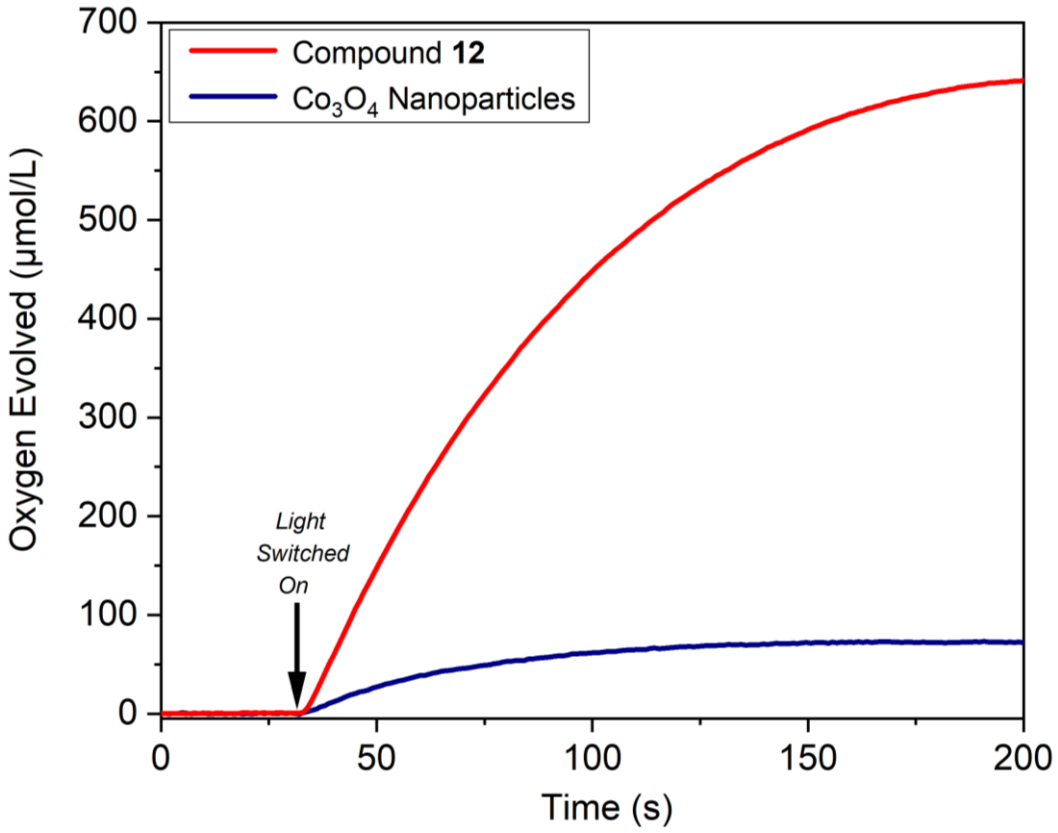

Figure 4.14: Comparison of the light-driven O_2 evolution activity between the two heterogeneous H_2O oxidation catalysts: Co_3O_4 nanoparticles (blue curve, commercially sourced, 50 – 80 nm) and **12** (red curve). Conditions: LED lamp (λ = 470, 10 mW cm^{-2}) 84 nmol catalyst, 2 mg $[Ru(bpy)_2(deeb)](PF_6)_2$ PS and 11.9 mg $Na_2S_2O_8$ SEA in 5 mL 0.01 M phosphate buffer (starting pH = 7). Constant temperature of 25 °C and stirring at 500 rpm maintained by immersion in a water bath.

The result of this experiment demonstrates that the OER proceeds with far faster kinetics when catalysed by **12** compared with the kinetics of the OER when catalysed by Co_3O_4 nanoparticles

under otherwise identical conditions. The quantity of O_2 evolved by **12** is 8.7 times greater than the amount of O_2 which is evolved by an equivalent Co molar quantity of Co_3O_4 nanoparticles in the first 170 seconds (3.21 µmol O_2 evolved by **12** compared with 0.37 µmol O_2 evolved by Co_3O_4 nanoparticles). Furthermore, the initial TOF of **12** was found to be 5.7 times larger than the initial TOF of Co_3O_4 nanoparticles under analogous conditions (TOF = 1.09 s^{-1} for **12** compared with a TOF = 0.19 s^{-1} for Co_3O_4 nanoparticles).

This experiment demonstrates that **12** is a kinetically superior OER catalyst to a common benchmark WOC (Co_3O_4 nanoparticles). Moreover, the contrasting activities manifested by **12** and Co_3O_4 nanoparticles is incompatible with the observed OER activity of **12** deriving from the *in-situ* formation of trace quantities of Co_3O_4 nanoparticles below the detection limit of Raman spectroscopy. Therefore, this test provides further indirect evidence that **12** is the true O_2 evolving species.

The results of the post-catalytic characterisation experiments strongly implicate **12** as the true O_2 evolving species in the light-driven OER experiments described. The formation of trace quantities of CoO_x species or Co–Pi could not be not be detected using Raman spectroscopy, and no leaching of Co^{II} from **12** into the supernatant was observed using UV-Vis spectroscopy. Moreover, as the observed kinetics for the light-driven H_2O oxidation by **12** are far superior to that of Co_3O_4 nanoparticles under the applied experimental conditions, the observed OER activity by **12** is highly unlikely to arise due to the formation of trace quantities of CoO_x species.

4.3.3 Electrochemical H_2O Oxidation Catalytic Properties of 12

Repetitive Cyclic Voltammetry at pH = 7.2

The electrocatalytic H_2O oxidation properties of **12** were established in a series of electrochemical experiments. In these tests, modified electrodes containing commercial carbon paste (CP) with 5% by weight (wt.-%) of the WOC **12** blended into the electrode (**12**/CP) were prepared for use in repetitive cyclic voltammetry (CV) experiments. The response of a **12**/CP electrode in a repetitive CV experiment under aqueous, phosphate-buffered conditions at pH = 7.2 throughout 150 cycles is shown in Fig. 4.15. Also plotted is the response of a control CP electrode without **12** for comparison.

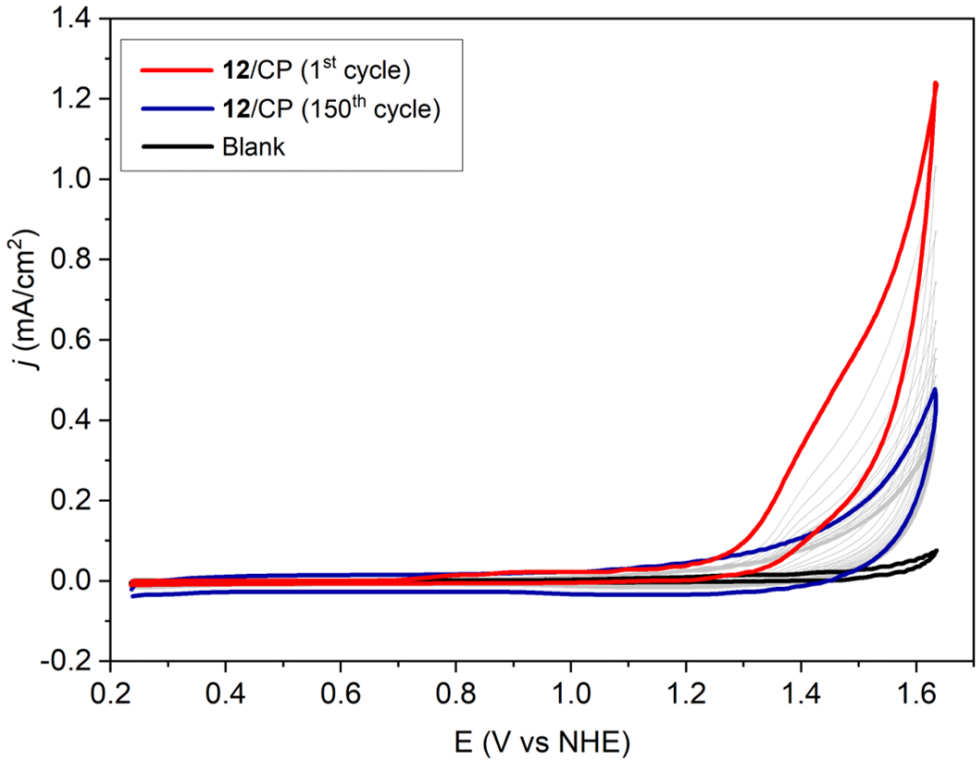

Figure 4.15: Repetitive CV at pH = 7.2 comparing the response of the **12**/CP electrodes during the first scan (red), the final scan after 150 cycles (blue) and a control experiment in the absence of **12** (black).

In this experiment, the **12**/CP electrodes clearly demonstrate catalytic activity which is not exhibited by the control electrode. OER activity by **12** occurs at a potential of 1.28 V vs. NHE, which corresponds to an onset overpotential for H_2O oxidation η = 465 mV at pH ≈ 7. This potential is low relative to the onset overpotential reported for many other earth-abundant

transition metal WOCs reported in the literature.[35,46,47] Furthermore, a shoulder in the response signal of the modified carbon paste electrode at *ca*. 1.45 V can be assigned to a one-electron oxidation of Co^{II} to Co^{III}.

In line with the WOC recycling experiments conducted under photocatalytic conditions, catalyst deactivation is observed over repeated cycles: The OER activity decreases within the first 10 cycles and then remains relatively stable for the remainder of the experiment. The maintained OER activity of **12** over repeated cycles can be attributed to the stabilizing effect of the carbon blend.[47]

Decomposition of **12** under the working conditions of this experiment leading to the *in-situ* formation of CoO_x or Co–Pi species would result in an increased current density at lower potentials over repeated cycles.[48,49,50] As this behavior is not observed in the repetitive CV experiment at pH = 7.2, it is rational to assume that **12** is not a precatalyst which forms CoO_x nanoparticles or Co–Pi *in-situ*. This observation, in combination with the post-catalytic characterization of **12** carried out ahead of light-induced O_2 evolution experiments strongly suggest that **12** is a genuine WOC at near-neutral pH.

Repetitive Cyclic Voltammetry at pH = 9.0

The response of a **12**/CP electrode containing 5 wt.-% of **12** in a repetitive CV experiment under basic conditions over 150 cycles is shown in Fig 4.16. The voltammogram shows that when the experiment is conducted using a borate buffer at pH = 9.0, the decomposition of **12** into CoO_x species is favoured. This transformation is associated with an observed increase in current density and OER activity at lower potentials after repeated cycles. This phenomenon has previously been reported in the literature, where Co^{II}-containing catalysts have been observed to decompose into CoO_x species under electrochemical conditions under basic, borate-buffered working conditions.[51]

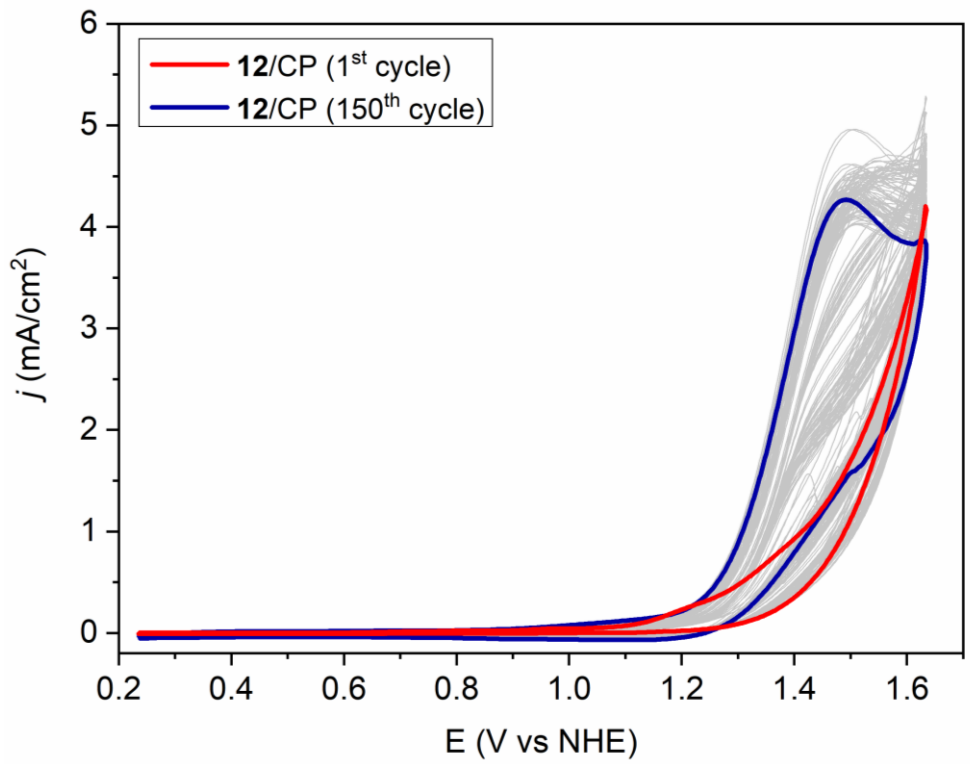

Figure 4.16: Repetitive CV experiment at pH = 9.0 comparing the response of **12**/CP electrodes during the first scan (red) and the response during the final scan after 150 cycles (blue).

The electrocatalytic investigations outlined confirm that **12** is active towards the OER under electro- and photochemical conditions. The overpotential required for the onset of catalytic activity (η = 465 mV) at neutral pH demonstrates the competency of **12** to catalyse the OER, corroborating the results of photocatalytic experiments using this H_2O oxidation catalyst.

4.3.4 Computational Analysis

A thermodynamic analysis at the DFT-B3LYP level employing a methodology by Van Voorhis *et al.*[52] was conducted by Dr. Joaquín Soriano-López to elucidate the mechanism of O_2 evolution by **12**. As pseudo first-order kinetics are observed in light-driven H_2O oxidation experiments, and because direct coupling between two oxo moieties is prohibited due to the separation of the Co^{II} centres of **12**, the O–O bond formation step was assumed to occur *via* a H_2O nucleophilic attack (WNA) pathway. Therefore, a single-site model in which **L3** was replaced by 1*H*-imidazol-4-ylmethylenenimine-phenyl (**L3'**) to give $[Co(\mathbf{L3'})_2(H_2O)_2]^{2+}$ was employed in the computational analysis. The proposed catalytic cycle for H_2O oxidation by **12** is presented in Fig. 4.17.

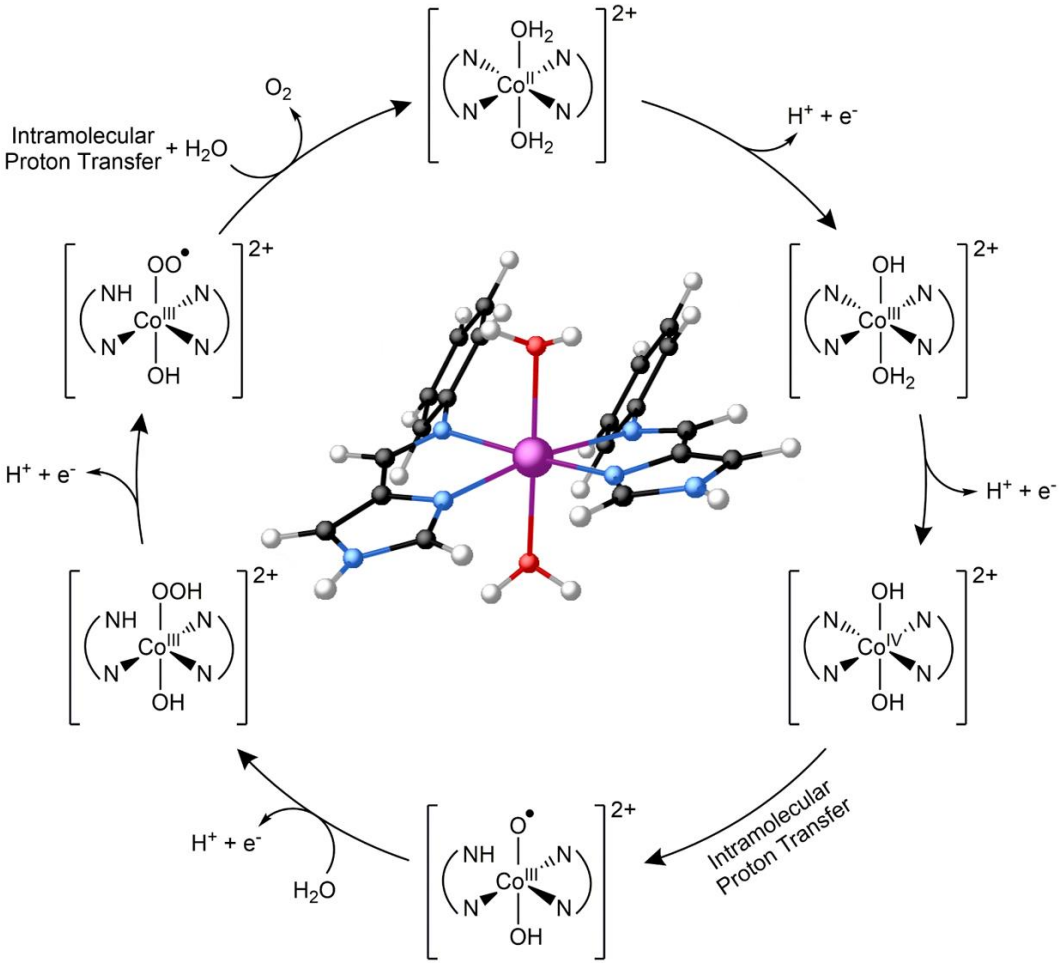

Figure 4.17: Proposed mechanism for O_2 evolution for $[Co(\mathbf{L3'})_2(H_2O)_2]^{2+}$ based on DFT calculations at the B3LYP level. Colour scheme: C black, N blue, O red, Co Violet.

DFT calculations reveal that the reaction proceeds *via* two PCET steps in which the two coordinated H_2O molecules are first deprotonated, followed by two one-electron oxidations of the Co^{II} centre generating $[Co^{IV}(\mathbf{L3'})_2(OH)_2]^{2+}$. These PCET events at 1.64 V and 1.67 V (vs. NHE at pH = 7) agree well with the experimental CV. Nucleophilic H_2O binding, followed by a PCET typically occurs when a WOC's oxo-group has an unoccupied molecular orbital localized at the O-atom, which acts as an electron acceptor.[53] Thus, for $[Co^{IV}(\mathbf{L3'})_2(OH)_2]^{2+}$ additional deprotonation events are required, as the LUMO of this species shows no contribution from the hydroxyl O-atoms (Fig. 4.18a).

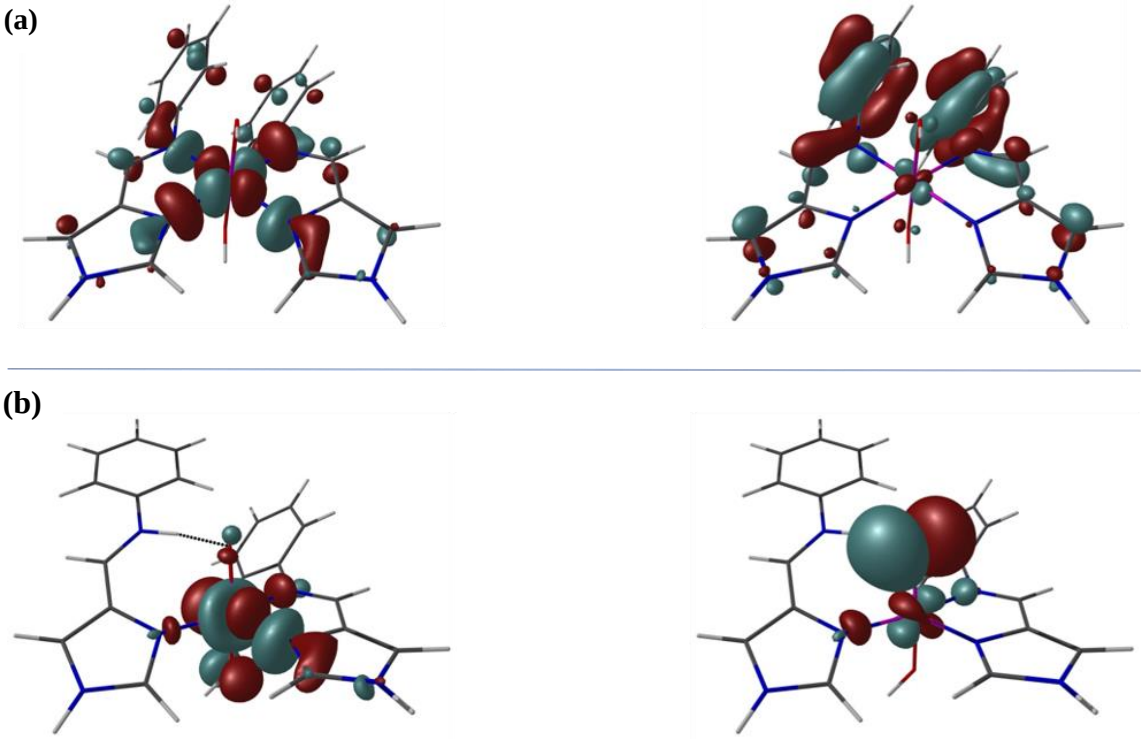

Figure 4.18: LUMOs of the alpha and beta electrons of the species $[Co^{IV}(\mathbf{L3'})_2(OH)_2]^{2+}$ (a), and the LUMOs of the alpha and beta electrons of the species $[Co^{III}(H\mathbf{L3'})(\mathbf{L3'})(O^{\bullet})(OH)]^{2+}$ (b). The LUMO of the beta electrons of the species $[Co^{III}(H\mathbf{L3'})(\mathbf{L3'})_2(O^{\bullet})(OH)]^{2+}$ is mainly localized on the oxyl radical, indicating that this is the active species for accepting the WNA. **L3'** = 1*H*-imidazol-4-ylmethylenenimine-phenyl.

Proton transfer then occurs intramolecularly, whereby the basic N-atom of the imine moiety of **L3'** acts as H^+-acceptor, yielding $[Co^{III}(H\mathbf{L3'})(\mathbf{L3'})(O^{\bullet})(OH)]^{2+}$, which formally represents a Co^{III}-oxyl radical. The formation of Co^{III}-oxyl over Co^{IV}-oxo species has previously been reported for other Co^{II}-based OER catalysts.[54] This

intramolecular proton transfer step requires a Gibbs energy of 0.20 eV, and the LUMO of the species is mainly localized at the O-atom of the Co^{III}-oxyl radical (Fig. 4.18b).

The alternative proton transfer from $[Co^{IV}(\mathbf{L3'})_2(OH)_2]^{2+}$ to the bulk solution would require a Gibbs energy of 1.69 eV, which renders this process highly unfavourable. Hence, the reaction is expected to form $[Co^{III}(H\mathbf{L3'})(\mathbf{L3'})(O^{\bullet})(OH)]^{2+}$ followed by a PCET event to yield $[Co^{III}(H\mathbf{L3'})(\mathbf{L3'})_2(OOH)(OH)]^{2+}$ requiring an overall Gibbs energy of 1.29 eV.

Finally, the formation of the superoxide species $[Co^{III}(H\mathbf{L3'})(\mathbf{L3'})_2(OO^{\bullet})(OH)]^{2+}$ at 0.56 V facilitates O_2 evolution. The catalyst is then regenerated with H_2O coordination, intramolecular proton transfer and reformation of the Co – N bond. This final mechanistic step is exergonic with a Gibbs free energy of −2.16 eV. This mechanism defines the second PCET event as the potential-determining step, which has a theoretical overpotential of 853 mV. This agrees well with the experimentally determined value of 846 mV to reach 1 mA/cm^2.

4.4 Conclusion and Future Work

In this chapter, the synthesis and physicochemical characterisation of an imine-stabilised Co^{II}-based polygon $[Co^{II}_3(\mathbf{L3})_2(H_2O)_6]^{6+}$ with a trigonal-disc-like structure is described. This metallo-supramolecular compound assembles through an extensive network of halogen and hydrogen bonding interactions to give rise to the halide-metal-organic framework structure $[Co^{II}_3(\mathbf{L3})_2(H_2O)_6]Cl_6 \cdot DMF \cdot 6H_2O$ (**12**).

For the first time, catalytic studies have demonstrated that **12** is a competent catalyst for the highly endergonic OER reaction under photo- and electrochemical conditions. A *max*. TON = 74.3 and TOF = 1.21 s^{-1} were achieved in photocatalytic experiments, and under electrocatalytic conditions, a low onset overpotential for catalytic H_2O oxidation of η = 465 mV was observed. Post-catalytic characterisation of **12** following use in the light-driven OER could not detect Co^{II} leaching into the supernatant, or the *in-situ* formation catalytically active CoO_x species or Co–Pi, strongly suggesting that **12** is a genuine WOC.

DFT calculations support the experimental data and attribute OER activity of **12** to a Co^{III}-oxyl species. This thermodynamic analysis also identified the beginning of a likely decomposition pathway, as a Co – N bond is cleaved and reformed during the catalytic cycle. This finding is in line with the detection of sub-components of the ligand **L3** in the post-catalytic reaction mixture using ESI mass spectroscopy. As **12** and other supramolecules are generated through sub-component synthesis,[4] reversible disassembly/assembly cycles may be applied in future H_2O splitting systems to prepare catalysts with prolonged activity, hence applying supramolecular concepts to create 'self-healing' WOCs.[55]

4.5 References

1 D. J. Tranchemontagne, Z. Ni, M. O'Keeffe and O. M. Yaghi, *Angew. Chem. Int. Ed.*, 2008, **47**, 5136–5147.

2 O. M. Yaghi, M. O'Keeffe, N. W. Ockwig, H. K. Chae, M. Eddaoudi and J. Kim, *Nature*, 2003, **423**, 705–714.

3 C. J. Brown, F. D. Toste, R. G. Bergman and K. N. Raymond, *Chem. Rev.*, 2015, **115**, 3012–3035.

4 M. Yoshizawa, J. K. Klosterman and M. Fujita, *Angew. Chem. Int. Ed.*, 2009, **48**, 3418–3438.

5 D. M. Kaphan, M. D. Levin, R. G. Bergman, K. N. Raymond and F. D. Toste, *Science*, 2015, **350**, 1235–1238.

6 B. Therrien, eds. M. Albrecht and E. Hahn, Springer Berlin Heidelberg, Berlin, Heidelberg, 2012, pp. 35–55.

7 J. Wang, C. He, P. Wu, J. Wang and C. Duan, *J. Am. Chem. Soc.*, 2011, **133**, 12402–12405.

8 M. D. Ward and P. R. Raithby, *Chem. Soc. Rev.*, 2013, **42**, 1619–1636.

9 H. Vardhan, M. Yusubov and F. Verpoort, *Coord. Chem. Rev.*, 2016, **306**, 171–194.

10 D. J. Tranchemontagne, Z. Ni, M. O'Keeffe and O. M. Yaghi, *Angew. Chem. Int. Ed.*, 2008, **47**, 5136–5147.

11 K. Byrne, M. Zubair, N. Zhu, X.-P. Zhou, D. S. Fox, H. Zhang, B. Twamley, M. J. Lennox, T. Düren and W. Schmitt, *Nat. Commun.*, 2017, **8**, 15268.

12 A. J. McConnell, C. M. Aitchison, A. B. Grommet and J. R. Nitschke, *J. Am. Chem. Soc.*, 2017, **139**, 6294–6297.

13 A. Ferguson, M. A. Squire, D. Siretanu, D. Mitcov, C. Mathonière, R. Clérac and P. E. Kruger, *Chem. Commun.*, 2013, **49**, 1597–1599.

14 W.-Y. Wu, X.-H. Fu, P. Jiang, T.-H. Tang, W.-Z. Li and R. Wan, *Inorg. Chem. Commun.*, 2018, **89**, 1–4.

15 R. A. Bilbeisi, J. K. Clegg, N. Elgrishi, X. de Hatten, M. Devillard, B. Breiner, P. Mal and J. R. Nitschke, *J. Am. Chem. Soc.*, 2012, **134**, 5110–5119.

16 B. M. Hunter, H. B. Gray and A. M. Müller, *Chem. Rev.*, 2016, **116**, 14120–14136.

17 D. Nesterov and O. Nesterova, *Catalysts*, 2018, **8**, 602.

18 J. Soriano-López, S. Goberna-Ferrón, L. Vigara, J. J. Carbó, J. M. Poblet and J. R. Galán-Mascarós, *Inorg. Chem.*, 2013, **52**, 4753–4755.

19 C. C. L. McCrory, S. Jung, I. M. Ferrer, S. M. Chatman, J. C. Peters and T. F. Jaramillo, *J. Am. Chem. Soc.*, 2015, **137**, 4347–4357.

20 I. McKeogh, PhD Thesis, Trinity College Dublin, 2015.

21 C. A. Hunter and J. K. M. Sanders, *J. Am. Chem. Soc.*, 1990, **112**, 5525–5534.

22 Q. Meng, J. Yang, S. Ma, M. Zhai and J. Lu, *Polymers*, 2017, **9**, 676.

23 S. Wang, W. Yao, J. Lin, Z. Ding and X. Wang, *Angew. Chem. Int. Ed.*, 2014, **53**, 1034–1038.

24 I. Krivokapic, M. Zerara, M. L. Daku, A. Vargas, C. Enachescu, C. Ambrus, P. Tregenna-Piggott, N. Amstutz, E. Krausz and A. Hauser, *Coord. Chem. Rev.*, 2007, **251**, 364–378.

25 G. Cavallo, P. Metrangolo, R. Milani, T. Pilati, A. Priimagi, G. Resnati and G. Terraneo, *Chem. Rev.*, 2016, **116**, 2478–2601.

26 C. F. Macrae, P. R. Edgington, P. McCabe, E. Pidcock, G. P. Shields, R. Taylor, M. Towler and J. van de Streek, *J. Appl. Crystallogr.*, 2006, **39**, 453–457.

27 J. J. Dannenberg, *J. Am. Chem. Soc.*, 1998, **120**, 5604.

28 R. Ramasamy, *Vibrational spectroscopic studies of imidazole*, 2015, vol. 8.

29 P. Drożdżewski, B. Pawlak and T. Głowiak, *J. Mol. Struct.*, 2003, **654**, 111–118.

30 M. D. Kärkäs, T. M. Laine, E. V Johnston and B. Åkermark, *Visible Light-Driven Water Oxidation Catalyzed by Ruthenium Complexes*, InTech, Rijeka, 2016.

31 W. Rüttinger and G. C. Dismukes, *Chem. Rev.*, 1997, **97**, 1–24.

32 A. Sartorel, M. Bonchio, S. Campagna and F. Scandola, *Chem. Soc. Rev.*, 2013, **42**, 2262–2280.

33 F. Evangelisti, P.-E. Car, O. Blacque and G. R. Patzke, *Catal. Sci. Technol.*, 2013, **3**, 3117–3129.

34 B. Schwarz, J. Forster, M. K. Goetz, D. Yücel, C. Berger, T. Jacob and C. Streb, *Angew. Chem. Int. Ed.*, 2016, **55**, 6329–6333.

35 M. D. Kärkäs and B. Åkermark, *Dalt. Trans.*, 2016, **45**, 14421–14461.

36 A. J. Bloomfield, S. W. Sheehan, S. L. Collom, R. H. Crabtree and P. T. Anastas, *New J. Chem.*, 2014, **38**, 1540–1545.

37 D. M. Robinson, Y. B. Go, M. Greenblatt and G. C. Dismukes, *J. Am. Chem. Soc.*, 2010, **132**, 11467–11469.

38 J. D. Blakemore, H. B. Gray, J. R. Winkler and A. M. Müller, *ACS Catal.*, 2013, **3**, 2497–2500.

39 H. Liu, M. Schilling, M. Yulikov, S. Luber and G. R. Patzke, *ACS Catal.*, 2015, **5**, 4994–4999.

40 S. J. Folkman and R. G. Finke, *ACS Catal.*, 2017, **7**, 7–16.

41 S. Fukuzumi and D. Hong, *Eur. J. Inorg. Chem.*, 2014, **2014**, 645–659.

42 J. Soriano-López, F. Song, G. R. Patzke and J. R. Galan-Mascaros, *Front. Chem.*, 2018, **6**, 302.

43 Y. Li, W. Qiu, F. Qin, H. Fang, V. G. Hadjiev, D. Litvinov and J. Bao, *J. Phys. Chem.*

C, 2016, **120**, 4511–4516.

44 C.-Z. Yuan, Y.-F. Jiang, Z. Wang, X. Xie, Z.-K. Yang, A. B. Yousaf and A.-W. Xu, *J. Mater. Chem. A*, 2016, **4**, 8155–8160.

45 S. Zhao, C. Li, H. Huang, Y. Liu and Z. Kang, *J. Mater.*, 2015, **1**, 236–244.

46 D. K. Dogutan, R. McGuire and D. G. Nocera, *J. Am. Chem. Soc.*, 2011, **133**, 9178–9180.

47 M. Blasco-Ahicart, J. Soriano-Lopez, J. J. Carbo, J. M. Poblet and J. R. Galan-Mascaros, *Nat. Chem.*, 2018, **10**, 24–30.

48 J. B. Gerken, J. G. McAlpin, J. Y. C. Chen, M. L. Rigsby, W. H. Casey, R. D. Britt and S. S. Stahl, *J. Am. Chem. Soc.*, 2011, **133**, 14431–14442.

49 X. Deng and H. Tüysüz, *ACS Catal.*, 2014, **4**, 3701–3714.

50 M. W. Kanan and D. G. Nocera, *Science*, 2008, **321**, 1072–1075.

51 Q. Daniel, R. B. Ambre, B. Zhang, B. Philippe, H. Chen, F. Li, K. Fan, S. Ahmadi, H. Rensmo and L. Sun, *ACS Catal.*, 2017, **7**, 1143–1149.

52 L.-P. Wang, Q. Wu and T. Van Voorhis, *Inorg. Chem.*, 2010, **49**, 4543–4553.

53 J. Soriano-López, W. Schmitt and M. García-Melchor, *Curr. Opin. Electrochem.*, 2018, **7**, 22–30.

54 J. Soriano-López, D. G. Musaev, C. L. Hill, J. R. Galán-Mascarós, J. J. Carbó and J. M. Poblet, *J. Catal.*, 2017, **350**, 56–63.

55 C. Costentin and D. G. Nocera, *Proc. Natl. Acad. Sci.*, 2017, **114**, 13380–13384.

Chapter Five

Porphyrin-Based Metallo-Supramolecular Systems: Towards Photoactive H_2O Splitting Systems

5.1 Mn^{II}-Based Supramolecular Assemblies

5.1.1 Introduction

The industrial-scale implementation of solar-to-fuel technologies is provisory on the cost-effectiveness of such systems.[1,2] Research into non-noble metal-based H_2O splitting catalysts is therefore of great societal significance.[3] To date, numerous WOCs have been synthesised using 1st row transition metals such as Mn[4,5] Fe,[6,7] Co,[8,9] Ni,[10,11] Cu[12,13] and others.[14,15] While significant progress has been made in this area in recent years, 1st row transition metal-based WOCs are typically more labile than their noble metal-based counterparts.[16] This presents an obstacle to the development of robust and efficient WOCs based on 1st row transition metals which are capable of withstanding the harshly oxidising conditions necessitated by the OER.[17]

An additional technological challenge is presented by the replacement of the widely employed noble metal-based PS's such as $[Ru(bpy)_3]Cl_2$ or $[Ir(bpy)_3]Cl_2$ for light-driven H_2O splitting catalysis. Substitution of these well-established PS's with cheaper, earth-abundant alternatives may significantly lower the investment costs associated with artificial photosynthetic systems.[18] Noble metal-free chromophores explored in the literature include among others: porphyrins,[19,20] phthalocyanines,[21] Cu^I species[22] and semiconductors,[23] all of which have demonstrated photosensitising behaviour for either OER or HER catalysis.

Despite significant challenges, considerable scope remains to enhance transition metal-based photocatalytic H_2O splitting systems. For example, a promising design strategy to improve the efficiency of state-of-the-art molecular artificial photosynthetic assemblies involves the direct tethering of a PS to a WOC *via* either coordinative or covalent linkages.[24] Karadas *et al.* exemplified this approach with the linkage of the porphyrin PS 5,10,15,20-tetra(4-pyridyl)-21*H*,23*H*-porphyrin (TPyP) to a Co-doped Prussian blue analogue *via* bridging $Fe(CN)_5$ groups, giving the noble metal-free chromophore-catalyst assembly [CoFe-TPyP].[25] This system was shown to sustain efficient light-driven photocatalytic OER activity in the presence of a SEA for upwards of three hours.

With the aim of generating supramolecular assemblies comprising intrinsic chromophore-catalyst dyads, a series of MMPFs composed of porphyrin linkers and potentially redox-active SBUs were synthesised. This design strategy was achieved using H_2**L1**-M metalloporphyrins (where M = Cu^{II} or Ni^{II}) as ligands in conjunction with Mn^{II}-based SBUs. These linkers were selected due to the established utility of Cu^{II} and Ni^{II} metalloporphyrin complexes as PS's for

light-driven H_2O splitting catalysis, and the redox properties, natural abundance and environmental benignity of Mn led to this metal's use.[26,27]

In this section, the syntheses, crystal structures and physicochemical characterisation of four novel Mn^{II}-based metallo-supramolecular assemblies constructed from H_2**L1**-Cu^{II} (**13** and **14**) or H_2**L1**-Ni^{II} (**15** and **16**) ligands are discussed. Following on from this, an investigation into the catalytic activities of **13** – **16** towards the light-driven OER and HER is described.

5.1.2 Synthesis, Characterisation and Catalytic Activity of Mn^{II}L1-Cu^{II} Frameworks

Drawing inspiration from Nature's paragon H_2O splitting complex: PS II, the applied synthetic strategy encompassed the creation of supramolecular structures constructed from porphyrin PS's and Mn reaction centres.[28,29] To achieve this aim, the dicarboxylic acid ligand H_2**L1**-Cu^{II} was combined with a variety of Mn salts under a range of solvothermal conditions. This approach resulted in the successful synthesis of two novel compounds: the 1D coordination polymer $[Mn^{II}(H$**L1**-$Cu^{II})_2(DEA)_2]\cdot DEA$ (**13**, DEA = *N*,*N*-diethylacetamide), and the 2D MMPF $[Mn^{II}($**L1**-$Cu^{II})(MeOH)_2]\cdot DEA\cdot MeOH$ (**14**).

The formation of **13** and **14** is reproducible and proceeds in good yield. Both products crystallise from the same reaction mixture and could not be manually separated as the crystals are indistinguishable based on their physical appearance. Moreover, because these closely structurally related compounds exhibit similar densities, attempts to purify **13** and **14** by suspending them in an organic solvent of appropriate density were unsuccessful. Changing the composition of the solvent system resulted in all of the suspended crystals simultaneously sinking or floating. In this section the synthesis, crystal structures, physicochemical characterisation and H_2O splitting properties of **13** and **14** are described.

5.1.2.1 Synthesis of [Mn^{II}(HL1-Cu^{II})$_2$(DEA)$_2$]·DEA (13) and [Mn^{II}(L1-Cu^{II})(MeOH)$_2$]·DEA·MeOH (14)

The 1D coordination polymer [Mn^{II}(H**L1**-Cu^{II})$_2$(DEA)$_2$]·DEA (**13**) and the 2D MMPF [Mn^{II}(**L1**-Cu^{II})(MeOH)$_2$]·DEA·MeOH (**14**) were synthesised in a reproducible reaction between H_2**L1**-Cu^{II} and $MnCl_2·2H_2O$ in a mixture of DEA and MeOH. Heating this reaction mixture under solvothermal conditions for three days, before slowly cooling to ambient temperature afforded the formation of uniform rod-shaped crimson crystals of **13** and **14** in good yield (40%). The crystals were of suitable quality for analysis using single crystal X-ray diffraction.

5.1.2.2 Crystal Structure of [Mn^{II}(HL1-Cu^{II})$_2$(DEA)$_2$]·DEA (13)

The crystal structure of **13** was solved in the monoclinic space group *C*2/c. **13** is a 1D coordination polymer featuring linear chains which extend in parallel with the (-1-11) crystallographic direction. **13** is characterised by octahedral Mn^{II} centres which are bridged by linear, ditopic porphyrin (H**L1**-Cu^{II})$^-$ linkers (Fig. 5.1a). Each Mn^{II} centre in the crystal structure of **13** is bridged by two (H**L1**-Cu^{II})$^-$ ligands, which gives rise to polymeric chains of mononuclear Mn^{II} SBUs connected by 'double-decker' porphyrin moieties (Fig. 5.1b).

The asymmetric unit of **13** contains one Mn^{II} ion which has a crystallographic occupancy of ½, one singly-deprotonated (H**L1**-Cu^{II})$^-$ metalloporphyrin linker, one DEA molecule which is coordinated to the Mn^{II} centre and one crystallographically half-occupied DEA constitutional solvent molecule. **13** is centrosymmetric, with the Mn^{II} ion locating on an inversion centre. Each Mn^{II} centre in the polymer chain is coordinated by four carboxylate moieties of four different bridging (H**L1**-Cu^{II})$^-$ linkers, all of which adopt monodentate η^1 coordination modes.

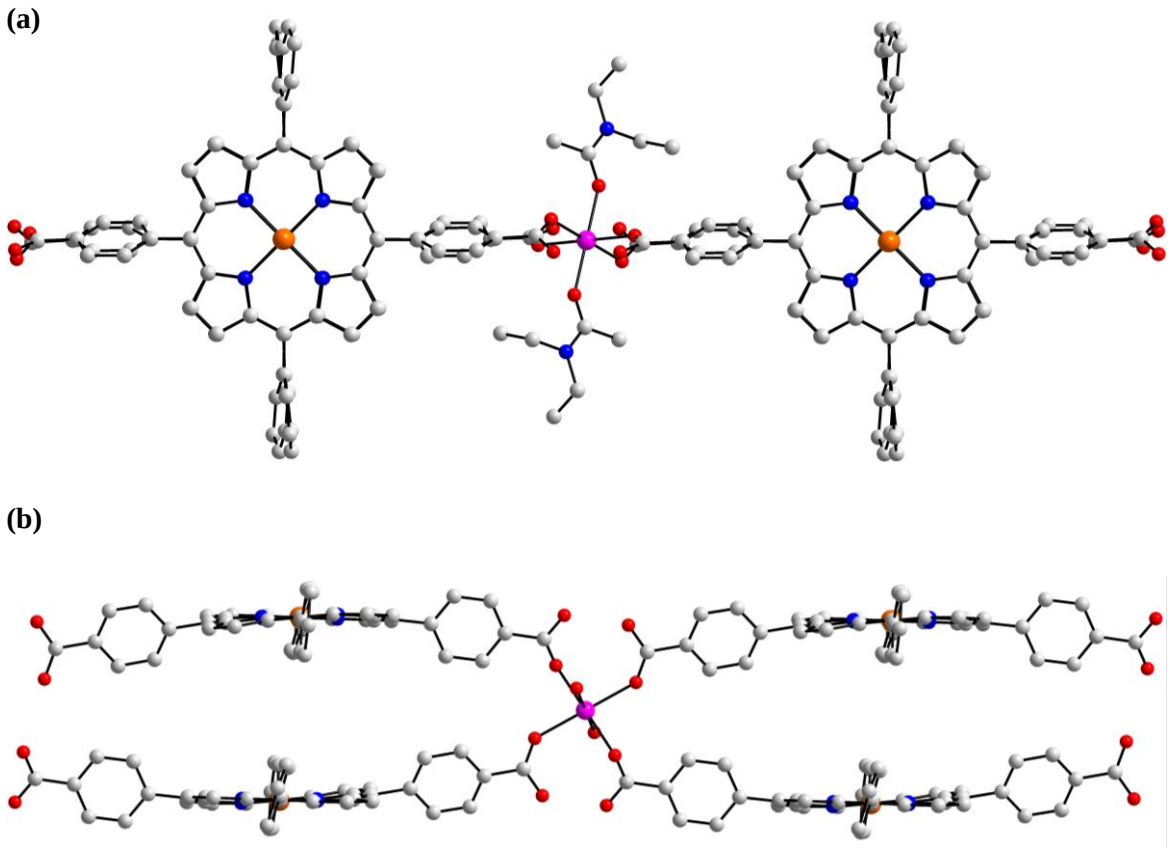

Figure 5.1: Ball-and-stick representation of the coordination polymer $[Mn^{II}(H\mathbf{L1}\text{-}Cu^{II})_2(DEA)_2]\cdot DEA$ (**13**) showing (a) the polymer chain which extends in parallel with the crystallographic [-1-11] direction, and (b) Mn^{II} centre coordinated by four $(H\mathbf{L1}\text{-}Cu^{II})^-$ linkers which adopt 'double-decker' configurations. Hydrogen atoms, constitutional and coordination solvent have been omitted for clarity. Colour scheme: C white, N blue, O red, Mn pink, Cu orange.

A detailed representation of the coordination environment of the Mn^{II} centre Mn(1) in **13** is displayed in Fig. 5.2. The binding geometry adopted by Mn(1) is distorted octahedral, and the coordination sphere constitutes four carboxylate O-donors O(2), O(2′), O(4) and O(4′) of four monodentate η^1 coordinating $(H\mathbf{L1}\text{-}Cu^{II})^-$ ligands, and two O-donors O(3) and O(3′) of two coordinated DEA solvent molecules. The carboxylate O-donors O(2), O(2′), O(4) and O(4′) coordinate at equatorial positions, whereas the two O-donors O(4) and O(4′) which derive from DEA solvent moieties coordinate *trans* with respect to one another and occupy axial positions of the coordination sphere.

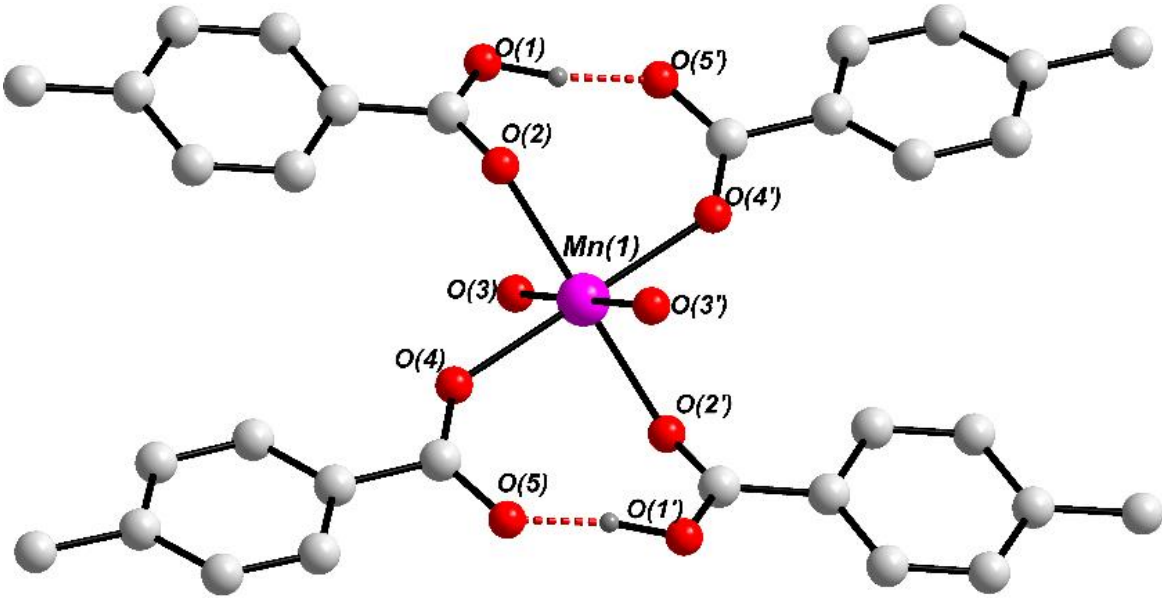

Figure 5.2: Ball-and-stick representation of the mononuclear Mn^{II} SBU of **13** and its coordination environment. Non-hydrogen bonding hydrogen atoms, constitutional solvent molecules and coordinated solvent molecules have been omitted for the purpose of clarity. Hydrogen bonds are represented as dashed red lines. Colour scheme: C white, H grey, O red, Mn pink.

The bond distances between Mn(1) and each of the monodentate carboxyl(ate) derived O-donors are 2.1521(2) Å for Mn(1) – O(2) and Mn(1) – O(2') and 2.1740(1) Å for Mn(1) – O(4) and Mn(1) – O(4'). The distance between the Mn^{II} centre and the O-donors of the DEA coordination solvent moieties is 2.1541(1) Å for Mn(1) – O(3) and Mn(1) – O(3'). The bond angles surrounding Mn(1) that deviate most significantly from the ideal octahedral angle of 90° are 87.73(1)° and 93.25(1)° for O(2)-Mn(1)-O(4) and O(3)-Mn(1)-O(4), respectively. These bond distances and angles render the coordination geometry of Mn(1) slightly distorted octahedral. The values are within expected ranges, and are consistent with the bond distances and angles of comparable Mn^{II}-based carboxylate complexes reported in the literature.[30]

Hydrogen bonding interactions stabilise the structure of **13**. These supramolecular forces propagate parallel with the direction of the polymer chain and are highlighted in Fig. 5.2. Each $(H\mathbf{L1}\text{-}Cu^{II})^{-}$ ligand forms two strong hydrogen bonds with two neighbouring $(H\mathbf{L1}\text{-}Cu^{II})^{-}$ linkers within the chain. The distance between the hydrogen bond donors and the hydrogen bond acceptors within **13** is 2.4311(1) Å, and the hydrogen bond angle O(1) – H···O(5') is 160.32(3)°. These values are consistent with hydrogen bond distances and angles reported in the literature.[31,32]

Neighbouring polymer chains in the crystal structure of **13** are stabilised by weak π – π interactions. The average distance between π – π stacking (H**L1**-Cu^{II})$^{-}$ linkers of two neighbouring polymeric strands is *ca*. 3.8 Å, which is within the typical range for a weak π – π interaction.[33] The interatomic distance between two connected Mn^{II} centres within a polymer chain is 22.1630(6) Å, and the distance between two (H**L1**-Cu^{II})$^{-}$ linkers within the same chain is *ca*. 6.8 Å.

The metalloporphyrin (H**L1**-Cu^{II})$^{-}$ moiety of **13** is shown in Fig. 5.3. The macrocycle adopts a saddle-shaped configuration and features a central tetracoordinate Cu^{II} ion Cu(1). The coordination geometry of this ion is distorted square-planar, and the bond angles between Cu(1) and the pyrrolic N-donors at opposite positions of the macrocycle's internal cavity are 177.45(2)° and 176.56(2)° for N(1)-Cu(1)-N(3) and N(2)-Cu(1)-N(4), respectively. This slight deviation from the ideal angle of 180° results in the non-planar arrangement of the linker, and also allows the relatively small Cu^{II} ion to be accommodated within the metalloporphyrin's central cavity.

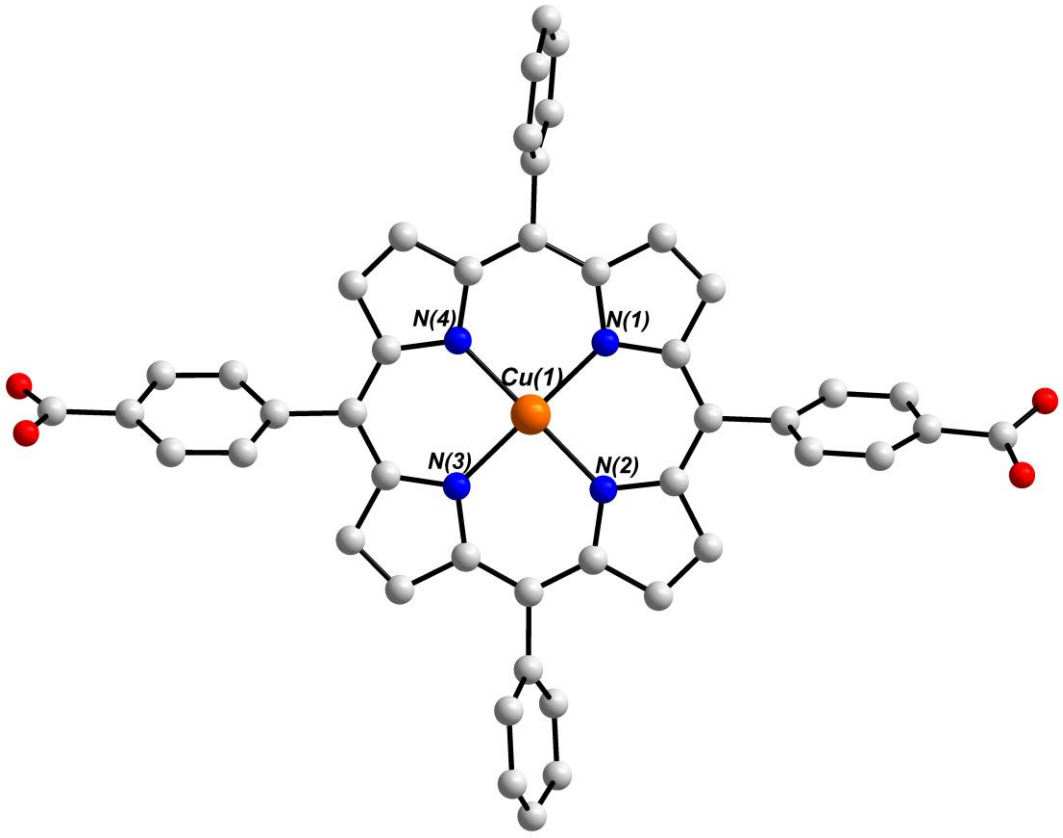

Figure 5.3: Ball-and-stick representation of the ditopic metalloporphyrin linker (H**L1**-Cu^{II})$^{-}$. Hydrogen atoms have been omitted for clarity. Colour scheme: C white, N blue, O red, Cu orange.

The dihedral angle between the carboxylate functionalised *meso* phenyl rings on opposite positions of the (H**L1**-Cu^{II})$^{-}$ linker is 11.53°. Similarly, the dihedral angle between the non-functionalised *meso* phenyl rings on opposite sides of the (H**L1**-Cu^{II})$^{-}$ linker is 14.93°. This configuration facilitates increased stabilisation of **13** through π – π stacking and hydrogen bonding interactions.

The (H**L1**-Cu^{II})$^{-}$ linker of **13** is deprotonated at two pyrrolic N – H moieties and one carboxylic acid moiety. The central Cu^{II} ion within the macrocycle gives the (H**L1**-Cu^{II})$^{-}$ ligand an overall charge of −1. As two (H**L1**-Cu^{II})$^{-}$ linkers coordinate per metal ion in **13**, Mn(1) must adopt an oxidation state of +2 in order to preserve charge neutrality. BVS analysis calculations were used to confirm the assignments of the oxidation states of the Mn^{II} and Cu^{II} ions in **13**.

The packing of **13** is illustrated in Fig. 5.4. Fig. 5.4a shows densely packed polymer chains which interdigitate, and small channels that extend in parallel with the crystallographic *b*-axis. Fig 5.4b depicts the layered architecture of **13**: Adjacent polymer chains stack on top of each other and are stabilized through π – π stacking interactions which extend in the direction of the crystallographic *b*-axis. These interactions generate a 2D supramolecular framework. The distance between porphyrin moieties of adjacent stacking polymer strands varies between 3.65 – 4.28 Å, which is consistent with distances reported in the literature for weak π – π stacking interactions.[34,33]

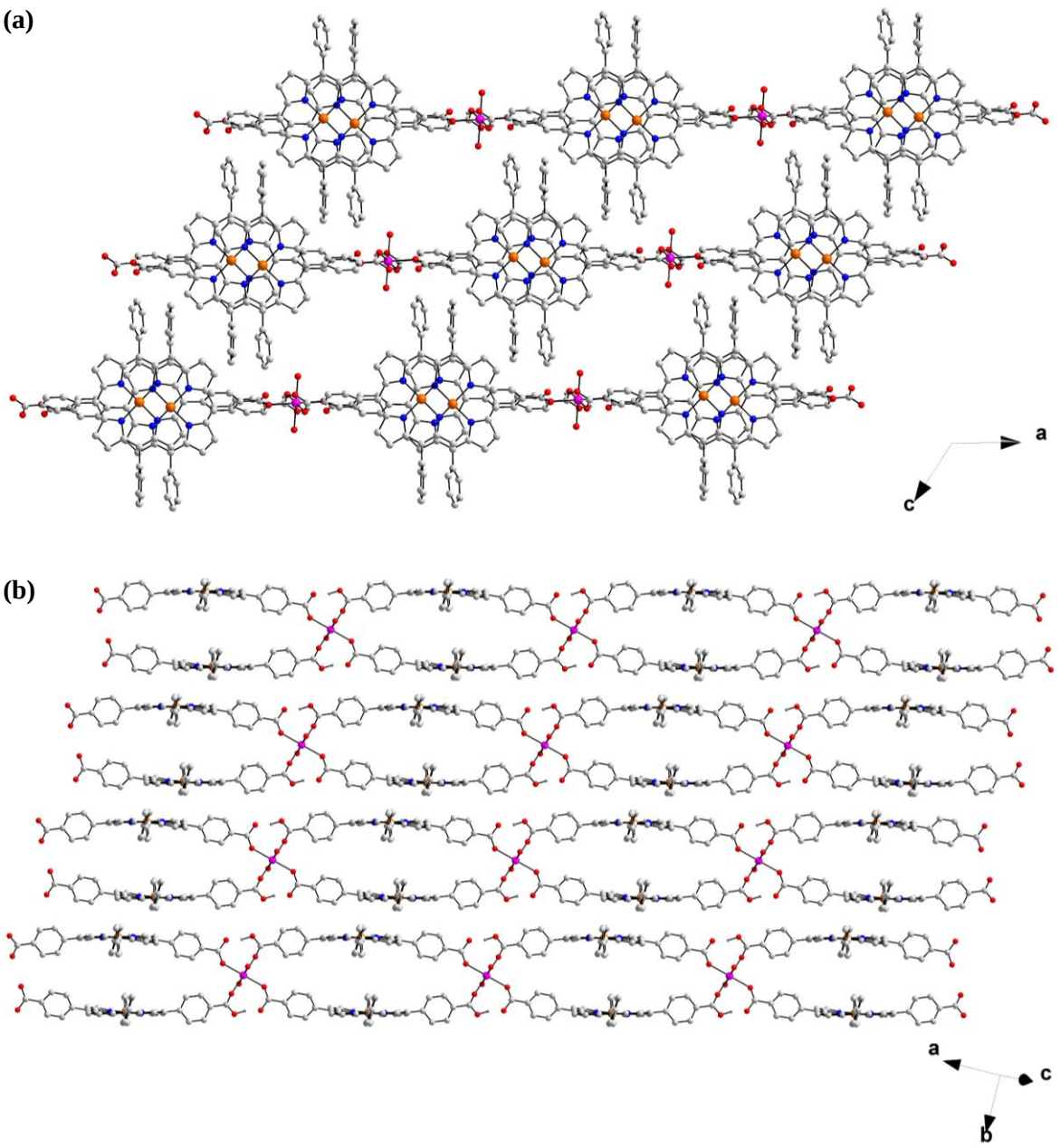

Figure 5.4: Ball-and-stick representation of the packing arrangement of **13** in the crystal structure showing (a) interdigitation between neighbouring polymer strands and (b) the 2D layered structure which is stabilised through π – π stacking interactions that extend approximately in the direction of the crystallographic *c*-axis. Constitutional solvent molecules, coordination solvent molecules and non-hydrogen bonding hydrogen atoms have been omitted for clarity. Colour scheme: C white, H grey, N blue, O red, Mn pink, Cu orange.

5.1.2.3 Crystal Structure of $[Mn^{II}(L1\text{-}Cu^{II})(MeOH)_2]\cdot DEA\cdot MeOH$ (14)

The 2D MMPF $[Mn^{II}(\mathbf{L1}\text{-}Cu^{II})(MeOH)_2]\cdot DEA\cdot MeOH$ (**14**) was identified as a 2nd product generated from the reproducible reaction which afforded the formation of **13**. Rod-shaped crimson crystals of **14** of suitable quality for single crystal X-ray analysis were obtained from the reaction outlined in section 5.1.2.1, allowing the crystal structure of **14** to be solved in the triclinic space group $P\bar{1}$.

The asymmetric unit of **14** comprises one octahedral Mn^{II} centre, to which one $(\mathbf{L1}\text{-}Cu^{II})^{2-}$ linker and two MeOH molecules coordinate. One DEA constitutional solvent molecule and one MeOH constitutional solvent molecule were also located in the asymmetric unit of **14**.

The MMPF **14** displays a 2D sheet architecture, featuring rod-shaped SBUs which extend infinitely in parallel with the direction of the crystallographic *a*-axis (Fig. 5.5). The SBU of **14** is composed of a chain of octahedrally coordinated Mn^{II} ions, each of which are bridged by four carboxylate moieties which derive from four different $(\mathbf{L1}\text{-}Cu^{II})^{2-}$ linkers. The bridging carboxylate functionalities of **14** adopt *syn-syn* bridging, $\mu_2\text{-}\eta^1\text{:}\eta^1$ binding modes.

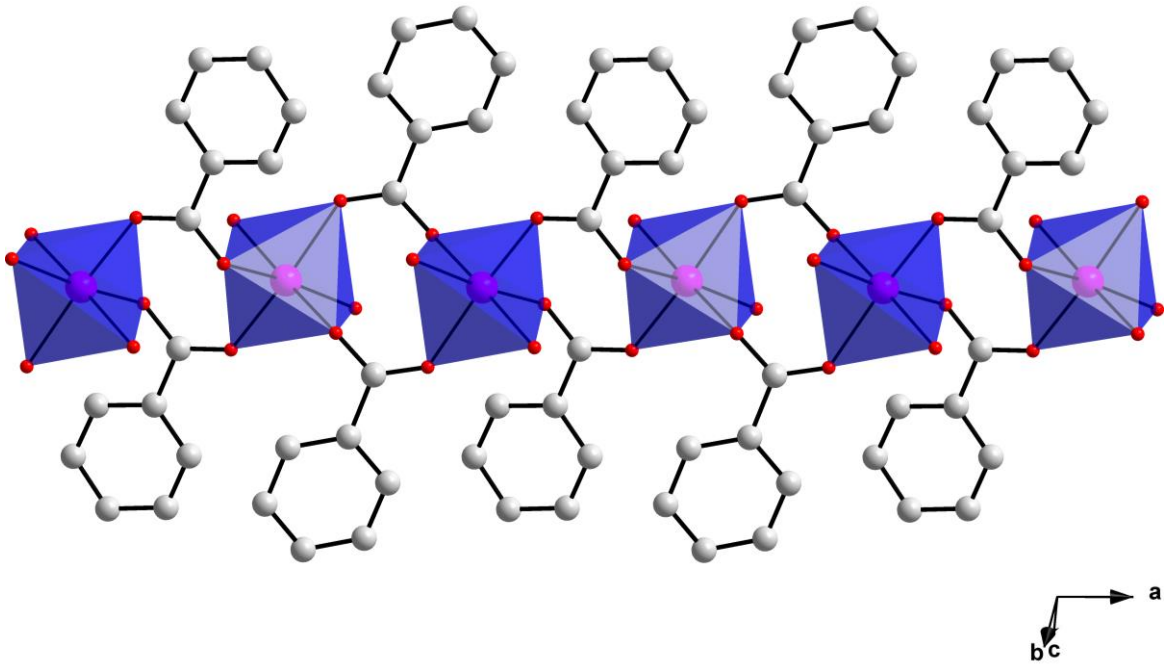

Figure 5.5: Ball-and-stick representation of the rod-shaped SBU of **14** which comprises an infinite 1D chain of octahedrally coordinated Mn^{II} centres. Mn^{II} ions within the SBU of **14** are linked through the *syn-syn* bridging carboxylate moieties of $(\mathbf{L1}\text{-}Cu^{II})^{2-}$ ligands. Hydrogen atoms, coordination solvent molecules and constitutional solvent molecules have been omitted for clarity. Colour scheme: C white, O red, Mn pink. Mn^{II} centres are represented as blue polyhedra.

The SBUs of **14** stack parallel, and each SBU is connected to two other SBUs *via* ditopic (**L1**-Cu^{II})$^{2-}$ linkers. This connectivity generates the 2D architecture of **14** which is shown in Fig. 5.6. The structure is stabilised by parallel-displaced π – π stacking interactions which extend approximately in parallel with the direction of the crystallographic *a*-axis. These interactions occur between adjacent porphyrin linkers within a 2D sheet which are separated by a distance of *ca*. 3.6 Å. The interatomic distance (Mn^{II} – Mn^{II}) between two connected rod-shaped SBUs of **14** is *ca*. 21.8 Å, whilst the interatomic distance between each Mn^{II} centre and the next Mn^{II} centre in a rod-shaped chain is *ca*. 4.6 Å.

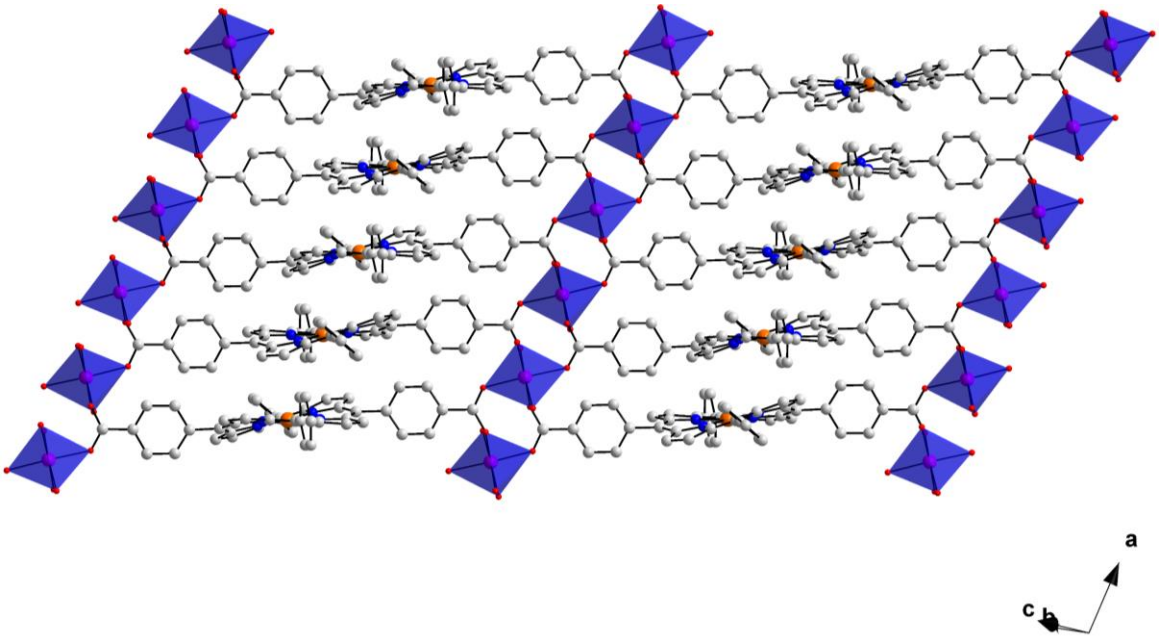

Figure 5.6: Ball-and-stick representation of the 2D sheet structure of **14** which is comprised of rod-shaped SBUs connected through (**L1**-Cu^{II})$^{2-}$ linkers. Crystallization solvent molecules, coordination solvent molecules and hydrogen atoms have been omitted for clarity. Colour scheme: C white, N blue, O red, Mn pink, Cu orange. Mn^{II} centres are shown as blue polyhedra.

A detailed representation of the coordination environment of the Mn^{II} centre Mn(1) in the SBU of **14** is displayed in Fig. 5.7. Mn(1) adopts a distorted octahedral coordination geometry. The coordination environment of Mn(1) comprises four O-donors O(1), O(3), O(5) and O(6) which derive from four *syn-syn* bridging, μ_2-η^1:η^1 binding carboxylate functionalities of four different (**L1**-Cu^{II})$^{2-}$ linkers. The coordination sphere of Mn(1) is completed by two O-donors O(2) and

O(4) that derive from two coordinated MeOH solvent moieties which occupy positions which are *cis* with respect to one another.

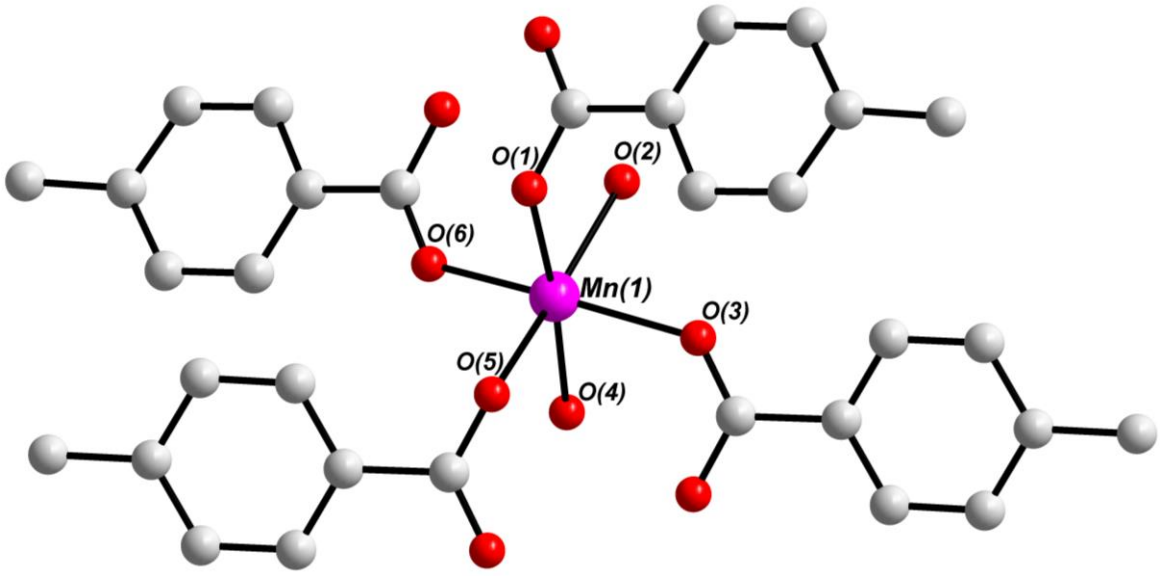

Figure 5.7: Ball-and-stick representation of the coordination environment of the Mn^{II} centre Mn(1) of **14**. Solvent of crystallisation, coordinated solvent molecules and hydrogen atoms have been omitted for clarity. Colour Scheme: C white, O red, Mn pink.

The bond distances between Mn(1) and each of the four carboxylate O-donors are 2.1721(1) Å, 2.1640(1) Å**,** 2.1507(6) Å and 2.1574(1) Å for Mn(1) – O(1), Mn(1) – O(3) Mn(1) – O(5) and Mn(1) – O(6), respectively. In contrast, the bond distances between Mn(1) and the O-donors which derive from coordinated MeOH molecules are 2.2275(1) Å and 2.2163(1) Å for Mn(1) – O(2) and Mn(1) – O(4), respectively. The relatively longer metal-oxygen bond lengths at the solvent coordination sites indicates that substitution of the more labile MeOH moieties may be possible. Exchange of these coordinated solvent molecules with a suitable substrate such as H_2O could precede catalytic transformations using **14**.

The bond angles which surround Mn(1) which deviate most significantly from the ideal octahedral angle of 90° are 86.37(4)° and 100.43(4)° for O(3)-Mn(1)-O(4) and O(1)-Mn(1)-O(3) respectively. Further, the bond angle surrounding Mn(1) exhibiting the greatest deviation from the ideal octahedral angle of 180° is 161.10(4)° for O(3)-Mn(1)-O(6). The bond distances and angles which surround Mn(1) render its coordination geometry distorted octahedral, and

are comparable with the bond distances and angles of other literature reported Mn^{II} – carboxylate complexes.[30,32]

The (**L1**-Cu^{II})$^{2-}$ linker in **14** is shown in Fig. 5.8. The metalloporphyrin ligand exhibits a saddle-shaped configuration and contains a central tetracoordinate Cu^{II} ion Cu(1). The bond angles between Cu(1) and the pyrrolic N-donors on opposite positions of the macrocycle's internal cavity are 172.08(5)° and 171.85(5)° for N(1)-Cu(1)-N(3) and N(2)-Cu(1)-N(4), respectively. These bond angles render the coordination geometry of Cu(1) distorted square planar.

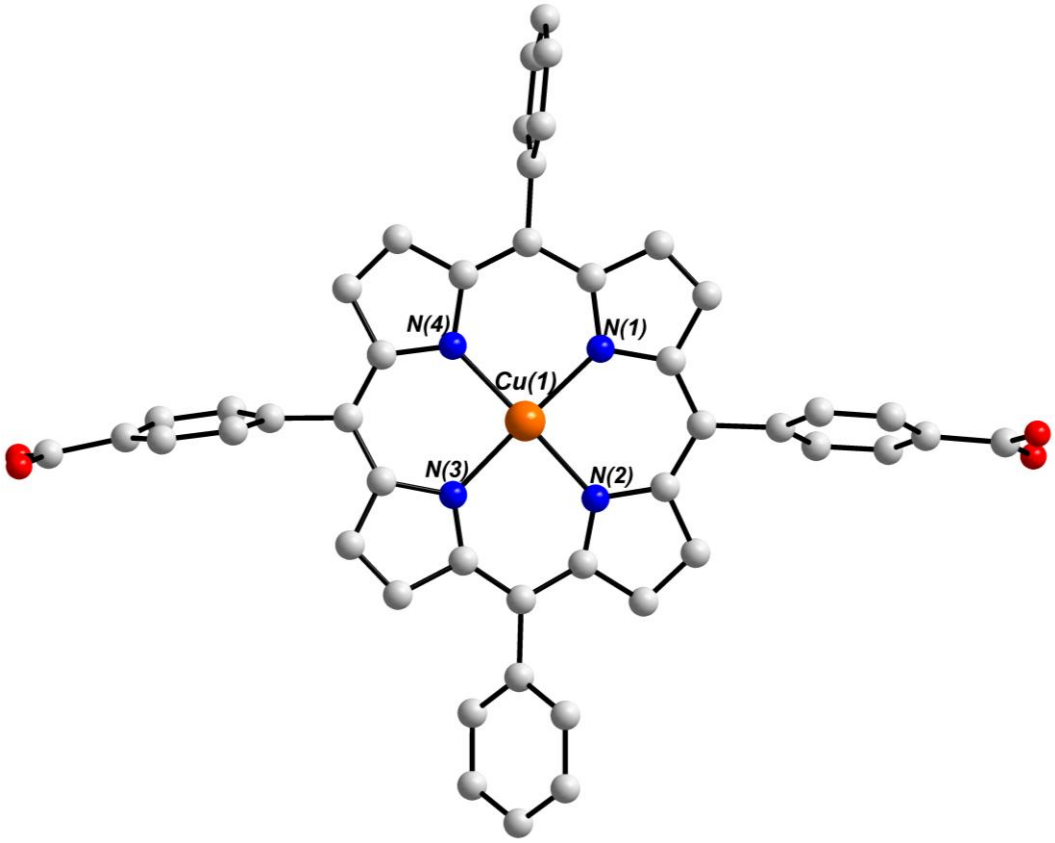

Figure 5.8: Ball-and-stick representation of the dicarboxylate metalloporphyrin (**L1**-Cu^{II})$^{2-}$. Hydrogen atoms have been removed for clarity. Colour scheme: C white, N blue, O red, Cu orange.

The dihedral angle between the carboxylate functionalised *meso* phenyl rings on opposite positions of the (**L1**-Cu^{II})$^{2-}$ linker is 26.5°, whereas the non-functionalised *meso* phenyl rings on opposite sides of the (**L1**-Cu^{II})$^{2-}$ linker are more staggered with a dihedral angle of 42.8°. This configuration facilitates increased stabilisation of **14** through π – π stacking interactions.

The (**L1**-Cu^{II})$^{2-}$ linkers in **14** are stabilized by two types of π – π stacking interactions: In addition to the parallel displaced π – π stacking interactions between porphyrin moieties within the same 2D sheet, T-shaped π – π stacking interactions occur between the non-functionalised *meso* phenyl rings and the tetrapyrrolic ring systems of porphyrin moieties of adjacent 2D layers. These interlayer interactions propagate in the direction of the crystallographic *b*-axis and extend the 2D structure into a 3D supramolecular framework. The distance between π – π stacking porphyrin moieties in **14** is within the range of *ca*. 3.4 – 3.9 Å, which is consistent with other π – π stacking interactions reported in the literature.[34,33]

The ditopic (**L1**-Cu^{II})$^{2-}$ linker is deprotonated at its two carboxylate binding sites, giving the linker a charge of −2. The porphyrin ligand is also deprotonated at its two N – H moieties, however this negative charge is balanced by the Cu^{II} ion Cu(1). As one porphyrin linker coordinates per metal centre in the crystal structure of **14**, it would be anticipated for Mn(1) to adopt an oxidation state of +2 to satisfy charge neutrality. The assignment of the oxidation states of the Mn^{II} and Cu^{II} ions in **14** was confirmed using BVS analysis calculations.

The packing of **14** in the crystal structure is displayed in Fig. 5.9. 2D sheets of **14** pack densely in the structure and porphyrin moieties interdigitate with neighbouring layers. Fig. 5.9a highlights small channels filled with constitutional solvent molecules which extend between layers in the direction of the crystallographic *a*-axis. The layered architecture of **14** is also depicted in Fig. 5.9b, in which infinite rod-shaped Mn^{II} chains *zig-zag* and extend in parallel with the crystallographic *a*-axis. The average distance between two neighbouring 2D sheets in **14** is *ca*. 14.5 Å.

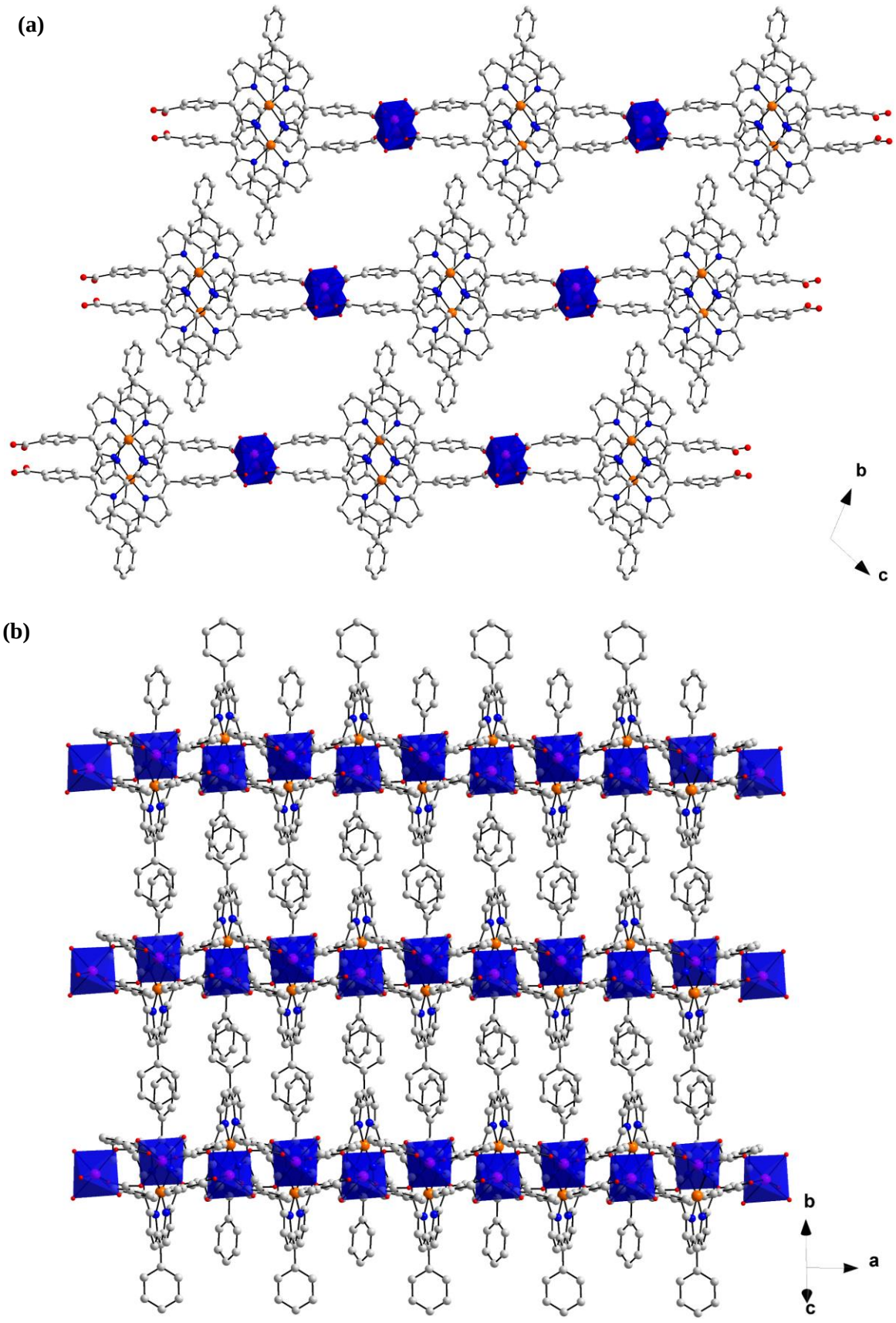

Figure 5.9: Ball-and-stick representation of the packing arrangement of **14** showing the structure's layered architecture. Solvent of crystallization, coordinated solvent molecules and hydrogen atoms have been omitted for clarity. Colour scheme: C white, N blue, O red, Mn pink, Cu orange. Mn^{II} centres are shown as blue polyhedra.

5.1.2.4 Physicochemical Characterisation of 13 and 14

As $[Mn^{II}(H\mathbf{L1}\text{-}Cu^{II})_2(DEA)_2]\cdot DEA$ (**13**) and $[Mn^{II}(\mathbf{L1}\text{-}Cu^{II})(MeOH)_2]\cdot DEA\cdot MeOH$ (**14**) have similar empirical compositions, form under the same reaction conditions and are indistinguishable based on their physical appearance, it is was necessary to characterise both materials as a mixture. In this section, the characterisation of a mixture of **13** and **14** using IR spectroscopy, TGA and PXRD analysis are described.

Infrared Spectroscopy

An FT-IR spectrum of **13** and **14** is presented in Fig. 5.10. Broad weak signals above 3000 cm^{-1} can be attributed to O – H stretching vibrations from the hydrogen bonding $(H\mathbf{L1}\text{-}Cu^{II})^{-}$ linkers of **13**, and from the constitutional MeOH solvent molecules of **13** and **14** which participate in hydrogen bonds.[35] A band at 2978 cm^{-1} can be associated with aromatic C – H stretching vibrations of the metalloporphyrin ligands of **13** and **14**. A signal at 1607 cm^{-1} can be assigned to a C = O stretching vibration of the DEA moieties of **13** and **14**.[36] A band at 1581 cm^{-1} can be associated with a carbonyl stretching vibration from the non-bridging η^1 carboxylate moiety of **13**.[37] Two strong signals at 1536 and 1398 cm^{-1} can be assigned to the asymmetric and symmetric stretching vibrational modes, respectively, of the bridging carboxylate moiety of **14**.[38] Finally, a sharp signal at 1001 cm^{-1} can be assigned to an in-plane deformation (ring breathing) of the $(\mathbf{L1}\text{-}Cu^{II})^{2-}$ linker.[39]

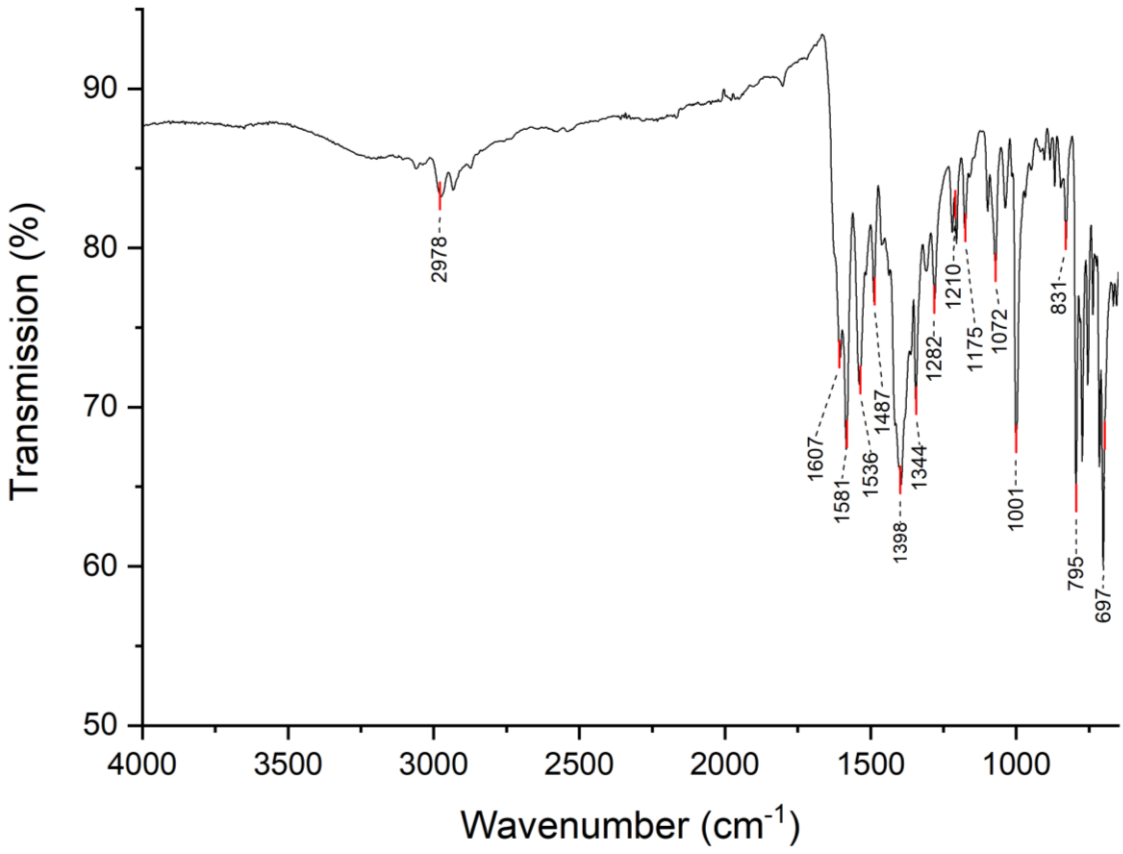

Figure 5.10: FT-IR spectrum of a mixture of **13** and **14**.

Thermogravimetric Analysis

Thermogravimetric analysis (TGA) was conducted on a crystalline sample of **13** and **14** under a constant stream of N_2 within a temperature range of 25 - 800 °C. The resulting TGA trace is plotted in Fig 5.11. When heated from 25 - 160 °C, the sample undergoes a weight loss of 3.4% which can be attributed to the loss of two constitutional MeOH solvent molecules (calculated: 3.0% for **13** or 5.1% for **14**). Other constitutional crystallisation solvent molecules are likely to have been lost before the TGA was performed. The next thermogravimetric step occurs between 160 – 450 °C and is associated with a weight loss of 12.6%. This can be accounted for by the loss of two DEA coordination solvent molecules from **13** and two MeOH coordination solvent molecules from **14** (calculated: 12.1% for **13** and 19.0% for **14**). Further heating of the mixture beyond 450 °C results in thermal decomposition of the product in two stages: Degradation of the organic components occurs from 450 – 520 °C and increasing the temperature above 520 °C can be associated with the formation of metal oxide species. As the magnitude of the thermal decomposition steps are more similar to the expected values for **13** than **14**, it can be assumed that the analysed sample contains a higher proportion of **13** than **14**.

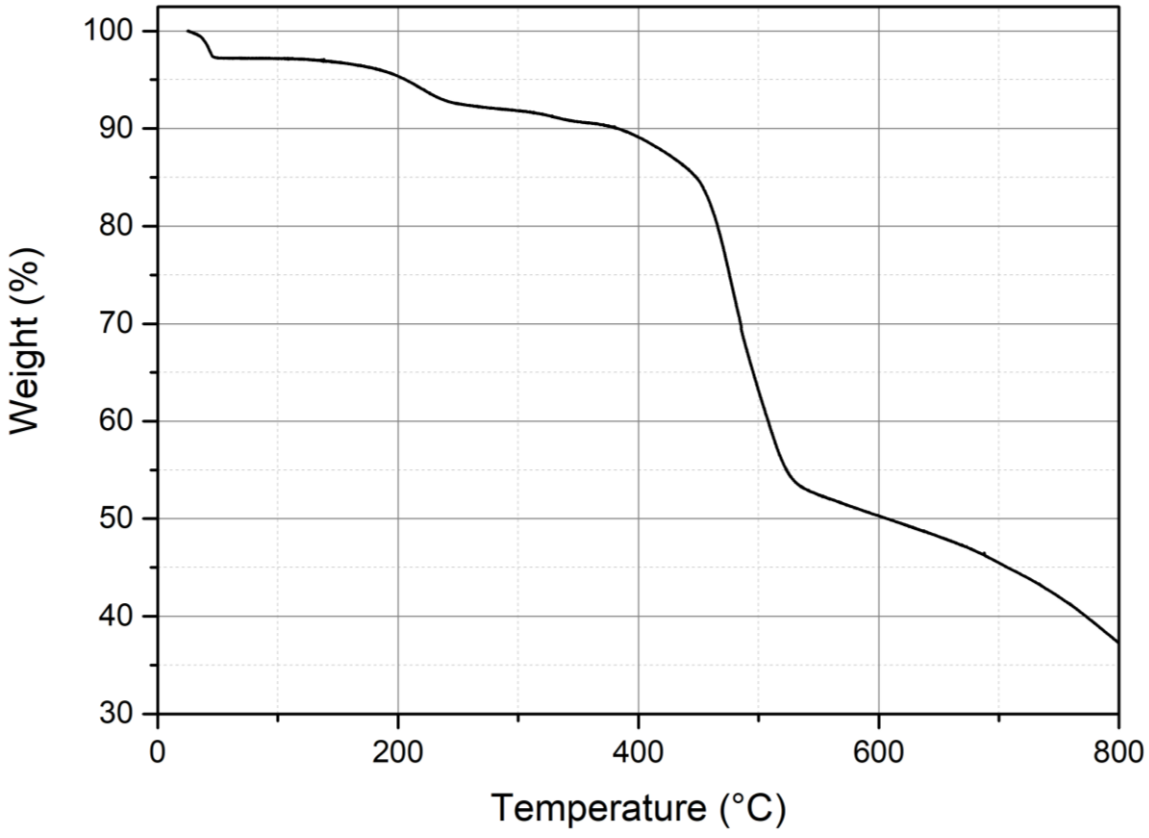

Figure 5.11: TGA trace of a mixture of **13** and **14**.

Powder X-Ray Diffraction Analysis

The powder X-ray diffraction (PXRD) pattern of a mixture of **13** and **14** (black) is compared with two simulated powder spectra which were calculated using the single crystal X-ray diffraction data of **13** (red) or **14** (blue) in Fig. 5.12. Upon removal of **13** and **14** from the mother liquor, the sample rapidly desolvates. Therefore, the sample was sealed inside a glass capillary before measuring. The experimentally obtained powder pattern agrees with the simulated spectra, as all of the signals of highest intensity in the measured powder pattern can be located in the calculated powder patterns of either **13** or **14**. Signals at $2\theta = 6.5°$ and $9.1°$ in the measured spectrum can be assigned to **13**, and a signal at $2\theta = 8.7°$ can be attributed to **14**. The fine structure is not completely resolved in the PXRD spectrum of **13** and **14**, which may result from preferred orientation effects in the sample or unrefined disordered solvent molecules in **13** and **14**. Based on the relative intensities of the signals assigned to **13** and **14**, the composition of the analysed sample can be estimated to contain a 2:1 ratio of **13** to **14**.

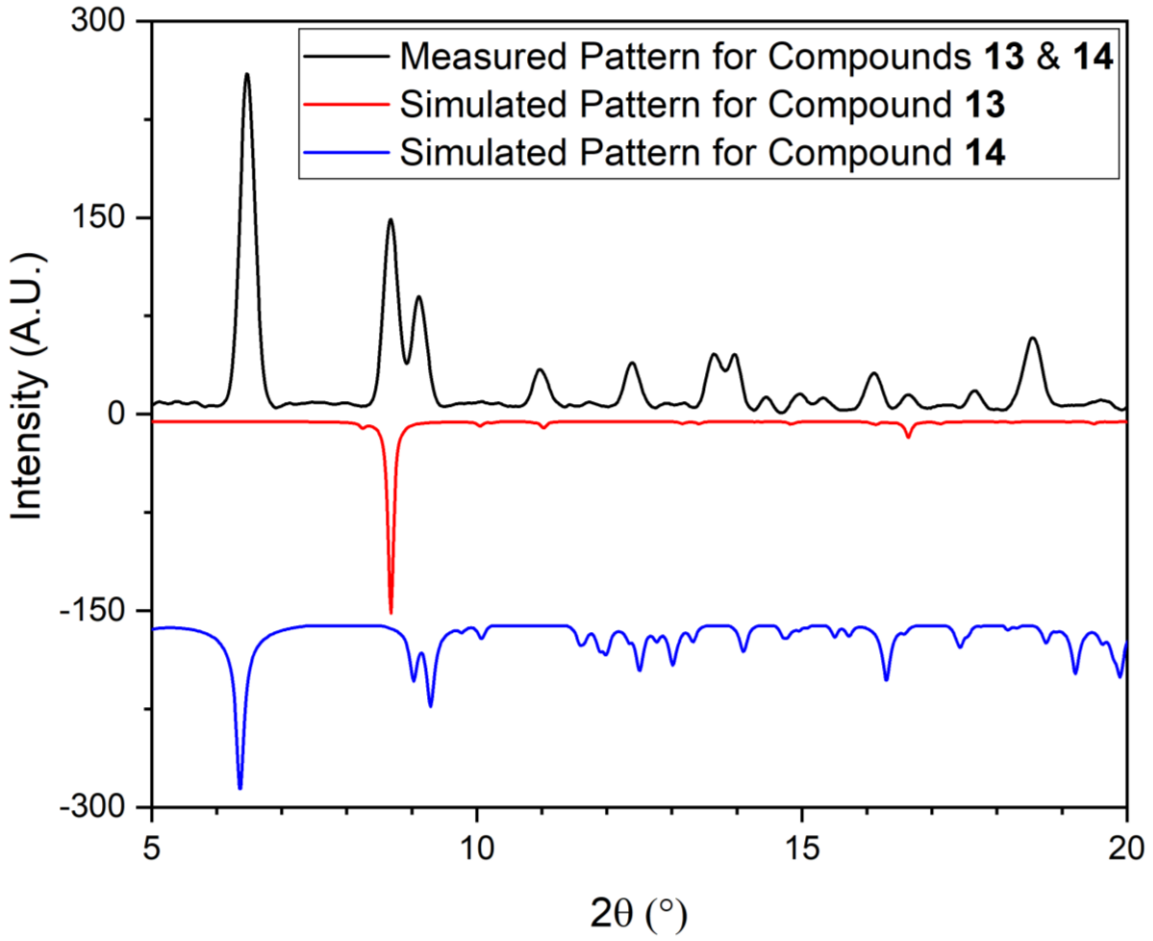

Figure 5.12: PXRD analysis comparing an experimentally obtained spectrum of a mixture of **13** and **14** (black) with simulated PXRD patterns calculated using the single crystal X-ray diffraction data of **13** (red) and **14** (blue)**.**

5.1.2.5 Catalytic Properties of 13 and 14

A mixture of **13** and **14** was screened for light-induced OER and HER activity to ascertain whether further catalytic studies whereby each compound would be isolated and investigated were warranted. Several attributes of the supramolecular assemblies **13** and **14** prompted this investigation: Firstly, both structures feature potentially redox-active Mn^{II}-based SBUs which are tethered to metalloporphyrin complexes that may serve as PS's for H_2O splitting reactions.[26,40] In addition, the coordination spheres of the Mn^{II} ions within the SBUs of **13** and **14** are partially occupied by labile solvent moieties. Exchange of these solvent molecules for either H_2O or H^+ substrates could precede OER or HER processes, respectively.

The Cu^{II}-based metalloporphyrin linkers of **13** and **14** represent another potentially viable catalytic constituent of these compounds. Notably, similar macrocyclic moieties have been employed as WOCs, indicating that the (**L1**-Cu^{II})$^{2-}$ ligands of **13** and **14** could display OER activity.[13,41] Finally, the metals Cu and Mn from which **13** and **14** are constructed are earth-abundant and environmentally benign. This array of favourable attributes led to **13** and **14** being examined as potential H_2O splitting photocatalysts. The results of this investigation are discussed in this section.

Initially, **13** and **14** were screened for catalytic activity towards the light-driven OER according to an modified literature protocol, and without the use of an external PS.[42] Prior to catalytic experiments, large individual crystals of **13** and **14** were manually picked, washed with H_2O and ground into a fine powder using a mortar and pestle. The powder (2 mg) was then added to an aqueous phosphate-buffered solution (5 mL, 0.01 M, initial pH = 7) containing $Na_2S_2O_8$ SEA (10 mM), before hermetically sealing this mixture inside a reaction vessel. The suspension was subsequently deoxygenated and irradiated using either a violet (λ = 405 nm) or a white (λ = 390 – 700 nm) LED while the dissolved O_2 concentration was simultaneously monitored in real-time using a Clark electrode. Unfortunately, the amount of O_2 evolved in this experiment was approximately equal to the quantity of O_2 released in a control experiment without **13** and **14** in the reaction mixture. Therefore, the experimental conditions were modified.

Unsuccessful attempts to use **13** and **14** as molecular chromophore-catalyst assemblies led to the photocatalytic OER experiment to be repeated, however with the addition of an external PS. O_2 evolution experiments were replicated as described above, however $[Ru(bpy)_2(deeb)](PF_6)_2$ PS (2 mg) was also added to the reaction mixture and the suspension

was irradiated using a blue LED (λ = 470 nm). The kinetics of light-driven O_2 evolution by a mixture of **13** and **14** (0.2 mg) in the presence of a $[Ru(bpy)_2(deeb)](PF_6)_2$ PS and $Na_2S_2O_8$ SEA are displayed in Fig. 5.13 (orange). The kinetics of a control experiment in which **13** and **14** were not added to the reaction vessel are also plotted for comparison (black).

Fig. 5.13 reveals that upon irradiation, the reaction mixture evolves O_2 for *ca*. 2 minutes, before the detected O_2 concentration inside the reactor reaches a plateau. The total quantity of O_2 evolved by **13** and **14** (72.5 nmol) is significantly higher than the O_2 yield of a control experiment in which no catalyst was added. However, this reaction is not truly catalytic as the TON < 1 (TON = 0.67 or 0.36 based on the molar masses of **13** and **14**, respectively). The TOF of the reaction was calculated as 2×10^{-3} s^{-1} based on the molar mass of **13** or 10^{-3} s^{-1} using the molar mass of **14**.

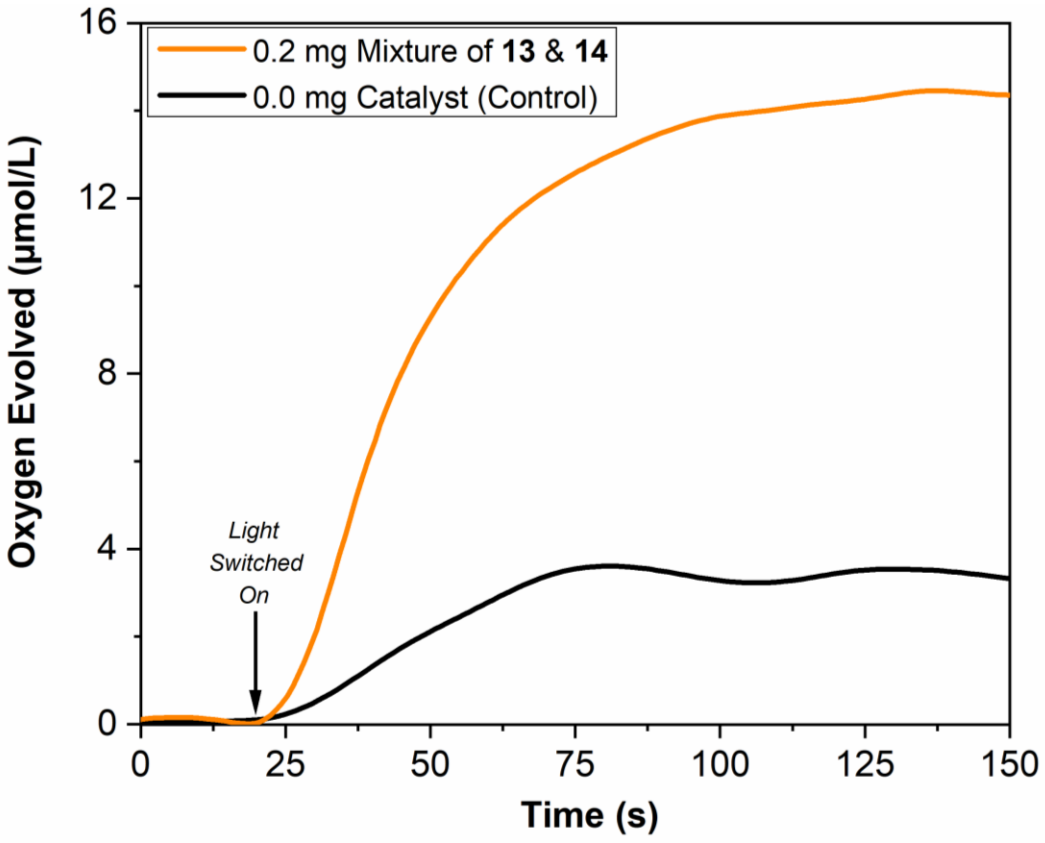

Figure 5.13: Kinetic monitoring (Clark electrode) of the light-driven OER using a mixture of $[Mn^{II}(H\mathbf{L1}\text{-}Cu^{II})_2(DEA)_2]\cdot DEA$ (**13**) and $[Mn^{II}(\mathbf{L1}\text{-}Cu^{II})(MeOH)_2]\cdot DEA\cdot MeOH$ (**14**) (0.2 mg, orange). The kinetics of O_2 evolution of a control experiment without **13** and **14** is also plotted for comparison (black). Conditions: LED light source (λ = 470, 10 mW cm^{-2}), $[Ru(bpy)_2(deeb)](PF_6)_2$ PS (2 mg), $Na_2S_2O_8$ SEA (10 mM) in a phosphate-buffered aqueous solution (5 mL, 0.01 M, initial pH = 7). Reaction temperature and stirring rate were maintained at 25 °C and 500 rpm, respectively.

For the TON and TOF values reported for **13** and **14**, the assumption was made that all of the catalysts' active sites are exposed to the substrate during catalysis. However, as **13** and **14** are non-porous heterogeneous catalysts, this approximation is unlikely to hold true. Therefore, the potential TONs and TOFs of **13** and **14** are most likely significantly higher than the values quoted. However, due to the low O_2 yield, slow OER kinetics exhibited by **13** and **14**, and because of the difficulty associated with characterising catalytic samples comprising multiple potentially active compounds, no further OER investigations were conducted using these compounds.

In addition to screening **13** and **14** for OER catalytic activity, the materials were also examined as potential catalysts for the light-driven HER. H_2 evolution experiments were conducted according to the same methodology described for H_2O oxidation experiments with some modifications: The O_2 sensing electrode employed in OER experiments was substituted for a H_2 sensing microsensor (Unisense H_2-NP), and the $Na_2S_2O_8$ SEA was replaced with a SED such as MeOH, ascorbic acid (AscH), triethylamine (TEA) or triethanolamine (TEOA). The precise reaction conditions employed were adapted from well-established literature protocols, and are documented in Table 5.1.[43,44,45,46] Unfortunately, mixtures of **13** and **14** did not exhibit HER activity under any of the applied conditions.

Table 5.1 – Reaction conditions used to asses the light-driven HER activity of 13 and 14.

Catalyst	External Photosensitiser	SED	Buffer Solution / Solvent System	Irradiation (λ, nm)	Evolved H_2
13 and **14** (0.1 mg)	None	AscH (0.3 M)	Aqueous NaPi buffer (5 mL, 1 M, pH = 6)	405	None
13 and **14** (0.1 mg)	None	AscH (0.3 M)	Aqueous NaPi buffer (5 mL, 1 M, pH = 6)	390 – 700	None
13 and **14** (0.1 mg)	$[Ru(bpy)_2(deeb)](PF_6)_2$ (2 mg)	AscH (0.3 M)	Aqueous NaPi buffer (5 mL, 1 M, pH = 6)	470	<1 nmol Evolved
13 and **14** (0.1 mg)	$Ru(bpy)_3]Cl_2$ (2 mg)	MeOH (1 mL)	Aqueous NaPi buffer (4 mL, 1 M, pH = 6)	470	None
13 and **14** (0.1 mg)	$[Ru(bpy)_3]Cl_2$ (2 mg)	TEA (0.5 mL)	Aqueous NaPi buffer (5 mL, 1 M, pH = 6)	470	None
13 and **14** (0.1 mg)	$[Ru(bpy)_3]Cl_2$ (2 mg)	TEOA (0.4 mL)	Acetonitrile (4.5 mL) and H_2O (0.1 mL)	470	None

In this section, the synthesis and crystal structures of two Mn^{II}-based supramolecular assemblies constructed from H_2**L1**-Cu^{II} linkers (**13** and **14**) were described. Elucidation of the crystal structures of **13** and **14** using single crystal X-ray diffraction revealed that **13** is a 1D coordination polymer and **14** is a 2D MMPF. As **13** and **14** form as an inseparable mixture under identical reaction conditions, the materials were characterised together using FT-IR spectroscopy, TGA and PXRD analysis. Examination of the crystal structures of **13** and **14** led to the identification of these compounds as potential H_2O splitting catalysts. Subsequent screening for activity towards the light-driven OER or HER revealed that these materials show only moderate, non-catalytic O_2 evolution behaviour, and do not exhibit HER activity under a range of experimental conditions.

5.1.3 Synthesis, Characterisation and Catalytic Activity of Mn^{II}L1-Ni^{II} Frameworks

Following on from the synthesis of the two bioinspired metallo-supramolecular assemblies **13** and **14**, a similar synthetic strategy was adopted using either H_2**L1**-Pt^{II} or H_2**L1**-Ni^{II} as ligands in place of H_2**L1**-Cu^{II}. The motivation for this was to determine whether assemblies which are isoreticular to **13** and **14** could be generated using alternative metalloporphyrin ligands, and to investigate how the catalytic properties of these novel structures would relate to the catalytic activity of their H_2**L1**-Cu^{II}-based analogues.

Initial synthetic efforts used H_2**L1**-Pt^{II} as a ligand due to the established attractive photoredox properties of similar Pt^{II} porphyrin complexes.[19,47] However, despite exploring an extensive range of synthetic conditions, crystals of suitable quality for X-ray analysis could not be obtained from reactions between H_2**L1**-Pt^{II} and a range of Mn^{II} salts. This outcome could be explained by the distortion effects exerted on metalloporphyrin moieties by their central metal ions. Porphyrin complexes of relatively small ions (such as Cu^{II} or Ni^{II}) typically adopt saddle-shaped or ruffled configurations. Such configurations decrease the size of the macrocycle's internal cavity, allowing smaller ions to be accommodated.[48] Conversely, for porphyrin complexes of larger ions such as Pt^{II}, planar configurations are often energetically more favourable.[49]

It can then be postulated that if a prerequisite for the self-assembly of **13** and **14** is the saddle-shaped configurations of the metalloporphyrin linkers, then the use of planar porphyrin ligands such as H_2**L1**-Pt^{II} may impede the formation of frameworks which are isoreticular to **13** and **14**. Further, it follows that metalloporphyrin complexes comprising smaller ions such as Ni^{II} are likely to adopt similar configurations to H_2**L1**-Cu^{II}, and therefore may be used to synthesise novel frameworks which are isostructural to **13** and **14**. Additionally, the established photosensitising[26] and OER catalytic[50] behaviour of Ni^{II}-based metalloporphyrins make them attractive building units for incorporation within supramolecular H_2O splitting assemblies.

The adoption of this strategy led to the successful synthesis of a further two Mn^{II}-based supramolecular structures using H_2**L1**-Ni^{II} as a ligand. The synthesis, crystal structures, physicochemical characterisation and catalytic properties of a coordination polymer $[Mn^{II}(H$**L1**-$Ni^{II})_2(DMF)_2]\cdot 3DMF$ (**15**) which is isoreticular to compound **13**, and a 2D MMPF $[Mn^{II}($**L1**-$Ni^{II})(DMF)_2]\cdot 4DMF$ (**16**) which is structurally related to compound **14** are discussed in this section. As with **13** and **14**, **15** and **16** form as an inseparable mixture under identical reaction conditions.

5.1.3.1 Synthesis of $[Mn^{II}(HL1\text{-}Ni^{II})_2(DMF)_2]\cdot 3DMF$ (15) and $[Mn^{II}(L1\text{-}Ni^{II})(DMF)_2]\cdot 4DMF$ (16)

The 1D coordination polymer $[Mn^{II}(H\mathbf{L1}\text{-}Ni^{II})_2(DMF)_2]\cdot 3DMF$ (**15**) and the 2D MMPF $[Mn^{II}(\mathbf{L1}\text{-}Ni^{II})(DMF)_2]\cdot 4DMF$ (**16**) were synthesised in a reproducible reaction between $H_2\mathbf{L1}\text{-}Ni^{II}$ and $MnCl_2\cdot 2H_2O$. Heating these reactants in a solution of DMF for three days under solvothermal conditions afforded the formation of uniform, crimson rod-shaped crystals of **15** and **16** which were indistinguishable by their appearance. The crystals formed in moderate yield (35%) and were suitable for analysis using single crystal X-ray diffraction.

5.1.3.2 Crystal Structure of $[Mn^{II}(HL1\text{-}Ni^{II})_2(DMF)_2]\cdot 3DMF$ (15)

The crystal structure of **15** was solved in the triclinic space group $P\bar{1}$. Structurally, **15** is similar to the polymer **13** which was solved in the monoclinic space group *C*2/c. **15** is a 1D coordination polymer which extends in parallel with the (-1-11) crystallographic direction and features octahedrally coordinated Mn^{II} centres which are doubly bridged by singly-deprotonated linear ditopic porphyrin $(H\mathbf{L1}\text{-}Ni^{II})^-$ linkers (Fig. 5.14a). Two $(H\mathbf{L1}\text{-}Ni^{II})^-$ linker moieties bridge each Mn^{II} ion, generating polymeric chains of **15** that are characterised by 'double-deckers' of bridging $(H\mathbf{L1}\text{-}Ni^{II})^-$ ligands (Fig. 5.14b).

The asymmetric unit of **15** contains one Mn^{II} ion with a crystallographic occupancy of ½, one singly-deprotonated $(H\mathbf{L1}\text{-}Ni^{II})^-$ metalloporphyrin linker, one coordinated DMF solvent molecule and three constitutional DMF solvent molecules. **15** is centrosymmetric, with the Mn^{II} centre locating on an inversion centre. As in **13**, the Mn^{II} ion of **15** is coordinated by four carboxylate moieties of four different bridging $(H\mathbf{L1}\text{-}Ni^{II})^-$ linkers, each of which adopts monodentate η^1 coordination modes.

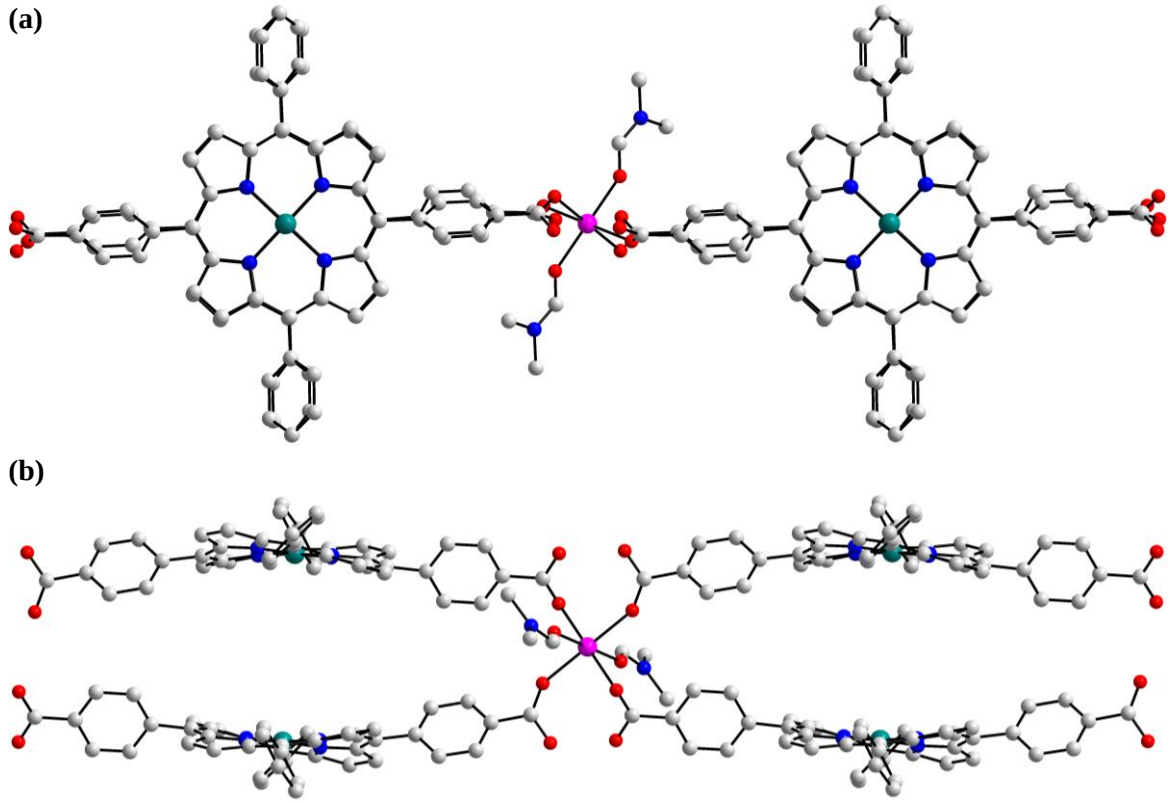

Figure 5.14: Ball-and-stick representation of the coordination polymer $[Mn^{II}(H\mathbf{L1}\text{-}Ni^{II})_2(DMF)_2]\cdot 3DMF$ (**15**) showing (a) the polymer chain which extends in parallel with the crystallographic (-1-11) direction, and (b) Mn^{II} centre bridged by four $(H\mathbf{L1}\text{-}Ni^{II})^-$ ligands which are arranged in 'double-decker' configurations. Constitutional solvent and hydrogen atoms have been omitted for clarity. Colour scheme: C white, N blue, O red, Mn pink, Ni teal.

The Mn^{II} centre of **15** Mn(1) has a distorted octahedral coordination geometry and is illustrated in Fig. 5.15. The coordination environment of Mn(1) is composed of four carboxylate O-donors O(2), O(2′), O(4) and O(4′) of four separate monodentate η^1 coordinating $(H\mathbf{L1}\text{-}Ni^{II})^-$ ligands, and two O-donors O(3) and O(3′) of two DMF coordination solvent molecules. The four $(H\mathbf{L1}\text{-}Ni^{II})^-$ carboxyl(ate)-derived O-donors O(2) and O(2′), O(4) and O(4′) occupy the four equatorial positions of the coordination sphere of Mn(1), whilst two O-donors O(4) and O(4′) of two DMF moieties coordinate *trans* with respect to one another and occupy axial positions of the coordination sphere.

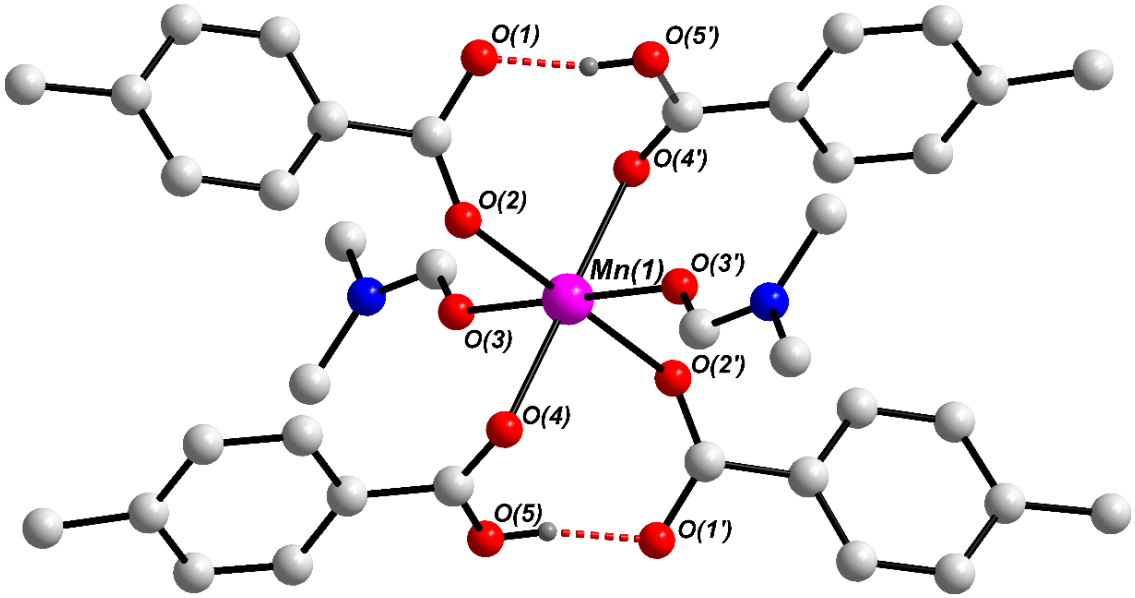

Figure 5.15: Ball-and-stick representation of the coordination environment of the Mn^{II} ion Mn(1) in **15.** Solvent of crystallization and non-hydrogen bonding hydrogen atoms have been omitted for clarity. Hydrogen bonds are represented as red dashed lines. Colour scheme: C white, H grey, N blue, O red, Mn pink.

The bond distances between Mn(1) and each of the monodentate carboxyl(ate)-derived O-donors are 2.1555(1) Å for Mn(1) – O(2) and Mn(1) – O(2'), and 2.1536(1) Å for Mn(1) – O(4) and Mn(1) – O(4'). The bond distance between the Mn^{II} centre and each of the O-donors of the DMF solvent moieties is 2.1516(1) Å for Mn(1) – O(3) and Mn(1) – O(3'). The bond distances surrounding Mn(1) fall within the range 2.1516(1) – 2.1555(1) Å, which gives the Mn^{II} centre of **15** a slightly distorted octahedral coordination geometry. The bond angles which surround Mn(1) that deviate most significantly from the ideal octahedral angle of 90° are 85.50(3)° and 94.50(3)° for O(2)-Mn(1)-O(4) and O(2)-Mn(1)-O(4'), respectively. The bond distances and angles which characterise Mn(1) are similar to the bond distances and angles surrounding the Mn^{II} ion of **13**, and are consistent with the values reported for other Mn^{II}-based carboxylate complexes reported in the literature.[30,32]

The (H**L1**-Ni^{II})$^{-}$ linker of **15** adopts a saddle-shaped configuration which is shown in Fig. 5.16. The central Ni^{II} ion Ni(1) of the metalloporphyrin exhibits a distorted square-planer coordination geometry. The bond angles between the central Ni^{II} ion Ni(1) and the pyrrolic N-donors on opposite corners of the macrocyclic cavity are 174.80(5)° and 175.64(5)° for N(1)-Ni(1)-N(3) and N(2)-Ni(1)-N(4), respectively. These angles deviate from the ideal octahedral angle of 180° to a greater extent in comparison with the equivalent bond angles of **13**. This is

in line with expectations, as the (H**L1**-Ni^{II})$^{-}$ linker of **15** is less planar than the (H**L1**-Cu^{II})$^{-}$ moiety of **13**.

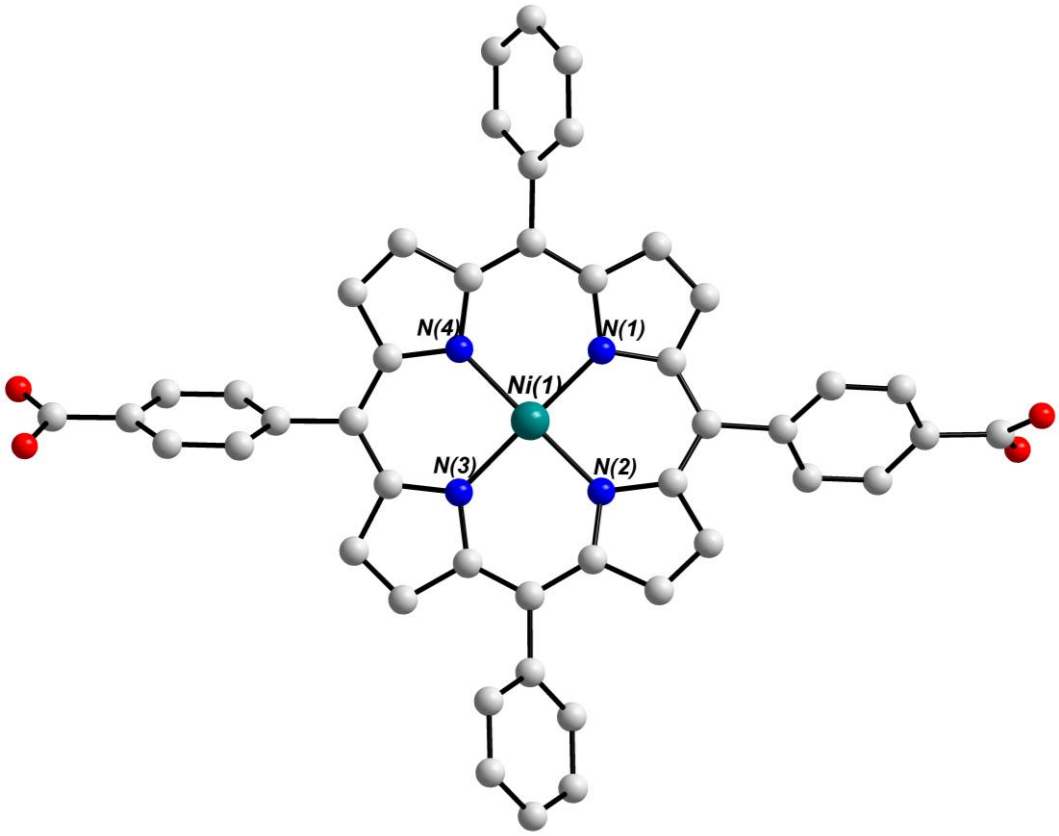

Figure 5.16: Ball-and-stick representation of the linear ditopic metalloporphyrin (H**L1**-Ni^{II})$^{-}$ linker moiety of **15**. Hydrogen atoms have been removed for clarity. Colour scheme: C white, N blue, O red, Ni teal.

The dihedral angle between the carboxylate functionalised *meso* phenyl rings on opposite positions of the (H**L1**-Ni^{II})$^{-}$ ligand is 70.49°, whereas the dihedral angle between the non-functionalised *meso* phenyl rings on opposite sides of the linker is 75.55°. This configuration facilitates increased stabilisation of **15** through π – π stacking and hydrogen bonding interactions. The *meso* phenyl groups of (H**L1**-Ni^{II})$^{-}$ are more staggered than the equivalent moieties of the (H**L1**-Cu^{II})$^{-}$ linker of **13**, which are more eclipsed on average by *ca*. 60°.

(H**L1**-Ni^{II})$^{-}$ linkers of neighbouring polymer chains are stabilised through π – π stacking interactions, and the average distance between metalloporphyrin moieties of two stacking chains is *ca*. 3.7 Å. This distance is within the expected range for π – π stacking interactions.[33]

The distance between two connected Mn^{II} ions in a polymer chain is 22.0208(7) Å, and the separation between two (H**L1**-Ni^{II})$^{-}$ linkers of the same chain is *ca*. 6.5 Å.

The charge of **15** is balanced in the same manner as compound **13**: Each (H**L1**-Ni^{II})$^{-}$ linker is deprotonated on one of its two binding sites giving a charge of −1. Two porphyrin ligands coordinate per metal centre in the crystal structure of **15**, therefore the oxidation state +2 is assigned to Mn(1) in order for the charge of the polymer to be neutral. BVS analysis calculations corroborate the assignment of the +2 oxidation state of Mn(1). The porphyrin ring has been deprotonated at two N – H moieties inside the porphyrin ring, giving a charge of −2. This negative charge is balanced by the square planar Ni^{II} ion which occupies the central cavity of the macrocycle. The assignment of the +2 oxidation state to the Ni^{II} metal ion was also confirmed using BVS analysis.

The packing of **15** in the crystal structure is depicted in Fig. 5.17. The packing diagram shows densely packed polymer chains in which porphyrin moieties interdigitate (Fig. 5.17a). Fig. 5.17b shows the layered architecture of **15**: Adjacent layers stack on top of each other and are stabilized through π – π interactions. These interactions extend in the direction of the crystallographic *a*-axis forming a 2D supramolecular framework. Interatomic distances between neighbouring stacking porphyrin moieties are within the range of *ca*. 3.7 – 4.3 Å, which is within the expected range for π – π stacking interactions.[34,33]

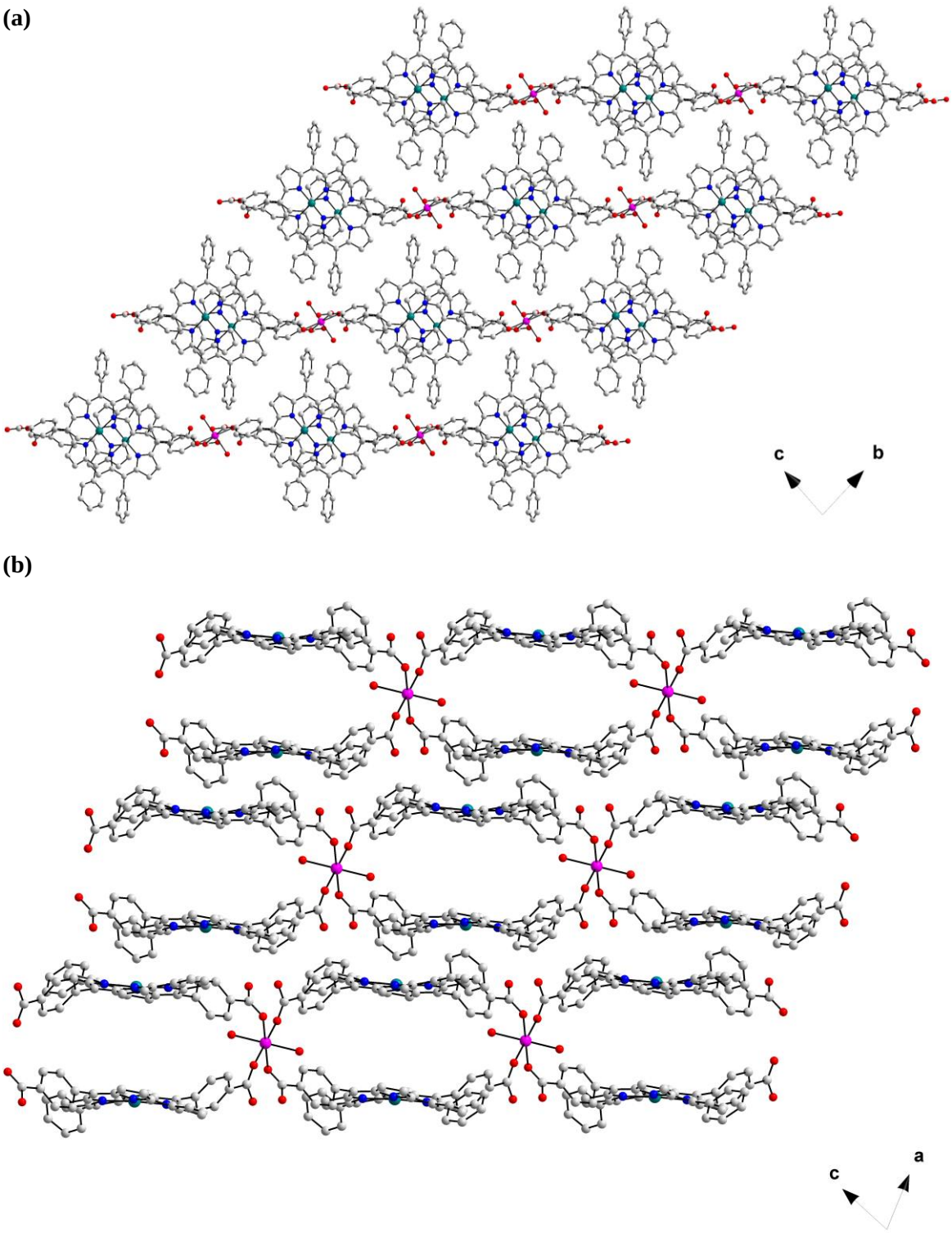

Figure 5.17: Ball-and-stick representation of the packing arrangement of **15** in the crystal structure revealing (a) interdigitation between neighbouring polymer strands viewed in the direction of the crystallographic *a*-axis and (b) the 2D layered architecture which is stabilised by π – π stacking interactions viewed in the direction of the crystallographic *b*-axis. Hydrogen atoms, constitutional solvent molecules and coordination solvent molecules have been omitted for the purpose of clarity. Colour scheme: C white, N blue, O red, Mn pink, Ni teal.

5.1.3.3 Crystal Structure of [(Mn^{II}(L1-Ni^{II})(DMF)$_2$]·4DMF (16)

The MMPF [(Mn^{II}(**L1**-Ni^{II})(DMF)$_2$]·4DMF (**16**), which is isoreticular to **14**, was obtained from the same reaction that afforded the formation of **15**. **16** was solved in the triclinic crystal system in the space group $P\bar{1}$. The asymmetric unit of **16** comprises two crystallographically independent octahedrally coordinated Mn^{II} centres, two (**L1**-Ni^{II})$^{2-}$ ligands, four coordinated DMF solvent molecules and four DMF crystallisation solvent molecules that locate within the small channels which extend between the 2D layers of **16**.

16 is a 2D MMPF which is characterised by infinite rod-shaped SBUs which extend in parallel with the crystallographic *b*-axis. The SBU of **16** (Fig. 5.18) is composed of an infinite chain of octahedrally coordinated Mn^{II} centres. Akin to **14**, each of these Mn^{II} ions are bridged by four *syn-syn* bridging, μ_2-η^1:η^1 binding carboxylate moieties from four distinct (**L1**-Ni^{II})$^{2-}$ linkers.

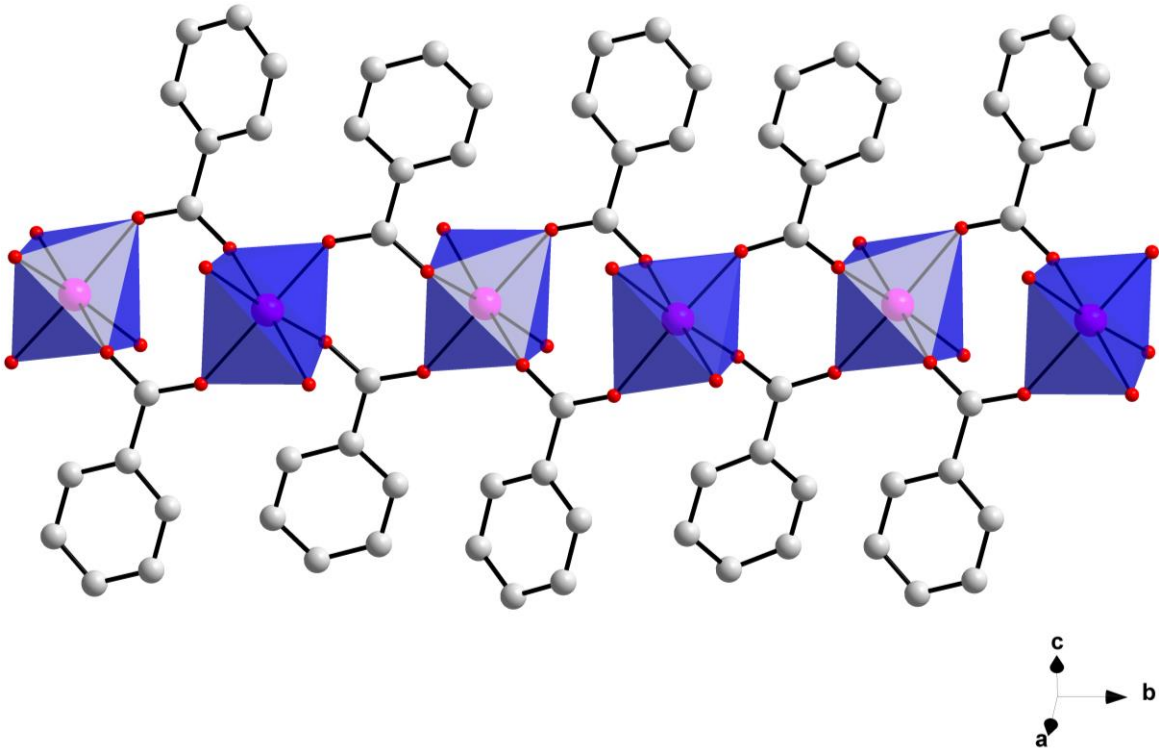

Figure 5.18: Ball-and-stick representation of the rod-shaped SBU of **16** which comprises an infinite 1D chain of octahedrally coordinated Mn^{II} centres that are bridged by *syn-syn* carboxylate functionalities of (**L1**-Ni^{II})$^{2-}$ ligands. Coordinated solvent molecules and hydrogen atoms have been omitted for clarity. Colour scheme: C white, N blue, O red, Mn pink. Mn^{II} centres are represented as blue polyhedra.

In a similar manner to **14**, the SBUs of **16** stack in parallel and are each connected to two other SBUs *via* ditopic (**L1**-Ni^{II})$^{2-}$ linkers, giving rise to the 2D layered structure of **16** (Fig. 5.19). The distance between each of the rod-shaped SBUs (Mn^{II} ··· Mn^{II}) within **16** is *ca*. 22.2 Å.

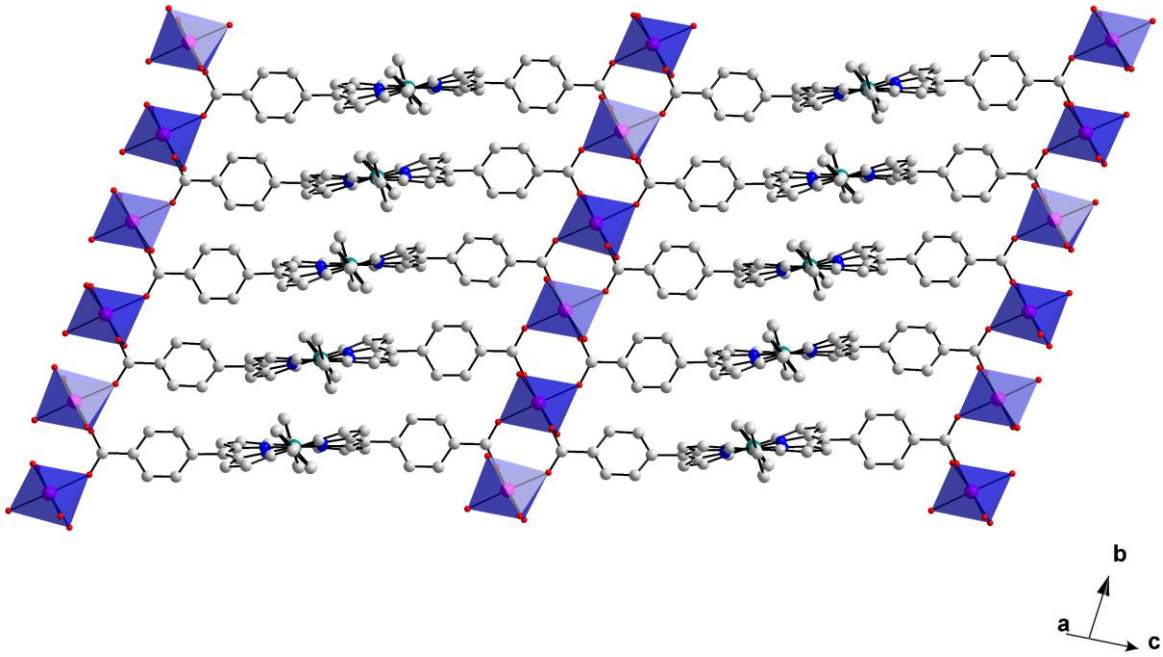

Figure 5.19: Ball-and-stick representation of the 2D layered structure of **16**. The 2D layers are comprised of rod-shaped SBUs, each of which is bridged by ditopic (**L1**-Ni^{II})$^{2-}$ linkers. Crystallization solvent molecules, coordination solvent molecules and hydrogen atoms have been omitted for clarity. Colour scheme: C white, N blue, O red, Mn pink, Ni teal. Mn^{II} centres are represented as blue polyhedra.

The coordination environments of the two crystallographically distinct Mn^{II} centres in the SBU of **16** are displayed Fig. 5.20. The coordination sphere of Mn(1) comprises four O-donors O(2), O(3), O(10) and O(12) which derive from the *syn-syn* bridging, μ_2-η^1:η^1 binding carboxylate functionalities of four distinct (**L1**-Ni^{II})$^{2-}$ linkers, and two O-donors O(1) and O(11) of two DMF solvent molecules which coordinate *cis* with respect to each other.

Similarly, the coordination environment of Mn(2) is composed of four carboxylate O-donors O(4), O(6), O(8) and O(9) from four (**L1**-Ni^{II})$^{2-}$ ligands and two O-donors O(5) and O(7) which derive from two *cis*-coordinated DMF molecules. The interatomic distance Mn(1) ··· Mn(2) is 4.8301(4) Å.

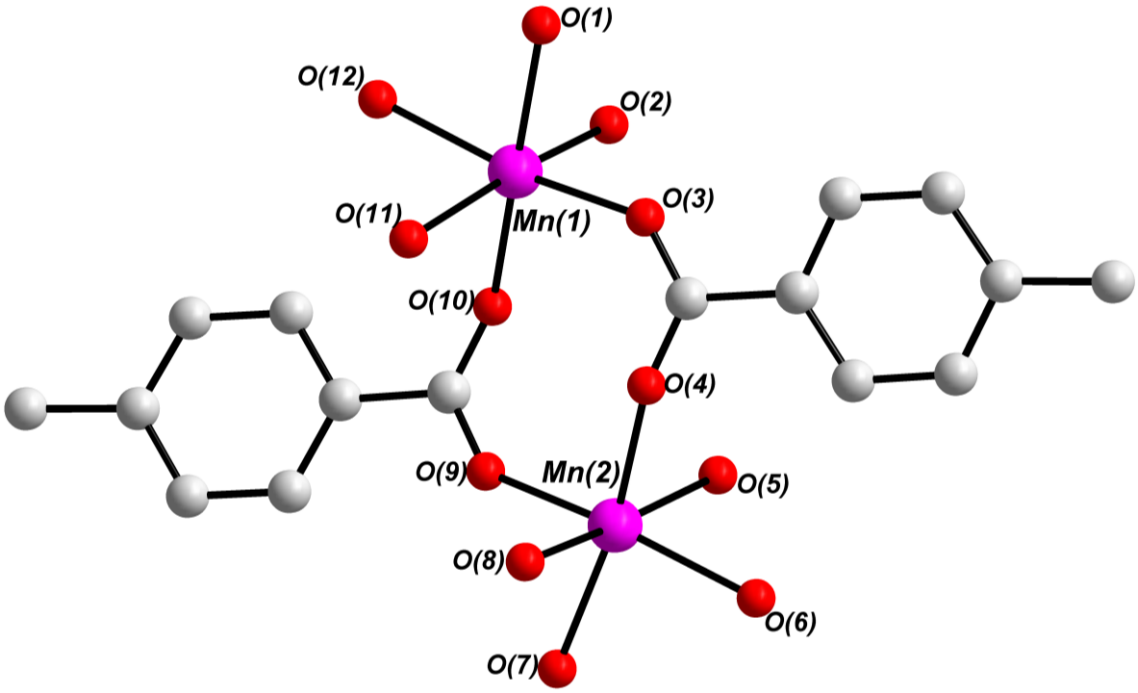

Figure 5.20: Ball-and-stick representation of the coordination environment of the two crystallographically distinct Mn^{II} centres Mn(1) and Mn(2) of **16**. Solvent of crystallization, coordinated solvent and hydrogen atoms have been omitted for clarity. Colour scheme: C white, O red, Mn pink.

The bond distances between Mn(1) and each of the four carboxylate O-donors are 2.1289(6) Å, 2.1568(8) Å**,** 2.1442(6) Å and 2.1366(7) Å for Mn(1) – O(2), Mn(1) – O(3) Mn(1) – O(10) and Mn(1) – O(12), respectively. However, the distances between Mn(1) and the O-donors of the coordinated DMF moieties are slightly longer: The bond distance Mn(1) – O(1) is 2.2633(6) Å, and the bond distance Mn(1) – O(11) is 2.2409(7) Å.

The bond angles surrounding Mn(1) which exhibit the greatest deviation from the ideal octahedral angle of 90° are 81.75(5)° and 100.57(4)° for O(11)-Mn(1)-O(12) and O(3)-Mn(1)-O(10), respectively. The bond angle surrounding Mn(1) deviating most significantly from the ideal octahedral angle of 180° is 162.86(5)° for O(3)-Mn(1)-O(12). The bond distances and angles surrounding Mn(1) render the coordination geometry of this metal ion distorted octahedral.

The distances between Mn(2) and each of the four carboxylate-derived O-donors are 2.1427(4) Å, 2.1529(7) Å**,** 2.1445(6) Å and 2.1572(8) Å for Mn(2) – O(4), Mn(2) – O(6) Mn(2) – O(8) and Mn(2) – O(9), respectively. The bond distances between Mn(2) and each of the O-donors

of the coordinated DMF solvent molecules are 2.2453(6) Å and 2.2140(8) Å for Mn(2) – O(5) and Mn(2) – O(7), respectively.

The bond angles which surround Mn(2) that deviate most significantly from the ideal octahedral angle of 90° are 79.26(4)° and 97.37(4)° for O(5)-Mn(2)-O(6) and O(4)-Mn(2)-O(9), respectively. Further, the bond angle surrounding Mn(2) that deviates to the greatest extent from the ideal octahedral angle of 180° is 163.05(5)° for O(6)-Mn(2)-O(9). These values give Mn(2) a distorted octahedral coordination geometry. The distortion of the coordination environment of Mn(1) and Mn(2) of **16** is similar to the degree of distortion of the Mn^{II} ion of **14.** In addition, the bond distances and angles surrounding Mn(1) and Mn(2) are consistent with the values reported for other Mn^{II} – carboxylate complexes reported in the literature.[30,32]

The two (**L1**-Ni^{II})$^{2-}$ linkers of **16** adopt saddle-shaped configurations and are displayed in Fig. 5.21. The central Ni^{II} ions of each of the (**L1**-Ni^{II})$^{2-}$ linkers exhibit distorted square-planar coordination geometries. The bond angles between Ni(1) and Ni(2) and the pyrrolic nitrogen atoms on opposite positions of the porphyrin's central cavity are 173.22(5)°, 173.78(2)°, 173.77(6)° and 173.70(5)° for N(1)-Ni(1)-N(3), N(2)-Ni(1)-N(4), N(5)-Ni(2)-N(6) and N(2)-Ni(2)-N(7), respectively.

The (**L1**-Ni^{II})$^{2-}$ linkers in **16** are stabilized through two types of π – π interactions: Parallel displaced π – π interactions between porphyrin moieties within the same 2D sheet propagate in the direction of the crystallographic *b*-axis, and T-shaped π – π interactions between the non-functionalised *meso* phenyl rings and pyrrole ring systems of (**L1**-Ni^{II})$^{2-}$ linker moieties of neighbouring 2D layers stabilise the structure. These interlayer π – π interactions extend the 2D MMPF **16** into a 3D supramolecular framework. The distance between stacking porphyrin moieties ranges between 3.66 – 3.91 Å, which is consistent with other π – π stacking interactions reported in the literature.[34, 33]

The average dihedral angle between the carboxylate functionalised *meso* phenyl rings on opposite positions of the (**L1**-Ni^{II})$^{2-}$ linkers of **16** is 43.22°. This is more staggered than the average dihedral angle between the non-functionalised *meso* phenyl rings of the (**L1**-Ni^{II})$^{2-}$ linkers, which is 24.49°. This configuration facilitates stabilisation of **16** through π – π stacking interactions which occur between neighbouring porphyrin moieties.

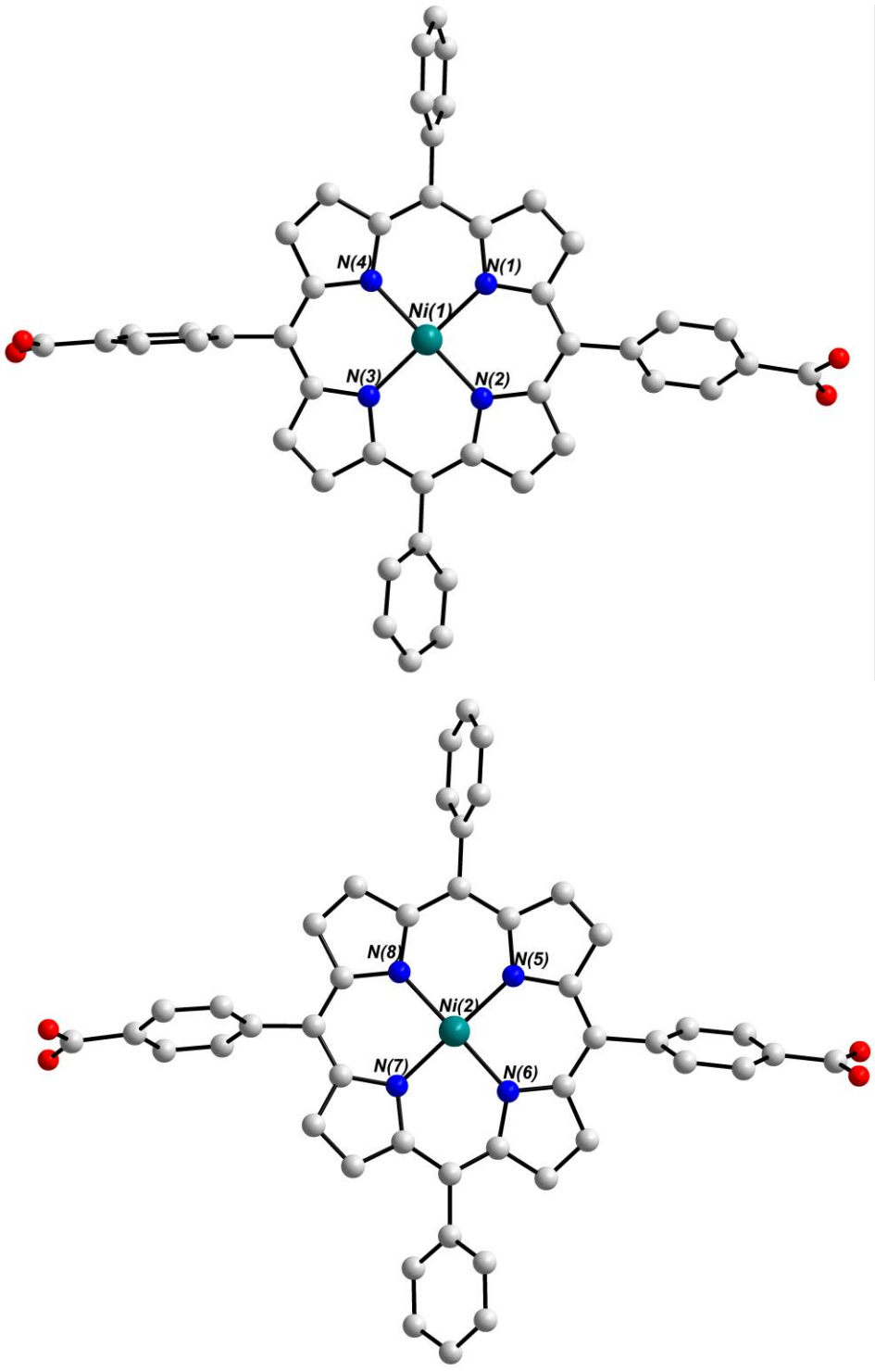

Figure 5.21: Ball-and-stick representation of the linear dicarboxylate metalloporphyrin (**L1**-Ni^{II})$^{2-}$ linker moieties of **16**. Hydrogen atoms have been removed for clarity. Colour scheme: C white, N blue, O red, Co purple, Ni teal.

Each of the ditopic (**L1**-Ni^{II})$^{2-}$ linkers are deprotonated at each of their two carboxylate binding sites giving a charge of −2. As one porphyrin linker coordinates per metal centre in the crystal

structure of **16**, it would be expected that each Mn centre would adopt an oxidation state of +2 to balance this charge. The (**L1**-Ni^{II})$^{2-}$ linker is also deprotonated at both of its pyrrolic N – H moieties inside the porphyrin ring, giving a charge of −2. This negative charge is balanced by a Ni^{II} ion which occupies the central cavity of the macrocycle. The assignments of the +2 oxidation state to both the Mn^{II} and Ni^{II} centres were corroborated using BVS analysis calculations.

The packing of **16** in the crystal structure is displayed in Fig. 5.22. 2D sheets of **16** pack densely and porphyrin moieties interdigitate with neighbouring layers. Small channels filled with constitutional solvent molecules extend between layers in parallel with the crytallographic *b*-axis (Fig. 5.22a). The layered architecture of **16** can be seen in Fig. 5.22b, which shows infinite chains of Mn^{II} ions which *zig-zag* and extend in parallel with the crystallographic *b*-axis. The average distance between two neighbouring 2D sheets is *ca*. 15.0 Å.

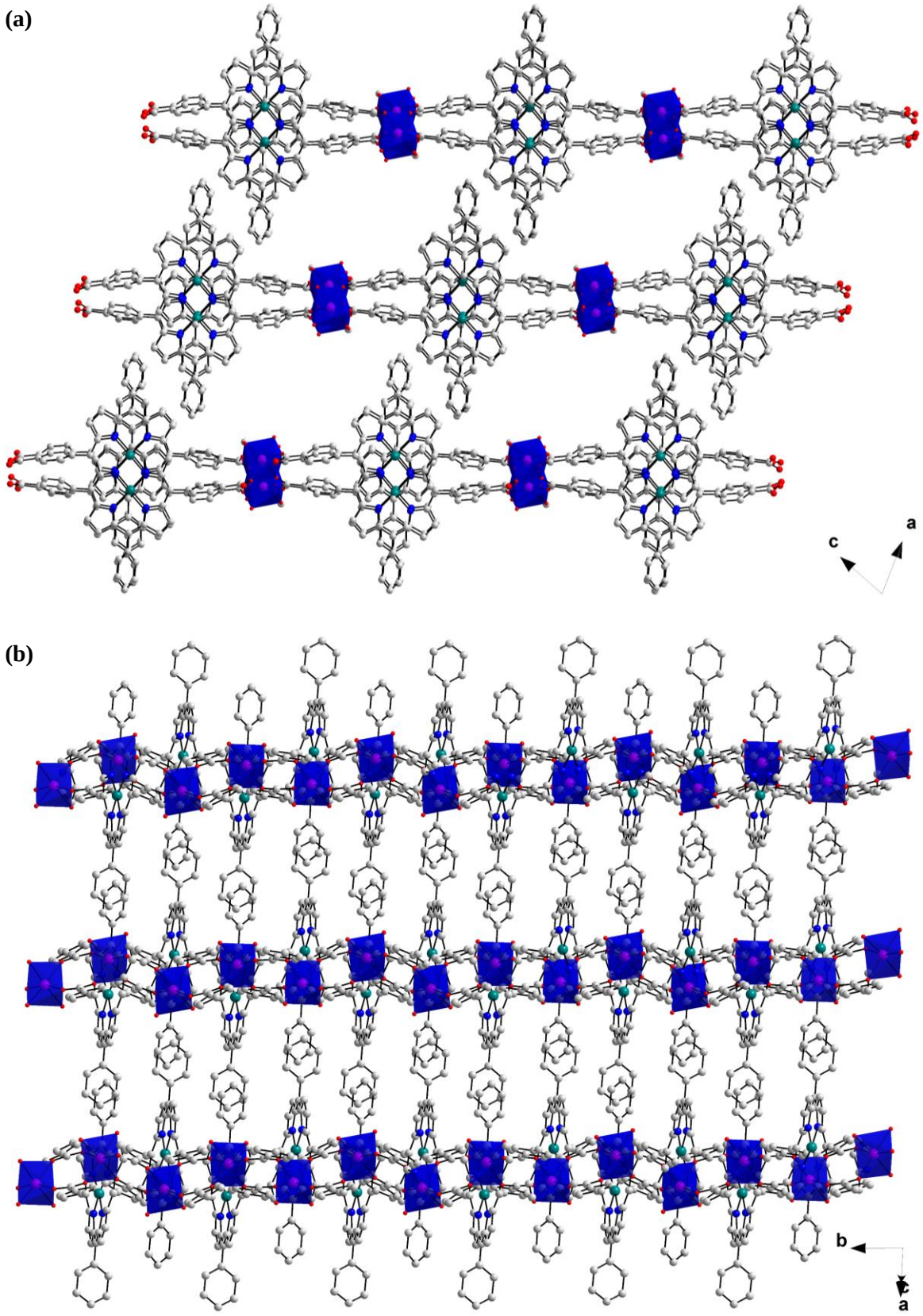

Figure 5.22: Ball-and-stick representation of the packing arrangement of **16** in the crystal structure. View is in the direction of the crystallographic: (a) *b*-axis and (b) *c*-axis. Solvent of crystallization and hydrogen atoms have been omitted for clarity. Mn^{II} centres are represented as blue polyhedra. Colour scheme: C white, N blue, O red, Mn pink, Ni

5.1.3.4 Physicochemical Characterisation of 15 and 16

The Mn^{II}-based metallo-supramolecular assemblies $[Mn^{II}(H\mathbf{L1}\text{-}Ni^{II})_2(DMF)_2]\cdot 3DMF$ (**15**) and $[Mn^{II}(\mathbf{L1}\text{-}Ni^{II})(DMF)_2]\cdot 4DMF$ (**16**) form under identical reaction conditions and are indistinguishable based on their physical appearance. Therefore, these compounds could not be separated manually. In addition, attempts to purify a mixture of **15** and **16** by suspending in an appropriate solvent system with a density that was between the densities of both compounds were unsuccessful. As a result of this, **15** and **16** were characterised as a mixture using FT-IR spectroscopy, TGA and PXRD spectroscopy.

Infrared Spectroscopy

An FT-IR spectrum of **15** and **16** is presented in Fig. 5.23. A broad signal around 3200 cm^{-1} can be associated with an O – H stretching vibration from the hydrogen bonded $(H\mathbf{L1}\text{-}Ni^{II})^{-}$ linkers of **15**.[35] A broad band at 3049 cm^{-1} can be attributed to aromatic C – H stretching vibrations of the porphyrin ligands of **15** and **16**.[35] A signal at 1656 cm^{-1} can be associated with a C = O stretching vibration of the DMF moieties of **15** and **16**.[36] A band at 1582 cm^{-1} can be attributed to a carbonyl stretching vibration of the non-bridging carboxylate moiety of **15**.[37] Strong signals at 1532 and 1394 cm^{-1} can be attributed to the asymmetric and symmetric stretching vibrations, respectively, of the μ_2 bridging carboxylate moiety of **16**.[38] Finally, a sharp band at 1003 cm^{-1} was assigned to an in-plane vibration (ring breathing) of the porphyrin linkers of **15** and **16**.[39]

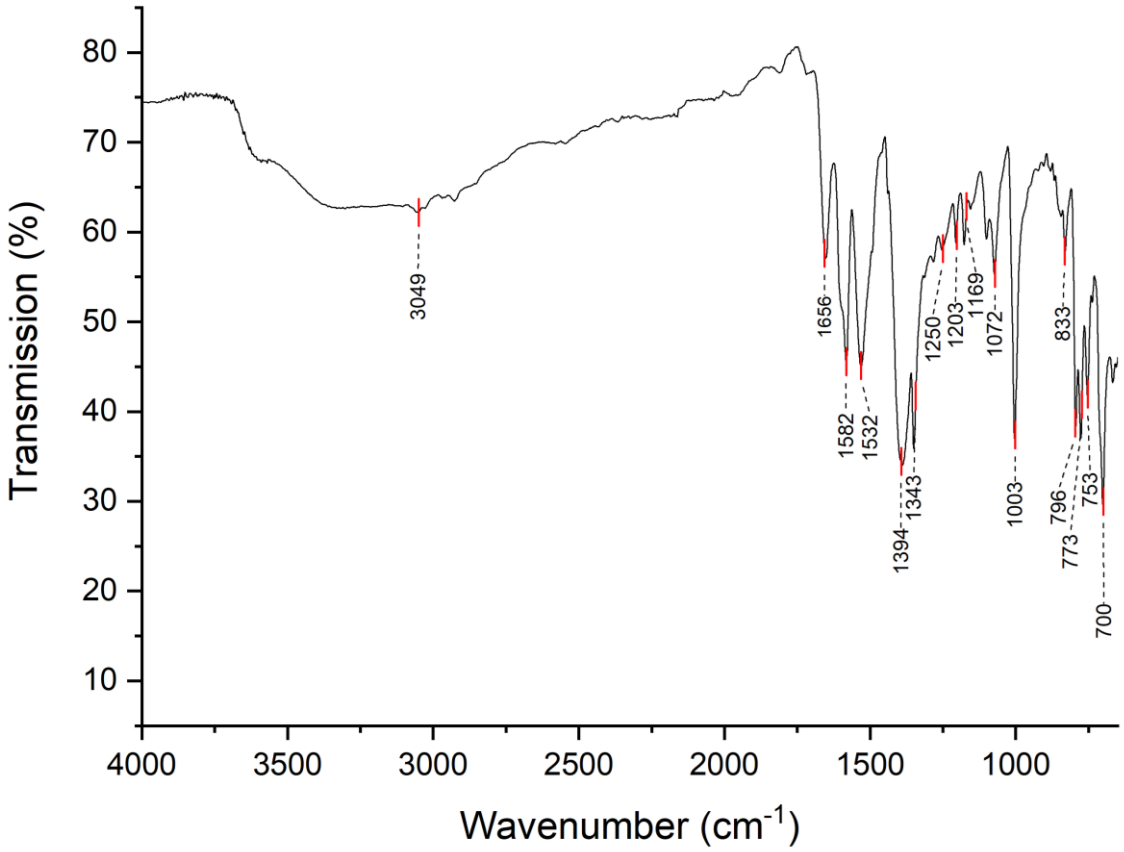

Figure 5.23: FT-IR spectrum of a mixture of **15** and **16**.

Thermogravimetric Analysis

TGA was performed on a mixture of **15** and **16** in the temperature range of 25 - 800 °C under a constant stream of N_2, and the resulting TGA trace is presented in Fig 5.24. Heating a mixture of **15** and **16** from 25 - 160 °C is associated with a sample weight loss of 4.0%. This may be attributed to the loss of one constitutional DMF solvent molecule (calculated 4.1% for **15** and 3.7% for **16**). Other constitutional solvent molecules were most likely lost before the TGA was carried out. The next thermogravimetric step occurs between 160 – 400 °C and has an associated weight loss of 7.0%. This can be accounted for by the loss of two coordinated DMF solvent molecules (calculated 7.1% for **15** and 7.8% for **16**). Heating the sample beyond 400 °C results in decomposition in two further steps: The organic components of **15** and **16** degrade between 400 – 480 °C and heating the sample above 480 °C is associated with the formation of metal oxide species. The TGA trace conforms more closely with the anticipated thermal decomposition behaviour of **15** than **16**, based on the formula masses of each compound. This is an indication that the analysed mixture comprises a higher proportion of **15** than **16**.

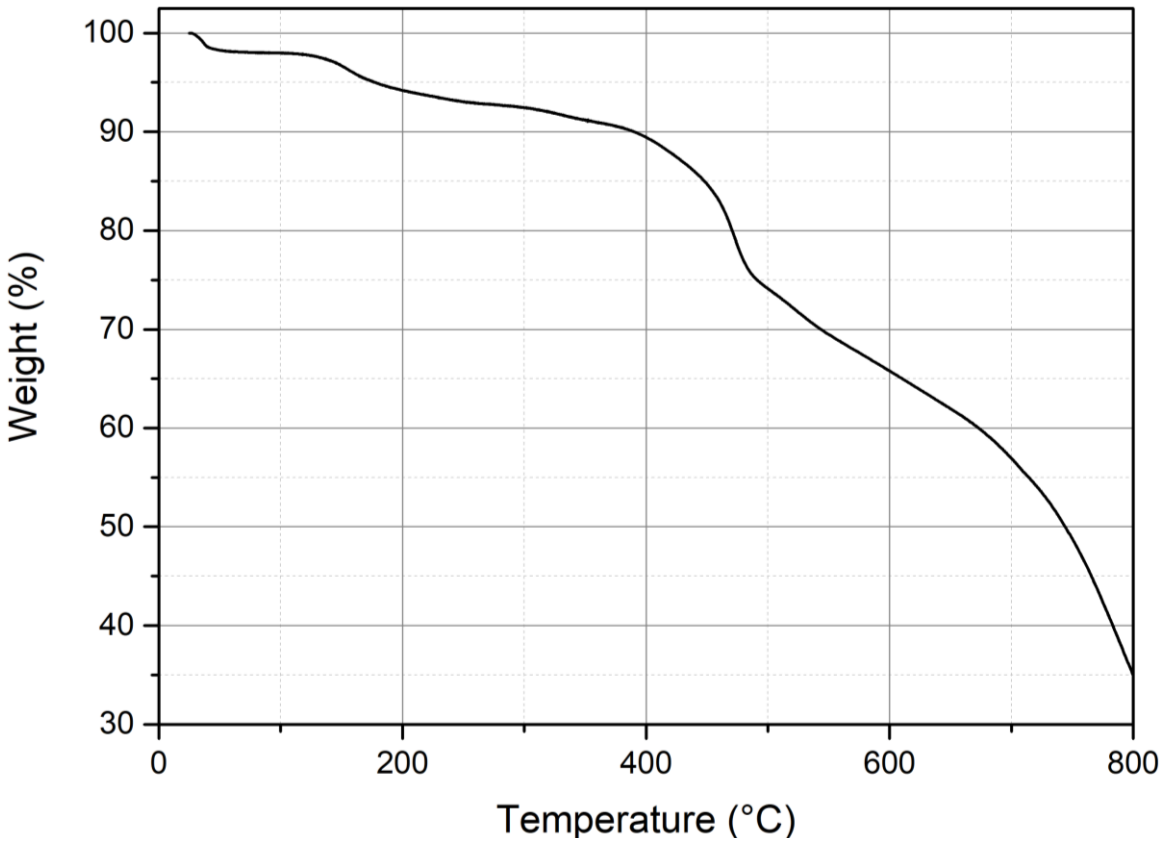

Figure 5.24: TGA trace of a mixture of **15** and **16**.

Powder X-Ray Diffraction Analysis

The PXRD spectrum of a mixture of **15** and **16** is compared with simulated powder spectra of **15** and **16** in Fig. 5.25. Removing **15** and **16** from the mother liquor results in sample desolvation. Therefore, the PXRD pattern was recorded by sealing the sample in a glass capillary. The experimental and calculated powder patterns are in good agreement, as all of the high intensity signals present in the measured pattern can be located in the simulated spectra of either **15** or **16**. Signals in the measured powder pattern of **15** and **16** at 2θ = 8.2°, 9.1°, 11.7°, 12.4°, 13.2°, 13.9°, 15.5°, 16.3° and 17.2° can be assigned to **15**, whilst signals in this spectrum at 2θ = 4.1°, 8.6° and 19.5° can be attributed to **16**. A signal of high intensity at 2θ = 6.2° is associated with both compounds **15** and **16**. Judging by the relative intensities of the signals assigned to **15** and **16**, the composition of the sample can be estimated to contain approximately a 2:1 ratio of **15** to **16**.

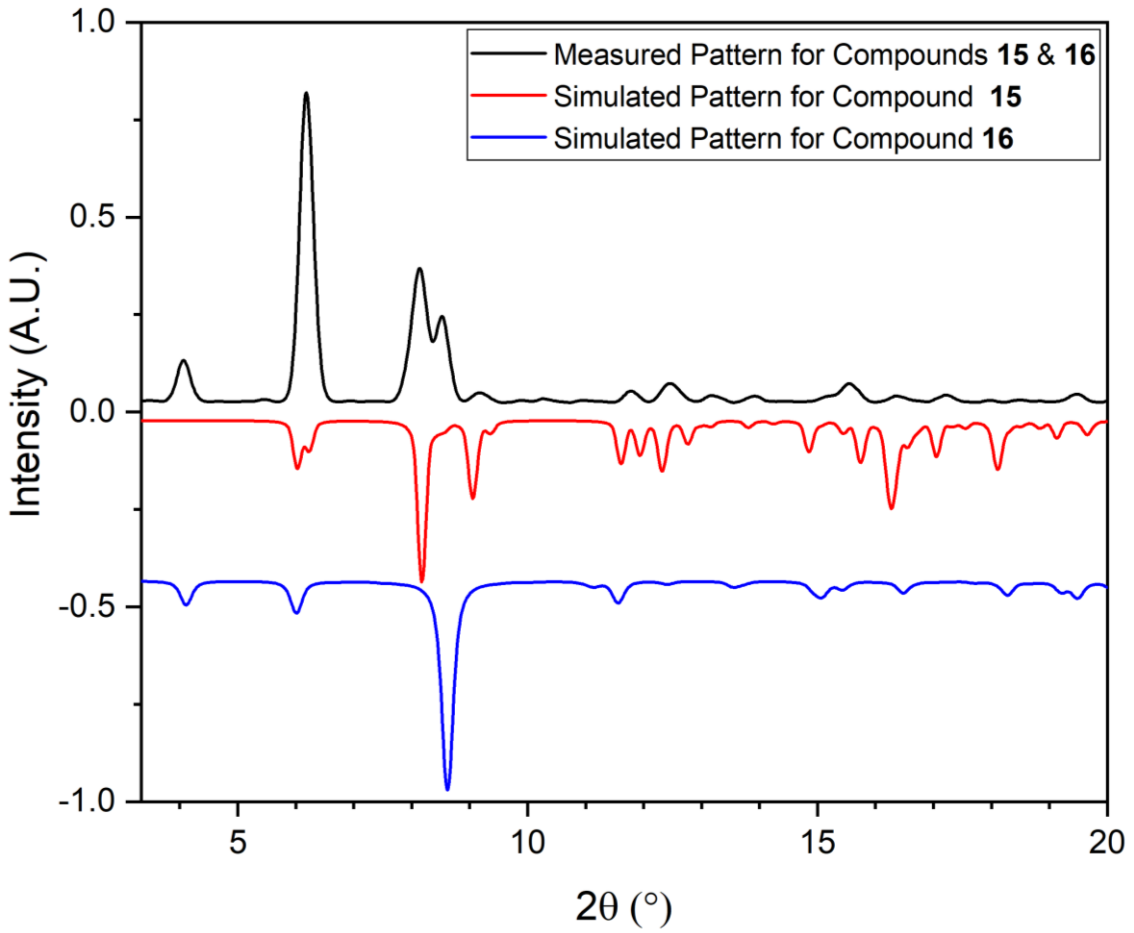

Figure 5.25: Comparison of a measured powder pattern obtained from a mixture of **15** and **16** (black) with simulated PXRD patterns calculated using the single crystal X-ray diffraction data of **15** (red) and **16** (blue).

5.1.3.5 Catalytic Properties of 15 and 16

A preliminary investigation into the propensity of a mixture of **15** and **16** to catalyse the light-driven OER was performed in order to gauge whether further catalytic studies in which these materials were isolated were worthwhile. The OER activity of **15** and **16** was assessed according to the literature-established protocol that was used to screen **13** and **14** for O_2 evolution activity.[42] In a preliminary OER experiment, **15** and **16** were suspended in a neutral, aqueous phosphate-buffered solution containing $Na_2S_2O_8$ SEA. This suspension was hermetically sealed in a reaction vial, deoxygenated and illuminated using either a violet or a white LED (λ = 405 or 390 – 700 nm) while the O_2 concentration inside the reactor was monitored in real time using a Clark electrode.

Unfortunately, O_2 evolution was not observed under these conditions. Therefore, the OER experiment was replicated with two modifications: $[Ru(bpy)_2(deeb)](PF_6)_2$ was added as an external PS and a blue LED (λ = 470 nm) was used to illuminate the suspension. Irradiation of this mixture of WOC, PS and SEA did result in OER activity. Fig. 5.26 compares the O_2 evolution kinetics using a mixture of **15** and **16** as a WOC (teal) with the kinetics of O_2 evolution in a control experiment in which **15** and **16** were not added to the reaction vessel (black).

The total quantity of O_2 evolved by a mixture of **15** and **16** in this experiment was 63.0 nmol, which is significantly higher than the amount of O_2 produced in a control experiment in which no catalyst was added. The TON for this reaction would be 0.61 based on the molar mass of **15**, or 0.39 based on the molar mass of **16**. If calculated using the molar mass of **15**, the TOF of the reaction is 6×10^{-4} s^{-1}, or alternatively the TOF = 4×10^{-4} s^{-1} using the molar mass of **16**. Due to the low yield and slow kinetics of O_2 evolution revealed in these experiments, no further H_2O splitting studies were conducted using **15** and **16**.

Comparatively, the robustness of **13** and **14** is similar to that of **15** and **16**: The average TON of **13** and **14** is 0.50 and the average TON of **15** and **16** is 0.49. However, the activity of **13** and **14** is significantly higher than that of **15** and **16** (TOF = 1.5×10^{-3} s^{-1} for **13** and **14** compared to TOF = 6×10^{-4} s^{-1} for **15** and **16**). This may be due to the presence of Cu^{II}-based metalloporphyrin moieties in **13** and **14** which could contribute towards the catalytic activity of these compounds.[13] This indicates that if the robustness of the catalyst could be improved, Cu^{II}-based metalloporphyrins might be a valuable structural moiety of earth-abundant WOCs with favourable activity.

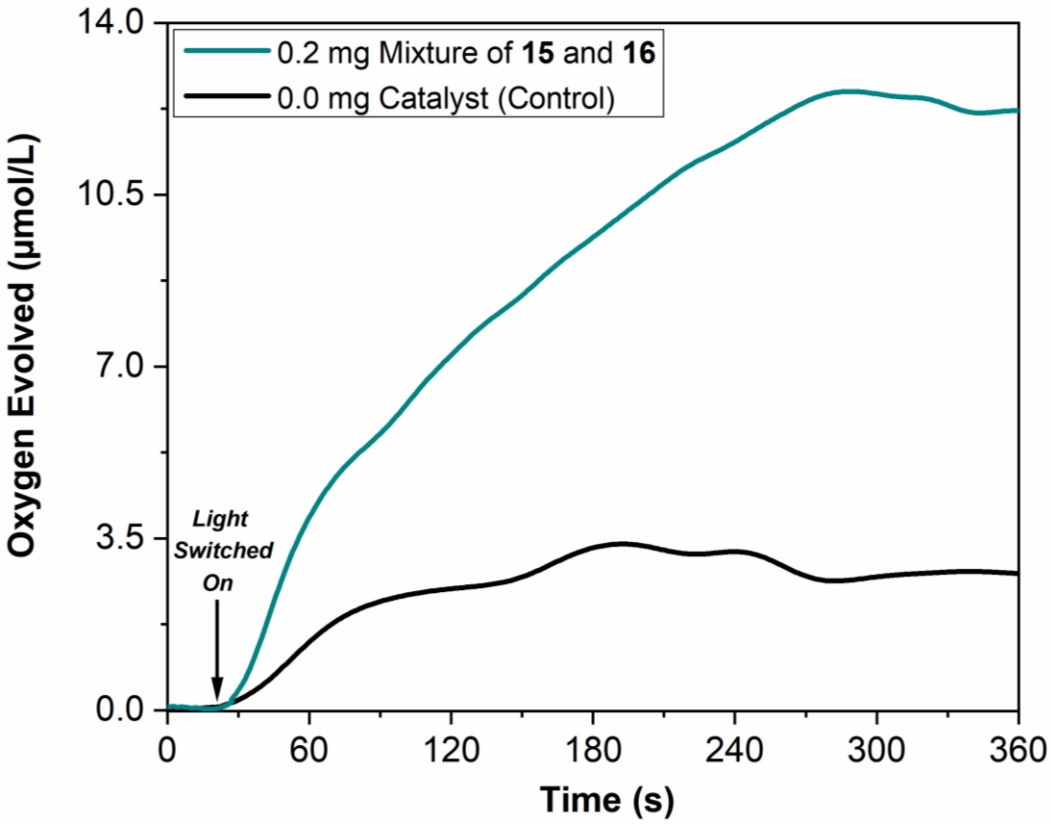

Figure 5.26: Kinetic monitoring (Clark electrode) of the light-driven OER using a mixture of **15** and **16** (0.2 mg, teal). Control test without WOC is plotted for comparison (black). Conditions: LED lamp (λ = 470, 10 mW cm^{-2}), $[Ru(bpy)_2(deeb)](PF_6)_2$ PS (2 mg) in an aqueous phosphate-buffered solution (5 mL, 0.01 M, initial pH = 7) containing $Na_2S_2O_8$ SEA (10 mM). Temperature and stirring rate were maintained at 25 °C and 500 rpm, respectively.

5.1.4 Conclusion & Future Work

A central ambition of this research project was to synthesise bioinspired metallo-supramolecular materials with potential H_2O splitting applications, as well as to characterise these compounds using single crystal X-ray diffraction in conjunction with other physicochemical techniques. This aim was achieved with the synthesis of four supramolecular assemblies comprising Mn^{II}-based SBUs connected *via* H_2**L1**-Cu^{II} (**13** and **14**) or H_2**L1**-Ni^{II} (**15** and **16**) metalloporphyrin proto-ligands. Compounds **13** – **16** were prepared in good yields, however **13** and **14** formed together as an inseparable mixture, as did **15** and **16**.

Single crystal X-ray diffraction was used to elucidate the structures of **13** – **16**. These analyses revealed **13** and **15** are isoreticular 1D coordination polymers featuring mononuclear SBUs, and **14** and **16** are structurally related 2D MMPFs which stack in the crystal structure and are composed of rod-shaped SBUs. The four frameworks **13** – **16** were characterised using FT-IR spectroscopy, TGA and PXRD spectroscopy. Interpretation of the PXRD spectra and TGA traces allowed the relative ratios of **13** to **14** and **15** to **16** in both samples to be estimated as 2:1.

A further objective of this work was to identify and investigate materials which may demonstrate catalytic activity towards either the OER or the HER. As **13** – **16** feature open metal sites, Mn^{II} building units and porphyrin linkers, it was rationalised that these structures were suitable candidates to use in H_2O splitting investigations. Accordingly, **13 – 16** were screened for photocatalytic OER or HER activity under a range of conditions. However, only very modest levels of O_2 evolution and poor robustness were observed using **13** – **16** as WOCs, with all four compounds exhibiting a TON of less than 1. The presence of Cu^{II}-based metalloporphyrin moieties in **15** and **16** was attributed to the higher TOFs of these compounds compared to **13** and **14**. H_2 evolution activity was unfortunately not exhibited by any of the structures. As a consequence of these findings, further H_2O splitting investigations were not carried out with these compounds.

The relatively low OER activity demonstrated these structures may be due to the dense packing of **13** – **16** in their crystal structures. As a result, only a small proportion of the potentially active sites of **13** – **16** are exposed H_2O substrate molecules.[51] Alternatively, the poor activity of **13** – **16** could be due to the structures not being robust enough to withstand the harsh conditions of the OER: Mn^{II}-based WOCs are typically susceptible to decomposition due to

their high lability, and porphyrins are vulnerable to attack by *in-situ* generated $^1O_2$ at their *meso* positions.[16,52]

Future work could encompass the optimisation of the syntheses of **13** – **16** in order to obtain these structures in a phase-pure form. Further, the activities of **13** – **16** may be improved using a pillaring synthetic strategy to generate pillar-layered MMPFs.[53,54] Such pillared MMPFs could benefit from increased porosity, thus allowing a greater proportion of the potentially active sites to be exposed to the substrate which may facilitate catalytic activity.

Additionally, the robustness of these compounds towards the OER may be improved by introducing blocking groups at the *meso* phenyl ring's *ortho* positions of the metalloporphyrin linkers of **13** – **16**. The introduction of bulky substituents such as F or Cl atoms, or methoxy groups at these positions has been demonstrated to sterically shield porphyrin macrocycles from attack by $^1O_2$.[55,56] Finally, future investigations may seek to explore the magnetic properties of the supramolecular structures **13** – **16**.

5.2 Additional Metalloporphyrin Supramolecular Structures

The porphyrin pro-ligand H_4**L1** was used to synthesise an additional two supramolecular assemblies: $[Zn^{II}_4O(\mathbf{L1}\text{-}Zn^{II})_3(H_2O)_3]$ (**17**) and $(TEAH)_2[In^{III}(H\mathbf{L1}\text{-}Cu^{II})_2(Ac)_2]Cl\cdot H_2O$ (**18**, TEAH = triethylammonium, Ac = acetate). **17** is a quadruply interpenetrated cubic Zn^{II}-based MMPF that was generated *via* a solvothermal reaction between H_4**L1** and $Zn(NO_3)_2\cdot 6H_2O$, whilst **18** is a mononuclear In^{III}-based porphyrin dimer which forms from a reaction between H_2**L1**-Cu^{II} and $InCl_3$.

Crystals of **17** and **18** of suitable quality for X-ray analysis were successfully prepared, allowing their structures to be elucidated. In this section the syntheses and crystal structures of **17** and **18** are discussed. Whilst structural analyses of these compounds were possible, **17** and **18** form in low yields.

5.2.1 $[Zn^{II}_4O(L1\text{-}Zn^{II})_3(H_2O)_3]$ (17)

MOF-5 ($[Zn^{II}_4O(BDC)_3]$, BDC = 1,4-benzenedicarboxylate) is regularly referred to as the archetypal MOF.[57,58,59] This quintessential framework features 6-connected $\{Zn^{II}_4O\}$ SBUs which are linked through dicarboxylate BDC ligands, generating MOF-5's primitive cubic (**pcu**) topology. The compound is characterised by a substantial pore volume of 1.04 $cm^3\ g^{-1}$ and the retention of its structural integrity upon desolvation.[60] These properties were unprecedented among porous materials known prior to the discovery of MOF-5 in 1999. As such, this MOF has been extensively investigated since its advent.[61]

Subsequent to Yaghi's seminal work on MOF-5, a plethora of analogous **pcu**-type frameworks comprising $\{Zn^{II}_4O\}$ SBUs and ditopic linkers have been designed through application of the principle of reticular synthesis.[62] Included among these structures are MOFs constructed from an array of elongated and functionalised ligands which have a broad range of potential applications.[57,63,64]

In this section, the synthesis, structure and physicochemical characterisation of an isoreticular analogue of MOF-5, $[Zn^{II}_4O(\mathbf{L1}\text{-}Zn^{II})_3(H_2O)_3]$ (**17**) are discussed. As in MOF-5, **17** forms a **pcu**-type framework encompassing $\{Zn^{II}_4O\}$ SBUs which are connected *via* linear dicarboxylate linkers. Unlike MOF-5, however, **17** comprises Zn^{II}-based metalloporphyrin ligands, which adds a further facet of functionality to this framework.

5.2.1.1 Synthesis of $[Zn^{II}_4O(L1\text{-}Zn^{II})_3(H_2O)_3]$ (17)

The MMPF $[Zn^{II}_4O(\mathbf{L1}\text{-}Zn^{II})_3(H_2O)_3]$ (**17**) was synthesized in a reaction between the freebase porphyrin pro-ligand $H_4\mathbf{L1}$ and $Zn(NO_3)_2{\cdot}6H_2O$ in a mixture of DMF and MeOH. Heating this mixture under solvothermal conditions for four days then gradually cooling to room temperature over a twelve hour period afforded the formation of pale orange, block-shaped crystals of **17** in low yield. The crystals were of suitable quality for analysis using single crystal X-ray diffraction, which facilitated the elucidation of the crystal structure of **17**.

5.2.1.2 Crystal Structure of $[Zn^{II}_4O(L1\text{-}Zn^{II})_3(H_2O)_3]$ (17)

The crystal structure of $[Zn^{II}_4O(\mathbf{L1}\text{-}Zn^{II})_3(H_2O)_3]$ (**17**) was solved in the trigonal space group $R\bar{3}c$. **17** is a four-fold interpenetrated 3D MMPF which is a symmetry-reduced, isoreticular version of MOF-5. One of the quadruply interpenetrated nets of **17** is displayed in Fig. 5.27. This framework is characterised by tetranuclear $\{Zn^{II}_4O\}$ SBUs which are coordinated by octahedral arrays of $(\mathbf{L1}\text{-}Zn^{II})^{2-}$ linkers. Each of the $\{Zn^{II}_4O\}$ nodes of **17** are connected to six other $\{Zn^{II}_4O\}$ SBUs *via* six ditopic $(\mathbf{L1}\text{-}Zn^{II})^{2-}$ ligands, generating a **pcu**-type network. The Zn atoms of the $\{Zn^{II}_4O\}$ nodes of **17** are disordered over two positions. However, for the purpose of clarity only one of these disordered positions is depicted in Figs. 5.27 – 5.32.

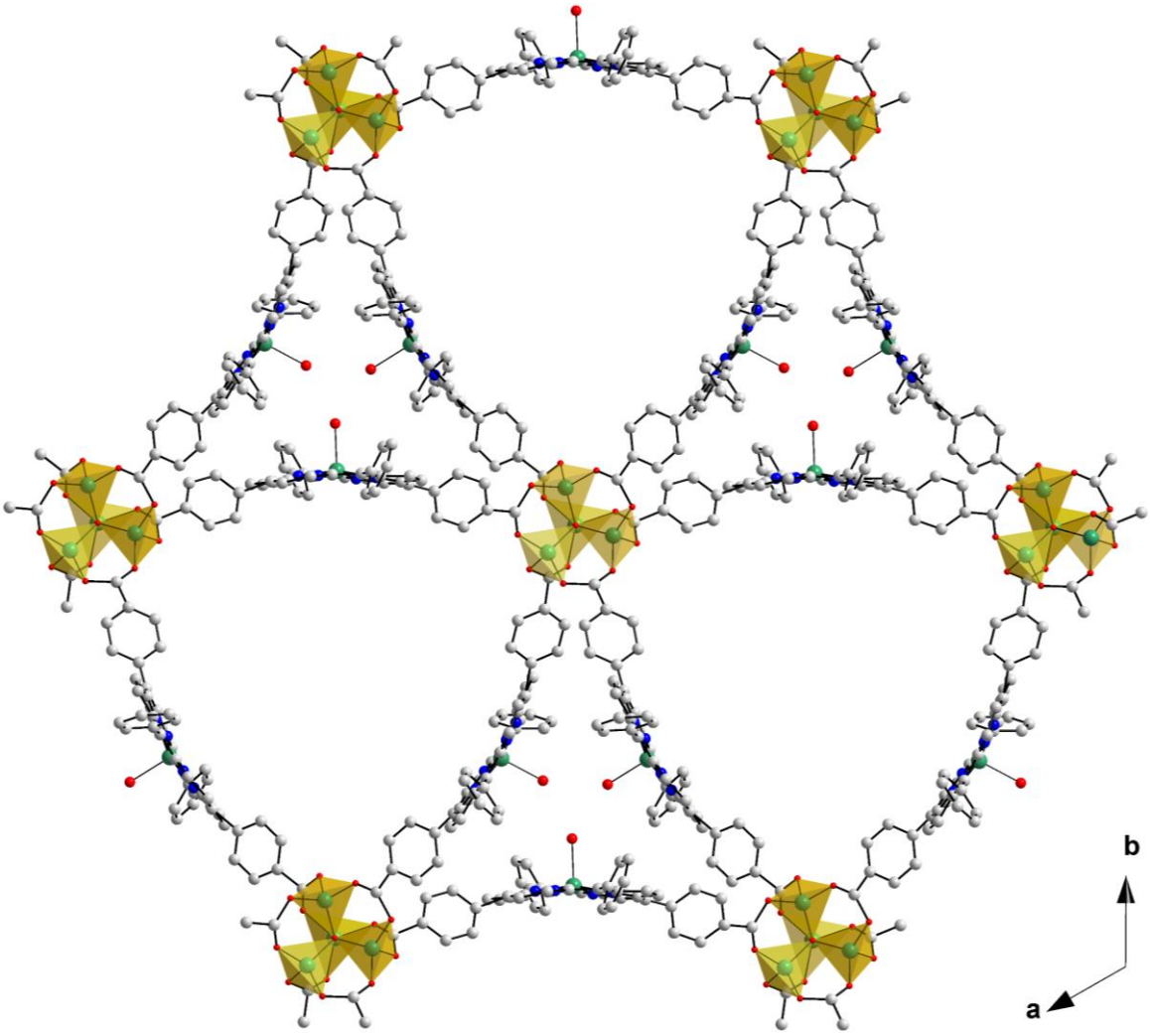

Figure 5.27: Ball-and-stick representation of one of the four-fold interpenetrated networks of the MMPF **17**, showing 6-connected $\{Zn^{II}_4O\}$ SBUs linked *via* ditopic $(\mathbf{L1}\text{-}Zn^{II})^{2-}$ ligands. Hydrogen atoms and one of the disordered positions of the $\{Zn^{II}_4O\}$ nodes have been omitted for clarity. Colour scheme: C white, N blue, O red, Zn green. Tetrahedral Zn^{II} centres are represented as yellow polyhedra.

The framework **17** can be visualised as a simple cubic net in which each of the vertices are substituted for $\{Zn^{II}_4O\}$ clusters, and the edges are replaced with $(\mathbf{L1}\text{-}Zn^{II})^{2-}$ linkers. The cubic structure of **17** can be seen clearly in Fig. 5.28. The interatomic distance between the central $\mu_4\text{-}O^{2-}$ ions of connected $\{Zn^{II}_4O\}$ clusters is *ca*. 24.7 Å. This distance is almost double the corresponding distance within MOF-5, which is *ca*. 12.9 Å.[60] This difference is due to the comparative lengths of the BDC linkers of MOF-5 and the $(\mathbf{L1}\text{-}Zn^{II})^{2-}$ ligands of **17**, which are *ca.* 12.7 Å and 19.6 Å for MOF-5 and **17**, respectively. Two $\mu_4\text{-}O^{2-}$ ions located at opposite vertices of the same cube in **17** are separated by an interatomic distance of *ca*. 30.2 Å or 46.1 Å. This variance highlights the tetragonal distortion which is exhibited by the framework **17**.

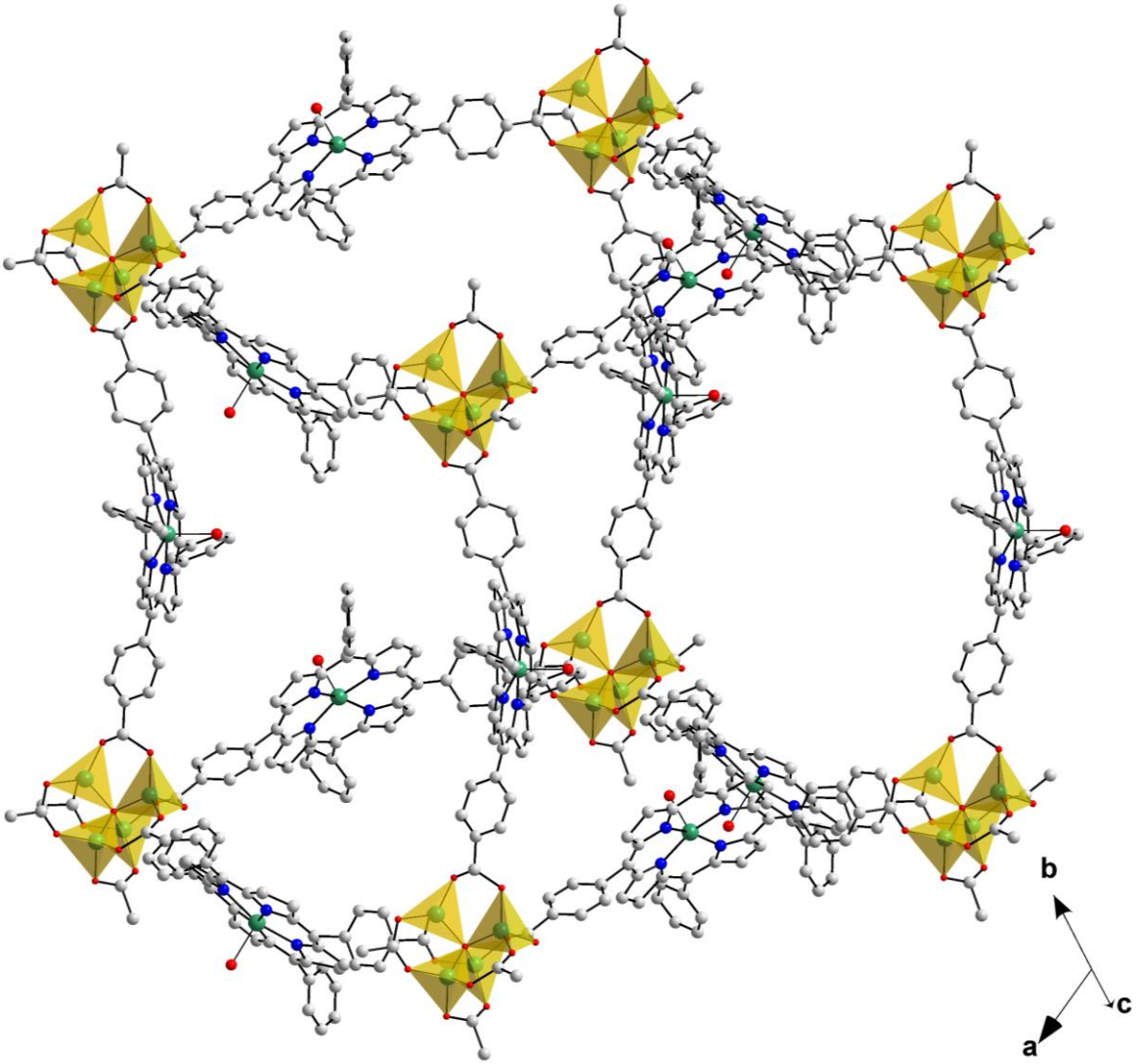

Figure 5.28: Ball-and-stick representation highlighting the cubic structure of the **pcu**-type MMPF **17** showing one of the four-fold interpenetrated networks of **17**. Hydrogen atoms and one of the disordered positions of the $\{Zn^{II}_4O\}$ node of **17** have been omitted for clarity. Colour scheme: C white, N blue, O red, Zn green. Tetrahedral Zn^{II} centres are represented as yellow polyhedra.

The asymmetric unit of **17** comprises two Zn^{II} centres and one μ_4-O^{2-} ion which derive from the SBU of **17**. Also present in the asymmetric unit of **17** are half of a $(\mathbf{L1}\text{-}Zn^{II})^{2-}$ linker moiety and one H_2O ligand which is terminally coordinated to the Zn^{II} centre of the metalloporphyrin ligand. The μ_4-O^{2-} ion and one of the Zn^{II} ions of the SBU of **17** are located on a three-fold rotoinversion axis, and the Zn^{II} ion of the $(\mathbf{L1}\text{-}Zn^{II})^{2-}$ linker is located on a two-fold inversion axis. As a result of the extensively interpenetrated nature of **17**, the solvent-accessible void volume of the structure is *ca*. 522 $Å^3$, which corresponds to just 2.6% of the unit cell volume (calculated using the CCDC-Mercury program and a probe radius of 1.2 Å). This void space is

occupied by disordered solvent molecules which could not be modelled, so were therefore accounted for using the Platon-Squeeze routine.[65]

Topologically, **17** can be described as a uninodal, 6-connected quadruply interpenetrated **pcu**-type network with the overall point symbol of $\{4^{12}\cdot6^3\}$. A topological reduction of **17** is presented in Fig. 5.29, which illustrates the four-fold interpenetrating **pcu**-type nets of this MMPF.

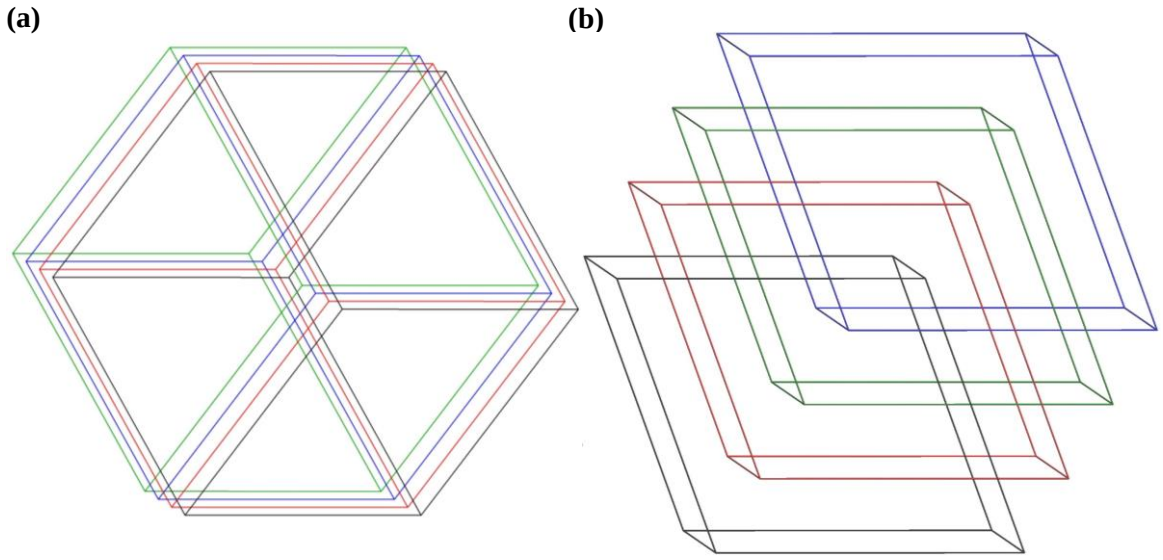

Figure 5.29: Topological reduction of **17** showing quadruply interpenetrated cubic **pcu**-type nets. Viewed approximately in the direction of the crystallographic (a) *c*-axis and (b) *b*-axis.

The $\{Zn^{II}_4O\}$ SBU of **17** is presented in detail in Fig. 5.30. The building unit comprises a μ_4-O^{2-} ion O(5) which is located at the centre of the cluster core. O(5) is coordinated by four Zn^{II} ions Zn(1), Zn(2), Zn(2') and Zn(2'') which form the vertices of a tetrahedron. Each of the metal centres are also bridged by three *syn-syn* μ_2-η^1:η^1 carboxylate moieties which derive from three different (**L1**-Zn^{II})$^{2-}$ linkers and constitute the edges of the tetrahedral node. A total of six bridging carboxylate groups, four Zn^{II} centres and one μ_4-O^{2-} ion embody the six-connected tetrahedral $\{Zn^{II}_4O\}$ node of **17**.

The Zn atoms of the $\{Zn^{II}_4O\}$ SBU are disordered over two positions in the crystal structure of **17**. Superimposition of the two disordered $\{Zn^{II}_4O\}$ tetrahedra generates an array of eight Zn^{II} centres which enclose the central, non-disordered μ_4-O^{2-} ion O(5). This array of Zn^{II} ions

displays a distorted cubic configuration, whereby each of the eight Zn^{II} centres locate at different vertices of a $\{Zn^{II}_8O\}$ 'cube'. This pattern of disorder has been observed in other isoreticular MOF-5 analogues.[64] For clarity in crystal structure representations of **17**, only one of the two disordered positions of the $\{Zn^{II}_4O\}$ node is depicted.

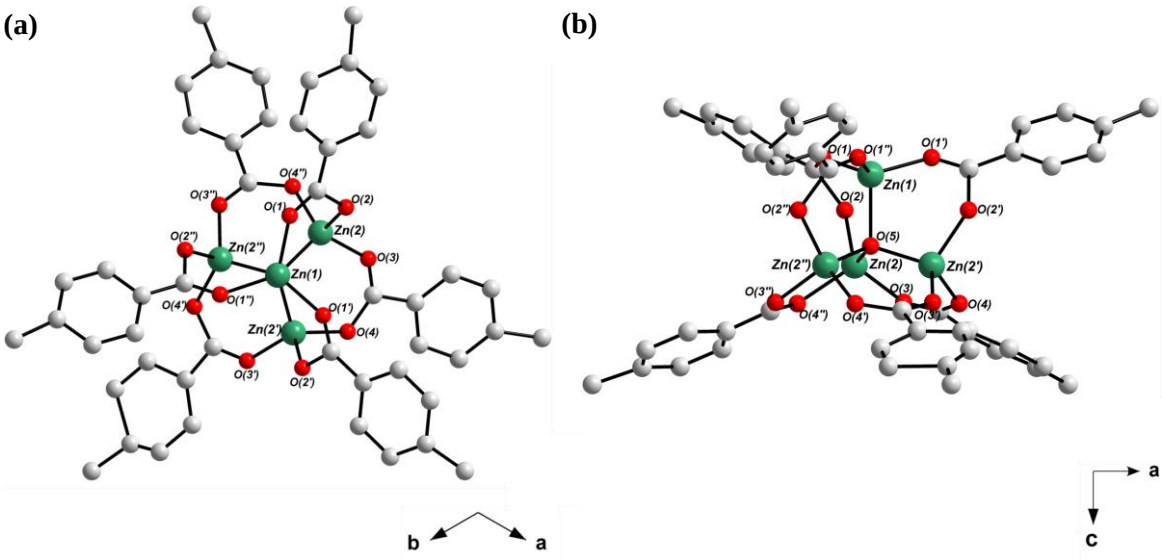

Figure 5.30: Ball-and-stick representation of the $\{Zn^{II}_4O\}$ SBU of **17**, viewed along the crystallographic (a) *c*-axis and (b) *b*-axis. Hydrogen atoms and half of the disordered Zn^{II} centres of the SBU are not shown for the purpose of clarity. Colour scheme: C white, N blue, O red, Zn green.

The coordination spheres of the four-coordinate Zn^{II} ions Zn(1) and Zn(2) are each composed of three O-donors which derive from the carboxylate moieties of three different $(\mathbf{L1}\text{-}Zn^{II})^{2-}$ linkers, and one μ_4-O^{2-} ion. The bond distance between Zn(1) and the three symmetry-related carboxylate O-donors O(1), O(1') and O(1'') is 1.9153(3) Å. This bond distance is marginally shorter than the distance between Zn(1) and the central μ_4-O^{2-} ion O(5), which is 2.0695(4) Å. The bond angles surrounding Zn(1) which deviate from the ideal tetrahedral angle of 109.5° are within the range of 113.80(8)° – 104.69(7)°. These bond distances and angles render the coordination geometry of Zn(1) distorted tetrahedral.

Similarly, the Zn^{II} ion, Zn(2) is characterised by metal – carboxylate O-donor bond distances of 1.9751(2) Å, 1.9882(2) Å and 1.9428(2) Å for Zn(2) – O(2), Zn(2) – O(3) and Zn(2) – O(4), respectively. The distance between Zn(2) and the central μ_4-O^{2-} ion O(5) is 1.9074(2) Å. The

tetrahedral bond angles surrounding Zn(2) vary between 107.29(8)° – 110.39(7)°, rendering the coordination geometry of this metal ion distorted tetrahedral.

The coordination sphere of the central, tetrahedrally coordinated μ_4-O^{2-} ion O(5) comprises four Zn^{II} ions Zn(1), Zn(2), Zn(2') and Zn(2''). The bond angles surrounding O(5) are 106.82(7)° for Zn(1)-O(5)-Zn(2), Zn(1)-O(5)-Zn(2') and Zn(1)-O(5)-Zn(2''), and 111.98(9)° for Zn(2)-O(5)-Zn(2'), Zn(2)-O(5)-Zn(2'') and Zn(2')-O(5)-Zn(2''). The bond distances and angles within the SBU of **17** are comparable with analogous $\{Zn^{II}_4O\}$ clusters reported in the literature.[60,66,67]

The (**L1**-Zn^{II})$^{2-}$ linker of **17** is displayed in Fig. 5.31. The ligand is characterised by a central, square pyramidally coordinated Zn^{II} ion Zn(3) which occupies the macrocycle's central cavity. As the freebase porphyrin H_4**L1** was used in the synthesis of **17**, metallation of the ligand occurs *in-situ*. (**L1**-Zn^{II})$^{2-}$ adopts a dome-shaped configuration, in which Zn(3) is positioned slightly above the mean porphyrin plane. The coordination environment of Zn(3) comprises four pyrrolic N-donors N(1), N(1'), N(2) and N(2') and one O-donor O(6) which derives from a terminally coordinated H_2O moiety. The four pyrrolic N-donors constitute the basal plane of the square pyramid, whereas the O-donor situates at an apical position perpendicular to the pyramid base.

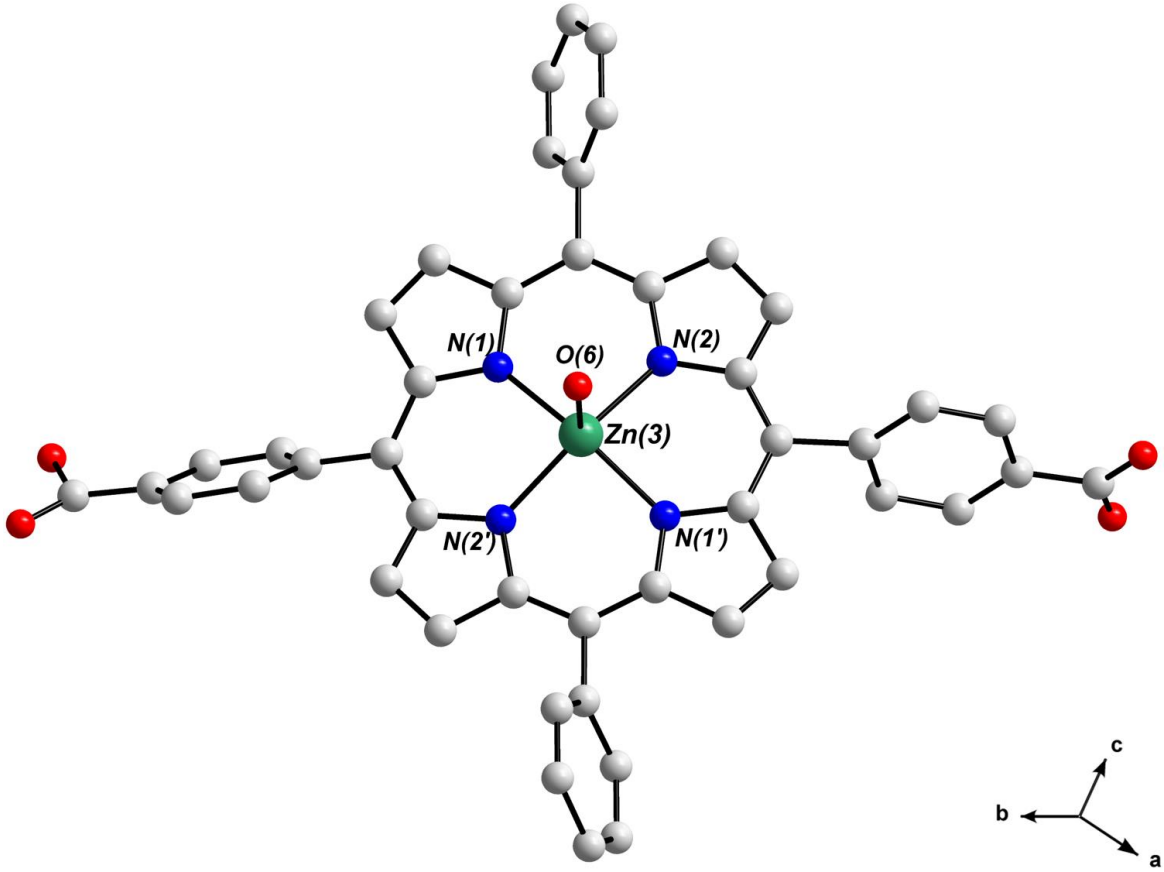

Figure 5.31: Ball-and-stick representation of the metalloporphyrin linker (**L1**-Zn^{II})$^{2-}$ of **17**. Hydrogen atoms have been omitted for clarity. Colour scheme: C white, N blue, O red, Zn green.

The bond distances between the central Zn^{II} ion Zn(3) and the four N-donors are 2.0480(3) Å for Zn(3) – N(1) and Zn(3) – N(1'), and 2.0486(3) Å for Zn(3) – N(2) and Zn(3) – N(2'). These distances are shorter than the bond distance between Zn(3) and the H_2O derived O-donor O(6), which is 2.2276(3) Å. The bond angles between N-donors which locate at opposite corners of the basal plane of the square pyramidal coordination environment of Zn(3) are 162.20(7)° and 164.80(9)° for N(1)-Zn(3)-N(1') and N(2)-Zn(3)-N(2'), respectively. The apical O-donor O(6) is situated perpendicular to the porphyrin plane, and the angle between Zn(3) – O(6) and the basal plane of the square pyramid is 90.00(2)°. The dihedral angles between the non-functionalised and carboxylate-functionalised *meso* phenyl rings of (**L1**-Zn^{II})$^{2-}$ are 46.38° and 53.46°, respectively. This configuration facilitates π – π stacking interactions which stabilise neighbouring interpenetrating **pcu** nets of **17**.

Two carboxylic acid moieties and two freebase amine sites of the porphyrin ligand are deprotonated. Taking the central Zn^{II} ion into account gives the (**L1**-Zn^{II})$^{2-}$ linker a formal

charge of −2. The four Zn^{II} ions which constitute the $\{Zn^{II}_4O\}$ SBU have a combined positive charge of +8. This positive charge is balanced in the crystal structure of **17** by three $(\mathbf{L1}\text{-}Zn^{II})^{2-}$ ligands and one central μ_4-O^{2-} ion O(5). The overall charge of **17** is therefore neutral, and the assigned oxidation states of the metal ions within **17** were substantiated using BVS analysis calculations.

The packing arrangement in one of the four-fold interpenetrating **pcu**-type frameworks of **17** is displayed in Fig. 5.32. The packing diagrams highlight, tetragonally distorted channels which extend in the direction of the crystallographic *a*- and *b*-axes. The tetragonal distortion of the channels of **17** is analogous to the channels of MOF-5, which can display either tetragonally distorted[68] or cubic[60] configurations depending on the conditions employed in the synthesis of the framework.[69]

(a)

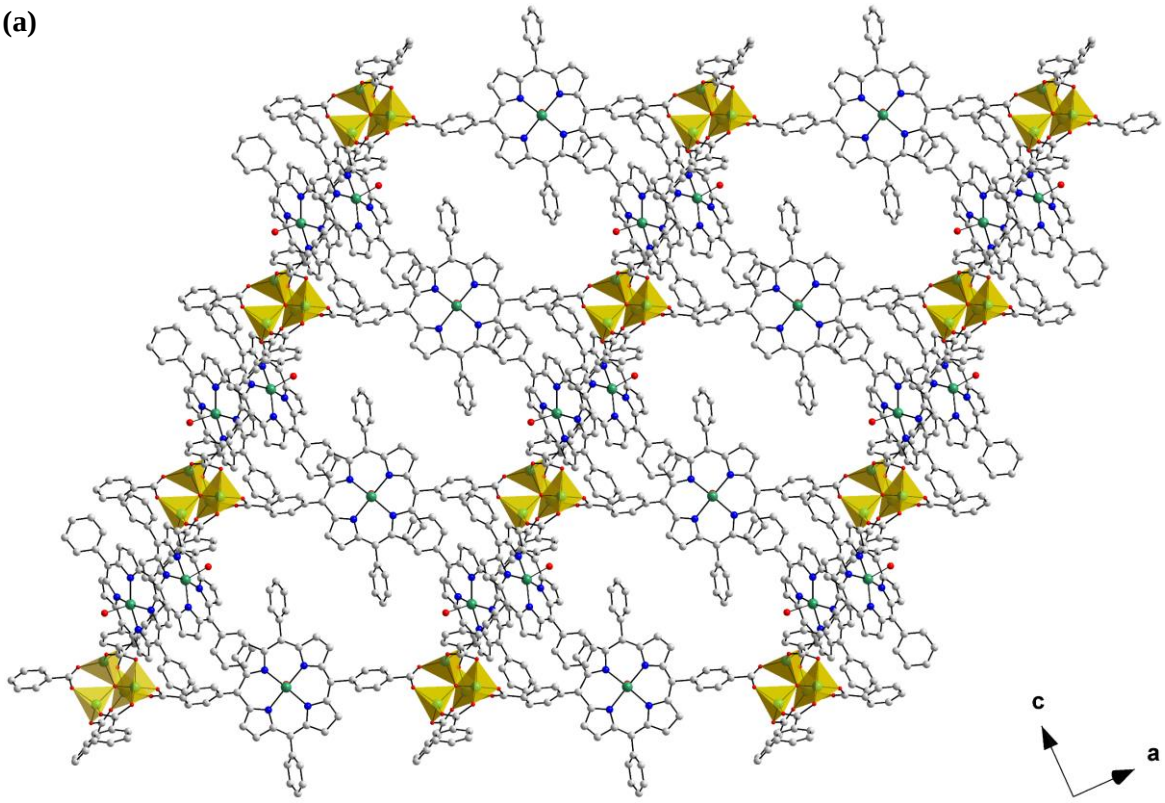

(b)

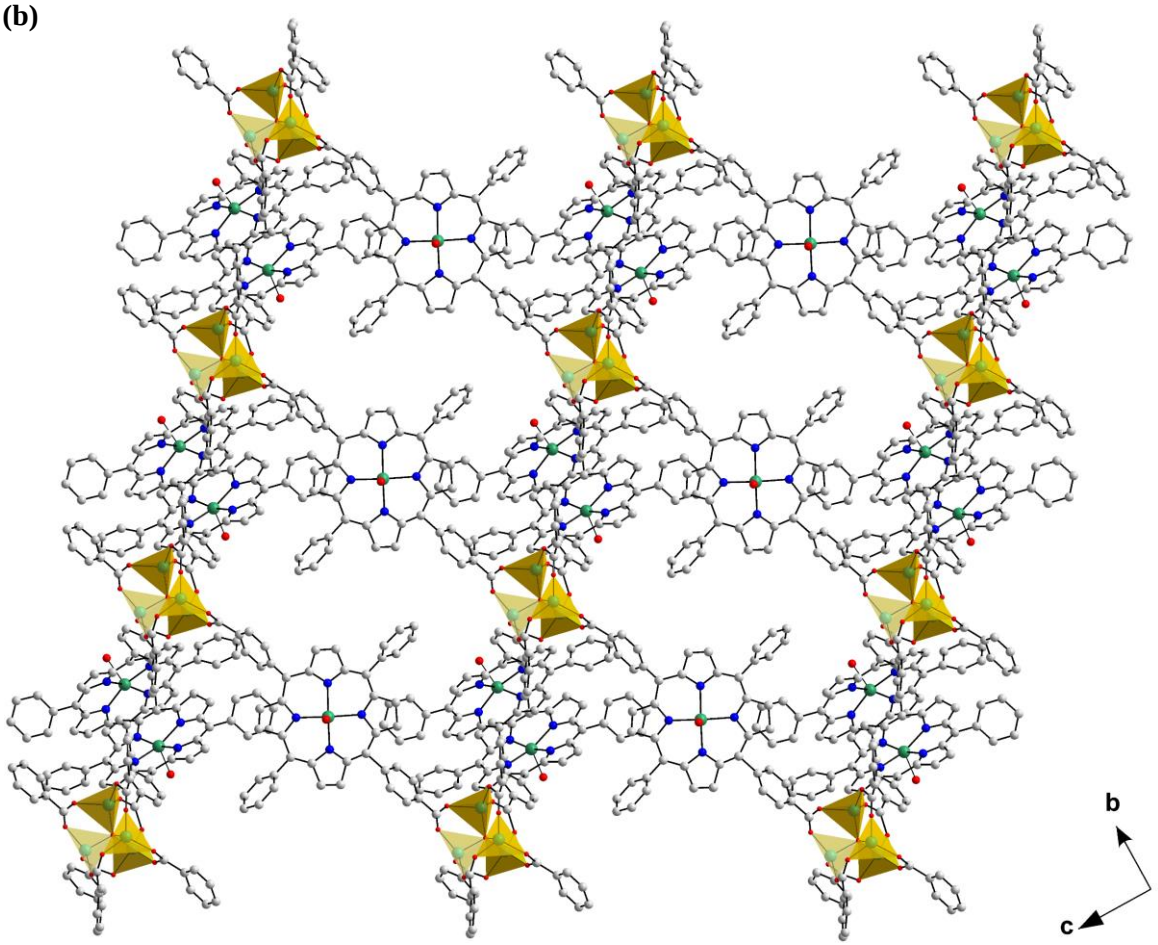

(c)

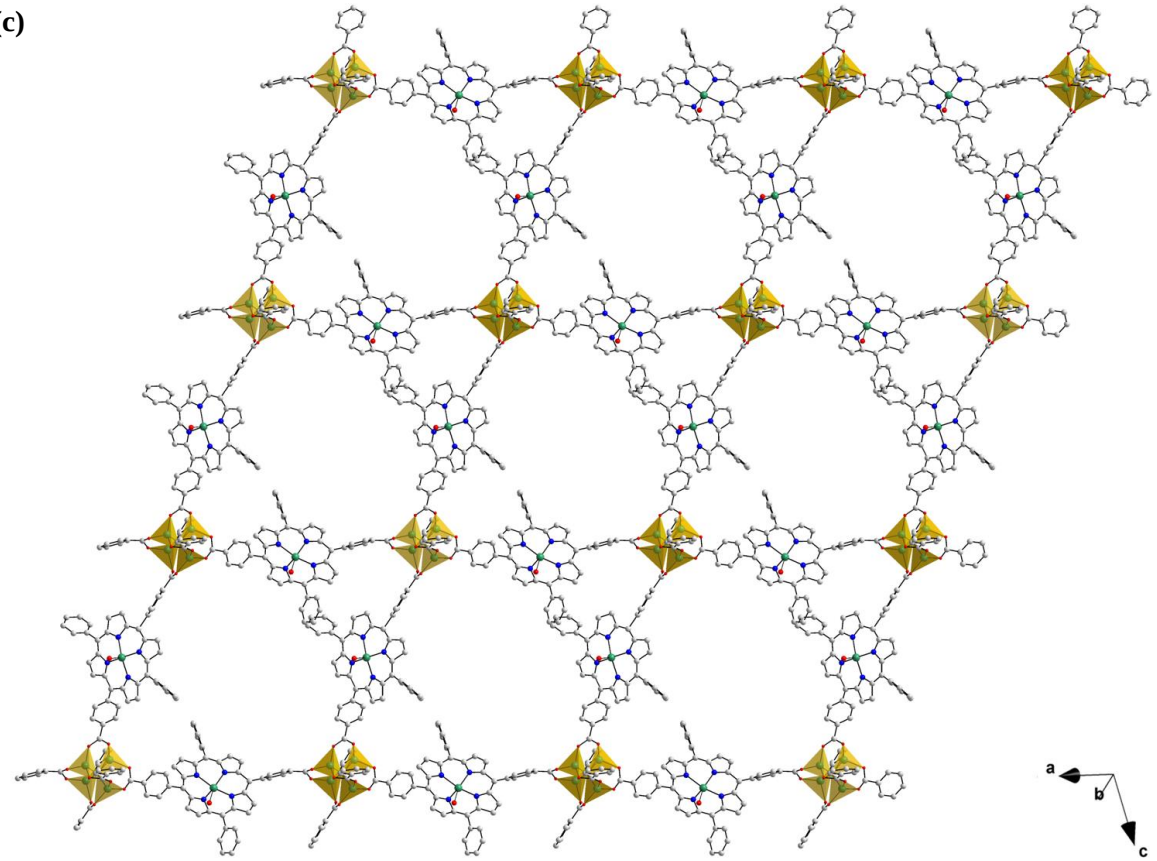

Figure 5.32: Packing diagram (ball-and-stick representation) of one of the four-fold interpenetrating cubic networks of **17**. View is in the direction of the (a) crystallographic *b*-axis, (b) crystallographic *a*-axis and (c) in the (−4,5,−1) crystallographic direction. Hydrogen atoms and half of the disordered positions of the Zn^{II} ions of the $\{Zn^{II}_4O\}$ SBUs have been omitted for the purpose of clarity. Colour scheme: C white, N blue, O red, Zn green. Zn^{II} centres are represented as yellow polyhedra.

5.2.1.3 Physicochemical Characterisation of 17

Infrared Spectroscopy

The MMPF **17** was characterised using IR spectroscopy. The FT-IR spectrum of **17** (presented in Fig. 5.33) exhibits a number of characteristic bands: Several signals around 3000 cm^{-1} can be assigned to C – H vibrations of **17**. Two bands at 1688 and 1533 cm^{-1} can be attributed to the asymmetric and symmetric stretching vibrational modes, respectively, of the carboxylate moieties of the $(\mathbf{L1}\text{-}Zn^{II})^{2-}$ linkers of **17**.[70,71,38] Two signals at 1392 and 1028 cm^{-1} can be attributed to C – N stretching and in-plane deformation (ring breathing) of the $(\mathbf{L1}\text{-}Zn^{II})^{2-}$ ligand, respectively.[39] Finally, the absence of a signal at above 3000 cm^{-1} which can be assigned to N – H vibrations of the macrocyclic ligands indicates that $H_4\mathbf{L1}$ is fully metallated *in-situ* during the synthesis of **17**.

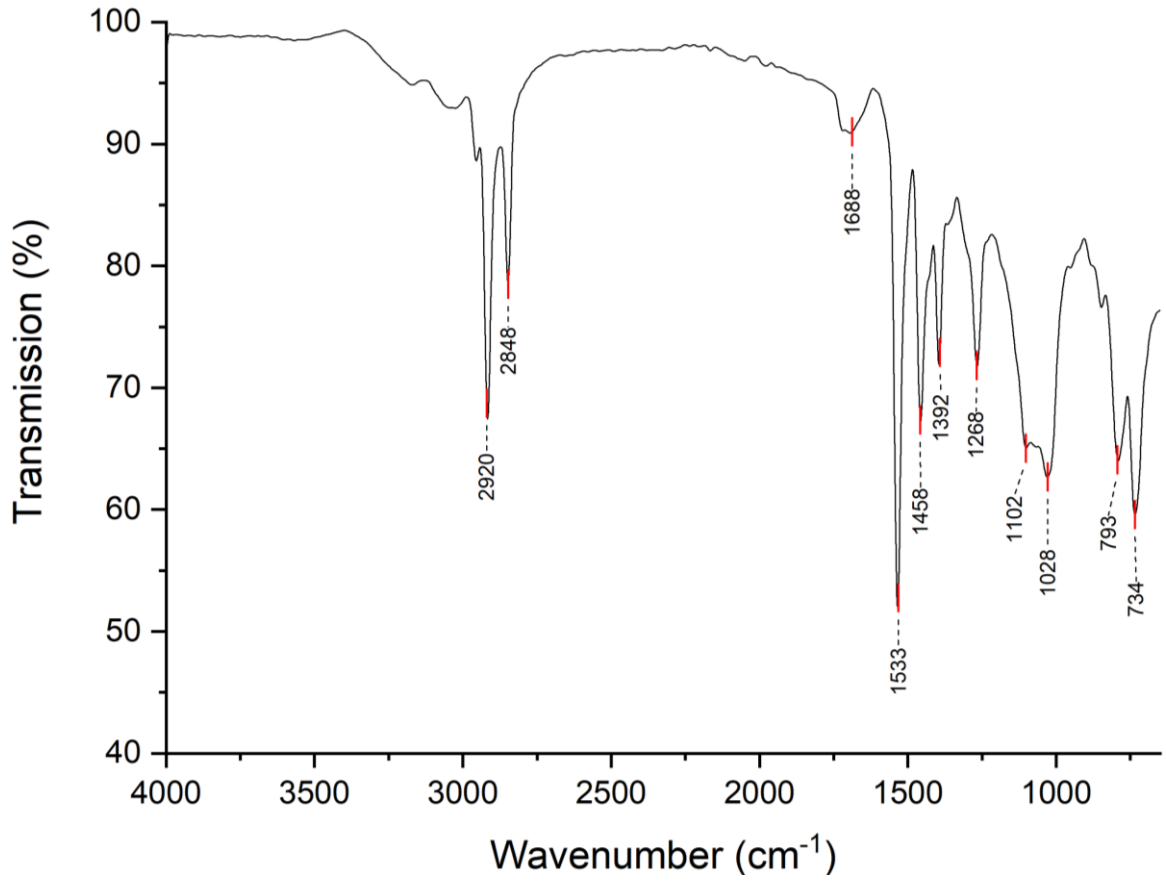

Figure 5.33: FT-IR spectrum of **17**.

5.2.2 $(TEAH)_2[In^{III}(HL1\text{-}Cu^{II})_2(Ac)_2]Cl\cdot H_2O$ (18)

Owing to the rich coordination chemistry of In^{III}, numerous supramolecular complexes and frameworks with diverse applications have been synthesised using this metal.[72,73,74] Due to the Lewis acidity and moisture stability of In compounds, they are particularly useful for mediating catalytic reactions.[75] Over the last thirty years many In-based catalysts have been prepared for a wide range of organic transformations.[76] More recently, however, In has been employed to catalyse the environmentally significant electrochemical reduction of CO_2 into formate.[77,78]

With the aim of synthesising supramolecular In-based assemblies with potential utility as photocatalysts for CO_2 or H^+ reduction, the pro-ligand H_2**L1**-Cu^{II} was reacted with $InCl_3$ under solvothermal conditions. With this, the mononuclear In^{III} metalloporphyrin dimer $(TEAH)_2[In^{III}(H$**L1**$\text{-}Cu^{II})_2(Ac)_2]Cl\cdot H_2O$ (**18**) was generated. **18** comprises a potentially redox-active In^{III} centre which is coordinated by two $(H$**L1**$\text{-}Cu^{II})^-$ ligand derivatives which may function as PS's.[26] In this section, the synthesis, crystal structure and physicochemical characterisation of **18** are discussed.

5.2.2.1 Synthesis of $(TEAH)_2[In^{III}(HL1\text{-}Cu^{II})_2(Ac)_2]Cl\cdot H_2O$ (18)

The metalloporphyrin dimer $(TEAH)_2[In^{III}(H$**L1**$\text{-}Cu^{II})_2(Ac)_2]Cl\cdot H_2O$ (**18**) was prepared in a reaction between H_2**L1**-Cu^{II} and $InCl_3$ in a mixture of DEA, MeOH and acetic acid. Heating this mixture to 120 °C under solvothermal conditions for four days afforded the formation of small, needle-shaped red crystals of **18** in low yield. These crystals were of suitable quality for analysis using single crystal X-ray diffraction.

5.2.2.2 Crystal Structure of $(TEAH)_2[In^{III}(HL1\text{-}Cu^{II})_2(Ac)_2]Cl\cdot H_2O$ (17)

The crystal structure of $(TEAH)_2[In^{III}(H$**L1**$\text{-}Cu^{II})_2(Ac)_2]Cl\cdot H_2O$ (**18)** was solved in the monoclinic space group *C*2/*c*. The structure of the In^{III}-bridged metalloporphyrin dimer **18** is displayed in Fig 5.34. **18** comprises a central In^{III} ion which is coordinated by a tetrahedral arrangement of four chelating (η^2) carboxylate ligands, two of which derive from two terminally coordinated $(H$**L1**$\text{-}Cu^{II})^-$ ligands, whilst the other two derive from two terminal acetate ligands. The coordination geometry adopted by the In^{III} centre is distorted square-antiprismatic.

The asymmetric unit of **18** is composed of one crystallographically half-occupied In^{III} ion which is located on a two-fold rotational axis, one $(H\mathbf{L1}\text{-}Cu^{II})^{-}$ ligand, one acetate ligand and a triethylammonium cation. Also present in the asymmetric unit of **18** are one Cl^{-} anion and one H_2O molecule, each of which are crystallographically ½ occupied and disordered over two positions. The proton of the non-coordinating carboxylic acid moiety of the $(H\mathbf{L1}\text{-}Cu^{II})^{-}$ ligand is also crystallographically half-occupied and disordered over two positions.

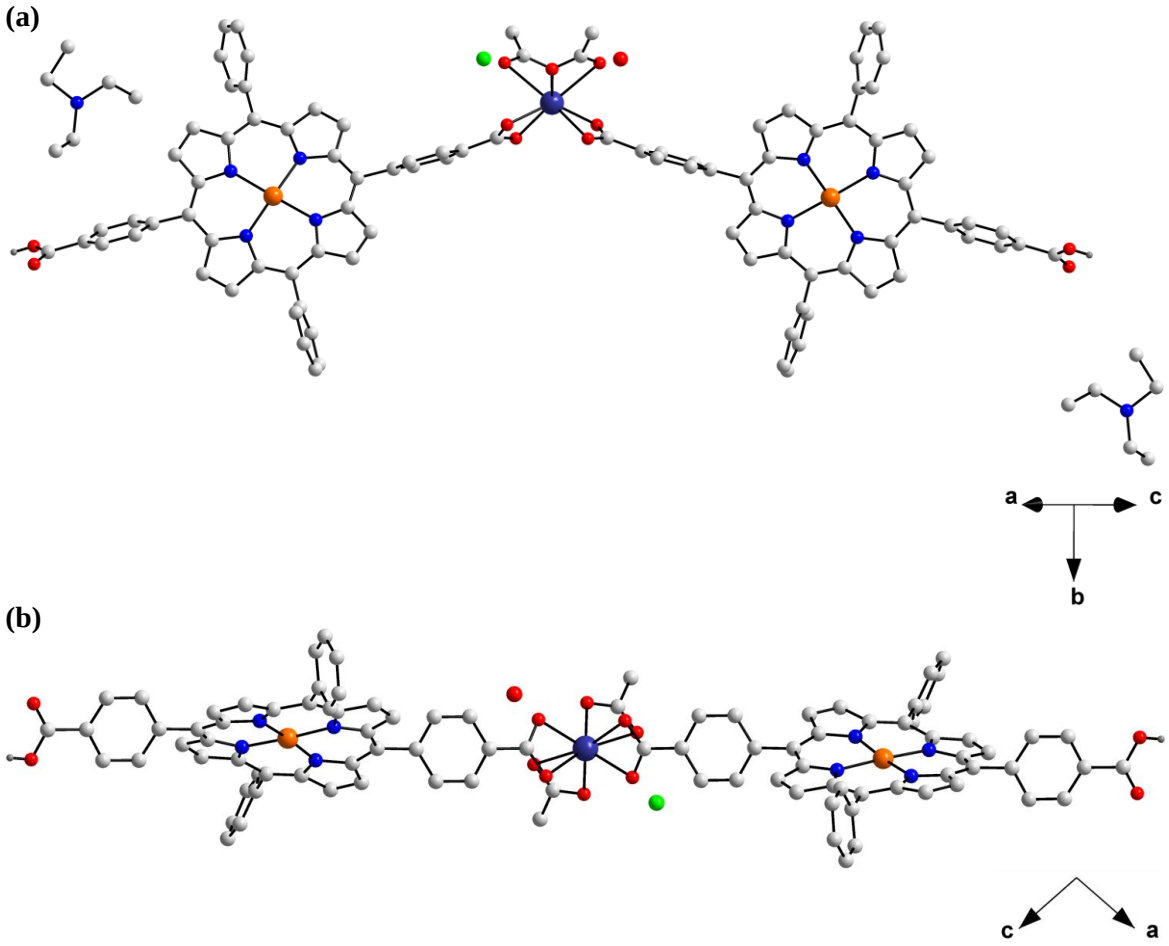

Figure 5.34: Ball-and-stick representation of the crystal structure of $(TEAH)_2[In^{III}(H\mathbf{L1}\text{-}Cu^{II})_2(Ac)_2]Cl\cdot H_2O$ (**18**). Non-carboxylic acid hydrogen atoms and, in Fig. 5.34b, triethylammonium cations have been omitted for the purpose of clarity. Colour scheme: C white, H grey, N blue, O red, Cl green, Cu orange, In indigo.

The coordination environment of the In^{III} ion, In(1) of **18** is depicted in detail in Fig. 5.35. The octacoordinated metal centre In(1) is surrounded by a distorted square-antiprismatic array of four O-donors O(1), O(1'), O(2) and O(2') which derive from two η^2 $(H\mathbf{L1}\text{-}Cu^{II})^{-}$ ligands, and

four O-donors O(3), O(3'), O(4) and O(4') of two η^2 acetate ligands. The two (H**L1**-Cu^{II})$^-$ ligands of the dimer **18** are *cis*-coordinated with respect to each other. Similarly, the two η^2 acetate ligands are *cis*-coordinated with respect to one another.

The porphyrin-derived O-donors O(1), O(1'), O(2) and O(2') locate at the vertices of one square face of the distorted antiprismatic coordination environment of In(1), whilst the carboxylate O-donors O(3), O(3'), O(4) and O(4') of the acetate ligands situate at the vertices of the other square face of the distorted antiprism. The In^{III} ion In(1) is sandwiched between the two square planes O(1)–O(1')–O(2)–O(2') and O(3)–O(3')–O(4)–O(4'), and the distance between these planes is 2.6029(9) Å. This configuration generates the square-antiprismatic coordination geometry of In(1).

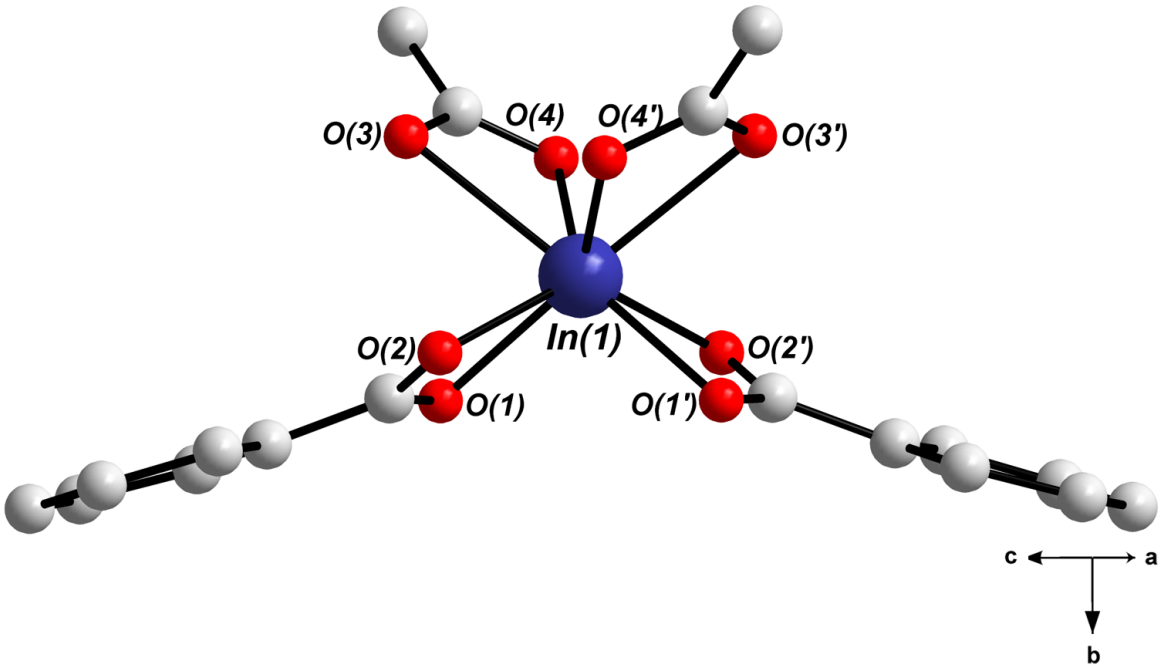

Figure 5.35: Ball-and-stick representation coordination environment of the eight-coordinate In^{III} centre of **18**. Hydrogen atoms and constitutional solvent molecules have been omitted for clarity. Colour scheme: C white, N blue, O red, In indigo.

The In^{III} centre In(1) is characterised by metal-oxygen distances of 2.2857(5) Å, 2.2309(7) Å, 2.5536(6) Å and 2.1641(7) Å for In(1) – O(1), In(1) – O(2), In(1) – O(3) and In(1) – O(4), respectively. The bite angle of the porphyrin carboxylate ligand O(1)-In(1)-O(2) is 58.17(4)°, which is slightly smaller than the bite angle of the acetate-derived carboxylate moiety O(3)-In(1)-O(4) of 54.15(4)°. These bond distances and angles are consistent with bond distances

and angles reported for other chelating carboxylate In^{III} complexes previously reported in the literature.[79]

Stabilising hydrogen bonding interactions occur between the carboxylic acid moieties of neighbouring porphyrin dimers in **18**. These interactions are highlighted in Fig. 5.36 create 1D chains of dimers through supramolecular forces. The hydrogen atom of this interaction is disordered over two positions and has a crystallographic occupancy of ½ in each position. O(5) and O(6) can, therefore, constitute either hydrogen bond acceptors or hydrogen bond donors. The hydrogen bond distance between two adjacent dimers O(6')···H – O(6) is 2.4474(9) Å, and the bond angle O(6')···H – O(6) is 155.34(4)°. These values are within expected ranges and are comparable to other hydrogen bonding interactions reported in the literature.[31]

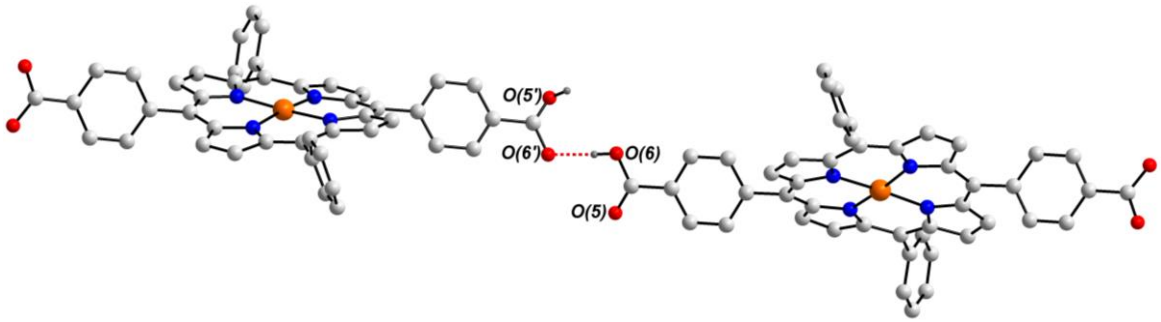

Figure 5.36: Ball-and-stick representation of the hydrogen bonding interactions which stabilise **18**. Hydrogen bond is represented as a dashed red line. Colour scheme: C white, N blue, O red, Cu orange.

The metalloporphyrin ligand of **18** is shown from two different viewing directions in Fig. 5.37. $(H\mathbf{L1}\text{-}Cu^{II})^{-}$ adopts a saddle-shaped configuration, and the dihedral angle between carboxylate functionalised phenyl rings on opposite *meso* positions of the porphyrin is 17.76(1)°. This configuration is relatively more staggered than the arrangement of the non-functionalised *meso* phenyl rings, which is 33.56(4)°. The $(H\mathbf{L1}\text{-}Cu^{II})^{-}$ ligand is deprotonated at its η^2 carboxylate binding site, and protonated at one of two positions at its non-bonding carboxylate moiety, giving the porphyrin ligand an overall charge of −1.

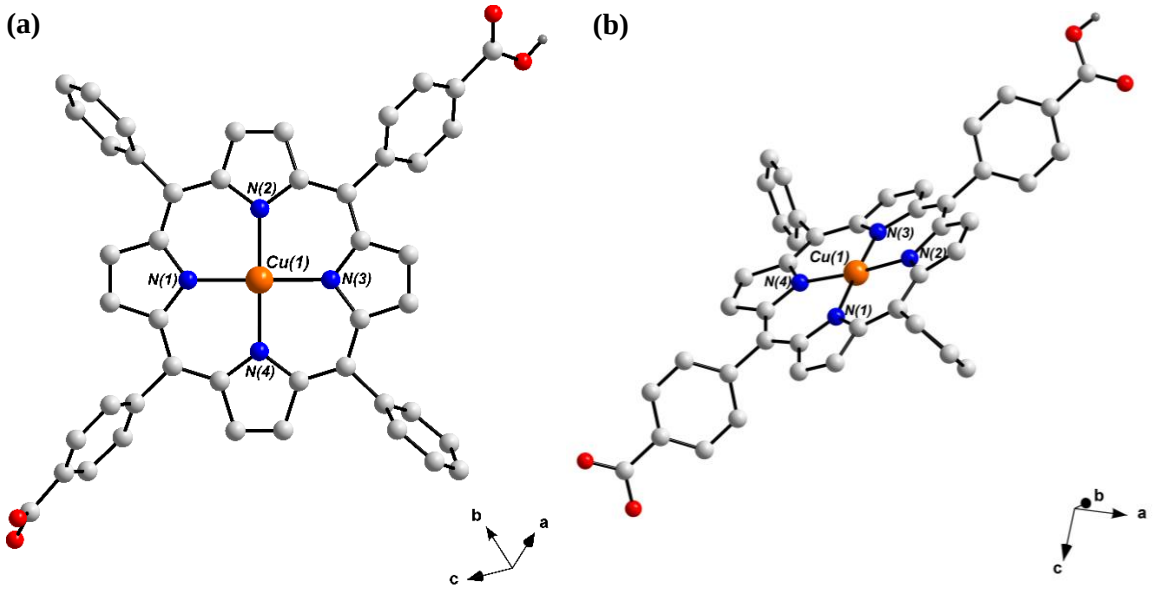

Figure 5.37: Ball-and-stick representation of the (H**L1**-Cu^{II})$^{-}$ ligand of **18**. Non-carboxylic acid hydrogen atoms not shown for clarity. Colour scheme: C white, H grey, N blue, O red, Cu orange.

The central cavity of the macrocycle is occupied by a square planar Cu^{II} ion Cu(1) which is coordinated by four pyrrolic N-donors N(1), N(2), N(3) and N(4). The bond distances surrounding Cu(1) are 1.9980(6) Å, 2.0009(5) Å, 1.9963(6) Å and 1.9975(5) Å for Cu(1) – N(1), Cu(1) – N(2), Cu(1) – N(3) and Cu(1) – N(4), respectively. The bond angles between N-donors on opposite sides of the macrocycle cavity are 176.85(5)° for N(1)-Cu(1)-N(3) and 174.59(2)° for N(2)-Cu(1)-N(4), giving the (H**L1**-Cu^{II})$^{-}$ ligand its saddle-shaped configuration.

Two deprotonated (H**L1**-Cu^{II})$^{-}$ ligands, two acetate ligands and a Cl^{-} anion give a combined negative charge of −5. This charge is balanced by a central In^{III} ion and two triethyl ammonium cations, giving **18** a net neutral charge. BVS calculations revealed that the BVS value of In(1) is 2.9, which supports the assignment of the +3 oxidation state for this ion.

The packing arrangement of **18** is displayed in Fig. 5.38. Dimers pack densely in the crystal structure and are held together by hydrogen bonding interactions which generate 1D chains with a wave-like shape. These wave-shaped chains stack on top of one another in the direction of the crystallographic *b*-axis, and the porphyrin moieties of neighbouring stacking chains interdigitate. Small solvent-filled channels locate between the interdigitating chains and extend in the direction of the crystallographic *a*-axis. The hydrogen bonded chains are further stabilised by π – π stacking interactions which extend in parallel with the crystallographic *a*-axis.

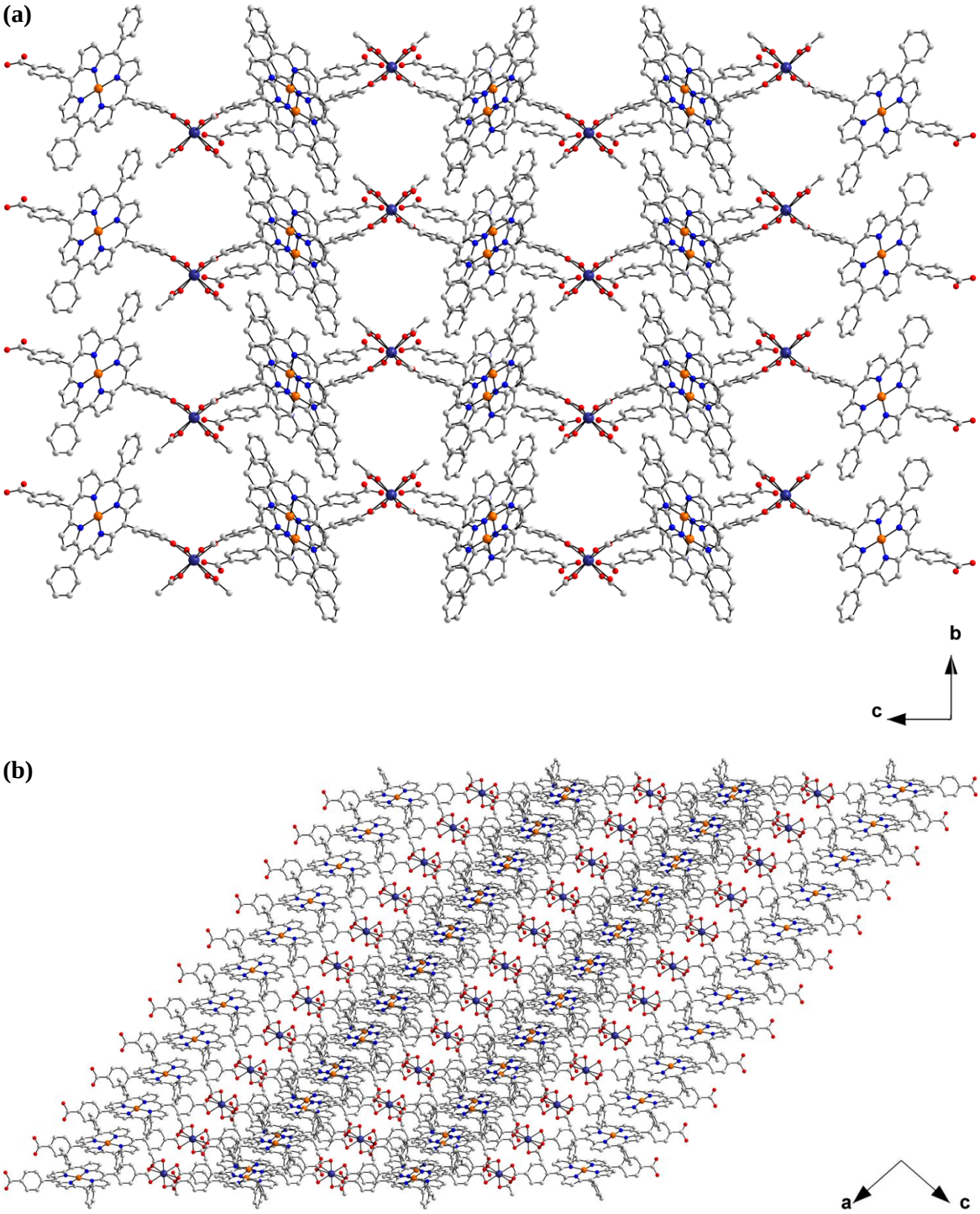

Figure 5.38: Ball-and-stick representation of the packing arrangement of **18**, showing wave-shaped chains which stack in the direction of the crystallographic *a*-axis and interdigitate. Hydrogen atoms, constitutional solvent molecules and counterionic species have been omitted for the purpose of clarity. Colour scheme: C white, N blue, O red, Cu orange, In indigo.

5.2.2.3 Physicochemical Characterisation of 18

Infrared Spectroscopy

18 was characterised using IR spectroscopy. The FT-IR spectrum of **18** is displayed in Fig. 5.39 and reveals a number of characteristic signals. A broad band at 3366 cm^{-1} can be assigned to O – H stretching vibrations of carboxylate moieties and constitutional H_2O solvent molecules of **18** which form hydrogen bonds. Broad signals above 3000 cm^{-1} can be associated with C – H stretching vibrations of the porphyrin ligands of **18**. A signal at 2962 cm^{-1} can be assigned to C – H vibrations of the aliphatic moieties within **18**. Two bands at 1713 and 1611 cm^{-1} can be attributed to asymmetric stretching vibrations of the carboxylic acid and carboxylate moieties, respectively, of the (H**L1**-Cu^{II})$^{-}$ ligands of **18**.[80] A signal at 1390 cm^{-1} can be associated with a symmetric vibration of the bidentate carboxylate moiety of (H**L1**-Cu^{II})$^{-}$.[70,71] Finally, two bands at 1257 and 1050 cm^{-1} can be assigned to C – N stretching vibrations and in-plane deformation (ring breathing), respectively, of the (H**L1**-Cu^{II})$^{-}$ ligand.[39]

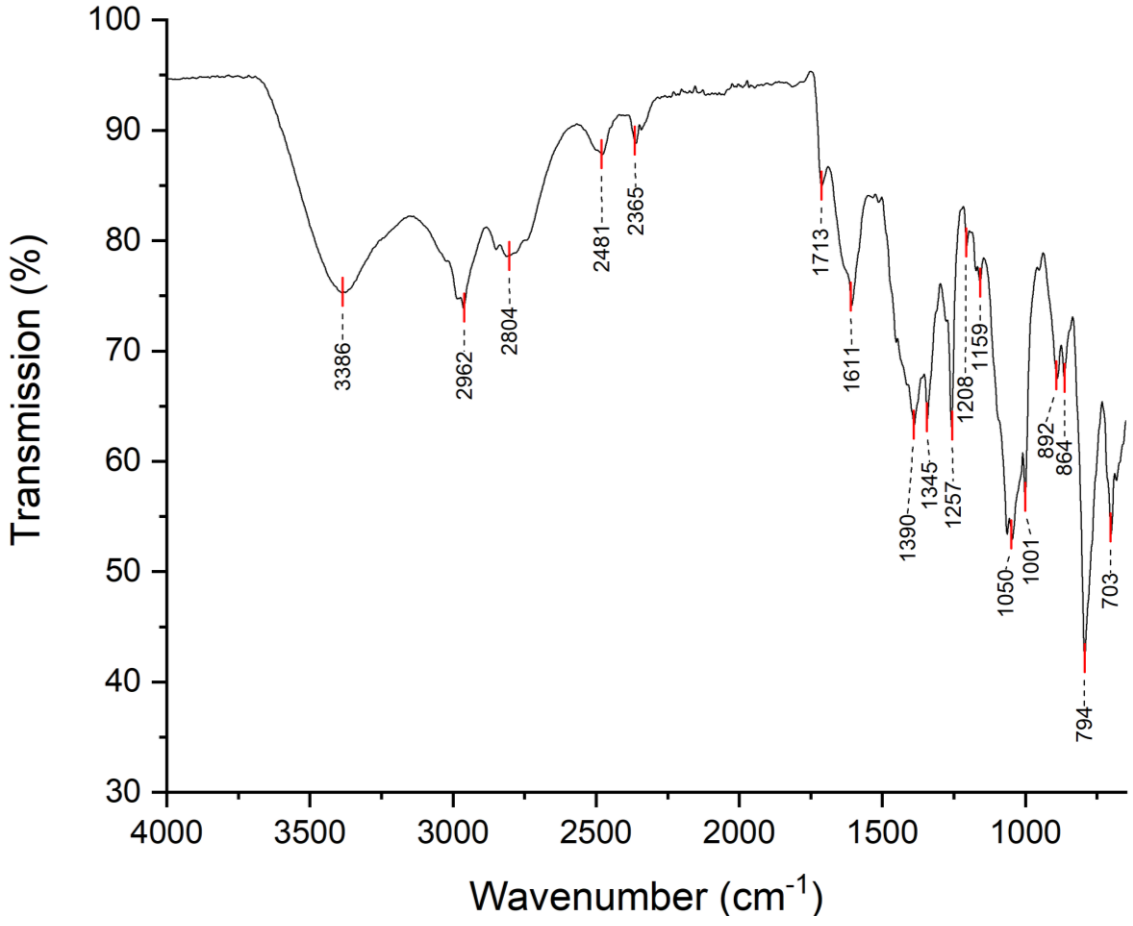

Figure 5.39: FT-IR spectrum of **18**.

5.2.3 Conclusion and Future Work

In conclusion, two metalloporphyrin-based supramolecular structures (**17** and **18**) have been synthesised and characterised using single crystal X-ray diffraction and IR spectroscopy. This analysis revealed that **17** is a quadruply interpenetrated **pcu**-type MMPF which comprises six-connected $\{Zn^{II}O_4\}$ SBUs and dicarboxylate (**L1**-Zn^{II})$^{2-}$ linkers, and that **18** is a mononuclear In^{III}-bridged (H**L1**-Cu^{II})$^{-}$ dimer.

The isoreticular MOF-5 analogue **17** was characterised using FT-IR spectroscopy, however, as the reaction which generates this compound yields only a few crystals of product further characterisation was not possible. Future investigations of **17** would initially require optimisation of the synthesis of this structure in order to improve the reaction yield. This might be achieved through careful exclusion of H_2O from the reaction mixture, as the $\{Zn^{II}O_4\}$ nodes which constitute the framework are likely to be susceptible to hydrolysis.[81] Obtaining an appreciable quantity of **17** would facilitate further characterisation of the material using TGA spectroscopy.

Additionally, post-synthetic modification (PSM) of **17** *via* transmetalation could be used to prepare analogous MMPFs to **17** which are decorated with sub-stoichiometric amounts of Mn^{2+}, Fe^{2+} or Co^{2+} ions.[82,83] This may endow newly created transmetalated frameworks with redox-activity. The successful PSM of **17** could then be confirmed using EDX spectroscopy.[84] Ultimately, these novel MMPFs could be explored as catalysts for reactions such as the OER, the HER or the reduction of CO_2.

The In^{III}-bridged metalloporphyrin dimer **18** was characterised using FT-IR spectroscopy. Future work involving **18** could entail optimising its synthesis to improve the yield of this compound, and additional physicochemical characterisation of the bulk material using thermal analysis and PXRD analysis. Finally, the photocatalytic activity of **18** towards the HER, the reduction of CO_2 or various organic transformations could be investigated.

5.3 References

1 R. J. Detz, J. N. H. Reek and B. C. C. van der Zwaan, *Energy Environ. Sci.*, 2018, **11**, 1653–1669.

2 H. L. Tuller, *Mater. Renew. Sustain. Energy*, 2017, **6**, 3.

3 H. Anthony, *Philos. Trans. R. Soc. A Math. Phys. Eng. Sci.*, 2013, **371**, 1996.

4 M. M. Najafpour, G. Renger, M. Hołyńska, A. N. Moghaddam, E.-M. Aro, R. Carpentier, H. Nishihara, J. J. Eaton-Rye, J.-R. Shen and S. I. Allakhverdiev, *Chem. Rev.*, 2016, **116**, 2886–2936.

5 G. Maayan, N. Gluz and G. Christou, *Nat. Catal.*, 2018, **1**, 48–54.

6 J. L. Fillol, Z. Codolà, I. Garcia-Bosch, L. Gómez, J. J. Pla and M. Costas, *Nat. Chem.*, 2011, **3**, 807–813.

7 D. R. Chowdhury, L. Spiccia, S. S. Amritphale, A. Paul and A. Singh, *J. Mater. Chem. A*, 2016, **4**, 3655–3660.

8 J. Soriano-López, S. Goberna-Ferrón, L. Vigara, J. J. Carbó, J. M. Poblet and J. R. Galán-Mascarós, *Inorg. Chem.*, 2013, **52**, 4753–4755.

9 M. L. Rigsby, S. Mandal, W. Nam, L. C. Spencer, A. Llobet and S. S. Stahl, *Chem. Sci.*, 2012, **3**, 3058–3062.

10 J.-W. Wang, W.-J. Liu, D.-C. Zhong and T.-B. Lu, *Coord. Chem. Rev.*, 2019, **378**, 237–261.

11 M. Gao, W. Sheng, Z. Zhuang, Q. Fang, S. Gu, J. Jiang and Y. Yan, *J. Am. Chem. Soc.*, 2014, **136**, 7077–7084.

12 K. J. Fisher, K. L. Materna, B. Q. Mercado, R. H. Crabtree and G. W. Brudvig, *ACS Catal.*, 2017, **7**, 3384–3387.

13 Y. Liu, Y. Han, Z. Zhang, W. Zhang, W. Lai, Y. Wang and R. Cao, *Chem. Sci.*, 2019, **10**, 2613–2622.

14 A. Singh and L. Spiccia, *Coord. Chem. Rev.*, 2013, **257**, 2607–2622.

15 F. Lu, M. Zhou, Y. Zhou and X. Zeng, *Small*, 2017, **13**, 1701931.

16 M. D. Kärkäs and B. Åkermark, *Dalt. Trans.*, 2016, **45**, 14421–14461.

17 B. Zhang and L. Sun, *Chem. Soc. Rev.*, 2019, **48**, 2216–2264.

18 T. Jafari, E. Moharreri, S. A. Amin, R. Miao, W. Song and L. S. Suib, *Mol.*, 2016, 21.

19 H.-C. Chen, D. G. H. Hetterscheid, R. M. Williams, J. I. van der Vlugt, J. N. H. Reek and A. M. Brouwer, *Energy Environ. Sci.*, 2015, **8**, 975–982.

20 P. Zhang, M. Wang, X. Li, H. Cui, J. Dong and L. Sun, *Sci. China Chem.*, 2012, **55**, 1274–1282.

21 W. A. V. Lozada, C. Diaz-Uribe, C. Quiñones, M. Lerma, C. Fajardo and K. Navarro, *Phthalocyanines: Alternative Sensitizers of TiO2 to be Used in Photocatalysis*, InTech,

Rijeka, 2017.

22 S.-P. Luo, E. Mejía, A. Friedrich, A. Pazidis, H. Junge, A.-E. Surkus, R. Jackstell, S. Denurra, S. Gladiali, S. Lochbrunner and M. Beller, *Angew. Chem. Int. Ed.*, 2013, **52**, 419–423.

23 T. Morikawa, S. Sato, K. Sekizawa, T. Arai and T. M. Suzuki, *ChemSusChem*, 2019, **12**, 1807–1824.

24 S. Berardi, S. Drouet, L. Francas, C. Gimbert-Surinach, M. Guttentag, C. Richmond, T. Stoll and A. Llobet, *Chem. Soc. Rev.*, 2014, **43**, 7501–7519.

25 T. G. U. Ghobadi, E. Yildiz, M. Buyuktemiz, S. S. Akbari, D. Topkaya, Ü. İsci, Y. Dede, H. G. Yaglioglu and F. Karadas, *Angew. Chem. Int. Ed.*, 2018, **57**, 17173–17177.

26 H.-C. Chen, J. N. H. Reek, R. M. Williams and A. M. Brouwer, *Phys. Chem. Chem. Phys.*, 2016, **18**, 15191–15198.

27 E. A. Malinka, G. L. Kamalov, S. V. Vodzinskii, V. I. Melnik and Z. I. Zhilina, *J. Photochem. Photobiol. A Chem.*, 1995, **90**, 153–158.

28 M. M. Najafpour and Govindjee, *Dalt. Trans.*, 2011, **40**, 9076–9084.

29 J.-R. Shen, *Annu. Rev. Plant Biol.*, 2015, **66**, 23–48.

30 J.-W. Lei, C.-X. Xie and H. Yang, *Acta Crystallogr. Sect. E*, 2012, **68**, 697–698.

31 T. Steiner, *Angew. Chem. Int. Ed.*, 2002, **41**, 48–76.

32 K. C. Mondal, O. Sengupta, M. Nethaji and P. S. Mukherjee, *Dalt. Trans.*, 2008, 767–775.

33 C. A. Hunter and J. K. M. Sanders, *J. Am. Chem. Soc.*, 1990, **112**, 5525–5534.

34 M. S. Deenadayalan, N. Sharma, P. K. Verma and C. M. Nagaraja, *Inorg. Chem.*, 2016, **55**, 5320–5327.

35 L. Li, X. Sun and B. Li, *Adv. Biosci. Biotechnol.*, 2012, **3**, 6.

36 M. B. Shundalau, A. I. Komyak, A. P. Zazhogin and D. S. Umreiko, *J. Appl. Spectrosc.*, 2012, **79**, 22–30.

37 V. Zeleňák, Z. Vargová and K. Györyová, *Spectrochim. Acta Part A Mol. Biomol. Spectrosc.*, 2007, **66**, 262–272.

38 B. Morzyk-Ociepa, M. Kokot, E. Różycka-Sokołowska, K. Giełzak-Koćwin, B. Filip-Psurska, J. Wietrzyk and D. Michalska, *Polyhedron*, 2014, **67**, 464–470.

39 L. J. Boucher and J. J. Katz, *J. Am. Chem. Soc.*, 1967, **89**, 1340–1345.

40 G. Landrou, A. A. Panagiotopoulos, K. Ladomenou and A. G. Coutsolelos, *J. Porphyr. Phthalocyanines*, 2016, **20**, 534–541.

41 T. Nakazono, A. R. Parent and K. Sakai, *Chem. – A Eur. J.*, 2015, **21**, 6723–6726.

42 J. Soriano-López, F. Song, G. R. Patzke and J. R. Galan-Mascaros, *Front. Chem.*, 2018, **6**, 302.

43 B. B. Beyene and C.-H. Hung, *Sustain. Energy Fuels*, 2018, **2**, 2036–2043.

44 A. Rajagopal, F. Venter, T. Jacob, L. Petermann, S. Rau, S. Tschierlei and C. Streb, *Sustain. Energy Fuels*, 2019, **3**, 92–95.

45 X. L. Ho, H. Shao, Y. Y. Ng, R. Ganguly, Y. Lu and H. Sen Soo, *Inorg. Chem.*, 2019, **58**, 1469–1480.

46 R. S. Sprick, B. Bonillo, R. Clowes, P. Guiglion, N. J. Brownbill, B. J. Slater, F. Blanc, M. A. Zwijnenburg, D. J. Adams and A. I. Cooper, *Angew. Chem. Int. Ed.*, 2016, **55**, 1792–1796.

47 P. Chen, O. S. Finikova, Z. Ou, S. A. Vinogradov and K. M. Kadish, *Inorg. Chem.*, 2012, **51**, 6200–6210.

48 J. Conradie and A. Ghosh, *ACS Omega*, 2017, **2**, 6708–6714.

49 H. D. Pranowo, F. Mulya, H. A. Aziz and G. A. Santoso, *Indones. J. Chem.*, 2018, **18**, 742.

50 Y. Han, Y. Wu, W. Lai and R. Cao, *Inorg. Chem.*, 2015, **54**, 5604–5613.

51 A. Dhakshinamoorthy, A. M. Asiri and H. Garcia, *Chem. Commun.*, 2014, **50**, 12800–12814.

52 R. Bonnett and G. Martínez, *Tetrahedron*, 2001, **57**, 9513–9547.

53 F. ZareKarizi, M. Joharian and A. Morsali, *J. Mater. Chem. A*, 2018, **6**, 19288–19329.

54 B. J. Burnett, P. M. Barron and W. Choe, *CrystEngComm*, 2012, **14**, 3839–3846.

55 A. M. S. Silva, M. G. P. M. S. Neves, R. R. L. Martins, J. A. S. Cavaleiro, T. Boschi and P. Tagliatesta, *J. Porphyr. Phthalocyanines*, 1998, **2**, 45–51.

56 T. Nakazono and K. Sakai, *Dalt. Trans.*, 2016, **45**, 12649–12652.

57 R. L. Martin, L.-C. Lin, K. Jariwala, B. Smit and M. Haranczyk, *J. Phys. Chem. C*, 2013, **117**, 12159–12167.

58 P. Falcaro, A. J. Hill, K. M. Nairn, J. Jasieniak, J. I. Mardel, T. J. Bastow, S. C. Mayo, M. Gimona, D. Gomez, H. J. Whitfield, R. Riccò, A. Patelli, B. Marmiroli, H. Amenitsch, T. Colson, L. Villanova and D. Buso, *Nat. Commun.*, 2011, **2**, 237.

59 J. H. Lee, S. Jeoung, Y. G. Chung and H. R. Moon, *Coord. Chem. Rev.*, 2019, **389**, 161–188.

60 H. Li, M. Eddaoudi, M. O'Keeffe and O. M. Yaghi, *Nature*, 1999, **402**, 276–279.

61 M. Eddaoudi, H. Li and O. M. Yaghi, *J. Am. Chem. Soc.*, 2000, **122**, 1391–1397.

62 M. Eddaoudi, *Science*, 2002, **295**, 469–472.

63 N. L. Rosi, *Science*, 2003, **300**, 1127–1129.

64 L. K. Macreadie, E. J. Mensforth, R. Babarao, K. Konstas, S. G. Telfer, C. M. Doherty, J. Tsanaktsidis, S. R. Batten and M. R. Hill, *J. Am. Chem. Soc.*, 2019, **141**, 3828–3832.

65 A. L. Spek, *Acta Crystallogr. Sect. C, Struct. Chem.*, 2015, **71**, 9–18.

66 H.-F. Zhou, B. Liu, L. Hou, W.-Y. Zhang and Y.-Y. Wang, *Chem. Commun.*, 2018, **54**, 456–459.

67 A. Kuc, A. Enyashin and G. Seifert, *J. Phys. Chem. B*, 2007, **111**, 8179–8186.

68 L. Huang, H. Wang, J. Chen, Z. Wang, J. Sun, D. Zhao and Y. Yan, *Microporous Mesoporous Mater.*, 2003, **58**, 105–114.

69 L. Zhang and Y. H. Hu, *Mater. Sci. Eng. B*, 2011, **176**, 573–578.

70 N. Iswarya, M. G. Kumar, K. S. Rajan and R. J. B. Balaguru, *Asian J. Sci. Res.*, 2012, **5**, 247–254.

71 R. Sabouni, H. Kazemian and S. Rohani, *Chem. Eng. J.*, 2010, **165**, 966–973.

72 L. M. Aguirre-Díaz, M. Iglesias, N. Snejko, E. Gutiérrez-Puebla and M. Á. Monge, *CrystEngComm*, 2013, **15**, 9562–9571.

73 H. Atallah, M. E. Mahmoud, A. Jelle, A. Lough and M. Hmadeh, *Dalt. Trans.*, 2018, **47**, 799–806.

74 J. Xia, J. Xu, Y. Fan, T. Song, L. Wang and J. Zheng, *Inorg. Chem.*, 2014, **53**, 10024–10026.

75 J. S. Yadav, A. Antony, J. George and B. V Subba Reddy, *European J. Org. Chem.*, 2010, **2010**, 591–605.

76 C. Frost and J. Hartley, *Mini. Rev. Org. Chem.*, 2004, **1**, 1–7.

77 W. Luo, W. Xie, M. Li, J. Zhang and A. Züttel, *J. Mater. Chem. A*, 2019, **7**, 4505–4515.

78 W. Ma, S. Xie, X.-G. Zhang, F. Sun, J. Kang, Z. Jiang, Q. Zhang, D.-Y. Wu and Y. Wang, *Nat. Commun.*, 2019, **10**, 892.

79 Y.-W. Peng, R.-J. Wu, M. Liu, S. Yao, A.-F. Geng and Z.-M. Zhang, *Cryst. Growth Des.*, 2019, **19**, 1322–1328.

80 K. Nakamoto 1922-2011, *Infrared and Raman spectra of inorganic and coordination compounds*, Wiley, New York, 5th ed., 1997.

81 K. Tan, N. Nijem, Y. Gao, S. Zuluaga, J. Li, T. Thonhauser and Y. J. Chabal, *CrystEngComm*, 2015, **17**, 247–260.

82 P. Deria, J. E. Mondloch, O. Karagiaridi, W. Bury, J. T. Hupp and O. K. Farha, *Chem. Soc. Rev.*, 2014, **43**, 5896–5912.

83 Z. Yin, S. Wan, J. Yang, M. Kurmoo and M.-H. Zeng, *Coord. Chem. Rev.*, 2019, **378**, 500–512.

84 S. Bommakanti and S. K. Das, *CrystEngComm*, 2019, **21**, 2438–2446.

Chapter Six

Experimental

6.1 Materials and Methods

6.1.1 Reagents

All chemicals and solvents were of reagent grade and purchased from the commercial suppliers Sigma-Aldrich Ltd., Fluka Chemica-Biochemica (U.K.), ABCR GmbH, Fluorochem Ltd. or local solvent suppliers and used as received without further purification unless stated otherwise. H_2O was distilled prior to use unless stated otherwise.

6.1.2 Single Crystal X-Ray Diffraction

X-ray analyses were performed by Dr. Brendan Twamley, Prof. Nianyong Zhu, Dr. Amal Cherian Kathalikkattil, Paul Wix and Friedrich Steuber. Data were collected using a Bruker APEX II DUO diffractometer equipped with a Cu-Kα (λ = 1.54184 Å) or a Mo-Kα (λ = 0.71073 Å) microfocus tube as a source. Diffraction frames were processed using the Bruker SAINT software packing, and structures were solved using BRUKER APEX v2011.8-0 software and refined using OLEX 2 software. Hydrogen atoms were refined anisotropically and assigned to their positions using a riding model. During structural refinements, the Platon-SQUEEZE routine was applied where structures contained a large amount of disordered solvent molecules that could not be resolved.[1] The solvent-accessible void volume was calculated using the 'voids' tool in Mercury (CCDC). For this calculation, a probe radius of 1.2 Å and a grid spacing of 0.7 Å were used.[2]

6.1.3 Mass Spectrometry

Samples were prepared prior to analysis by adding the material (*ca*. 0.5 mg) to a suitable HPLC grade solvent (*ca*. 1 mL) and sonicating for 10 minutes to dissolve the sample. Solid particles were removed from aqueous or organic suspensions by passing the sample through a nylon or Teflon filter, respectively, which had a pore diameter of 200 µm. Prepared samples were then analysed by either Dr. Martin Feeney or Dr. Gary Hessman. ESI mass spectra were acquired using a Micromass Time-of-Flight LCT Electrospray mass spectrometer supplied by Waters Corp. in the positive or negative mode as required. MALDI spectra were acquired using a Waters Corp Maldi Q-Tof Premier using *trans*-2-[3-4-tert-butylphenyl)-2-methyl-2-propenylidene]malononitrile as a MALDI matrix in the positive or negative mode.

6.1.4 Powder X-Ray Diffraction

Powder X-ray diffraction (PXRD) analyses of structurally robust samples were performed using a Bruker D2 Phaser equipped with a Cu-Kα (λ = 1.54184 Å) 30 kV and 10 mA source. Samples were ground using an agate mortar and pestle before loading on a zero-background sample holder. Data were collected between 2θ values of 5 – 55° at 25 °C and spectra were processed using the Bruker DIFFRAC.EVA software package.[3]

PXRD samples for compounds which were sensitive to desolvation effects were prepared by adding a finely ground sample of crystalline material under solvent to a glass capillary which was subsequently flame-sealed. PXRD spectra were then obtained either by Prof. Dr. Nianyong Zhu or Dr. Amal Cherian Kathalikkattil by mounting and centring the capillary on a goniometer head on a Bruker APEX II diffractometer. The data were collected upon 360° φ rotational frames at a detector distance of 120 mm. Data were processed using the Bruker APEX II XRD2-Eval subprogram.

6.1.5 Fourier Transform Infrared Spectroscopy

Infrared spectra were recorded using a PerkinElmer Spectrum One FT-IR spectrometer with a universal Attenuated Total Reflectance (ATR) sampling accessory and processed using Spectrum v5.01 (2002 PerkinElmer Instrument LLC) software. The scan rate used was 16 scans per minute with a resolution of 4 scans within the range of 650 – 4000 cm^{-1}. The following abbreviations were used to describe peak intensities: vs, very strong; s, strong; m, medium; w, weak; vw, very weak; br, broad and vbr, very broad.

6.1.6 Raman Spectroscopy

Raman spectroscopy measurements were performed using a Renishaw-1000 micro-Raman spectrometer equipped with a 50 × magnification objective and a cooled camera system, which was calibrated prior to measurements using an internal Si standard. The spectral resolution of the spectrometer was 1 cm^{-1}. Each spectrum was averaged over 12 measurements with an accumulation time of 10 seconds per measurement. Spectra were analysed using the Renishaw WIRE software package. Samples were excited using a 785 nm laser.

6.1.7 Nuclear Magnetic Resonance Spectroscopy

^{1}H and ^{13}C NMR spectra were recorded on a Bruker DPX 400 spectrometer operating at 400.13 MHz or 100.14 MHz, respectively, by Dr. John O'Brien or Dr. Manuel Rüther. Samples were analysed in deuterated solvents that are listed for each spectrum. Standard abbreviations were used for spectral assignments: s, singlet; d, doublet; t, triplet; q, quaternary; m, multiplet; br, broad; vbr; very broad; J, coupling constant.

6.1.8 UV-Visible Spectroscopy

UV-Vis spectra were recorded in the range 300 – 800 nm on a Cary Scan spectrophotometer at 20 °C using disposable cells with a path length of 1 cm.

6.1.9 Thermogravimetric Analysis

Thermogravimetric analyses were performed using a Perkin Elmer Pyriss-1 Thermogravimetric analyser which was equipped with an ultra-micro balance with a sensitivity of 0.1 µg which had been calibrated to Ni and Fe standards. Samples were placed in a ceramic crucible and held at 25° C for 1 minute before heating to 800 °C at a rate of 2 °C or 5 °C per minute under a nitrogen atmosphere.

6.1.10 Elemental Analysis

Quantitative elemental analysis was carried out by Rónán Crowley or Ann Connolly using an Exeter Analytical CE 440 elemental analyser in the Microanalysis Lab at the School of Chemistry and Chemical Biology of University College Dublin, Belfield.

6.1.11 Dynamic Light Scattering

Hydrodynamic radii distributions were obtained using a Malvern Zetasizer Nano ZS analyser. Samples were suspended in Millipore water in disposable cells with a path length of 1 cm prior to measurement.

6.1.12 Light-Driven O_2 Evolution Measurements

Materials

A schematic representation of the setup used to measure photocatalytic H_2O splitting reactions can be found in Section 2.5.1 on page 88. In light-driven OER catalytic experiments, borosilicate crimp top vials (5, 10 or 20 mL) were used to house the reaction mixture. A Unisense O_2-sensing Clark electrode equipped with a piercing needle tip (model: OX-NP) was used to determine the O_2 concentration inside the reactor. This microsensor was connected to a Unisense Microsensor Multimeter to amplify the signal, which was connected to a computer operating the Logger routine of the SensorTrace Suite software package.

Data were recorded at a rate of 1 data point per second, and a two-point calibration method was employed prior to each measurement, using (a) a zero-O_2 determination of an anoxic water solution (prepared using a mixture of NaOH and sodium ascorbate) and (b) air-saturated distilled water at a known temperature which was prepared by vigorously bubbling air for 10 minutes into a 300 mL Unisense Calibration Chamber (CAL300). Various LED light sources (Prizmatix, $\lambda = 390 – 700$, 405 or 470 nm) of adjustable intensity which were connected to a fibre optic cable were used to irradiate photocatalytic mixtures.

Methodology

In a typical experiment, a three-component photocatalytic mixture comprising a WOC, a PS and a SEA was added to a 5 mL crimp top vial equipped with a stir bar.[4,5,6] The reaction vessel was then hermetically sealed using a butyl rubber septum to prevent O_2 exchange with the surrounding environment and wrapped in aluminium foil to exclude ambient light. The reaction mixture was stirred at a constant rate of 500 rpm and the vial was kept at 25 °C by immersing in a temperature-controlled water bath.

Following this, an aqueous phosphate buffer solution was injected into the reactor through the rubber septum (for investigations of homogeneous OER catalysts, the WOC was introduced in the solution phase at this stage). The Clark electrode and a grounding cable were then inserted into the solution *via* the septum and the O_2 quantities were monitored thereafter in real-time. N_2 was then bubbled through the aqueous mixture until it was fully deoxygenated, before removing the N_2 inlet and waiting for a consistent, steady O_2 reading. At this point, the aluminium foil surrounding the reaction vial was removed and its content was irradiated using the LED light source ($\lambda = 470$ nm, 10 mW cm^{-2}) until no more O_2 evolution was detected.

The TONs and TOFs and O_2 yields of photocatalytic reactions were calculated as follows:

$$\mathrm{TON} = \mathrm{n}_{(\mathrm{O}_2)}/\mathrm{n}_{(\mathrm{catalyst})},$$

$$\mathrm{TOF} = \mathrm{n}_{(\mathrm{O}_2)}/\left(\mathrm{n}_{(\mathrm{catalyst})} \times \mathrm{t}\right) \text{ and}$$

$$\mathrm{O}_2\mathrm{Yield}\ (\%) = \frac{\Delta[\mathrm{O}_2]\ \times 2}{[\mathrm{Na}_2\mathrm{S}_2\mathrm{O}_8]} \times 100$$

where $\mathrm{n}_{(\mathrm{O}_2)}$ is quantity (moles) of O_2 produced, $\mathrm{n}_{(\mathrm{catalyst})}$ is quantity (moles) of WOC used, t is the time elapsed in seconds, $\Delta[O_2]$ is the change in O_2 concentration and $[Na_2S_2O_8]$ is the initial concentration of $Na_2S_2O_8$ SEA added to the reaction vial. The time period considered for TOF calculation was the first 10 seconds following the onset of the O_2 evolution.

6.1.13 Functional Testing and Control Experiments

To verify that the developed setup and methodology was suitable measuring catalytic O_2 evolution, several control experiments were carried out. Initially, a literature known WOC (commercially obtained Co_3O_4 nanoparticles, 50 – 80 nm) was irradiated (λ = 470 nm) in the presence of $Na_2S_2O_8$ SEA and $[Ru(bpy)_2(deeb)](PF_6)_2$ PS under phosphate-buffered aqueous conditions as the dissolved O_2 concentration was recorded using a Clark electrode.[7,8] Next, the light-induced O_2 evolution responses of $Na_2S_2O_8$ and $[Ru(bpy)_2(deeb)](PF_6)_2$ were established in the absence of a WOC. To this end, aqueous phosphate-buffer solutions containing either $[Ru(bpy)_2(deeb)](PF_6)_2$, $Na_2S_2O_8$, or $[Ru(bpy)_2(deeb)](PF_6)_2$ and $Na_2S_2O_8$ were irradiated while the O_2 concentration inside the reactor was monitored. The recorded O_2 evolution responses of these control experiments are plotted in Fig. 6.1.

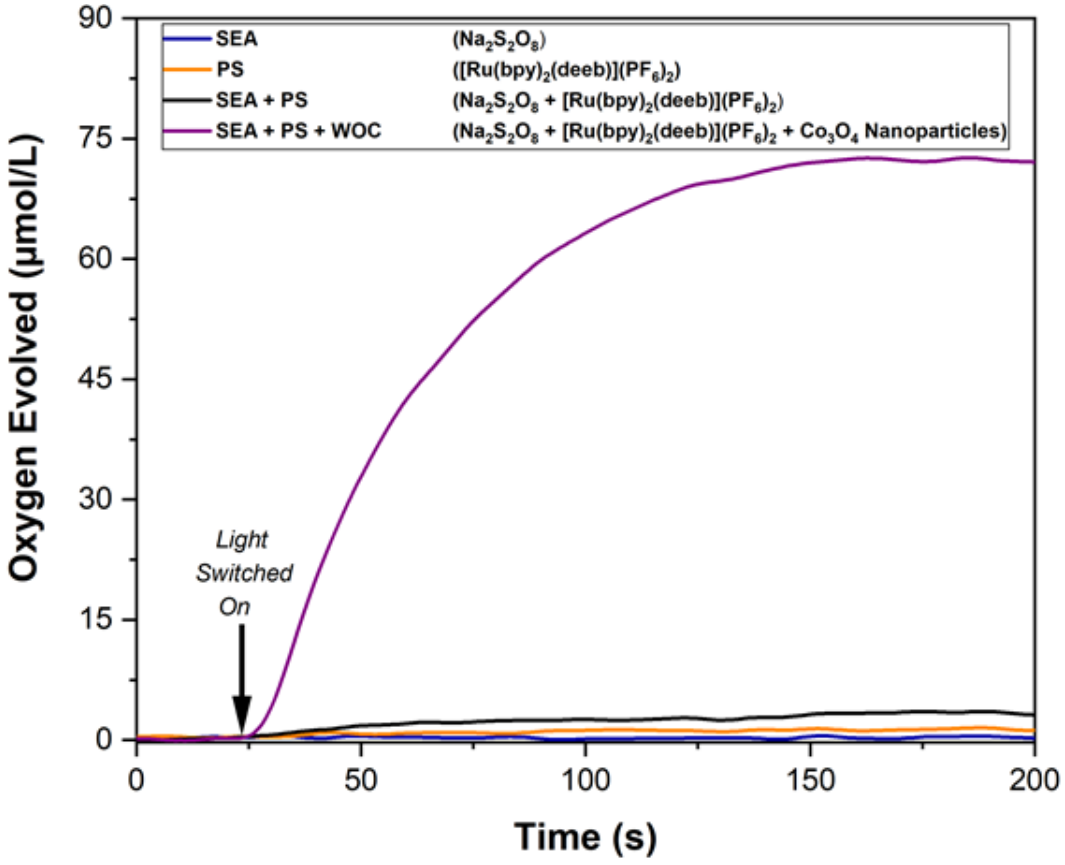

Figure 6.1: Kinetic monitoring (Clark electrode) of the O_2 evolution responses of $Na_2S_2O_8$ (10 mM, navy), $[Ru(bpy)_2(deeb)](PF_6)_2$ (2 mg, 2.33 µmol, orange), $[Ru(bpy)_2(deeb)](PF_6)_2$ (2 mg, 2.33 µmol) and $Na_2S_2O_8$ (10 mM, black) and $[Ru(bpy)_2(deeb)](PF_6)_2$ (2 mg, 2.33 µmol), $Na_2S_2O_8$ (10 mM) and Co_3O_4 nanoparticles (50 – 80 nm, 20 µg, 84 nmol, purple) in phosphate-buffered aqueous solutions (5 mL, 0.01 M, pH = 7). LED lamp (λ = 470, 10 mW cm^{-2}). The mixtures were stirred at a rate of 500 rpm and maintained at 25 °C by immersing the reaction vessel in a water bath.

Importantly, these control experiments establish that phosphate-buffered aqueous solutions at pH = 7 containing $Na_2S_2O_8$ (navy), $[Ru(bpy)_2(deeb)](PF_6)_2$ (orange) or $Na_2S_2O_8$ and $[Ru(bpy)_2(deeb)](PF_6)_2$ (black) do not give rise to significant quantities of O_2 upon illumination. Furthermore, only irradiation of a combination of a WOC, SEA and a PS (purple) gave rise to significant O_2 evolution (35 nmol). Therefore, when evaluating a potential OER catalyst in the presence of this SEA and PS, any observed O_2 evolution can rationally be attributed to the WOC under investigation. Finally, the functional test performed using Co_3O_4 nanoparticles illustrated that the employed setup and methodology are suitable for measuring the kinetics of photocatalytic O_2 evolution of a known WOC.

6.1.14 Light-Driven H_2O Oxidation Optimisation

The conditions of O_2 evolution were optimised in a series of photocatalytic experiments. In these tests, several experimental parameters including SEA concentration, PS concentration, buffer solution ionic strength and light intensity were individually modified while the OER response of an established WOC was recorded. These experiments revealed that O_2 evolution activity increased with increasing concentrations of $Na_2S_2O_8$, up to 10 mM. Increasing the SEA concentration beyond this had no impact on O_2 production. Therefore, H_2O oxidation experiments were conducted using 10 mM $Na_2S_2O_8$ solutions.

A similar trend was observed when varying the employed concentration of $[Ru(bpy)_2(deeb)](PF_6)_2$. Increasing the quantity of this PS up to 2 mg per 5 mL buffer solution resulted in increased O_2 evolution. However, further increases in PS loading beyond this did not result in improved OER performance. As such 2 mg $[Ru(bpy)_2(deeb)](PF_6)_2$ was used in typical OER experiments. The influence of phosphate buffer molarity and light intensity was also tested. The highest OER activity was observed using a buffer strength of 0.01 M, and the optimal light intensity of the incident radiation at the centre of the reactor was determined to be 10 mW cm^{-2}. A control experiment was also performed using borate-buffered aqueous solutions (initial pH = 8). Irradiating a PS and a SEA in this buffer resulted in significant O_2 evolution (*ca*. 3 μmol). This activity is attributed to decomposition of the PS into OER active species under the basic working conditions.[9] As a result of these experiments, initial testing of catalysts for light-induced OER activity was conducted using a blue (λ = 470) LED with an intensity of of 10 mW cm^{-2} under aqueous phosphate-buffered conditions (5 mL, 0.01 M, initial pH = 7) in the presence of $Na_2S_2O_8$ (10 mM) and $[Ru(bpy)_2(deeb)](PF_6)_2$ (2 mg, 2.33 μmol).

6.1.15 Mn-Oxo Compounds Screened for Light-Driven OER Activity

Several materials investigated for OER catalytic activity were synthesised and characterised by my colleagues in the Schmitt Group. Phase-pure samples of **3**, **4**, **5**, **6** and **9** were provided by Dr. Lei Zhang, **7** was prepared Dr. Colm Healy, **8** was synthesised by Swetanshu Tandon whilst **10** and **11** were provided by Dr. Ayuk M. Ako. **3** – **11** were used as received in catalytic experiments unless stated otherwise. The formulae used to determine the molar masses of these compounds for the calculation of their respective TONs and TOFs are listed in Table 6.1.

Table 6.1 – Structural formulae of the Mn-oxo compounds 3 – 11 which were screened for light-driven H_2O oxidation catalytic activity (see Chapter 3).

Compound	Structural Formula
3	$[Mn^{II}Mn^{III}_{12}(\mu_4\text{-}O)_8(\mu_4\text{-}Cl)_6(t\text{BuPO}_3)_8][Mn^{II}(MeCN)_6]Cl_2\cdot 6CH_3CN\cdot 5.25H_2O$
4	$(\text{ApyH})_3[Mn^{II}_3Mn^{III}_{10}(\mu_4\text{-}O)_6(\mu_3\text{-}O)(\mu_3\text{-}OH)(\mu_4\text{-}Cl)_4(Cl)$ $(t\text{BuPO}_3\text{H})(t\text{BuPO}_3)_9]\cdot 3CH_3CN\cdot 2H_2O$
5	$(\text{ApyH})_2[Mn^{II}_3Mn^{III}_{11}(\mu_4\text{-}O)_6(\mu_3\text{-}O)(\mu_3\text{-}OH)(\mu_2\text{-}OH)(\mu_4\text{-}Cl)_4$ $(t\text{BuPO}_3\text{H})(t\text{BuPO}_3)_{10}(\text{Apy})]\cdot\text{Apy}\cdot 3\text{MeCN}\cdot 2H_2O$
6	$[(Mn^{II}_{0.5}Mn^{III}_{0.5})Mn^{III}_{12}(\mu_4\text{-}O)_6(\mu\text{-}OH)_2(\mu\text{-}CH_3O)_4$ $(CH_3OH)_2(t\text{BuPO}_3)_{10}(\text{Pic})]Cl_{0.5}\cdot 1.5H_2O$
7	$[(Mn^{II}_{0.5}Mn^{III}_{0.5})Mn^{III}_{12}Ca^{II}_2(\mu_4\text{-}O)_6(\mu_3\text{-}O)_2(\mu\text{-}\text{OMe})_4$ $(\text{MeOH})_6(t\text{BuPO}_3)_{10}(\text{Piv})_2(Ph_2PO_2)_2]$
8	$[ClMn^{III}_6(t\text{BuPO}_3)_8(\text{Py})_6][Mn^{III}_{11}Mo^{VI}_2O_2(\mu_4\text{-}O)_2(\mu_3\text{-}O)_4$ $(\mu\text{-}O)_4(\mu\text{-}OH)_2(t\text{BuPO}_3)_{10}(\text{Py})_4]\cdot 4.5\text{MeCN}$
9	$[(Mn^{II}_{0.5}Mn^{III}_{0.5})Mn^{III}_{12}(\mu_4\text{-}O)_6(\mu\text{-}OH)_2(\mu\text{-}\text{OMe})_4$ $(\text{MeOH})_2(t\text{BuPO}_3)_{10}(\text{TDP})_4]Cl_{0.5}\cdot 8\text{MeOH}$
10	$[Mn^{III}_{12}Mn^{II}_6Sr^{II}(\mu_4\text{-}O)_8(\mu_3\text{-}Cl)_8(\text{H}\mathbf{L2})_{12}(\text{MeCN})_6]Cl_2\cdot 15\text{MeOH}$
11	$[Mn^{III}_{12}Mn^{II}_7(\mu_4\text{-}O)_8(\mu_3\text{-}OCH_3)_2(\mu_3\text{-}Br)_6(\text{H}\mathbf{L2})_{12}$ $(\text{MeOH})_5(\text{MeCN})]Br_2\cdot 9\text{MeCN}\cdot\text{MeOH}$

The crystal structures of **3** and **8** contain the co-crystallised cationic complexes $[Mn^{II}(CH_3CN)_6]^{2+}$ and $[Mn^{III}_6(t\text{BuPO}_3)_8\text{9(Cl)(Py)}_6]^{+}$. These structures have previously been isolated and demonstrated as catalytically inactive towards the light-driven OER. Therefore, catalytic activity observed using **3** and **8** can rationally be attributed to the larger co-crystallised clusters.

6.1.16 Light-Driven H_2 Evolution Measurements

Materials

Light-driven H_2 evolution experiments were carried out in an analogous manner to photocatalytic OER experiments. A Unisense H_2-sensing Clark-type electrode equipped with a piercing needle tip (model H_2-NP) was used to monitor the H_2 concentration inside the reactor in real time. This microsensor was connected to a Unisense Microsensor Multimeter and a computer operating the SensorTrace Suite package (Logger routine); data were recorded at speed of one data point per second. A two-point calibration method was employed, whereby readings were taken from (a) air (zero-H_2 reading) and (b) a vial filled with H_2 at atmospheric pressure (pure H_2 reading) prior to measuring.

Methodology

In a typical experiment, a 5 mL crimp vial equipped with a stir bar was loaded with a suspected HEC, PS ($[Ru(bpy)_3]Cl_2$, 1.88 mg, 2.33 μmol) and SED (MeOH, 1 mL, 2.47 mmol). The vial was then hermetically sealed using a butyl rubber septum and protected from light by wrapping in aluminium foil. Stirring was maintained at 500 rpm and the vial immersed in a temperature-controlled water bath to maintain a constant temperature of 25 °C. Following, an aqueous phosphate-buffered solution (4.0 mL, 0.01 M, initial pH = 7) was injected through the septum into the vial. The H-NP H_2 electrode (Unisense) and grounding cable were then inserted into the solution phase through the septum, and the real-time H_2 concentration was monitored thereafter. O_2 was then purged from the sample by bubbling N_2 into the vial for several minutes, before removing the N_2 inlet and waiting for a steady reading to be obtained from the sample. At this point, the content of the vial was illuminated, and HER activity was recorded.

The TONs and TOFs of photocatalytic H_2 evolution experiments were calculated in the same manner as for light-driven O_2 evolution experiments. However, the quantity of H_2 evolved was considered instead of the quantity of O_2 liberated.

6.1.17 Electrochemical H_2O Oxidation Experiments

LSV measurements (Chapter 3) were conducted using a Biologic VSP potentiostat. Ohmic drop compensations were applied prior to each experiment using the positive feedback compensation method as implemented in the instrumental setup. A typical three-electrode setup comprised an Ag/AgCl (KCl, 3M) reference electrode, carbon paste working electrodes (surface area = 0.07 cm^2), and a Pt wire counter-electrode for these experiments. LSV measurements were carried out in a potassium phosphate buffer solution (50 mM) using KNO_3 (1 M) as electrolyte at pH = 7.2. The carbon paste blends were prepared by grinding carbon paste and the desired quantities of catalyst in an agate mortar and pestle. The resulting mixtures were inserted inside the carbon paste electrode pocket. The LSV measurements were conducted using an ALS RRDE-3A set-up with a carbon paste rotating disc electrode (surface area = 0.07 cm^2) at 1,600 r.p.m. and at a scan rate of 10 mV s^{-1}.

Cyclic voltammetry experiments (Chapter 4) were performed using a three-electrode set up employing a modified carbon paste electrode with 5 wt.-% of **12** as the working electrode. The system was completed with a Pt wire as a counter electrode and an Ag/AgCl (KCl 1M) as a reference electrode. The ohmic drop was determined and compensated using the positive feedback compensation implemented in the instrument. The scan rate was set to 100 mV s^{-1}.

All applied potentials (E_{app}) were converted to the NHE reference scale using $E_{NHE} = E_{Ag/AgCl} + 0.210$ (V). The overpotentials were calculated by subtracting the thermodynamic H_2O oxidation potential ($E^0_{H_2O}$) from E_{app} as: $\eta = E_{app} - E^0_{H_2O/O_2}$, whereby $E^0_{H_2O/O_2}$ was corrected by the pH value by employing the Nernst equation, $E^0_{H_2O/O_2} = 1.229 - (0.059 \times pH)$ (V) vs. NHE at 25 °C. The geometrical surface area of the carbon paste electrode was used to calculate the current densities. The onset potentials were estimated from the intersection point between the tangent lines of the Faradaic current at 1 mA cm^{-2} and the non-Faradic current.

6.2 Synthesis of the PS Complex $[Ru(bpy)_2(deeb)](PF_6)_2$

The PS $[Ru(bpy)_2(deeb)](PF_6)_2$ was prepared in a three-step synthesis (summarised in Scheme 6.1) according to adapted literature protocols outlined by Ma *et al.*[10] and Meyer *et al.*[11]

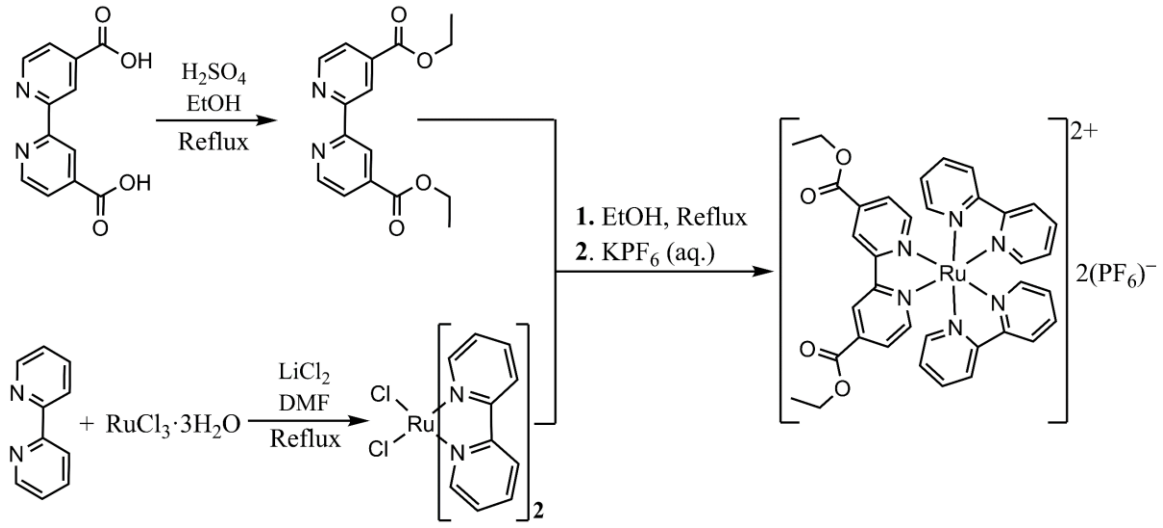

Scheme 6.1: Three-step synthetic route to afford the formation of the heteroleptic polypyridyl PS $[Ru(bpy)_2(deeb)](PF_6)_2$.

6.2.1 Synthesis of Diethyl 2,2'-bipyridine-4,4'-dicarboxylate (deeb)

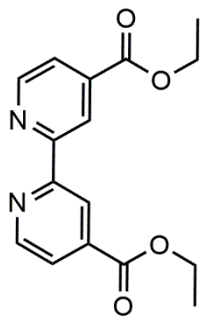

Diethyl 2,2'-bipyridine-4,4'-dicarboxylate (deeb) was synthesized according to a modified literature procedure outlined by Ma *et al.*[10] Initially, 2,2'-bipyridine-4,4'-dicarboxylic acid (0.30 g, 1.228 mmol) and concentrated H_2SO_4 (1 mL) were refluxed in EtOH (10 mL) for 4 hours. The reaction mixture was then allowed to cool to room temperature and distilled water (30 mL) was added. The resulting white precipitate was then collected by filtration and washed with MeOH before drying under vacuum. Yield: 0.28 g, 1.02 mmol, 82%.

^{1}H NMR (400 MHz, CD_3CN): δ (ppm) = 8.93 (m, 2H, pyridyl-H), 8.84 (d, 2H, pyridyl-H), 7.92 (d, 2H, pyridyl-H), 4.42 (q, 2H, CH_2), 1.38 (t, 3H, CH_3).

FT-IR υ_{max}: 3340 (w, br), 3109 (w), 2974 (w), 1728 (s), 1599 (w), 1559 (m), 1457 (w), 1369 (m), 1292 (s), 1248 (s), 1138 (s), 1088 (m), 1013 (s), 951 (m), 914 (w), 863 (m), 815 (w), 757 (s), 716 (w), 683 (s), 513 (w) cm^{-1}.

MS (ESI): Found *m/z* = 301.1148. Calculated *m/z* = 301.1188 for $[C_{16}H_{17}N_2O_4]^+$.

6.2.2 Synthesis of $[Ru(bpy)_2]Cl_2$

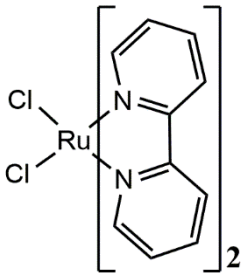

The ruthenium polypyridine precursor $[Ru(bpy)_2]Cl_2$ was synthesized according to an adapted literature procedure outlined by Meyer *et al*.[11] $RuCl_3 \cdot 3H_2O$ (2.00 g, 7.649 mmol), bpy (2.39 g, 15.298 mmol) and LiCl (2.15 g, 50.715 mmol) were refluxed together in reagent grade DMF (14 mL) for 8 hours. The reaction mixture was then cooled to 0 °C, causing the product to precipitate which was subsequently collected by filtration. The black crystalline product obtained was then washed with distilled H_2O (3 × 10 mL) followed by diethyl ether (3 × 10 mL) before allowing the product to dry in air. Yield: 1.593 g, 3.290 mmol, 43%.

^{1}H NMR (400 MHz, DMSO-d_6): δ (ppm) = 9.96 (d, 1H, pyridyl-H), 8.63 (d, 1H, pyridyl-H), 8.48 (d, 1H, pyridyl-H), 8.07 (t, 1H, pyridyl-H), 7.76 (t, 1H, pyridyl-H), 7.67 (t,1H, pyridyl-H) 7.49 (d, 1H, pyridyl-H), 7.10 (t, 1H, pyridyl-H).

FT-IR υ_{max} = 3473 (m, br), 3064 (w), 1611 (m), 1451 (m), 1419 (m), 1308 (w), 1269 (w), 1123 (w), 1020 (w), 967 (w), 895 (w), 799 (w), 764 (s), 725 (m), 653 (m) cm^{-1}.

MS (MALDI-TOF): Found *m/z* = 483.9837. Calculated *m/z* = 483.9795 for $[C_{20}H_{16}Cl_2N_4Ru]$.

6.2.3 Synthesis of $[Ru(bpy)_2(deeb)](PF_6)_2$

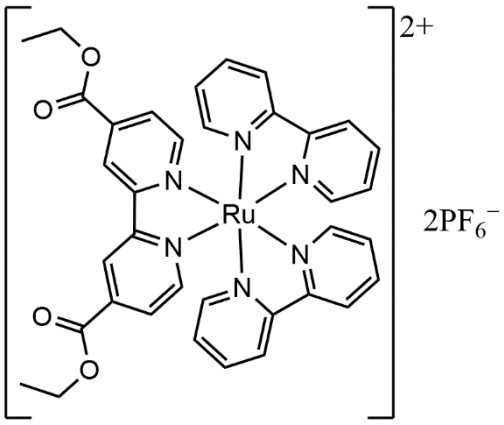

The polypyridyl PS $[Ru(bpy)_2(deeb)](PF_6)_2$ was synthesized according to an adapted literature procedure described by Ma *et al*.[10] $Ru(bpy)_2Cl_2$ (38.0 mg, 0.08 mmol) and deeb (50.0 mg, 0.16 mmol) were refluxed in EtOH (10 mL) under an atmosphere of nitrogen for 48 hours. The solvent was then evaporated under reduced pressure, and the resulting residue was recrystallized from an aqueous saturated KPF_6 solution to afford the formation $[Ru(bpy)_2(deeb)](PF_6)_2$ as a red powder. Yield: 60.1 mg, 0.057 mmol, 69%.

^{1}H NMR (400 MHz, DMSO-d_6): δ (ppm) = 9.30 (m, 2H, pyridyl-H), 8.87 (t, 4H, pyridyl-H), 8.20 (m, 4H, pyridyl-H), 7.99 (d, 2H, pyridyl-H), 7.91 (m, 2H, pyridyl-H), 7.76 (d, 2H, pyridyl-H), 7.71 (d, 2H, pyridyl-H), 7.76 (d, 2H, pyridyl-H), 7.50 (d, 2H, pyridyl-H), 4.44 (q, 4H, CH_2), 1.37 (t, 6H, CH_3).

FT-IR υ_{max}: 3119 (w, br), 1722 (m), 1606 (w), 1556 (w), 1468 (w), 1443 (w), 1368 (w), 1315 (m), 1255 (s), 1112 (w), 1022 (w), 876 (w), 828 (s), 763 (s), 725 (w), 663 (w) cm^{-1}.

MS (MALDI-TOF): Found *m/z* = 714.1584 and 859.1202. Calculated *m/z* = 714.1529 and 859.1170 for $[C_{36}H_{32}N_6O_4Ru]$ and $[C_{36}H_{32}N_6O_4PF_6Ru]$, respectively.

6.3 Synthesis of 5,15-Bis(4-carboxyphenyl)-10,20-diphenylporphyrin (H_4**L1**) and Metalloporphyrin Complexes

In this section, the syntheses of the ditopic porphyrin ligand 5,15-bis(4-carboxyphenyl)-10,20-diphenylporphyrin (H_4**L1**) and its Cu^{II}-, Ni^{II}- and Pt^{II}-metallated analogues are described.

6.3.1 Synthesis of 5-(4-Carbomethoxyphenyl)dipyrromethene

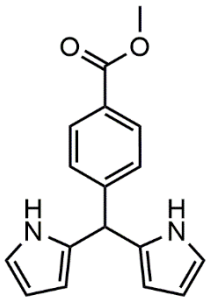

The *meso*-substituted dipyrromethane 5-(4-carbomethoxyphenyl)dipyrromethane was prepared using an adapted literature procedure outlined by Lindsey *et al*.[12] Under an inert atmosphere and while shielding from light, TFA (0.23 mL 0.343 mmol) was added to a solution of methyl-4-formyl benzoate (5.00 g, 30.4 mmol) in pyrrole (150 mL, 2.162 mol), and the solution was stirred for 3 hours. NaOH (3.60 g, 0.090 mol) was then added and the reaction was stirred for a further 1 hour. The reaction mixture was then filtered, and the filtrate was concentrated by evaporation of the solvent under reduced pressure. Excess pyrrole was saved for later use. The obtained crude product was subsequently purified by silica gel column chromatography using a mixture of hexane, DCM, ethyl acetate and TEA in a ratio of 4:2:1:0.05 (vol/vol) as the eluting solvent before washing with cold ethyl acetate yielding 5-(4-carbomethoxyphenyl)dipyrromethane as an off-white powder. Yield: 4.26 g, 15.2 mmol, 50%.

^{1}H NMR (400 MHz, CD_3CN): δ (ppm) = 8.94 (m, 2H, NH), 7.92 (m, 2H, aryl-H), 7.32 (m, 2H, aryl-H), 6.66 (m, 2H, pyrrole-H), 6.02 (m, 2H, pyrrole-H), 5.77 (m, 2H, pyrrole-H), 5.52 (s, 1H, CH), 3.85 (s, 3H, CH_3).

^{13}C NMR (100 MHz, CD_3CN): δ (ppm) = 167 (s, 1C, carboxy-C), 150 (s, 1C aryl-C), 133 (s, 2C, pyrrole-C), 130 (s, 2C, aryl-C) 129 (s, 1C, aryl-C), 129 (s, 2C aryl-C), 119 (s, 2C, pyrrole-C), 109 (s, 2C, pyrrole-C), 108 (s, 2C, pyrrole-C), 53 (s, 1C, CH_3), 45 (s, q, 1C, CH).

FT-IR υ_{max}: 3332 (s), 1701 (s), 1607 (m), 1555 (w), 1508 (w), 1434 (m), 1416 (w), 1290 (s), 1261 (m), 1199 (m), 1179 (m), 1115 (s), 1097 (m), 1032 (s), 962 (m), 868 (w), 803 (w), 781 (m), 729 (vs) cm^{-1}.

MS (ESI): Found *m/z* = 279.1128 and 280.1242. Calculated *m/z* = 279.1134 and 280.1218 for $[C_{17}H_{15}N_2O_2]^-$ and $[C_{17}H_{16}N_2O_2]^-$, respectively.

6.3.2 Synthesis of 5,15-Bis(4-carbomethoxyphenyl)-10,20-diphenylporphyrin (Me_2H_2L1)

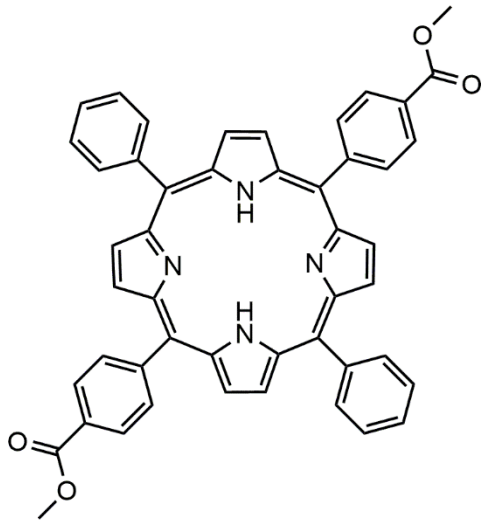

Under an inert atmosphere shielded from light, benzaldehyde (3.6 mL, 35.3 mmol) was added to a solution of 5-(4-carbomethoxyphenyl)dipyrromethane (9.60 g, 34.5 mmol) in dry DCM (3.3 L). To this solution, TFA (6.6 mL) was then added dropwise over 1 minute. The reaction was then stirred for 3 hours before adding *p*-chloranil (12.48g, 50.7 mmol) and stirring overnight. TEA (6.6 mL) was then added to quench the reaction, before removing the solvent under reduced pressure. The crude product was then dry loaded onto silica and purified using silica gel column chromatography with CH_3Cl as the eluent. A purple powder consisting of a number of different methoxy ester-substituted porphyrins was obtained as the second purple band after tetraphenylporphyrin. This mixture was then subjected to a second dry loaded silica column using DCM/hexane in a ratio of 2:1 (vol/vol) as the eluent to obtain the desired diester porphyrin in the third purple band. Evaporation of the solvent under reduced pressure afforded 5,15-bis(4-carbomethoxyphenyl)-10,20-diphenylporphyrin (Me_2**L1**) as a purple powder. Yield: 0.6 g, 0.817 mmol, 17%.

^{1}H NMR (400, MHz $CDCl_3$): δ (ppm) = 8.80 (m, 4H, pyrrole-H), 8.75 (m, 4H, pyrrole-H), 8.45 (d, 4H, benzyl-H, J = 9.2 Hz,), 8.28 (d, 4H, benzyl-H, J = 6.9 Hz), 8.20 (d, 4H, aryl-H, J = 9.2 Hz), 7.78 (m, 6H, aryl-H), 4.12 (s, 6H, CH_3), -2.78 (br, s, 2H, pyrrole-H).

MS (MALDI-TOF): Found *m/z* = 730.2417. Calculated *m/z* = 730.2580 for [$C_{48}H_{34}N_4O_4$].

FT-IR υ_{max}: 3316 (w), 2948 (w), 1716 (s), 1601 (m), 1555 (w), 1471 (w), 1436 (m), 1401 (w), 1345 (w), 1271 (s), 1183 (m), 1103 (s), 1022 (w), 962 (m), 871 (w), 794 (s), 727 (s) cm^{-1}.

UV-Vis (DMF): λ_{max}/nm (ε/L mol^{-1} cm^{-1}) = 415 (1.8 × 10^5, Soret band, π – π*), 513 (9.0 × 10^3, Q band, π – π*), 546 (4.0 × 10^3, Q band, π – π*), 590 (3.4 × 10^3, Q band, π – π*), 645 (2.9 × 10^3, Q band, π – π*).

6.3.3 Synthesis of 5,15-Bis(4-carboxyphenyl)-10,20-diphenylporphyrin (H_4**L1**)

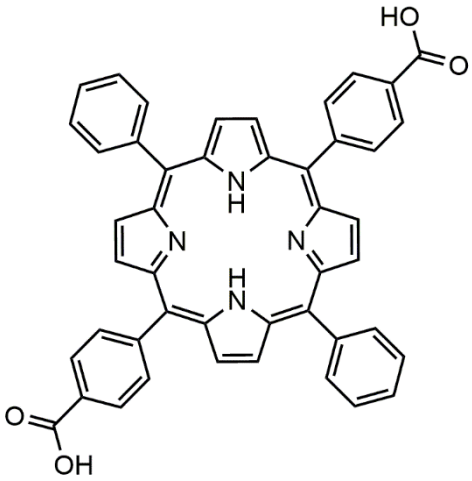

The ester 5,15-bis(4-carbomethoxyphenyl)-10,20-diphenylporphyrin (H_2Me_2**L1**) was hydrolysed according to an adapted literature procedure outlined by Zhu *et al.*[13] Me_2H_2**L1** (0.10 g, 13.7 mmol) was first dissolved in a mixture of THF and MeOH (1:1 vol/vol, 60.0 mL) before adding an aqueous solution of KOH (6.00 mL, 1.78 M) and heating to reflux for 2 days. The reaction mixture was then cooled to ambient temperature and the organic solvent was removed under reduced pressure before dissolving the solid residue in distilled water (100 mL). The resulting solution containing the dipotassium porphyrin salt was subsequently acidified using 1M HCl until no further precipitation was observed. Following this, the precipitate was collected by filtration before washing thoroughly using copious amounts of hot distilled water and hexane. Finally, the porphyrin dicarboxylic acid H_4**L1** was obtained as a purple crystalline powder. Yield: 0.09 g, 13.0 mmol, 95%.

^{1}H NMR (400 MHz, DMSO-d_6): δ (ppm) = 8.86 (br, m, 8H, pyrrole-H), 8.36 (d, 4H, benzyl-H, J = 8.0 Hz), 8.29 (d, 4H, benzyl-H, J = 8.0 Hz), 8.21 (m, 4H, aryl-H) 7.85 (m, 6H, aryl-H), 2.93 (s, 2H, pyrrole-H).

MS (MALDI-TOF): Found *m/z* = 702.2281. Calculated *m/z* = 702.2267 for [$C_{46}H_{30}N_4O_4$].

UV-Vis (DMF): λ_{max}/nm (ε/L mol^{-1} cm^{-1}) = 415 (1.8×10^5, Soret band, π – π*), 512 (4.7×10^3, Q band, π – π*), 546 (3.5×10^3, Q band, π – π*), 590 (3.3×10^3, Q band, π – π*), 644 (2.2×10^3, Q band, π – π*).

FT-IR υ_{max}: 3315 (w, vbr) 2923 (w), 2853 (w), 2531 (w), 1687 (s), 1599 (s), 1533 (m), 1472 (w), 1393 (s), 1281 (m), 1174 (w), 1134 (w), 1078 (w), 964 (s), 875 (w), 841 (w), 801 (s), 703 (vs) cm^{-1}.

6.3.4 Synthesis of [5,15-Bis(4-carboxyphenyl)-10,20-diphenylporphyrinato]-Cu^{II} (H_2**L1**-Cu^{II})

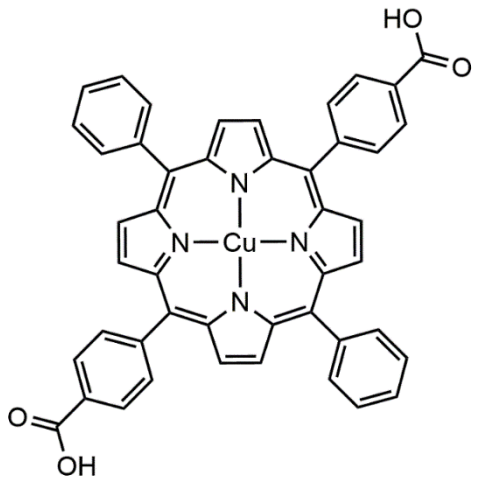

The porphyrin [5,15-bis(4-carboxyphenyl)-10,20-diphenylporphyrinato]-Cu^{II} (H_2**L1**-Cu^{II}) was synthesised according to adapted literature procedures outlined by Zhu *et al*. and Cheng *et al*.[13,14] A saturated solution of $Cu(OAc)_2$ (65.0 mg, 357 µmol) in MeOH was added to a solution of Me_2H_2**L1** (120 mg, 164 µmmol) in $CHCl_3$ (20 mL), and the resulting mixture was refluxed for 3 hours in the dark until complete metalation was confirmed by TLC. The resulting solution was subsequently diluted with water (100 mL) and extracted using $CHCl_3$. The organic layer was then washed with brine before drying over $MgSO_4$. The solvent was then removed under reduced pressure, and the residue was recrystallized in DCM and MeOH (1:1 vol/vol) to obtain orange crystals of the metalloporphyrin ester, [5,15-bis(4-carboxyphenyl)-10,20-diphenylporphyrinato]-Cu (Me_2**L1**-Cu^{II}). This ester was subsequently dissolved in 60 mL of a mixture of THF and MeOH (1:1 vol/vol), before adding an aqueous solution of KOH (6.0 mL, 1.78 M) to the mixture and heating to reflux for 24 hours. After confirming completion of the hydrolysis by TLC, the reaction mixture was cooled to ambient temperature and the organic solvent was concentrated under reduced pressure. The residue was then diluted with 50 mL of water, before acidifying the resulting dipotassium salt with 1 M HCl until no further precipitation was observed. Following this, the organic acid was collected by filtration before thoroughly washing with hot water and hexane. Finally, the porphyrin dicarboxylic acid product [5,15-bis(4-carboxyphenyl)-10,20-diphenylporphyrinato]-Cu^{II} (H_2**L1**-Cu^{II}) was obtained as an orange powder. Yield: 90.0 mg, 118 µmmol, 72%.

^{1}H NMR (400 MHz, DMSO-d_6): δ (ppm) = 8.73 (br, m, 8H, pyrrole-H), 8.30 (d, 4H, benzyl-H, J = 7.8 Hz), 8.11 (d, 4H, benzyl-H, J = 7.8 Hz), 8.05 (d, 4H, aryl-H, J = 6.9 Hz), 7.76 (br, m, 6H, aryl-H).

MS (MALDI-TOF): Found *m/z* = 763.1435. Calculated *m/z* = 763.1407 for [$C_{46}H_{28}CuN_4O_4$].

UV-Vis (DMF): λ_{max}/nm (ε/L mol^{-1} cm^{-1}) = 408 (1.6×10^5, Soret band, π – π*).

FT-IR υ_{max}: 3619 (w, br), 2849 (w, vbr) 2544 (w, br), 1678 (vs), 1601 (m), 1444 (w), 1421 (m), 1284 (m), 1188 (w), 997 (s), 866 (w), 808 (s), 756 (w), 697 (s) cm^{-1}.

6.3.5 Synthesis of [5,15-Bis(4-carboxyphenyl)-10,20-diphenylporphyrinato]-Ni^{II} (H_2**L1**-Ni^{II})

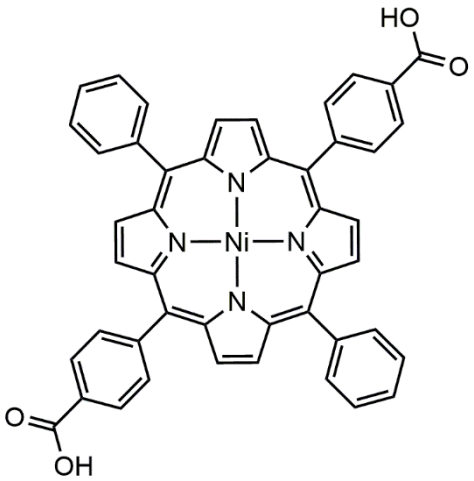

The metalloporphyrin [5,15-bis(4-carboxyphenyl)-10,20-diphenylporphyrinato]-Ni^{II} was synthesized according to a procedure adapted from Zhu *et al*. and Cheng *et al*.[13,14] A solution of Me_2H_2**L1** (119 mg, 163 µmol) in toluene was refluxed at 110 °C with $Ni(acac)_2$ (56 mg, 0.220 mmol) for 2 days under darkness. After complete metallation was confirmed by TLC, the mixture was poured into distilled H_2O (50 mL) and extracted in $CHCl_3$. The organic layer was subsequently washed with H_2O (50 mL) and then brine (50 mL) before drying over anhydrous $MgSO_4$. The solvent was then evaporated under reduced pressure and the residue was recrystallised in a mixture of $CHCl_3$ and MeOH (1:1 vol/vol) which afforded the formation of orange crystals of the metalloporphyrin ester [5,15-bis(4-carbomethoxyphenyl)-10,20-di-phenylporphyrinato]-Ni^{II} (Me_2**L1**-Ni^{II}). This ester was then dissolved in 60 mL of a THF/MeOH (1:1 vol/vol) mixture before adding an aqueous solution of KOH (6.0 mL, 1.78 M) and heating to reflux in the dark for 2 days. After confirming complete metallation using TLC, the mixture was cooled to ambient temperature and the organic solvent was evaporated under reduced pressure. The solid residue was then diluted with distilled H_2O (50.0 mL) before acidifying with 1M HCl until no further precipitation was observed. Following this, the suspension was filtered and washed thoroughly with hot H_2O and hexane. Finally, the porphyrin dicarboxylic acid H_2**L1**-Ni^{II} was obtained as an orange powder. Yield: 83.0 mg, 109 µmol, 67%.

^{1}H NMR (400 MHz, DMSO-d_6): δ (ppm) = 13.28 (vbr, s, 2H, COOH) 8.73 (br, m, 8H, pyrrole-H), 8.30 (d, 4H, benzyl-H, J = 7.8 Hz), 8.13 (d, 4H, benzyl-H, J = 7.8 Hz), 8.02 (d, 4H, aryl-H, J = 6.9 Hz) 7.77 (m, 6H, aryl-H).

MS (MALDI-TOF): Found *m/z* = 758.1432. Calculated *m/z* = 758.1464 for [$C_{46}H_{28}NiN_4O_4$].

UV-Vis (DMF): λ_{max}/nm (ε/L mol^{-1} cm^{-1}) = 395 (1.5×10^5, Soret band, π – π*).

FT-IR υ_{max}: 2845 (w, vbr) 2539 (w, br), 1683 (vs), 1604 (m), 1569 (w), 1472 (w), 1421 (m), 1288 (m), 1203 (w), 1174 (w), 1072 (w), 1004 (s), 865 (w), 796 (s), 699 (s) cm^{-1}.

6.3.6 Synthesis of [5,15-Bis(4-carboxyphenyl)-10,20-diphenylporphyrinato]-Pt^{II} (H_2**L1**-Pt^{II})

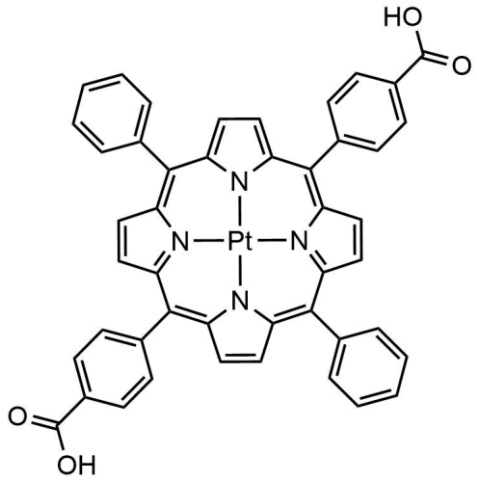

The metalloporphyrin [5,15-bis(4-carboxyphenyl)-10,20-diphenylporphyrinato]-Pt^{II} was synthesized according to a procedure adapted from Zhu *et al*. and Cheng *et al*.[13,14] $PtCl_2$ (0.45 g, 1.69 mmol) was added to a solution of Me_2H_2**L1** (1.00 g, 1.08 mmol) in benzonitrile (112 mL) under N_2 and refluxed for 6 hours while shielding the reaction from light. After complete metallation of the porphyrin was confirmed by TLC, the product was concentrated by evaporating the solvent under reduced pressure. Remaining traces of benzonitrile were removed from the crude product by entrainment by triturating with toluene (3 × 100 mL). Removal of the volatile components under reduced pressure afforded a red solid which was taken into CH_3Cl (500 mL) and washed with distilled H_2O (3 × 100 mL) before drying over anhydrous $MgSO_4$. Evaporation the solvent under reduced pressure afforded a red residue was recrystallised in a mixture of $CHCl_3$ and MeOH (1:1 vol/vol), which yielded red crystals of the metalloporphyrin ester [5,15-bis(4-carbomethoxyphenyl)-10,20-di-phenylporphyrinato]-Pt^{II} (Me_2**L1**-Pt^{II}). This ester was then dissolved in THF and MeOH (1:1 vol/vol, 60.0 mL), before adding an aqueous KOH solution (6.0 mL, 1.78 M) to the mixture and heating to reflux for 2 days under darkness. After cooling to ambient temperature, the organic solvent was evaporated under reduced pressure and the resulting residue was dissolved in distilled H_2O (50.0 mL). The dipotassium salt solution was then acidified using 1M HCl until no further precipitation was observed, and the product was collected by filtration and washed thoroughly with hot water and hexane. Finally, the product was purified by recrystallising in a mixture of acetone and EtOH (1:1 vol/vol) to obtain the metalloporphyrin dicarboxylic acid (H_2**L1**-Pt^{II}) as a red powder. Yield: 0.07 g, 0.08 mmol, 57%.

^{1}H NMR (400 MHz, DMSO-d_6): δ (ppm) = 13.30 (vbr, s, 2H, COOH), 8.75 (m, 8H, pyrrole-H), 8.37 (d, 4H, benzyl-H, J = 7.8 Hz), 8.30 (d, 4H, benzyl-H, J = 7.8 Hz), 8.18 (d, 4H, aryl-H, J = 7.0 Hz), 7.84 (6H, m aryl-H).

MS (MALDI-TOF): Found *m/z* = 895.1777. Calculated *m/z* = 895.1758 for [$C_{46}H_{28}PtN_4O_4$].

UV-Vis (DMF): λ_{max}/nm (ε/L mol^{-1} cm^{-1}) = 406 (1.7×10^5, Soret band, π – π*).

FT-IR υ_{max}: 2925 (w, vbr) 2546 (w, br), 2383 (w), 1681 (C=O, s), 1604 (m), 1587 (w), 1505 (w), 1424 (m), 1357 (m), 1315 (m), 1268 (m), 1211 (w), 1177 (m), 1078 (m), 1013 (vs), 887 (w), 833 (w), 791 (s), 769 (m), 702 (s) cm^{-1}.

6.4 Synthesis of Inorganic Complexes and Frameworks

The syntheses of the complexes and frameworks **1**, **2** and **11** – **18** are described in this section.

6.4.1 Synthesis of [(L1-Cu^{II})$_4$$Co^{II}_4$($H_2O$)$_4$]·2DEA·8MeOH (1)

H_2**L1**-Cu^{II} (1.4 mg, 1.82 μmol) and $CoCl_2$ (5.2 mg, 40.0 μmol) were dissolved in DEA (1 mL) and MeOH (0.6 mL) by sonicating the mixture for 30 minutes. This solution was then filtered into a glass vial, which was placed inside an autoclave and heated to 80 ˚C for 3 days. Following this, the reaction mixture was gradually cooled to ambient temperature over a period of 1 day. Following this period, crimson rod-shaped crystals had formed inside the vial which were suitable for analysis by single crystal X-ray diffraction. Prior to use in catalytic experiments, large single crystals of **1** were manually picked, filtered and washed with DMF and MeOH before grinding into a fine powder using a mortar and pestle. Yield: 0.9 mg, 0.268 μmol, 59%.

FT-IR υ_{max}: 3629 (br, w), 3056 (br, w), 2972 (vbr, w), 2353 (w), 2121 (br, w), 1807 (w), 1604 (w), 1575 (m), 1533 (m), 1382 (s), 1342 (m), 1206 (w), 1182 (w), 1142 (w), 1105 (w), 1070 (w), 996 (s), 826 (w), 793 (s), 776 (s), 759 (m), 717 (s), 704 (vs) cm^{-1}.

6.4.2 Synthesis of [(L1-Cu^{II})Co^{II}(DEA)]·H_2O·3MeOH (2)

H_2**L1**-Cu^{II} (1.2 mg, 1.56 μmol) and $CoCl_2$ (1.5 mg, 11.5 μmol) were dissolved in DEA (1 mL) and MeOH (0.5 mL) by sonicating for thirty minutes. Following this, 1 drop of acetic acid was added to the solution, before heating the reaction mixture to 120 ˚C for 4 days. After this time, the reaction mixture was allowed to slowly cool to ambient temperature. This afforded the formation of red, plate-shaped crystals in moderate yield which were suitable for analysis using single crystal X-ray diffraction. Yield: 0.6 mg, 0.608 μmol, 39%.

FT-IR υ_{max}: 2969 (vbr, m), 1594 (s), 1548 (m), 1373 (s), 1334 (s), 1276 (m), 1204 (w), 1181 (w), 1067 (w), 994 (s), 832 (w), 797 (s), 773 (s), 699 (s) cm^{-1}.

Elemental Analysis (%): Expected for $[C_{52}H_{39}CoCuN_5O_5]\cdot 12H_2O$: C 54.19, H 5.51, N 6.08. Found: C 54.02, H 4.59, N 7.06.

6.4.3 Synthesis of $[Mn^{III}_{12}Mn^{II}_{7}(\mu_4\text{-}O)_8(\mu_3\text{-}OCH_3)_2(\mu_3\text{-}Br)_6(HL2)_{12}(MeOH)_5(MeCN)]Br_2\cdot 9MeCN\cdot MeOH$ (11)

The nonadecanuclear Mn-oxo cluster $[Mn^{III}_{12}Mn^{II}_{7}(\mu_4\text{-}O)_8(\mu_3\text{-}OCH_3)_2(\mu_3\text{-}Br)_6(H\mathbf{L2})_{12}(MeOH)_5(MeCN)]Br_2\cdot 9MeCN\cdot MeOH$ (**11**) was prepared according to an adapted literature procedure.[15,16] The ligand 2,6-bis(hydroxymethyl)-*p*-cresol ($H_3\mathbf{L2}$) (0.17 g, 1.01 mmol), $MnBr_2\cdot 4H_2O$ (0.3 g, 1.05 mmol) and TEA (0.17g, 2.88 mmol) were stirred in MeCN (25 mL) and MeOH (5 mL) for 2 hours at 30 °C. This mixture was then heated to reflux for 2 hours, before allowing cool slowly to ambient temperature. The reaction mixture was then filtered twice and allowed to crystallise by slow evaporation. After several days, uniform deep-red coloured needle-shaped single crystals of **11** which were suitable for analysis using X-ray diffraction had formed in moderate yield. Prior to catalytic measurements using **11**, the mother liquor was decanted, and the crystals were washed carefully using distilled water before drying in air and grinding into a fine powder using an agate mortar and pestle. Yield: 98.0 mg, 23.6 μmol, 28%.

FT-IR υ_{max}: 3208 (w, br), 2932 (w), 2881 (w), 2828 (w), 2363 (s), 2337 (m), 1646 (w), 1609 (m), 1468 (s), 1351 (w), 1303 (w), 1255 (s), 1226 (s), 1160 (s), 1027 (s), 982 (s), 953 (w), 897 (m), 860 (m), 814 (m), 767 (w), 634 (s), 599 (s), 573 (s), 543 (s), 512 (s), 474 (s) cm^{-1}.

Elemental analysis (%): Expected for $[C_{117}H_{149}Br_8Mn_{19}NO_{51}]\cdot MeOH\cdot 9MeCN$: C 36.55; H 4.04; N 3.03. Found: C 36.62; H 4.23; N 3.25.

6.4.4 Synthesis of $[Co^{II}_3(L3)_2(H_2O)_6]Cl_6 \cdot DMF \cdot 6H_2O$ (12)

The trinuclear complex **12** was prepared according to a procedure developed within the Schmitt group.[17] A solution of 4-imidazolecarboxaldehyde (0.29 g, 3.0 mmol) in MeOH (30 mL) was added drop-wise to a solution of 1,3,5-tris(4-aminophenyl)benzene (0.50 g, 1.08 mmol) in MeOH (30 mL). A few drops of acetic acid were then added to the resulting solution, before heating the mixture to reflux overnight. The solvent was then evaporated under reduced pressure, and the resulting solid was recrystallised from MeCN to give *N*,*N*',*N*''-tris-(1-methyl)-1*H*-imidazol-4-ylmethylene)-1,3,5-triphenyl benzene (**L3**) as a cream coloured powder. The resulting Schiff base **L3** (100 mg, 0.17 mmol) and $CoCl_2 \cdot 6H_2O$ (60 mg, 0.25 mmol) were then dissolved in DMF (7 mL) and heated to 75 °C for 2 hours. The resulting green solution was then filtered before slowly diffusing THF into the filtrate over 24 hours, which afforded uniform orange crystals of **12** that were suitable for analysis using single crystal X-ray diffraction. Prior to catalytic experiments, crystals of **12** were collected by filtration and washed in MeOH before grinding into a fine powder using a mortar and pestle. Yield: 50 mg, 26.4 µmol, 31%.

FT-IR υ_{max}: 3354 (br, w), 3335 (vbr, w), 3127 (w), 2979 (s), 2885 (m), 2362 (w), 1622 (s), 1592 (s), 1503 (s), 1446 (s), 1392 (s), 1347 (m), 1295 (w), 1251 (w), 1157 (w), 1090 (m), 1016 (w), 957 (w), 895 (w), 828 (s), 761 (m), 737 (w), 702 (w) cm^{-1}.

Elemental Analysis (%): Expected for $[Co_3C_{72}H_{66}N_{18}O_6Cl_6] \cdot DMF \cdot 9H_2O$: C, 48.93; H, 5.22; N, 13.38. Found: C, 48.8; H, 5.46; N, 13.01.

6.4.5 Synthesis of $[Mn^{II}(HL1\text{-}Cu^{II})_2(DEA)_2]\cdot DEA$ (13) and $[Mn^{II}(L1\text{-}Cu^{II})(MeOH)_2]\cdot DEA\cdot MeOH$ (14)

H_2**L1**-Cu^{II} (15.0 mg, 19.7 μmol) and $MnCl\cdot 2H_2O$ (3.20 mg, 19.8 μmol) were dissolved in DEA (11.0 mL) and MeOH (6.00 mL) by sonicating the mixture for 30 minutes. The resulting solution was then transferred into an autoclave and heated to 120 °C for 4 days, before allowing to cool slowly to ambient temperature. Following this, morphologically indistinguishable crimson rod-shaped crystals of **13** and **14** formed in the reaction mixture which were suitable for analysis using single crystal X-ray diffraction. Yield: 4.78 mg, corresponding to 2.46 μmol **13** (33%) or 4.64 μmol **14** (24%).

FT-IR υ_{max}: 2978 (br, w), 1607 (m), 1581 (s), 1536 (m), 1487 (w), 1366 (vs), 1282 (w), 1210 (w), 1175 (w), 1012 (w), 1001 (s), 831 (w), 796 (s), 697 (s) cm^{-1}.

6.4.6 Synthesis of $[Mn^{II}(HL1\text{-}Ni^{II})_2(DMF)_2]\cdot 6DMF$ (15) and $[(Mn^{II}(L1\text{-}Ni^{II})(DMF)_2]\cdot 4DMF$ (16)

H_2**L1**-Ni^{II} (5.00 mg, 6.60 μmol) and $MnCl_2\cdot 2H_2O$ (3.20 mg, 19.8 μmol) were dissolved in DMF (1 mL) by sonicating for 30 minutes. The resulting solution was then heated to 120 °C for a period of 3 days, before allowing to cool slowly to ambient temperature. Following this, uniform orange rod-shaped crystals of **15** and **16** had formed which were suitable for analysis using single crystal X-ray diffraction. Yield: 3.59 mg, corresponding to 1.86 μmol **15** (56%) or 2.87 μmol **16** (43%).

FT-IR υ_{max}: 3629 (w, br), 3049 (w, vbr), 2979 (w, vbr), 1656 (w), 1583 (m), 1532 (m), 1394 (s), 1343 (s), 1250 (w), 1203 (w), 1169 (w), 1072 (w), 1003 (s), 833 (w), 796 (s), 773 (m), 753 (w), 700 (s) cm^{-1}.

6.4.7 Synthesis of $[Zn_4O(HL1\text{-}Zn^{II})_3(H_2O)_3]$ (17)

H_4**L1**^{II} (0.5 mg, 0.712 μmol) and $Zn(NO_3)_2 \cdot 6H_2O$ (0.7 mg, 3.70 μmol) were dissolved by sonicating in a mixture of DMF (0.5 mL) and MeOH (0.7 mL) for 30 minutes. Following this, the mixture was heated in an autoclave to 120 °C for 4 days before slowly cooling to ambient temperature. After this period, a few transparent, block-shaped crystals of **12** had formed which were suitable for analysis using single crystal X-ray diffraction. Yield: <0.1 mg.

FT-IR υ_{max}: 2920 (m), 2848 (w), 1688 (w), 1533 (s), 1458 (m), 1392 (w), 1268 (m), 1102 (m, br), 1028 (m, br), 793 (m), 734 (m) cm^{-1}.

6.4.8 Synthesis of $(TEAH)_2[In^{III}(HL1\text{-}Cu^{II})_2(Ac)_2]Cl \cdot H_2O$ (18)

H_2**L1**-Cu^{II} (0.90 mg, 1.17 μmol) and InCl3 (1.2 mg, 5.4 μmol) were dissolved in DEA (1.10 mL) and MeOH (0.20 mL) by sonicating the mixture for an hour. The resulting solution was then transferred to a glass vial which was placed inside an autoclave and heated to 80 °C for 4 days, before allowing to cool slowly to ambient temperature. Following this, orange block-shaped crystals of **18** had formed in the vial which were suitable for analysis by single crystal X-ray diffraction. Yield: <0.1 mg.

FT-IR υ_{max}: 3386 (br, m), 2962 (br, m), 2804 (br, m), 2481 (w), 2365 (w), 1713 (w), 1611 (m), 1390 (s), 1345 (s), 1257 (s), 1208 (w), 1159 (m), 1050 (s), 1001 (s), 892 (m), 864 (m), 794 (vs), 703 (s) cm^{-1}.

6.5 References

1 A. L. Spek, *Acta Crystallogr. Sect. C, Struct. Chem.*, 2015, **71**, 9–18.

2 C. F. Macrae, P. R. Edgington, P. McCabe, E. Pidcock, G. P. Shields, R. Taylor, M. Towler and J. van de Streek, *J. Appl. Crystallogr.*, 2006, **39**, 453–457.

3 *DIFFRAC. EVA, Version 4.1*, Bruker AXS Inc., Karlsruhe, Germany, 2015.

4 B. Limburg, E. Bouwman and S. Bonnet, *ACS Catal.*, 2016, **6**, 5273–5284.

5 M. Orlandi, R. Argazzi, A. Sartorel, M. Carraro, G. Scorrano, M. Bonchio and F. Scandola, *Chem. Commun.*, 2010, **46**, 3152–3154.

6 M. D. Kärkäs, T. M. Laine, E. V Johnston and B. Åkermark, *Visible Light-Driven Water Oxidation Catalyzed by Ruthenium Complexes*, InTech, Rijeka, 2016.

7 X. Deng and H. Tüysüz, *ACS Catal.*, 2014, **4**, 3701–3714.

8 J. D. Blakemore, H. B. Gray, J. R. Winkler and A. M. Müller, *ACS Catal.*, 2013, **3**, 2497–2500.

9 M. Hara, C. C. Waraksa, J. T. Lean, B. A. Lewis and T. E. Mallouk, *J. Phys. Chem. A*, 2000, **104**, 5275–5280.

10 H. Xia, Y. Zhu, D. Lu, M. Li, C. Zhang, B. Yang and Y. Ma, *J. Phys. Chem. B*, 2006, **110**, 18718–18723.

11 B. P. Sullivan, D. J. Salmon and T. J. Meyer, *Inorg. Chem.*, 1978, **17**, 3334–3341.

12 J. K. Laha, S. Dhanalekshmi, M. Taniguchi, A. Ambroise and J. S. Lindsey, *Org. Process Res. Dev.*, 2003, **7**, 799–812.

13 J. Miao and L. Zhu, *Chem. Asian J.*, 2010, **5**, 1634–1641.

14 C. He, Q. He, C. Deng, L. Shi, D. Zhu, Y. Fu, H. Cao and J. Cheng, *Chem. Commun.*, 2010, **46**, 7536–7538.

15 A. M. Ako, B. Burger, Y. Lan, V. Mereacre, R. Clérac, G. Buth, S. Gómez-Coca, E. Ruiz, C. E. Anson and A. K. Powell, *Inorg. Chem.*, 2013, **52**, 5764–5774.

16 A. M. Ako, V. Mereacre, R. Clérac, W. Wernsdorfer, I. J. Hewitt, C. E. Anson and A. K. Powell, *Chem. Commun.*, 2009, **0**, 544–546.

17 I. McKeogh, PhD Thesis, Trinity College Dublin, 2015.

Chapter Seven

Conclusion

7.1 Conclusion

The artificial photosynthetic production of H_2 from H_2O and sunlight is a promising solution to reduce our reliance on fossil fuels as it is renewable, carbon-free and energy-dense.[1,2] Switching to an economy based on H_2 may mitigate many of the challenges faced by contemporary society by securing our energy supply, limiting GHG emissions and preventing pollution arising due to the extraction and transportation of fossil fuels.[3,4] The current bottleneck of H_2O splitting is the four-electron OER, owing to the high complexity and endergonicity of this half-reaction.[5] Thus, the development of stable, inexpensive WOCs is a significant contemporary scientific challenge.[6] Despite extensive efforts, no cost-effective solution for sustainable solar fuel synthesis currently exists. Therefore, the discovery of novel OER catalysts constructed from earth-abundant materials is a scientific imperative.[7,8]

Inspiration for the design of molecular WOCs may be drawn from Nature.[9] In PS II, an intricate assembly of proteins and light-absorbing porphyrin cofactors funnel solar energy towards a catalytic $\{Mn_4CaO_5\}$ cubane cluster.[10] This Mn-oxo moiety mediates H_2O oxidation with exceptional efficiency and is stabilised by several amino acid residues including a closely associated Y_z, which facilitates electron abstraction from the OEC.[11,12] The preparation of metalloenzyme-mimicking MOFs that incorporate catalytically active SBUs and have high surface areas was recognised as one possible avenue to design supramolecular, PS II-inspired OER catalysts. Another approach highlighted to emulate the OEC was to use Mn-based clusters with cubane motifs and that are stabilised by redox-active, Y_z-like ligands.

The aims of this project were to synthesise and characterise supramolecular, bioinspired complexes and extended structures using metalloporphyrin ligands. A further aim was to identify transition metal-based materials with potential catalytic H_2O oxidation activity. The final aim was to assess the catalytic OER activity of Mn- and Co-based compounds.

These aims were achieved with the synthesis of four bifunctional porphyrin ligands H_4**L1**, H_2**L1**-Cu^{II}, H_2**L1**-Ni^{II} and H_2**L1**-Pt^{II} which were used to prepare five novel transition metal-based MMPFs **1**, **2**, **13**, **15** and **17**, two new Mn-based coordination polymers **14** and **16**, and one novel transition metal-based complex **18**. Moreover, a novel polymorph **11** was discovered. Following this, an experimental protocol was developed to measure light-driven H_2O splitting catalysis. Testing a wide range of novel and literature-known materials suspected of harbouring previously uncharted OER properties resulted in the discovery of twelve compounds **1** – **12** that exhibit excellent O_2 evolution properties. Indeed, the nonadecanuclear

cluster **11** yields the highest turnover characteristics of any known molecular heterogeneous Mn-based WOC under neutral conditions, whilst the activities of **1** and **12** compare favourably with the activities of other earth-abundant metal-based OER catalysts in the literature. Electrochemical investigations using **11** and **12** corroborate the results of photocatalytic experiments, confirming the high activities of these compounds. In addition, post-catalytic characterisation tests confirm that **1**, **11** and **12** are true molecular WOCs, whilst computational studies of **12** support empirical data and reveal a mechanism for catalytic H_2O oxidation by this compound.

A brief summary of the work discussed in each chapter of this report follows:

In chapter 2, the four dicarboxylic acid-functionalised porphyrin ligands H_4**L1**, H_2**L1**-Cu^{II}, H_2**L1**-Ni^{II} and H_2**L1**-Pt^{II} were synthesised and characterised, and an experimental setup and methodology was designed to measure the activity of OER or HER catalysts. H_2**L1**-Cu^{II} was then employed in the synthesis of two novel Co^{II}-based bioinspired frameworks (**1** and **2**). The 3D MMPF **1** comprises a previously unreported, 8-connected partially hydrated $\{Co^{II}_4\}$ SBU and features large solvent-accessible 1D channels. In contrast, **2** is a 2D framework constructed from rod-shaped SBUs that are composed of alternating tetrahedral and octahedral Co^{II} centres. In the solid state, **2** forms corrugated stacking sheets which are stabilised by $\pi - \pi$ interactions.

Both of the bioinspired frameworks **1** and **2** feature potentially redox-active, labile coordination sites suggesting either may be able to catalyse the OER. However, owing to the four terminal aqua ligands present on the tetranuclear SBU of **1** and its large channels, this compound was selected to use in OER studies. Hence, **1** was employed in a series of photocatalytic O_2 evolution experiments. These tests revealed that **1** displays excellent catalytic H_2O oxidation activity which compared favourably to cutting-edge transition metal-based WOCs.[13,14] Furthermore, the O_2 evolution behaviour of **1** could not be attributed to *in-situ* CoO_x or Co–Pi formation.

In Chapter 3, a collection of compounds with structural similarities to the OEC were screened for light-driven H_2O oxidation activity. This assay resulted in the identification of eight Mn-oxo clusters and one Mn-oxo cluster-derived coordination polymer (**3** – **11**) which display O_2 evolution activity. Prior to this work the catalytic OER properties of **3** – **11** had not been described in the literature.

The nonadecanuclear Mn-oxo cluster $[Mn^{III}_{12}Mn^{II}_7(\mu_4\text{--}O)_8(\mu_3\text{--}OCH_3)_2(\mu_3\text{-}Br)_6(H\mathbf{L2})_{12}(MeOH)_5(MeCN)]Br_2\cdot 9MeCN\cdot MeOH$ (**11**) revealed the highest activity towards

light-driven H_2O oxidation out of all of the structures screened. Therefore, this compound was resynthesized and characterised using single crystal X-ray diffraction and other supplementary techniques. This led to the discovery of a novel polymorph containing a known Mn-oxo cluster core. Following on from this, **11** was employed in a series of additional photo- and electrocatalytic investigations which confirmed that **11** is a genuine, highly active molecular WOC.

In electrochemical experiments using **11**, a catalytic response was elicited at a low applied onset overpotential of η = 255 mV. Under photochemical conditions, a *max*. TOF = 0.57 s^{-1} and a TON = 80 were achieved using this catalyst. The exceptional catalytic performance of **11** was attributed to a synergistic effect between the cluster's Mn-oxo core and its stabilising, Y_Z-like, redox-active *p*-cresol (H**L2**)$^-$ ligand derivatives.[15,16]

In chapter 4, the synthesis and characterisation of a Co^{II}-based halide-MOF $[Co^{II}_3(\mathbf{L3})_2(H_2O)_6]Cl_6 \cdot DMF \cdot 6H_2O$ (**12**) was described. This supramolecular structure was successfully employed as a heterogeneous WOC under electro- and photochemical conditions. Catalytic experiments demonstrated that **12** is a competent catalyst for H_2O oxidation, exhibiting a *max*. TON = 74.3 and TOF = 1.21 s^{-1} in the presence of a SEA and PS, and a reasonably low onset overpotential for catalytic H_2O oxidation of η = 465 mV as part of a modified CP electrode. This activity surpasses that of many transition metal-based WOCs in the literature.[17,18] Furthermore, post-catalytic characterisation experiments indicated that the observed catalytic activity stems solely from **12**. DFT calculations were performed to propose a catalytic mechanism for O_2 evolution which agrees well with the experimental data.

In Chapter 5, the use of the porphyrin ligands H_4**L1** H_2**L1**-Cu^{II} and H_2**L1**-Ni^{II} in the synthesis of an additional six novel frameworks, coordination polymers and complexes (**13** – **18**) is described. Each of these compounds were characterised using single crystal X-ray analysis and other supplementary characterisation techniques. **13** and **15** are 1D coordination polymers that stack *via* $\pi - \pi$ interactions to generate a 2D supramolecular framework, whilst **14** and **16** are 2D MMPFs with characteristic layered architectures. **13** and **15** form under the same reaction conditions as an inseparable mixture, as do **14** and **16**. Physicochemical characterisation indicated that the 1D coordination polymer is the dominant compound in both product mixtures. **17** is a quadruply interpenetrated 3D MMPF comprising six-connected $\{Zn^{II}O_4\}$ SBUs connected through (**L1**-Zn^{II})$^{2-}$ ligand derivatives, whereas **18** is an In^{III}-based (H**L1**-Cu^{II})$^-$ dimer.

As **13** – **16** each feature labile solvent moieties that coordinate to potentially redox-active Mn^{II} centres, these novel structures were rationalised as promising materials to use in catalytic OER and HER investigations. Thus, the heterogeneous catalytic activities of **13** – **16** were assessed under photocatalytic conditions. In these experiments the O_2 or H_2 evolution activities of **13** – **16** were found to exceed that of control experiments where no WOC or HEC was present. However, these Mn-based extended structures did not exhibit true catalytic behaviour, as their calculated TONs were less than 1. This was attributed to the lack of substrate-accessible metallic centres in the crystal structures of these compounds.

7.2 Future Work

There are a number of possible directions in which this work could be continued. Several general areas (❖) for future investigations and specific avenues (➢) which could advance this research follow:

❖ Modification of the porphyrin ligands H_4**L1**, H_2**L1**-Cu^{II} and H_2**L1**-Ni^{II} to synthesise structural analogues of **1**, **2** and **13** – **18** with improved catalytic properties.

- ➢ Alternative metals ions such as Zn^{II}, Mn^{II} or Co^{II} could be incorporated within the metalloporphyrin ligands to tune their photophysical and redox catalytic properties.
- ➢ Porphyrins with greater resistance to attack by reactive oxygen species might be prepared by incorporating Cl or F atoms at the *ortho* positions of these ligand's *meso* substituted aryl groups.[19] These modified macrocycles may be used to synthesise more robust MMPF WOCs.[20]
- ➢ Finally, the metalloporphyrin H_2**L1**-Cu^{II} could be extended by incorporating additional alkenyl or aryl 'spacer' groups to increase the ligand's length along its longest axis. This extended linker could then be used to prepare isoreticular analogues of **1** with larger channels, higher surface areas and (potentially) faster catalytic kinetics.[21]

❖ Modification of the $\{Mn_{19}\}$ system (**11**).

- ➢ Synthesising derivatives of the *p*-cresol ligand H_3**L2** could allow various analogues of **11** to be prepared with potentially enhanced catalytic properties. For example, adding electron donating substituents to H_3**L2** may stabilise the Mn-oxo core during the OER.[22] Further, derivatives of the ligand H_3**L2** containing more robust binding groups such as carboxylates could be employed to generate clusters with heightened stability.
- ➢ Incorporation of heterometallic ions into the $\{Mn_{19}\}$ system such as Ca^{II} or Ba^{II}.[23] Catalytic testing of these mixed-metal variants would be interesting to see how their activities compare with that of **11**.

- Continued investigation of the catalytic OER and HER properties of **1** – **11**.

  - Electrochemical experiments using **1** could be conducted to further characterise the catalytic OER behaviour of this compound, and to corroborate the results of light-driven H_2O oxidation experiments outlined in Chapter 2
  - Photo- and electrochemical tests could be performed to establish the catalytic H_2O oxidation activity of the 2D Co^{II}-based MMPF **2**. The catalytic activities of **1** and **2** might then be compared.
  - Further characterisation and optimisation of the OER catalytic behaviour of the Mn-oxo compounds **3** – **10**, paying particular attention to **6** as this system displayed highly promising O_2 evolution properties.
  - Post-catalytic characterisation of **3** – **10** could be carried out.
  - Computational modelling could be employed to elucidate the mechanism of catalytic H_2O oxidation by the Mn-oxo cluster **11** to better understand the exceptional activity of this WOC.

- Optimisation and modification of the applied reaction conditions.

  - The employed reaction parameters in the synthesis of **1** – **18** such as temperature, pressure, solvent system, pH value, reaction time, metal to ligand ratio, metal counterion identity and the presence of modulators could be modified to either increase the yields of these compounds or to generate novel and interesting structures.
  - The dimensionality of the 2D MMPFs **2**, **14** and **16** could be increased by employing a pillaring strategy. Adding a ditopic N-donor linker such as bpy at a late stage in the synthesis of these materials could give rise to 3D MMPFs with permanent porosity.
  - The synthesis of the Zn^{II}-based framework **17** and the In^{III}-based dimer **18** could be optimised to improve their yields, thus facilitating further characterisation and catalytic testing of these compounds.
  - Post-synthetic modification of **17** could be carried out to generate a 3D MMPF which features photoactive linkers and catalytically active nodes.

7.3 References

1 M. D. Kärkäs, O. Verho, E. V Johnston and B. Åkermark, *Chem. Rev.*, 2014, **114**, 11863–12001.

2 N. P. Brandon and Z. Kurban, *Philos. Trans. R. Soc. A Math. Phys. Eng. Sci.*, 2017, **375**, 20160400.

3 *Nat. Energy*, 2016, **1**, 16127.

4 F. Perera, *Int. J. Environ. Res. Public Health*, 2017, **15**, 16.

5 B. Zhang, X. Zheng, O. Voznyy, R. Comin, M. Bajdich, M. Garcia-Melchor, L. Han, J. Xu, M. Liu, L. Zheng, F. P. Garcia de Arquer, C. T. Dinh, F. Fan, M. Yuan, E. Yassitepe, N. Chen, T. Regier, P. Liu, Y. Li, P. De Luna, A. Janmohamed, H. L. Xin, H. Yang, A. Vojvodic and E. H. Sargent, *Science*, 2016, **352**, 333–337.

6 B. Zhang and L. Sun, *Chem. Soc. Rev.*, 2019, **48**, 2216–2264.

7 S. Ye, C. Ding and C. Li, in *Water Oxidation Catalysts*, eds. R. van Eldik and C. D. B. T.-A. in I. C. Hubbard, Academic Press, 2019, vol. 74, pp. 3–59.

8 H. Inoue, T. Shimada, Y. Kou, Y. Nabetani, D. Masui, S. Takagi and H. Tachibana, *ChemSusChem*, 2011, **4**, 173–179.

9 E. Y. Tsui, J. S. Kanady and T. Agapie, *Inorg. Chem.*, 2013, **52**, 13833–13848.

10 G. Renger and T. Renger, *Photosynth. Res.*, 2008, **98**, 53–80.

11 D. Narzi, D. Bovi and L. Guidoni, *Proc. Natl. Acad. Sci.*, 2014, **111**, 8723–8728.

12 M. M. Najafpour and Govindjee, *Dalt. Trans.*, 2011, **40**, 9076–9084.

13 M. D. Kärkäs and B. Åkermark, *Dalt. Trans.*, 2016, **45**, 14421–14461.

14 J. Soriano-López, F. Song, G. R. Patzke and J. R. Galan-Mascaros, *Front. Chem.*, 2018, **6**, 302.

15 M. M. Najafpour, G. Renger, M. Hołyńska, A. N. Moghaddam, E.-M. Aro, R. Carpentier, H. Nishihara, J. J. Eaton-Rye, J.-R. Shen and S. I. Allakhverdiev, *Chem. Rev.*, 2016, **116**, 2886–2936.

16 R. Brimblecombe, A. Koo, G. C. Dismukes, G. F. Swiegers and L. Spiccia, *J. Am. Chem. Soc.*, 2010, **132**, 2892–2894.

17 A. J. Bloomfield, S. W. Sheehan, S. L. Collom, R. H. Crabtree and P. T. Anastas, *New J. Chem.*, 2014, **38**, 1540–1545.

18 D. M. Robinson, Y. B. Go, M. Greenblatt and G. C. Dismukes, *J. Am. Chem. Soc.*, 2010, **132**, 11467–11469.

19 A. M. S. Silva, M. G. P. Neves, R. R. L. Martins, J. A. S. Cavaleiro, T. Boschi and P. Tagliatesta, *J. Porphyr. Phthalocyanines*, 1998, **2**, 45–51.

20 T. Nakazono and K. Sakai, *Dalt. Trans.*, 2016, **45**, 12649–12652.

21 A. Kirchon, L. Feng, H. F. Drake, E. A. Joseph and H.-C. Zhou, *Chem. Soc. Rev.*, 2018, **47**, 8611–8638.

22 P. Garrido-Barros, I. Funes-Ardoiz, S. Drouet, J. Benet-Buchholz, F. Maseras and A. Llobet, *J. Am. Chem. Soc.*, 2015, **137**, 6758–6761.

23 M. Blasco-Ahicart, J. Soriano-López, J. J. Carbó, J. M. Poblet and J. R. Galan-Mascaros, *Nat. Chem.*, 2017, **10**, 24.

Appendix

Crystallographic Information and Refinement Parameters

Table 8.1 – Crystal data and structural refinement parameters for 1.

Compound 1	
Empirical formula	$C_{92}H_{59}Co_2Cu_2N_8O_{11.5}$
Formula weight	1705.41
Temperature/K	99.98
Crystal system	Orthorhombic
Space group	Pbcn
a/Å	17.2902(7)
b/Å	29.5685(10)
c/Å	43.6523(16)
α/°	90
β/°	90
γ/°	90
Volume/Å^3	22317.0(14)
Z	8
ρ_{calc}g/cm^3	1.015
μ/mm^{-1}	3.116
F(000)	6968.0
Crystal size/mm^3	0.13 × 0.1 × 0.02
Radiation	CuKα (λ = 1.54178)
2Θ range for data collection/°	2.02 to 102.54
Index ranges	$-17 \leq h \leq 12$, $-26 \leq k \leq 29$, $-44 \leq l \leq 43$
Reflections collected	93119
Independent reflections	12091 [R_{int} = 0.0683, R_{sigma} = 0.0489]
Data/restraints/parameters	12091/14/1033
Goodness-of-fit on F^2	1.042
Final R indexes [I>=2σ (I)]	R_1 = 0.0598, wR_2 = 0.1843
Final R indexes [all data]	R_1 = 0.0759, wR_2 = 0.1992
Largest diff. peak/hole / e Å^{-3}	0.78/-0.33

Table 8.2 – Crystal data and structural refinement parameters for 2.

Compound 2	
Empirical formula	$C_{52}H_{39}CoCuN_5O_5$
Formula weight	936.35
Temperature/K	215(2)
Crystal system	Monoclinic
Space group	P2/c
a/Å	8.668(3)
b/Å	14.858(5)
c/Å	39.439(14)
α/°	90
β/°	94.76(2)
γ/°	90
Volume/Å^3	5062(3)
Z	4
ρ_{calc}g/cm^3	1.229
μ/mm^{-1}	3.473
F(000)	1928.0
Crystal size/mm^3	0.18 × 0.10 × 0.02
Radiation	CuKα (λ = 1.54184)
2Θ range for data collection/°	4.496 to 105.11
Index ranges	$-8 \leq h \leq 7$, $-15 \leq k \leq 15$, $-28 \leq l \leq 40$
Reflections collected	28227
Independent reflections	5758 [R_{int} = 0.0465, R_{sigma} = 0.0415]
Data/restraints/parameters	5758/0/578
Goodness-of-fit on F^2	1.056
Final R indexes [I>=2σ (I)]	R_1 = 0.0607, wR_2 = 0.1699
Final R indexes [all data]	R_1 = 0.0726, wR_2 = 0.1784
Largest diff. peak/hole / e Å^{-3}	0.40/-1.26

Table 8.3 – Crystal data and structural refinement parameters for 11.

Compound 11	
Empirical formula	$C_{265.5}H_{333.5}Br_{16}Mn_{38}N_{17}O_{104}$
Formula weight	8793.25
Temperature/K	99.99
Crystal system	Monoclinic
Space group	$P2_1/n$
a/Å	14.5729(10)
b/Å	33.050(2)
c/Å	17.6322(12)
α/°	90
β/°	93.3150(10)
γ/°	90
Volume/Å^3	8478.2(10)
Z	1
ρ_{calc}g/cm^3	1.722
μ/mm^{-1}	3.323
F(000)	4388.0
Crystal size/mm^3	0.2 × 0.09 × 0.08
Radiation	MoKα (λ = 0.71073)
2Θ range for data collection/°	3.058 to 58.314
Index ranges	$-19 \leq h \leq 19$, $-45 \leq k \leq 45$, $-24 \leq l \leq 24$
Reflections collected	329005
Independent reflections	22828 [R_{int} = 0.0668, R_{sigma} = 0.0302]
Data/restraints/parameters	22828/117/1104
Goodness-of-fit on F^2	1.151
Final R indexes [I>=2σ (I)]	R_1 = 0.0585, wR_2 = 0.1458
Final R indexes [all data]	R_1 = 0.0860, wR_2 = 0.1647
Largest diff. peak/hole / e Å^{-3}	1.71/-2.11

Table 8.4 – Crystal data and structural refinement parameters for 12.

Compound 12	
Empirical formula	$C_{72}H_{98}Cl_6Co_3N_{18}O_{21}$
Formula weight	1941.17
Temperature/K	123(2)
Crystal system	Hexagonal
Space group	$P6_522$
a/Å	24.2974(14)
b/Å	24.2974(14)
c/Å	53.285(4)
α/°	90
β/°	90
γ/°	120
Volume/Å^3	27243(4)
Z	6
ρ_{calc}g/cm^3	0.710
μ/mm^{-1}	0.397
F(000)	6042.0
Crystal size/mm^3	0.30 × 0.25 × 0.05
Radiation	MoKα (λ = 0.71073)
2Θ range for data collection/°	1.936 to 50.144
Index ranges	$-28 \leq h \leq 28$, $-28 \leq k \leq 28$, $-63 \leq l \leq 63$
Reflections collected	296060
Independent reflections	16106 [R_{int} = 0.1484, R_{sigma} = 0.0946]
Data/restraints/parameters	16106/32/504
Goodness-of-fit on F^2	0.936
Final R indexes [I>=2σ (I)]	R_1 = 0.0707, wR_2 = 0.1762
Final R indexes [all data]	R_1 = 0.1220, wR_2 = 0.1912
Largest diff. peak/hole / e Å^{-3}	0.59/-0.33
Flack parameter	0.10(4)

Table 8.5 – Crystal data and structural refinement parameters for 13.

Compound 13	
Empirical formula	$C_{108.72}H_{88.15}Cu_2MnN_{10.82}O_{10.82}$
Formula weight	1901.22
Temperature/K	100(2)
Crystal system	Monoclinic
Space group	C2/c
a/Å	42.9827(13)
b/Å	10.8296(3)
c/Å	25.7438(8)
α/°	90
β/°	123.6450(10)
γ/°	90
Volume/Å^3	9976.0(5)
Z	4
ρ_{calc}g/cm^3	1.266
μ/mm^{-1}	2.026
F(000)	3943.0
Crystal size/mm^3	0.240 × 0.230 × 0.040
Radiation	CuKα (λ = 1.54178)
2Θ range for data collection/°	4.938 to 136.962
Index ranges	$-51 \leq h \leq 51$, $-12 \leq k \leq 12$, $-31 \leq l \leq 30$
Reflections collected	75407
Independent reflections	9130 [R_{int} = 0.0575, R_{sigma} = 0.0351]
Data/restraints/parameters	9130/3/664
Goodness-of-fit on F^2	1.042
Final R indexes [I>=2σ (I)]	R_1 = 0.0502, wR_2 = 0.1402
Final R indexes [all data]	R_1 = 0.0576, wR_2 = 0.1469
Largest diff. peak/hole / e Å^{-3}	0.84/-0.58

Table 8.6 – Crystal data and structural refinement parameters for 14.

Compound 14	
Empirical formula	$C_{52.25}H_{44.01}CuMnN_{4.63}O_{7.36}$
Formula weight	973.06
Temperature/K	100(2)
Crystal system	Triclinic
Space group	P-1
a/Å	8.9816(4)
b/Å	14.5078(7)
c/Å	19.8421(10)
α/°	108.876(3)
β/°	97.599(3)
γ/°	95.625(3)
Volume/Å^3	2397.5(2)
Z	2
ρ_{calc}g/cm^3	1.348
μ/mm^{-1}	3.156
F(000)	1006.0
Crystal size/mm^3	0.280 × 0.040 × 0.030
Radiation	CuKα (λ = 1.54178)
2Θ range for data collection/°	4.78 to 137.328
Index ranges	$-9 \leq h \leq 10$, $-17 \leq k \leq 17$, $-23 \leq l \leq 23$
Reflections collected	27291
Independent reflections	8701 [R_{int} = 0.0864, R_{sigma} = 0.1053]
Data/restraints/parameters	8701/9/642
Goodness-of-fit on F^2	1.082
Final R indexes [I>=2σ (I)]	R_1 = 0.1295, wR_2 = 0.3524
Final R indexes [all data]	R_1 = 0.1543, wR_2 = 0.3694
Largest diff. peak/hole / e Å^{-3}	3.02/-1.51

Table 8.7 – Crystal data and structural refinement parameters for 15.

Compound 15	
Empirical formula	$C_{116}H_{110}MnN_{16}Ni_2O_{16}$
Formula weight	2156.55
Temperature/K	100(2) K)
Crystal system	Triclinic
Space group	P-1
a/Å	11.6826(5)
b/Å	15.5000(7)
c/Å	15.6690(7)
α/°	79.6331(14)°.
β/°	68.2046(13)°
γ/°	76.2617(14)°
Volume/Å^3	2545.9(2)
Z	1
ρ_{calc}g/cm^3	1.407
μ/mm^{-1}	0.669
Crystal size/mm^3	0.310 x 0.170 x 0.140 mm3
Radiation	CuKα (λ = 1.54178)
2Θ range for data collection/°	2.954 to 53.194
Index ranges	-16≤h≤16, -21≤k≤21, -22≤l≤22
Reflections collected	116084
Independent reflections	15137 [R(int) = 0.0246]
Data/restraints/parameters	15137 / 1 / 692
Goodness-of-fit on F^2	1.033
Final R indexes [I>=2σ (I)]	R1 = 0.0295, wR2 = 0.0762
Final R indexes [all data]	R1 = 0.0361, wR2 = 0.0805
Largest diff. peak/hole / e Å^{-3}	0.897 and -0.436

Table 8.8 – Crystal data and structural refinement parameters for 16.

Compound 16	
Empirical formula	$C_{58}H_{54}MnN_8NiO_8$
Formula weight	1104.74
Temperature/K	173(2)
Crystal system	Triclinic
Space group	P-1
a/Å	14.771(3)
b/Å	17.982(3)
c/Å	21.039(4)
α/°	83.51(3)
β/°	69.80(3)
γ/°	89.48(3)
Volume/Å^3	5208.2(18)
Z	4
ρ_{calc}g/cm^3	1.409
μ/mm^{-1}	0.669
F(000)	2300.0
Crystal size/mm^3	0.50 × 0.35 × 0.06
Radiation	MoKα (λ = 0.71073)
2Θ range for data collection/°	2.954 to 53.194
Index ranges	$-18 \leq h \leq 18$, $-22 \leq k \leq 22$, $-26 \leq l \leq 26$
Reflections collected	39368
Independent reflections	21370 [R_{int} = 0.0504, R_{sigma} = 0.0917]
Data/restraints/parameters	21370/0/1369
Goodness-of-fit on F^2	1.057
Final R indexes [I>=2σ (I)]	R_1 = 0.0760, wR_2 = 0.2006
Final R indexes [all data]	R_1 = 0.1341, wR_2 = 0.2336
Largest diff. peak/hole / e Å^{-3}	1.47/-0.53

Table 8.9 – Crystal data and structural refinement parameters for 17.

Compound 17	
Empirical formula	$C_{138}H_{78}N_{12}O_{16}Zn_7$
Formula weight	2617.71
Temperature/K	100(2)
Crystal system	Trigonal
Space group	R-3c
a/Å	39.117(8)
b/Å	39.117(8)
c/Å	14.884(3)
α/°	90
β/°	90
γ/°	120
Volume/Å^3	19723(9)
Z	6
ρ_{calc}g/cm^3	1.322
μ/mm^{-1}	1.930
F(000)	7968.0
Radiation	CuKα (λ = 1.54184)
2Θ range for data collection/°	12.85 to 82.174
Index ranges	$-22 \leq h \leq 21$, $-31 \leq k \leq 32$, $-7 \leq l \leq 12$
Reflections collected	5590
Independent reflections	1384 [R_{int} = 0.0383, R_{sigma} = 0.0347]
Data/restraints/parameters	1384/3/228
Goodness-of-fit on F^2	1.140
Final R indexes [I>=2σ (I)]	R_1 = 0.0782, wR_2 = 0.2311
Final R indexes [all data]	R_1 = 0.0885, wR_2 = 0.2404
Largest diff. peak/hole / e Å^{-3}	0.66/-0.44

Table 8.10 – Crystal data and structural refinement parameters for 18.

Compound 18	
Empirical formula	$InCu_2ClO_{13}N_{10}C_{104}H_{84}$
Formula weight	1959.16
Temperature/K	215.01
Crystal system	Monoclinic
Space group	C2/c
a/Å	11.726(4)
b/Å	24.198(8)
c/Å	33.800(11)
α/°	90
β/°	97.81(4)
γ/°	90
Volume/Å^3	9501(6)
Z	4
ρ_{calc}g/cm^3	1.370
μ/mm^{-1}	3.253
F(000)	4024.0
Crystal size/mm^3	0.26 × 0.06 × 0.01
Radiation	CuKα (λ = 1.54184)
2Θ range for data collection/°	5.278 to 125.162
Index ranges	$-13 \leq h \leq 13$, $-25 \leq k \leq 26$, $-38 \leq l \leq 37$
Reflections collected	30028
Independent reflections	7459 [R_{int} = 0.0626, R_{sigma} = 0.0552]
Data/restraints/parameters	7459/6/567
Goodness-of-fit on F^2	1.099
Final R indexes [I>=2σ (I)]	R_1 = 0.0810, wR_2 = 0.2213
Final R indexes [all data]	R_1 = 0.0930, wR_2 = 0.2279
Largest diff. peak/hole / e Å^{-3}	1.31/-0.98

Attached CD-ROM

The attached CD-ROM contains various files related to this thesis. The folder ’CIF’ contains crystallographic information files for each of the novel compounds presented in this work. The folder ‘Organic Characterisation’ contains NMR, MS, FT-IR and UV-Vis data for the organic compounds presented in Chapter 6. The folder ‘PDF’ contains an electronic copy of this thesis.